THERMAL-HYDRAULIC ANALYSIS OF GAS-COOLED REACTOR CORE FLOWS

AMIR KESHMIRI

JULY 2010

A Thesis Submitted to the University of Manchester for the Degree of Doctor of Philosophy in the Faculty of Engineering and Physical Sciences

School of Mechanical, Aerospace and Civil Engineering (MACE), The University of Manchester, Manchester, M60 1QD, United Kingdom.

Dedicated to the Loving Memory of My Sister, Arezoo ...

LIST OF CONTENTS

Total word count: 73,000

LIST OF FIGURES

LIST OF TABLES

ABSTRACT

In this thesis a numerical study has been undertaken to investigate turbulent flow and heat transfer in a number of flow problems, representing the gas-cooled reactor core flows.

The first part of the research consisted of a meticulous assessment of various advanced RANS models of fluid turbulence against experimental and numerical data for buoyancy-modified mixed convection flows, such flows being representative of low-flow-rate flows in the cores of nuclear reactors, both presently-operating Advanced Gas-cooled Reactors (AGRs) and proposed 'Generation IV' designs. For this part of the project, an in-house code ('CONVERT'), a commercial CFD package ('STAR-CD') and an industrial code ('Code_Saturne') were used to generate results. Wide variations in turbulence model performance were identified. Comparison with the DNS data showed that the Launder-Sharma model best captures the phenomenon of heat transfer impairment that occurs in the ascending flow case; v^2-f formulations also performed well. The k-ω-*SST* model was found to be in the poorest agreement with the data. Cross-code comparison was also carried out and satisfactory agreement was found between the results.

The research described above concerned flow in smooth passages; a second distinct contribution made in this thesis concerned the thermal-hydraulic performance of rib-roughened surfaces, these being representative of the fuel elements employed in the UK fleet of AGRs. All computations in this part of the study were undertaken using STAR-CD. This part of the research took four continuous and four discrete design factors into consideration including the effects of rib profile, rib height-to-channel height ratio, rib width-to-height ratio, rib pitch-to-height ratio, and Reynolds number. For each design factor, the optimum configuration was identified using the 'efficiency index'. Through

comparison with experimental data, the performance of different RANS turbulence models was also assessed. Of the four models, the v^2-f was found to be in the best agreement with the experimental data as, to a somewhat lesser degree were the results of the k-ω-*SST* model. The k-ε and Suga models, however, performed poorly. Structured and unstructured meshes were also compared, where some discrepancies were found, especially in the heat transfer results.

The final stage of the study involved a simulation of a simplified 3-dimensional representation of an AGR fuel element using a 30° sector configuration. The v^2-f model was employed and comparison was made against the results of a 2D rib-roughened channel in order to assess the validity and relevance of the precursor 2D simulations of rib-roughened channels. It was shown that although a 2D approach is extremely useful and economical for 'parametric studies', it does not provide an accurate representation of a 3D fuel element configuration, especially for the velocity and pressure coefficient distributions, where large discrepancies were found between the results of the 2D channel and azimuthal planes of the 3D configuration.

DECLARATION

No portion of the work referred to in the dissertation has been submitted in support of an application for another degree or qualification of this or any other university or other institute of learning;

COPYRIGHT STATEMENT

i. The author of this thesis (including any appendices and/or schedules to this thesis) owns certain copyright or related rights in it (the "Copyright") and s/he has given The University of Manchester certain rights to use such Copyright, including for administrative purposes.

ii. Copies of this thesis, either in full or in extracts and whether in hard or electronic copy, may be made only in accordance with the Copyright, Designs and Patents Act 1988 (as amended) and regulations issued under it or, where appropriate, in accordance with licensing agreements which the University has from time to time. This page must form part of any such copies made.

iii. The ownership of certain Copyright, patents, designs, trade marks and other intellectual property (the "Intellectual Property") and any reproductions of copyright works in the thesis, for example graphs and tables ("Reproductions"), which may be described in this thesis, may not be owned by the author and may be owned by third parties. Such Intellectual Property and Reproductions cannot and must not be made available for use without the prior written permission of the owner(s) of the relevant Intellectual Property and/or Reproductions.

iv. Further information on the conditions under which disclosure, publication and commercialisation of this thesis, the Copyright and any Intellectual Property and/or Reproductions described in it may take place is available in the University IP Policy in any relevant Thesis restriction declarations deposited in the University Library, The University Library's regulations and in The University's policy on presentation of Theses.

THE AUTHOR

The author graduated from UMIST in 2005 with a 2(i) Honours degree in Mechanical Engineering. In the same year, he started his Masters degree in Thermal Power and Fluids Engineering in the School of Mechanical, Aerospace and Civil Engineering ('MACE') of The University of Manchester. After obtaining his M.Sc. (with Distinction) in September 2006, he was appointed to an EPSRC-funded Ph.D. award under the auspices of the EPSRC 'Keeping the Nuclear Option Open' (KNOO) project.

ACKNOWLEDGEMENTS

I would like to begin by expressing my sincere gratitude to my supervisors Dr. Mark A. Cotton and Professor Dominique Laurence for their inspiring supervision and constant guidance and support throughout the project.

I am also grateful to the UK Engineering and Physical Sciences Research Council for providing funding under grant EP/C549465/1, 'Keeping the Nuclear Option Open' (KNOO) and Mr. J. Gotts of British Energy for kindly supplying information concerning AGR design and operating conditions.

I am indebted to Dr. Yacine Addad and Dr. Juan Uribe for their generous and extremely useful assistance with my problems and questions over the past four years and their time in reviewing parts of my thesis. I also offer my thanks to Professor Michael Fairweather and Dr. Alistair Revell for agreeing to examine this work.

I would also like to thank all my friends and colleagues in the school, for creating an unforgettable environment in which my research was carried out, especially Hamid, Mahyar, Tohid and Rasool and my office mates in the past few years Flavien, Stefano and Neil.

The most important person to thank is my fiancé, Parhun with whom I have spent the best days of my life. In fact, she was the first reason why I decided to stay in Manchester and start my PhD. I am grateful to her and her parents for all their encouragement and support throughout the course of this study and simply without their love, I could never have got through the most tragic time of my life when I lost my beloved sister, Arezoo.

For their endless and immeasurable love and inspiration, I would like to thank my my parents, my brother, Amin and my sister, Armaghan who patiently endured my absence miles away from home for a decade to continue my studies abroad. Without

any doubt, I would have never got where I am, had they not given me their love and support.

NOMENCLATURE

A	Cross-sectional area of the channel
a_{ij}	Stress anisotropy tensor, $\overline{u_i u_j} / k - 2/3\delta_{ij}$
b	Rib base
Bo	Buoyancy parameter, $8\times10^4\, Gr/(Re^{3.425} Pr^{0.8})$
c_f	Local friction coefficient
c_p	Specific heat capacity at constant pressure
C_p	Pressure coefficient, $(p-p_{ref})/(0.5\rho U_b^2)$
C_μ	Coefficient or function in eddy viscosity models
D	Pipe diameter
D_e	Hydraulic diameter, $4A/P$
E	Constant in velocity log-law equation
E_ε	Source term in ε-equation
f_μ	Damping function in LRN turbulence models
f_S	Damping function in the CI turbulence model
g_i	Acceleration due to gravity
Gr	Grashof number, $\frac{\beta g D^4 \dot{q}}{\lambda \nu^2}$
h	Convection coefficient
H	Channel height
k	Turbulence kinetic energy, $\overline{u_i u_j} / 2$
k	Rib height
L	Length scale
l_m	Mixing-length scale

$\dot{m}$	Mass flow rate
Nu	Nusselt number, $\dot{q}D_h/\left(\lambda(T_w - T_b)\right)$ or hL/λ
p	Pressure
P	Pitch between two ribs
P	wetted perimeter
P_G	Production of turbulent kinetic energy due to buoyancy, $-\beta\, g_i\, \overline{u_i\theta}$
P_k	Rate of production of k, $-\overline{u_i u_j}\left(\partial U_i / \partial x_j\right)$
p_s	Static pressure at the wall
Pr	Prandtl number, $\frac{\mu c_p}{\lambda}$
$\dot{q}$	Wall heat flux
q^+	Heat loading parameter, $\dot{q}/(\rho_b U_b c_{pb} T_b)$
Re	Reynolds number, $U_b D_e/\nu$
Re_t	Turbulent Reynolds number, $k^2/(\nu\varepsilon)$
Re_τ	Reynolds number based on frictional velocity, $\frac{D\,U_\tau}{\nu}$
S_{ij}	Mean strain rate tensor, $\partial U_i/\partial x_j + \partial U_j/\partial x_i$
S_ϕ	General source term
T	Temperature
T_s	Turbulent timescale
T_τ	Non-dimensional temperature, $q/(\rho c_p U_\tau)$
t	Time
$\overline{u_i u_j}$	Turbulent stress tensor
$\overline{u_j\theta}$	Turbulent heat flux vector

U_τ	Frictional velocity, $(\tau_w / \rho)^{1/2}$
U_i, u_i	Mean, fluctuating velocity components in Cartesian tensors
x,y	Streamwise and wall-normal coordinates
Y	Yap Term
y^+	Dimensionless wall distance, yU_τ / ν

Greek Symbols:

α	Molecular diffusivity, $\lambda / \rho c_p$
α_t	Turbulent diffusivity
β	Coefficient of volumetric expansion
δ_{ij}	Kronecker delta
ε	Dissipation rate of turbulence kinetic energy
$\tilde{\varepsilon}$	Homogenous dissipation rate, $\varepsilon - 2\nu(\partial k^{1/2} / \partial x_i)^2$
ϕ	Scalar quantity
Γ	Turbulent exchange coefficient
η	Efficiency index, $(Nu / Nu_0) / (c_f / c_{f0})^{1/3}$
κ	Von Karman constant
λ	Thermal conductivity
μ	Dynamic viscosity
μ_t	Turbulent viscosity
ν	Kinematic viscosity, μ / ρ
ν_t	Turbulent kinematic viscosity
θ	Temperature fluctuation
ϑ	Velocity scale

ρ	Density
σ_k	Turbulent Prandtl number for diffusion of k
σ_t	Turbulent Prandtl number
σ_ε	Turbulent Prandtl number for diffusion of ε
τ_w	Wall shear stress
Ω_{ij}	Mean vorticity tensor, $\partial U_i / \partial x_j - \partial U_j / \partial x_i$
$\tilde{\Omega}$	Non-dimensional vorticity, $k / \varepsilon \sqrt{1/2(\Omega_{ij}\Omega_{ij})^2}$
ω	Dissipation rate per unit of kinetic energy, $\varepsilon / C_\mu k$

Subscripts

b	Bulk
i,j	Scalar node position
in	Initial value
b	Bulk
ref	Reference
s	Static
t	Turbulent
w	Wall

Superscripts

+	Non-dimensionless quantity normalized by U_τ, T_τ and ν

Acronyms:

AGR	Advanced Gas-cooled Reactor
BC	Boundary Condition

BPG	Best Practice Guidelines
CFD	Computational Fluid Dynamics
CI	Cotton-Ismael Model
DNS	Direct Numerical Simulation
ERCOFTAC	European Research Community on Fluids, Turbulence and Combustion
EVM	Eddy-Viscosity Model
FVM	Finite Volume Method
GGDH	Generalized Gradient Diffusion Hypothesis
GUI	Graphical User Interfaces
LCL	Lien, Chen, and Leschziner Model
LES	Large Eddy Simulation
LEVM	Linear Eddy-Viscosity Model
LRN	Low Reynolds Number
LS	Launder-Sharma Model
MLH	Mixing Length Hypothesis
NLEVM	Non-Linear Eddy-Viscosity Model
RANS	Reynolds Averaged Navier-Stokes
RSM	Reynolds Stress Model
SGDH	Simple Gradient Diffusion Hypothesis
VHTR	Very High Temperature Reactor

Additional symbols are defined in the text.

CHAPTER 1

INTRODUCTION

1.1 COMPUTATIONAL FLUID DYNAMICS

'Computational Fluid Dynamics (CFD)' is the name given to a set of physical models and computational techniques for solving problems involving fluid flow and heat transfer (and any other related phenomena). Nowadays, thanks to the rapid growth of computer power and the introduction of user-friendly Graphical User Interfaces (GUI), CFD has become an important industrial tool and enjoys a wide range of engineering applications including in aerodynamics, power plant analysis, turbomachinery and meteorology, as well as nuclear engineering and other areas. Compared to experimentally-based approaches, CFD has many advantages including substantial reductions in time and cost, the possibility of obtaining practically unlimited levels of detail (at least of the mean field), and the ability to simulate almost any flow problem. Despite all these benefits, CFD has one main problem and that is a lack of general reliability, especially in turbulent flow predictions; this is due to the nature of turbulent

flow, where the flow is irregular quasi-random, and unsteady. Although it is possible to improve the reliability of CFD, it is done at an extremely high price in terms of the computational time and resources that it requires. This is why, even after four decades, turbulent flow CFD is still an on-going research topic with lots of questions yet to be answered.

1.2 TURBULENCE MODELLING SCHEMES

Turbulence is composed of eddies of various length-scales. Energy is extracted from the mean flow and is cascaded down to the smallest eddies by essentially inviscid mechanism. Turbulence is a phenomenon of great complexity and has exercised many eminent scientists including Osborne Reynolds, the finest professor of engineering at the University of Manchester, and after who the 'Reynolds number' is named.

Turbulent flow is characterised by three-dimensional motion of the fluid on a wide range of scales both in time and space. Mathematically, this means that a very small distance between discretized points is required which results in the computations becoming longer and more expensive. This is why a number of approximations have been introduced to represent the turbulence and effectively make the simulation more feasible.

The different approaches that have been developed to compute turbulent flows can be broadly categorised into the following three groups: 1) Direct Numerical Simulations, 2) Large Eddy Simulations, and 3) Reynolds-Averaged Navier-Stokes analysis.

In Direct Numerical Simulation (DNS), all the fluid scales of motion are resolved by solving the Navier-Stokes and continuity equations. Since all the fluid scales need to be taken into account, DNS requires a very fine grid spacing of the order of Kolmogorov scales. Despite obtaining accurate results, DNS is not an option for

complex industrial flow problems and is currently limited to applications of academic interest, and then only at low Reynolds numbers.

Large Eddy Simulation (LES) is another technique for computing turbulent flows in which large scales are resolved, while the small scales are modelled. LES emerged over 40 years ago, initially for meteorological applications (Pope, 2000). The idea behind LES technique is that large scales in the flow are anisotropic and thus not universal and need to be resolved, while small scales can be approximated since they are isotropic, dissipative, and more universal. The large scales can be separated from the small scales through applying a filter to the velocity field and decomposing it into filtered (resolved) and modelled (sub-grid) components. The size of this filter is determined by the resolution of the grid. Although LES has proved to be accurate on a range of industrial and non-industrial applications whilst requiring less computational resources than DNS, the cost of LES still exceeds the cost of a RANS simulation (introduced below) by at least few orders of magnitude. Therefore it has been predicted that LES calculations for complex geometries, especially at high Reynolds-number may not be feasible for several decades to come (Spalart, 2000).

If instantaneous flow parameters are not required, a more practical alternative to DNS and LES is the Reynolds-Averaged Navier-Stokes (RANS) technique. In RANS, instantaneous flow quantities are decomposed into mean and fluctuating components. This decomposition and subsequent averaging results, however, in the loss of some information on the turbulent fluctuations and this is where turbulence models emerge as a tool to close these sets of equations. Many turbulence models have been developed so far, ranging from simple algebraic equations to more complicated differential expressions. RANS is currently the most economical and flexible, and thus the most commonly-adopted, approach for predicting turbulent flows and is widely used in industry for design and analysis of various flow problems, even though its accuracy is

strongly dependent on the choice of turbulence model. Since it is not possible to have a universal turbulence model, it is very important for CFD users to know which turbulence models are the more accurate and thus reliable for use in various flow problems. This need has resulted in extensive CFD verification and validation assessments, and still remains a topic of research and debate across the international community.

CFD V&V

One of the industrial sectors in which CFD is widely used these days is nuclear engineering. Application of CFD for nuclear reactor safety problems requires that simulation tools have reached a sufficient degree of maturity and reliability, and that the users of CFD have high levels of expertise in selecting appropriate turbulence models and numerical schemes. Therefore, Best Practice Guidelines (BPG) have been provided by a number of organizations (see ERCOFTAC, 2000 and Menter, 2002, for example) in response to increasingly pressing demands from industry and government to place 'error bars' around CFD results. One of the best attempts to produce BPG for CFD was the ERCOFTAC SIG 15 (ERCOFTAC, 2000) which has been a voluntary and unfunded academic benchmarking activity for the past 2 decades. More recently, in an attempt to keep these databases alive and open to everyone in the CFD community, the CFD/Turbulence Modelling group at the school of Mechanical, Aerospace and Civil Engineering at the University of Manchester has launched a new website (www.CFDtm.org) to improve the overall quality of CFD by bringing together scientists, researchers, users, and developers from industry and academia and has created an interactive database* consisting of a large number of test cases concerning CFD 'Quality and Trust' in relation to nuclear reactor safety. This attempt, as a

* 'http://cfd.mace.manchester.ac.uk/twiki/bin/view/Saturne/TestCases'

Validation &Verification (V&V) activity, has recently attracted wide academic and industrial support. One of the aims of the present study, therefore, is to contribute towards updating this database by uploading all the simulations presented in this work to the CFDtm website.

1.3 ADVANCED GAS-COOLED NUCLEAR REACTORS

Advanced Gas-cooled Reactors (AGRs) are the second generation of British gas-cooled reactors which were developed from the Magnox reactor, but which are capable of operating at higher temperatures thus have higher thermal efficiencies. AGRs have a graphite moderator and use pressurized CO_2 as coolant. Uranium dioxide (UO_2) pellets, enriched to 2.5-3.5%, are used as fuel. There are currently 7 AGR stations in the UK including Dungeness, Hartlepool, Heysham, Hinkley Point, Hunterston and Torness, all owned and operated by British Energy (part of 'EdF Energy' since 5 January 2009); these together account for just under 20% of the UK's electricity production. A schematic of an AGR is shown in Figure 1.1. The pressurized CO_2 circulates through the core, reaching approximately 650°C, and then passes over the boiler tubes. The rate of nuclear reaction (i.e. fission) is controlled by 'control rods' which penetrate the graphite moderator. Control rods are made of neutron-absorbing materials and thus inserting them fully inside the core can shut-down the reactor. (In AGRs there are also secondary and tertiary shut-down systems which operate by injecting nitrogen into the coolant and injecting boron spheres into the reactor, respectively.)

The reactor core consists of over 300 fuel elements. Eight fuel elements are held together vertically by a tie bar which passes through the centres of the elements to form a fuel stringer. Each fuel element (as shown in Figure 1.2) comprises 36 stainless steel fuel pins, which are housed in graphite sleeves (a hollow cylindrical graphite sleeve of

1040 mm long × 240 mm outer diameter × 24 mm wall thickness). Each fuel pin contains 64 fuel pellets, with each pellet being approximately equivalent to 1.5 tonnes of coal. The 36 fuel pins and a central guide tube are supported by a stainless steel grid and two stainless steel braces which maintain the spatial arrangement of the fuel pins. The main structural component of the fuel element is the graphite sleeve which supports the pin cluster and the whole of the stringer above it. The fuel element sleeves, by engaging with lugs attached to the grids and braces, restrict possible axial, rotational and lateral movements of the fuel cluster (Burridge and Naylor, 1991). A typical fuel element assembly weighs approximately 85 kg of which 28 kg is made up by the graphite sleeve.

1.3.1 Mixed Convection under Post-Trip Conditions

Conduction, convection and radiation are the three mechanisms by which thermal energy may be transferred from one point in space (and time) to another. Convective heat transfer is said to occur when there is a transport of thermal energy by molecular conduction and bulk fluid motion and it is traditionally divided into the regimes of ‘forced’ convection (where motion is in response to an externally-applied pressure difference) and ‘free’ convection (where motion is due to density variations within the fluid). However, both mechanisms may operate simultaneously; where there is a buoyancy-modified forced flow, the heat transfer regime is termed ‘mixed’ (or ‘combined’) convection. The effects on heat transfer performance are complex, and forced and free convection influences do not combine in a simple additive manner. It is also worth noting that forced convection may be regarded as the limiting case of mixed convection when the variations of body force become negligible.

Mixed convection occurs in a variety of engineering applications including nuclear reactors. Generally, nuclear reactors incorporate a dual heat exchanger configuration,

which transfers the heat generated by the fission process to a primary coolant circuit and then to a secondary boiler/stream generator circuit. In the currently-operating UK fleet of Magnox and Advanced Gas-cooled Reactor stations, and also in proposed 'Generation IV' Very High Temperature Reactor (VHTR) designs, the core coolant flows vertically. The coolant in AGRs is carbon dioxide and the principal flow ascends through the core; in VHTRs the coolant is helium and the flow descends. At low flow rates, associated with post-trip conditions, density variations affect the flow, and heat transfer levels with respect to the corresponding forced convection flow at the same Reynolds and Prandtl numbers may be quantified in terms of a Nusselt number ratio, Nu/Nu_0, where subscript 0 denotes the forced convection condition. Although mixed convection would not be expected to occur under normal reactor operation, it may, as noted above, occur during post-trip decay heat removal, where the heat loading from the fuel elements is relatively large in relation to the low primary coolant flow rate. Under such conditions buoyancy effects have the potential to cause wholesale modifications to the turbulence structure. In the case of descending flow, heat transfer levels are always enhanced. In the ascending flow case, however, heat transfer levels may be either impaired (at moderate heat loadings), or enhanced (at very high heat loadings), see Figure 1.3.

It is worth noting that in the preset study all mixed convection computations are done in pipes with smooth surfaces. The thermal-hydraulics of channels and pipes with roughened surfaces are also investigated and are briefly discussed below.

1.3.2 Thermal-Hydraulics of the Fuel Elements

An important feature of AGR fuel pins is the rib-roughening applied to the heat transfer surface which can be seen in Figure 1.4. Applying roughness to the fuel pins of a

nuclear reactor could potentially result in either an improvement or reduction in performance, depending upon the relative increases in heat transfer and flow resistance.

Two-Dimensional Rib-Roughness

For many years, rough surfaces have been used to enhance convective heat transfer by the promotion of higher turbulence levels. The penalty associated with such roughening is an increase in drag and consequently much effort has been devoted to the optimization of roughness designs.

Despite numerous studies on heat transfer, turbulence and turbulent boundary layer in rough surface problems, the detailed physics of these flow problems are still a topic of research (see Chapter 2 for further details). Most of the standard measurement techniques have proved to be inaccurate for rough surfaces mainly due to high turbulence intensities near the roughness elements and this is why computational studies are becoming more common these days especially thanks to continuously improving computational power.

Depending on the surface configuration, one can divide rib-roughened surfaces into two categories. The first category corresponds to a geometry where the spacing between adjacent ribs is small and is occupied by a recirculating flow, as shown in Figure 1.5(a). This type of roughness is known as "*d*-type" roughness. The second type refers to a situation where the gap between the ribs is larger. This type of roughness is characterized by eddies that form behind a roughness element. This type of roughness is known as "*k*-type" roughness (see Figures 1.5 b & c) (Jiménez, 2004).

In fact, the distinction between *d*- and *k*-type roughness was first made by Perry et al. (1969) who observed that in flow over plates roughened by narrow spanwise square grooves, the effective roughness (Nikuradse 'sand-grain' roughness), k_s, was not proportional to the roughness height (k), but to the boundary-layer thickness (d), and thus this type of roughness was named *d*-type (Jiménez, 2004). On the other hand, they

found that for rough surfaces where the gap between the grooves was greater, roughness effects showed clear dependence on the roughness height, hence *k*-type roughness.

In a little more detail, flow over rib-roughness can be divided into the following three regimes, as shown in Figure 1.5:

- 'Skimming flow' in which the cavity between the ribs is occupied by a recirculating flow (*d*-type roughness).
- 'Un-reattached flow' in which the separated regions downstream of the first rib and upstream of the second rib merge with the consequence that viscous skin friction is relatively insignificant (*k*-type roughness).
- 'Reattached flow' in which the separated flow behind the first rib reattaches to the smooth surface in the cavity and thus viscous skin friction is significant (a second form of *k*-type roughness).

Apart from the significance of the spacing between ribs, the roughness height is also crucial. According to Jiménez (2004), the channel height, H, should be at least $40k$ in order to eliminate the direct effect of the roughness elements on the outer flow, otherwise it is likely that direct roughness effects will be felt across the entire boundary layer and thus the flow would no longer be categorized as flow over roughness elements, but rather as flow over surface-mounted bluff bodies. Discussed further in Chapter 6.

A simple method of approaching the problem of rib-roughness on AGR fuel pins is to simulate the flow in a plane between two fuel pins as shown in Figure 1.6. This allows one to carry out a 'parametric study' without having to simulate the whole fuel element. This approach is also advantageous since there are many experimental and DNS data available for 2D rib-roughened surfaces and comparison with these data can

be made to ensure the accuracy of the computations. This approach was adopted in this project and the results are presented in Chapter 6.

Three-Dimensional Investigation of Flow over Fuel Elements

Although a 2D representation of fuel elements is an extremely efficient method for parametric studies, it clearly does not resolve 3D flow features. Therefore, 3-dimensional simulations of the fuel element are required to capture possible interactions among different fuel pins and sub-channels. In addition, a 3D representation of a fuel element is necessary in order to compute the pressure, temperature and velocity distributions across the whole fuel element, which are in fact crucial for design and safety purposes (Morrison, 2003). Computation of the 3D case can provide a fuller picture and valuable detailed information concerning the thermal-hydraulics of AGR core coolant flows. To date there is no 3-dimensional simulation of AGR fuel elements, and the present work represents the first attempt to compute the whole fuel element. Further details of the 3D computations are given in Chapter 7.

1.4 OBJECTIVES OF THE PRESENT STUDY

The present work was carried out as part of Work Packages I & IV of 'Keeping the Nuclear Option Open' (KNOO) project[†], a four-year initiative (2006-2010) addressing challenges related to safety, reliability, and sustainability of nuclear power. Through collaboration between key industrial and governmental stakeholders, and also international partners, KNOO was sought to maintain and develop skills relevant to nuclear power generation. Funded through the 'Towards a Sustainable Energy Economy Programme' of Research Councils UK, it represented the largest single nuclear research programme in the United Kingdom for more than 30 years. This £6.1million programme

[†] The titles of WP1 and WP4 are:

WP1: Fuel, thermal-hydraulics and reactor systems.

WP4: Safety and performance for a new generation of reactor designs.

considered various issues concerning nuclear reactors. One of these issues was to investigate the thermal-hydraulics of currently-operating (and also Generation IV; WP4) nuclear reactors through collaboration with industrial partners including British Energy. The attention of this thesis is thus focused on this issue, aiming to shed some light on some current industrial concerns.

Accordingly, this project has three aims, first to assess various advanced RANS models of fluid turbulence against experimental and numerical data for buoyancy-modified mixed convection flows, such flows being representative of reactor core flows under post-trip conditions (see Section 1.3.1 for more details). The research has application both to current AGR designs and proposed Generation IV VHTR core configurations. For this part of the project, an in-house code ('CONVERT'), a commercial CFD package ('STAR-CD') and an industrial code ('Code_Saturne') are used to generate results (presented in Chapter 5).

The second aim is to investigate the thermal-hydraulic performance of flow over rib-roughened fuel elements in AGRs, including a parametric study of flow in a 2-dimensional channel (see Section 1.3.2). This part of the research takes various factors into consideration including the effects of rib height-to-channel height ratio, rib width-to-height ratio, rib pitch-to-height ratio, rib profile, Reynolds number, near-wall treatment, and mesh type. Through comparison with experimental data, the performance of different RANS turbulence models is assessed. Other practical issues such as the effects of carbon deposition on the roughened surfaces are also addressed.

Finally, the third aim is to simulate a simplified 3-dimensional representation of an AGR fuel element similar to the Transverse and Multi-Start designs (where the latter is the only current design). This part of the research is intended to link the findings of the precursor 2-dimensional rib-roughness analysis to a 3D flow problem, in addition to

provide information on the performance of RANS models in capturing 3D flow features.

1.5 OUTLINE OF THE THESIS

Work is presented in this thesis as follows. Chapter 2 gives a review of the literature on vertical mixed convection flows, 2-dimensional rib-roughened surfaces, and AGR fuel elements. Previous experimental and numerical works are reviewed. Chapter 3 provides an overview of existing RANS turbulence models and includes details of all the turbulence models used in the present project. Chapter 4 then introduces some theoretical concepts related to the test cases computed here and also summarises the details of the codes used in this thesis. Results of mixed convection heat transfer in a vertical heated pipe are presented in Chapter 5. In Chapter 6, the effects of various design factors are examined using 2-dimensional rib-roughened channels. Chapter 7 presents results for the case of the flow over a 3-dimensional representation of a fuel element. Finally, Chapter 8 includes conclusions together with suggestions for future work.

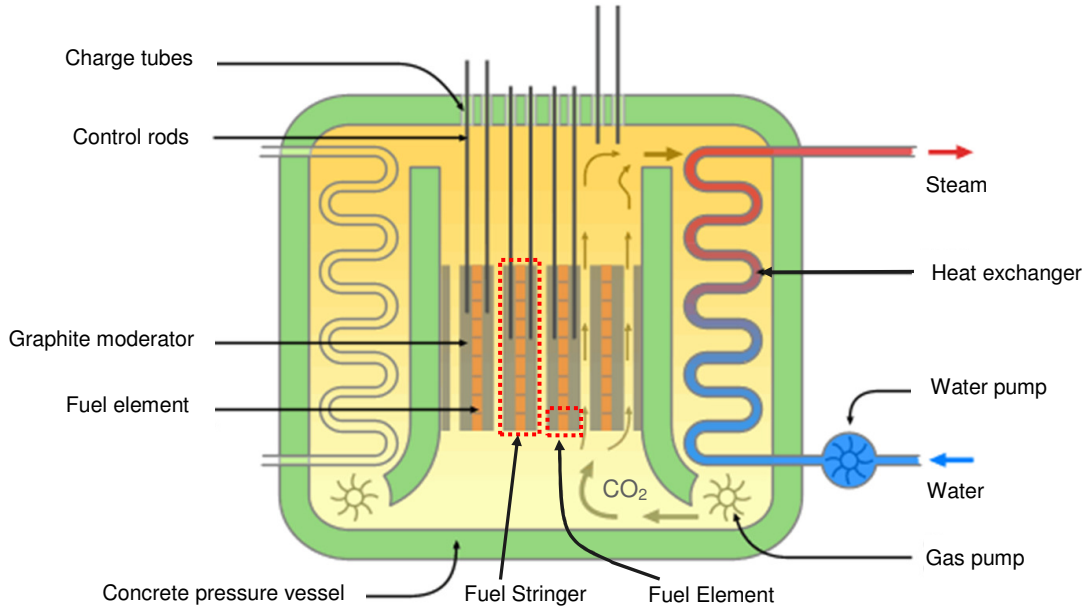

Figure 1.1 – Schematic of an AGR. (Adapted from http://www.ecology.at.)

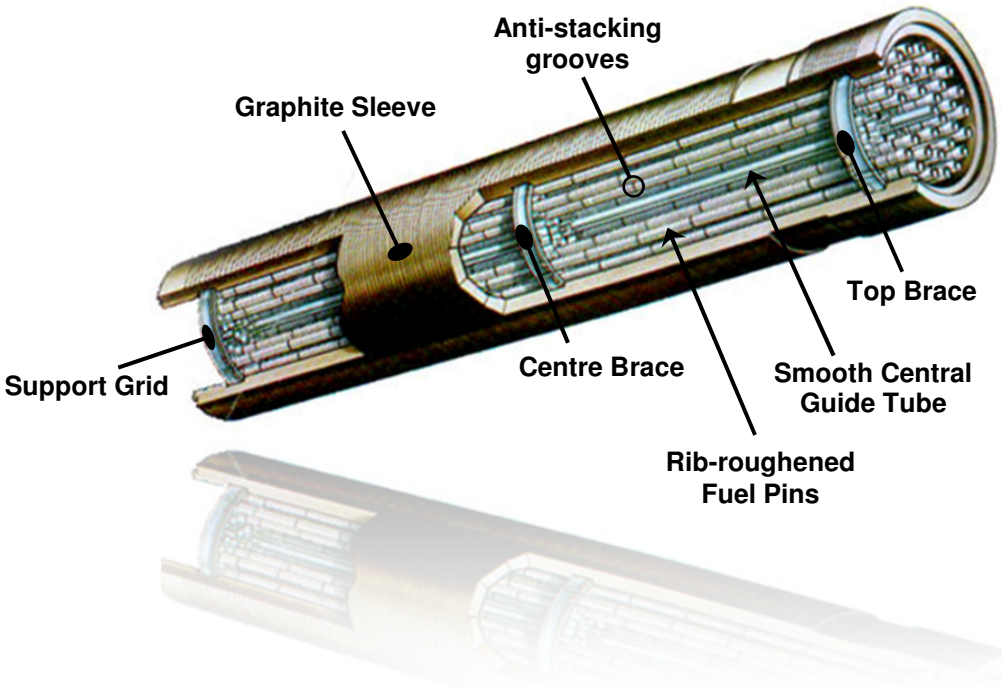

Figure 1.2 – Schematic of an AGR fuel element. (Adapted from CORE, 1999.)

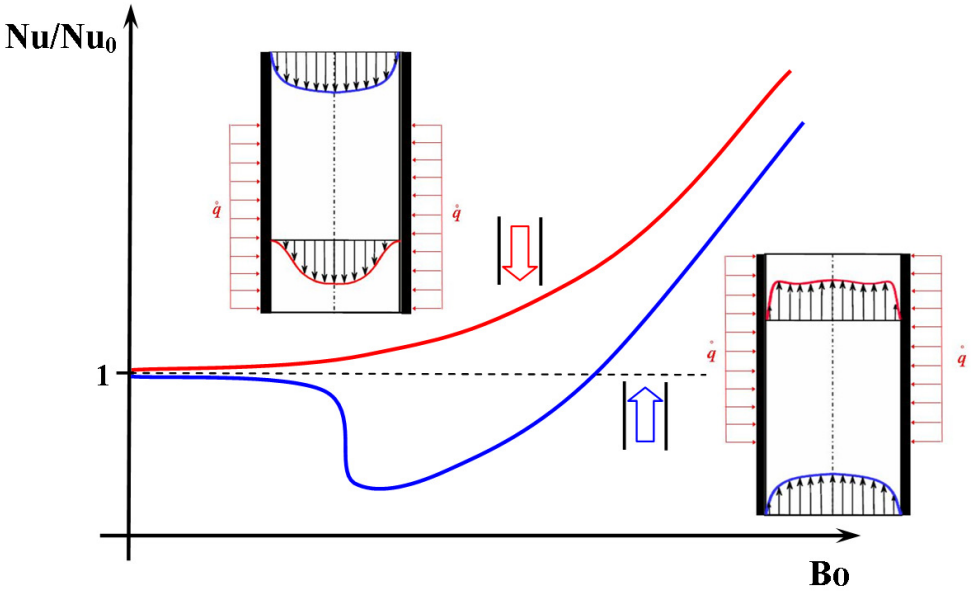

Figure 1.3 – Trends of Nusselt number impairment and enhancement for ascending and descending mixed convection flows.

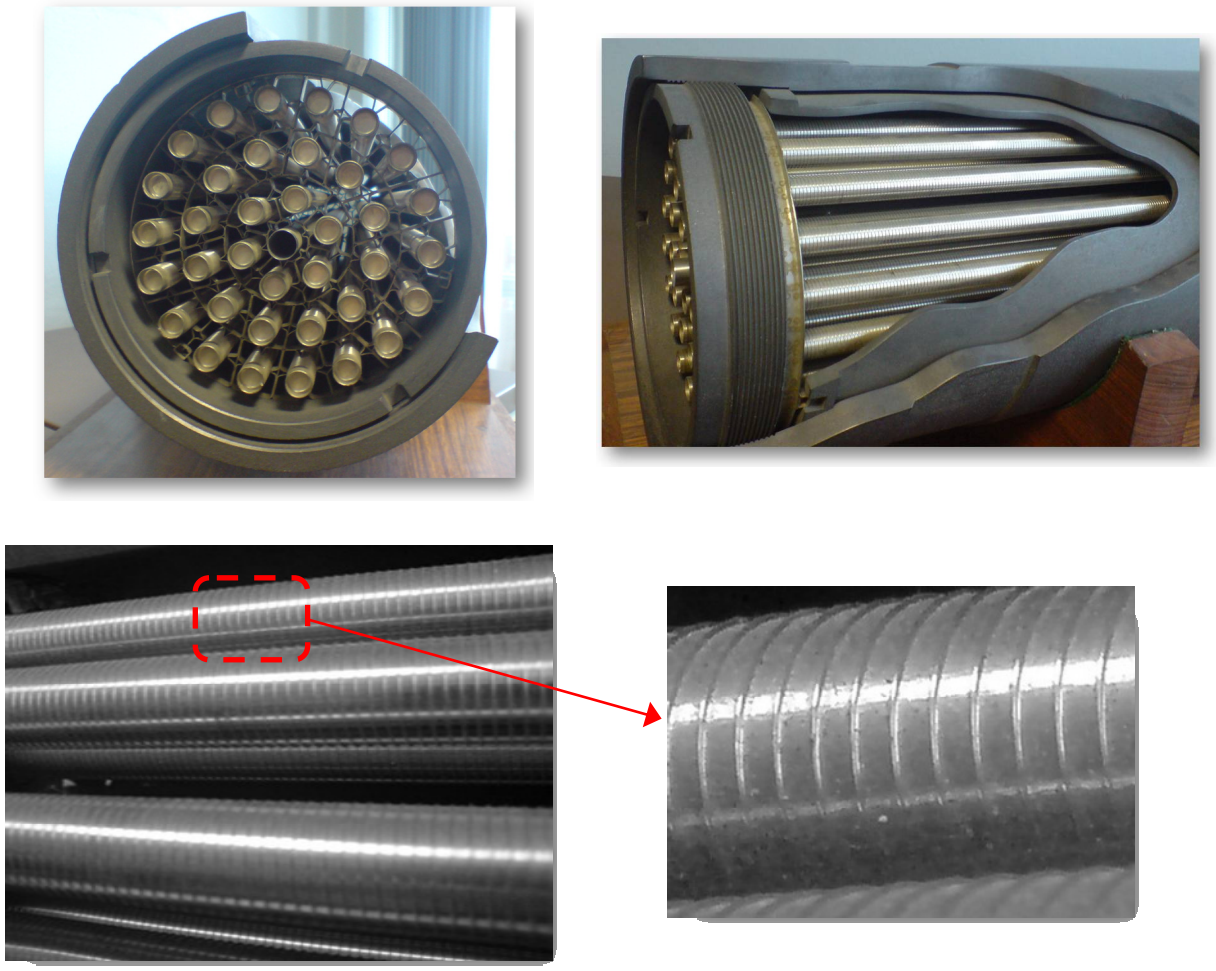

Figure 1.4 – An early design of AGR fuel pins with transverse ribs.

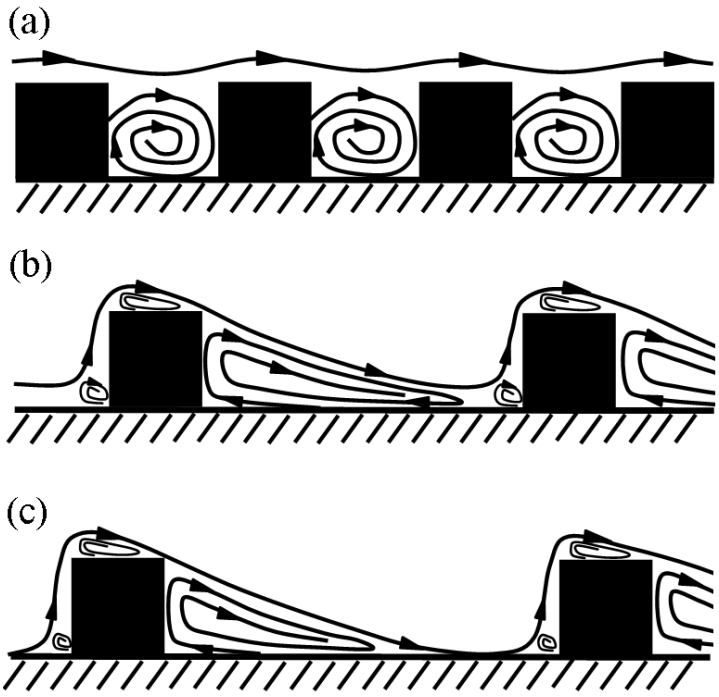

Figure 1.5 – Regimes of the mean flow over rod roughness (a) Skimming flow (*d*-type) (b) Un-reattached flow (*k*-type) (c) Reattached flow (*k*-type).

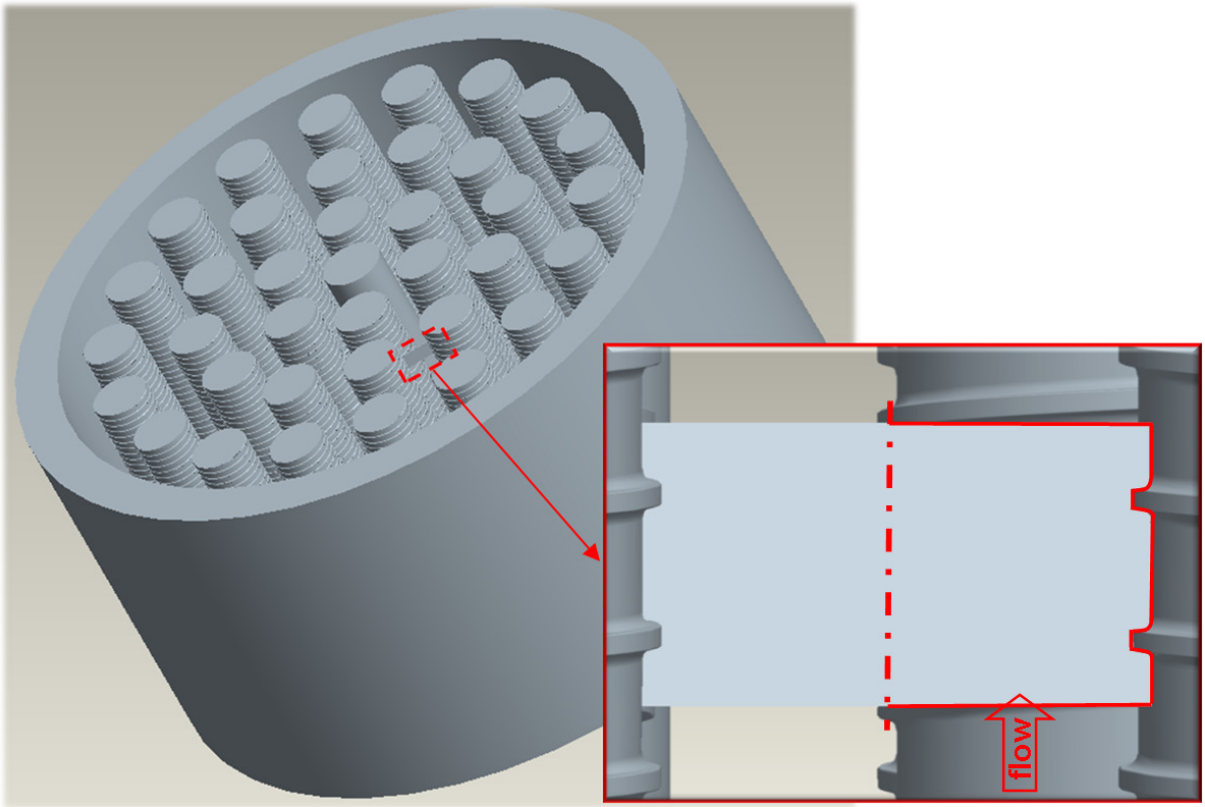

Figure 1.6 – A 2-dimensional representation of AGR fuel elements.

CHAPTER 2

LITERATURE REVIEW

2.1 PRELIMINARY REMARKS

In this chapter, a literature review is presented on three main topics: 1) Mixed convection heat transfer in vertical flow, 2) Flow and heat transfer over rib-roughened surfaces, and 3) The thermal-hydraulics of the fuel elements of Advanced Gas-cooled Reactors (AGRs). Clearly experimental works provide a crucial tool for the validation of numerical studies. Therefore, for each topic, after a short introduction, a brief review of previous experimental works is presented. Earlier numerical works are then presented under the three categories of DNS, LES, and RANS. Previous numerical works using RANS are of particular interest in the context of this work and therefore are discussed in more detail.

2.2 MIXED CONVECTION HEAT TRANSFER IN VERTICAL FLOWS

2.2.1 Introduction

The complex phenomena associated with the mixed convection regime are discussed in the monograph of Petukhov and Polyakov (1988) and the review papers of Jackson et al. (1989) and Jackson (2006).

In the examination of mixed convection, an important parameter is a dimensionless group known as the 'buoyancy parameter', *Bo*, which is widely used to characterize the degree of buoyancy influence. The buoyancy parameter was originally developed in a semi-empirical analysis pursued by Hall and Jackson (1969). Works from the late-1980s onwards have tended to adopt a revised form of the parameter (Cotton, 1987; Jackson et al., 1989):

$$Bo = 8\times10^{4}\,\frac{Gr}{Re^{3.425}\,Pr^{0.8}} \tag{2.1}$$

Variable property effects other than those associated with buoyancy become significant where the temperature variations in a flow are large. An appropriate dimensionless measure of axial and radial temperature variations is provided by the 'heat loading parameter', q^{+}:

$$q^{+} = \frac{\dot{q}}{\rho_b U_b c_{pb} T_b} \tag{2.2}$$

The geometry studied in the present mixed convection investigation is that of a vertical pipe with the fluid either ascending or descending. The thermal boundary is one of uniform wall heat flux (Figure 2.1).

In the case of ascending flow an increase of buoyancy influence rapidly leads to heat transfer levels, represented by the Nusselt number, *Nu*, being impaired with respect

to forced convection values. 'Laminarization' of the flow occurs due to a reduction in shear stress and turbulence production. With a further increase in buoyancy influence, however, heat transfer levels recover and may be enhanced above forced convection values. The purpose of the first part of the present work is to investigate this interesting phenomenon in depth.

As was noted in Chapter 1, the coolant flow in AGRs is carbon dioxide; however, due to a lack of data for carbon dioxide, attention here is restricted to air flows.

2.2.2 Experimental Works

Currently there exists an extensive set of experimental studies of mixed convection in vertical pipes, the majority of which are related to upward flow. However, despite the practical importance of mixed convection flows, only a limited number of flow profile measurements have been reported in the literature and many experimental investigations have been concerned solely with the determination of heat transfer coefficients. The fluids tested in these experimental works are air, water, mercury, sodium, helium and nitrogen.

Experimental studies of ascending turbulent mixed convection air flows include the works of Steiner (1971), Carr et al. (1973), Polyakov and Shindin (1988), Vilemas et al. (1992) and Shehata and McEligot (1995). In contrast, Parlatan et al. (1996) used water as the working fluid. Despite the primary focus of the present work being on gas-cooled reactors, comparison with the data of Parlatan et al. is reported below. (This is justified on the basis that a 'buoyancy parameter', defined earlier, includes a Prandtl number dependence.)

The experiment by Steiner (1971) was amongst the first on ascending air flow, and the impairment of heat transfer coefficient and distortion of velocity and temperature

profiles was demonstrated. It was concluded that the effect of buoyancy was to reduce turbulence levels and thus to impair the effectiveness of heat transfer.

Carr et al. (1973) performed their tests at Re = 5,000 - 14,000, with the aim of obtaining accurate flow profiles. They focused their attention on the region of maximum impairment and therefore had low-to-medium buoyancy influence. Since all their cases had weak variable property effects and relatively low bulk temperature rises, their results can be treated as constant property experiments (i.e. the Boussinesq approximation is valid).

Polyakov and Shindin (1988) carried out tests at Re = 5,100 and 9,000. They reported the results for Nusselt number development, velocity, temperature, Reynolds stresses, and turbulent heat flux profiles. By measuring the turbulent transport quantities, they showed that the rapid reduction of heat transfer levels is due to turbulent heat transport being suppressed to a greater degree than the momentum transport.

Vilemas et al. (1992) carried out tests at Re = 3,000 - 50,000 and reported the results of twelve cases which spanned a wide range of buoyancy influence (including some value of Bo for which most of turbulence models are unable to produce any solution). This wide range of Bo resulted in large property variation for some cases. Data were provided for Nusselt number and wall temperature development.

Shehata and McEligot (1995; see also Shehata and McEligot, 1998), report the results of tests which were conducted for heating rates causing significant property variation with limited mixed convection influence. Reynolds number was varied between 4,000 and 6,000. Flow development was studied by obtaining streamwise velocity and temperature profiles at various axial locations.

Parlatan et al. (1996) investigated the behaviour of friction factor and heat transfer coefficient for both aiding and opposing transitional and turbulent flow of water for Reynolds numbers between 4,000 and 9,000 and with $Bo < 1.3$. The measured

development of friction factor and heat transfer coefficient were compared with other experimental data including those of Steiner (1971), Carr et al. (1973) and Easby (1978). Comparison was also made with the correlation of Jackson et al. (1989) and the numerical results of Cotton and Jackson (1990). The heat transfer results of Parlatan et al. agreed well with previous studies.

Figure 2.2 and Figure 2.3 compare the range of buoyancy influence (*Bo*) and heat loading parameter (q^+) encompassed by the experimental works mentioned above.

Finally, Easby (1978) and Axcell and Hall (1978) carried out experiments on descending flow with nitrogen and air, respectively. In both cases, monotonic enhancement of heat transfer levels was reported.

2.2.3 Numerical Works

In this section, earlier numerical studies of turbulent mixed convection flows are reviewed under the following three headings: 1) DNS, 2) LES, and 3) RANS.

DNS

In recent years the body of experimental data on turbulent mixed convection existing in the literature has been complemented by the appearance of Direct Numerical Simulation (DNS) results. One of the earliest studies of this kind was undertaken by Kasagi and Nishimura (1997) who carried out a simulation of mixed convection between two vertical parallel plates maintained at different uniform temperatures.

Another DNS of turbulent pipe flow with strong heating and variable fluid properties was carried out by Satake et al. (2000). Good agreement was found when they compared their mean velocity and temperature profiles against the data of Shehata and McEligot (1998).

A focus of the present study is the recent DNS of You, Yoo and Choi (2003) who conducted a study of turbulent mixed convection in a vertical uniformly-heated pipe for

constant property conditions; buoyancy was accounted for using the Boussinesq approximation. You et al. restricted their attention to conditions of hydrodynamically and thermally fully-developed flow. Adoption of the Boussinesq approximation framework is attractive from the viewpoint of turbulence model/computer code validation because it permits an examination of buoyancy effects in isolation from other variable property phenomena (thus q^+, Eqn. (2.2) above, is not a relevant parameter of the simulations). You et al. compared their Nusselt number and friction coefficient values against various sets of experimental data and found good agreement with the data. In the present study, most of the results on mixed convection flow will be examined against the data of You et al. (see Chapter 5 for details).

LES

The work of Xu, Lee, Pletcher, Shehata and McEligot (2004) was amongst the first Large Eddy Simulations (LES) to appear in the literature. They performed their computations for the same conditions as the experiments of Shehata and McEligot (1998). Xu et al. obtained good agreement for mean velocity and temperature profiles as well as bulk Nusselt number.

A second LES for mixed convection was carried out by Addad and Laurence (2008) (also reported in Keshmiri et al. 2008a; 2008b). They compared their results against the DNS of You et al. (2003). LES runs were generated for seven values of the buoyancy parameter, four of which corresponded directly to the cases of You et al. In relation to forced convection, the DNS value of Nusselt number was over-predicted by the LES by approximately 10%. The LES study also showed an earlier onset of heat transfer impairment. However, in examining mean velocity, temperature, and Reynolds shear stress distributions, Addad and Laurence's LES produced acceptably close results to the DNS.

RANS

In the review of Jackson et al. (1989), computational works on mixed convection published up to the late-1980s were divided into the following categories:

1) Prescribed eddy diffusivity models
2) Mixing length models
3) One-equation transport models
4) Two-equation transport models
5) Higher order models

Attention here is restricted to two-equation transport models.

Walklate (1976) used three different formulations of the k-ε model (based on the proposals of Launder and Spalding, 1972). One of the models tested was a standard high-Reynolds-number formulation with wall functions based on the van Driest mixing-length equation. The other two models employed damping functions in the constitutive equation to account for near-wall effects (i.e. partial low-Reynolds-number models). Walklate concluded that, for an ascending pipe flow, a partial low-Reynolds-number models gave improved predictions of the mean flow when compared to the data of Carr et al. (1973). Furthermore, such partial low-Reynolds-number models generally performed better than the high-Reynolds-number model in predicting heat transfer. However, this agreement was not found when the models were compared against the experimental data of Axcell and Hall (1978) for descending flow.

Abdelmeguid and Spalding (1979) applied the high-Reynolds-number k-ε model of Launder and Spalding (1974) together with wall functions to both ascending and descending flows. The model successfully reproduced the correct trends of heat transfer impairment and enhancement for both upward and downward flows. The velocity and temperature profiles were also in reasonable agreement with the experimental results of

Buhr et al. (1974) which were obtained for an upward flow of mercury in a heated pipe. However, despite obtaining fairly good results with the k-ε model, they adopted a simple form of near wall treatment which could be the likely cause of some discrepancies found between computational results of these types of turbulence models and experimental data (Jackson et al., 1989).

Tanaka et al. (1987) used a slightly modified version of the k-ε model due to Jones and Launder (1972) and compared their results against their own experimental data for a heated upflow of nitrogen at Reynolds numbers of 3,000 and 5,000. Tanaka et al. generally found good agreement between the measured and calculated Nusselt numbers. Their experimental data, however, did not include measurements in the laminarization region.

The contribution of the present study is a continuation of a series of numerical studies carried out at the University of Manchester over the past 2 decades and including the works of Cotton (1987), Yu (1991), Mikielewicz (1994) and Kirwin (1995). These investigations are described below. The main tool in these computational investigations is an in-house computer code 'CONVERT' which was originally developed by Cotton (1987; based on the discretization procedures of Leschziner, 1982). Details of CONVERT will be given in Chapter 4.

Cotton (1987; see also Cotton and Jackson, 1990) applied the low-Reynolds-number k-ε model of Launder and Sharma (1974; hereafter LS model) in a constant property formulation and compared his results against experimental data for ascending (Steiner, 1971; Byrne and Ejiogu, 1971; Carr et al., 1973) and descending (Easby, 1978; Axcell and Hall, 1978) turbulent mixed convection flows. Fairly good agreement was found when the results of this model were compared with experimental data, the exception being the heat transfer data of Axcell and Hall (1978) at higher Bo values. Nevertheless, Cotton and Jackson (1990) found that inclusion of the length-scale

correction term of Yap (1987) produced marked improvement in the degree of accord with the data of Axcell and Hall.

Yu (1991) continued the work of Cotton (1987) and Cotton and Jackson (1990) by again employing the LS model, but now extending it by taking the variation of flow properties into account. These properties included density, thermal conductivity, and dynamic viscosity. Yu found that including variable property effects yielded better agreement with data. She also carried out calculations for other fluids including water, mercury, and liquid sodium and undertook extensive comparisons against the experimental data of Jacoby (1972), Kenning et al. (1974), Buhr et al. (1974) and Rouai (1987). Her results were generally in a good agreement with the data, except at very high levels of buoyancy influence, where some discrepancies were found. However, for very low Prandtl number liquid metals, in particular sodium ($Pr \approx 0.005$), for which there was no data available at the time, Yu found rather different heat transfer behaviour. For buoyancy-aided sodium flow, heat transfer levels were generally enhanced while for buoyancy-opposed flow, little or no impairment in Nu was found. These phenomena were discussed by Cotton, Jackson and Yu (1989).

Mikielewicz (1994) further extended the Manchester programme of work by implementing a number of turbulence models (with various degrees of sophistication), and sought to compare the response of those models to the influences of buoyancy and variable property effects in heated vertical pipes. Overall, twelve different turbulence models were tested, each varying in complexity from zero-order models through to more advanced one- and two-equation models. Mikielewicz considered three different fluids and compared his results against a number experiments, including the works of Steiner (1971), Weinberg (1972), Carr et al. (1973), Rouai (1987), Vilemas et al. (1992), Buyucalaca (1993), Li (1994) and Shehata and McEligot (1995). His computations for water showed that only the LS model could correctly predict the heat

transfer coefficient over a range of *Bo* for both ascending and descending flows, while the Jones and Launder (1972) and Chien (1982) models proved to perform better at higher values of *Bo*. For ascending supercritical pressure carbon dioxide, where strong buoyancy and significant property variation effects are present, the LS model was again the best model in capturing heat transfer trends, except in the recovery region. Finally, for air, the LS model was generally the most successful model in responding to buoyancy effects. However, some limitations of the LS model became evident at high Reynolds numbers when the influence of both buoyancy and variable properties was strong.

Kirwin (1995) studied the performance of three different turbulence models, namely those of Launder and Sharma (1974), Michelassi, Rodi and Scheuerer (1991) and Wilcox (1988). He carried out calculations for a heated vertical pipe flow for both ascending and descending flow, and with both constant and variable property formulations. Comparison was made against experimental data including those of Steiner (1971), Carr et al. (1973), Axcell and Hall (1978), Polyakov and Shindin (1988), Vilemas et al. (1992) and Shehata and McEligot (1995). He concluded that the LS model was the most accurate of the models. Kirwin also developed a variant of the LS model (importantly with the same Re_t – parameterization) to investigate whether it was possible to improve the calculation of forced convection flow while retaining good performance in mixed convection. However, no major improvement over the standard LS closure could be demonstrated for mixed convection flow (see also Cotton and Kirwin, 1995).

Despite the record of success of the LS model, Cotton and Ismael (1998) argued that a fundamental weakness exists in the assumption of the stress/rate-of-strain constitutive equation of EVMs (this applying to both low- and high-Reynolds versions). They developed a new from of EVM based upon the definition of a ‘strain parameter’,

S, which formed the subject of a third transport equation. A new damping function was introduced which was made to depend principally upon *S*. (Further details on the model are given in Chapter 3.) The Cotton-Ismael model has been applied to a number of problems including mixed convection flows with variable fluid properties. Cotton and Ismael concluded that their new model returned results similar to those of the LS model, with the exception that in examining axial thermal development large discrepancies were found in comparison with the experimental data of Vilemas et al. (1992).

Later, Cotton, Ismael and Kirwin (2001) applied the three-equation strain parameter model to ascending mixed convection flows and they examined the results against those generated using the LS model. Comparison was made with four sets of experimental heat transfer data and it was demonstrated that both turbulence models are generally successful in resolving Nusselt number developments along the lengths of mixed convection flow passages, although for computed Reynolds stress profiles, the k-ε-S model generally returned better results.

Using the commercial CFD package 'FLUENT', Richards, Spall and McEligot (2004) tested six turbulence models including three versions of k-ε model, two versions of k-ω model, and a variant of the v^2-f formulation (due to Cokljat, Kim, Iaccarino and Durbin, 2003). Comparison was made against the experimental data of Shehata and McEligot (1995) where the variation in fluid properties was strong. Richards et al. showed that the v^2-f model was greatly superior to the other turbulence models in predicting the mean flow and heat transfer.

Recently, Kim, Jackson and He (2008) carried out an extensive study on the application of various turbulence models to ascending mixed convection flows in vertical pipes with constant fluid properties. They applied ten different low-Reynolds-number, two- and four-equation, turbulence models of the eddy viscosity type. Kim et al. simulated the DNS results of You et al. (2003). They attempted to understand the

reasons for the diverse performance of the various models in simulating this type of flow. Kim et al. showed that the LS model reproduced the general trends of the effects of buoyancy influence most closely. Other turbulence models including the k-ε model of Cotton and Kirwin (1995) and the v^2-f model of Behnia, Parneix and Durbin (1998) could also capture the impairment and recovery of heat transfer levels, while the predictions of the k-ω model of Wilcox (1988) were poor. An interesting conclusion which could be drawn from the work of Kim et al. is that the reason why some classical turbulence models such as the LS model can predict eddy viscosity reasonably well is due to the cancelling effect of inaccurate predictions of the two components (i.e. k^2 / ε and f_μ).

Recently, Billard, Uribe and Laurence (2008) proposed a new segregated (Code-friendly) formulation of the v^2-f model (also known as $\varphi - \alpha$, where $\varphi = v^2/k$ and α is a blending parameter) which is based on elliptic blending with the intention of improving the original v^2-f model and its previous formulations. This new formulation was applied to a few different test cases, including an ascending mixed convection flow with constant fluid properties. In relation to the Nusselt number distributions, the model showed good agreement with the DNS data of You et al. (2003). The profiles of mean velocity, temperature, and turbulent kinetic energy were also in close accord with the DNS. Details of this new model and its results will be discussed further in subsequent chapters.

There also have been some attempts to apply higher order turbulence models including Reynolds Stress Model (RSM) to buoyant flows including the work by Craft, Ince and Launder (1996a). For a review on the progress of RSM until late-1980s, the interested reader is referred to the article of Launder (1989).

2.3 RIB-ROUGHENED SURFACES

2.3.1 Introduction

In this section, a brief history of research on rough surfaces is presented followed by a review of previous works done on two-dimensional rib-roughened surfaces in channel flows (see Figure 2.4). Although there are also a number of publications which present results for more complex three-dimensional flows in stationary and rotating ribbed ducts, they are not discussed here (although the interested reader is referred to Iacovides, 1998). An extensive review of the literature on rough-wall boundary layers is also given by Raupach, Antonia and Rajagopalan (1991).

History

In relation to rough surfaces, a brief overview of a number of landmark contributions is given below (see also Schlichting, 1979; Pope, 2000; Jiménez, 2004):

- In 1776, Coulomb showed that surface roughness has an effect on friction resistance.
- In 1854, Hagen observed a sudden increase in the pressure drop by increasing the mass flow rate and reported that there might be two regimes of viscous flow in the pipe.
- In 1933, Nikuradse carried out a very important experiment where he selected a few smooth pipes of diameter 25, 50 and 100 mm and covered their inside surface with carefully selected uniform grains of sand and introduced the non-dimensional number of ε/d where, ε and d were the diameters of the sand grains and the pipe, respectively. He then measured the velocity profile and the pressure drop and calculated the friction factor and Reynolds number for each case and plotted his results for the range of $0.002 \leq \varepsilon/d \leq 0.06$. Based on his findings, he then introduced

the roughness Reynolds number, $\varepsilon^+ = \rho\ \varepsilon\ u_\tau / \mu$, where ε is a geometrical quantity, but ε^+ is a flow quantity.

- In 1936, Schlichting continued Nikuradse's work on sand-grain roughness and carried out further experiments but this time he tested the effects of choosing various types of sand grain roughness and he introduced the concept of 'equivalent sand-grain roughness', k_s, which relates the resistance of any type of roughness to its corresponding sand-grain roughness at the same Reynolds number.
- In 1944, Moody's famous paper included the first universal method of calculating flow resistance for fully developed flow in pipes and now is commonly and widely used in the fluid mechanic problems.

2.3.2 Experimental Works

The years from the late-1970s to the present day have witnessed a continuing high level of experimental activity related to flow over ribbed (and other roughened) surfaces. A recent review is given by Jiménez (2004) who pays particular attention to very rough surfaces.

Laboratory studies of flow over repeated-rib surfaces date back at least as far as 1950s; see, for example, the discussion of Webb, Eckert and Goldstein (1971). In their own experimental programme Webb et al. investigated pipe flow with repeated rectangular ribs, focusing upon the effects of geometrical factors on flow resistance and heat transfer (Reynolds and Prandtl number effects were also studied). In line with established findings for sand-roughened surfaces (see Schlichting, 1979, for example), it was found that flow resistance and heat transfer levels increased with relative roughness (i.e. the ratio of rib height to pipe diameter, *k/D*). Pitch-to-height ratios of $10 \leq P/k \leq 40$ were examined and it was established that flow resistance and heat transfer decreased monotonically as *P/k* was increased over this range. (For comparison, the helical ribs of

AGR fuel pins have $P/k \approx 5.5 – 6.5$, the exact value depending upon whether pitch is measured normal to the ribs or in the axial direction; Fairbairn, 2009.) The maximum value of relative roughness studied by Webb et al. was $k/D = 0.04$. They also proposed an empirical correlation for the heat-transfer roughness function based on the analogy between heat and momentum transfer.

Han, Glicksman and Rohsenow (1978) later conducted experiments on a rectangular channel with rib-roughened upper and lower walls. k/D_e (where D_e is the 'hydraulic diameter' and is defined as D_e = 4x[flow area]/[wetted perimeter]) was extended up to 0.102. The work of Han et al. encompassed an examination of the effect of rib cross-section on the flow thermal-hydraulics; it was established that rib profile had a significant effect on the flow resistance, but only a very limited effect on heat transfer. The influence of the rib shape on heat transfer, completely disappeared at higher Reynolds numbers ($10{,}000 < Re < 30{,}000$) where the flow was in a completely rough region.

Park et al. (1992) carried out experiments on 2-side ribbed rectangular channels to investigate the combined effects of the channel aspect ratio, rib angle-of-attack, and Reynolds number on heat transfer and pressure drop. The aspect ratio (width-to-height) was varied from 1/4 to 4 and the Reynolds number range was 10,000 to 60,000. Park et al. found that narrower channels (width-to-height < 1) have better heat transfer performance. It was also found that for $30{,}000 \leq Re \leq 60{,}000$, heat transfer levels and friction coefficients were only slightly increased.

Through a series of Laser Doppler Velocimetry (LDV) measurements made in a rectangular channel with ribs on two opposite walls, Liou et al. (1990; 1993b) studied the effects of Reynolds number as well as the P/k and k/D ratios. Those authors examined P/k ratios of 5, 10, and 15. It was found that the reattachment length behind the ribs varied only slightly with Reynolds number (within the range $12{,}000 \leq Re \leq$

120,000). It was further established that increasing the P/k ratio resulted in an increase in pressure loss. The value $P/k = 10$ was found to be optimal from the standpoint of heat transfer enhancement.

Okamoto et al. (1993) measured the flow structure over repeated two-dimensional square ribs, in this case mounted on one wall only. Data for mean velocity, static pressure, velocity vectors, turbulence intensity, and the integral scale were obtained. Okamoto et al. examined various P/k ratios ($2 \leq P/k \leq 17$) and found that turbulence intensity, heat transfer and pressure loss were all maximized at $P/k = 9$. Furthermore, their results indicated that the point of maximum heat transfer is nearly coincident with the reattachment point between ribs.

Taslim and Wadsworth (1997) conducted a series of tests in a square duct roughened with staggered 90° ribs. The objective was to investigate the effects of rib height (k/D_e = 0.133, 0.167 and 0.25), pitch-to-height ratio (P/k = 5, 7, 8.5 and 10) and Reynolds number (Re = 10,000 ~ 50,000). It was found that increasing the rib height results in an increase in heat transfer levels. It their experiments, $P/k = 8.5$ produced the highest heat transfer levels. Taslim and Wadsworth also showed that the overall thermal performance was decreased by increasing the Reynolds number.

The results presented in Chapter 6 of the present work have been generated mainly for comparison against the data of Rau, Çakan, Moeller and Arts (1998) who employed two geometrically (and dynamically) similar square cross-section test sections: a smaller one for heat transfer measurements and a larger version designed to give good resolution of the flow field. Air was the working fluid, and the Reynolds number based on the bulk velocity and equivalent diameter was fixed at Re = 30,000. In both cross-sections square ribs could be mounted on the lower surface only (‘1s’), or on both the lower and upper surfaces (‘2s’). In all cases, a large blockage ratio was imposed (k/H = 0.1) and the surfaces may be considered to have a high degree of roughness. Rau et al.

reported 1s channel results for P/k = 6, 9, and 12, while P/k was set to 9 in the 2s section.

As noted above, the flow channels studied experimentally by Rau et al. (1998), (and simulated in the present work and shown in Chapter 6), are very rough, with k/H = 0.1. Jiménez (2004) used an approximate analysis to show that roughness effects might be expected to extend well into the logarithmic region for flows in which $\delta/k \leq 40$ (or $k/\delta \geq 0.025$; δ is a boundary layer thickness or channel half-width). Jiménez suggested that flows with such high blockage ratios, might be better described as 'flows over obstacles' rather than 'classical' rough surface flows.

In relation to AGR fuel channels, Keshmiri et al. (2009) estimated on the basis of design data provided by Fairbairn (2009) that k/D_e is an order of magnitude less than the k/H value in the experiments of Rau et al. (1998). Nevertheless, the ratio of k to D_e in AGRs is still sufficiently high to raise the possibility that there will be significant restructuring of the logarithmic layer. (Also, the distance between adjacent fuel pins is somewhat less than D_e; consequently normalization of k by inter-pin distance will indicate a greater degree of relative roughness.)

More recent experiments include the hot-wire measurements of Krogstad, Andersson, Bakken and Ashrafian (2005) and the Particle Image Velocimetry (PIV) measurements of Lee, Kim and Sung (2008). These works focus on the effects of surface roughness on the turbulent Reynolds stresses and spatially-developing characteristics of rough wall boundary layers. In these experiments, the P/k and k/H ratios were fixed. One of the conclusions of Lee et al. was that the effective sand roughness height (k_s) is a more appropriate length scale for representing the extent of roughness effect rather than the roughness height (k). Jiménez (2004) plotted the equivalent sand roughness (k_s/δ) versus k/δ for d-type roughness and suggested that this

plot only partially supports the conclusion that k_s/δ is independent of the roughness dimension.

2.3.3 Numerical Works

In this section, the numerical studies of flow over two-dimensional rib-roughened surfaces are again divided into the following three categories: 1) DNS, 2) LES, and 3) RANS.

DNS

Direct numerical simulations of channel flows with only one wall roughened by rectangular ribs were performed by Miyake et al. (2001), Leonardi et al. (2003), Nagano et al. (2004) and Ikeda and Durbin (2007).

Miyake et al. (2001) studied two types of roughness: sand-grain roughness and two-dimensional transverse square rib roughness. In the rib-roughened case, the k/H ratio was fixed at 0.07. The authors showed that the major effect of the roughness elements was to enhance turbulent mixing and hence heat exchange. They also showed that away from the wall, both the mean velocity and thermal fields are little influenced by the condition of the wall surface but instead depends on total drag, except for the layer close to the wall where direct interference with roughness elements manifests itself.

Leonardi et al. (2003) carried out a similar DNS and presented results for Re = 4,200 and the k/H ratios of 0.1 and 0.2 (although only the results of k/H = 0.2 were reported). A wide range of pitch-to-height ratio ($1.33 \leq P/k \leq 20$) was studied and it was found that the minimum skin frictional drag and maximum form drag occurred at P/k = 8.

Again using a DNS approach, the effects of rib spacing, width and height on heat transfer and drag were studied by Nagano et al. (2004). It was found that for $P/k \geq 4$ (k-type roughness), increasing the rib height had the effect of increasing both heat transfer

and drag. However, decreasing the rib height, resulted in an enhancement in heat transfer with a small increase in drag, and the heat transfer characteristic improves i.e. the rib with the lowest height was the most efficient design. On the other hand, in the *d*-type roughness case, heat transfer characteristics could not be improved regardless of the rib spacing. The heat transfer augmentation was found to be smaller than that in the *k*-type roughness with the same roughness height.

Recently, Ikeda and Durbin (2007) performed a DNS study of rib-roughness in a channel flow where they computed and visualized detailed statistical and instantaneous data. They also studied a case with uneven rib heights (having ±15% height difference) to imitate random roughness. The *P/k* ratio was kept at 10 for both the even and uneven rib height cases. One of the conclusions Ikeda and Durbin drew from their work was that, similar to sand-grain roughness, two-dimensional rib roughness produces three-dimensional random motions of vortices that disturb the viscous sublayer. This is consistent with the findings of some earlier DNS works including those of Ashrafian et al. (2004) and Nagano et al. (2004).

A common feature of all the aforementioned computer simulations is that only one channel wall was roughened, while the other wall was assumed to be smooth. The rib height-to-channel height ratio (*k/H*) was typically between 5 to 10%. For the first time, however, Ashrafian et al. (2004; see also Ashrafian, 2004) performed a DNS of a pressure-driven turbulent channel flow where both walls were roughened by square rods with a height of only 1.7% of the channel height (*P/k* = 8). Their main objective was to examine the effects of roughness on the mean and turbulent flow fields and to see how far from the viscous sublayer these effects are felt. It was found that outside the roughness sublayer (i.e. $y > 5k$), no apparent streamwise variation of the mean velocity and second-order statistics could be observed. However, significant differences in the turbulence field were observed between smooth- and rough-wall layers.

In a similar work, Krogstad et al. (2005) investigated a fully turbulent channel flow with rib-roughened walls using both hot-wire anemometry and DNS and compared their results against a smooth channel. They showed that surface roughness does not affect the outer region, and, for both smooth and rough surfaces, the Reynolds stresses appeared to be very similar beyond $y \approx 5k$.

LES

One of the early LES studies was undertaken by Ciofalo and Collins (1992). They performed LES of a channel flow with and without transverse ribs on one of the walls. The authors employed a general-purpose code with a simple Smagorinsky model and van Driest damping near the walls. Relatively coarse grids were used in the simulations as the focus was on a demonstration of the feasibility of LES for simple and complex flows, rather than accuracy. Comparison was made against experimental data, k-ε predictions and large eddy simulations of Moin and Kim (1982). They found that the mean flow rate and the turbulence levels in the bulk flow region were over-predicted by LES when compared to experimental data and RANS simulations, while the overall flow structure was in reasonable agreement with data.

Cui, Patel and Lin (2003) used LES to investigate the effects of varying the P/k ratio in a channel with one wall roughened by square ribs. They tested P/k = 2, 5 and 10 to represent d- and k-type roughness, and an intermediate roughness between the two. They showed that LES can be used to identify the pressure and frictional components of resistance in a rib-roughened channel. However, no heat transfer results were reported.

More recently, Liu, Tucker and Iacono (2006) carried out a series of simulations using RANS and hybrid RANS/LES approaches. The three RANS models they used were the one-equation Spalart-Allmaras (S-A) model, the zonal k-l/EASM (Explicit Algebraic Stress Model) and a k-l/NLEVM (Non-Linear Eddy Viscosity Model). k-l modelling in the last two approaches was employed only in near-wall regions. Liu et al.

also used *k-l* based zonal LES (ZLES) method as well as a S-A based Detached Eddy Simulation (DES) approach. It was found that both ZLES and DES returned similar results and were capable of capturing complex unsteady flow features associates with flow separation and reattachment while the *k-l*/EASM model under-predicted the velocity and heat transfer, especially in the recirculation region. (Similar findings were reported by Bredberg and Davidson, 1999.) For heat transfer levels, the S-A model, despite its simplicity, returned results closest to the data.

RANS

There are a number of computational studies reported in the literature which employ high-Reynolds number turbulence models with wall functions; these include the works of Acharya et al. (1993), Liou et al. (1993a) and Prakash and Zerkle (1995). However, it is well known that application of wall functions which are based on the log-law is not suitable for separated flows with heat transfer (Launder, 1984; 1988).

Acharya et al. (1993) applied both the standard linear *k-ε* model of Launder and Spalding (1974) and a non-linear *k-ε* model due to Speziale (1987) to repeating two-dimensional rectangular ribs in a 1-sided rough channel and found that the performances of the two models were similar, although the non-linear model produced more realistic Reynolds stress distributions than the linear form in the region immediately above the ribs. Both models, however, under-predicted the local *Nu* distribution, a result that was attributed to the use of wall functions. Comparison with their own experimental data revealed that both models performed poorly in the recirculation region downstream of the ribs, which was thought to be due to the adoption of a constant turbulent Prandtl number.

Liou et al. (1993a) used the *k-ε-A* algebraic stress model (due to Rodi and Leschziner, 1981) with wall functions for both the turbulent stresses and heat fluxes. The algebraic model could reproduce both qualitatively and quantitatively the local *Nu*

distributions. They also found satisfactory agreement for mean velocity, turbulent kinetic energy, and temperature profiles when compared to their own interferometry data and the LDV measurements of Drain and Martin (1985). However, the model under-predicted the reattachment length for which the use of wall functions was again partially blamed.

Prakash and Zerkle (1995) using a high-Reynolds number k-ε model with a generalized wall function (due to Rosten and Worrell, 1988), predicted turbulent flow and heat transfer in a stationary and rotating rectangular channel with a 2:1 aspect ratio and with square ribs on the two shorter sides. The ribs were in a staggered arrangement and normal to the flow direction. For the stationary case, heat transfer results were compared against the correlation of Han (1988). For a range of Re = 30,000 – 90,000, Nusselt number was under-predicted by about 20% while the friction factor was over-predicted by about 25%.

Iacovides and Raisee (1999; 2001) examined the capabilities of the low-Reynolds-number LS model and second moment closures in predicting convective heat transfer in ribbed annular channels, pipes and plane channels. They showed that the most reliable results were obtained using the low-Reynolds-number second moment closures. The authors also obtained a more realistic variation of heat transfer levels in the separation region and by employing a differential form of the Yap length-scale correction term (originally introduced by Yap, 1987) in the ε-equation.

Apart from the LS model and second moment closures, Raisee (1999) applied two- and three-equation variants of the Non-Linear Eddy Viscosity Model (NLEVM) of Suga (1995; see also Craft, Launder and Suga, 1996b). Raisee showed that both these models need further refinements because severe problems with numerical stability were encountered. He investigated these problems and found that, for the two-equation non-linear k-ε model, the use of a C_μ function results in too high values of that term in

regions of recirculation. Later, Craft, Iacovides and Yoon (1999) carried out a numerical study to further improve this model by modifying the definition of C_μ; they also incorporated the differential form of Yap term (developed by Iacovides and Raisee, 1999). Later, Raisee, Noursadeghi and Iacovides (2004) used this new formulation of NLEVM (which they termed 'NLEVM2') to predict heat transfer in two-dimensional and axi-symmetric rib roughened passages. It was found that the heat transfer predictions of NLEVM2 were much closer to the data than the original NLEVM.

Ooi, Iaccarino, Durbin and Behnia (2002) carried out simulations of the flow and heat transfer in 3-dimensional rib-roughened ducts using the v^2-f and Spalart-Allmaras (S-A) turbulence models; they compared their results with the experimental data of Rau et al. (1998) and the k-ε simulations of Chen and Patel (1988). Configurations with various geometrical parameters including pitch, rib height, and cavity depth were considered. It was shown that, while the k-ε model severely underestimates heat transfer levels, the S-A model gave results that were closer to the experimental data, but nonetheless the computed values of Nu were still far from the measured values. The authors reported that heat transfer results generated by the v^2-f model were closest to the experimental values of Rau et al. (1998). However, none of the above models could capture the secondary flow structure which consequently led to incorrect predictions of Nu on the heated side wall.

Iaccarino, Ooi, Durbin and Behnia (2002) presented a detailed analysis of the capabilities of the v^2-f model in predicting heat transfer in rib-enhanced passages. It was shown that the computed average values of the Nusselt number closely matched the experimental data. However, local values of the Nusselt number very close to the ribs were strongly affected by the rib thermal boundary condition. Their numerical data showed that heat transfer is dominated by convection upstream and conduction downstream of the rib.

Manceau, Parneix and Laurence (2000) implemented the v^2-f model in an industrial code based on a finite element discretization. In this work, the v^2-f model was applied to a number of test cases including a 2D periodic ribbed-channel. Two different types of boundary condition at the rough wall were also applied. In the first type, the fluid problem was coupled with the conduction problem in the rib (i.e. closer to the physics, but more difficult to compute), while in the second type, the constant heat flux which was imposed at the lower face of the rib was equally distributed on the other faces. Both boundary conditions produced identical Nusselt number distributions, except on the rib faces and in the vicinity of the lower corners of the rib. (Similar observations were also reported by Iaccarino et al., 2002.) It was also shown that a very simple model for the heat fluxes is sufficient to successfully predict the Nusselt number distribution. Manceau et al. concluded that the v^2-f model is a good compromise between simplicity and accuracy for simulating separated flows and it is a robust turbulence model especially in estimating the near-wall turbulence anisotropy which is essential for reproducing the correct levels of heat transfer.

Bredberg and Davidson (1999) applied three different eddy viscosity models to a rib-roughened 2D channel. These turbulence models consisted of the two-layer k-ε model of Chen and Patel (1988) and two k-ω models, one of which was based on the original k-ω model of Wilcox (1988) and was termed, the 'ARG k-ω model' (due to Abid, Rumsey and Gatski, 1995), while the other one was similar to the LRN version of Wilcox (1993a) and was termed 'PDH k-ω model' (due to Peng, Davidson and Holmberg, 1997). Bredberg and Davidson found that although the results for the flow field were in good agreement with the data, none of these turbulence models could return satisfactory heat transfer results.

In a similar work, Bredberg, Davidson and Iacovides (2000), again applied the ARG k-ω model' (Abid et al., 1995), the two-layer k-ε model of Chen and Patel (1988),

and the LS model (with the Yap-term) to a periodic 2D channel with ribs on one wall. The aim of this work was to study the connection between flow field and heat transfer predictions. Comparison was made against two different experiments done by Nicklin (1998). It was found that the results of the k-ω and LS models were closer to the data.

Later, Bredberg, Peng and Davidson (2002) extended their work and modified the k-ω formulation in an attempt to improve its performance in recirculating flows. Comparison was made against the experimental data of Rau et al. (1998) and three other EVMs including the k-ε model of Abe, Kondoh and Nagano (1994), the k-ω model of Wilcox (1993a), and the v^2-f model of Lien and Kalitzin (2001). For the Nusselt number distribution, it was found that both their proposed model and the v^2-f model gave reasonable predictions, while the Wilcox k-ω model under-predicted the Nusselt number. Once again they confirmed that there exists a close connection between heat transfer and turbulence level.

Recently, Ryu, Choi and Patel (2007b) carried out a series of simulations using the k-ω model of Wilcox (1998) to obtain the resistance coefficient and velocity profile for a turbulent flow in channels with 2D ribs and 3D blocks. Various rib configurations were tested including ribs with square, triangular, semicircular, and wavy cross-sections over a range of rib pitch and Reynolds numbers. It was found that the k-ω model can successfully capture essential features of the flow. It was also found that the square and wavy ribs resulted in maximum and minimum resistance, respectively. This work was extended in Ryu, Choi and Patel (2007a) to study heat transfer from these rough surfaces, where the k-ω-θ^2-ε_θ model was applied with near-wall treatment for velocity and temperature fields. It was found that the geometry with the highest average Nusselt number corresponds to that of a maximum resistance coefficient for both 2D ribs and 3D blocks.

Very recently, Kamali and Binesh (2008; 2009) have used the *k-ω-SST* model to study the effects of the Reynolds number, *P/k* ratio and the rib shape in 2D rib-roughened channels. Four different rib shapes were tested including a square, triangular, trapezoidal with a decreasing height in the flow direction, and a trapezoidal with an increasing height in the flow direction. It was shown that the heat transfer coefficient is strongly affected by the rib shape and was also found that the trapezoidal shaped rib with a decreasing height in the flow direction had the highest value of heat transfer, while, the trapezoidal shaped rib with an increasing height in the flow direction had the lowest friction factor. In Kamali and Binesh (2009), the effects of having grooves in the space between the ribs were tested and it was shown that these grooves can lead to an increase in heat transfer coefficient. It should be noted however, that Kamali and Binesh (2008; 2009) did not compare their results with any experimental or DNS data.

2.4 AGR FUEL ELEMENTS

2.4.1 Introduction

In this section, attention is restricted to the works which were done directly on AGR fuel elements. In the past 6 decades, a number of experimental works have been carried out on various designs of AGR fuel elements, mostly by the UK Atomic Energy Authority (UKAEA) and the British Energy. Most of these experiments were based on measurements of heat transfer and pressure drop from annuli with heated roughened inner and unheated smooth outer surface. As there are currently no numerical works on three-dimensional AGR fuel elements, only the available experimental works are reviewed here.

2.4.2 Experimental Works

One of the earliest experiments in this field was carried out by Wilkie (1966). In a single-start transverse rib-roughened fuel pin, Wilkie tested the effects of varying the rib height ($0.1 < k/D_e < 1.6$), P/k ratio ($2.5 < P/k < 50$), rib profile, rib width, rib helix angle and the Reynolds number. In this work, the transformation method of Hall (1962) waas applied which permitted the measurements of heat transfer and friction for a roughened surface to be isolated from those for a passage with mixed surfaces. One of the conclusions drawn from Wilkie's work was that although the value of P/k giving the maximum heat transfer rate varies with k/D_e and Re, at large k/D_e, the maximum heat transfer occurs at $P/k \approx 6$, irrespective of Re. It was also found that slight chamfering of very sharp ribs reduced friction coefficient by 6-8%, while further chamfering or rounding had no more effects. The Hall transformation was also found to be wholly invalid in this experiment.

In a similar experiment, White and Wilkie (1967) measured heat transfer and friction factor over a range of Reynolds number (Re = 60,000 - 200,000) for eight tubes roughened externally by square-section wires in the form of single-start and multi-start rib design (number of starts included 1, 4, 10, and 16). White and Wilkie studied the effects of varying the P/k ratio (P/k = 8 & 16) as well as the rib helix angle (3° to 63°) and found that the heat transfer and the friction coefficient fall off with increasing the helix angle (i.e. increasing the number of starts). However, since the friction coefficient falls off more rapidly, there is generally a gain in thermal performance. It was estimated that the maximum gain of approximately 6% to occur at P/k = 8 and Re = 200,000. These findings played a major role in making the decision of replacing the single-start fuel pins by the multi-start ones.

A few years later, Wilkie (1983b; a) carried out new experiments to compare the single- and multi-start design to a design with longitudinal fins with approximately

triangular cross-section (Figure 2.5) and listed some of the advantages and disadvantages of each design. In comparing transverse and multi-start designs, Wilkie found that the principal advantage of the multi-start configuration is that the much enhanced coolant mixing of heat due to swirl induced by the ribs, reduced across-channel temperature gradients and hence reduced peak temperature. In addition, hotspots in the 'anti-stacking grooves'* were eliminated. The good mixing also flattened out the coolant temperature profiles in all channels making the tie-bar cooler. Since the ribs were higher, they were less sensitive to any rib wear, rib oxidation and deposition while their strength was increased. Also, the can† temperatures were less sensitive to pin displacement (due to pin bow). The only certain disadvantage of the multi-start design was the increased neutron absorption, although this could be offset by a small reduction in can thickness or by reducing the rib width.

Some of the works done by the British Energy on the AGR fuel elements were reported in Pirie (1987), Morrison (2003) and Gotts and Xu (2006).

Pirie (1987) carried out tests to measure the pressure drop of a fuel element containing multi-start fuel pins. The measurements were used to calculate the resistance of a complete stringer. Comparison was also made with the recommended value of resistance of the same fuel element but with transverse fuel pins. One of the main findings of this work was that the flow resistance of the stringers with multi-start and transverse fuel pins were found to be nearly the same for most of the flow range with the maximum difference of 2.2%.

Recently, in an attempt to optimize the fuel resistance of the multi-start fuel elements, Morrison (2003) calculated the effects of the followings:

* 'Anti-stacking grooves', as shown in Figure 1.2, are indentations which are spaced along the length of each fuel pin. For transverse design, the spacing between these grooves is usually about 80 mm.

† 'Can' is a commonly referred name for a fuel pin.

1) Slightly increasing the sleeve bore (i.e. widening the bore of the graphite sleeve). This results in achieving higher mass flow rate without increasing the peak of pressure drop (i.e. dome ΔP).
2) Replacing the fabricated streamlined brace with the machined streamlined brace. The lower resistance of the latter will give a small increase in the mass flow rate, which in this case is accompanied by an increase in the velocity of the coolant flow.
3) Using thinner and optimized can walls. This would be expected to increase the free flow area of the fuel channel, hence reducing resistance.

Calculations of Morrison showed that, by incorporating the above changes to the fuel element, the fuel resistance can be reduced by 19%. However, in practice, none of these changes were made to the existing AGRs (Gotts, 2009).

On the other hand, one of the current problems with the AGR fuel elements is associated with the carbon particle deposition on fuel pins which results in heat transfer impairment and in turn higher fuel pin temperatures. Recently, Gotts and Xu (2006) investigated this problem in details with the aim of understanding the nature of the problem and recommending a way to resolve it. In general, carbon deposition acts through two basic mechanisms:

1) The carbon forms an insulating layer across which there is a temperature gradient i.e. 'insulating effects'
2) The carbon, if it deposits more in the space between the ribs than on the rib tips, reduces the effective rib height i.e. 'rib height effect'. According to Gotts (2009), the deposition between the ribs ranges from 16 to 200 μm, while the deposition on the rib tips, is usually about 2/3 of that between the ribs. There is also a weak effect from changing the rib profile and rib width but these have been shown to be small (Mantle, 1985). In Chapter 6, the effects of changing the

rib height, rib width, and the rib profile are further discussed, in the context of the 2D rib roughness.

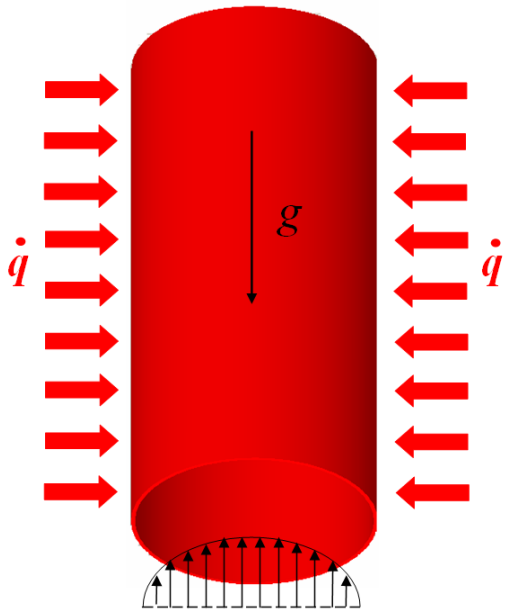

Figure 2.1 – Schematic diagram of ascending mixed convection flow.

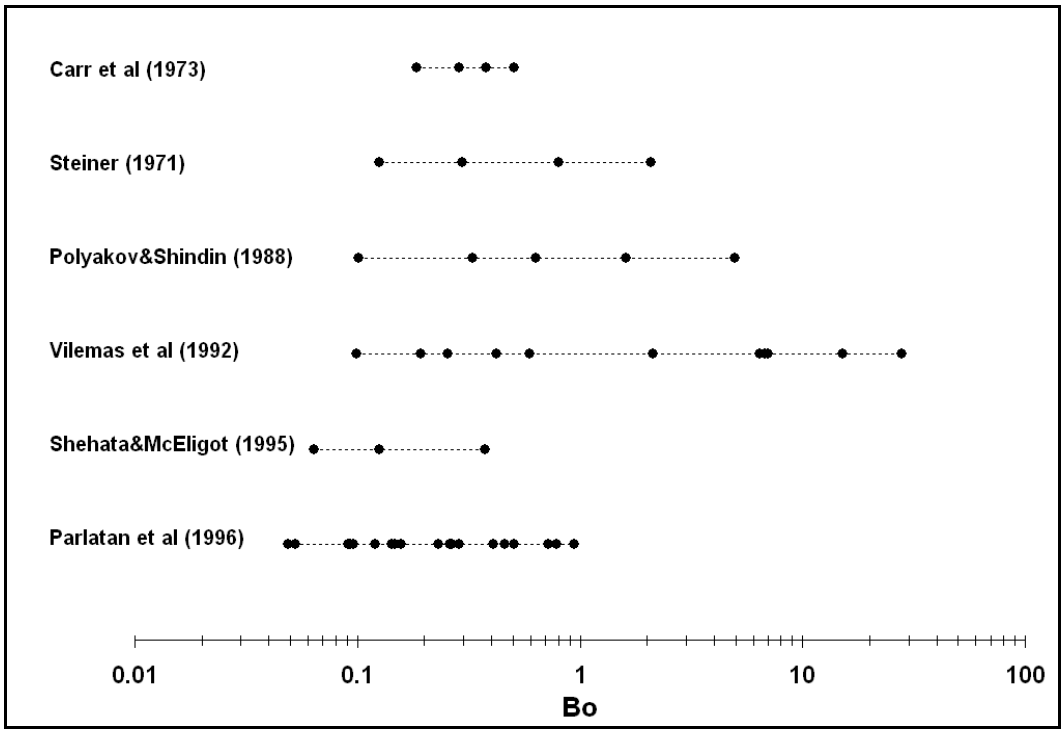

Figure 2.2 – Range of Buoyancy influence encompassed by mixed convection data.

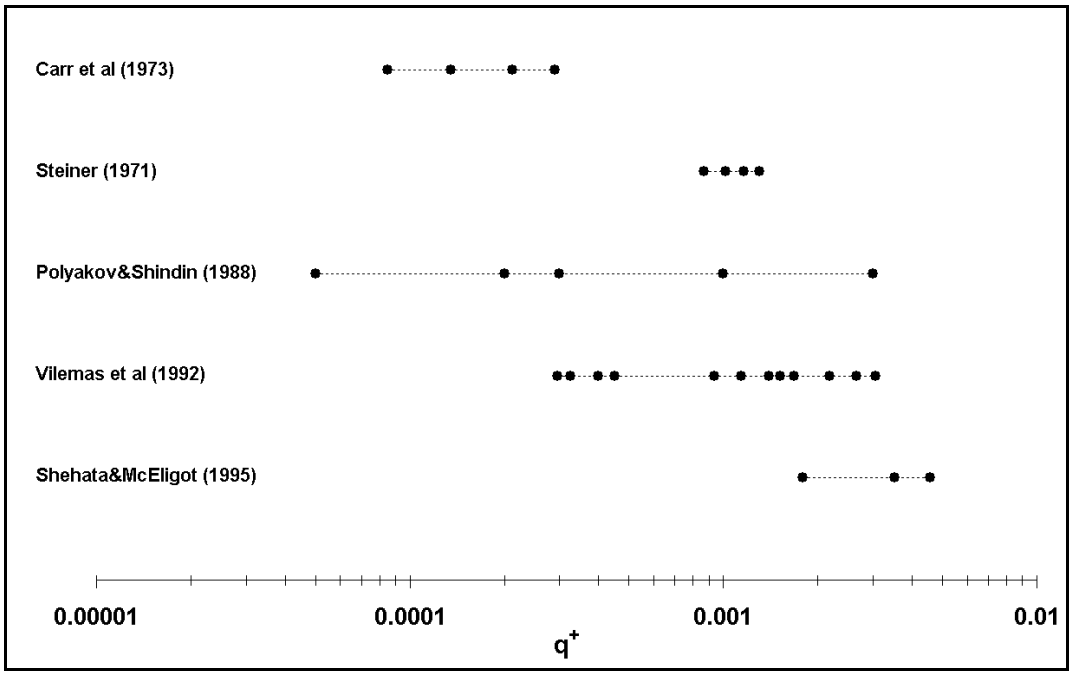

Figure 2.3 – Range of heat loading parameter encompassed by mixed convection data.

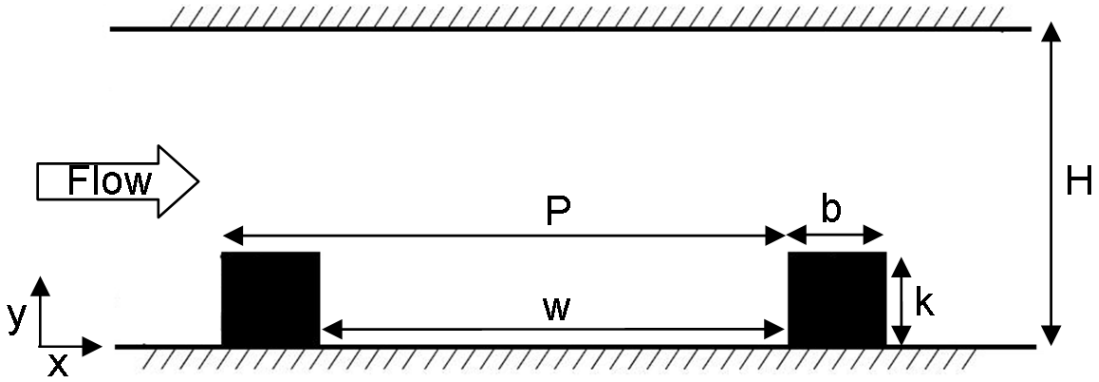

Figure 2.4 – Schematic diagram of a rib-roughened surface.

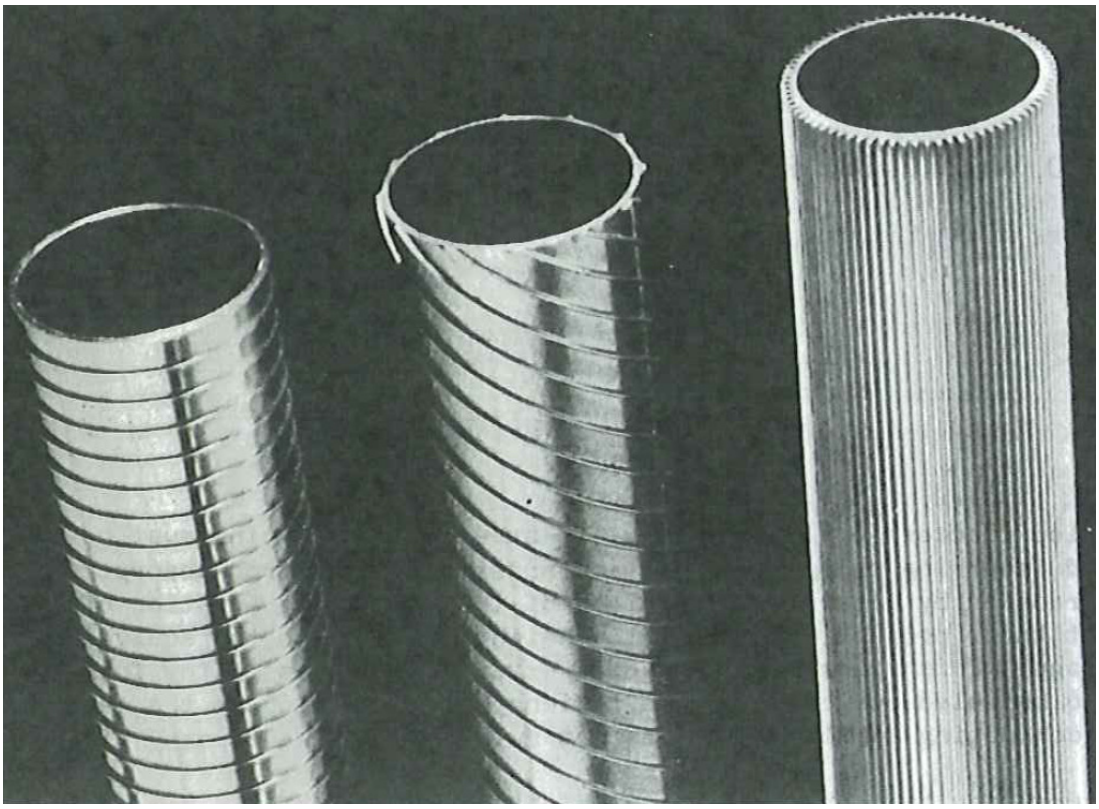

Figure 2.5 – Schematics of transverse-ribbed, multi-start ribbed and longitudinally finned fuel pins (from Wilkie, 1983b)

CHAPTER 3

MATHEMATICAL MODELLING OF TURBULENCE

3.1 PRELIMINARY REMARKS

The presence of turbulence significantly affects the dynamic and thermal fields of a flow, and since most of industrial problems are of a turbulent nature, it is very important to devise an efficient method to model these effects. This chapter generally focuses on Reynolds-Averaged Navier-Stokes (RANS) modelling which remains the most common method of dealing with turbulence within the framework of CFD. Firstly, the Navier-Stokes equations are introduced followed by a description of the basics of the RANS approach. Next Eddy Viscosity Models are introduced. Some of the methods used to take near-wall effects into account are then briefly discussed. Finally, the specific turbulence models used in the present study are described in detail.

3.2 NAVIER-STOKES EQUATIONS

The Navier-Stokes equations (named after two 19th century scientists, Claude-Louis Navier and George Gabriel Stokes) are the fundamental partial differential equations that describe the motion of a fluid. They are obtained by applying Newton's Law of Motion and linear stress/strain relationship to a fluid element. In general, for a Newtonian fluid, the continuity, momentum, and energy equations can be written in tensor notation as

$$\frac{\partial}{\partial t}\left(\tilde{\phi}\right)+\frac{\partial}{\partial x_j}\left(\tilde{U}_j\tilde{\phi}\right)=\frac{\partial}{\partial x_j}\left(\Gamma_\phi\frac{\partial\tilde{\phi}}{\partial x_j}\right)+S_\phi \tag{3.1}$$

where $\tilde{\phi}$ represents a variable and Γ_ϕ and S_ϕ are the diffusion coefficient and source term, respectively. $\tilde{U}_j$ is the velocity component in the x_j direction. (Note that the tilde indicates an instantaneous value.) Table 3.1 indicates the equivalence of ϕ, Γ_ϕ and S_ϕ in the continuity, momentum, and energy equations.

Equation	ϕ	Γ_ϕ	S_ϕ
Continuity	1	0	0
Momentum	U,V,W	ν	$-(1/\rho)(\partial P/\partial x_i)$
Energy	T	ν/Pr	0

Table 3.1 – Variables appearing in the Navier-Stokes Equations

These equations can be expressed for an incompressible flow as follows:

$$\frac{\partial\tilde{U}_j}{\partial x_j}=0 \tag{3.2}$$

$$\frac{\partial\tilde{U}_i}{\partial t}+\frac{\partial}{\partial x_j}\left(\tilde{U}_j\tilde{U}_i\right)=\left(-\frac{1}{\rho}\frac{\partial\tilde{P}}{\partial x_i}\right)+\frac{\partial}{\partial x_j}\left(\nu\frac{\partial\tilde{U}_i}{\partial x_j}\right) \tag{3.3}$$

$$\frac{\partial \tilde{T}}{\partial t} + \frac{\partial}{\partial x_j}\left(\tilde{U}_j \tilde{T}\right) = \frac{\partial}{\partial x_j}\left(\frac{\nu}{Pr}\frac{\partial \tilde{T}}{\partial x_j}\right) \tag{3.4}$$

These equations can be solved analytically for some laminar flows. They can also be solved directly using DNS. As discussed earlier, this approach is extremely expensive in terms of computational storage and CPU time and therefore, has only very limited industrial application. An alternative approach is to average the instantaneous Navier-Stokes equations to obtain RANS equations, and this is discussed below in more detail.

3.3 REYNOLDS-AVERAGED NAVIER-STOKES (RANS) EQUATIONS

A turbulence model is a mathematical formulation used to close the system of mean flow equations. It is desirable that a turbulence model should have a broad range of applicability, while also being as simple as possible. For most engineering purposes it is unnecessary to resolve the details of the turbulent fluctuations and only a statistical description of the flow, and the effects of the turbulence on the mean flow are usually sought. One of the most common methods of computationally modelling turbulent flows is known as the 'Reynolds Averaged Navier-Stokes' (RANS) approach which is based on time-averaging the Navier-Stokes equations. The Reynolds decomposition of the instantaneous velocities $\tilde{U}_i$, pressure $\tilde{P}$, and temperature $\tilde{T}$ into averaged and fluctuating parts can be written as

$$\tilde{U}_i = U_i + u_i \qquad \tilde{P} = P + p' \qquad \tilde{T} = T + \theta \tag{3.5}$$

where the upper case symbols represent the mean quantities, and u_i, p' and θ correspond to the fluctuating part. The mean of velocity, pressure and any scalar quantities can be defined as

$$\overline{\phi}(x_i) = \lim_{T\to\infty} \frac{1}{T}\int_0^T \tilde{\phi}(x_i, t)dt \tag{3.6}$$

Now, by taking the average of Eqns. (3.2)-(3.4) and replacing the flow variables in these equations by the mean and fluctuating parts (obtained by the Reynolds decomposition), the RANS equations are obtained as

$$\frac{\partial U_i}{\partial x_i} = 0 \tag{3.7}$$

$$\frac{\partial U_i}{\partial t} + \frac{\partial}{\partial x_j}\left(U_j U_i\right) = -\frac{1}{\rho}\frac{\partial P}{\partial x_i} + \frac{\partial}{\partial x_j}\left(\nu\frac{\partial U_i}{\partial x_j} - \overline{u_i u_j}\right) \tag{3.8}$$

$$\frac{\partial T}{\partial t} + \frac{\partial}{\partial x_j}\left(U_j T\right) = \frac{\partial}{\partial x_j}\left[\frac{\nu}{Pr}\frac{\partial T}{\partial x_j} - \overline{u_j\theta}\right] \tag{3.9}$$

For the two-dimensional, incompressible and steady flows considered in the present work, the above equations are re-written as follows:

Continuity: $$\frac{\partial U}{\partial x} + \frac{\partial V}{\partial y} = 0 \tag{3.10}$$

U-Momentum: $$\frac{\partial}{\partial x}(UU) + \frac{\partial}{\partial y}(UV) = -\frac{1}{\rho}\frac{\partial P}{\partial x} + \left[\frac{\partial}{\partial x}\left(\nu\frac{\partial U}{\partial x} - \overline{uu}\right) + \frac{\partial}{\partial y}\left(\nu\frac{\partial U}{\partial y} - \overline{uv}\right)\right] \tag{3.11}$$

V-Momentum: $$\frac{\partial}{\partial x}(UV) + \frac{\partial}{\partial y}(VV) = -\frac{1}{\rho}\frac{\partial P}{\partial y} + \left[\frac{\partial}{\partial x}\left(\nu\frac{\partial V}{\partial x} - \overline{uv}\right) + \frac{\partial}{\partial y}\left(\nu\frac{\partial V}{\partial y} - \overline{vv}\right)\right] \tag{3.12}$$

Energy: $$\frac{\partial}{\partial x}(UT) + \frac{\partial}{\partial y}(VT) = \frac{\partial}{\partial x}\left[\frac{\nu}{\mathrm{Pr}}\frac{\partial T}{\partial x} - \overline{u\theta}\right] + \frac{\partial}{\partial y}\left[\frac{\nu}{\mathrm{Pr}}\frac{\partial T}{\partial y} - \overline{v\theta}\right] \tag{3.13}$$

The left-hand sides of Eqns. (3.11) and (3.12) represent the convective terms, while the right-hand sides consist of the pressure gradient, the diffusive terms (containing viscous effects), and the turbulent Reynolds stresses. One of the drawbacks of RANS equations is that information is lost in the averaging process which gives rise to the appearance of the Reynolds stress tensor $\overline{u_i u_j}$ and thus, it is the role of turbulence models to provide an approximation to these terms. Similarly, the turbulent heat fluxes

$\overline{u_j\theta}$ which appear in the Energy Equation, Eqn. (3.13) need to be modelled too. Generally, there are two major types of turbulence models for closing RANS equations: Eddy Viscosity Models (EVMs) and Reynolds Stress Models (RSMs). The basis for the vast majority of common turbulence models stems from the Eddy Viscosity model which is discussed below. In an Eddy Viscosity Model, the Reynolds stresses and turbulent heat fluxes are directly linked to the local gradients of the mean flow field through a turbulent viscosity and diffusivity, where the turbulent viscosity itself is determined by a characteristic velocity- and length-scale. The choice of scales is wide, ranging from prescribed diffusivity profiles to widely-used two-equation models.

On the other hand, Reynolds Stress Models (also known as the Second-Moment Closure) focus directly on the transport equations for the Reynolds stresses rather than supposing the stress and strain fields to be directly linked via an eddy viscosity. RSMs require the solution of seven transport equations, one for each of the Reynolds stresses themselves, and an additional equation to obtain the length-scale of the local turbulence. Despite higher computational costs compared to the EVMs, Reynolds Stress Models have shown to perform successfully in more complex flows where the stress field is highly anisotropic. However, the focus of the present work is restricted only to the EVMs and therefore RSMs are not discussed here any further, although the interested reader is referred to Launder et al. (1975) and Launder (1989) for more information.

3.4 EDDY VISCOSITY MODELS (EVMS)

3.4.1 Introduction

In Eddy Viscosity Models (EVMs) the Reynolds stress tensor is modelled by the Boussinesq hypothesis (see Pope, 2000) which assumes the turbulent stress to be proportional to the mean strain rate, via an 'eddy viscosity', ν_t, that is

$$-\overline{u_i u_j} = 2\nu_t S_{ij} - \frac{2}{3} k \delta_{ij} \tag{3.14}$$

where δ_{ij} is the Kronecker delta (which is equal to 1 when i and j are equal, and zero otherwise) and k is the turbulent kinetic energy. The mean strain rate tensor, S_{ij}, is defined as

$$S_{ij} = \frac{1}{2}\left(\frac{\partial U_i}{\partial x_j} + \frac{\partial U_j}{\partial x_i} \right) \tag{3.15}$$

Currently, there are many different turbulence models for calculating the turbulent viscosity: zero-, one- and two-equation models, which are discussed below in more detail. It should be noted that in contrast to the molecular viscosity, ν, the eddy viscosity, ν_t, is dependent on local flow conditions. One can also define the effective viscosity as

$$\nu_{eff} = \nu + \nu_t \tag{3.16}$$

Replacing the molecular viscosity by the effective viscosity in the Navier-Stokes equations is helpful in numerical terms. The practice tends to improve numerical stability by introducing additional diffusivity into the momentum equation.

The Reynolds stress tensor, $\overline{u_i u_j}$, is a three-by-three matrix:

$$\overline{u_i u_j} = \begin{bmatrix} \overline{uu} & \overline{uv} & \overline{uw} \\ \overline{vu} & \overline{vv} & \overline{vw} \\ \overline{wu} & \overline{wv} & \overline{ww} \end{bmatrix} \tag{3.17}$$

The normal stresses (i.e. $\overline{uu}$, $\overline{vv}$, and $\overline{ww}$) are always zero or positive since they include squared velocity fluctuations. An isotropic state is when these normal stresses have the same value and are equal to 2/3 of the turbulent kinetic energy i.e. $\overline{uu} = \overline{vv} = \overline{ww} = 2/3k$. Therefore, it would be useful to introduce a parameter representing deviation from isotropic state. This parameter is called ‘stress anisotropy tensor’, a_{ij}, and is defined as

$$a_{ij} = \frac{\overline{u_i u_j}}{k} - \frac{2}{3}\delta_{ij} \tag{3.18}$$

The linear EVM assumes that the anisotropy is determined by the local velocity gradients. This means that in simple shear flows, this term depends on the only non-zero component of Reynolds stress i.e. $\overline{uv}$. Despite this apparently major simplification, EVMs have proved to be robust in many flow problems, except in flows with strong anisotropy, where these models struggle to return accurate results.

3.4.2 Zero-Equation Models

One of the simplest approaches to calculate ν_t is via the so-called 'Mixing Length Hypothesis' (MLH) introduced by Prandtl in 1925 (see Pope, 2000):

$$\nu_t = {l_m}^2 \sqrt{\left(\frac{\partial U_i}{\partial x_j} + \frac{\partial U_j}{\partial x_i}\right)^2} \tag{3.19}$$

where l_m is an algebraic expression for a turbulence length-scale and can be approximated using a simple linear relationship, $l_m = \kappa\, y$; the product of the von Kármán constant, $\kappa = 0.41$, and the wall distance. The MLH is also known as a zero-equation model because it has no additional transport equations. In fact, zero-equation models are over-simplistic and are not appropriate for more complex flows. In addition, the MLH depends on wall distance and thus in regions where the velocity gradients become zero, Eqn. (3.19) incorrectly returns $\nu_t = 0$.

van Driest proposed the inclusion of a damping function to account for the reduction in the length-scale as a solid boundary is approached. Thus, the mixing length becomes

$$l_m = \kappa\, y\left(1 - \exp\left(\frac{-y^+}{26}\right)\right) \tag{3.20}$$

where $\kappa = 0.41$ is the van Driest constant; $y^+ = y\,u_\tau / \nu$ is the non-dimensional distance from the wall; $u_\tau = \sqrt{\tau_w / \rho}$ is the friction velocity and $\tau_w = \mu(dU/dy)_{wall}$ is the wall shear stress. Figure 3.1 shows the variation of the mixing length against the distance from the wall.

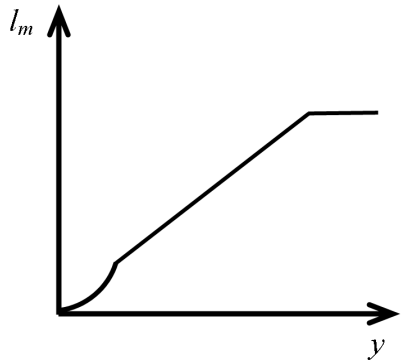

Figure 3.1 – Variation of the mixing length with distance from the wall.

3.4.3 One-Equation Models

In order to allow turbulence to be non-zero in regions where source terms may be zero, it was proposed solving a differential transport equation for at least one turbulence scale and thus eliminating the need to prescribe a velocity-scale. These models became known as one-equation models. In 1945, Prandtl proposed a one-equation model which calculated the turbulent viscosity through

$$\nu_t = C_\mu\, k^{1/2}\, l \tag{3.21}$$

where C_μ is a constant, k is the turbulent kinetic energy (for which a transport equation is solved) and the algebraic prescription of the length-scale, l, is analogous to that of the mixing length, l_m. However, similar to zero-equation models, this model is not reliable for situations where the prescription of the length-scale is complex, e.g. in recirculating and separating flows.

One of most popular one-equation models was proposed by Spalart and Allmaras (1992). They used a transport equation for the eddy viscosity in order to over-come the

above problem. Although this model has been applied to many aerospace applications, the problem of prescribing the length-scale still exists, which yields inaccurate results for recirculating and separating flows.

3.4.4 Two-Equation Models

As was mentioned earlier, in many flow problems which one would encounter in CFD, the convection and diffusion of turbulence quantities cannot be ignored and thus prescription of the length-scale becomes infeasible. As a result, two-equation models evolved out of the desire to eliminate the need to prescribe the turbulent length-scale in an ad hoc manner. Two-equation models employ a differential transport equation for the length-scale as well as one for the velocity-scale. Many two-equation models have been proposed in the past few decades, most of which solve the transport equation for k and some other turbulent quantity that can be used to calculate the turbulent viscosity. Therefore, these models differ mainly in the choice of the second variable. Some models solve a transport equation for the rate of dissipation of turbulent kinetic energy, ε, as the second variable, while others use the turbulent frequency, ω (where $\omega \sim \varepsilon / k$). There are further models that solve directly for the k and turbulent-length scale, l, or for k and turbulent dissipation time (Wilcox, 1993b).

In the standard k-ε model (due to Launder and Spalding, 1974), the eddy viscosity is calculated as

$$\nu_t = C_\mu \frac{k^2}{\varepsilon} \tag{3.22}$$

where C_μ is a constant.

As was noted before, most k-ε models are based on model transport equations for k and ε. The transport equation for k is derived from the exact equation, while the model

transport equation for ε is obtained using physical reasoning and bears little resemblance to its exact equation obtained from the Navier-Stokes equations.

The standard k-ε model of Launder and Spalding is a High-Reynolds-Number (HRN) model and it assumes that the flow is fully turbulent, and that the effects of molecular viscosity are negligible, i.e. this model should only be used for wall-bounded flows outside the viscous sub-layer. The modelled transport equations for k and ε, in the HRN form are given as

$$\frac{Dk}{Dt} = \frac{\partial}{\partial x_j}\left[\frac{\nu_t}{\sigma_k}\frac{\partial k}{\partial x_j}\right] + P_k - \varepsilon \tag{3.23}$$

$$\frac{D\varepsilon}{Dt} = \frac{\partial}{\partial x_j}\left[\frac{\nu_t}{\sigma_\varepsilon}\frac{\partial \varepsilon}{\partial x_j}\right] + C_{\varepsilon 1}\frac{\varepsilon}{k}P_k - C_{\varepsilon 2}\frac{\varepsilon^2}{k} \tag{3.24}$$

where the substantive derivative for a variable ϕ is defined as

$$\frac{D\phi}{Dt} = \frac{\partial \phi}{\partial t} + U_k\frac{\partial \phi}{\partial x_k} \tag{3.25}$$

and the production of turbulent kinetic energy, P_k, is expressed as

$$P_k = -\overline{u_i u_j}\frac{\partial U_i}{\partial x_j} \tag{3.26}$$

The generally accepted set of coefficients in the standard k-ε model is given in Table 3.2.

C_μ	$C_{\varepsilon 1}$	$C_{\varepsilon 2}$	σ_k	σ_ε
0.09	1.44	1.92	1.0	1.3

Table 3.2 – Constants appearing in the standard k-ε model.

These coefficients have been optimized over a range of benchmarked turbulent flows. C_μ is defined empirically based on flow under local equilibrium conditions and it is usually taken to be 0.09. The value of $C_{\varepsilon 1}$ has significant effects on the spreading

rates of free-shear flows and therefore it is set by computer optimization by calibration against free flows, whereas $C_{\varepsilon 2}$ is independently fixed from considering the decay of grid turbulence.

Despite its shortcomings, the k-ε model is far superior to zero- and one-equation models and remains very widely used. It was the first complete turbulence model that could be solved in general flow configurations without the need for ad hoc assumptions that depend on geometry. A major criticism, however, is its reliance on the Boussinesq eddy viscosity hypothesis. It is now well accepted that the eddy viscosity should be anisotropic and is only theoretically justified for turbulent flows that are close to equilibrium.

All the above two-equation models belong to the Linear Eddy Viscosity Model (LEVM) category, in which Reynolds stress anisotropy is directly linked to the mean strain rates (see Eqn. (3.18)), which naturally results in $a_{ij} = 0$ when the strain rate goes to zero. LEVMs also tend to return incorrect normal stress anisotropy even in simple shear flows. An alternative approach to overcome these problems is to define the anisotropy tensor a_{ij} explicitly as a non-linear function of the strain and vorticity terms. This was a starting point in development of what later became known as Non-Linear Eddy Viscosity Models (NLEVMs). Pope (1975) first proposed a more general expression for the anisotropy tensor and showed that if a_{ij} is exclusively dependent on strain tensor, S_{ij}, and vorticity tensor, Ω_{ij}, it can be expressed as follows:

$$\begin{aligned} a_{ij} &= \beta_1 S_{ij} + \beta_2 \left(S_{ik}\Omega_{kj} - \Omega_{ik}S_{kj} \right) + \beta_3 \left(S_{ik}S_{kj} - 1/3 S_{lk}S_{kl}\delta_{ij} \right) \\ &+ \beta_4 \left(\Omega_{ik}\Omega_{kj} - 1/3 \Omega_{lk}\Omega_{kl}\delta_{ij} \right) + \beta_5 \left(\Omega_{il}S_{lm}S_{mj} - S_{il}S_{lm}\Omega_{mj} \right) \\ &+ \beta_6 \left(\Omega_{il}\Omega_{lm}S_{mj} - S_{il}\Omega_{lm}\Omega_{mj} - 2/3 S_{lm}\Omega_{mn}\Omega_{nl}\delta_{ij} \right) \\ &+ \beta_7 \left(\Omega_{ik}S_{kl}\Omega_{lm}\Omega_{mj} - \Omega_{ik}\Omega_{kl}S_{lm}\Omega_{mj} \right) \\ &+ \beta_8 \left(S_{ik}\Omega_{kl}S_{lm}S_{mj}\Omega_{mj} - S_{ik}S_{kl}\Omega_{lm}\Omega_{mj} \right) \\ &+ \beta_9 \left(\Omega_{ik}\Omega_{kl}S_{lm}S_{mj} + S_{ik}S_{kl}\Omega_{lm}\Omega_{mj} - 2/3 S_{kl}S_{lm}\Omega_{mn}\Omega_{nk}\delta_{ij} \right) \end{aligned} \tag{3.27}$$

where the coefficients β_i may be defined as functions of k, ε and ν_t.

NLEVMs have been adopted since they not only have the relative simplicity of LEVMs, but also have the ability to account for the effects of turbulence anisotropy in complex strain fields. In fact, the computing times required for the NLEVMs are typically only 10% more than that of LEVMs. One of the more recent formulations of a NLEVM was proposed by Craft, Launder and Suga (1996b) which introduced quadratic and cubic functions of strain rate and vorticity.

It should be noted that, while all the turbulence models used in the present work belong to the class of two-equation EVMs, each has a different physical parameterization. Consequently, as will be seen in Chapters 5 and 6, each model responds differently to externally-imposed conditions. This makes it difficult to evaluate the overall performance of the two-equation models as a whole. Therefore, one of the goals of the present work is to identify which turbulence model returns the most accurate results in two different flow problems, both having applications to the Gas-cooled Reactors, namely mixed convection heat transfer in vertical flows, and recirculating flows in 2D and 3D rib-roughened channels.

Details of all the turbulence models used in the present work are given in Section 3.6.

3.5 NEAR-WALL TREATMENTS

3.5.1 Introduction

The presence of solid wall along with no-slip condition has significant effects on a turbulent boundary layer, since viscous stresses become dominant (compared to the turbulent stresses) in the near-wall regions. Near-wall regions are low-Reynolds-number zones and accurate resolution of these is generally desirable in highly non-equilibrium flows, or in computing heat transfer problems. Thus, the method of dealing with these

wall effects can significantly affect the overall performance of any turbulence model. In general, the effects of the wall can be divided into the following two categories:

1) Dynamic effects
   1) No-slip condition which results in large tangential mean velocity gradients in the near-wall region.
   2) Low-Reynolds-number effects which results in the largest and smallest scales of turbulence having the same order; the assumption of isotropic dissipation becomes invalid.
   3) Two-component nature of turbulence as the wall is approached which implies that $v'v' \sim y^4$ while $u'u'$ and $w'w' \sim y^2$. This is achieved by exploring the wall-limiting behaviour of u', v', w' using Taylor series expansion and then applying the continuity equation would result in $\partial v'/\partial y = 0$.

2) Non-local effects
   1) Wall blocking effects: The impermeability condition at the wall implies $V = 0$ which affects the flow via the pressure field, i.e. damping of the normal fluctuations results in an increase in the pressure that can be felt up to an integral length-scale away from the wall (Manceau, Wang and Laurence, 2001).
   2) Wall reflection (or echo) effects: In the near-wall regions, the pressure correlations have two contributions, one due to the free-space Green's function and the second one is called 'wall reflection' effects which is due to the contribution of the 'image points' on the other side of the wall (Pope, 2000).

In relation to the wall effects on turbulent boundary layer, as shown in Figure 3.2, one can divide turbulent boundary layers into four regions:

1) The 'Viscous Sub-Layer': This is a very thin layer (typically $y^+ < 5$) across which there are only limited turbulent fluctuations and inertial effects can be neglected when compared to viscous effects. In this layer, the mean velocity profile has a universal form, which follows the relationship $U^+ = y^+$.

2) The 'Buffer Layer': In this layer ($5 < y^+ < 30$), the turbulent eddies are quickly damped and consequently turbulent shear stresses are lower than the viscous stresses. This is essentially a transition region between the viscosity-dominated and the turbulence-dominated parts of the flow.
3) The 'Inner Region': In this region ($30 < y^+ < 50$), the size of the turbulent eddies is proportional to wall distance.
4) The 'Outer Region': In this region ($y^+ > 50$), the size of the turbulent eddies is constant (independent of the Reynolds number) and proportional to the thickness of the boundary layer, δ.

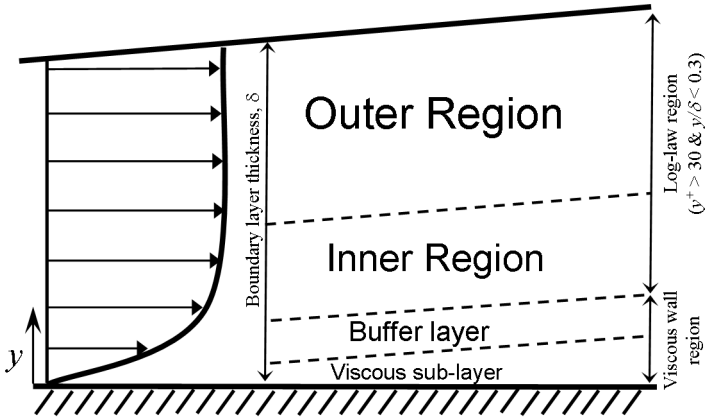

Figure 3.2 – Schematic of various wall regions and layers in a boundary layer (adapted from Iacovides, 2006).

In the boundary layer there exists a region known as the 'log-law region' ($y^+ > 30$ & $y/\delta < 0.3$), where the length-scale of the dominant eddies is proportional to wall distance. Assuming that there is a local equilibrium between production and dissipation of energy, the mean velocity profile can be obtained from (Pope, 2000):

$$U^+ = \frac{1}{\kappa} \ln y^+ + A \tag{3.28}$$

where non-dimensional velocity, U^+, is defined as $U^+ = U / U_\tau$, and U_τ is the friction velocity:

$$U_\tau = \sqrt{\tau_w / \rho} \tag{3.29}$$

In the literature there are various suggestion for the values ascribed to the log-law constants, which are generally within 5% of $A = 5.2$ and $\kappa = 0.41$.

As far as turbulence models are concerned, there are currently two main approaches for taking wall effects into account: 1) using 'Low-Reynolds-Number' models, 2) applying 'Wall Functions'. These approaches are discussed below in more detail.

3.5.2 Low-Reynolds-Number Models

The first approach examined here to represent near-wall flow behaviour is the use of Low-Reynolds-Number (LRN) models which incorporate a single set of equations throughout the flow. This is achieved by modifying the transport and constitutive equations of the turbulence model for example by including viscous damping functions, and thus various model developments have incorporated different modifications to the standard HRN version to obtain LRN versions. The LRN models require a fine near wall mesh in order to resolve the large gradients of the mean and turbulent flow variables (the first cell should usually satisfy $y^+ < 1$), which in turn results in higher computational cost. Another disadvantage of LRN method is that the models which are based on damping functions are still empirical and thus, to some extent, only mimic the turbulence reduction in near-wall regions rather than taking the full physics into account.

Despite their drawbacks, RANS models, in particular LRN versions, have been widely adopted over the past three decades mainly because of their relatively low computational cost and often acceptable accuracy. In the present work attention is principally on eddy viscosity models, mainly at the two-equation level including LRN effects.

3.5.2.1 LRN Modifications to the Launder-Spalding Model

As was mentioned earlier, modifications have to be made to turbulence models if one seeks to apply them in near-wall regions. Here some proposed modifications are discussed. Here, the focus is on the k-ε model of Launder-Sharma (1974; hereafter, the 'LS' model) which has achieved some status as a 'baseline' low-Reynolds-number model.

In the LS model, there are four main modifications used to account for LRN effects in k- and ε-transport equations:

1) Changes to the constitutive equation,
2) Introduction of the 'homogenous dissipation',
3) Adding a source term to ε-equation, and
4) Inclusion of viscous diffusion.

In addition, another modification was later made by Yap (1987) for length-scale correction.

The above modifications are discussed below in more details.

- **Changes to the constitutive equation**

In its high-Reynolds number form, the strain-stress relation is given by

$$\frac{\overline{uv}}{k} = -C_\mu \left(\frac{k}{\varepsilon} \frac{\partial U}{\partial y} \right) = -C_\mu S \tag{3.30}$$

In a local equilibrium boundary region, $S \approx 3.3$ and $|\overline{uv}/k| \approx 0.3$, giving $C_\mu \approx 0.09$. However, the turbulent viscosity needs to be reduced across the viscous region. Therefore, a damping function is added to the constitutive equation as

$$\nu_t = C_\mu f_\mu \frac{k^2}{\varepsilon} \tag{3.31}$$

The function f_μ is defined such that it takes a value of unity in the fully-turbulent part of the flow, and then decreases across the viscous sub-layer. f_μ is made a function of the turbulent Reynolds number, Re_t. Launder and Sharma (1974) proposed

$$f_\mu = \exp\left[\frac{-3.4}{\left(1+\frac{Re_t}{50}\right)^2}\right] \tag{3.32}$$

where the turbulent Reynolds number is defined as

$$Re_t = \frac{k^2}{\nu\varepsilon} \tag{3.33}$$

- **Introduction of the homogenous dissipation:**

It is clear that at the wall, k has the simple boundary condition, $k = 0$, while ε is non-zero at the wall (in fact DNS has revealed that ε reaches a maximum at the wall). Fluctuating quantities can be expanded in Taylor series in terms of y (the normal direction to the wall). By using such Taylor series, one can find the wall-value of dissipation, ε_w as

$$\varepsilon_w = 2\nu\left(\frac{\partial k^{1/2}}{\partial y}\right)_w^2 \tag{3.34}$$

This equation could be rather difficult to implement in a numerical scheme, and so instead, Launder and Sharma have opted to solve a transport equation for the 'homogenous dissipation rate', $\tilde{\varepsilon}$, which is defined as

$$\tilde{\varepsilon} = \varepsilon - 2\nu\left(\frac{\partial k^{1/2}}{\partial x_j}\right)^2 \tag{3.35}$$

The advantage of using this homogenous dissipation rate is that outside the viscous sub-layer, $\tilde{\varepsilon}$ and ε are identical, which means all the earlier modelling considerations are still valid. However, at the wall, $\tilde{\varepsilon} = 0$ by virtue of Eqns. (3.34) and (3.35).

- **Adding a source term to ε-equation**

The third modification made by Launder and Sharma was to introduce a new source term, commonly known as the 'E-term', in the ε-transport equation. E_ε is defined as

$$E_\varepsilon = 2\nu\nu_t\left(\frac{\partial^2 U_i}{\partial x_j \partial x_j}\right)^2 \tag{3.36}$$

This term acts to increase the dissipation rate in the near wall region, where velocity gradients are changing rapidly.

- **Inclusion of viscous diffusion**

The fourth modification to account for LRN effects was to include the viscous diffusion in the k- and ε-transport equations:

$$\frac{Dk}{Dt} = \frac{\partial}{\partial x_j}\left[\left(\nu + \frac{\nu_t}{\sigma_k}\right)\frac{\partial k}{\partial x_j}\right] + P_k - \varepsilon \tag{3.37}$$

$$\frac{D\varepsilon}{Dt} = \frac{\partial}{\partial x_j}\left[\left(\nu + \frac{\nu_t}{\sigma_\varepsilon}\right)\frac{\partial \varepsilon}{\partial x_j}\right] + C_{\varepsilon 1}\frac{\varepsilon}{k}P_k - C_{\varepsilon 2}\frac{\varepsilon^2}{k} \tag{3.38}$$

- **Inclusion of the Yap-term:**

Yap (1987) added a further new term to the ε-transport equation which was used as a length-scale correction term and defined as

$$Y = \max\left[0.83\left(\frac{l}{l_e} - 1\right)\left(\frac{l}{l_e}\right)^2 \frac{\varepsilon^2}{k},\ 0\right] \tag{3.39}$$

where $l = k^{3/2} / \varepsilon$ and $l_e = 2.55\ y$.

This new source term was designed to prevent the LS model from returning excessively large length-scales, especially in reattaching and impinging flows. Thus, only when the predicted turbulent length-scale exceeds the equilibrium length-scale, does this term come into effect. It should be noted that in complex geometries, similar to other wall-normal distance dependent parameters, the Yap term can be difficult to

implement. The effects of this term in affecting the overall performance of the LS model in buoyancy-affected flows will be considered in Chapter 5.

3.5.2.2 Elliptic Relaxation

In the context of Reynolds Stress Models (RSM), along with production and dissipation of turbulence, redistribution is an important process in the balance of the Reynolds stresses. Consequently, its modelling is crucial, and the subject of extensive research. From a theoretical point of view, the modelling of the redistribution term in terms of local quantities is questionable for strongly inhomogeneous flows. In addition, in the near-wall regions, it is inaccurate and undesirable to use various ad hoc viscous damping functions or any explicit use of a geometrical parameter, such as the wall distance.

Durbin (1993) introduced a novel approach to address the above issues. He proposed modelling the pressure-rate-of-strain based on the solution of an elliptic equation (similar to the Poisson equation). This, and related 'elliptic relaxation models', have had some success in the calculation of near-wall flows (Pope, 2000). Durbin (1991) proposed modelling the two-point correlation directly instead of modelling the pressure-strain term which results in non-local effects (such as wall-blocking and wall-echo effects) to be accounted for. In Durbin's approach, in addition to k and ε, another set of variables, f_{ij} is solved for, which essentially represents the sum of the redistribution terms and dissipation anisotropy (= $\varepsilon_{ij} - 2/3\ \varepsilon\ \delta_{ij}$) in the RSM. Since Launder (1986) showed that only the wall-normal stress component provides the correct velocity scale near the wall, the full $\overline{u_i u_j} - f_{ij}$ model is reduced to $\overline{v^2} - f_{22}$ model. This was the starting point for Durbin (1991; 1995) to develop a closure known as the $\overline{v^2} - f$ model. Compared to EVMs, this closure requires only two extra equations (i.e. one for the wall-normal velocity, $\overline{v^2}$, and one for its corresponding elliptic distribution,

f_{22}). In general, the elliptic relaxation model has led to very encouraging results, especially as applied to the $\overline{v^2}-f$ (or $k-\varepsilon-\overline{v^2}$) model. Further details of the $\overline{v^2}-f$ model and elliptic relaxation will be given in Sections 3.6.5 and 3.6.6. In the present work, the $\overline{v^2}-f$ formulation as implemented in STAR-CD is tested for both buoyancy-affected flows (shown in Chapter 5) and rib-roughened 2D and 3D passages (shown in Chapters 6 and 7).

3.5.3 Wall Functions

3.5.3.1 Introduction

The second method used to deal with the wall effects is based on so-called 'wall functions'. The idea of the wall function approach (Launder and Spalding, 1972) is to apply boundary conditions (based on the log-law) some distance away from the wall, thus eliminating the need to have a fine mesh all the way down to the wall. This approach is used in conjunction with a high-Reynolds-number turbulence model. The usual assumptions of a conventional wall function approach are:

1) The first near-wall grid node is located far enough from the wall (at a distance y_p) to ensure that the first cell is placed in the inner region of the boundary layer. The first near-wall cell should usually be at $y^+ \geq 30$.
2) The flow over this region is assumed to obey the inner law of the wall, Eqn. (3.28).
3) Local equilibrium conditions are assumed in order to estimate the wall shear stress and to evaluate the source terms in the transport equations of the turbulence model (e.g. in the k- and ε-transport equations of the k-ε model)

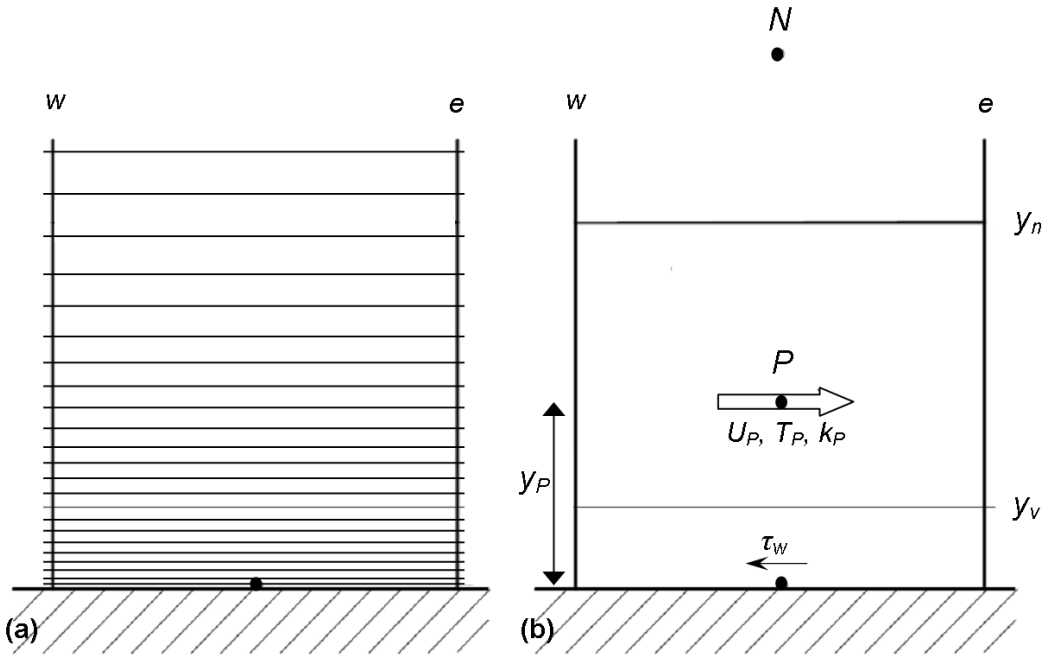

Figure 3.3 – Near-wall treatment approaches; (a) Low-Reynolds number approach (b) Wall Function approach.

There has been a great deal of efforts in developing and refining various wall functions in the past few decades, most of which were done at UMIST (now the University of Manchester). Some of the currently-used wall functions include the standard (Launder and Spalding, 1974), analytical (Gerasimov, 2003), numerical (Gant, 2003) and scalable (Grotjans and Menter, 1998; Uribe, 2006). In the present work, only the standard wall function is of relevance and therefore is discussed below.

3.5.3.2 Standard Wall Functions (SWF)

In the derivation of the standard log-law (Launder and Spalding, 1974), it is assumed that for a high-Reynolds number zero-pressure-gradient boundary layer, the log-law (Eqn. (3.28)) can be written as:

$$U^* = \frac{1}{\kappa}\ln\left(EC_\mu{}^{0.25}y^*\right) \tag{3.40}$$

where

$$U^* = \frac{\rho U_P C_\mu^{0.25} k_P^{0.5}}{\tau_w} \tag{3.41}$$

and

$$y^* = \frac{y k_P^{0.5}}{\nu} \tag{3.42}$$

where for a smooth wall, the von Kármán constant, κ, and wall roughness constant, E, take the values of 0.42 and 9.79, respectively.

Combining and rearranging Eqns. (3.40) and (3.41) results in the wall shear stress to be calculated from:

$$\tau_w = \frac{\rho \kappa U_P C_\mu^{0.25} k_P^{0.5} U_P}{\ln\left(E C_\mu^{0.25} y_P^*\right)} \tag{3.43}$$

The above equation is adopted in accounting for the forces applied to the near-wall cell, for the momentum component parallel to the wall (see Figure 3.3 (b)).

In the SWF approach, it is assumed that the dimensionless viscous sub-layer thickness is at $y_v^* = 20$ (where $y_v^* = y_v k_P^{0.5} / \nu$) and thus if the near-wall control volume lies above this region, it is assumed to be in the fully turbulent flow region and consequently τ_w can be calculated using Eqn. (3.43). However, if the first node is located inside the viscous sub-layer, then the flow in the near-wall cell is assumed to be laminar and wall shear stress is assumed to be totally viscous i.e. $\tau_w = \mu U_P / y_P$.

In order to calculate the cell-averaged turbulent kinetic energy production, $\overline{P_k}$, it is assumed that in the near-wall cell, turbulence energy is generated by simple shear i.e. $\overline{P_k} = -\rho \overline{u'v'} \partial U / \partial y$. Equilibrium condition yields (Craft et al., 2002)

$$-\rho \overline{u'v'} = \tau_w \text{ and } U = \frac{\tau_w}{\rho \kappa C_\mu^{0.25} k_P^{0.5}} \ln\left(E \frac{y k_P^{0.5}}{\nu} \right) \tag{3.44}$$

Thus,

$$\overline{P_k} = \frac{{\tau_w}^2}{\rho\kappa C_\mu^{0.25} {k_P}^{0.5} y} \tag{3.45}$$

The above expression assumes that the turbulent shear stress is constant over the control volume and is equal to τ_w. Now, P_k can be integrated over the control volume (not over the entire control volume, but rather between y_v and y_n) by setting k constant and equal to k_P. This leads to

$$\overline{P_k} = \frac{1}{y_n}\int_{y_v}^{y_n} \tau_w \frac{\tau_w}{\rho\kappa C_\mu^{0.25} {k_P}^{0.5} y} dy = \frac{{\tau_w}^2}{\rho\kappa C_\mu^{0.25} {k_P}^{0.5} y_n} \ln\left(\frac{y_n}{y_v}\right) \tag{3.46}$$

Similarly, for the cell-averaged dissipation rate, $\overline{\varepsilon}$, it is assumed that outside of the viscous sub-layer, the variation of ε is according to the equilibrium length-scale (Craft et al., 2002):

$$\varepsilon = \frac{k^{1.5}}{l} = \frac{{k_P}^{1.5}}{c_l y} \tag{3.47}$$

where c_l = 2.55. However, within the viscous sub-layer, ε can be taken as its wall-limiting value of

$$\varepsilon = \frac{2\nu k_P}{{y_v}^2} \tag{3.48}$$

Now integration of $\overline{\varepsilon}$ leads to

$$\begin{aligned}\overline{\varepsilon} &= \frac{1}{y_n}\left[\int_0^{y_v} \frac{2\nu k_P}{{y_v}^2} dy + \int_{y_v}^{y_n} \frac{{k_P}^{1.5}}{c_l y} dy\right] = \frac{1}{y_n}\left[\frac{2\nu k_P}{{y_v}^2} + \frac{{k_P}^{1.5}}{c_l} \ln\left(\frac{y_n}{y_v}\right)\right] \\ &= \frac{1}{y_n}\left[\frac{2{k_P}^{1.5}}{y_v^*} + \frac{{k_P}^{1.5}}{c_l} \ln\left(\frac{y_n}{y_v}\right)\right]\end{aligned} \tag{3.49}$$

The transport equation for ε is not solved in the near-wall cell. Instead, the value of dissipation at the near-wall node, ε_P, is prescribed as

$$\varepsilon_P = \frac{k_P^{1.5}}{c_l y_P} \tag{3.50}$$

The SWF is a relatively simple approach and has been implemented in many industrial and commercial CFD codes. The main disadvantage of the SWF is that the universality of the wall function becomes highly questionable for flows with effects such as separation, reattachment and curvature. This will be discussed further in Section 6.4.3 where the SWF is applied to a 2D rib-roughened channel and comparison is made against the LRN computations.

Another problem associated with this type of wall function is that one has to make sure that the first cell is positioned at $y^+ \geq 30$. In practice, making sure that first cell has a specific value of y^+ can be difficult as it first requires the solution of the velocity field.

3.6 MODEL FORMULATIONS

In this section, the equations of all the turbulence closures used in the present work are listed. These turbulence models which are all EVM-based, are implemented in one or more of the three CFD codes used in this study i.e. CONVERT, STAR-CD, and Code_Saturne. A description of these codes is presented in Chapter 4.

3.6.1 Launder-Sharma k-ε Model (CONVERT)

One of the most successful and widely used two-equation models is the *k-ε* model of Launder and Sharma (1974) which is a refinement of a previous model developed by Jones and Launder (1972). Despite the early appearance of the LS closure, it remains one of the more conceptually advanced, and accurate, of a large group of two-equation model variants (Patel, Rodi and Scheuerer, 1985; Cotton and Kirwin, 1995).

In this model, the eddy viscosity is calculated as

$$\nu_t = C_\mu f_\mu \, k^2 / \tilde{\varepsilon} \tag{3.51}$$

where C_μ is a constant and the damping function, f_μ is defined as

$$f_\mu = \exp\left[-3.4/\left(1+\left(Re_t/50\right)\right)^2\right] \tag{3.52}$$

Within the LS model k and $\tilde{\varepsilon}$ are determined from the following transport equations:

$$\frac{Dk}{Dt} = P_k + \frac{\partial}{\partial x_j}\left[\left(\nu + \frac{\nu_t}{\sigma_k}\right)\frac{\partial k}{\partial x_j}\right] - \left[\tilde{\varepsilon} + 2\nu\left(\frac{\partial (k)^{1/2}}{\partial x_j}\right)^2\right] \tag{3.53}$$

$$\frac{D\tilde{\varepsilon}}{Dt} = C_{\varepsilon 1}\frac{\tilde{\varepsilon}}{k}P_k + \frac{\partial}{\partial x_j}\left[\left(\nu + \frac{\nu_t}{\sigma_\varepsilon}\right)\frac{\partial \tilde{\varepsilon}}{\partial x_j}\right] - C_{\varepsilon 2} f_\varepsilon \frac{\tilde{\varepsilon}^2}{k} + E_\varepsilon + Y \tag{3.54}$$

where $P_k = -\overline{u_i u_j}\left(\partial U_i/\partial x_j\right)$ and $f_\varepsilon = 1 - 0.3\exp\left(-Re_t^2\right)$. E_ε and Y are defined by Eqns. (3.36) and (3.39), respectively.

The coefficients of the LS k-ε model are quoted in Table 3.3.

C_μ	$C_{\varepsilon 1}$	$C_{\varepsilon 2}$	σ_k	σ_ε
0.09	1.44	1.92	1.0	1.3

Table 3.3 – Constants appearing in the LS model.

3.6.2 Lien-Chen-Leschziner k-ε Model (STAR-CD)

The low-Reynolds-number k-ε model of Lien, Chen and Leschziner (1996; the 'LCL' model), is termed the 'Standard Low-Reynolds-Number k-ε Model' in the STAR-CD documentation (CD-Adapco, 2006). The closure of Lien et al. (1996) carries two turbulence transport equations, i.e. the k- and ε-transport equations, the latter being somewhat modified from the standard form (Launder and Spalding, 1974; Launder and Sharma, 1974), in part to improve the convergence properties of the model.

Eddy viscosity in the LCL model is obtained as

$$\nu_t = C_\mu f_\mu k^2/\varepsilon \tag{3.55}$$

where

$$f_\mu = \left(1 - e^{-0.0198 \ \ Re_y}\right)\left[1 + \left(5.29 / Re_y\right)\right] \tag{3.56}$$

The transport equations for the turbulent kinetic energy, k and its dissipation rate, ε, are given as

$$\frac{Dk}{Dt} = P_k + \frac{\partial}{\partial x_j}\left[\left(\nu + \frac{\nu_t}{\sigma_k}\right)\frac{\partial k}{\partial x_j}\right] - \varepsilon \tag{3.57}$$

$$\frac{D\varepsilon}{Dt} = C_{\varepsilon 1}\frac{\varepsilon}{k}\left(P_k + P_k^{'}\right) + \frac{\partial}{\partial x_j}\left[\left(\nu + \frac{\nu_t}{\sigma_\varepsilon}\right)\frac{\partial \varepsilon}{\partial x_j}\right] - C_{\varepsilon 2} f_\varepsilon \frac{\varepsilon^2}{k} \tag{3.58}$$

where

$$P_k^{'} = 1.33 f_\varepsilon \left[P_k + 2\nu \frac{k}{y^2}\right] e^{-0.00375 Re_y{}^2} \tag{3.59}$$

$$Re_t = k^2 /(\nu\varepsilon) \tag{3.60}$$

$$Re_y = \frac{y\sqrt{k}}{\nu} \tag{3.61}$$

$$f_\varepsilon = 1 - 0.3\exp\left(-Re_t{}^2\right) \tag{3.62}$$

In the LCL model, $P_k^{'}$ is introduced to ensure that the correct level of near-wall turbulence-energy dissipation is returned. From Eqn. (3.59), it is clear that $P_k^{'}$ has dependence on the wall-normal distance which is an undesirable feature in complex geometries. However, Lien et al. (1996) argues that the ε-equation of the LCL model does not include terms of the type $2\nu\left[\partial^2 u /\left(\partial x_k \partial x_l\right)\right]^2$ (similar to the E_ε term in the LS model; Eqn. (3.36)) which is difficult to expand in general 3D coordinates and also provokes a high level of sensitivity to near-wall grid resolution.

The coefficients of the LCL k-ε model are quoted in Table 3.4.

C_μ	$C_{\varepsilon 1}$	$C_{\varepsilon 2}$	σ_k	σ_ε
0.09	1.44	1.92	1.0	1.22

Table 3.4 – Constants appearing in the LCL k-ε model.

3.6.3 Wilcox k-ω Model

The two-equation k-ω model of Wilcox (1993b) is available in many CFD packages including STAR-CD and Code_Saturne. Although this model was not used in the present work, a brief description is given here for the sake of completeness. The model is based on an idea, first proposed by Kolmogorov in 1942, which is to use the dissipation rate per unit turbulent kinetic energy (i.e. $\omega \sim \varepsilon / k$) as the second variable. In this model, the turbulent viscosity is defined as

$$\nu_t = \frac{k}{\omega} \tag{3.63}$$

The transport equations for k and ω are written as

$$\frac{Dk}{Dt} = P_k + \frac{\partial}{\partial x_j}\left[\left(\nu + \frac{\nu_t}{\sigma_k}\right)\frac{\partial k}{\partial x_j}\right] - \beta^* k\omega \tag{3.64}$$

$$\frac{D\omega}{Dt} = \alpha\frac{\omega}{k}P_k + \frac{\partial}{\partial x_j}\left[\left(\nu + \frac{\nu_t}{\sigma_\omega}\right)\frac{\partial \omega}{\partial x_j}\right] - \beta\omega^2 \tag{3.65}$$

The coefficients are given in Table 3.5.

σ_k	σ_ω	α	β	β^*
2.0	2.0	0.55	0.075	0.09

Table 3.5 – Constants appearing in the standard k-ω model.

The dissipation of the turbulent kinetic energy and length-scale can be obtained through

$$\varepsilon = \beta^* k\omega \quad \text{and} \quad l = \sqrt{k}/\omega \tag{3.66}$$

It should be noted that, ω will tend to infinity at the wall as $k = 0$ while $\varepsilon \neq 0$. Thus, a new boundary condition must be derived for ω near the wall. Since in the near-wall region, viscous diffusion and dissipation terms have the largest values, one can assume

$$\nu\left(\frac{\partial^2 \omega}{\partial y^2}\right) - \beta\omega^2 = 0 \tag{3.67}$$

The above equation reduces to

$$\omega = \frac{6\nu}{\beta(\Delta y)^2} \tag{3.68}$$

where Δy is the distance to next point adjacent to the wall. This is the boundary condition for ω which is applied at the near-wall cell.

One of the advantages of the k-ω model is that it does not need any damping functions to compute the near-wall turbulence. This model is still very attractive for wall bounded calculations since it has been proved to have a better performance in separated flows (Wilcox, 1993b). It also performs better in cases with variable pressure gradients and has similar numerical properties to the k-ε model, but it is extremely sensitive to the free-stream boundary condition on ω. In fact, the reason for not using this model in the present work is in part due to findings of Kirwin (1995) where it was shown that this model performs very poorly in ascending mixed convection flows, especially at higher values of buoyancy influence.

3.6.4 Standard k-ω-SST Model (STAR-CD & Code_Saturne)

Advantages of both the k-ε and k-ω models are combined in the Shear Stress Transport (SST) model of Menter (1994). Through a blending function this model effectively uses a LRN formulation of the k-ω model in the boundary layer and a version of the k-ε model in the free shear layer. This is based on the observations that the k-ε model is much less sensitive to the free-stream value of ε than the k-ω model is to ω. Apart from

this unique feature, the main differences between the standard k-ω model and the SST model are the following:

- The SST model includes a damped cross-diffusion derivative term, as well as a blending function, in the ω-transport equation.
- The definition of the turbulent viscosity in the SST was modified to improve the prediction of the turbulent shear stress.
- The coefficients of the model were modified to improve the overall performance of the model.

In the SST model, two transport equations are solved for the turbulent kinetic energy, k, and turbulent frequency, ω ($= \varepsilon / C_\mu k$):

$$\frac{Dk}{Dt} = \hat{P}_k + \frac{\partial}{\partial x_j}\left[\left(\nu + \frac{\nu_t}{\sigma_k}\right)\frac{\partial k}{\partial x_j}\right] - \beta^* k\omega \tag{3.69}$$

$$\frac{D\omega}{Dt} = \alpha\left(\frac{\partial U_i}{\partial x_j} + \frac{\partial U_j}{\partial x_i}\right)^2 + \frac{\partial}{\partial x_j}\left[\left(\nu + \frac{\nu_t}{\sigma_\omega}\right)\frac{\partial \omega}{\partial x_j}\right] - \beta\omega^2 + 2\frac{(1-F_1)}{\sigma_{\omega 2}}\frac{1}{\omega}\frac{\partial k}{\partial x_j}\frac{\partial \omega}{\partial x_j} \tag{3.70}$$

where

$$\hat{P}_k = \begin{cases} P_k & STAR-CD \\ \min\left(P_k, 10\beta^* k\omega\right) & Code\_Saturne \end{cases} \tag{3.71}$$

Any coefficient α used in the model is calculated from

$$\alpha = F_1\alpha_1 + (1-F_1)\alpha_2 \tag{3.72}$$

where subscript 1 corresponds to the original coefficient of the k-ω model and subscript 2 represents the coefficients of the transformed k-ε model. The blending function F_1, is defined as

$$F_1 = \tanh\left(\arg_1{}^4\right) \tag{3.73}$$

where

$$\arg_1 = \min\left[\max\left(\frac{\sqrt{k}}{\beta^* \omega y}, \frac{500\nu}{y^2 \omega} \right), \frac{4\rho k}{\sigma_{\omega 2} CD_{k\omega} y^2} \right] \tag{3.74}$$

$$CD_{k\omega} = \max\left(2\rho \frac{1}{\sigma_{\omega 2} \omega} \frac{\partial k}{\partial x_j} \frac{\partial \omega}{\partial x_j}, 10^{-20} \right) \tag{3.75}$$

This definition of the blending function assures a smooth transition from the *k-ω* model at the wall to the *k-ε* model far from it.

The eddy-viscosity is expressed as

$$\nu_t = \frac{c_1 k}{\max(c_1 \omega, \Omega F_2)} \tag{3.76}$$

$$F_2 = \tanh\left(\arg_2^2\right) \tag{3.77}$$

$$\arg_2 = \max\left(\frac{2\sqrt{k}}{\beta^* \omega y}, \frac{500\nu}{y^2 \omega} \right) \tag{3.78}$$

$$\Omega = \sqrt{2\Omega_{ij}\Omega_{ij}} \tag{3.79}$$

where y is the distance to the nearest wall and the model coefficients are shown in Table 3.6.

α_1	β_1	c_1	$\sigma_{\omega 1}$	σ_{k1}	κ
$\beta_1 / \beta^* - \kappa^2 / \left(\sigma_{\omega 1} \sqrt{\beta^*}\right)$	0.075	0.31	2.0	1.176	0.41
α_2	β_2	β^*	$\sigma_{\omega 2}$	σ_{k2}	
$\beta_2 / \beta^* - \kappa^2 / \left(\sigma_{\omega 2} \sqrt{\beta^*}\right)$	0.0828	0.09	1.168	1.0 (STAR-CD) 2.0 (Code_Saturne)	

Table 3.6 – Constants appearing in the *k-ω-SST* model.

Note that following the recommendations of Menter et al. (2003), in addition to introducing a production limiter (Eq. (3.71)), the denominator of Eq. (3.76) was modified to $\max(c_1 \omega, SF_2)$. These modifications have been implemented into Code_Saturne, while the *k-ω-SST* model in STAR-CD uses the original formulation of Menter (1994) (except the value of σ_{k1} which in the original version is $\sigma_{k1} = 2$).

The wall boundary condition for ω proposed by Menter is given by

$$\omega_w = 10\frac{6\nu}{\beta_1(\Delta y)^2} \tag{3.80}$$

where Δy is the distance to the next point away from the wall.

3.6.5 The v²-f Model (STAR-CD)

The original v^2-f model (Durbin, 1991) has as its starting point, the two-equation k-ε model of the Launder & Sharma (1974). It was designed to handle wall effects in turbulent boundary layers and to accommodate non-local effects. The v^2-f model is a general low-Reynolds-number turbulence model that is valid all the way up to solid walls, and therefore does not need to make use of wall functions. Despite being a low Reynolds number model, it does not require wall distance (in common with the LS model); a quantity that is difficult and costly to calculate, especially in complicated geometries. In addition, no damping function is needed to adjust the behaviour of turbulence quantities (although comparing the constitutive equations of the v^2-f and k-ε models would indicate that in the v^2-f model, v^2/k represents an 'effective damping function'). Instead, a third transport equation is included for $\overline{v^2}$ (or simply v^2), one of the three Reynolds normal stresses (v is the wall-normal component of the fluctuating velocity vector). v^2 is used in a revised definition of turbulent viscosity given by the flowing equations:

$$\nu_t = C_\mu v^2 \, T_s \tag{3.81}$$

where

$$T_s = \max\left[\frac{k}{\varepsilon}, C_{kT}\left(\frac{\nu}{\varepsilon}\right)^{0.5}\right] \tag{3.82}$$

In addition, an elliptic equation for the redistribution term in the v^2-equation, f_{22}, is included to account for near-wall and non-local effects.

STAR-CD uses a variant of Durbin (1995) version of the v^2-f model. The governing equations of this particular model are given in Iaccarino (2001) as follows:

$$\frac{Dk}{Dt} = P_k + \frac{\partial}{\partial x_j}\left[\left(\nu + \frac{\nu_t}{\sigma_k}\right)\frac{\partial k}{\partial x_j}\right] - \varepsilon \tag{3.83}$$

$$\frac{D\varepsilon}{Dt} = \frac{C_{\varepsilon 1}^z}{T_s}P_k + \frac{\partial}{\partial x_j}\left[\left(\nu + \frac{\nu_t}{\sigma_\varepsilon}\right)\frac{\partial \varepsilon}{\partial x_j}\right] - \frac{C_{\varepsilon 2}}{T_s}\varepsilon \tag{3.84}$$

$$\frac{D\overline{v^2}}{Dt} = \frac{\partial}{\partial x_j}\left[\left(\nu + \frac{\nu_t}{\sigma_k}\right)\frac{\partial \overline{v^2}}{\partial x_j}\right] + k\, f_{22} - 6\overline{v^2}\frac{\varepsilon}{k} \tag{3.85}$$

$$L^2 \nabla^2 f_{22} - f_{22} = \frac{(1-C_1)}{T_s}\left(\frac{2}{3} - \frac{\overline{v^2}}{k}\right) - C_2\frac{P_k}{k} - 5\frac{\overline{v^2}}{kT_s} \tag{3.86}$$

where $\nabla^2 \equiv \nabla.\nabla$ is the Laplacian operator and

$$L = C_L\, max\left(k^{3/2}/\varepsilon, C_\eta(\nu^3/\varepsilon)^{1/4}\right) \tag{3.87}$$

$$C_{\varepsilon 1}^z = 1 + 0.045\sqrt{k/\overline{v^2}} \tag{3.88}$$

The coefficients of the v^2-f model in STAR-CD are given in Table 3.7.

C_μ	σ_k	σ_ε	$C_{\varepsilon 1}$	$C_{\varepsilon 2}$	C_1	C_2	C_L	C_η	C_{kT}
0.22	1.0	1.3	1.4	1.9	1.4	0.3	0.23	70.0	6.0

Table 3.7 – Constants appearing in the v^2-f model.

It is worth mentioning that the above model bears a close resemblance to the v^2-f formulation due to Lien and Kalitzin (2001), the only difference being in the definition of $C_{\varepsilon 1}^z$. In the Lien and Kalitzin model, $C_{\varepsilon 1}^z$ is defined as:

$$C_{\varepsilon 1}^z = 1 + 0.05\sqrt{k/\overline{v^2}} \tag{3.89}$$

(cf. Eqn. (3.88).)

3.6.6 Manchester v^2-f Model (Code_Saturne)

The v^2-equation includes a redistributive source term, f which represents a modelled form of the pressure-strain correlation. An elliptic equation is used in the determination of the source term, a feature that allows cognizance to be taken of non-local effects. Unfortunately, incorporation of the original scheme in an industrial segregated solver (where the governing equations are solved sequentially) gave rise to numerical problems related to the 'stiffness' of the equation set, and it is this consideration that has led to the development of a number of alternative approaches, including the current revised formulation.

Lien and Durbin (1996) subsequently developed a 'code-friendly' version of the scheme which sought to overcome the numerical issues alluded to above. However, a source term in the f-equation was neglected in the Lien-Durbin formulation, an omission that had the effect of causing the revised scheme to return results that were significantly different from those of the original model. Two later attempts were made to produce a form of the v^2-f closure that would be suitable for use in industrial segregated codes (Laurence et al., 2004; Hanjalić et al., 2004). The models of Laurence et al. (2004) and Hanjalić et al. (2004) solved a transport equation for a dimensionless variable $\varphi = v^2 / k$ in place of v^2. The terms neglected in the φ-based variants were less significant than those of Lien and Durbin (1996); however, numerical problems persisted and the models were prone to be unstable, particularly in near-wall regions.

The refinement of the v^2-f model (the Manchester v^2-f model) which was proposed at the University of Manchester (Billard et al., 2008), uses an 'elliptic blending' approach (Manceau, 2005) in order to strengthen the coupling between φ and f. Thus, an elliptic equation is solved for a 'blending parameter', α:

$$L^2 \nabla^2 \alpha - \alpha = -1 \tag{3.90}$$

where

$$L = C_L \; max\left(k^{3/2}/\varepsilon, C_\eta(\nu^3/\varepsilon)^{1/4}\right) \tag{3.91}$$

The blending parameter varies the weighting between a near-wall sub-model (Eqn. (3.92), below) and a homogeneous sub-model (Eqn. (3.93)) that appear in the φ-equation (Eqn. (3.94)):

$$f_{wall} = -\frac{\varepsilon}{k}\varphi \tag{3.92}$$

$$f_{hom} = -\frac{1}{T_t}(C_1 + C_2\frac{P_k}{\varepsilon} - 1)(\varphi - \frac{2}{3}) \tag{3.93}$$

$$\frac{D\varphi}{Dt} = \alpha^3 f_{hom} + (1-\alpha^3) f_{wall} - P_k\frac{\varphi}{k} + \frac{2}{k}\left(\frac{\nu_t}{\sigma_k}\right)\frac{\partial k}{\partial x_j}\frac{\partial \varphi}{\partial x_j} + \frac{\partial}{\partial x_j}\left[\left(\nu + \frac{\nu_t}{\sigma_\varphi}\right)\frac{\partial \varphi}{\partial x_j}\right] \tag{3.94}$$

The wall boundary condition applied to Eqn. (3.90) is α = 0, an aspect of the current proposal that greatly alleviates the problems experienced by other workers in relation to the stiffness of the equation set. The transport equations for turbulent kinetic energy and its dissipation rate read as follows:

$$\frac{Dk}{Dt} = P_k - \varepsilon + \frac{\partial}{\partial x_j}\left[\left(\nu + \frac{\nu_t}{\sigma_k}\right)\frac{\partial k}{\partial x_j}\right] \tag{3.95}$$

$$\frac{D\varepsilon}{Dt} = \frac{C_{\varepsilon 1}P_k - C_{\varepsilon 2}\varepsilon}{T_t} + \frac{\partial}{\partial x_j}\left[\left(\nu + \frac{\nu_t}{\sigma_\varepsilon}\right)\frac{\partial \varepsilon}{\partial x_j}\right] \tag{3.96}$$

The functions and constants appearing in the Manchester v^2-f model are listed in Table 3.9.

$C_{\varepsilon 1}$				$C_{\varepsilon 2}$	C_1	C_2
$1.44(1+0.04(1-\alpha^3)\sqrt{\frac{1}{\varphi}})$				1.83	1.7	1.2
σ_k	σ_ε	σ_φ	C_η	C_μ	C_L	C_T
1.0	1.22	1.0	90	0.22	0.22	6.0

Table 3.8 – Constants appearing in the Manchester v^2-f model.

Full details of this model, along with its recent updates and modifications, can be found in Billard et al. (2008) and Billard (2010).

$C_{\varepsilon 1}$				$C_{\varepsilon 2}$	C_1	C_2
$1.44(1+0.04(1-\alpha^3)\sqrt{\frac{1}{\varphi}})$				1.83	1.7	1.2
σ_k	σ_ε	σ_φ	C_η	C_μ	C_L	C_T
1.0	1.22	1.0	90	0.22	0.22	6.0

Table 3.9 – Constants appearing in the Manchester v^2-f model.

3.6.7 Cotton-Ismael k-ε-S Model (CONVERT)

Cotton and Ismael (1998) argued that a fundamental weakness exists in the stress/rate-of-strain relationship of high-Reynolds-number EVMs. Thus, for example, one might consider the constitutive equation of the 'standard' k-ε model (Launder and Spalding, 1974): under the influence of simple shear, the structural ratio $-\overline{uv}/k$ as determined by this model varies linearly with the group $(k/\varepsilon)\partial U/\partial y$:

$$-\overline{uv}/k = C_\mu (k/\varepsilon)\partial U/\partial y \tag{3.97}$$

where C_μ is a constant.

The expression above represents the ratio of the large-scale turbulence timescale (k/ε) to the mean strain timescale, $(\partial U/\partial y)^{-1}$. Alternatively, it may be considered as total strain ($t.\partial U/\partial y$) truncated on the turbulence timescale. In a preliminary step Cotton and Ismael advanced a generalization of the above relationship based upon dimensional analysis. Hence, quite simply, the structural ratio is now expressed as

$$-\overline{uv}/k = f\left[(k/\varepsilon)\partial U/\partial y\right] \tag{3.98}$$

where f is a function to be determined.

The second stage of the development is based upon the proposals of Townsend (1970) and Maxey (1982) and consists of the introduction of an additional transport equation for a 'strain parameter', S:

$$\frac{DS}{Dt} = \frac{1}{2}\frac{k}{\tilde{\varepsilon}}\left(\frac{\partial U_i}{\partial x_j} + \frac{\partial U_j}{\partial x_i}\right)^2 + \frac{\partial}{\partial x_j}\left(\frac{\nu_t}{\sigma_S}\frac{\partial S}{\partial x_j}\right) - \frac{S}{(k/\tilde{\varepsilon})} \tag{3.99}$$

where ε has now been replaced by $\tilde{\varepsilon}$ (cf. the LS model, above). Under equilibrium conditions, S takes the value $\left[(k/\tilde{\varepsilon})\,\partial U/\partial y\right]^2$; where the flow is a non-equilibrium state, Eqn. (3.99) mimics some aspects of Rapid Distortion Theory (RDT), see for example Hunt and Carruthers (1990). Eddy viscosity in the Cotton-Ismael model (the 'CI' model) is obtained as

$$\nu_t = C_\mu f_\mu(Re_t) f_S(S) k^2/\tilde{\varepsilon} \tag{3.100}$$

where

$$f_\mu(Re_t) = 1 - 0.3\exp\left[-Re_t/50\right] \tag{3.101}$$

$$f_S(S) = \frac{2.88}{1+0.165S} \times \left\{1 - 0.55\,\exp\left[-\left(0.135S + 0.0015S^3\right)\right]\right\} \tag{3.102}$$

Note that, in contrast to EVMs in which damping effects are attributed wholly to viscous effects, Eqn. (3.101) rapidly asymptotes to unity. The k-equation of the CI model is identical to that of the LS scheme, while the ε-equation differs only in the value assigned to σ_ε and the prescription of the functions f_ε and E_ε. Thus the ε-equation is written

$$\frac{D\tilde{\varepsilon}}{Dt} = C_{\varepsilon 1}\frac{\tilde{\varepsilon}}{k}P_k + \frac{\partial}{\partial x_j}\left[\left(\nu + \frac{\nu_t}{\sigma_\varepsilon}\right)\frac{\partial \tilde{\varepsilon}}{\partial x_j}\right] - C_{\varepsilon 2} f_\varepsilon \frac{\tilde{\varepsilon}^2}{k} + E_\varepsilon \tag{3.103}$$

where $f_\varepsilon = 1$ and $E_\varepsilon = 0.9\nu\nu_t\left(\dfrac{\partial^2 U_i}{\partial x_j \partial x_k}\right)^2$

The coefficients of the CI model are quoted in Table 3.10.

C_μ	σ_k	σ_ε	σ_s	$C_{\varepsilon 1}$	$C_{\varepsilon 2}$
0.09	1.0	1.21	6.0	1.44	1.92

Table 3.10 – Constants appearing in the CI model.

3.6.8 Suga Non-Linear k-ε Model (CONVERT & STAR-CD)

In a research effort that proceeded in parallel with the development of the CI model, Craft et al. (1996b) developed a two-equation model (this model was originally developed by Suga (1995), thus it is usually known as the 'Suga' model) in which quadratic and cubic mean strain and vorticity terms were introduced into the constitutive equation – see the general stress-strain relationship in Eqn. (3.27). (A subsequent refinement of the approach included a third transport equation for A_2, the second invariant of the stress anisotropy tensor.)

Similar to the LS model, the transport equations for k and $\tilde{\varepsilon}$ in the Suga model take the following forms:

$$\frac{Dk}{Dt} = P_k + \frac{\partial}{\partial x_j}\left[\left(\nu + \frac{\nu_t}{\sigma_k}\right)\frac{\partial k}{\partial x_j}\right] - \left[\tilde{\varepsilon} + 2\nu\left(\frac{\partial (k)^{1/2}}{\partial x_j}\right)^2\right] \tag{3.104}$$

$$\frac{D\tilde{\varepsilon}}{Dt} = C_{\varepsilon 1}\frac{\tilde{\varepsilon}}{k}P_k + \frac{\partial}{\partial x_j}\left[\left(\nu + \frac{\nu_t}{\sigma_\varepsilon}\right)\frac{\partial \tilde{\varepsilon}}{\partial x_j}\right] - C_{\varepsilon 2} f_\varepsilon \frac{\tilde{\varepsilon}^2}{k} + E_\varepsilon + Y \tag{3.105}$$

where $P_k = -\overline{u_i u_j}\left(\partial U_i / \partial x_j\right)$ and $\tilde{\varepsilon} = \varepsilon - 2\nu\left(\partial k^{1/2} / \partial x_j\right)^2$. Y represents the Yap correction term, defined in (3.39). Note that in STAR-CD, the Yap term is included in the $\tilde{\varepsilon}$-equation by default, while it is optional in Code_Saturne.

The turbulent viscosity is defined as

$$\nu_t = C_\mu f_\mu \, k^2 / \tilde{\varepsilon} \tag{3.106}$$

Craft et al. (1996b) proposed the following functional form of C_μ:

$$C_\mu = \frac{0.3}{1 + 0.35(\max(\tilde{S}, \tilde{\Omega}))^{1.5}}\left(1 - \exp\left[\frac{-0.36}{\exp(-0.75\max(\tilde{S}, \tilde{\Omega}))}\right]\right) \tag{3.107}$$

where dimensionless strain and vorticity invariants are defined as

$$\tilde{S} = k/\tilde{\varepsilon}\sqrt{1/2(S_{ij}S_{ij})} \quad , \quad \tilde{\Omega} = k/\tilde{\varepsilon}\sqrt{1/2(\Omega_{ij}\Omega_{ij})} \tag{3.108}$$

As before, the mean strain rate and vorticity tensor are

$$S_{ij} = \left(\frac{\partial U_i}{\partial x_j} + \frac{\partial U_j}{\partial x_i} \right) \quad , \quad \Omega_{ij} = \left(\frac{\partial U_i}{\partial x_j} - \frac{\partial U_j}{\partial x_i} \right) \tag{3.109}$$

Although this new definition of C_μ would improve the performance of the model in such a way that, for example, $\overline{uv}$ is better represented in non-equilibrium shear flows, but it cannot solve the general problem of linear eddy viscosity models, namely returning isotropic normal stresses. Therefore, in the NLEVM additional terms are added to the stress-strain relation which consequently makes the Reynolds stresses a more general function of mean velocities and vorticities. Thus, the equation for the Reynolds shear stresses becomes

$$\begin{aligned}
\overline{u_i u_j} &= (2/3)k\delta_{ij} - \nu_t S_{ij} \\
&+ c_1 \nu_t \frac{k}{\tilde{\varepsilon}} \left(S_{ik} S_{jk} - 1/3 S_{kl} S_{kl} \delta_{ij} \right) \\
&+ c_2 \nu_t \frac{k}{\tilde{\varepsilon}} \left(\Omega_{ik} S_{kj} + \Omega_{jk} S_{ki} \right) \\
&+ c_3 \nu_t \frac{k}{\tilde{\varepsilon}} \left(\Omega_{ik} \Omega_{jk} - 1/3 \Omega_{kl} \Omega_{kl} \delta_{ij} \right) \\
&+ c_4 \nu_t \frac{k^2}{\tilde{\varepsilon}^2} \left(S_{ki} \Omega_{lj} + S_{kj} \Omega_{li} \right) S_{kl} \\
&+ c_5 \nu_t \frac{k^2}{\tilde{\varepsilon}^2} \left(\Omega_{il} \Omega_{lm} S_{mj} + S_{il} \Omega_{lm} \Omega_{mj} - 2/3 S_{lm} \Omega_{mn} \Omega_{nl} \delta_{ij} \right) \\
&+ c_6 \nu_t \frac{k^2}{\tilde{\varepsilon}^2} S_{ij} S_{kl} S_{kl} + c_7 \nu_t \frac{k^2}{\tilde{\varepsilon}^2} S_{ij} \Omega_{kl} \Omega_{kl}
\end{aligned} \tag{3.110}$$

Craft et al. (1996b) optimized the coefficients over a range of flows including simple shear, impinging, curved and swirling flows. Their proposed values for the coefficients used in Eqn. (3.110) are listed in Table 3.11.

c_1	c_2	c_3	c_4	c_5	c_6	c_7
-0.1	0.1	0.26	-10 C_μ^2	0	-5 C_μ^2	5 C_μ^2

Table 3.11 – Constants appearing in the Reynolds shear stress equation of the Suga model.

Although, in the definition of turbulent viscosity (Eqn. (3.106)), an additional Reynolds number-dependent damping function is required, its effects are substantially less that that used in LEVMs, since in NLEVM, most of near-wall strain-related damping is provided through the new definition of C_μ (Eqn. (3.107)).

Craft et al. (1996b) proposed the following expression for f_μ and f_ε:

$$f_\mu = 1 - \exp\left[-(Re_t/90)^{1/2} - (Re_t/400)^2\right] \tag{3.111}$$

$$f_\varepsilon = 1 - 0.3\exp\left(-Re_t^{\,2}\right) \tag{3.112}$$

where as before, the turbulent Reynolds number is $Re_t = k^2/\nu\tilde{\varepsilon}$.

The near-wall source term, E_ε, is expressed as

$$E_\varepsilon = \begin{cases} 0.0022\ \dfrac{\tilde{S}\,\nu_t k^2}{\tilde{\varepsilon}}\left(\dfrac{\partial^2 U_i}{\partial x_j \partial x_k}\right)^2 & \text{for } Re_t \le 250 \\ 0 & \text{for } Re_t > 250 \end{cases} \tag{3.113}$$

It can be seen that this new expression for E_ε is different from its original form in the LS model (Eqn. (3.36)). It has been modified in order to reduce its dependence on Reynolds number.

The coefficients in the *k*- and $\tilde{\varepsilon}$ -transport equations are listed in Table 3.12.

$C_{\varepsilon 1}$	$C_{\varepsilon 2}$	σ_k	σ_ε
1.44	1.92	1.0	1.3

Table 3.12 – Constants appearing in the Suga model.

In is worth noting that, in simple shear flows such as the flow to be discussed in Chapter 5, the equation of the Reynolds shear stress (see Eqn. (3.110)) is simplified to

$$\overline{uv} = -\nu_t \frac{\partial U}{\partial y} + \frac{\nu_t k^2}{\tilde{\varepsilon}^2}\left(\frac{\partial U}{\partial y}\right)^3 \left(-2c_5 + 2c_6 + 2c_7\right) \tag{3.114}$$

Note that the above equation reduces to $\overline{uv} = -\nu_t (\partial U / \partial y)$ as a result of values given in Table 3.11 for c_5, c_6 and c_7.

Finally, for comparison Table 3.13 lists different functions appearing in the turbulence models of Launder-Sharma, Cotton-Ismael, Lien-Chen-Leschziner and Suga.

Variable	LS k-ε model	LCL k-ε model	CI k-ε-S model	Suga k-ε model
$\overline{u_i u_j}$ §	$-\nu_t\left(\frac{\partial U_i}{\partial x_j}\right)$	$-\nu_t\left(\frac{\partial U_i}{\partial x_j}\right)$	$-\nu_t\left(\frac{\partial U_i}{\partial x_j}\right)$	$\frac{2}{3}k\delta_{ij}-\nu_t S_{ij}+c_1\nu_t\frac{k}{\varepsilon}(S_{ik}S_{jk}-\frac{1}{3}S_{kl}S_{kl}\delta_{ij})$ $+c_2\nu_t\frac{k}{\varepsilon}(\Omega_{ik}S_{kj}+\Omega_{jk}S_{ki})$ $+c_3\nu_t\frac{k}{\varepsilon}(\Omega_{ik}\Omega_{jk}+\frac{1}{3}\Omega_{lk}\Omega_{lk}\delta_{ij})$ $+c_4\nu_t\frac{k^2}{\varepsilon^2}(S_{ki}\Omega_{lj}+S_{kj}\Omega_{li})S_{kl}$ $+c_5\nu_t\frac{k^2}{\varepsilon^2}(\Omega_{il}S_{mj}+S_{il}\Omega_{mj}-\frac{2}{3}S_{ln}\Omega_{mn}\delta_{ij})\Omega_{lm}$ $+c_6\nu_t\frac{k^2}{\varepsilon^2}S_{ij}S_{kl}S_{kl}+c_7\nu_t\frac{k^2}{\varepsilon^2}S_{ij}\Omega_{kl}\Omega_{kl}$
P_k' †	0	$1.33\left(1-0.3e^{-Re_t^2}\right)\times$ $\left[P_k+2\nu\frac{k}{y^2}\right]e^{-0.00375Re_y^2}$ where $Re_y=\frac{y\sqrt{k}}{\nu}$	0	0
C_μ ‡	0.09	0.09	0.09	$\frac{0.3}{1+0.35\left(\max(\tilde{S},\tilde{\Omega})\right)^{1.5}}\times$ $\left(1-\exp\left[\frac{-0.36}{\exp\left(-0.75\max(\tilde{S},\tilde{\Omega})\right)}\right]\right)$
f_μ ‡	$\exp\left[-3.4/\left(1+\frac{Re_t}{50}\right)^2\right]$	$\left(1-e^{-0.0198\ Re_y}\right)$ $\times\left[1+\left(5.29/Re_y\right)\right]$	$1-0.3\exp\left[\frac{-Re_t}{50}\right]$	$1-\exp\left[-(Re_t/90)^{1/2}-(Re_t/400)^2\right]$
f_S ‡	1	1	$\frac{2.88}{1+0.165S}\times$ $\left\{1-0.55\ e^{\left[-\left(0.135S+0.0015S^3\right)\right]}\right\}$	1
f_ε †	$1-0.3\exp\left(-Re_t^2\right)$	$1-0.3\exp\left(-Re_t^2\right)$	1	$1-0.3\exp\left(-Re_t^2\right)$
D *	$2\nu\left(\frac{\partial(k)^{1/2}}{\partial x_j}\right)^2$	0	$2\nu\left(\frac{\partial(k)^{1/2}}{\partial x_j}\right)^2$	$2\nu\left(\frac{\partial(k)^{1/2}}{\partial x_j}\right)^2$
E_ε †	$2\nu\nu_t\left(\frac{\partial^2 U_i}{\partial x_j\partial x_k}\right)^2$	0	$0.9\nu\nu_t\left(\frac{\partial^2 U_i}{\partial x_j\partial x_k}\right)^2$	$0.0022\frac{\tilde{S}\nu_t k^2}{\tilde{\varepsilon}}\left(\frac{\partial^2 U_i}{\partial x_j\partial x_k}\right)^2$

* $\frac{Dk}{Dt}=P_k+\frac{\partial}{\partial x_j}\left[\left(\nu+\frac{\nu_t}{\sigma_k}\right)\frac{\partial k}{\partial x_j}\right]-\left(\tilde{\varepsilon}+D\right)$

† $\frac{D\tilde{\varepsilon}}{Dt}=C_{\varepsilon 1}\frac{\tilde{\varepsilon}}{k}\left(P_k+P_k'\right)+\frac{\partial}{\partial x_j}\left[\left(\nu+\frac{\nu_t}{\sigma_\varepsilon}\right)\frac{\partial\tilde{\varepsilon}}{\partial x_j}\right]-C_{\varepsilon 2}f_\varepsilon\frac{\tilde{\varepsilon}^2}{k}+E_\varepsilon$

‡ $\nu_t=C_\mu f_\mu f_S\frac{k^2}{\varepsilon}$

§ $P_k=-\overline{u_i u_j}\left(\partial U_i/\partial x_j\right)$

Table 3.13 – Functions appearing in the LS, CI, LCL and Suga models.

CHAPTER 4

THEORETICAL FORMULATION

4.1 PRELIMINARY REMARKS

In this chapter, after introducing the finite volume method, some theoretical concepts related to the test cases computed in the present work are briefly discussed. The three CFD codes used during the course of this project are then introduced. For each code, some relevant details are also included.

4.2 DISCRETIZATION

4.2.1 Introduction

The numerical solution of differential equations cannot produce a continuous distribution of the variables over the solution domain, thus the aim instead becomes to produce a set of discrete values at a number of nodes that cover the solution domain.

There are however, different ways to approximate the flow variables (Versteeg and Malalasekera, 1995):

- **Finite Difference:** Describes an unknown variable ϕ by means of point samples at node points. Truncated Taylor series expansions are used to generate finite difference approximations to the derivatives of ϕ at each grid point and its immediate neighbours.
- **Finite Volume:** Developed as a variant of the finite difference formulation. This is the method used in the present study and therefore will be discussed in depth in the next section.
- **Finite Element:** Uses simple piecewise functions (e.g. linear or quadratic) valid on individual elements to describe the local variation of ϕ. The governing equations are precisely satisfied by the exact solution of ϕ. As a result, one can obtain a set of algebraic equations for the unknown coefficients of the approximating functions.
- **Spectral Method:** Approximates the unknowns by means of truncated Fourier series or a series of Chebyshev polynomials. Unlike Finite Difference or Finite Element, the approximations are not local but are valid throughout the entire computational domain.

4.2.2 Finite Volume Method

The Finite Volume (FV) method has three main steps:

1) Formal integration of the governing equations over a control volume.
2) Conversion of the integral equations into a system of algebraic equations by substitution of a variety of Finite-Difference-type approximations for different terms in the governing equations.

3) Solution of the algebraic equations by an iterative method.

An important feature of the FV method is the conservation of flow properties for each finite volume.

The generic equation for the transport of a scalar ϕ in steady flows is of the form:

$$div\left(\rho \underline{u}\phi - \Gamma_\phi \, grad\phi\right) = S_\phi \tag{4.1}$$

where $\underline{u}$ is the velocity vector representing the fluid velocity, while Γ_ϕ and S_ϕ are the diffusivity and the source term of the scalar ϕ, respectively.

As was mentioned above, the first step in the FV method is to integrate the governing equation over the control volume, which for an arbitrary volume V bounded by a closed surface S can be written as

$$\int_S \underline{n} \cdot \left(\rho \underline{u}\phi - \Gamma_\phi \, grad\phi\right) dS = \int_V S_\phi dV \tag{4.2}$$

where $\underline{n}$ is the unit vector in the direction normal to the control volume surface. Now, if V and S are respectively assumed to be the cell volume (V_c) and discrete faces of a computational cell (S_j) (see Figure 4.1), the above equation can be re-written as

$$\underbrace{\sum_{j=1}^{N_f} \int_{S_j} \underline{n} \cdot \left(\rho \underline{u}\phi - \Gamma_\phi \, grad\,\phi\right) dS}_{\text{convection and diffusion terms}} = \underbrace{\int_{V_c} S_\phi dV}_{\text{source terms}} \tag{4.3}$$

where N_f is the number of faces of the cell.

The left hand side of Eqn. (4.3) contains both diffusion (D_j) and convection (C_j) terms. Each of these terms is expressed in terms of approximated average values over cell faces, donated by $(\,)_j$. Thus:

$$\sum_j \left(\rho \underline{u}\phi \cdot \underline{n}S\right)_j - \sum_j \left(\Gamma_\phi \, grad\phi \cdot \underline{n}S\right)_j = \sum_j C_j - \sum_j D_j \tag{4.4}$$

The diffusion terms D_j are approximated by face-centred expressions of the form

$$D_j \approx \Gamma_{\phi,j}\left[\underbrace{f_j^l(\phi_N-\phi_P)}_{\text{term 1}}+\underbrace{\left(grad\phi\cdot\underline{n}S-f_j^l\,grad\phi\cdot\underline{d}_{PN}\right)_j}_{\text{term 2}}\right] \tag{4.5}$$

where f_j^l correspond to geometrical factors and $\underline{d}_{PN}$ is the distance vector between the two neighbouring cell centres. Term 1 is the normal diffusion between cell *P* and the neighbouring cell-centred node *N*, and term 2 represents the cross-diffusion.

To approximate the convective term, there are several schemes including first-order Upwind Differencing (UD), second-order Central Differencing (CD) and more advanced Quadratic Upstream Interpolation for Convection Kinetics Scheme (QUICK). Some of the convection schemes used in the present work are discussed further in Section 4.7.2.3 in conjunction with STAR-CD.

Finally, the source terms in Eqn. (4.3) generally contain components representing sources or sinks for the transported property and additional flux terms.

4.3 BOUNDARY LAYER APPROXIMATIONS

As was mentioned earlier, the mean flow equations consist of the continuity, momentum, and energy equations. In the computations carried out using the in-house code, CONVERT (see Section 4.7.1 for a description of the code), these equations may be written in the 'thin shear' or 'boundary layer' approximation form, where there is a clear principal flow direction and a direction of principal gradients which is normal to the flow direction. Thus,

$$|U| >> |V| \quad \text{and} \quad |\partial/\partial y| >> |\partial/\partial x| \tag{4.6}$$

Thus, in Cartesian tensor notation (where U_j represents a mean velocity component), the mean flow conservation equations are as follows:

Continuity:

$$\frac{\partial U_j}{\partial x_j} = 0 \tag{4.7}$$

Momentum:

$$U_j \frac{\partial U_i}{\partial x_j} = -\frac{1}{\rho}\frac{\partial p}{\partial x_i} + \frac{\partial}{\partial x_j}\left[(\nu + \nu_t)\frac{\partial U_i}{\partial x_j}\right] + g_i \tag{4.8}$$

where $i = 1$ and

$$g_i = \begin{cases} -g \ \ for\ ascending\ \ flow \\ +g \ \ for\ descending\ \ flow \end{cases} \tag{4.9}$$

Energy:

$$U_j \frac{\partial T}{\partial x_j} = \frac{\partial}{\partial x_j}\left[\left(\frac{\nu}{Pr} + \frac{\nu_t}{\sigma_t}\right)\frac{\partial T}{\partial x_j}\right] \tag{4.10}$$

where, following standard modelling practice, e.g. Launder and Sharma (1974), the turbulent Prandtl number is set to a constant value, $\sigma_t = 0.9$.

These approximations lead to significant reduction in the number of terms appearing in the governing equations.

4.4 BOUSSINESQ APPROXIMATION

Another approximation for the mean flow equations which was employed in all three codes used in the present work is concerned with partial elimination of variable property effects from the equation set and is known as the 'Boussinesq approximation'. In this approximation all fluid properties, with the exception of density appearing in the body force term of the momentum equation, are taken as constant. Density appearing in the body force term is written as a linear function of local-to-reference temperature difference:

$$\rho = \rho_0 \left[1 - \beta(T - T_0)\right] \tag{4.11}$$

where ρ_0 is density corresponding to the reference temperature, T_0. β is the coefficient of volumetric expansion.

Therefore, in the Boussinesq formulation, the momentum equation becomes:

$$\rho \frac{\partial}{\partial x_j}\left(U_j U_i\right) = -\frac{\partial p}{\partial x_i} + \frac{\partial}{\partial x_j}\left((\mu + \mu_t)\frac{\partial U_i}{\partial x_j}\right) + \rho_0 g_i \left[1 - \beta(T - T_0)\right] \tag{4.12}$$

As a 'rule of thumb', the Boussinesq approximation is applicable for bulk temperature rises of less than 10% of the initial absolute temperature (Gray and Giorgini, 1976).

4.5 BUOYANCY PRODUCTION TERM

In addition to momentum equation, for buoyancy affected problems, an extra term could be introduced in both k and ε transport equations. This term is known as the 'production of turbulent kinetic energy due to buoyancy' or 'P_G'. For buoyant flows, therefore, the k and ε transport equations of the Launder-Sharma model (Launder and Sharma, 1974) could be extended to read as:

$$\frac{Dk}{Dt} = P_k + P_G + \frac{\partial}{\partial x_j}\left[\left(\nu + \frac{\nu_t}{\sigma_k}\right)\frac{\partial k}{\partial x_j}\right] - \left[\tilde{\varepsilon} + 2\nu\left(\frac{\partial (k)^{1/2}}{\partial x_j}\right)^2\right] \tag{4.13}$$

$$\frac{D\tilde{\varepsilon}}{Dt} = C_{\varepsilon 1}\frac{\tilde{\varepsilon}}{k}P_k + C_{\varepsilon 1}\frac{\tilde{\varepsilon}}{k}P_G + \frac{\partial}{\partial x_j}\left[\left(\nu + \frac{\nu_t}{\sigma_\varepsilon}\right)\frac{\partial \tilde{\varepsilon}}{\partial x_j}\right] - C_{\varepsilon 2} f_\varepsilon \frac{\tilde{\varepsilon}^2}{k} + E_\varepsilon \tag{4.14}$$

where

$$P_G = \frac{1}{\rho} g_i \overline{\rho' u_i} \tag{4.15}$$

In the above equation, g_i has the same definition as in Eqn. (4.9) and ρ' represents the fluctuating temperature-dependent density.

In the present work, the buoyancy production term was generally omitted for all buoyancy-affected flows. However, as will be discussed in Chapter 5, in a series of calculations where P_G was included, two modelling strategies were adopted. In both cases, the starting point was to re-cast Eqn. (4.15) in terms of fluctuating temperature, θ. Thus, in accordance with the Boussinesq approximation

$$P_G = -\beta\, g_i\, \overline{u_i\theta} \tag{4.16}$$

where $\overline{u_i\theta}$ is the turbulent heat flux and is described below.

4.6 TURBULENT HEAT FLUX MODELLING

In order to calculate heat transfer, the energy equation must be closed, i.e. a model for the turbulent heat fluxes are required. As far as the present work is concerned, in order to model the turbulent heat fluxes, $\overline{u_i\theta}$, two methods are used and are briefly described below:

- **Simple Gradient Diffusion Hypothesis (SGDH)**

This approach to modelling the turbulent heat fluxes relies upon the concept of an isotropic turbulent thermal conductivity

$$\rho\, c_p \overline{u_i\theta} = -\lambda_t \frac{\partial T}{\partial x_i} \tag{4.17}$$

where

$$\lambda_t = \frac{c_p\, \mu_t}{\sigma_t} \tag{4.18}$$

where the turbulent Prandtl number, $\sigma_t = 0.9$. Combining the above two equations results in

$$\overline{u_i\theta} = -\frac{\nu_t}{\sigma_t} \frac{\partial T}{\partial x_i} \tag{4.19}$$

Therefore, the buoyancy production term becomes

$$P_G = \beta\, g_i \frac{\nu_t}{\sigma_t} \frac{\partial T}{\partial x_i} \tag{4.20}$$

It is well known that in a simple shear flow with only wall-normal temperature variations, the heat flux in the streamwise direction is usually significantly larger than in the wall-normal direction. Therefore, in spite of λ_t being notionally isotropic, equations of the form of Eqn. (4.17) may lead to a poor approximation to the axial turbulent heat flux since temperature variations are negligible in this direction. (Cotton and Jackson, 1990).

- **Generalized Gradient Diffusion Hypothesis (GGDH)**

This method which was first introduced by Daly and Harlow (1970) may provide a better model for P_G in comparison to SGDH. In Generalized Gradient Diffusion Hypothesis (GGDH), the turbulent heat flux is modelled as

$$\overline{u_i\theta} = -c_\theta \frac{k}{\varepsilon} \overline{u_i u_j} \frac{\partial T}{\partial x_j} \tag{4.21}$$

where $c_\theta = 0.3$. Therefore, the buoyancy production term becomes

$$P_G = \beta\, g_i\, c_\theta \frac{k}{\varepsilon} \overline{u_i u_j} \frac{\partial T}{\partial x_j} \tag{4.22}$$

It has been reported by Cotton (1987) that inclusion of P_G in the k and ε transport equations has an insignificant effect when modelled in accordance with the SGDH and only a second-order effect when modelled using the GGDH. The effects of including the Buoyancy production term and modelling the turbulent heat flux using both the SGDH and the GGDH are discussed further in Chapter 5.

4.7 DESCRIPTION OF THE CODES USED

4.7.1 In-house Code: CONVERT

4.7.1.1 Introduction

An in-house Fortran Code, known as 'CONVERT' (for Convection in Vertical Tubes) is one of the codes used to generate results in this project. CONVERT is a computer program written in Fortran 77, and was originally developed by Cotton (1987) as a modification of the code 'PASSABLE' developed by Leschziner (1982); CONVERT was later extended by some other workers including Yu (1991), Mikielewicz (1994), Kirwin (1995) and the present author. CONVERT differs from PASSABLE principally in that the overall mass continuity constraint is satisfied using the 'exact' method of Raithby and Schneider (1979). Details of CONVERT can be found in Cotton (1987) and Yu (1991), therefore only a brief overview is given here.

In CONVERT the differential equations to be solved are first formally integrated over a control volume and then discretized in accordance with the finite volume/finite difference scheme of Leschziner (1982). After converting the differential equations to a set of algebraic ones and forming a tri-diagonal matrix, solution is obtained using the Tri-Diagonal Matrix Algorithm (TDMA). The governing equations are 'parabolic' (i.e. the flow is unaffected by the downstream conditions), thus the program is 'marching' in the streamwise direction. Solution is obtained iteratively at each station (i.e. axial solution position) and is then advanced to the next station.

4.7.1.2 Computational procedure

The geometry defined in CONVERT has 101 grid nodes in the radial direction with 100 control volumes, the surfaces of which are placed mid-way between two adjacent grid nodes (except the wall and centre-line control volumes).

An expanding distribution of nodes is employed to ensure good resolution of the near-wall flow. The grid distribution in the radial direction is based on specifying the value of y^+ at 51st and 100th node (the 1st and the 101st node being at the centre-line and wall, respectively). Typical values used in the present work are $y^+ = 50$ for the 51st and $y^+ = 0.5$ for the 100th node. Small steps (of 0.001R) are taken in the axial direction.

The initial axial step length is made small (0.001R). However, the user has an option of choosing constant or variable step sizes. Although using variable step size is more efficient in terms of computational time, it may not be very accurate, especially in mixed convection problems, as development of the flow may occur in an unpredictable manner along the entire length of the pipe, which means constant and small steps are more desirable and are therefore used in the present study.

At each station, for the solution to be deemed to be converged, a normalized difference between two successive iterations at that particular station, should be less than a pre-defined value, known as 'convergence criterion'. The user can specify a different convergence criterion for the velocity and temperature fields, as well as for the turbulent kinetic energy. In the present work, however, the convergence criterion for all three was set to 0.0001. Once the convergence criteria are satisfied, the computation is advanced to the next station downstream.

Use of an under-relaxation factor can promote convergence by causing changes in variables to occur gradually. In CONVERT under-relaxation was applied to the k and ε fields, immediately following solution of each field for second and subsequent iterations. A typical value of under-relaxation factor in the present study is 0.2, but it might be varied slightly for different turbulence models.

As illustrated in Figure 4.2, in order to perform a mixed convection computation, first, an initial isothermal/forced convection run ($g_i = 0$) ('RUN 1') is made in which the dynamic field is allowed to develop from approximate initial profiles to a fully-

developed state as determined by the particular turbulence model in use. In the present work, RUN 1 was typically set to 50*D*. Next, a mixed convection run (RUN 2) reads the fully-developed mean flow and turbulence profiles from RUN 1 at $x = 0$. A uniform wall heat flux is applied and the buoyancy force term is activated in Eqn. (4.8). In those cases where it is required that the mixed convection run should itself reach a hydrodynamically and thermally fully-developed state, RUN 2 is extended 500 diameters downstream of $x = 0$, although, as will be seen later, in the case of one particular Eddy Viscosity Model (EVM) the domain had to be restricted to 50*D* because of convergence difficulties.

Three EVMs have been examined using CONVERT: 1) The Launder and Sharma model (Launder and Sharma, 1974), the 'LS model', 2) The Cotton-Ismael three-equation scheme (Cotton and Ismael, 1998), the 'CI model', and 3) The Suga non-linear EVM (Craft et al., 1996b), the 'Suga model'. More detailed descriptions of the three turbulence models are given in Chapter 3.

The accuracy of the computational procedure has been tested by Cotton (1987), Yu (1991) and Kirwin (1995) through carrying out various sensitivity tests. These sensitivity tests involved changing various parameters including the radial and axial spacing of grid nodes, the convergence criteria, and the relaxation factors. For example, Kirwin (1995) found an increase of 2.1% in Nusselt number by decreasing the relaxation factor from 0.2 to 0.05 when the convergence criterion was set to 0.001. Kirwin also showed that making the convergence criteria more stringent than those used in the present study, would only change the Nusselt number by less than 0.2%. In addition, in Chapter 5, similar sensitivity tests have also been conducted by the present author.

4.7.2 Commercial Code: STAR-CD

4.7.2.1 Introduction

STAR-CD (a product of CD-Adapco; see CD-Adapco, 2006) is a general-purpose commercial finite-volume CFD package. The code is a self-contained and fully-integrated package providing the three main elements of pre-processor, solver, and post-processor. STAR-CD offers a wide range of turbulence models. The RANS turbulence models in the code range from a simple algebraic model and different variants of the k-ε and k-ω models to advanced second-moment closures models. This code also incorporates two sub-grid-scale based models for LES, namely the classical Smagorinsky model and a one-equation sub-grid model. A full description of the code can be found in the STAR-CD manual (CD-Adapco, 2006). Only some relevant details are briefly discussed here for the sake of completeness.

STAR-CD was used to generate results for all the cases studied during the course of this project including ascending flow in vertical heated pipes, 2D rib-roughened channels, and 3D AGR fuel elements.

4.7.2.2 Boundary Conditions

STAR-CD can apply a variety of boundary conditions. Two of these boundary conditions are used the most in the present study and are described below.

Symmetry Boundaries

Symmetry boundary conditions are those that arise by viewing the computational domain as a sub-region of some larger domain which possesses planes or axes of symmetry (Figure 4.3). In STAR-CD, plane two-dimensional flows can be simulated using a single layer of cells bounded on its sides by symmetry planes, since there is no velocity component in the spanwise direction. This type of boundary condition can also be applied to axially symmetric flows, for instance by generating a single segment of

cells and applying the symmetry conditions on the segment surfaces. Applying symmetry boundary conditions can significantly reduce the mesh size and consequently results in considerable savings in computational time. It should be noted, however, that symmetry boundary conditions cannot be used in LES and DNS, where full resolution of the domain is required.

Periodic (Cyclic) Boundaries

This type of boundary condition consists of pairs of geometrically identical boundaries at which all flow conditions are matched. In STAR-CD these operations are performed automatically at declared cyclic pairs. A simple example is that of a 2-dimensional channel with both walls roughened by a repeating obstacle (Figure 4.3). By using symmetry and cyclic boundary conditions, it is possible to solve only a small section made up of one symmetry plane and one pair of cyclic boundary conditions.

In applying periodic boundary conditions, special treatment of the transport equations is required: by adding extra source terms to the momentum and energy equations, the streamwise pressure drop and temperature increase due to heating are accounted for.

In a periodic fully-developed region, the pressure, P, and temperature, T, can be decomposed as

$$P = P^*(x, y) - \beta x \text{ and } T = T^*(x, y) + \gamma x \tag{4.23}$$

Now the governing equations based on RANS for an incompressible fluid with constant properties are re-written as

$$\frac{\partial U_i}{\partial x_i} = 0 \tag{4.24}$$

$$\frac{\partial}{\partial x_j}\left(U_j U_i\right) = \frac{\beta}{\rho}\delta_{i1} - \frac{1}{\rho}\frac{\partial P^*}{\partial x_i} + \frac{\partial}{\partial x_j}\left(\nu\frac{\partial U_i}{\partial x_j} - \overline{u_i u_j}\right) \tag{4.25}$$

$$\frac{\partial}{\partial x_j}\left(U_j T^*\right)=\frac{\partial}{\partial x_j}\left[\frac{\nu}{Pr}\frac{\partial T^*}{\partial x_j}-\overline{u_j\theta}\right]-U_j\gamma\delta_{1j} \tag{4.26}$$

where the extra source term in the momentum equation, assuming a linear pressure drop characteristics in the streamwise direction, is

$$\beta=\frac{\partial P}{\partial x_i} \tag{4.27}$$

The pressure P^* behaves periodically and gives no contribution to the pressure drop over a unit cell with periodic boundary conditions. The extra source term in the energy equation is

$$\gamma=\frac{\partial T_b}{\partial x}=\frac{\dot{q}\,A_{ht}}{\dot{m}\,c_p\left(x_{out}-x_{in}\right)} \tag{4.28}$$

where $\dot{q}$ is the wall heat flux, A_{ht} is the wall heat transfer area, and $\dot{m}$ is the mass flow rate. The functions $P^*(x,y)$ and $T^*(x,y)$ are repeated from x_{in} to x_{out} and indicate the local departure of the pressure and the temperature from the linear decrease given by $-\beta x$ and the linear increase given by γx, respectively (Liou et al., 1993a).

4.7.2.3 Convection Discretization Schemes

In this section various schemes available in STAR-CD for discretization of the convection term are presented (CD-Adapco, 2006).

Upwind Differencing (UD)

This first-order scheme takes into account the direction of the flow by setting the value of variable ϕ at a cell face equal to its value at the upstream node (see Figure 4.4). Thus:

$$C_j \equiv F_j\begin{cases}\phi_P & \text{for} \quad F_j \geq 0\\ \phi_{N+} & \text{for} \quad F_j < 0\end{cases} \tag{4.29}$$

Despite being a stable and bounded scheme, the UD method is only first-order accurate. Another disadvantage of this scheme is that it can produce 'false diffusion'. Such false diffusion tends to stabilise the flow calculation by reducing gradients in ϕ, consequently resulting in inaccurate solutions in regions with steep flow gradient, particularly where the flow and grid-lines are not aligned. It has been shown that false diffusion can be large enough to give physically incorrect results (Leschziner, 1980).

Linear Upwind Differencing (LUD)

LUD is another scheme in STAR-CD which is a specially adapted, second-order accurate scheme formulated for non-structured meshes. In comparison to UD, the LUD scheme produces less false diffusion, but can produce solutions that are outside physical limits on ϕ (i.e. the scheme is unbounded).

Central Differencing (CD)

The CD scheme is second-order accurate and interpolates linearly between nearest neighbour values. Thus

$$C_j \equiv F_j\left[f_+ \phi_P + (1-f_+)\phi_{N+}\right] \tag{4.30}$$

where f_+ is a geometrical interpolation factor ($f_+ = 0.5$ for regular grids).

One of the major disadvantages of CD scheme is that it admits an influence at node P from the directions of all its neighbours to calculate convective fluxes and consequently it cannot recognize the direction of the flow or the strength of convection relative to diffusion. In comparison to UD scheme, however, it produces less false diffusion and therefore is recommended for use in DNS and LES calculations.

Monotone Advection and Reconstruction Scheme (MARS)

MARS which is specific to STAR-CD is a multidimensional second-order accurate differencing scheme. Unlike the above schemes, MARS is a monotone scheme, which

means it does not lead to an oscillatory behaviour of the numerical solution (Hirsch, 1990). MARS operates in two separate steps:

1) **Reconstruction:** A set of monotone gradients are computed using a multidimensional Total Variation Diminishing (TVD) scheme (TVD schemes cannot create new local extrema. In addition, the value of an existing local minimum cannot be decreased and that of a local maximum cannot be increased i.e. ensures convergence).
2) **Advection:** The reconstructed cell-face flow properties are used to compute the face fluxes for all advected properties using a monotone and bounded advection scheme.

The advantage of MARS is that it does not rely on any problem-dependent parameters to operate and it can automatically handle all flow problems and mesh types supported by STAR-CD (CD-Adapco, 2006). In this scheme the user has the option of choosing a value between 0 and 1 as a 'compression level', with the default value being 0.5. Lower compression levels produce a computationally efficient scheme at the expense of sharpness of resolution, while increasing the compression level improves the resolution, but also results in an increase in the number of iterations. Compared to other schemes available in STAR-CD, MARS is the least sensitive to mesh structure and skewness, features which make it a common choice in practice.

Blended Differencing (BD)

In this approach a higher-order scheme such as CD or LUD is blended with the lower-order UD scheme, thus:

$$C_j^{BD} \equiv \gamma C_j^{CD/LUD} + (1-\gamma) C_j^{UD} \tag{4.31}$$

where the blending factor γ is defined by the user. Optimum results with this scheme are often obtained through trial-and-error.

Finally, it is worth mentioning that a particular feature of STAR-CD is that it enables the user to choose different discretization schemes for individual transport equations. In the present work, CD and UD schemes have been used for the momentum and turbulence transport equations, respectively. (Although, as will be seen in Chapter 7, in the computations of the 3D fuel element, UD scheme was used for both the momentum and turbulence transport equations in order to reach a converged solution.) In addition, MARS with the compression level set to 0.5 was used for the energy equation in all the cases studied in the present study.

4.7.2.4 Standard Wall Function

Standard Wall Functions (SWFs) were briefly introduced in Section 3.5.5. In the present work, SWF was applied to a 2-dimensional rib-roughened channel and comparison was made against low-Reynolds-number computations (see Section 6.4.3 for further detail). In this section, the formulation of the SWF implemented in STAR-CD for calculating velocity are discussed (CD-Adapco, 2006):

Velocity

Velocity is calculated based on the log-law discussed earlier in Section 3.5:

$$u^+ = \begin{cases} y^+ & for\ y^+ \le y_m^+ \\ \dfrac{1}{\kappa}\ln(Ey^+) & for\ y^+ \ge y_m^+ \end{cases} \tag{4.32}$$

where $u^+ = (u - u_w)/u_\tau$

u = tangential fluid velocity

u_w = tangential wall velocity

$u_\tau = (\tau_w/\rho)^{1/2}$

τ_w = wall shear stress

$y^+ = \rho\, u_\tau\, y / \mu \approx \rho\, C_\mu^{1/4}\, k^{1/2}/\mu$

$E = 9.0$

$\kappa = 0.419$

y_m^+ satisfies the following:

$$y_m^+ - \frac{1}{\kappa}\ln(Ey_m^+) = 0 \tag{4.33}$$

The SWF in STAR-CD has specific treatments for semi- and fully-rough surfaces, where Eqn. (4.32) is re-defined as

$$u^+ = \begin{cases} y^+ & for\ y^+ \le y_m^+ \\ A + \frac{1}{\kappa}\ln\left[\frac{y^+ - D^+}{B + CR^+}\right] & for\ y^+ \ge y_m^+ \end{cases} \tag{4.34}$$

where A, B, and C are constants and D^+ and R^+ are defined as

$$D^+ = \rho C_\mu^{1/4} k^{1/2} \frac{D}{\mu} \tag{4.35}$$

$$R^+ = \rho C_\mu^{1/4} k^{1/2} \frac{y_0}{\mu} \tag{4.36}$$

where D is the displacement thickness and y_0 the equivalent roughness height. Figure 4.5 shows how D and y_0 are defined in a fully-rough example. Note that the fluid velocity goes to zero at $y = y_0 + D$ from the wall.

Based on the measurements of Nikuradse for sand-roughness (Schlichting, 1968), STAR-CD takes the following values by default: $A = 8.5$, $B = 0$, $C = 1$, and $D = 0$.

Note that the energy and turbulence transport equations are not discussed here. However, the interested reader is referred to the STAR-CD manual for more details (CD-Adapco, 2006).

4.7.3 Industrial Code: Code_Saturne

Code_Saturne is an industrial code developed by Electricité de France (EdF) for the principal purpose of performing thermo-hydraulic computations related to power generation applications. Code_Saturne has three-dimensional capability and may be used for steady or transient, single-phase laminar or turbulent flows. The code is based

on a finite volume approach and stores the flow variables in a fully-collocated arrangement. Structured and unstructured meshes with different types of cell shape including hybrid meshes with arbitrary interfaces can be used. Velocity-pressure coupling is obtained using a predictor-corrector scheme (Archambeau et al., 2004).

Code_Saturne can be divided into two separate software elements:

1) The 'Kernel' which performs the numerical solution.
2) The 'Shell' which processes the mesh and creates output readable by post-processing software.

Since 1996, this code has been continuously developing both at EdF and at the University of Manchester and has been validated over a wide range of academic and complex industrial cases. Examples cited in the paper of Archambeau et al. (2004) show the capability of the code to tackle a wide range of flow problems.

The first officially-approved version of the code (Code_Saturne 1.0) was released in 2001 and had only two RANS-based turbulence models. Code_Saturne now features many turbulence models (standard k-ε, k-ω-*SST*, v^2- f and second moment closure). It also uses the Smagorinsky and dynamic LES formulations.

The code adopts a second-order centred scheme in space and time. A global Crank-Nicholson scheme is used for both convection and diffusion. Non-linearity is treated by evaluating the mass flux using an Adams-Bashforth extrapolation. Velocity and pressure coupling is ensured by a predictor-corrector method with a SIMPLEC algorithm. The results obtained using Code_Saturne are presented in Chapter 5.

Finally, Table 4.1 shows an overview of the test cases studied in the present work using all three codes that were discussed in this chapter. The turbulence models used for each test case are also included in this table.

Code	Case(s) studied	Turbulence model(s) used*
CONVERT	Vertical Heated Pipe	LS, CI and Suga
STAR-CD	Vertical Heated Pipe	LCL k-ε, k-ω-SST, v^2-f, Suga and LES†
	2D Rib-Roughened Channel	LCL k-ε, k-ω-SST, v^2-f and Suga
	3D AGR Fuel Element	v^2-f
Code_Saturne	Vertical Heated Pipe	k-ω-SST and Manchester v^2-f‡

Notes:
* See Chapter 3 for more information on the turbulence models used in the present study.
† The computations using this model were carried out by Yacine Addad (also reported in Addad and Laurence, 2008 and Keshmiri et al., 2008a).
‡ The computations using this model were carried out by Flavien Billard (also reported in Billard et al., 2008).

Table 4.1 – Summary of the codes used in the present work for different test cases using various turbulence models.

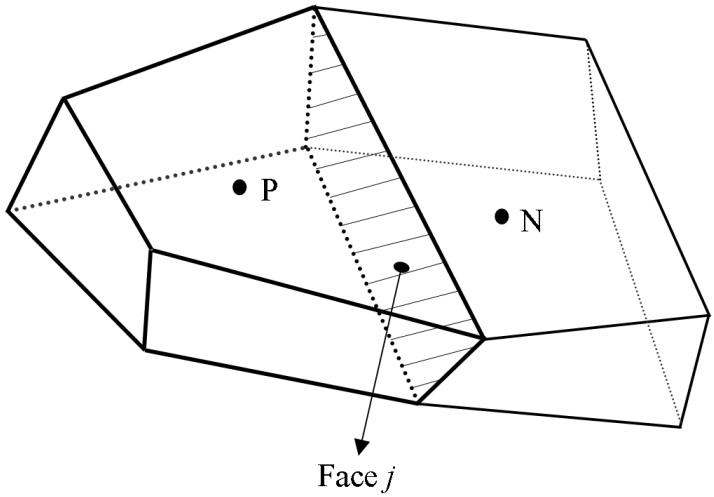

Figure 4.1 – A typical cell centred with node P and neighbour cell centred with node N.

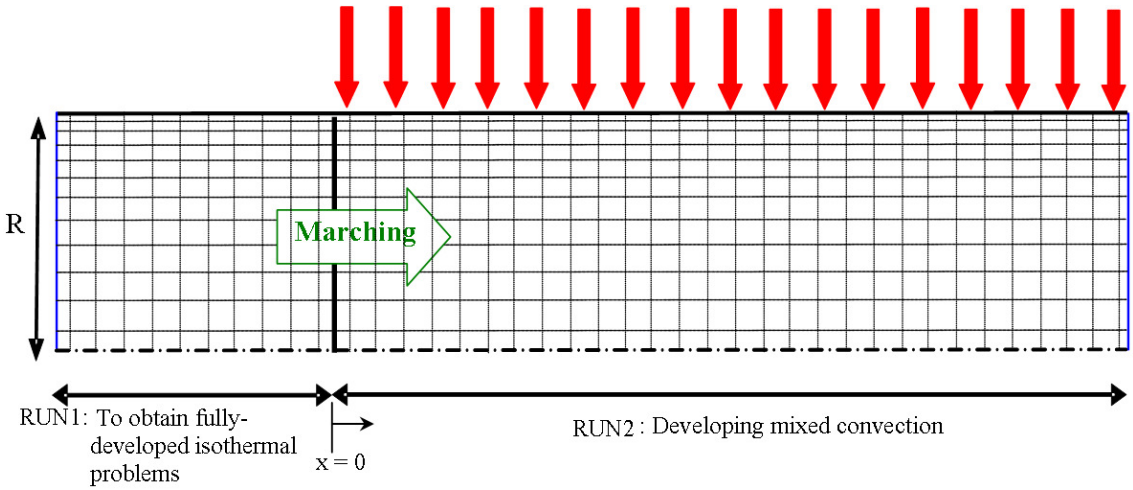

Figure 4.2 – CONVERT solution sequence.

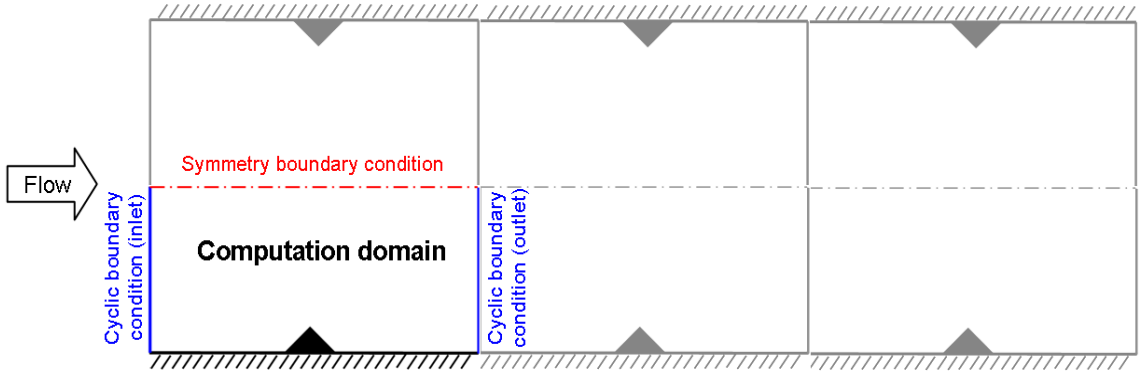

Figure 4.3 – Definition of 'Symmetry' and 'Cyclic' boundary conditions.

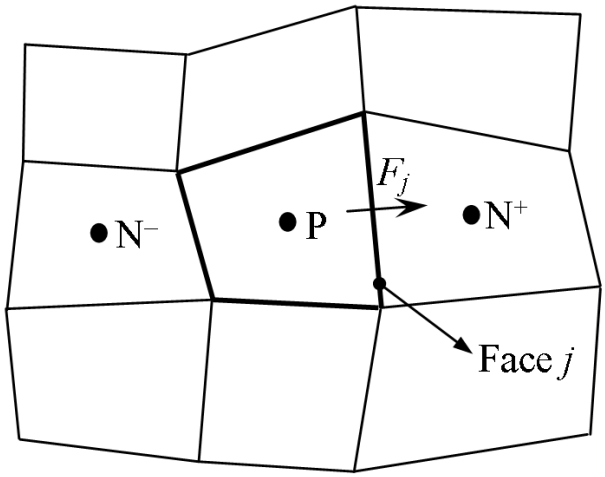

Figure 4.4 – Node labelling convention for flux discretization.

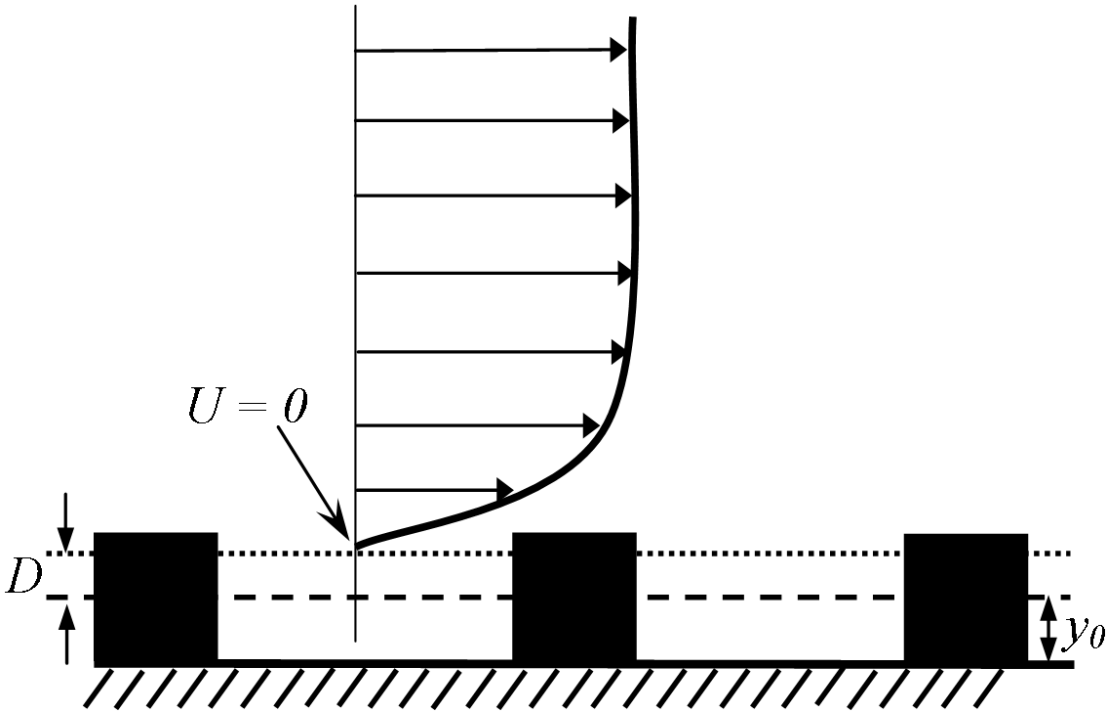

Figure 4.5 – Definition of the standard wall function in STAR-CD.

CHAPTER 5

VERTICAL HEATED PIPE

5.1 PRELIMINARY REMARKS

In this chapter, heat transfer performance of mixed convection flows is investigated using a range of refined Reynolds-Averaged-Navier-Stokes (RANS) turbulence models. While all belong to the broad class of Eddy Viscosity Models (EVMs), the various RANS closures have different physical parameterizations and might therefore be expected to show different responses to externally-imposed conditions. Comparison is made against various experimental data including the works of Steiner (1971), Carr et al. (1973), Easby (1978), Polyakov and Shindin (1988) and Parlatan et al. (1996) (in contrast, Parlatan et al. (1996) used water as the working fluid, although the primary focus of the present work being on gas-cooled reactors). In addition, mean flow and turbulence profiles are compared against the recent results of You et al. (2003) who conducted a DNS study on turbulent mixed convection in a heated vertical pipe for conditions of constant properties with buoyancy accounted for using the Boussinesq

approximation. This feature of their computations enables the effects of buoyancy to be studied in isolation from other influences associated with the non-uniformity of fluid properties and flow acceleration. Large Eddy Simulation (LES) results generated by author's colleagues as part of this project are also reported.

Three different CFD codes have been employed in the work: 'CONVERT', 'STAR-CD', and 'Code_Saturne', which are respectively in-house, commercial, and industrial packages.

Attention in the present chapter is mainly focused on ascending flow case (although some results on descending flow cases are also reported), and the geometry, which consists of a long vertical pipe, is illustrated in Figure 5.1.

Throughout this chapter, the dimensionless 'buoyancy parameter', *Bo*, is used to characterize the extent of buoyancy influence. The buoyancy parameter here is defined in the form quoted by Jackson et al. (1989):

$$Bo = 8\times10^{4}\,\frac{Gr}{Re^{3.425}\,Pr^{0.8}} \tag{5.1}$$

where the Grashof number, *Gr*, is defined as

$$Gr = \beta g D^{4}\dot{q}/(\lambda\nu^{2}) \tag{5.2}$$

Here the results of various turbulence models are presented in two main sections: in the first section local heat transfer and friction coefficients for a range of *Bo* are presented and the present EVM computations are compared against several sets of experimental data and the DNS results of You et al. (2003). In the second section, mean flow and turbulence profiles are presented for each model and comparison is again made with the DNS data of You et al.

The next group of calculations provides greater detail of thermal-hydraulic development by plotting *Nu* vs. *x/D*. However, it is the case that fewer models are employed; and comparison is made with the experimental data of Polyakov and Shindin

(1988). In the final part of this chapter, the effects of Reynolds number on the heat transfer and friction coefficient are examined.

5.2 CASE DESCRIPTION

5.2.1 Introduction

The geometry studied here consists of a long vertical pipe for which the thermal boundary condition is one of uniform wall heat flux. The working fluid is assumed to be standard air and the Reynolds number based on the pipe diameter is set to Re = 5,300 (except in Section 5.6 where computations are carried out for a range of Reynolds numbers). The Prandtl number of standard air (Pr = 0.71) is used throughout calculations. In addition, all fluid properties are assumed to be constant and buoyancy is accounted for within the Boussinesq approximation. The values of some other parameters used in the present simulations are given in Table 5.1.

Parameter	**symbol**	**units**	**values**
Reference Temperature	T_{ref}	$°K$	293
Density	ρ	kg/m^3	1.205
Specific heat coefficient at constant pressure	c_p	$J/kg°K$	1005
Conductivity	λ	$W/m°K$	0.0257
Molecular viscosity	μ	Kg/ms	1.82×10^{-5}
Coefficient of volumetric expansion	β	$°K^{-1}$	0.003413
gravitational acceleration	g	m/s^2	9.81
Pipe diameter	D	m	0.2
Pipe length (only in CONVERT)	L	m	500D

Table 5.1 – The fluid properties used in the present simulations.

In computing mixed convection flows, You et al. (2003) retained the same Reynolds and Prandtl numbers and varied buoyancy influence via the Grashof number. A total of

four simulations were performed and these are detailed in Table 5.2. In each case a brief description of the thermal-hydraulic regime is included in the table. The mean flow and turbulence profiles presented in Section 5.4 are reported for the four thermal-hydraulic regimes indicated in Table 5.2.

Case	Gr/Re^2	Bo	Thermal-Hydraulic Regime
A	0	0	Forced convection
B	0.252	0.13	Early-onset mixed convection
C	0.348	0.18	Laminarization
D	0.964	0.50	Recovery

Table 5.2 – DNS cases of You et al. (2003).

5.2.2 Mesh and Numerical Details

5.2.2.1 CONVERT

The in-house code, CONVERT was introduced in Section 4.7.1. Some of its features are briefly reviewed here again.

Three EVMs have been examined using CONVERT:

1) The Launder and Sharma model (Launder and Sharma, 1974), the 'LS model',
2) The Cotton-Ismael three-equation scheme (Cotton and Ismael, 1998), the 'CI model', and
3) The Suga non-linear EVM (Suga, 1995; Craft et al., 1996b), the 'Suga model'.

The Suga model was implemented in CONVERT by the author (verification and validation tests of this model are shown in Appendix B). A more detailed description of above turbulence models can be found in Section 3.6.8.

The mesh used in CONVERT is a radial mesh consisting of 100 control volumes and a double expansion technique is employed to ensure good resolution of the near-wall flow (the wall-adjacent node is typically located at $y^+ = 0.5$ and half the nodes are

located between the wall and y^+ = 50). Small steps (of 0.001R) are taken in the axial direction and at-station iteration is applied to ensure a converged solution before the computation is advanced to the next location downstream.

As illustrated in Figure 5.2, each mixed convection run is preceded by an 'isothermal run' in order to generate fully-developed velocity and turbulence profiles at entry to the heated mixed convection section (the isothermal run is started from approximate initial profiles). In order to ensure the flow is fully developed, the pipe length in CONVERT is set to 500D (however, as will be seen later, in the case of the Suga model the flow domain was limited to 50D since converged solutions could not be obtained downstream of that location).

Sensitivity Tests

To ensure that the computational solutions are not affected by making the standard procedures of running CONVERT more stringent, sensitivity tests must be applied. A 'standard run' is introduced as shown in Table 5.3 and the parameters described in this table are, by turn, made more stringent. If the resulting change in the computed Nusselt number or friction coefficient is greater than 1%, then the original procedure is to be deemed unacceptable.

The sensitivity tests are done through applying eight different tests, for two cases of forced convection (case A) and mixed convection (case D). The Launder-Sharma model has been used for these sensitivity tests and the results are listed in Table 5.4 and Table 5.5, respectively. The description of each test run in these two tables is as follows:

i) The pipe length was increases to 250D to ensure that the flow is fully developed.

ii) The step length was reduced by one order of magnitude.

iii) Variable step length was used and the step length modification criterion was reduced to 5%.

iv) Variable step length was used and the maximum step length was halved.

v) The position of the 51st node was moved to $y^+ = 30$.

vi) The position of the 100th node was moved to $y^+ = 0.25$.

vii) The relaxation factor was changed to 0.3.

viii) The convergence criteria for the velocity, turbulent and thermal fields were reduced to 10E-8.

Variable	Value
Reynolds number	5300
Prandtl number	0.711
Diameter [m]	0.1
Length	100D
Initial step length	0.01 - fixed
Step length modification criterion	10%
Maximum step length	0.1 (= 10 × Initial step-length)
y^+ at 51st node	30
y^+ at 100th node	0.5
Convergence Criterion (for U, k and T)	10^{-4}
Relaxation factor	0.2

Table 5.3 – Different parameters and their values for the 'standard run'.

Note that the output profiles of a standard run with the 'isothermal run' were used as the initial profiles for the validation tests in order to ensure that the results are independent of initial profiles.

The results shown in Table 5.4 and Table 5.5 serve to demonstrate that the standard procedures adopted in using CONVERT yield accurate solutions of the equation set and in fact, represent a conservative approach to the specification of numerical criteria.

Test	Nu	$[(Nu-Nu_{ref})/Nu_{ref}]\times100$ (%)	c_f	$[(c_f-c_{f\,ref})/c_{f\,ref}]\times100$ (%)
reference	15.833	-	7.299×10^{-3}	-
i	15.833	0	7.299×10^{-3}	0
ii	15.833	0	7.299×10^{-3}	0
iii	15.833	0	7.299×10^{-3}	0
iv	15.833	0	7.299×10^{-3}	0
v	15.833	0	7.299×10^{-3}	0
vi	15.833	0	7.299×10^{-3}	0
vii	15.833	0	7.299×10^{-3}	0
viii	15.833	0	7.299×10^{-3}	0

Table 5.4 – Sensitivity tests for forced convection; Case (A).

Test	Nu	$[(Nu-Nu_{ref})/Nu_{ref}]\times100$ (%)	c_f	$[(c_f-c_{f\,ref})/c_{f\,ref}]\times100$ (%)
reference	9.8769	-	11.633×10^{-3}	-
i	9.9166	0.40	11.629×10^{-3}	-0.03
ii	9.8768	0	11.634×10^{-3}	0.01
iii	9.9019	0.25	11.593×10^{-3}	-0.34
iv	9.8791	0.02	11.630×10^{-3}	-0.03
v	9.8769	0	11.633×10^{-3}	0
vi	9.8769	0	11.633×10^{-3}	0
vii	9.8769	0	11.633×10^{-3}	0
viii	9.8769	0	11.633×10^{-3}	0

Table 5.5 – Sensitivity tests for mixed convection; Case (D).

5.2.2.2 STAR-CD & Code_Saturne

The mesh used for the present STAR-CD and Code_Saturne computations is shown in Figure 5.3. The domain consists of a 2-degree sector of the pipe cross-section. Periodic boundary conditions are applied in the streamwise (x) direction, while symmetry

boundary conditions are applied at the two azimuthal (θ) faces. The face at $r = R$ represents the pipe wall. In principle, only one cell is necessary in the streamwise direction, however, five are used to promote convergence. There are 120 cells in the radial direction and the wall-adjacent cell is positioned at $0.15 < y^+ < 0.2$.

The following two turbulence models are used in the STAR-CD computations:

1) The *k-ω-SST* model of Menter (1994) (the model of Menter is also implemented in Code_Saturne, and direct comparison of the two codes is reported here).
2) The LCL *k-ε* model (due to Lien, Chen and Leschziner, 1996; termed the 'standard LRN *k-ε* model').

In the Code_Saturne computations, only the *k-ω-SST* model of Menter (1994) was used. It is worth mentioning that the results of the Manchester v^2-*f* scheme (Billard et al., 2008) developed by the author's colleagues at the University of Manchester is also included in the present work. (The Manchester v^2-*f* scheme, in view of its recent development, was discussed in Chapter 3 in some detail.)

5.3 RESULTS OF LOCAL NUSSELT NUMBER AND FRICTION COEFFICIENT

Results in this section are presented in three main parts: In the first part, there is an evaluation of model hydrodynamic and thermal performance in forced convection. All eddy viscosity models and LES computations are compared against the experimental data of Polyakov and Shindin (1988) and the DNS data of You et al. (2003). The second part includes an examination of mixed convection impairment or enhancement of Nusselt number and local friction coefficient with respect to forced convection values. The attention in this part is restricted only to the results of CONVERT. For both ascending and descending flows, the results are examined against several sets of experimental data and the DNS results of You et al. In the last part of this section, the

focus is on ascending flows and fully-developed Nu/Nu_0 and c_f/c_{f0} are plotted against the buoyancy parameter, Bo. The present EVM computations using all three codes are again compared against several sets of experimental and DNS data as well as the LES computations of Addad and Laurence (2008).

5.3.1 Forced Convection

Since forced convection Nusselt number and friction coefficient are to supply the normalizing parameter in the presentation of heat transfer and friction coefficient impairment/enhancement effects, it is appropriate first to assess model performance in the computation of buoyancy-free pipe flows. All runs are performed for Re = 5,300 (or Re_τ = 360 based on pipe diameter) and Pr = 0.71, the values selected by You et al. (Note, however, that the presentation below of mixed convection results in terms of the buoyancy parameter of Eqn. (5.1) does allow cautious extrapolation to other flow conditions.)

The results of this initial assessment are summarized in Table 5.6 and Figure 5.4 which show values of local Nusselt number and friction coefficient computed using the eight turbulence model/code combinations and single LES approach. The first points on the left of Figure 5.4 and the horizontal broken lines represent the DNS results of You et al. It is immediately apparent that, even for this simple 'baseline' case, there is significant disparity between the various schemes.

Naturally, an under- or over-prediction of Nu_0 and c_{f0} will affect the absolute level of mixed convection deduced from values of Nu/Nu_0 and c_f/c_{f0} to be examined next. Such discrepancies between the DNS figure and other possible 'reference' values of Nu_0 and c_{f0} is naturally a cause for concern. This concern relates directly to the preceding comparisons of forced convection Nusselt number and friction coefficient; it also extends to the evaluation of turbulence model computations of mixed convection heat

transfer and friction coefficient levels where there might be expected to be similar discrepancies within the reference database.

Models/Techniques	Nu_0	% diff.	c_{f0}	% diff.
DNS of You et al. (2003)	18.3	–	9.28×10^{-3}	–
Expt. of Polyakov and Shindin (1988)	19.6	+7.1	–	–
Launder & Sharma (CONVERT)	17.4	–4.9	8.52×10^{-3}	–8.2
Cotton & Ismael (CONVERT)	18.9	+3.3	9.17×10^{-3}	–1.2
Suga NLEVM (CONVERT)	18.3	0	8.93×10^{-3}	–3.8
LCL k-ε (STAR-CD)	17.9	–2.2	7.63×10^{-3}	–17.8
v^2-f (STAR-CD)	17.4	–4.9	9.08×10^{-3}	–2.2
Manchester v^2-f (Code_Saturne)	18.6	+1.6	8.95×10^{-3}	–3.6
k-ω-SST (STAR-CD)	21.9	+19.7	9.84×10^{-3}	+6.0
k-ω-SST (Code_Saturne)	19.8	+8.2	9.62×10^{-3}	+3.7
LES (STAR-CD)	20.1	+9.8	9.39×10^{-3}	+1.2

Table 5.6 – Results for fully-developed forced convection.

From Table 5.6, it is seen that the DNS value of Nu_0 is itself 7% lower than that found from the experiments of Polyakov and Shindin (1988)[*] (the data of Polyakov and Shindin are discussed further in Section 5.5.2 below) while the DNS value of c_{f0} is well within 1% of the friction coefficient obtained from the Blasius equation, viz. $c_{f0} = 0.079Re^{-0.25} = 9.26\times10^{-3}$.

It is noted that the long-established Launder-Sharma model somewhat under-predicts the DNS values of Nu_0 and c_{f0}. A particularly large discrepancy in the value of Nu_0 is returned by the STAR-CD *k-ω-SST* model (+19.7%), while the LCL *k-ε* formulation implemented in STAR-CD produces too low a value of c_{f0} (-17.8%). It is also seen that the Cotton-Ismael model and LES values of c_{f0} are in closest agreement

[*] Polyakov and Shindin's experiments were conducted at Re = 5100. The value of Nu_0 = 19.6 appearing in Table 5.6 has been obtained by scaling the present authors' determination of Nu_0 = 19.0 by a factor of $(5300/5100)^{0.8}$.

with the DNS data. Moreover, the value of Nu_0 returned by the Suga model lies closest to the DNS data.

The value of Nusselt number for forced convection condition can also be found through the modified form of the Dittus-Boelter equation (Kays and Leung, 1963):

$$Nu_0 = 0.022 Re^{0.8} Pr^{0.5} \tag{5.3}$$

Comparison of the DNS value of Nusselt number with above equation ($Nu_0 = 0.022 Re^{0.8} Pr^{0.5} = 17.7$), reveals the DNS value of Nu_0 to be approximately 3% higher than the correlation (the LS model is within 2% of this latter value).

It is of some interest (and relevance to the present study) to compare different correlations of the Dittus-Boelter type. Kays and Leung report that Eqn. (5.3) has been used to correlate a large amount of data for heat transfer to gases; they show good agreement with their own air flow data for $10^4 \leq Re \leq 10^5$. The Kays and Leung equation may be compared with the Dittus-Boelter expression in its generally quoted form (McAdams, 1954, p. 219):

$$Nu_0 = 0.023 Re^{0.8} Pr^{0.4} \tag{5.4}$$

Eqn. (5.4) is ostensibly valid for $Pr \approx$ O(1)-O(100). Considering Pr = 0.71, the equation returns values of Nu_0 that are 8% higher than Eqn. (5.3). Finally, it is noted that if the coefficient of Eqn. (5.4) is reduced to 0.021 (specifically in order to correlate data for air flow; McAdams, footnote to p. 219), the resulting form agrees with Eqn. (5.3) to within around 1%.

5.3.2 CONVERT; Ascending and Descending Flow

Turning next to mixed convection flows, Figure 5.5 provides an overview of heat transfer performance in ascending and descending flow computed using CONVERT. Nusselt number in mixed convection, Nu is normalized by the corresponding forced

convection value evaluated at the same Reynolds and Prandtl numbers, and Nu/Nu_0 is plotted against the buoyancy parameter, Eqn. (5.1). Present turbulence model results are shown together with the ascending and descending flow DNS data of You et al. (2003) and the experimental results of Steiner (1971), Carr et al. (1973), Parlatan et al. (1996) and Easby (1978). The first three experimental papers report results for ascending air flow, whereas Easby made measurements on a descending flow of nitrogen.

In their direct simulations You et al. adopted the Boussinesq approximation and cast the governing equations in fully-developed form. The Reynolds and Prandtl numbers of the seven simulations (one forced convection and six mixed convection) in the DNS of You et al. (2003) were 5300 and 0.71. The conditions of the present EVM runs therefore match exactly those of the DNS, and comparisons between the present computations and the direct simulation data are effectively in terms of Nu/Nu_0 vs. Gr (rather than Bo).

In contrast to the DNS of You et al., the three sets of experimental data all span a range of Reynolds number. It follows that some uncertainty is introduced into the comparisons because any functional dependence of Nu/Nu_0 on Bo is not exact. A second uncertainty is introduced because the experimental works do not report values for forced convection Nusselt number. Measured values of mixed convection Nusselt number are consequently normalized using Nu_0 determined from Eqn. (5.3) (with $Pr = 0.71$).

Examining the experimental data, especially for the 'Recovery' region ($Bo \geq 0.2$), a general observation might be made that there is considerable scatter in the measurements, a feature that may be due in part to variable property effects. In practice, variable property effects are minor in the case of the ascending flow data of Carr et al., while temperature variations in Steiner's test cases are sufficiently large to warrant the use of a full variable properties formulation in the computational simulation of the data (Cotton et al., 2001). Easby's descending flow data are also subject to significant property variations. The water data of Parlatan et al. suggest the sudden drop of heat

transfer to occur at a slightly smaller buoyancy parameter ($Bo \approx 1.5$).

An immediately striking feature of the ascending flow portion of Figure 5.5 is the catastrophic onset of large-scale heat transfer impairment that occurs at $Bo \approx 0.2$. Examining the EVM results, it is seen that the LS model is in closest agreement with the direct simulation data; the CI model returns a similar minimum level of heat transfer, but indicates that this is attained at higher Bo. Significantly lower levels of heat transfer impairment are returned by the Suga model and the onset of impairment is delayed considerably (these results are for $x/D = 50$ because, for cases with relatively high Bo, converged solutions could not be obtained at locations further downstream). In the 'recovery' region ($Bo \geq 0.5$) the LS and CI models are in close agreement, but the Suga model yields lower Nu/Nu_0.

Consideration of the descending flow region of Figure 5.5 reveals that there is little difference between the heat transfer enhancement levels of the Suga and CI models. The Nu/Nu_0 vs. Bo curve of the LS model lies above the other two EVM schemes, while the three DNS points suggest a lower trajectory. Easby's data for Nu/Nu_0 do not asymptote to unity at low Bo. If, however, the 'original' form of the Dittus-Boelter correlation, Eqn. (5.4), is used to supply Nu_0, the asymptotic behaviour is improved (Easby, 1978; Cotton, 1987). The implication that Nu_0 from Eqn. (5.3) is too 'low' does not appear to be related to variable property effects since a temperature-ratio correction to Eqn. (5.3) or (5.4) of the form $(T_w/T_b)^n$ would serve to *reduce* forced convection Nusselt number ($n \approx -0.55$; Kays and Perkins, 1973, p. 7-163).

Turning to examine friction coefficient, Figure 5.6 shows normalized local friction coefficient plotted against the buoyancy parameter. In the case of ascending flow all three models indicate little or no reduction in friction coefficient below the c_{f0} level. In the case of the LS model this is in part related to its under-prediction of c_{f0} (see Table 5.6). This in turn results in an earlier onset of enhancement in friction coefficient

compared to the experimental results of Carr et al. (1973) and DNS data. In comparison to the LS and CI models, the results of the Suga model show higher gradient of enhancement. Considerable scatter in the experimental measurements of Parlatan et al. (1996) can also be seen, especially for higher *Bo*.

For the descending flow, all models and the DNS data suggest that the local friction coefficient is rather a weak function of buoyancy parameter. While the LS and CI models as well as the DNS data predict a slightly increasing trend for the friction coefficient at higher *Bo*, the Suga model returns an opposite for c_f/c_{f0} against *Bo*.

Finally, it is worth noting that in Figure 5.6 some discrepancies can be seen between the results of different experiments and the DNS data of You et al. (2003). The reason for this discrepancy lies in the method of measuring c_f in different experiments. You et al. argued that their results in both ascending and descending flows do not agree with the experimental data obtained by using the total pressure drop (e.g. Easby, 1978 and Parlatan et al., 1996), but agree with those obtained by measuring velocity gradient in the case of ascending flow (e.g. Carr et al., 1973).

5.3.3 Cross-Code Comparison; Ascending Flow

In this section, the local heat transfer and friction coefficient results obtained from CONVERT (which were presented in the previous section) are compared against the computations carried out by STAR-CD and Code_Saturne. The attention here however, is restricted only to the ascending flow case.

Similar to the previous section, where available, all sets of data and the present computations are normalized using the corresponding Nu_0 and c_{f0} values of that particular test case.

Similar to Figure 5.5, the most remarkable point to note from Figure 5.7 is the abrupt and dramatic reduction in heat transfer levels occurring at around $0.15 < Bo <$

0.25. DNS Case C (Bo = 0.18) is representative of this laminarized state in which heat transfer levels are only approximately 4/10ths of those found in forced convection under otherwise identical conditions. As was noted before, the formulation in closest agreement with the three DNS data points is the LS model (as implemented in CONVERT). Other models that perform well are the Manchester v^2-f scheme (Code_Saturne) of Billard et al. (2008) and the v^2-f model (STAR-CD), although these two schemes are not as close to the DNS point at the lowest level of buoyancy influence (Case B; Bo = 0.13). The Large Eddy Simulations (STAR-CD) of Addad and Laurence (2008) indicate that significant heat transfer impairment occurs at a lower value of Bo, and interestingly these results, at least at lower levels of buoyancy influence, are in good agreement with the water data of Parlatan et al. (1996) when both the LES and data are presented in terms of Bo.

The k-ω-SST model (STAR-CD and Code_Saturne) performs particularly poorly, but there is at least quite close agreement between the two codes (see Section 5.4.6.3 below). Finally in relation to the turbulence models, it is observed that the LCL k-ε model (STAR-CD) returns somewhat different results from the LS scheme, mainly for lower values of Bo. This is mainly due to its somewhat different formulation to the LS model (see Section 3.6 for more details).

Figure 5.8 shows normalized local friction coefficient plotted against the buoyancy parameter. From the DNS data, it can be seen that with increasing the buoyancy influence, the normalized friction coefficient initially decreases, taking a value lower than unity. As Bo further increases, however, the trend reverses and the friction coefficient increases. Of the turbulence models considered, the STAR-CD v^2-f and Manchester v^2-f models are in closest agreement with the three DNS points of You et al. (2003) and the data of Carr et al. (1973). The Large Eddy Simulations show an early onset of c_f -reduction (cf. Figure 5.7 for Nu/Nu_0); it is also seen that the LES

computations return the lowest values of c_f/c_{f0} found in the present study. Again there is quite good agreement between the two codes when the *k-ω-SST* model is used, although some discrepancies emerge between the results at higher values of buoyancy parameter ($Bo > 0.4$). The *k-ω-SST* model also fails to return any friction coefficient below the value of c_{f0}.

By comparing Figure 5.7 to Figure 5.8, the similarities between the Nusselt number and friction coefficient distributions become apparent. However, the reduction of friction coefficient due to laminarization is significantly less than that of heat transfer. In addition, c_f/c_{f0} rises to a value greater than unity for Case (C) ($Bo = 0.18$), while at the same *Bo*, the heat transfer coefficient is much lower than one. These differences lead to a conclusion that in a buoyancy-influenced flow the relationship between momentum transfer and heat transfer is less direct than in forced convection (Kim et al., 2008).

It is worth noting again that the performance of each model in predicting normalized local Nusselt number and friction coefficient greatly depends on the calculated *Nu* and c_f at forced convection condition (Table 5.6 and Figure 5.4). In fact, having normalized all the results in Figure 5.7 and Figure 5.8 by the same value of Nu_0 and c_{f0}, the performance of each model could be different from what was observed above.

Finally, it is necessary to sound a note of caution in relation to the evaluation of turbulence model performance by comparison with the maximum impairment condition: this is because of the extreme sensitivity to flow conditions of the 'catastrophic' laminarization process that is the cause of large-scale heat transfer impairment.

5.4 MEAN FLOW AND TURBULENCE PROFILES

In this section, mean flow and turbulence profiles are presented for each turbulence model tested in the present work. The profiles are compared against the DNS data of You et al. (2003). Attention here is restricted to ascending (buoyancy-aided) flows only.

For the sake of completeness, mean flow and turbulence profiles obtained by the Manchester v^2-f model (Billard et al., 2008) and LES (Addad and Laurence, 2008) are also included in Appendix B.

5.4.1 Results of the Launder-Sharma Model (CONVERT)

This section presents the results of the Launder-Sharma k-ε model (Launder and Sharma, 1974; or the 'LS model') for an ascending flow using CONVERT. Mean flow and turbulence profiles for four different thermal-hydraulic regimes (Table 5.2) are reported and comparison has been made against the DNS data of You et al (2003).

As can be seen from Figures 5.9 (a) and (b), velocity profiles returned by the LS model are in good agreement with the DNS data for cases (A) and (B), where the thermal-hydraulic regime is mainly of forced convection (although case B is a combination of forced and mixed convection). For case (C) the velocity profile is very much flattened in the core (in fact showing a slightly inverted shape) and the turbulence quantities are reduced to a very low level (see Figure 5.9 e). It is worth noting that very close to the wall (shown as an inset to Figure 5.9 a), the velocity gradients for all four cases is somewhat different from those of the DNS. The effects of this inaccuracy in predictions could be seen in the friction coefficient distributions in Figure 5.6.

In Figures 5.9 (a) and (b), while overall agreement between the LS results and the data is good, the maximum discrepancy occurs near the pipe centre-line (the maximum discrepancy is about 3.4% for case C). Figure 5.9 (b), where the mean velocity profiles are plotted in wall coordinates ($y^+ = y.U_\tau/\nu$ against $U^+ = U/U_\tau$, where $U_\tau = (\tau_w/\rho)^{0.5}$), shows the pronounced departure from near-wall 'universality' under conditions of turbulent mixed convection. Thus, any assumption of universality made in order to construct wall functions for use with 'high-Reynolds-number' turbulence models applied to mixed convection are clearly highly questionable (Cotton and Jackson, 1990).

In Figure 5.9 (c), the temperature profiles returned by the LS model are in very good agreement with the DNS data. When plotting the temperature profiles in wall units in Figure 5.9 (d) ($y^+ = y.U_\tau / \nu$ against $T^+ = (T_w\text{-}T)/T_\tau$, where $T_\tau = q/\rho.c_p.U_\tau$), some discrepancies occur between the LS results and the DNS data, mainly due to an inaccurate estimation of τ_w by the model (see also friction coefficient distributions in Figure 5.6). Consequently, the estimated values of U_τ and Re_τ (= $D.U_\tau / \nu$) for all four cases would also be inaccurate. For instance, as shown in Table 5.7, for the forced convection case, the LS model under-estimates the value of Re_τ by about 4% compared to the DNS data.

Case	DNS - A	LS - A	LS - B	LS - C	LS - D
Re_τ	360	345.70	342.60	342.28	404.32

Table 5.7 – Estimated values of Re_τ obtained by the LS model and the DNS data.

Profiles of the turbulent kinetic energy, k, and its dissipation rate, ε, are shown in Figures 5.9 (e) and (f). The results of the turbulence kinetic energy in forced convection and early-onset mixed convection (cases A and B) show large under-estimation of the peak (which occurs at $y^+ \approx 20$) compared to the DNS data. This shortcoming of the LS model in predicting the peak of the turbulent kinetic energy has also been reported by a number of other researchers including Cotton and Kirwin (1995) and Cotton and Ismael (1998). This under-estimation even exists for cases (C) and (D), where the model predicts negligible turbulent kinetic energy levels up to $y^+ \approx$ 30-40. The effect of buoyancy on turbulence reduction, however, is well captured by the LS model (case C) and so is the recovery of k for case (D). A similar trend can also be seen for the dissipation rate, ε. Although no profile was reported for ε by You et al. (2003), the profiles shown in Figure 5.9 (f) are not expected to be in good agreement with the DNS

data especially near the wall due to highly approximate nature of ε-equation (Cotton and Ismael, 1998).

Reynolds shear stress profiles are shown in Figure 5.9 (g). It can be seen that cases (A) and (B) have similar shear stress profiles which are positive and have a peak at $y^+ \approx$ 20-30. For case (C) it is seen that the DNS data of You et al. indicates large-scale laminarization of the flow and a change in sign of the Reynolds stress in the core region. The reduction in stress levels is captured by the LS model which, in fact, indicates an almost complete laminarization of the near-wall flow. The DNS data for case (D) continue to show a modest level of Reynolds shear stress in the near-wall region, but increased stress levels in the core flow. The LS model captures the general trends of the data, but fails to resolve the detail of the near-wall stress distribution (similar under-prediction was seen for the levels of turbulent kinetic energy for cases C and D in Figure 5.9 e).

Based on the findings above regarding the under-predictions of k and $\overline{uv}$ by the LS model in the near-wall regions, the good agreement of the heat transfer with the DNS data (in Figure 5.5 and Figure 5.7) could perhaps be viewed as being fortuitous. In fact, Kim et al. (2008) argued that the excellent heat transfer agreement seen by the LS model in this type of flow problem is achieved as a result of two incorrectly re-produced effects cancelling each other out, namely under-predicted turbulent diffusion and an over-predicted advection.

Generally, as was discussed in Chapter 3, in eddy viscosity models μ_t links the turbulence model to the mean flow and thus the performance of a turbulence model strongly depends on μ_t. In the low-Reynolds number form of the LS model, the turbulent viscosity is defined as

$$\mu_t = \rho C_\mu f_\mu \frac{k^2}{\varepsilon} \tag{5.5}$$

where C_μ is a constant (= 0.09 in the LS model) and f_μ is a damping function defined as

$$f_\mu = \exp\left[-3.4/\left(1+\left(Re_t/50\right)\right)^2\right] \tag{5.6}$$

where the turbulent Reynolds number, Re_t, is given by

$$Re_t = k^2/(\nu\varepsilon) \tag{5.7}$$

Now in order to further understand the performance of the LS model in the present flow problem, the profiles of the turbulent viscosity, damping function, and the turbulent Reynolds number are examined below.

Figure 5.9 (h) shows profiles of the normalized turbulent viscosity for all four cases compared with those extracted from the DNS data. It is seen that when the buoyancy influence is weak (cases A and B), μ_t in the near-wall region is zero up to $y^+ \approx 10$ mainly due to turbulence levels being negligible since viscous forces are dominant within this region. As buoyancy influence increases further to Bo = 0.18, the flow laminarizes and the region with negligible μ_t extends up to $y^+ \approx 50$. The extent of the region over which the turbulent viscosity is zero reduces (to $y^+ \approx 40$) as Bo is further increased to 0.5 (Case D). In comparison to the DNS data, it can be seen that the LS model can capture the general trend, while the extent to which the turbulent viscosity is zero is predicted with very good accuracy. Correctly predicting the length of the 'region with μ_t = 0' has a crucial effect in returning correct trends of heat transfer impairment/enhancement (see Figure 5.5).

In Figure 5.9 (i) very similar trends to those of μ_t/μ can be seen for the distributions of the turbulent Reynolds number, Re_t, since both are functions of k^2/ε. However, the extent over which $Re_t = 0$, is slightly smaller than that of $\mu_t/\mu = 0$ due to the effects of the damping function (since $\mu_t \propto f_\mu k^2/\varepsilon$).

Damping function profiles are shown in Figure 5.9 (j). It is seen that in all four cases the value of the damping function starts off with an initial constant value ($f_\mu = e^{-3.4} \approx 0.033$ – Eqn. (5.6)) which is followed by a sharp increase in the values. Far away from the wall ($y^+ > 100$) where the gradient of Re_t profile decreases, the value of the damping function tends to a constant value. From Eqn. (5.6) it is clear that the damping function in the LS model is dependent solely upon the turbulent Reynolds number. While this feature has been shown to be somewhat undesirable for some flow problems, it performs well under mixed convection conditions (Cotton et al., 2001).

Attention is turned next to Nusselt number and friction coefficient developments, shown in Figures 5.9 (k) and (l), respectively. The developments are plotted against the streamwise distance, x/D over the entire pipe length (x/D = 500). These plots are important as they indicate the minimum length required in order to obtain a stable and fully-developed solution. In the literature, in both numerical and experimental works, Nusselt number developments have been presented for various test cases, however, friction coefficient developments have rarely been reported. These figures indicate that in cases (A) and (B), where the buoyancy influence is not significant, variations in Nu and c_f are small and they reach full-developed status even before $x/D \approx 50$. However, the situation is very different for cases (C) and (D), where the buoyancy effects are strong. In case (C) heat transfer impairment and friction coefficient enhancement take place gradually and the flow reaches a full-developed condition only after $x/D \approx 350$ (the significance of this development and its effects on the mean flow profiles will be examined in Section 5.5.1). For case (D) it can be seen that there is a sharp drop in Nu and abrupt increase in c_f within $0 \leq x/D \leq 50$, followed by a series of minima and maxima up to $x/D \approx 150$, after which fully-developed status is reached. This rather complex development of Nusselt number is due to an interaction between the development of the thermal boundary layer and buoyancy.

Moreover, it is worth noting that case (D) has the highest level of c_f (nearly 1.4 times greater than the average value of c_f for the other 3 cases) since:

$$c_f = \frac{\tau_w}{0.5\rho U_b^{\,2}} \tag{5.8}$$

where wall shear stress, τ_w is calculated as

$$\tau_w = \mu\left(\frac{\partial U}{\partial y}\right)_{wall} \tag{5.9}$$

From the inset to Figure 5.9 (a), it is evident that case (D) has the highest velocity gradient in near wall region and consequently the highest friction coefficient.

Budgets of the turbulent kinetic energy

Although plotting the turbulent kinetic energy or the rate of its dissipation against the distance from the wall shows the level of that quantity, it does not indicate the contribution of each individual term in their respective transport equations. Therefore, in order to see the effects of changing a function in a model or to see how different terms affect the *k*- and *ε*-profiles, graphical output of each term is required for a balance, or budget, of the individual terms of the transport equations.

In this section, the budgets of the turbulent kinetic energy for the forced convection and laminarization cases (i.e. cases A and C) are plotted and shown in Figures 5.10 (a) and (b).

The *k*-equation of the LS model applicable to constant property flows is given as

$$\frac{Dk}{Dt} = \underbrace{\frac{\partial}{\partial x_j}\left(\nu\frac{\partial k}{\partial x_j}\right)}_{Viscous\,Diffusion} + \underbrace{\frac{\partial}{\partial x_j}\left(\frac{\nu_t}{\sigma_k}\frac{\partial k}{\partial x_j}\right)}_{Turbulent\,Diffusion} + \underbrace{\nu_t\left(\frac{\partial U_i}{\partial x_j}+\frac{\partial U_j}{\partial x_i}\right)\frac{\partial U_i}{\partial x_j}}_{Production} - \underbrace{\left[\tilde{\varepsilon} + 2\nu\left(\frac{\partial (k)^{1/2}}{\partial x_j}\right)^2\right]}_{Dissipation} \tag{5.10}$$

As can be seen in above equation, there are four terms to be examined: viscous diffusion, turbulent diffusion, production, and dissipation. The convective terms (*Dk*/*Dt*) are not calculated since they have no effect in steady-state fully-developed flows.

Figure 5.10 (a) shows the balance of terms in the *k*-equation, calculated for a fully-developed forced convection (case A) using the LS model. It is seen that the budgets are largely dominated by the production and dissipation, except in the near-wall region. Very near to the wall, the dissipation is balanced with the viscous diffusion and the maximum production and dissipation of *k*, occur at $y^+ \approx 12$. Also note that the viscous and turbulent diffusions change sign at approximately $y^+ \approx 10$ and $y^+ \approx 13$, respectively.

In Figure 5.10 (b), a dramatically different balance from that of forced convection is shown for the laminarized case (case C). It can be seen that the values are also much smaller than those of forced convection (with nearly two orders of magnitude). In this case all the elements of the *k*-budget are equal to zero up to $y^+ \approx 20$. The production of *k* is zero at the position of the velocity maximum ($y^+ \approx 40$ – Figure 5.9 b). Unlike case (A), in the core region the production is balanced with the diffusion and dissipation terms.

Effects of Buoyancy production term

As was discussed in Section 4.5, in buoyancy affected problems, the buoyancy production term (P_G) could be added to both *k* and ε transport equations. The buoyancy production term in accordance with the Boussinesq approximation is defined as

$$P_G = -\beta\, g_i\, \overline{u_i \theta} \tag{5.11}$$

where g_i is negative for ascending and positive for descending flows and $\overline{u_i \theta}$ is the turbulent heat flux.

In all the results presented so far, the buoyancy production term was not included in the *k*- and ε-transport equations. In this section, the effects of including this term when modelled using the Simple Gradient Diffusion Hypothesis (SGDH) and Generalized Gradient Diffusion Hypothesis (GGDH) are examined (see Section 4.6 for a description of the SGDH and GGDH).

Figure 5.11 shows the effects of including the buoyancy production term on the local Nusselt number and friction coefficient. It can be seen that the effects of including this term (modelled using both the SGDH and GGDH) are negligible. With the GGDH, however, there is a slight under-prediction of the maximum Nusselt number impairment near the re-laminarization region (shown in the inset to Figure 5.11 a). The results in Figure 5.11 indicate that the buoyancy production term plays an insignificant role in mixed convection in vertical channels (they are rather important in buoyancy-driven cavity flows and buoyancy-influenced horizontal flows; Ince and Launder, 1989). Similarly, Kim et al. (2008) investigated the effects of including the buoyancy production term (modelled using both the SGDH and GGDH) in the two-equation model of Abe et al. (1994) and found insignificant differences in the heat transfer results.

Furthermore, distribution of the buoyancy production term (P_G) for all four thermal-hydraulic regimes using the GGDH and SGDH are shown in Figures 5.12 (a) and (b), respectively. Also shown in Figure 5.12 (a) are the DNS data of You et al. (2003). From the DNS data, it is evident that for cases (A) and (B), the effect of buoyancy production term is negligible, while in laminarized and recovery conditions (cases C and D) the effect of P_G becomes more significant. The buoyancy production term modelled using the GGDH returns values that are comparable with the DNS data, although the production levels are under-predicted for cases (C) and (D). However, as shown in Figure 5.12 (b) when the turbulent heat flux is modelled using the SGDH, the magnitudes of the buoyancy production term become nearly three orders of magnitude smaller compared to the DNS data. In addition, in contrast to the DNS data, in Figure 5.12 (b) the maximum value of buoyancy production occur at the pipe centre-line (y/R = 1). As was discussed earlier in Section 4.6, the SGDH results in a poor approximation of $\overline{u\theta}$ since temperature variations are negligible in the streamwise direction.

Effects of Yap term

In some buoyancy-affected problems such as turbulent flows in cavities, the results were found to be improved by including an additional source term to the ε-transport equation (Ince and Launder, 1989). This source term which acts as a length-scale correction term, is known as the 'Yap term' (Yap, 1987) and is defined as

$$Y = \max\left[0.83\left(\frac{l}{l_e}-1\right)\left(\frac{l}{l_e}\right)^2\frac{\varepsilon^2}{k},\ 0\right] \tag{5.12}$$

where $l = k^{3/2} / \varepsilon$ and $l_e = 2.55\ y$. This term has not been included in the calculations presented so far, and in this section the effects of including this term is examined on the local Nusselt number and friction coefficient for a range of buoyancy parameter.

It is clear from Figures 5.13 (a) and (b) that in ascending mixed convection flows, including the Yap term has no effects on heat transfer and friction coefficient. Generally, the Yap term becomes active when the predicted turbulent length-scale exceeds the equilibrium length-scale. This, however, is not the case in an ascending flow problem and therefore, has negligible effects on the results. In fact, Cotton and Jackson (1990) carried out a test on the ascending flow 'Run N13' of Carr et al. (1973) and found that *Nu* changed by only 0.3% in response to inclusion of the Yap term.

Including the Yap term for descending flow computations, however, produces marked improvement in the degree of accord with the data due to limitations of the modelling of the ε-equation in the LS model (Yu, 1991; Cotton and Jackson, 1990).

5.4.2 Results of the Cotton-Ismael Model (CONVERT)

In this section, the results of the Cotton and Ismael (1998) model (the 'CI model') for an ascending flow problem are presented.

Before running the code for the present mixed convection problem, a series of validation tests were carried out to ensure the accuracy of the implementation of the CI

model in CONVERT. These tests were based on validating the results of a channel flow obtained by Cotton and Ismael (1998). The results of Cotton and Ismael (1998) for a channel flow at Re = 5,600 and 13,750 were successfully re-produced by the present author (the results of these validations tests can be found in Appendix A of the author's first year PhD report[†]).

Mean flow and turbulence profiles for four different thermal-hydraulic regimes (Table 5.2) are shown in Figure 5.14 and comparison has been made against the DNS data of You et al (2003).

Table 5.8 lists the values of the turbulent Reynolds number, Re_τ, obtained by the CI model for all four cases. The value of Re_τ for the forced convection (case A) is in much better agreement with the DNS data (with less than 0.5% under-prediction) compared to the LS model.

Case	DNS - A	CI - A	CI - B	CI - C	CI - D
Re_τ	360	358.02	355.12	352.96	393.80

Table 5.8 – Estimated values of Re_τ obtained by the CI model and the DNS data.

In Figures 5.14 (a) and (b), except for case (C), the general trends of the data are captured by the CI model, although the velocity magnitude is generally under-predicted near the pipe centre-line. The CI model returns essentially unchanged velocity profiles for cases (A, B and C); it clearly fails to capture the laminarization regime for case C (see also Figure 5.5). The maximum discrepancy between the results of the CI model and the DNS data for case (C) is about 8% and it is at the pipe centre-line.

Similar to the velocity profiles, in Figures 5.14 (c) and (d), it is seen that except for case (D), the CI model returns very similar temperature profiles for cases (A-C). The maximum discrepancy between the results of the CI model and the DNS data occurs for

[†] available from www.CFDtm.org

case (C), with the maximum difference of 8.8% at the pipe centre-line. The results for the recovery regime (case D), however, is in good agreement with the data with slight over-prediction near the centre-line. The discrepancies between the CI results and the DNS data are more significant when temperature profiles are plotted in wall units (Figure 5.14 d).

Figures 5.14 (e) and (f) show profiles of the turbulent kinetic energy and its dissipation rate, respectively. Figure 5.14 (e) clearly shows the advantage of the CI model over the LS formulation (cf. Figure 5.9 e) in predicting the levels of k, for cases with no or low buoyancy effects i.e. cases (A) and (B). (In fact, such good agreement with the data is not surprising since constants and functions of the CI model were tuned by reference to isothermal channel and heated mixed convection flows.) Once again, it is seen that the flow is not laminarized in case (C) and still high levels of k and ε are returned by the model. This delay in the turbulence response of the CI model is directly related to the late onset of heat transfer impairment in Figure 5.5. For case (D), although the recovery of the flow has been captured by the CI model, the levels of k are under-predicted up to $y^+ \approx 80$. Furthermore, it should be noted that the values of the dissipation rate at the wall for cases (A) and (B) in Figure 5.14 (f) are nearly an order of magnitude greater than those returned by the LS model (see Figure 5.9 f). In addition, unlike the LS model, the CI model returns a non-zero dissipation rate for case (C).

From Figure 5.14 (g), it can be seen that for the forced convection condition (case A) the predictions of the Reynolds shear stress is in good agreement with the DNS data as, to a lesser degree are the results for cases (B) and (D). It is worth noting that unlike the LS model, for case (D) the initial near-wall positive region is captured by the CI model (although with some delay compared to the DNS data). Again, the model returns the least accurate results for case (C), where the shear stress is severely over-predicted.

As was discussed in Chapter 3, eddy viscosity in the CI model is obtained as

$$\mu_t = \rho C_\mu f_\mu(Re_t) f_S(S) k^2 / \varepsilon \tag{5.13}$$

where

$$f_\mu(Re_t) = 1 - 0.3\exp[-Re_t / 50] \tag{5.14}$$

$$f_S(S) = \frac{2.88}{1 + 0.165 S} \times \left\{1 - 0.55 \exp\left[-\left(0.135 S + 0.0015 S^3\right)\right]\right\} \tag{5.15}$$

Figure 5.14 (h) shows the profiles of the normalized turbulent viscosity. It is seen that the results for cases (A) and (B) are in good agreement with the data for near-wall regions and core, while near the centre-line the CI model tends to over-predict the values of the turbulent viscosity. The reason for obtaining relatively good agreement for cases (A) and (B) is because of calculating the levels of k with good accuracy (Figure 5.14 e). The turbulent viscosity is severely over-predicted by the CI model for case (C), for the reasons discussed above. For case (D), for about $y^+ < 30$, the model correctly returns zero turbulent viscosity, however, in the core and centre-line regions, the level of turbulent viscosity predicted by the model is nearly half of that found by the DNS data.

Profiles of the turbulent Reynolds number are shown in Figure 5.14 (i). The definition of the turbulent Reynolds number in both the CI and LS models is the same i.e. $k^2/\nu\varepsilon$. It is seen that for cases (A) and (B), the profiles have higher gradients in the near-wall region ($y^+ < 20$) compared to the LS model. Very different profile is predicted for case (D), where buoyancy effects are significant. However, the value of Re_t for cases (A) and (D) become nearly equal for $y^+ > 100$.

With reference to the LS model, the turbulent viscosity returned by the CI model has two main differences: 1) It has an extra damping function $f_s(S)$, and 2) The definition of f_μ is slightly different. The reason for introducing $f_s(S)$ in the constitutive equation in the CI model is that as a wall is approached, Re_t tends to zero and therefore viscous properties of a turbulent flow must be taken into account. Consequently, the role of $f_s(S)$

would primarily be to effectively reduce C_μ, instead of a viscous-dependent variable (Cotton et al., 2001).

Profiles of $f_s(S)$ are shown in Figure 5.14 (j). At $y^+ = 0$, for all cases $f_s(S) = 1.296$ since the strain rate ($S = k/\varepsilon\left|\partial U/\partial y\right|$) is zero at the wall. Note that the damping function $f_s(S)$ varies inversely with S (see Eqn. (5.15)). In Figure 5.14 (j), the values of $f_s(S)$ suddenly drop to less than 0.1 at $y^+ \approx 10$ and then, except for case (D), the values gradually increase until they reach the maximum value of about 1.2 for $y^+ > 100$. For case (D), the maximum value of $f_s(S)$ occurs at $y^+ \approx 40$; this point approximately corresponds to the position of velocity profile inversion (see Figure 5.14 b).

Profiles of f_μ are shown in Figure 5.14 (k). In contrast to the LS model in which damping effects are attributed wholly to viscous effects, Eqn. (5.14) rapidly asymptotes to unity (after $y^+ \approx 10$), except for case (D), where it reaches unity only after $y^+ \approx 40$.

The overall effects of both damping functions are shown in Figure 5.14 (l) where the trends of the profiles are dominated by the shape of $f_s(S)$ rather than f_μ.

Finally, in Figures 5.14 (m) and (n) the developments of Nu and c_f are plotted against the streamwise distance, x/D. It is seen that for cases (A-C), the developments reach fully-developed condition relatively quickly ($x/D < 50$), however, for case (D), similar to the LS model, the developments of both Nu and c_f involve a series of minima and maxima before reaching a fully-developed condition. Again it is apparent that the pipe should be at least $350D$ in length for cases with high buoyancy influence (e.g. case D) in order to reach fully-developed status.

Budgets of the turbulent kinetic energy

Budgets of the turbulent kinetic energy for cases (A) and (C) are shown in Figure 5.15. It can be seen that in both cases, the distribution of different terms are similar, although the magnitudes are somewhat smaller for case (C). It is seen that the budgets are largely dominated by the production and dissipation terms, except in the near-wall region. Also,

in both cases (in contrast to the LS model) the dissipation and viscous diffusion are not zero at the wall. For the forced convection case, the distributions of the production and turbulent diffusion are similar to those of the LS model, while for case (C) the distributions of the LS and CI models are entirely different due to the delay in capturing the laminarization effects by the CI model.

5.4.3 Results of the Suga Model (CONVERT and STAR-CD)

5.4.3.1 CONVERT

In this section, the results of the cubic non-linear eddy viscosity model due to Suga (1995; and also Craft et al., 1996b) (the 'Suga model') for an ascending airflow are presented. Similar to the LS and the CI models, the results of this section, have been obtained using the in-house code, CONVERT.

The Suga model was implemented in CONVERT by the author. The implementation of the model was then verified and validated against the results presented in Suga (1995) for a channel flow at Re = 5,600 and 14,000 (based on the DNS data of Kim et al., 1987). The results of the validations tests for Re = 5,600 are shown in Appendix B.

The numerical details and fluid properties used in generating the results in this section, are the same as those considered for the LS and CI models with an exception of the pipe length which was limited to 50D (instead of 500D), since converged solution could not be obtained downstream of that location. Stability problems in the solutions became more severe by increasing the buoyancy influence. Similar stability problems were also encountered when the Suga model as implemented in STAR-CD was applied to the same flow problem. In fact, these problems were so severe in STAR-CD that for case (D), no solution could be obtained at all (see Section 5.4.3.2 for more detail).

Table 5.9 shows the values of the turbulent Reynolds number, $Re_{\tau,}$ which was estimated by the Suga model for all four cases. For comparison, the value of Re_τ obtained by the DNS of You et al. (2003) is also included in this table for the forced convection case. Similar to the LS and CI models, Re_τ is under-predicted for case (A) by about 1.7%.

Case	DNS - A	Suga - A	Suga - B	Suga - C	Suga - D
$\mathbf{Re_\tau}$	360	353.92	352.92	351.88	402.34

Table 5.9 – Estimated values of Re_τ obtained by the Suga model and the DNS data.

Mean flow and turbulence profiles are shown in Figure 5.16. Similar to the results of the CI model, in Figures 5.16 (a) and (b) it can be seen that the results for the first three cases (cases A-C) are essentially unchanged, which implies that laminarization of the flow is not correctly captured by this model. For case (D), an M-shape velocity profile emerges which shows the reaction of this model to the buoyancy effects at higher *Bo* numbers. In the velocity profiles, the maximum discrepancy between the results of the Suga model and the DNS data occurs for case (C) and it is at the pipe centre-line.

From the temperature profiles shown in Figures 5.16 (c) and (d), it can be seen that there is good agreement with the DNS data for cases (A) and (B), while for case (D), there is a maximum of 4.4% over-prediction at the centre-line (Figure 5.16 c). Again the model returns the least accurate results for case (C).

Profiles of the turbulent kinetic energy are shown in Figure 5.16 (e). Compared to the DNS data, for cases (A) and (B) the Suga model performs better than the LS model, but not as good as the CI model in predicting correct levels of *k*. However, the results of the Suga model for cases (C) and (D) are severely over- and under-predicted, respectively. In Figure 5.16 (f) for the recovery regime, the levels of the dissipation rate become negligible compared to cases (A-C). Unlike the LS model the dissipation rate at

the wall is not zero for case (C). The discrepancies found between the results of the LS and Suga models for the dissipation rate are partly associated with different definitions of the 'E-term' in the ε-transport equations of the models.

In Figure 5.16 (g), it can be seen that profiles of the turbulent shear stress for cases (A) and (B) are in reasonable agreement with the data. The results in cases (C) and (D), however, are poor as a result of inaccurate predictions of k and ε.

Profiles of the normalized turbulent viscosity are shown in Figure 5.16 (h). As was discussed in Section 3.6.8, the turbulent viscosity in the Suga model is defined as

$$\mu_t = \rho C_\mu f_\mu \, k^2 / \tilde{\varepsilon} \tag{5.16}$$

where

$$C_\mu = \frac{0.3}{1 + 0.35(\max\,(\tilde{S}, \tilde{\Omega}))^{1.5}} \left(1 - \exp\left[\frac{-0.36}{\exp(-0.75 \max\,(\tilde{S}, \tilde{\Omega}))} \right] \right) \tag{5.17}$$

$$f_\mu = 1 - \exp\left[-(Re_t / 90)^{1/2} - (Re_t / 400)^2 \right] \tag{5.18}$$

The turbulent viscosity profiles for cases (A-C) show quasi-linear form and thus are in rather poor agreement with the DNS data, especially in the core. Severe under-predictions are returned by the model for the recovery regime (case D).

Profiles of the turbulent Reynolds number in Figure 5.16 (i) are somewhat similar to those returned by the CI model, except for case (D), where much lower values are returned by the Suga model especially in the core region.

Profiles of the damping function, f_μ, are given in Figure 5.16 (j). Although the definition of f_μ in the Suga model is slightly different from that used in the LS model, the performance is somewhat similar, at least for cases (A) and (B). The profiles for cases (C) and (D), however, are very different from those returned by the LS model, mainly due to differences in the profiles of k and ε. It should be noted that even in non-linear eddy viscosity models, a Reynolds-number dependent damping term (i.e. f_μ) is

required for near-wall flows, but its influence is considerably less than that used in linear EVMs, since a substantial amount of the near-wall strain-related damping is now provided by the functional form of C_μ, given in Eqn. (5.17) (Craft et al., 1996b).

Attention is turned next to the developments of Nu and c_f, as shown in Figures 5.16 (k) and (l), respectively. Except for case (D), relatively smooth and steady developments are returned by the Suga model for both Nu and c_f. The Nusselt number development in case (D) has a steeper decay compared to the other cases, while the c_f development has a completely different trend; it increases very sharply up to $x/D \approx 5$ and after a local drop, it recovers and continuously increases over $x/D > 25$. The developments in Figure 5.16 (k) indicate that the domain length of $50D$ seems to be long enough for obtaining fully-developed condition; however, the picture which emerges from Figure 5.16 (l) is rather contrary. In addition, as was seen from the results of the LS and CI models, to reach a fully-developed status, much longer pipe length is required for case (D), therefore, the results obtained for this case using the Suga model perhaps should be assumed not to be fully-developed.

In the past, there have been a few attempts to trace the stability problems of the Suga model (see Raisee, 1999 and Craft et al., 1999, for example). The investigations of Raisee (1999) on ribbed passages found that the dependence of C_μ on the strain rate was the source of these stability problems. To further investigate this point here, the distributions of C_μ and non-dimensional strain rate, $\tilde{S}$, are plotted for case (D) and are shown in Figure 5.17.

In Figure 5.17 (a) it can be seen that there is a sudden increase in the value of C_μ over $40 < y^+ < 60$, which corresponds to a region of low strain rate (see Figure 5.17 b). In fact, at $y^+ \approx 45$, the strain rate goes to zero which in turn has a direct effect on C_μ (the region indicated by a dashed line). This point corresponds to the position of the velocity maximum (Figure 5.16 b). The above findings show that the stability problems

encountered in the present work, especially in case (D), may be linked to the current formulation of C_μ and its dependence on the stain rate.

Budgets of the turbulent kinetic energy

Budgets of the turbulent kinetic energy for cases (A) and (C) are shown in Figure 5.18. It can be seen that both cases have similar distributions for all four terms (although the magnitudes are slightly lower for case C), which again indicates that the Suga model fails to capture the flow laminarization in case (C). Similar to the *k*-budgets obtained using the CI model, both cases (A) and (B) have non-zero dissipation and viscous diffusion at the wall. The budgets are largely dominated by the production and dissipation, except in the near-wall region.

5.4.3.2 CONVERT vs. STAR-CD

The only turbulence model available in both STAR-CD and CONVERT is the cubic non-linear model of Suga. Therefore, as a cross-code comparison test, here the results presented in the previous section are compared with the results obtained using the Suga model in STAR-CD. However, the Suga model in STAR-CD also proved to be numerically unstable for cases with high buoyancy influence (similar to CONVERT) and consequently no solution could be obtained for $Bo = 0.5$ (case D).

In Figure 5.19 to Figure 5.21, comparison is made for the profiles of the velocity, temperature, and turbulent kinetic energy for cases (A-C).

In the forced convection case in Figure 5.19, both codes return nearly identical velocity and temperature profiles, while STAR-CD returns a turbulent kinetic energy profile that is lower than that returned by CONVERT.

In Figure 5.20, the results of both codes are somewhat different for case (B); the velocity and temperature profiles obtained using CONVERT return lower values,

especially near the pipe centre-line. As can be seen in Figure 5.20 (c) the prediction of the Suga model in CONVERT for k is closer to the DNS data.

For the laminarized regime (case C) in Figure 5.21, the discrepancies in the results of both codes are again negligible for the velocity and temperature profiles, while for the turbulent kinetic energy, STAR-CD returns lower values with the maximum difference of about 12%.

It is worth noting that as was mentioned earlier, the governing equations in CONVERT are parabolic and therefore, the code marches in the streamwise direction, while in STAR-CD a cyclic boundary condition with constant mass flow rate has been employed at inlet and outlet. This implies that, while in CONVERT the pipe length is set to $50D$, in STAR-CD the pipe length can be assumed to be infinite as a result of using cyclic boundary condition. This difference along with the differences associated with the mesh size and type used in both codes could perhaps be blamed for the discrepancies found between the results.

5.4.4 Results of the Lien-Chen-Leschziner k-ε Model (STAR-CD)

The results obtained using the LCL k-ε model (due to Lien-Chen-Leschziner, 1996) in STAR-CD are presented in this section. See Section 3.6.2 for more details.

The velocity profiles are shown in Figures 5.22 (a) and (b). In Figure 5.22 (a) the profiles are in good agreement with the data. The model successfully captures the M-shaped distortion of the velocity profiles for cases (C) and (D), although with a slight under-prediction near the pipe centre-line. The velocity profiles in cases (A) and (B) though, when plotted in wall units (Figure 5.22 b) are in poor agreement with the data mainly due to under-predicting the wall shear stress.

The temperature profiles in Figures 5.22 (c) and (d) are in good agreement with the DNS data, except for the forced convection case, where the model slightly under-predicts the temperature near the pipe centre-line.

Profiles of the turbulent kinetic energy and Reynolds shear stress are shown in Figures 5.22 (e) and (f), respectively. The profiles are similar to those obtained using the LS model (presented earlier in Figures 5.9 e and g). The levels of turbulent kinetic energy are severely under-predicted, especially in near-wall and core regions. However, unlike the results of the CI and Suga models, the turbulence collapse for case (C) is captured by the LCL k-ε model which resulted in returning relatively accurate local heat transfer impairment in Figure 5.7. Predictions of the Reynolds shear stress are relatively in a better agreement with the DNS data, although for cases (A) and (B), the model tends to under-predict the shear stress.

5.4.5 Results of the v^2-f Model (STAR-CD)

In this section, mean flow and turbulence profiles obtained using the v^2-f model in STAR-CD are presented. Details of the v^2-f model implemented in STAR-CD are given in Section 3.6.5.

In Figure 5.23 (a), it is seen that the velocity profiles are in good agreement with the DNS data, except for case (D), where the model under-predicts the velocity magnitude by about 6% near the pipe centre-line. In Figure 5.23 (b), the maximum velocity magnitude for cases (C) and (D) are over-predicted, which could again be due to under-predicting the wall shear stress.

Temperature profiles are shown in Figure 5.23 (c). The general trends of the DNS data are captured by the v^2-f model. In case (B), the model returns a temperature profile that is essentially unchanged from the forced convection distribution. In Figure 5.23 (d), the temperature profiles are plotted in wall units, where it is seen that the results of case

(C) is in least agreement with the data.

Profiles of the turbulent kinetic energy are shown in Figure 5.23 (e). The general trends of the DNS data are well captured by the v^2-f model. In fact, the levels of turbulent kinetic energy returned by this model for cases (C) and (D) are in the closest agreement with the data compared to all the other models studied so far.

In Figure 5.23 (f), profiles of the Reynolds shear stress are shown. Except for case (C), the magnitude of the shear stress is generally over-predicted by the model. Unlike other models, the shear stress in the near-wall regions for cases (C) and (D) are not zero as a result of returning non-zero turbulent kinetic energy for these cases (Figure 5.23 e).

It is worth noting that as was seen earlier in Figure 5.7, the value of *Bo* at which the maximum heat transfer impairment occurs was very well predicted by the v^2-f model, while the magnitude of heat transfer impairment itself was under-predicted. On the other hand, in Figure 5.8 it was seen that the v^2-f model returned the most accurate results for the local friction coefficient (although the maximum friction coefficient impairment was somewhat over-predicted).

5.4.6 Results of the k-ω-SST Model (STAR-CD and Code_Saturne)

5.4.6.1 STAR-CD

Mean flow and turbulence profiles obtained using the *k-ω-SST* model in STAR-CD are presented in this section. The velocity and temperature profiles in Figures 5.24 (a)-(d), show that for cases (B) and (C), the model returns profiles that are essentially unaffected from the forced convection case. For the recovery regime (case D), the model clearly fails to predict an M-shape velocity profile and consequently the velocity magnitudes are over-predicted over $y/R > 0.4$. Similar results can be seen in Figure 5.24 (b), where the velocity is over-predicted in case (D) over $y^+ > 50$.

The temperature profiles are also in poor agreement with the data, especially for

cases (C) and (D). Discrepancies between the results and the DNS data are more evident when the temperature profiles are plotted in wall units (Figure 5.24 d).

Figure 5.24 (e) shows that the *k-ω-SST* model fails to return correct levels of turbulent kinetic energy for all four cases. Turbulence reduction predicted by the model for cases (C) and (D) are considerably less than that found in the DNS data. Consequently, poor Reynolds shear stress profiles are returned by the model (Figure 5.24 f).

Such a poor performance of the *k-ω-SST* model was also seen in Figure 5.7 and Figure 5.8, where much lower impairment for heat transfer and nearly negligible impairment for friction coefficient was predicted.

5.4.6.2 Code_Saturne

Mean flow and turbulence profiles obtained using the *k-ω-SST* model in Code_Saturne are shown in Figure 5.25. The profiles are very much similar to those returned by the *k-ω-SST* model in STAR-CD (Figure 5.24). The model broadly fails to detect the laminarization condition for case (C) which results in returning nearly identical velocity and temperature profiles for cases (A-C). In addition, the model significantly under-predicts the buoyancy influence on mean flow and turbulence profiles for case (D). This poor performance of the *k-ω-SST* model in predicting the mean flow and turbulence profiles could also be anticipated from the local heat transfer and friction coefficient distribution plotted against the buoyancy parameter (Figure 5.7 and Figure 5.8).

5.4.6.3 STAR-CD vs. Code_Saturne

In this section, comparison is made for the results obtained using the *k-ω-SST* model in STAR-CD and Code_Saturne. Profiles of the normalized velocity, temperature, turbulent kinetic energy, and Reynolds shear stress for cases (A) and (D) are compared in Figure 5.26 and Figure 5.27.

In the forced convection condition (case A) in Figure 5.26, the profiles obtained from both codes are acceptably close, except for the turbulence kinetic energy (Figure 5.26 c) where the *k-ω-SST* model in STAR-CD returns levels that are lower by about 15% (at $y^+ \approx 50$).

The largest discrepancies between the results of STAR-CD and Code_Saturne occur in the recovery regime (case D; $Bo = 0.5$), as shown in Figure 5.27. While the velocity profiles are reasonably close, the temperature profiles returned by STAR-CD seem to be more turbulent that that found by Code_Saturne (in spite of both codes returning very close values of Nu/Nu_0 at $Bo = 0.5$ – see Figure 5.7).

In Figure 5.27 (c) similar to case (A), STAR-CD returns somewhat lower levels of turbulent kinetic energy up to $y^+ \approx 50$. However, the turbulent kinetic energy profile returned by Code_Saturne has a slightly steeper gradient thus, returning lower values of k beyond $y^+ \approx 50$. For the Reynolds shear stress shown in Figure 5.27 (d), STAR-CD returns values that are higher by approximately 20% (at $y^+ \approx 50$).

5.5 NUSSELT NUMBER DEVELOPMENT

5.5.1 Streamwise Development of Nu and c_f for Case (C)

In this section, mean flow and turbulence profiles for the laminarized regime (case C) obtained at four different streamwise locations are examined. The calculations shown in Figure 5.28 are computed profiles for ascending flow at x/D = 200, 300, 350, and 500 (Re = 5,300, Pr = 0.71) using the Launder-Sharma *k-ε* model – see Figures 5.28 (a) and (b). (Note that the profiles obtained at x/D = 500 are the fully-developed profiles reproduced from Figure 5.9 above.)

From Figure 5.28, it is evident that the profiles demonstrate marked development effects. The discrepancies apparent in these profiles arise as a consequence of local recoveries in Nu- and c_f -developments. In all the profiles shown in Figure 5.28, it is

seen that at *x/D* = 200 the profiles are quite similar to the profiles obtained for conditions at which buoyancy influence is low e.g. cases (A) and (B) in Table 5.2. At *x/D* = 300 and 350, however, the flow begins to laminarize, but it is only at *x/D* = 500 where the flow can be assumed to be fully-developed i.e. complete laminarization occurs.

From Figures 5.28 (c)-(f) it is seen that the velocity and temperature profiles at *x/D* = 350 and 500 are relatively close, however, there are rather large discrepancies in the profiles shown in Figures 5.28 (g)-(j). Such diverse performances of flow at different *x/D* show the importance of the pipe length (computational domain) in numerical simulations of this type. It is also clear that in ascending flows, the mean flow equations and turbulence models must be cast in a developing flow framework in order to capture the complex thermo-fluid development (Cotton and Jackson, 1990).

It should be noted, however, that the experimental studies of mixed convection heat transfer have usually adopted much shorter pipe lengths (Table 5.10 below), therefore, when numerical results are compared against experimental results, care should be taken to match the measurement lengths (i.e. *x/D*) too (even if the flow is not fully-developed at that particular *x/D*).

Experiments	**Total Pipe Length**	**Length of Heated Section**
Steiner (1971)	60D	37.5D
Carr et al. (1973)	113D	100D
Polyakov and Shindin (1988)	85.5D	68.5D
Parlatan et al. (1996)	131D	80D
Shehata and McEligot (1998)	82D	32D

Table 5.10 – Pipe lengths in a number of experiments carried out on ascending mixed convection flows.

5.5.2 The Experiments of Polyakov and Shindin

Heat transfer development is examined next and comparison is made with the experimental data of Polyakov and Shindin (1988). CONVERT is used to run the LS, CI, and Suga models. Conditions at the start of heating are given in Table 5.11 together with the bulk temperature rise along the test section. In Run 5 ΔT_b is sufficiently large to invalidate the Boussinesq approximation (see Gray and Giorgini, 1976, for example). Comparison with Run 5 is included only for completeness since for these conditions a full variable properties formulation (e.g. Kirwin, 1995) should be adopted.

Figure 5.29 shows plots of Nusselt number against axial position arranged in order of increasing buoyancy influence. Forced convection flow is represented by Figure 5.29 (a) from which it is seen that the CI model is closest to the measurements, while the Suga and LS models return lower values of *Nu*. The average value of forced convection Nusselt number obtained from the data of Polyakov and Shindin is $Nu_0 = 19.0$ (for $30 < x/D < 65$). Now, Polyakov and Shindin's experiments were conducted for $Re = 5100$ (cf. $Re = 5300$ in the DNS of You et al., 2003). If Nu_0 is taken to vary as $Re^{0.8}$, the experimental result can be scaled to yield $Nu_0 = 19.0 \times (5300/5100)^{0.8} = 19.6$ at the higher Reynolds number. (The scaled value of Nu_0 appeared in Table 5.6 and Figure 5.4, above.)

Run	Re	Pr	Gr	Bo	q^+	ΔT_b (^{o}C)
1	5100	0.709	0	0	0	-
2	5100	0.709	4.80×10^6	0.1010	5.64×10^{-5}	4.8
3	5100	0.709	1.55×10^7	0.3280	1.84×10^{-4}	15.6
4	5100	0.709	3.00×10^7	0.6320	3.53×10^{-4}	30.0
5	5100	0.709	7.67×10^7	1.6190	9.01×10^{-4}	76.8

Table 5.11 – Conditions at the start of heating in the experiments of Polyakov and Shindin (1988).

Figures 5.29 (b) and (c) are for values of *Bo* associated respectively with early-onset mixed convection and heat transfer recovery. The LS model is closest to the data of Figure 5.29 (b), and, while no model accurately captures the development history of Figure 5.29 (c), the LS scheme is in best agreement with the measurements made in the downstream region. Further into the recovery region, Figure 5.29 (d) shows that the LS model performs better than the other two schemes. As indicated previously, variable property effects in Run 5 (Figure 5.29 e) render the Boussinesq approximation inapplicable, and it would be inadvisable to draw any firm conclusions from these results.

5.6 EFFECTS OF THE REYNOLDS NUMBER

In this section, the effects of changing the Reynolds number on heat transfer and friction coefficient are examined. Six Reynolds numbers are selected in a range between 5,000 and 25,000. At each Reynolds number, the Grashof number was varied (by changing the heat flux) so as to cover all four regimes in Table 5.2. The k-ε model of Launder-Sharma implemented in CONVERT has been used to carry out the computations in this section.

Values of fully-developed Nusselt number (Nu_0) and friction coefficient (c_{f0}) at different Reynolds numbers are shown in Table 5.12. These values are compared against the modified form of the Dittus-Boelter equation ($Nu = 0.022\ Re^{0.8}\ Pr^{0.5}$) and the Blasius equation ($c_f = 0.079\ Re^{-0.25}$). Compared to the correlations, the LS model under-estimates the Nusselt number and friction coefficient by an average of 2.2% and 8.7%, respectively.

Re	**Nu_0**	**$0.022\,Re^{0.8}\,Pr^{0.5}$**	**% diff.**	**c_{f0}**	**$0.079\,Re^{-0.25}$**	**% diff.**
5,000	16.69	16.90	-1.2	8.69×10^{-3}	9.39×10^{-3}	-7.5
7,500	22.97	23.37	-1.7	7.75×10^{-3}	8.49×10^{-3}	-8.7
10,000	28.81	29.42	-2.1	7.18×10^{-3}	7.90×10^{-3}	-9.1
12,500	34.34	35.17	-2.4	6.78×10^{-3}	7.47×10^{-3}	-9.2
15,000	39.64	40.69	-2.6	6.49×10^{-3}	7.14×10^{-3}	-9.2
25,000	59.33	61.24	-3.1	5.75×10^{-3}	6.28×10^{-3}	-8.5

Table 5.12 – Results for fully-developed forced convection using the Launder-Sharma model at different Reynolds numbers.

In Figure 5.30 normalized Nusselt number is plotted against the buoyancy parameter (*Bo*) for different Reynolds numbers. As was noted above, the buoyancy parameter is generally quoted in the form given by Eqn. (5.1). Its origins lie in the analysis of Hall and Jackson (1969) who considered the reduction in total shear stress, τ that occurs in a heated ascending pipe flow due to the action of buoyancy. In Figure 5.30 it is seen that the general trend of the Nusselt number is broadly the same for different Reynolds numbers. A dramatic reduction in heat transfer levels is evident in all cases at around $0.15 < Bo < 0.2$, except for $Re = 25{,}000$ where the heat transfer impairment is not as sudden as in other cases. After the maximum impairment point, by increasing the buoyancy influence, the heat transfer levels enhance in proportion to approximately $Bo^{0.32}$.

In addition, it is seen that the original definition of *Bo* (Eqn. (5.1)) results in collapsing curves of Nu/Nu_0 obtained at different *Re* in recovery region i.e. $Bo > 0.25$. It is, however, unable to produce a satisfactory collapse of the family of curves at lower levels of buoyancy influence (i.e. to the left of the maximum impairment point). These findings initiated the work of Cotton and Keshmiri (2008) to advance the original definition of *Bo* with an aim of improving the collapse of computed heat transfer results. Although the modified *Bo* proposed by Cotton and Keshmiri lead to a better collapse of

Nu/Nu_0 at lower levels of buoyancy influence, the degree of collapse was actually worsened for the recovery region (i.e. to the right of the maximum impairment point). The work on improving the definition of *Bo* is still in progress.

In Figure 5.31 normalized friction coefficient is plotted against the buoyancy parameter. Similar to Figure 5.30, the collapse of computed friction coefficient for the recovery region ($Bo > 0.25$) is much better than the region with lower levels of buoyancy influence. Note that in the recovery region, by increasing *Bo*, the friction coefficient increases in proportion to approximately $Bo^{0.34}$ (cf. $Bo^{0.32}$ for the heat transfer enhancement). This indicates that in the recovery region, the rates at which the normalized Nusselt number and friction coefficient enhance are very similar, regardless of the Reynolds number.

5.7 SUMMARY

In this chapter, ascending and descending turbulent mixed convection pipe flows, representing the gas-cooled reactor core flows, were simulated using a number of eddy viscosity turbulence models. Three different CFD codes were employed: 'CONVERT', 'STAR-CD', and 'Code_Saturne', which are respectively in-house, commercial, and industrial packages. Comparison was made against experimental and DNS data. The various turbulence closures adopted a range of different strategies to account for departures from the 'universality' of flow behaviour that is associated with fully-developed forced convection conditions. Wide variations in turbulence model performance were identified. The LS model generally had the best performance in capturing the phenomenon of heat transfer impairment in the ascending flow case. The v^2-*f* model and Large Eddy Simulation also returned satisfactory results. The effects of including the Yap term and buoyancy production term (modelled as the SGDH and GGDH) were also investigated and were found to have insignificant effects in heat

transfer results. In addition, cross-code comparison was carried out between CONVERT and STAR-CD using the Suga model and between STAR-CD and Code_Saturne using the *k-ω-SST* model. In both cases, a relatively good agreement was obtained between the codes. Mean flow and turbulence profiles at four different streamwise locations were compared for the laminarized case (case C) using the LS model, where wide variations were found between the profiles. The performance of the LS, CI and Suga models were next evaluated in comparison with the data of Polyakov and Shindin (1988) for developing forced and mixed convection flows. Finally, the effects of increasing the Reynolds number (Re = 5,000 – 25,000) on heat transfer and friction coefficients were also investigated using the LS model.

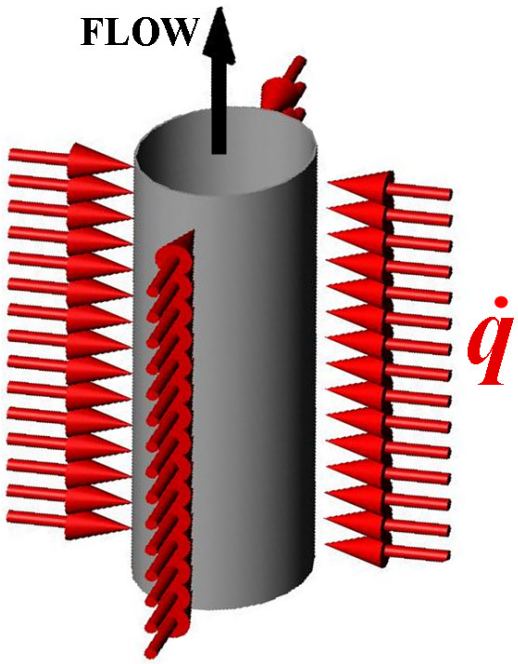

Figure 5.1 – Schematic diagram of an ascending mixed convection flow.

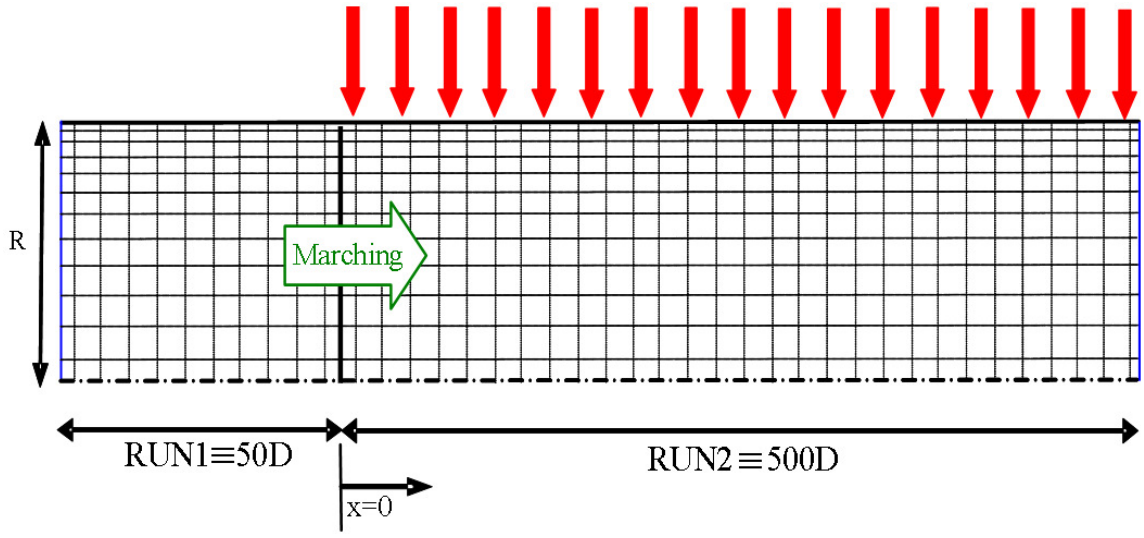

Figure 5.2 – CONVERT solution sequence.

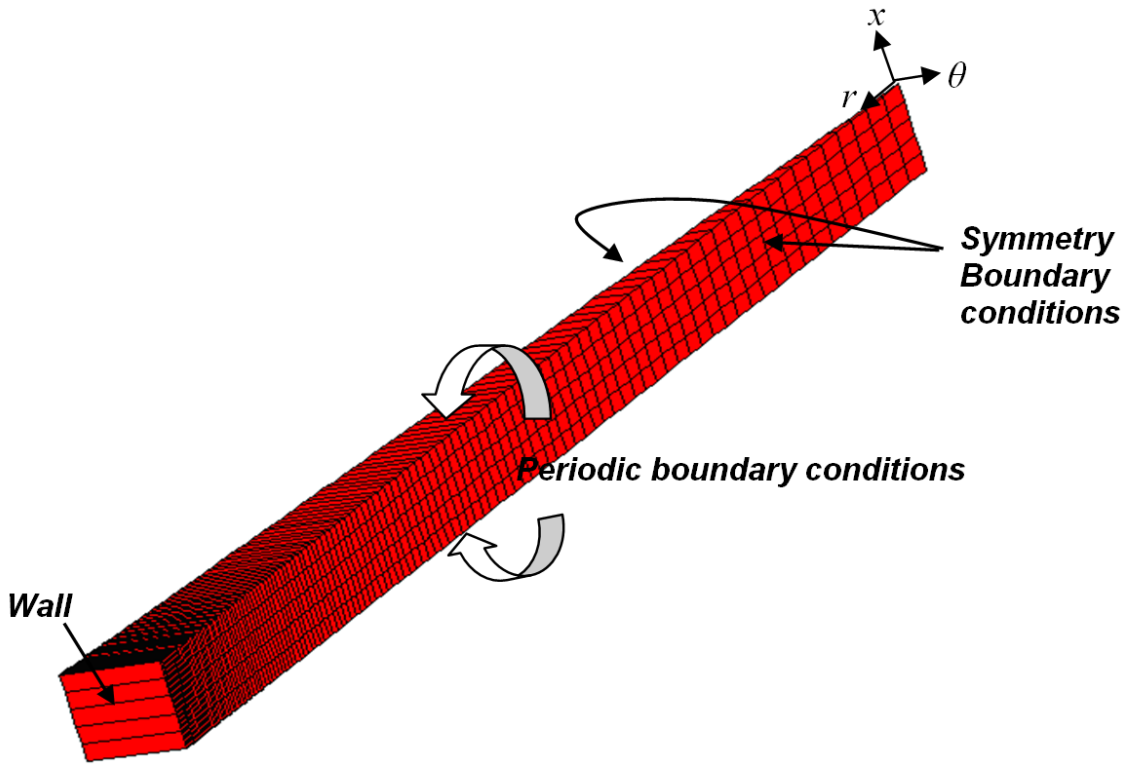

Figure 5.3 – Schematic of the mesh used in STAR-CD and Code_Saturne.

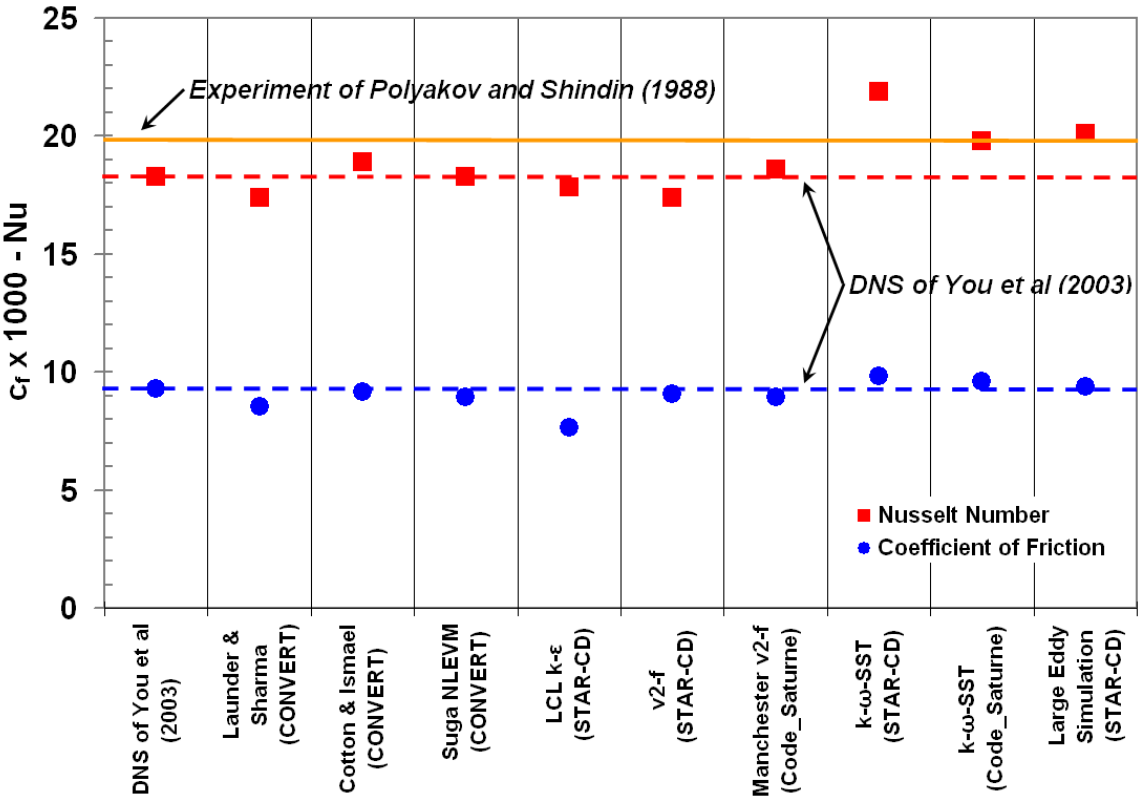

Figure 5.4 – Results for fully-developed forced convection. (The computations using Manchester v^2-f model and LES were carried out by F. Billard and Y. Addad, respectively, and are also reported in Billard et al., 2008, Addad and Laurence, 2008 and Keshmiri et al., 2008a; b).

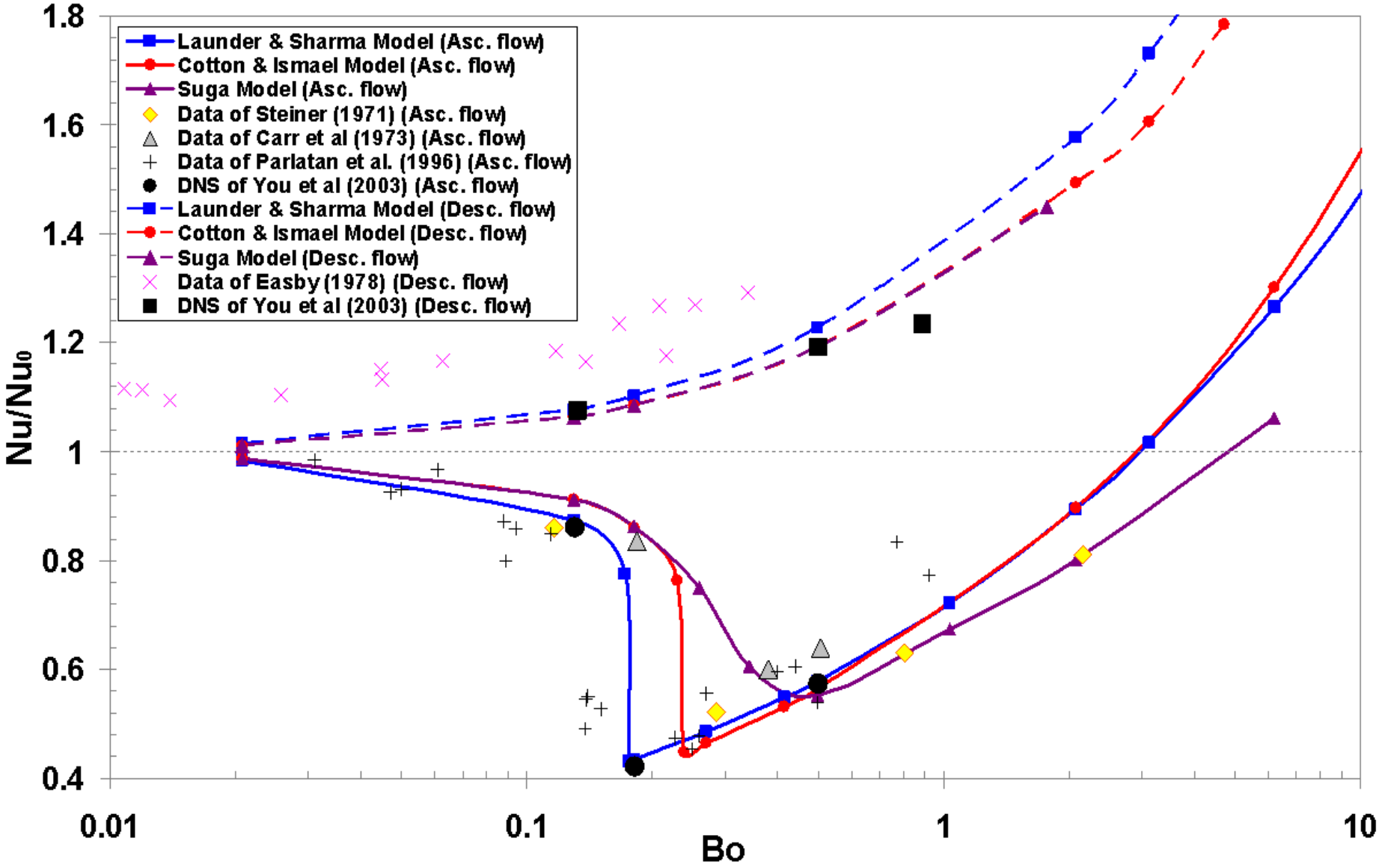

Figure 5.5 – Heat transfer impairment and enhancement in ascending and descending mixed convection flows using CONVERT.

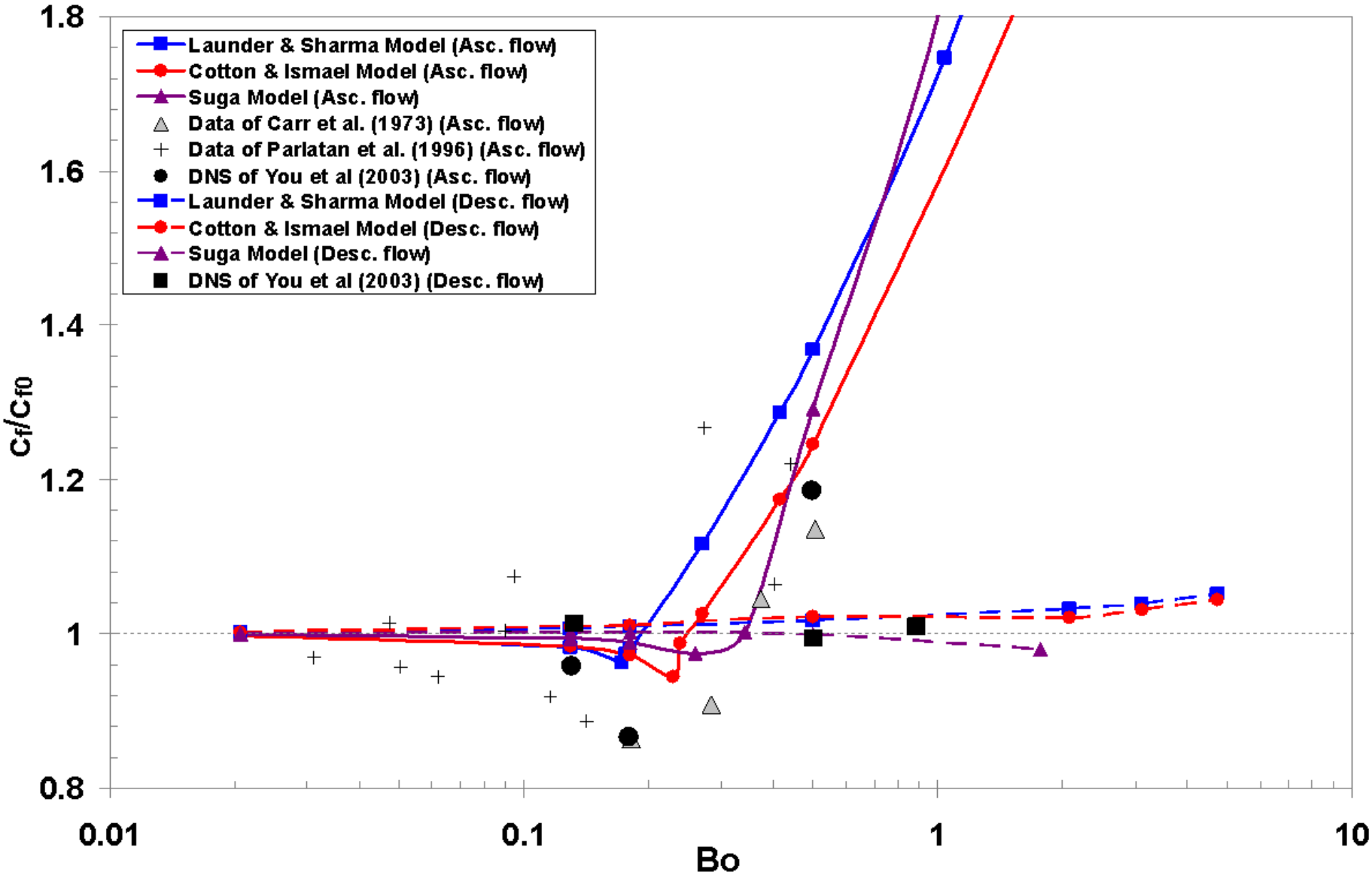

Figure 5.6 – Friction coefficient impairment and enhancement in ascending and descending mixed convection flows using CONVERT.

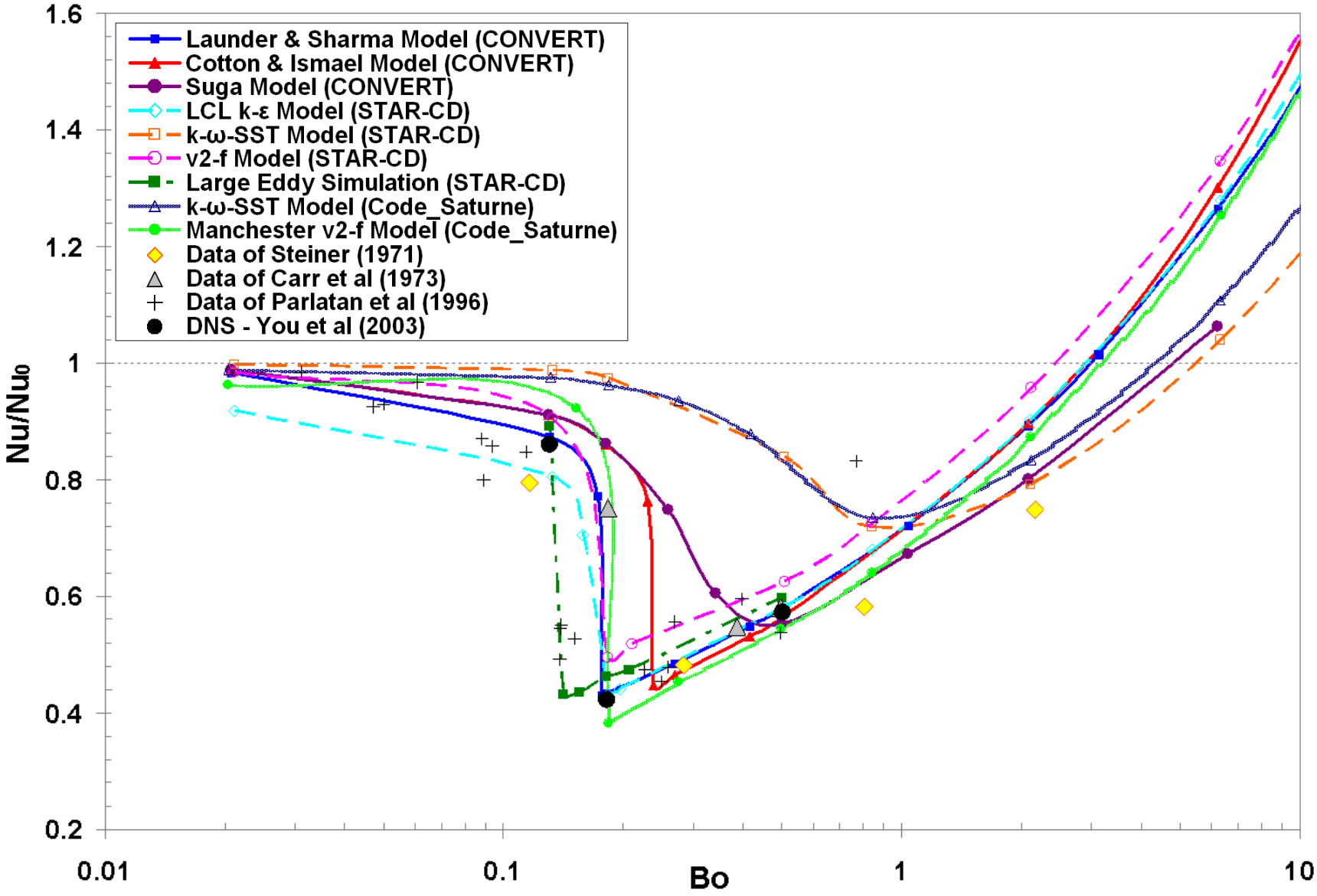

Figure 5.7 – Cross-code comparison of heat transfer impairment and enhancement in ascending mixed convection flows.

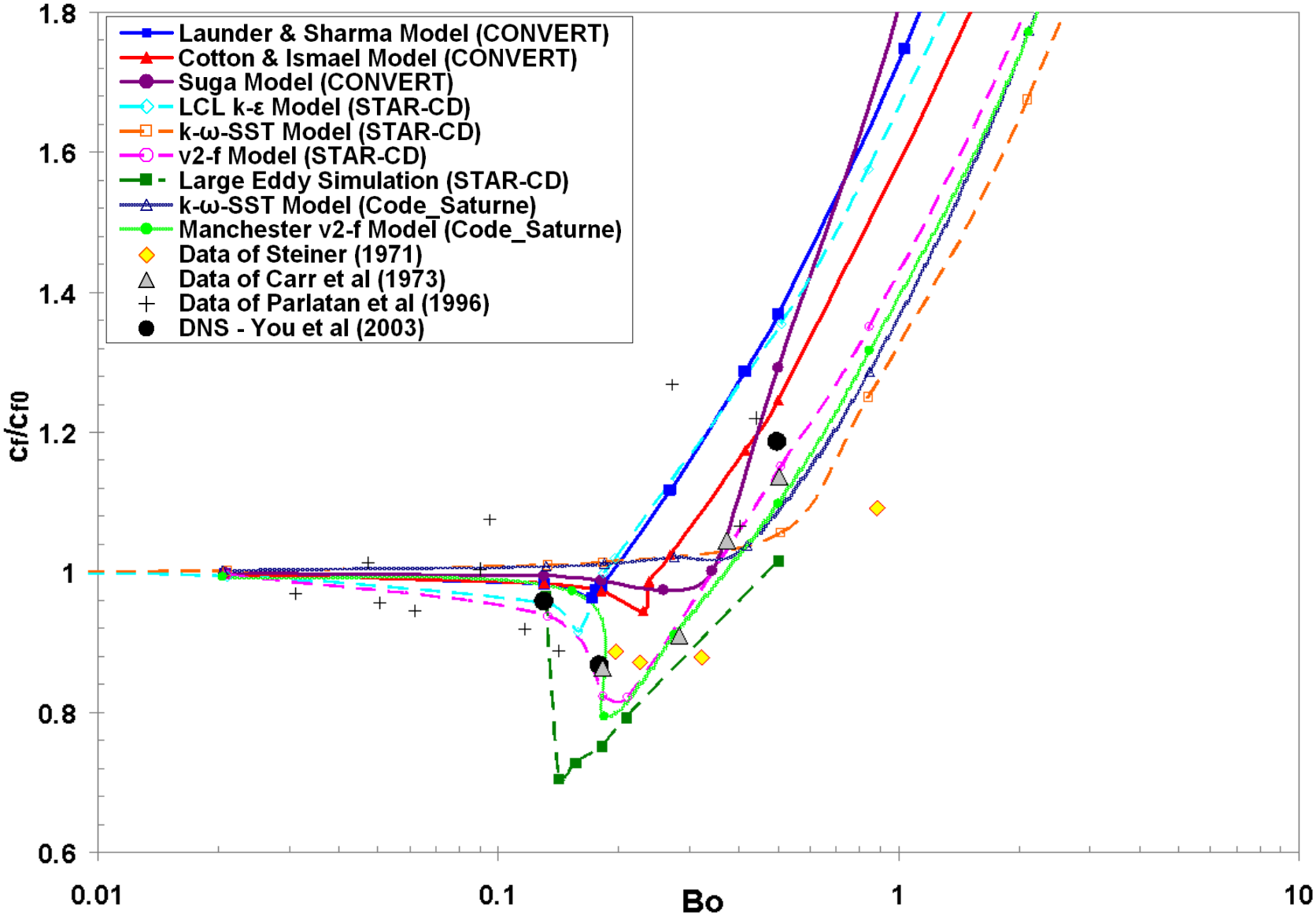

Figure 5.8 – Cross-code comparison of friction coefficient impairment and enhancement in ascending mixed convection flows.

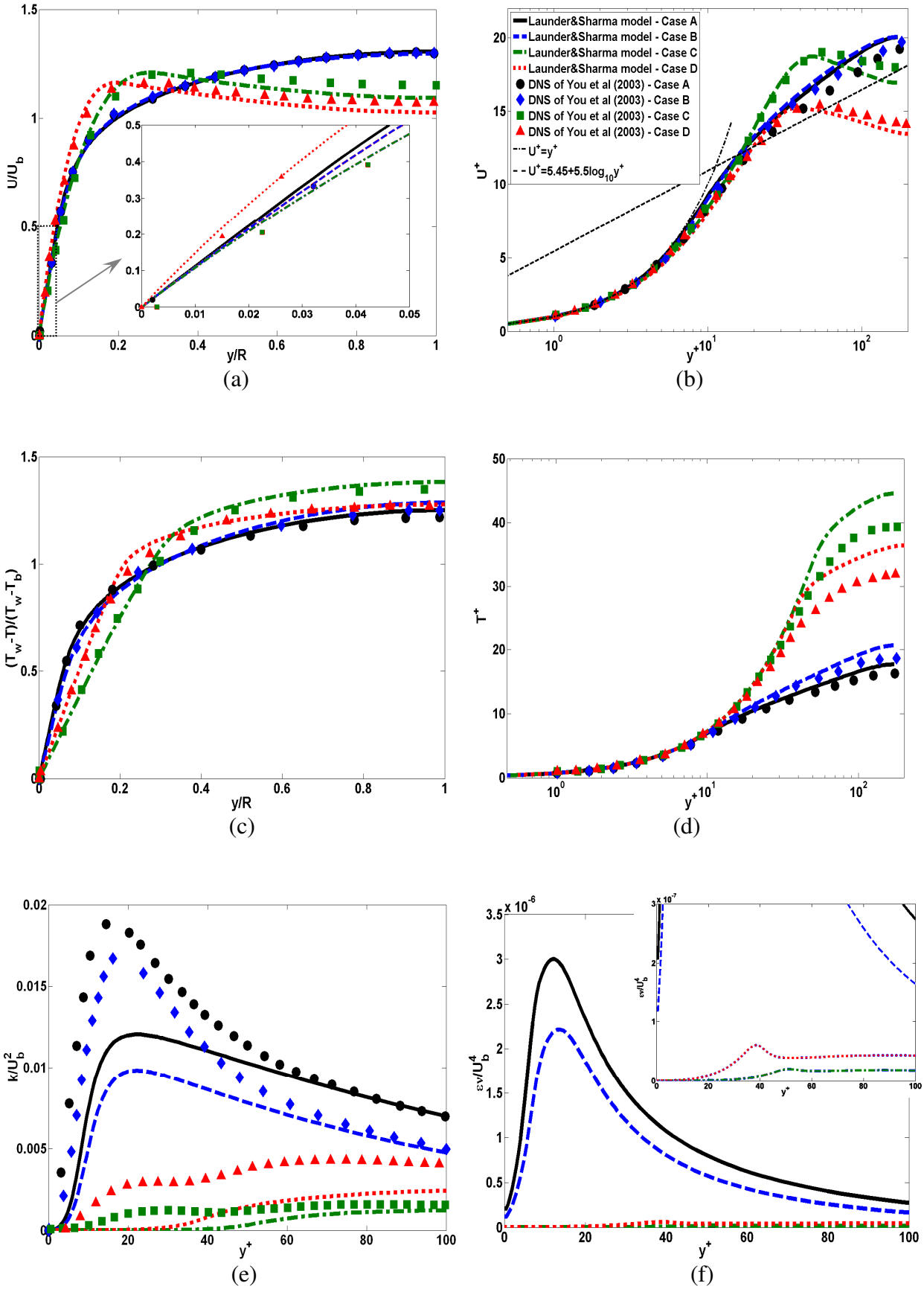

Figure 5.9 – Mean flow and turbulence profiles obtained using the Launder-Sharma model in CONVERT.

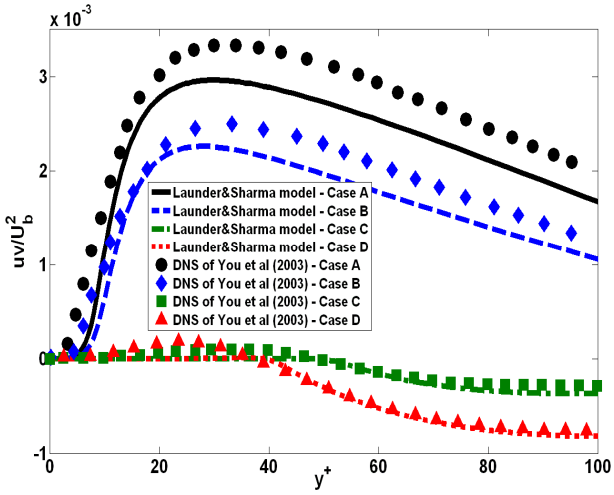

(g)

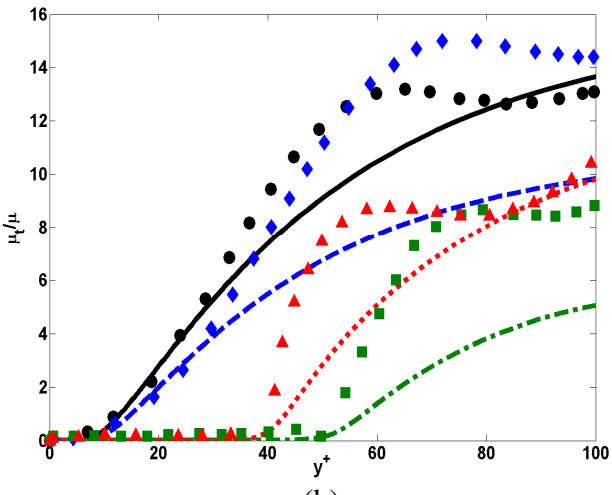

(h)

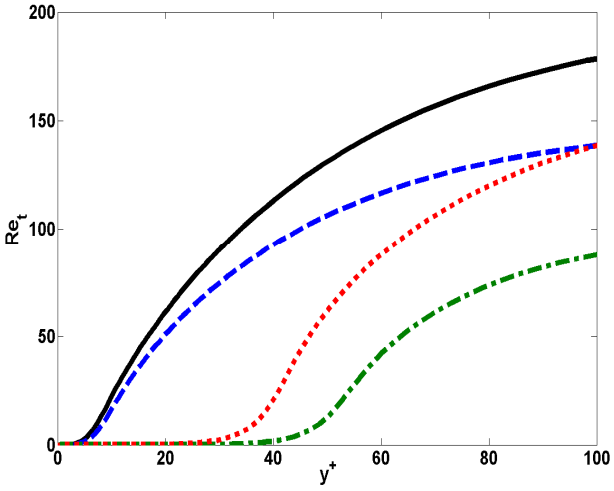

(i)

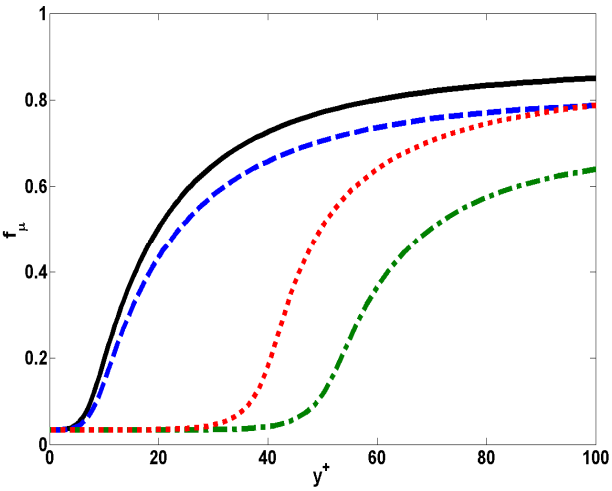

(j)

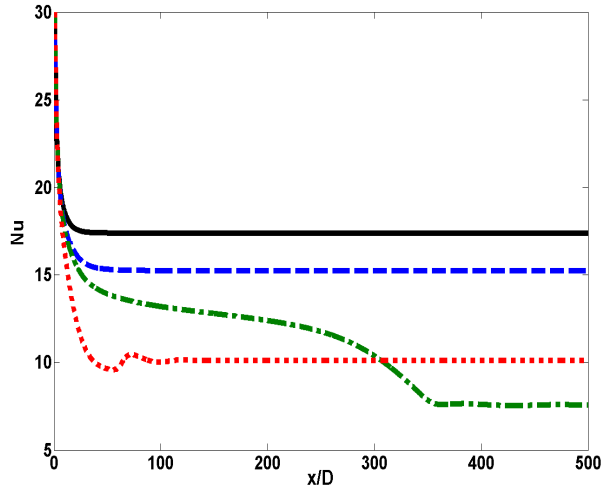

(k)

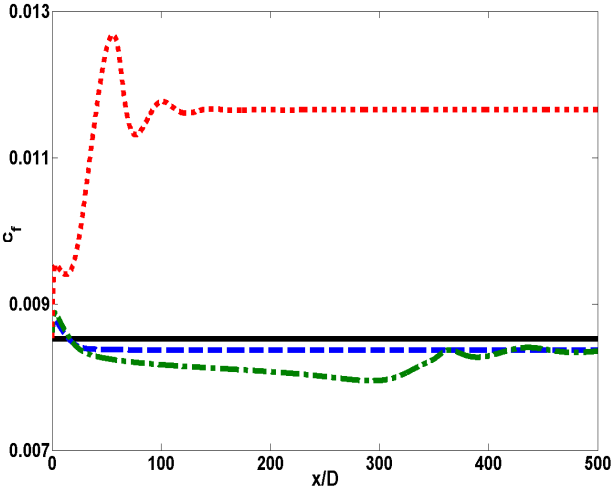

(l)

Figure 5.9 continued.

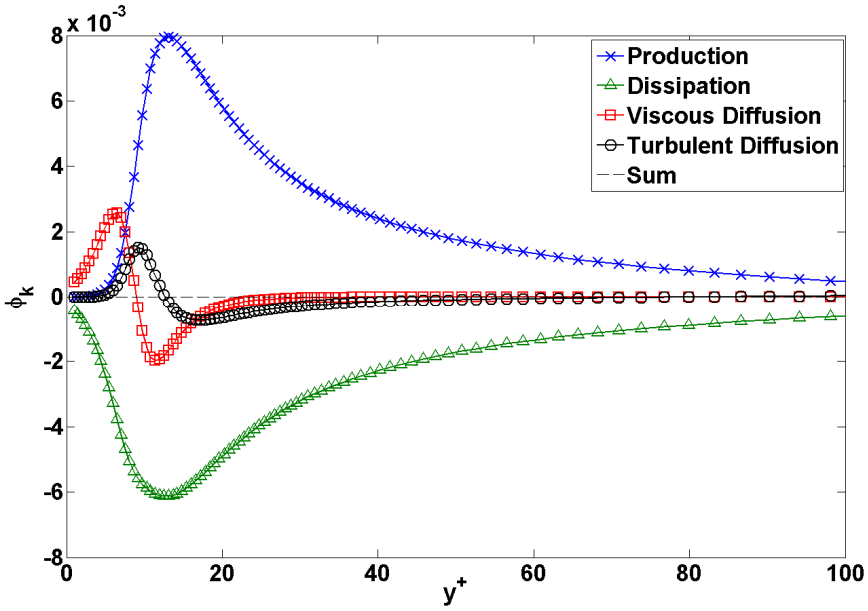

(a)

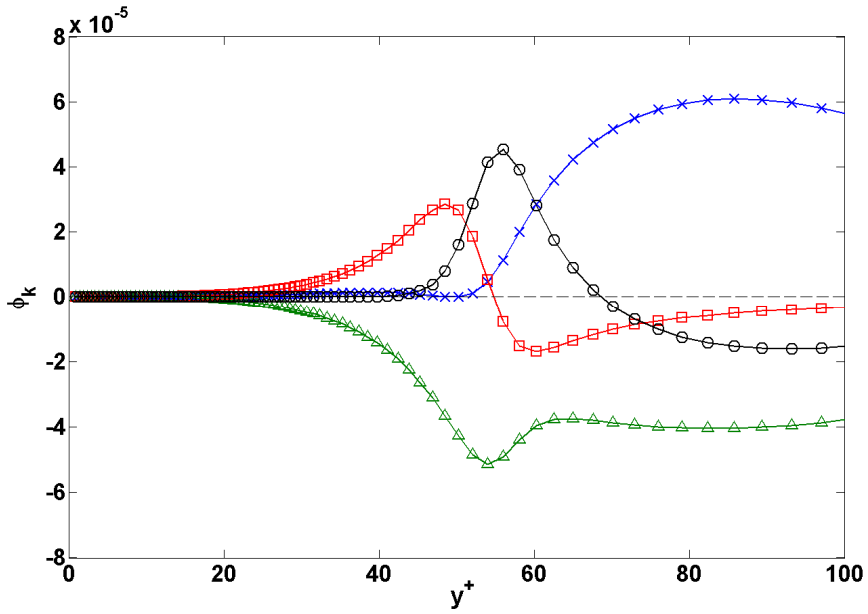

(b)

Figure 5.10 – Budgets of the turbulent kinetic energy [m^2/s^3] obtained using the Launder-Sharma model in CONVERT (a) case A (b) case C.

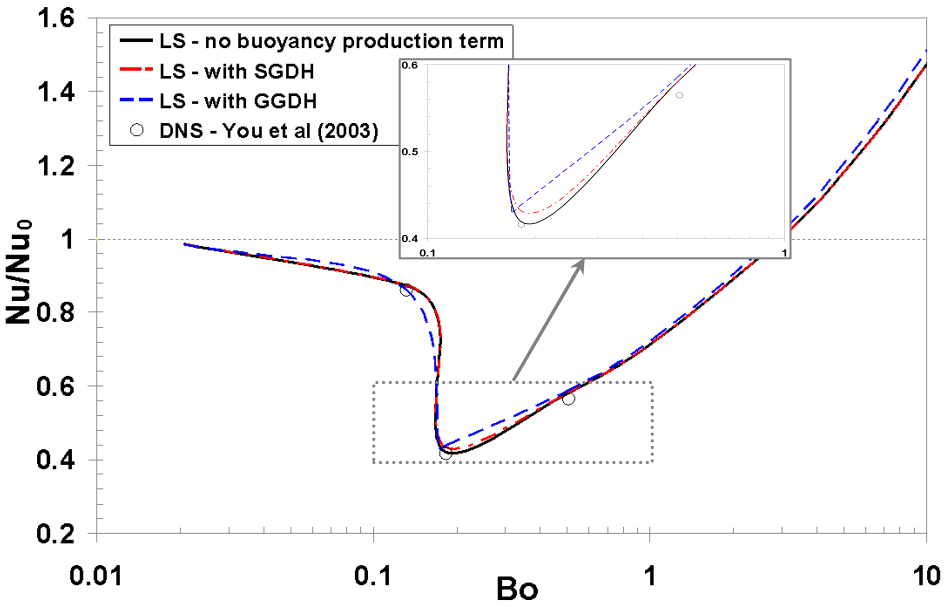

(a)

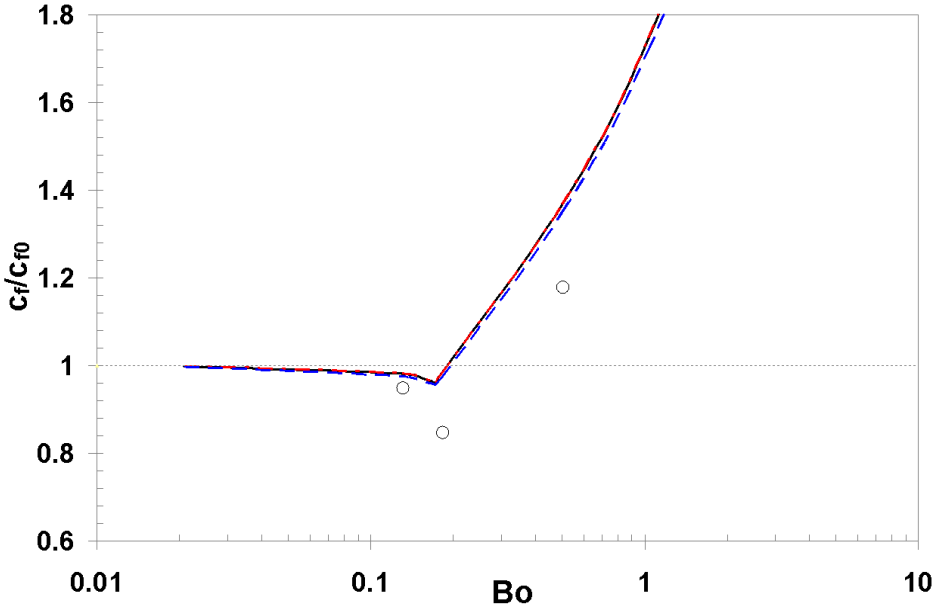

(b)

Figure 5.11 – Effects of including the buoyancy production term on the heat transfer and friction coefficient impairment/enhancement.

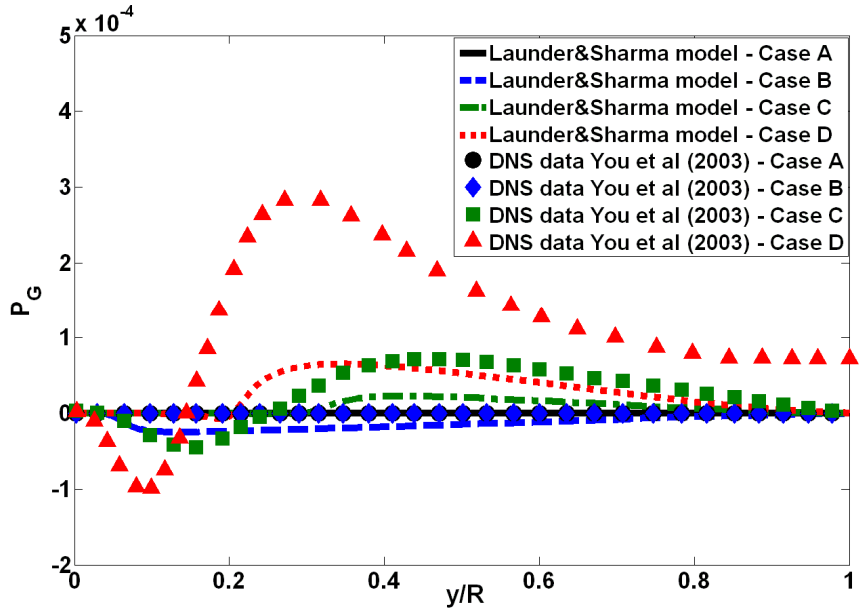

(a)

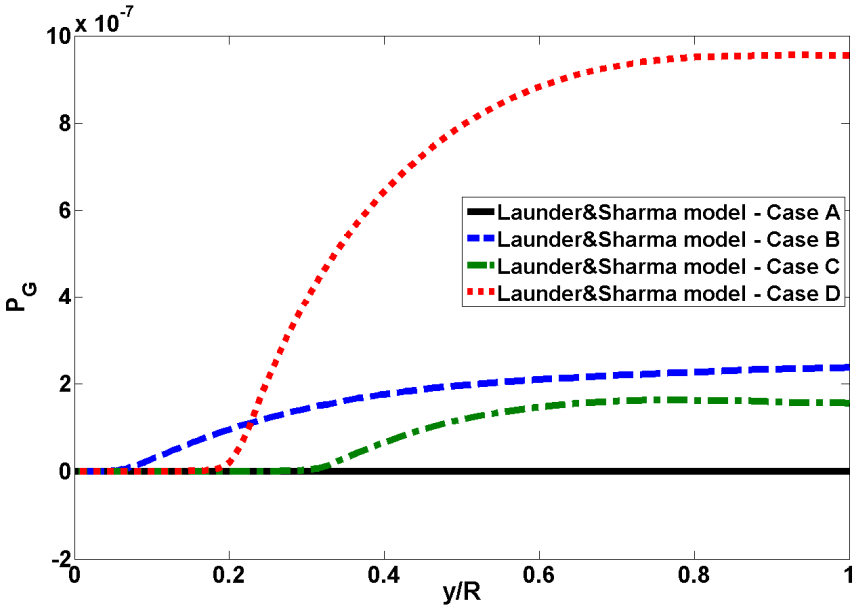

(b)

Figure 5.12 – Effects of the heat flux models on the buoyancy production term [m^2/s^3] using (a) Generalized Gradient Diffusion Hypothesis (GGDH) and (b) Simple Gradient Diffusion Hypothesis (SGDH).

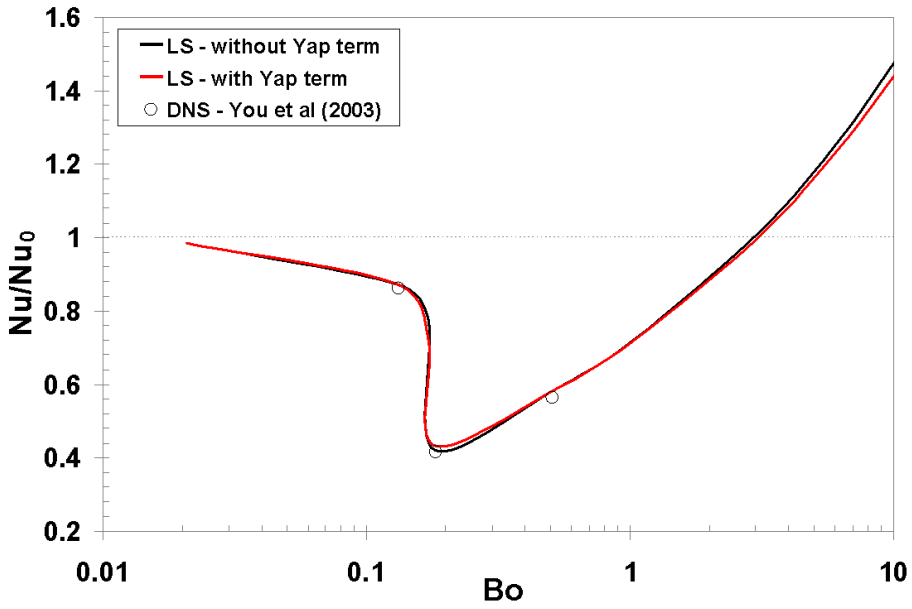

(a)

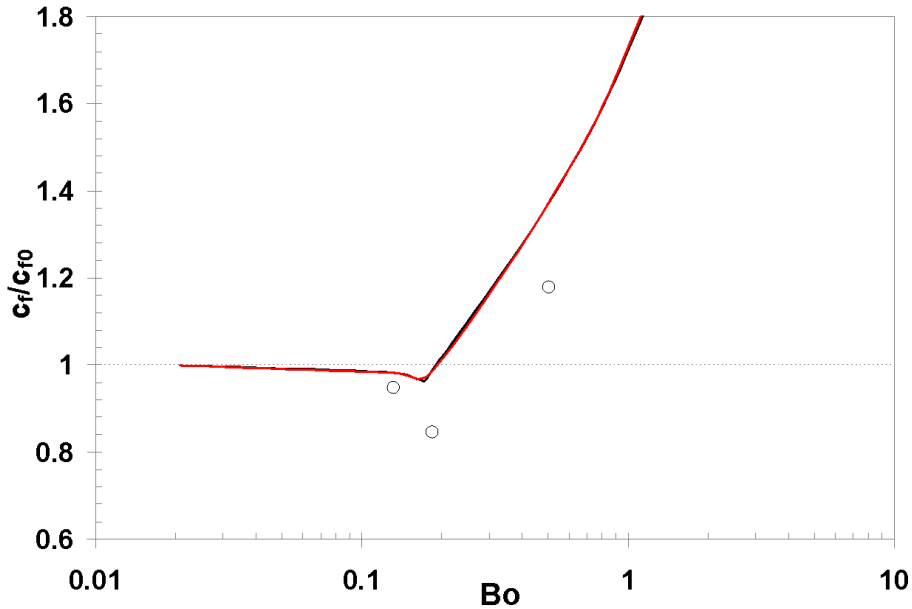

(b)

Figure 5.13 – Effects of including the Yap term on the local Nusselt number and friction coefficient.

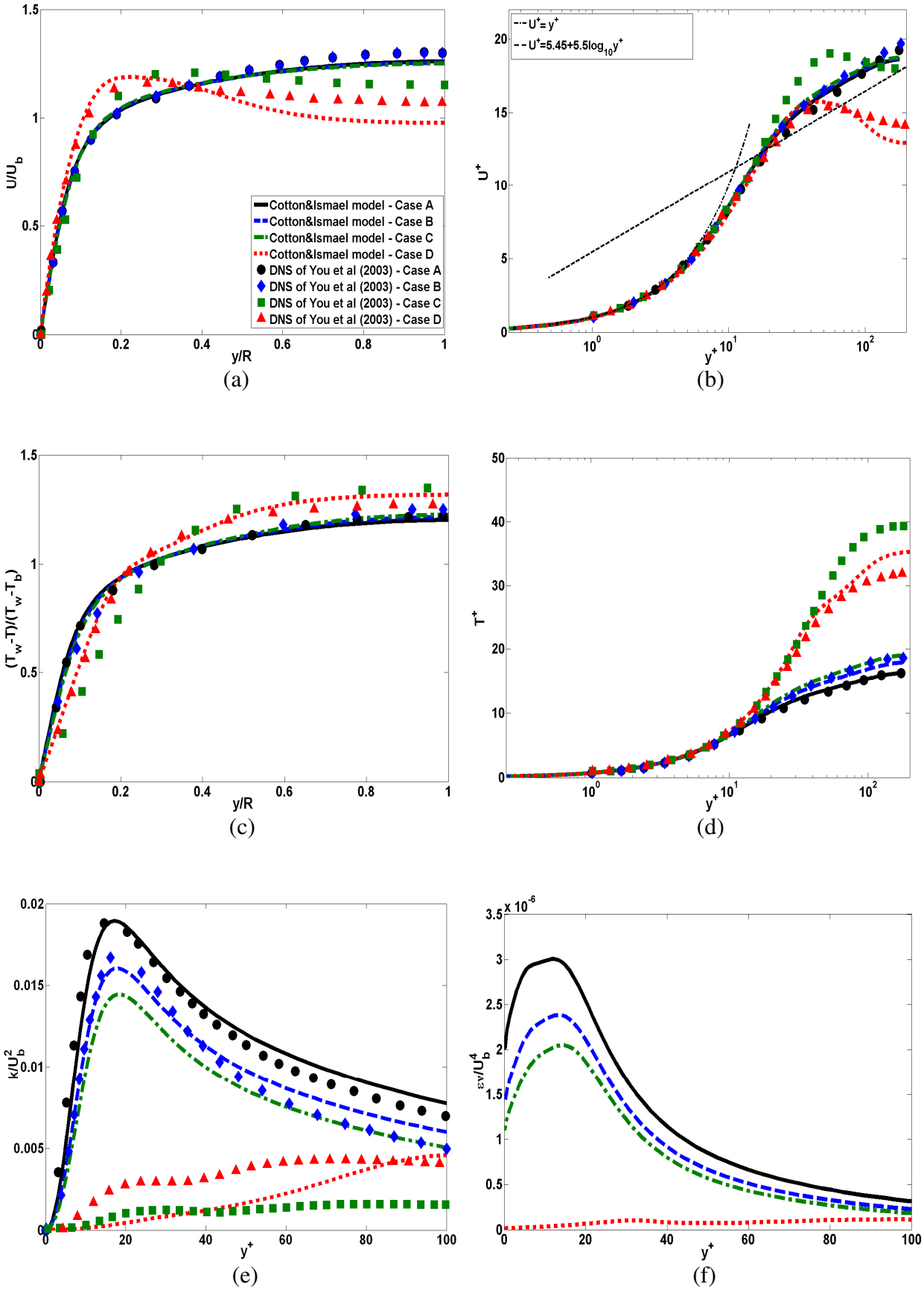

Figure 5.14 – Mean flow and turbulence profiles obtained using the Cotton-Ismael model in CONVERT.

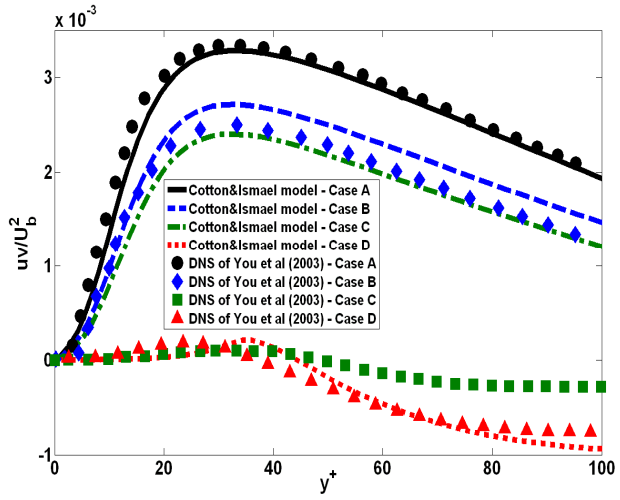

(g)

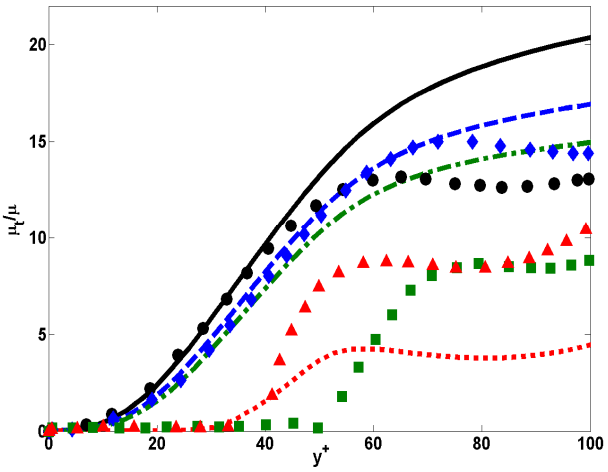

(h)

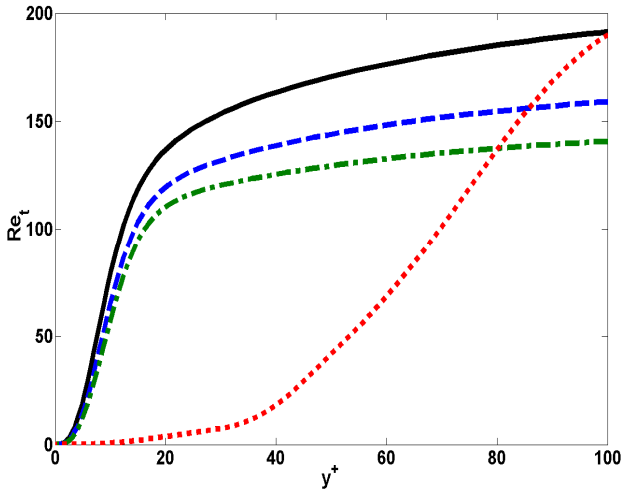

(i)

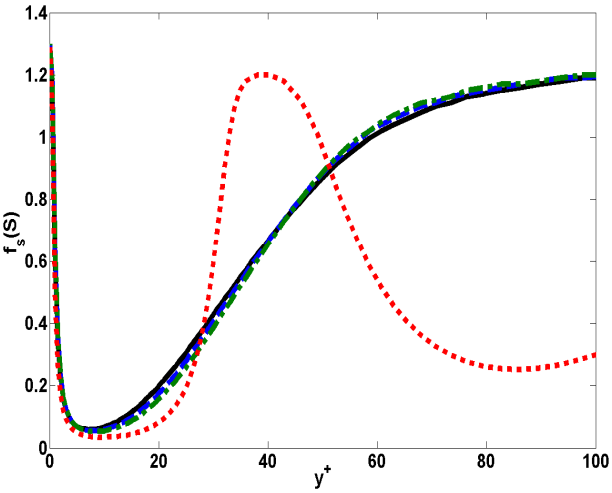

(j)

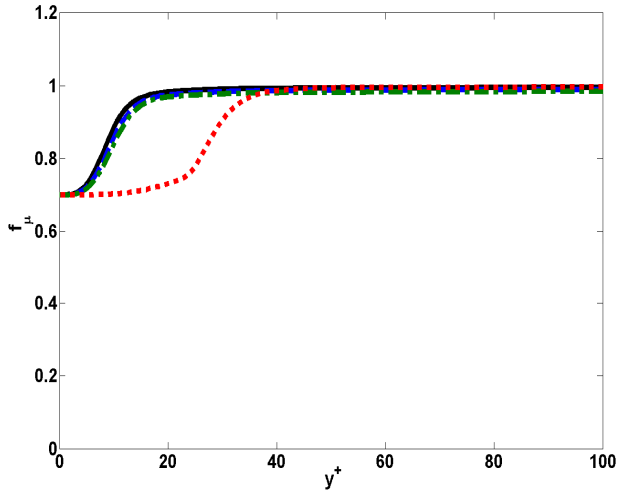

(k)

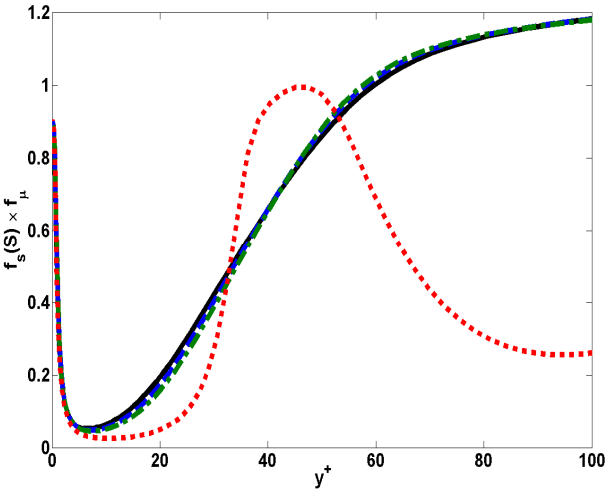

(l)

Figure 5.14 continued.

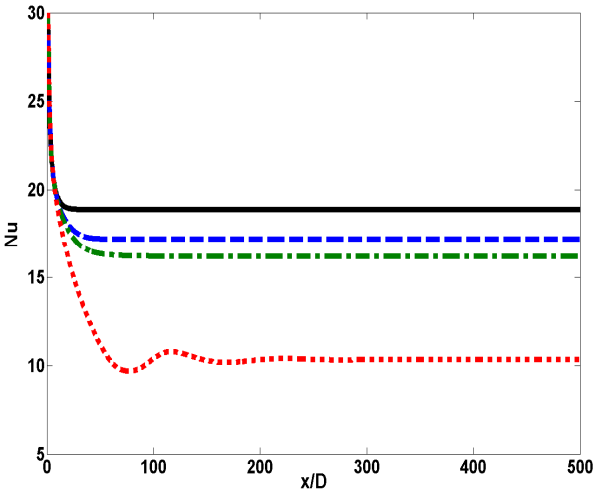

(m)

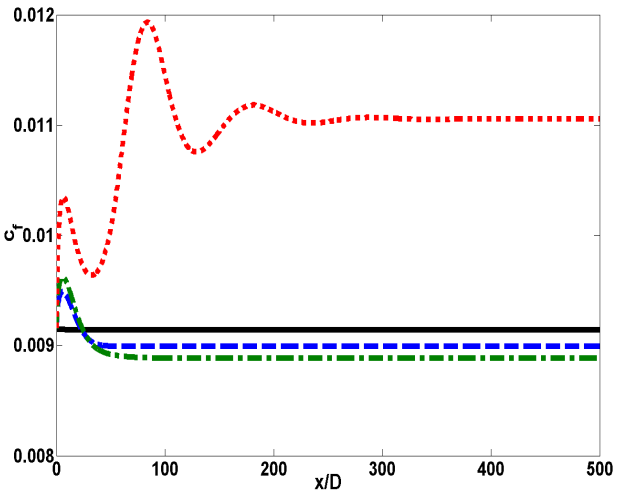

(n)

Figure 5.14 continued.

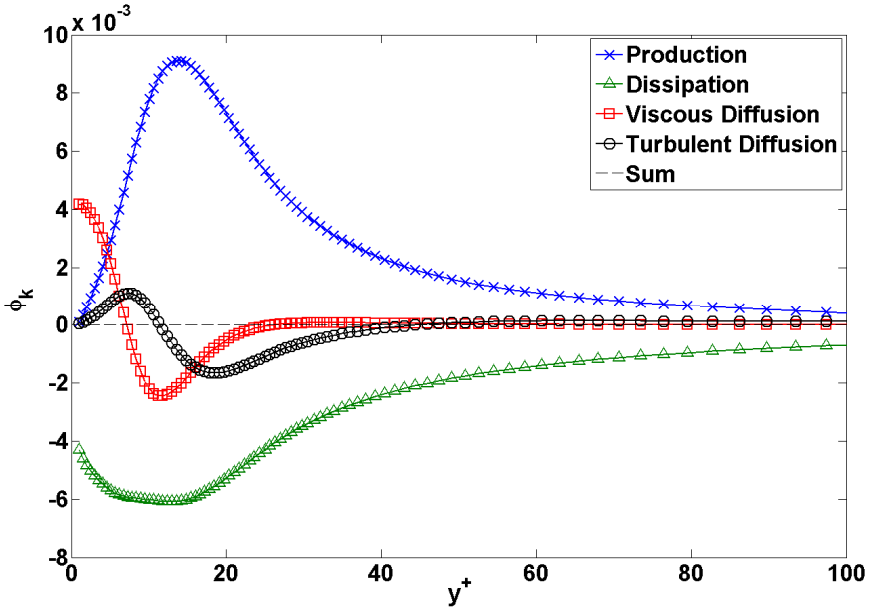

(a)

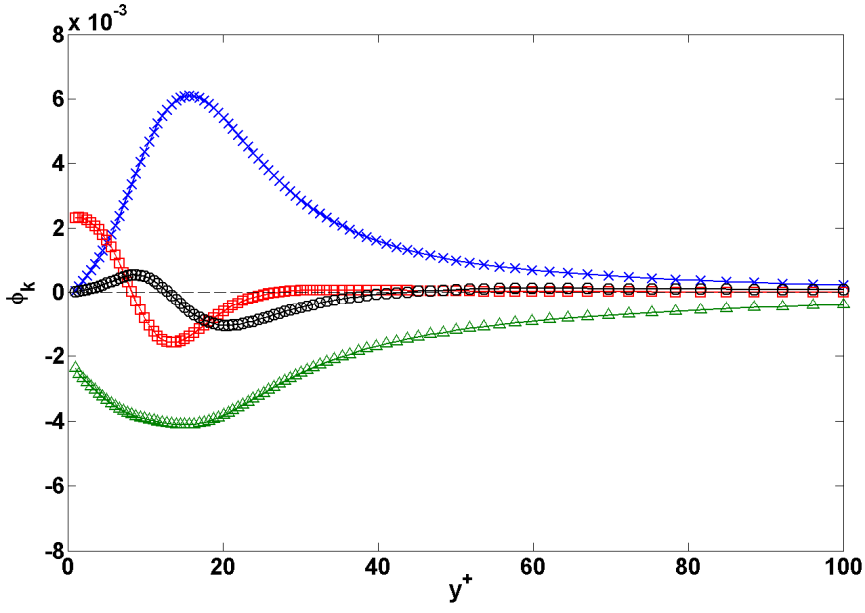

(b)

Figure 5.15 – Budgets of the turbulent kinetic energy [m^2/s^3] obtained using the Cotton-Ismael model in CONVERT (a) case A (b) case C.

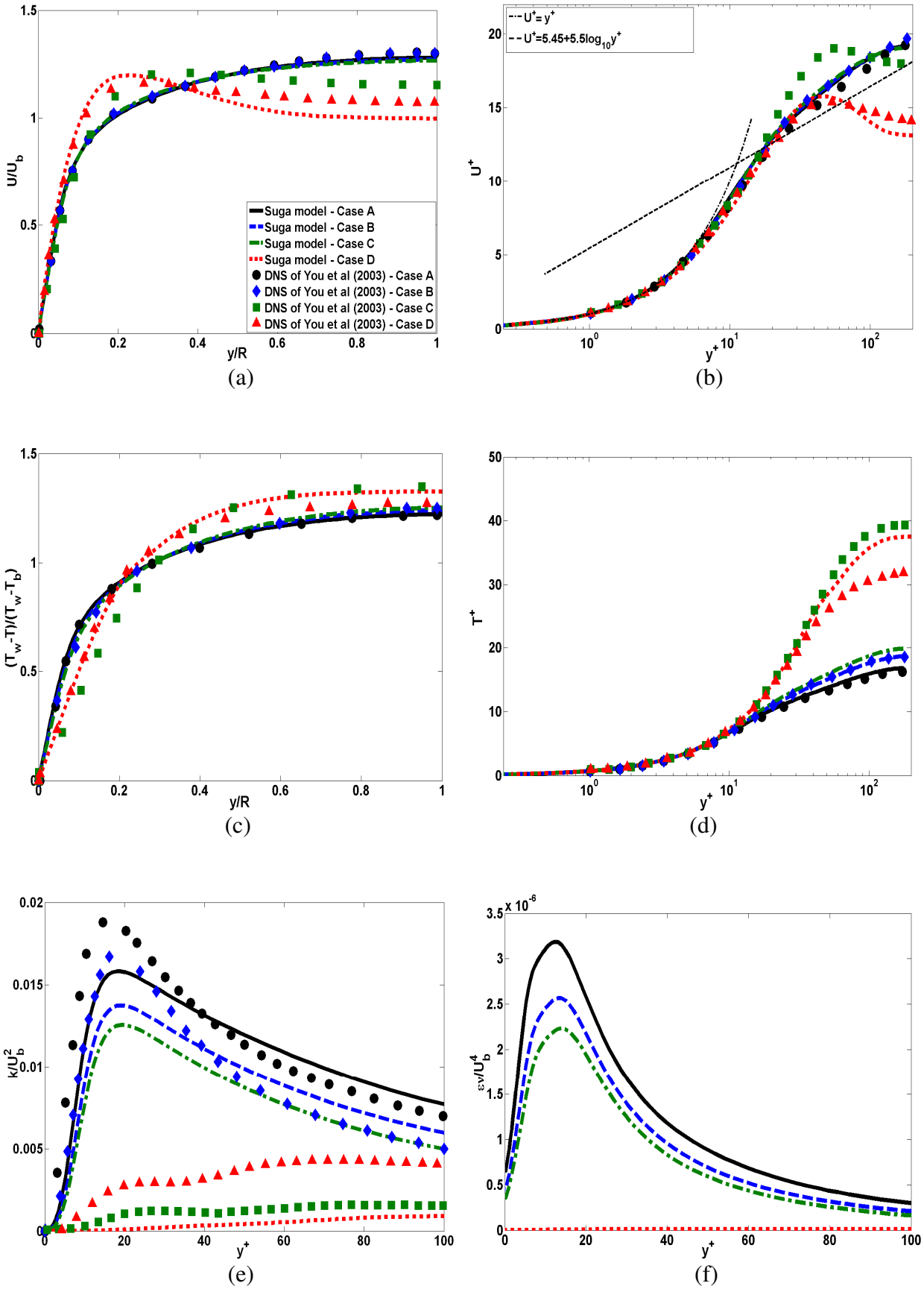

Figure 5.16 – Mean flow and turbulence profiles obtained using the Suga model in CONVERT.

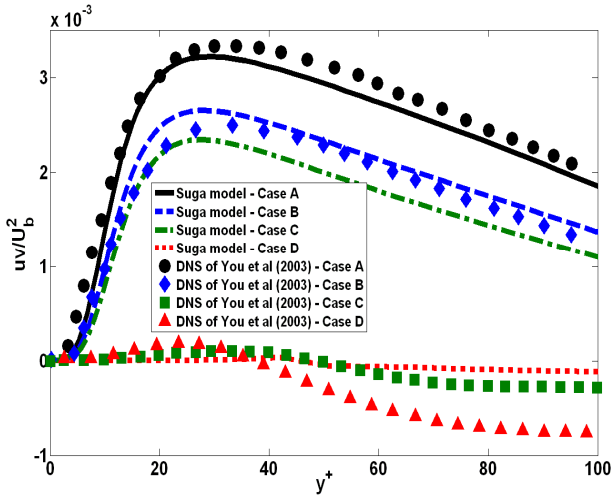

(g)

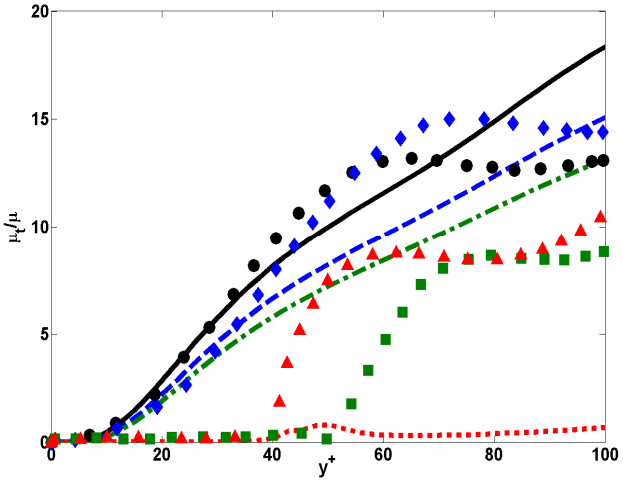

(h)

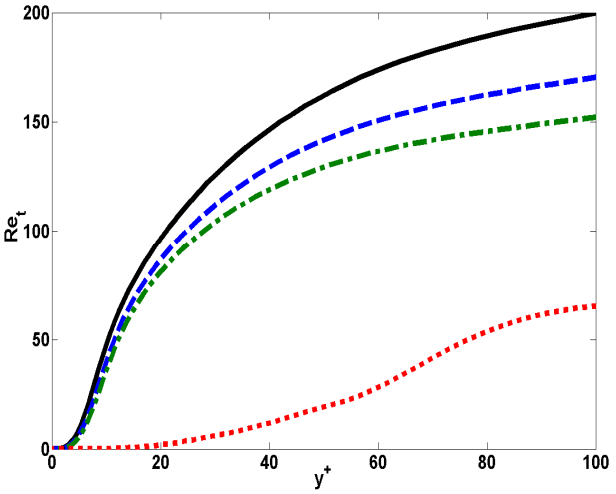

(i)

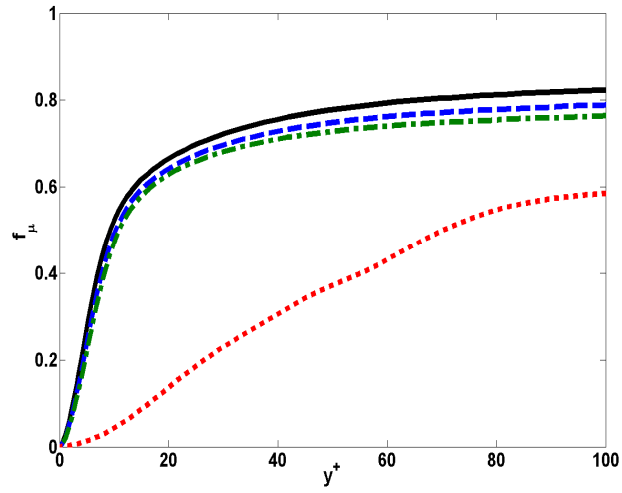

(j)

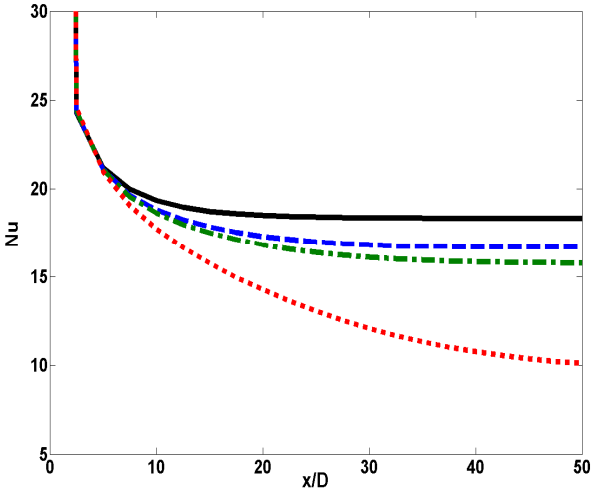

(k)

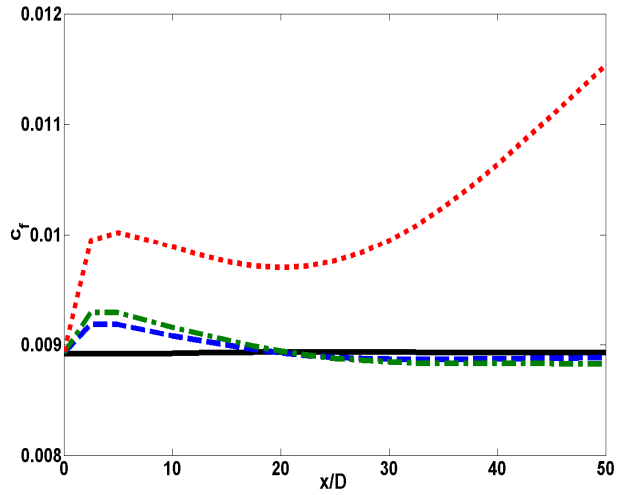

(l)

Figure 5.16 continued.

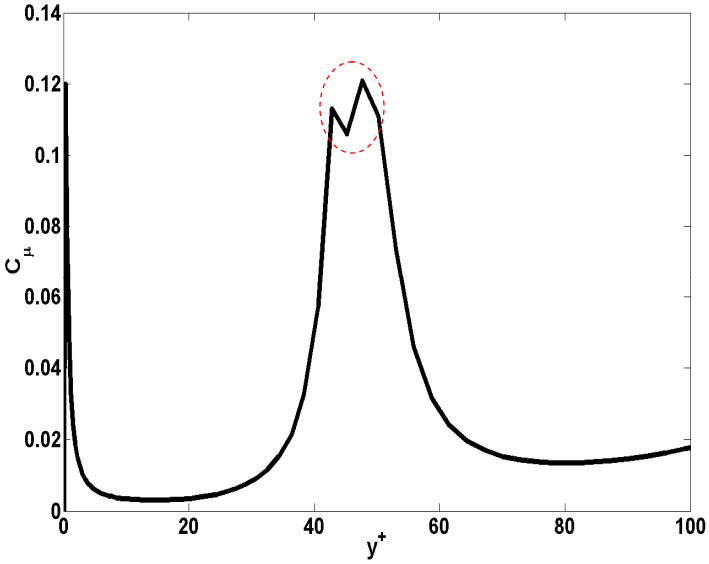

(a)

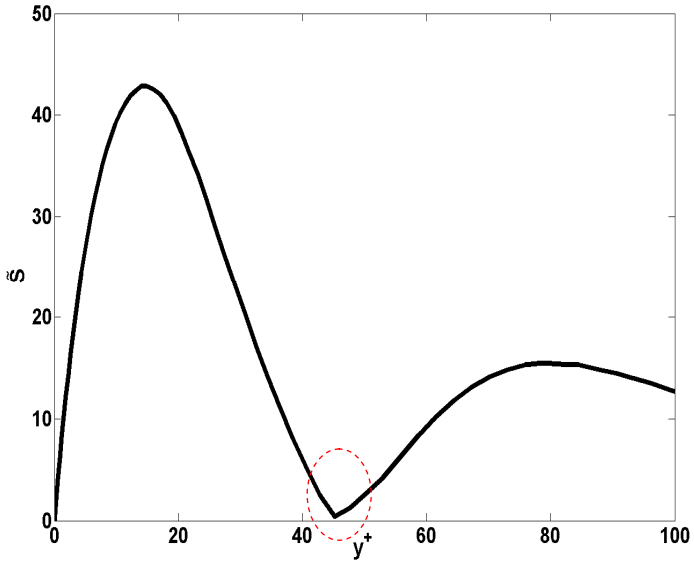

(b)

Figure 5.17 – Distribution of C_μ and non-dimensional strain rate $\tilde{S}$ for case (D) using the Suga model in CONVERT.

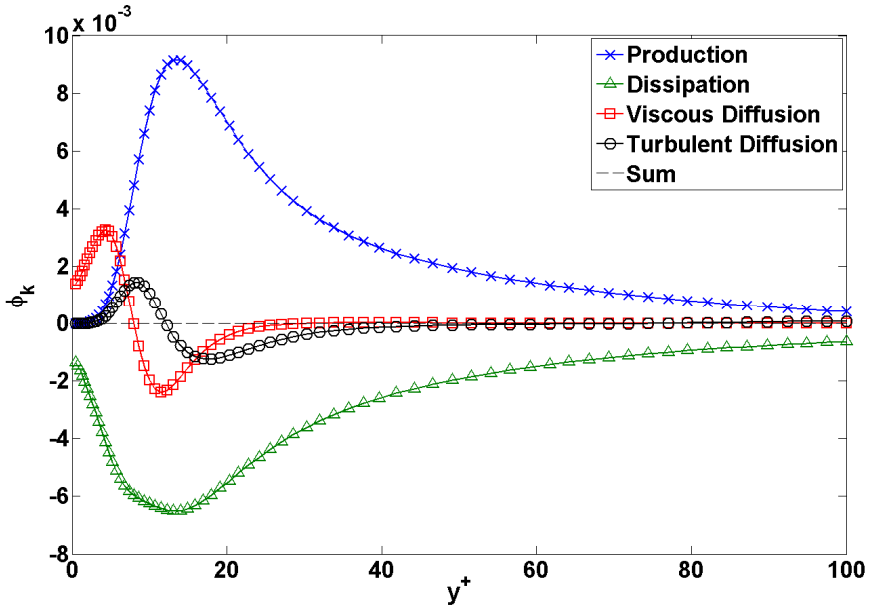

(a)

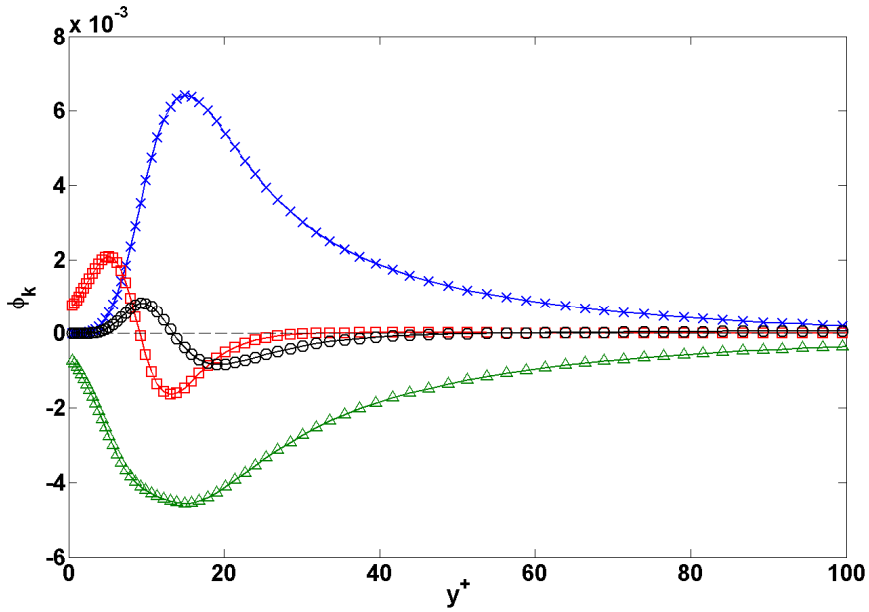

(b)

Figure 5.18 – Budgets of the turbulent kinetic energy [m^2/s^3] obtained using the Suga model in CONVERT (a) case A (b) case C

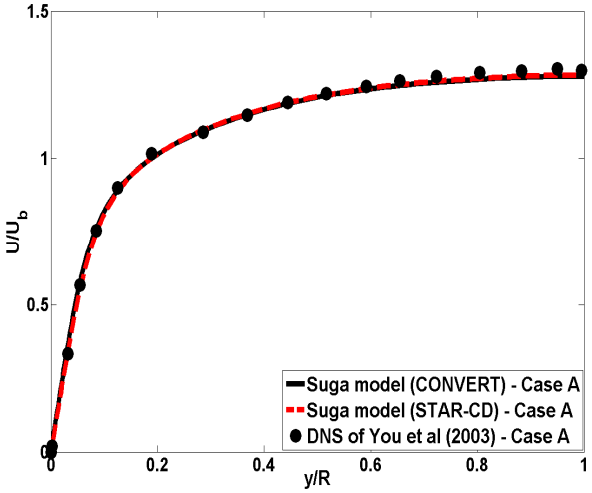

(a)

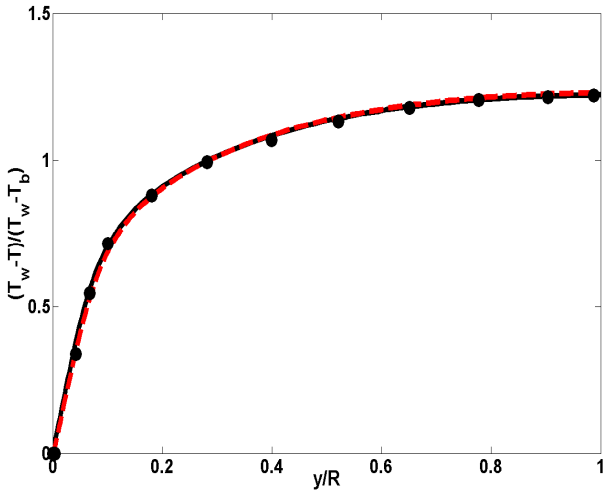

(b)

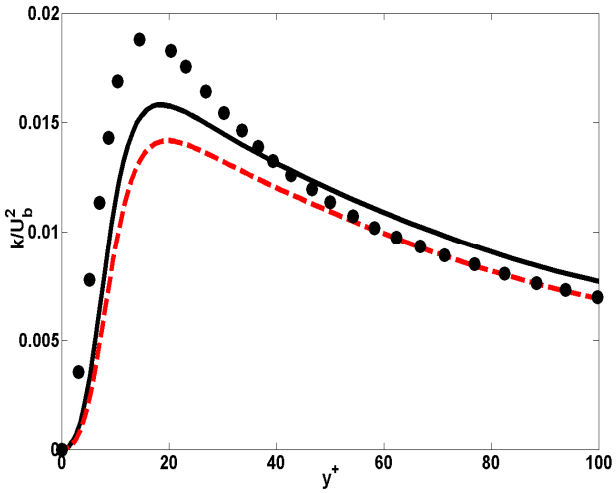

(c)

Figure 5.19 – Comparison of the results for case (A) obtained using the Suga model in CONVERT and STAR-CD.

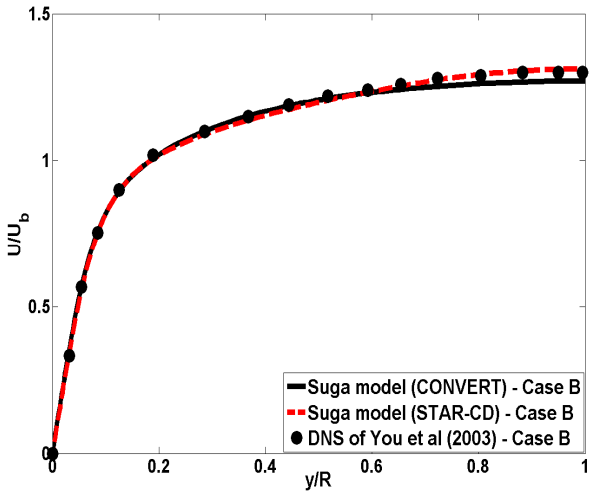

(a)

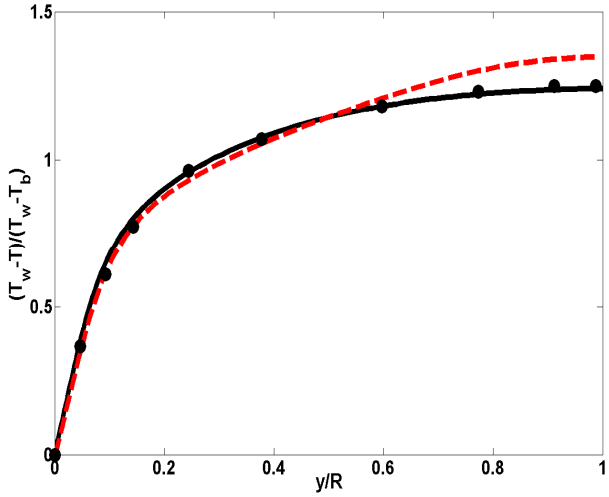

(b)

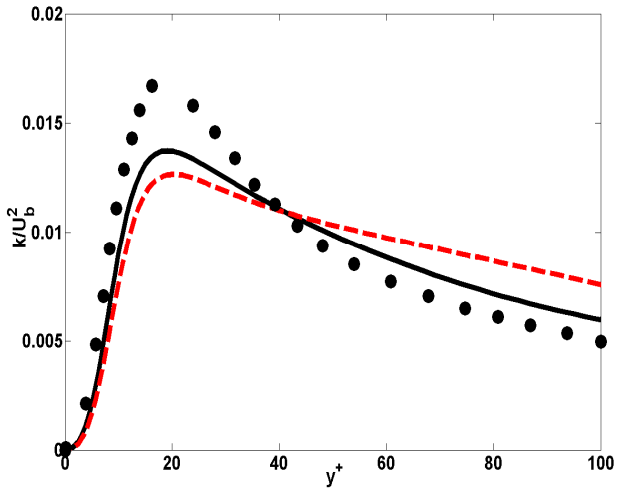

(c)

Figure 5.20 – Comparison of the results for case (B) obtained using the Suga model in CONVERT and STAR-CD.

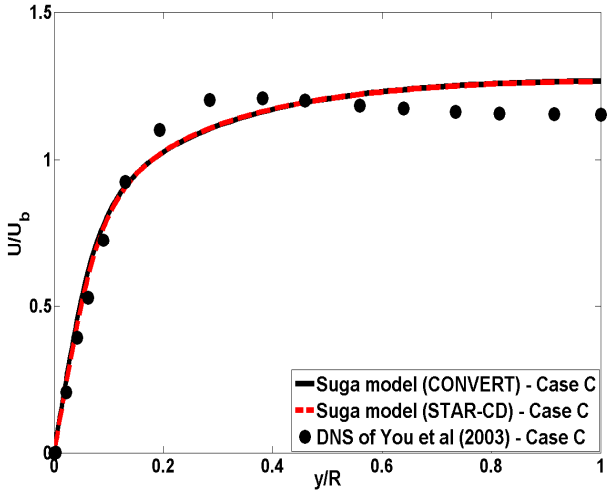

(a)

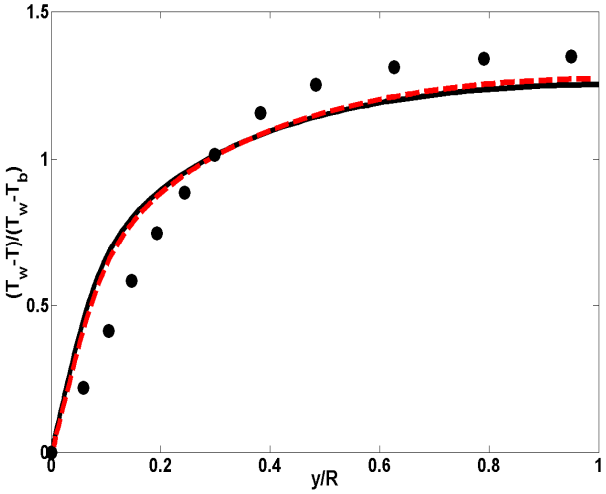

(b)

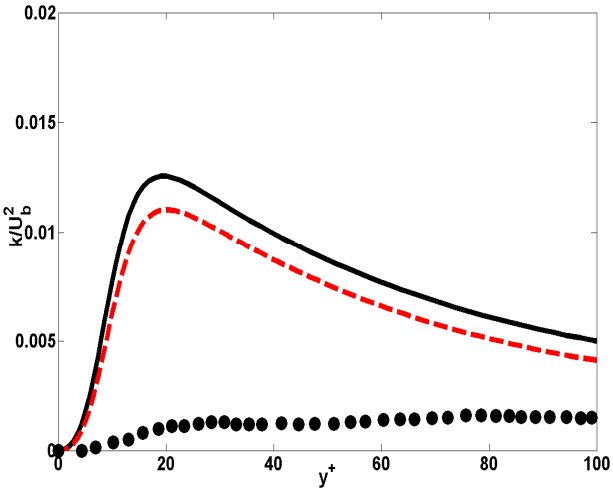

(c)

Figure 5.21 – Comparison of the results for case (C) obtained using the Suga model in CONVERT and STAR-CD.

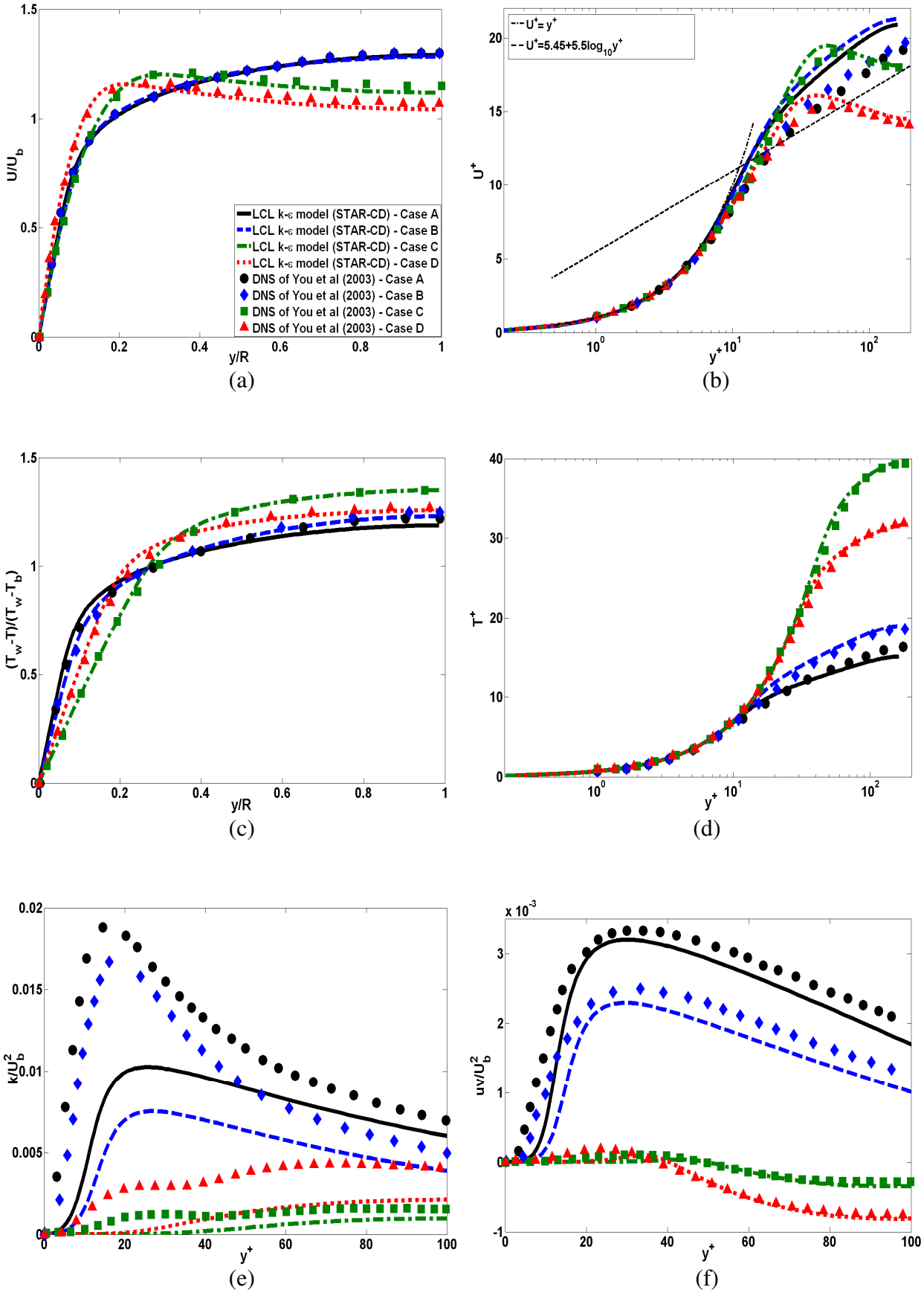

Figure 5.22 – Mean flow and turbulence profiles obtained using the LCL *k*-ε model in STAR-CD.

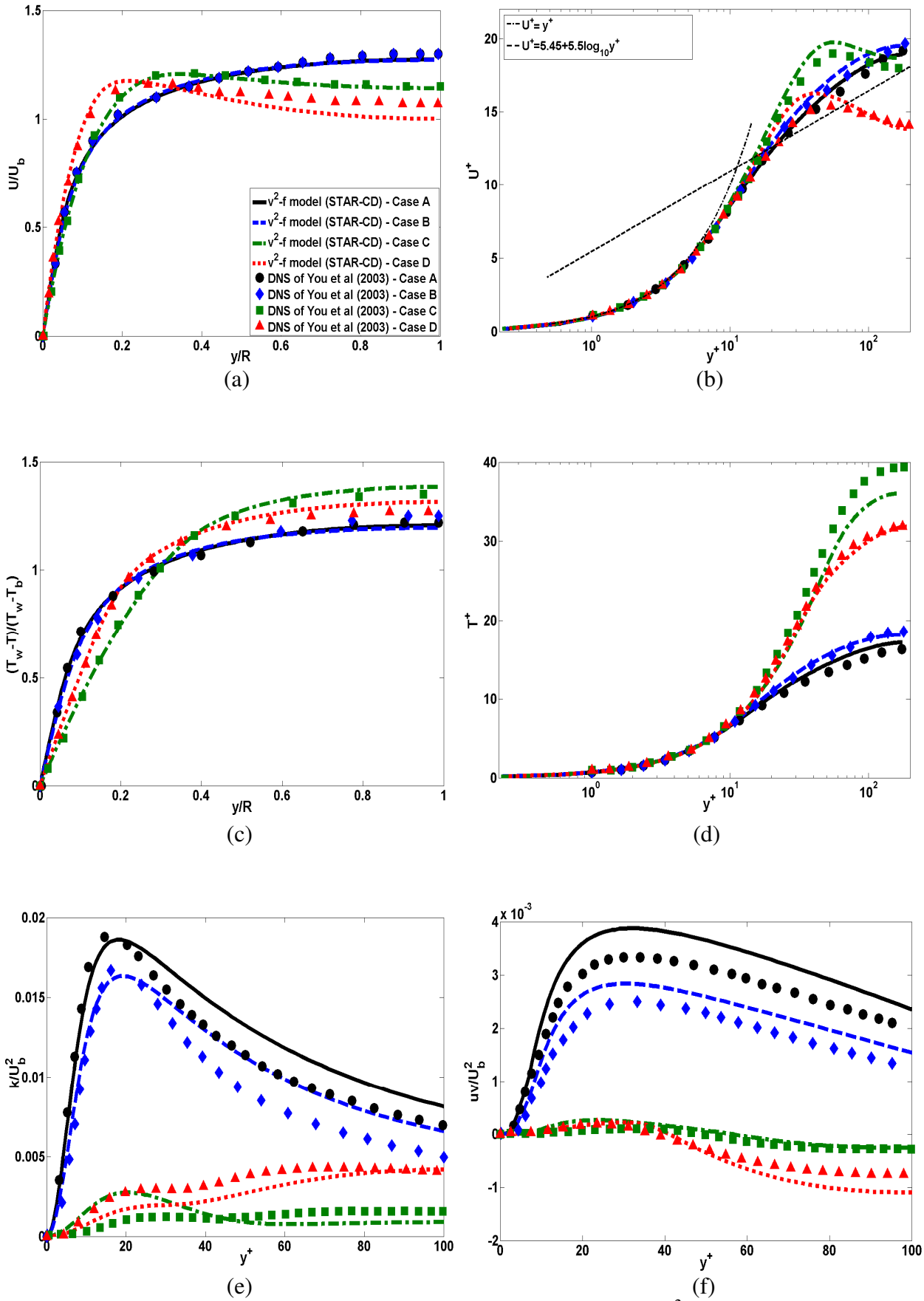

Figure 5.23 – Mean flow and turbulence profiles obtained using the v^2-f model in STAR-CD.

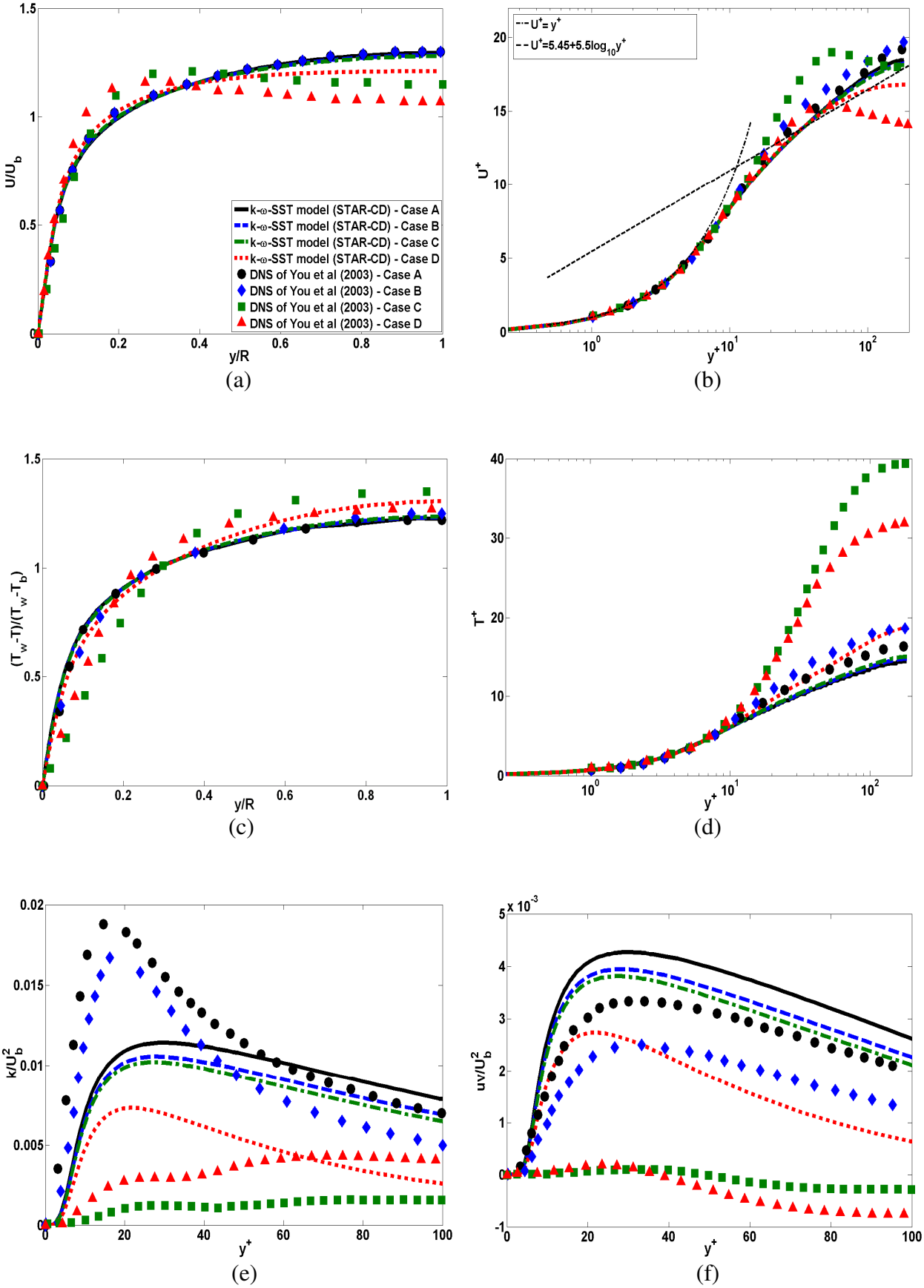

Figure 5.24 – Mean flow and turbulence profiles obtained using the standard *k-ω-SST* model in STAR-CD.

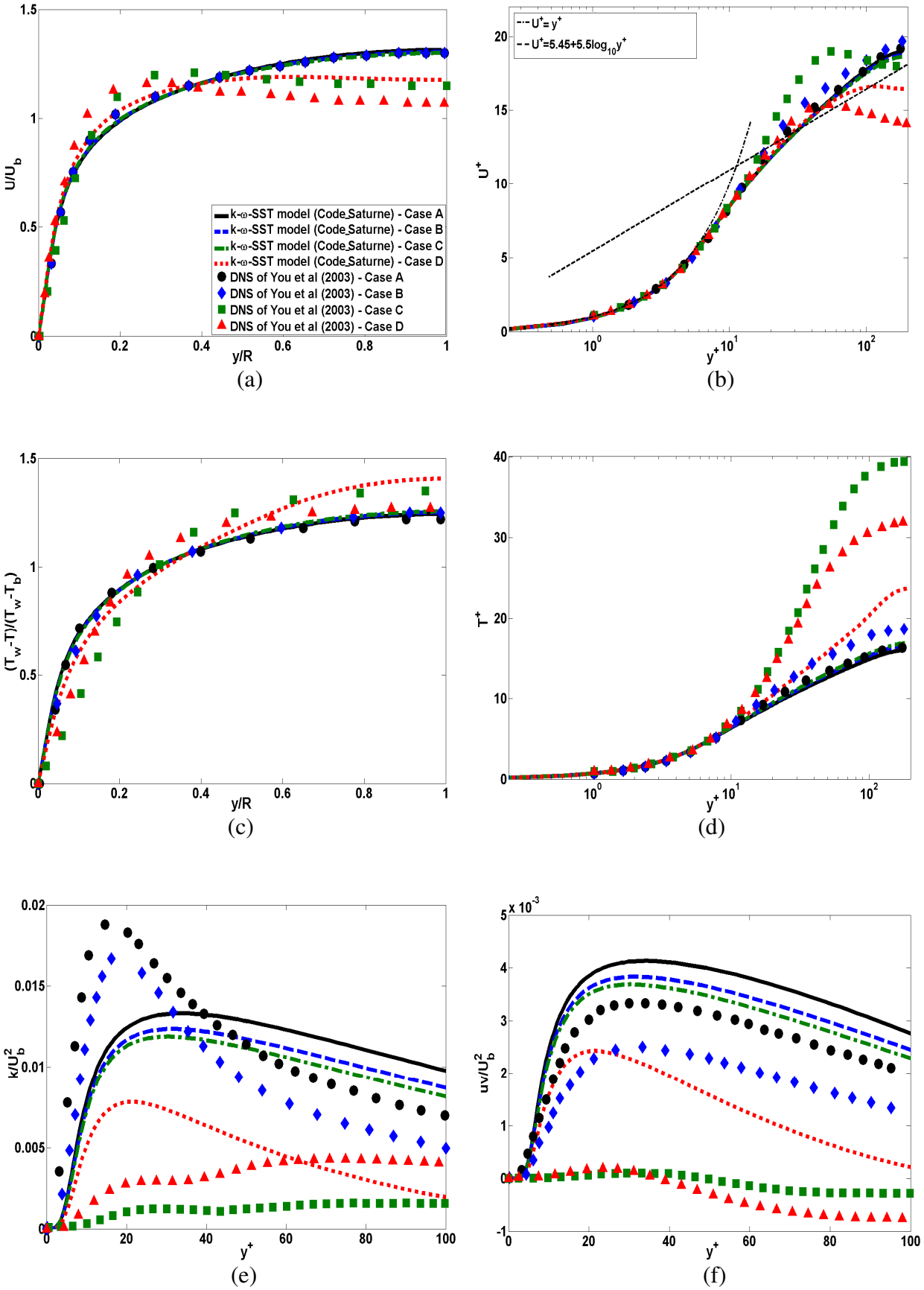

Figure 5.25 – Mean flow and turbulence profiles obtained using the standard *k-ω-SST* model in Code_Saturne.

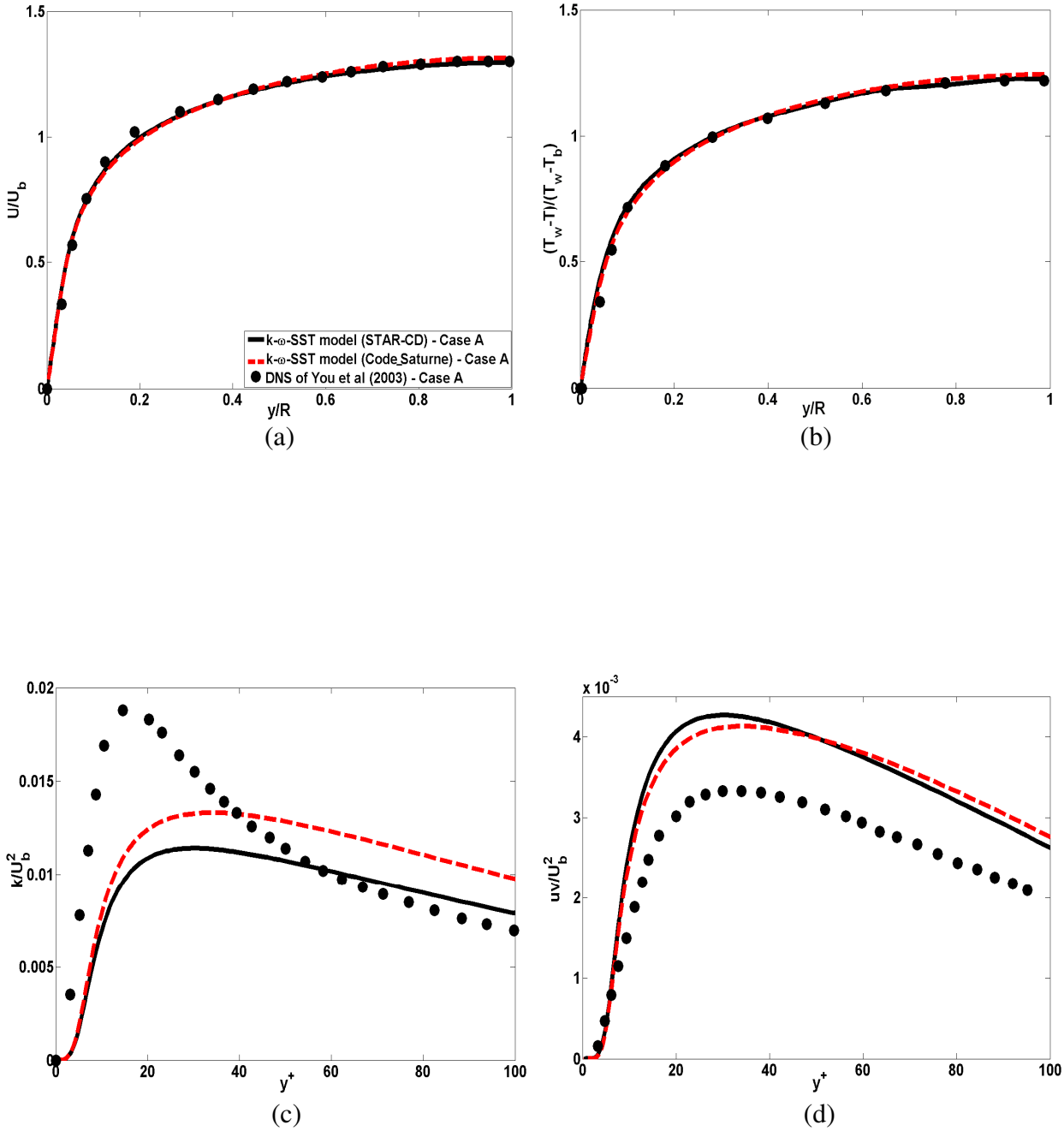

Figure 5.26 – Comparison of mean flow and turbulence profiles for case (A) obtained using the standard *k-ω-SST* model in STAR-CD vs. Code_Saturne.

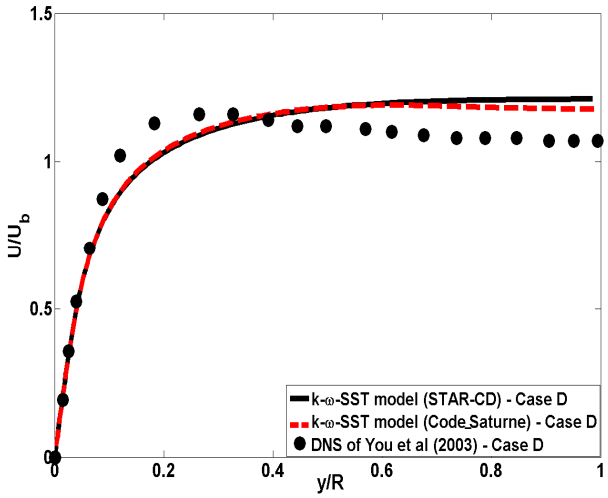

(a)

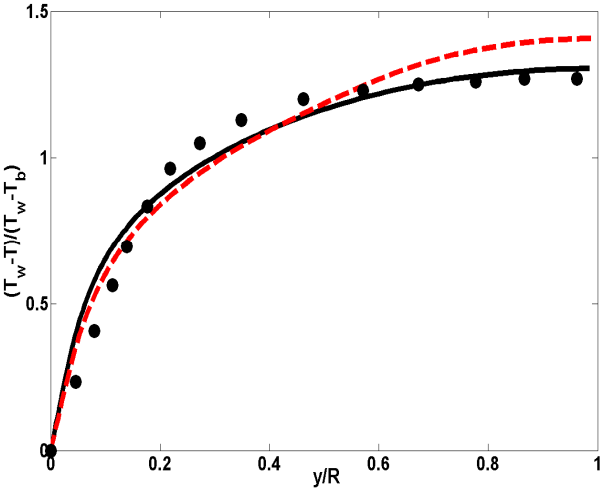

(b)

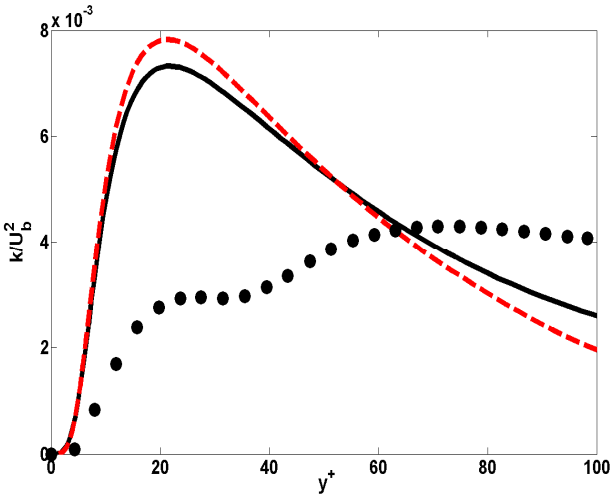

(c)

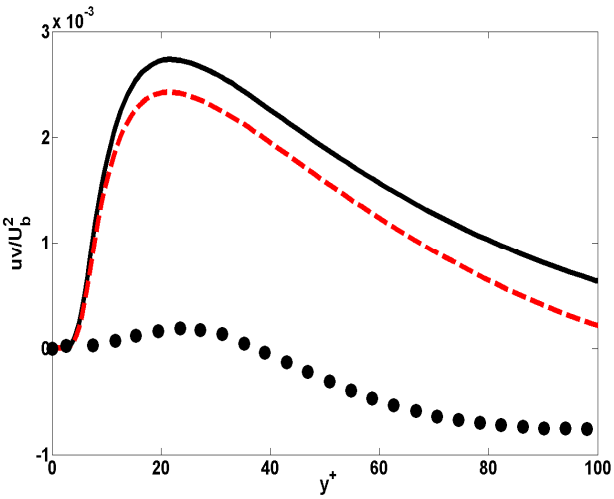

(d)

Figure 5.27 – Comparison of mean flow and turbulence profiles for case (D) obtained using the standard *k-ω-SST* model in STAR-CD vs. Code_Saturne.

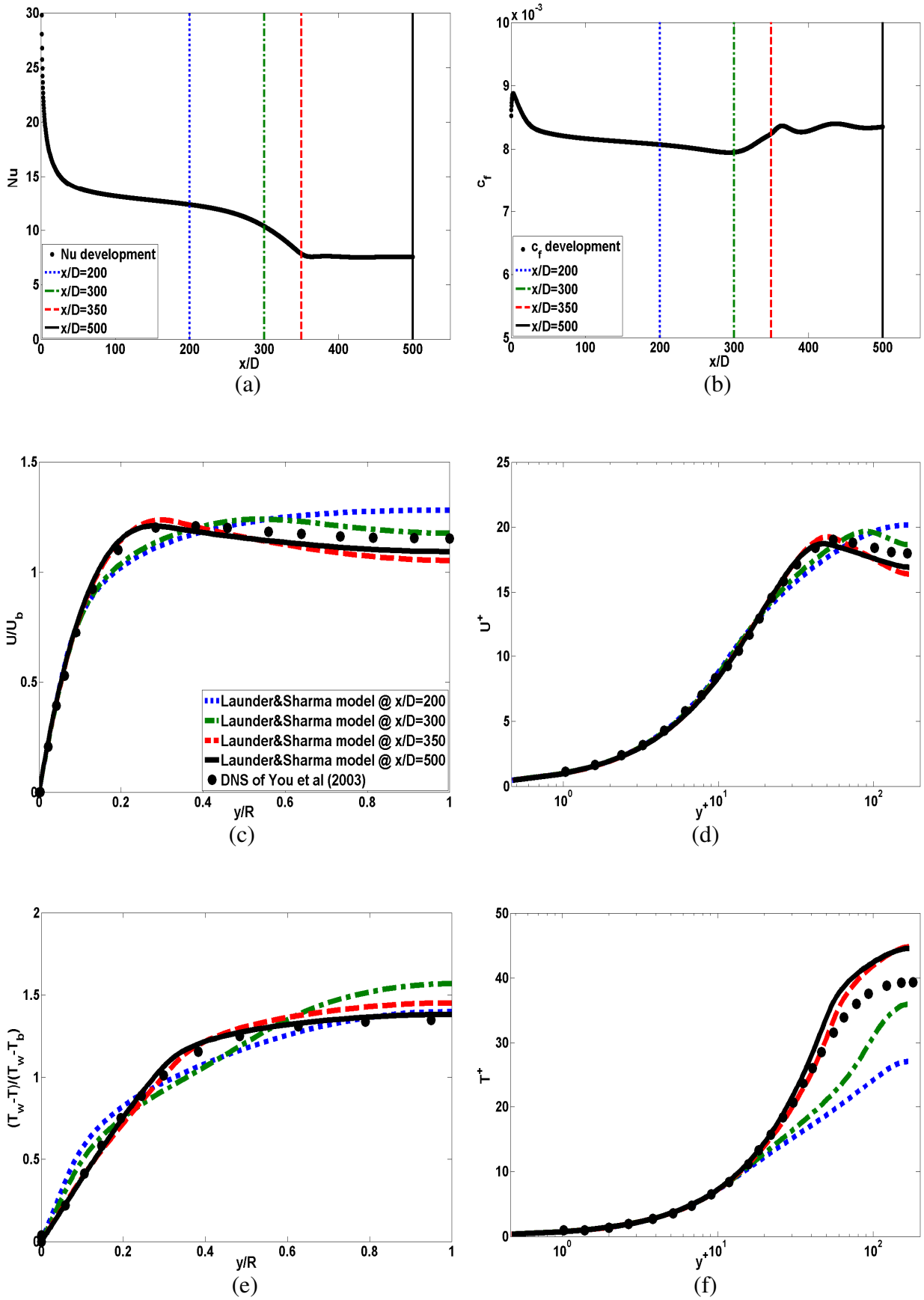

Figure 5.28 – Mean flow and turbulence profiles for case (C) at different streamwise locations obtained using the Launder-Sharma model in CONVERT.

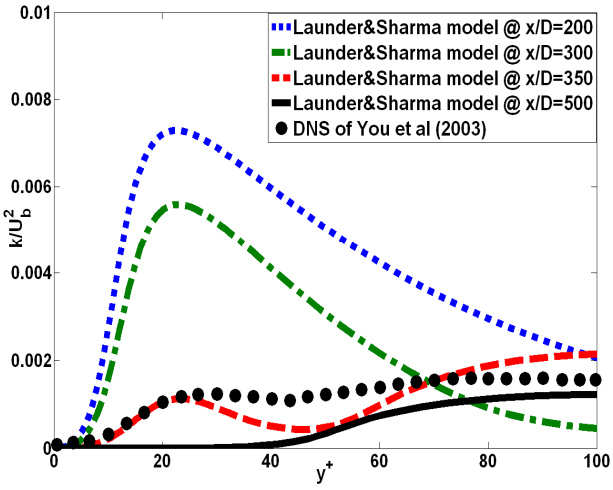

(g)

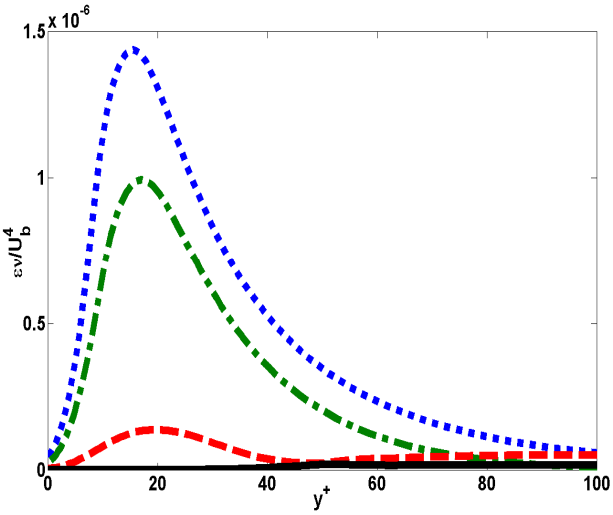

(h)

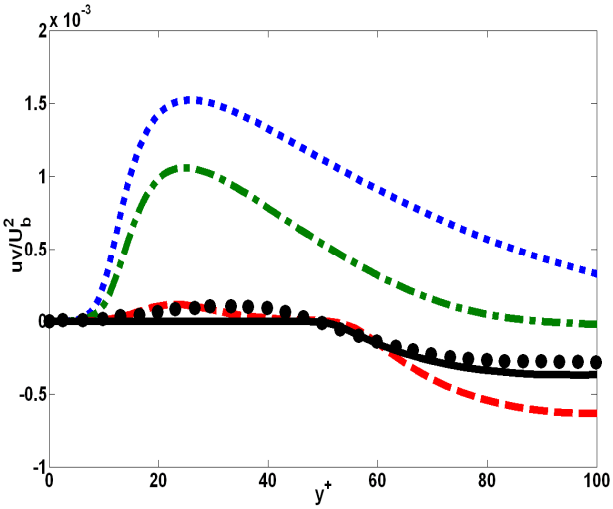

(i)

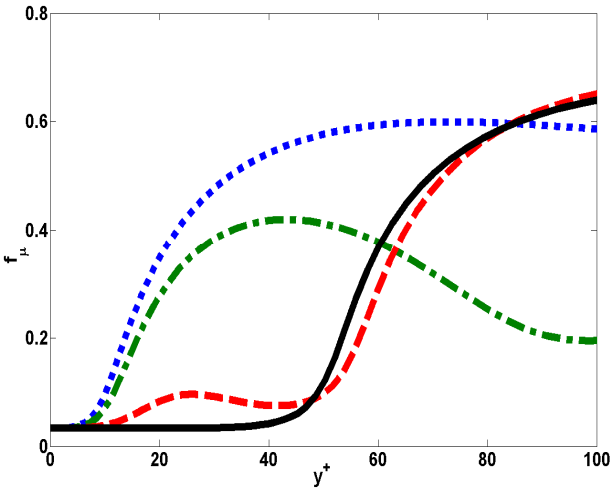

(j)

Figure 5.28 continued.

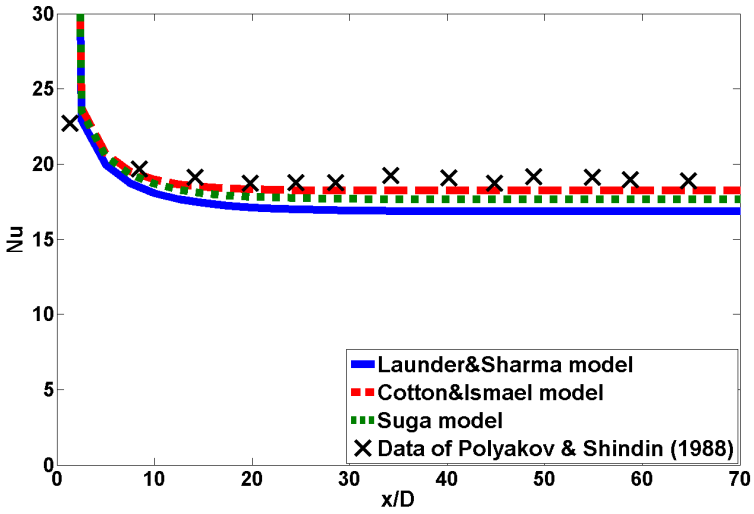

(a)

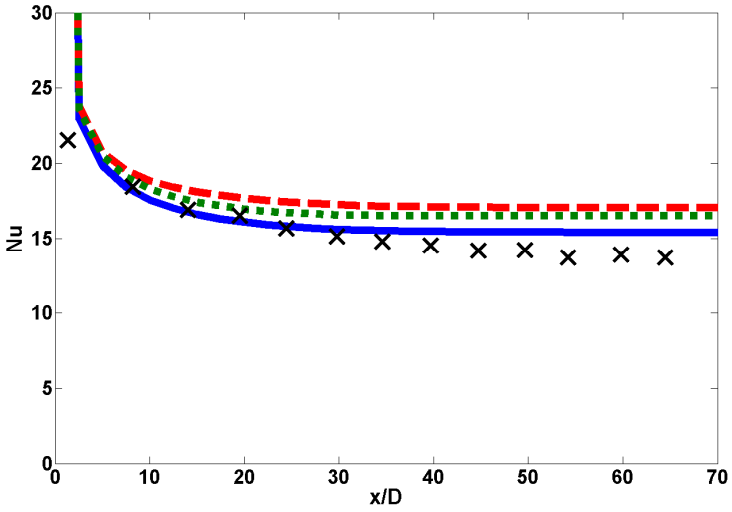

(b)

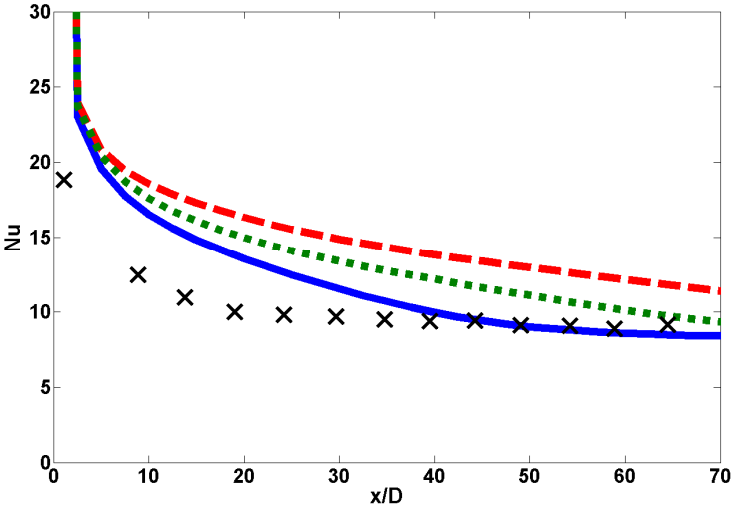

(c)

Figure 5.29 – Nusselt number development against the experiments of Polyakov and Shindin (1988) (Runs 1-5 in Table 5.11)

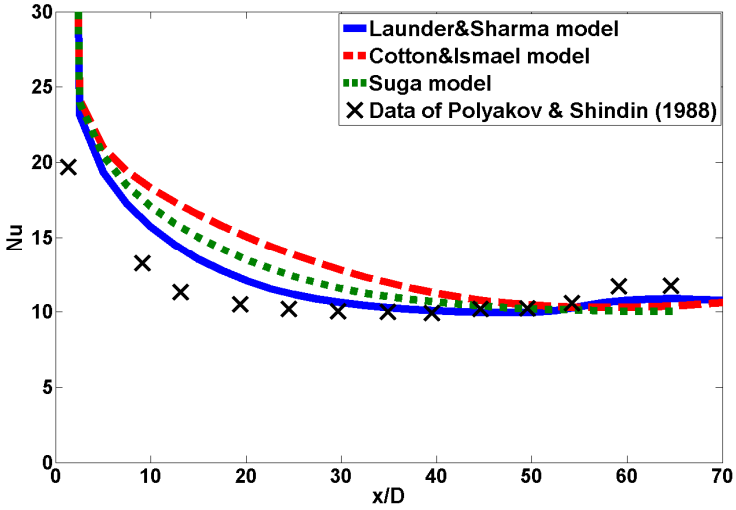

(d)

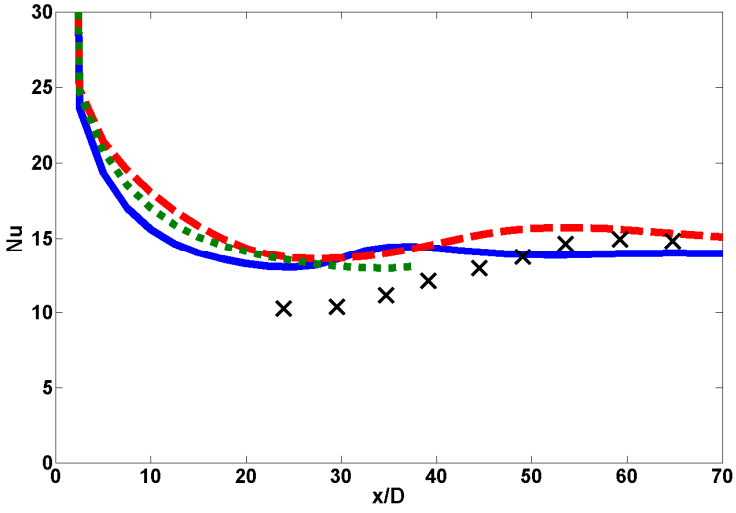

(e)

Figure 5.29 continued.

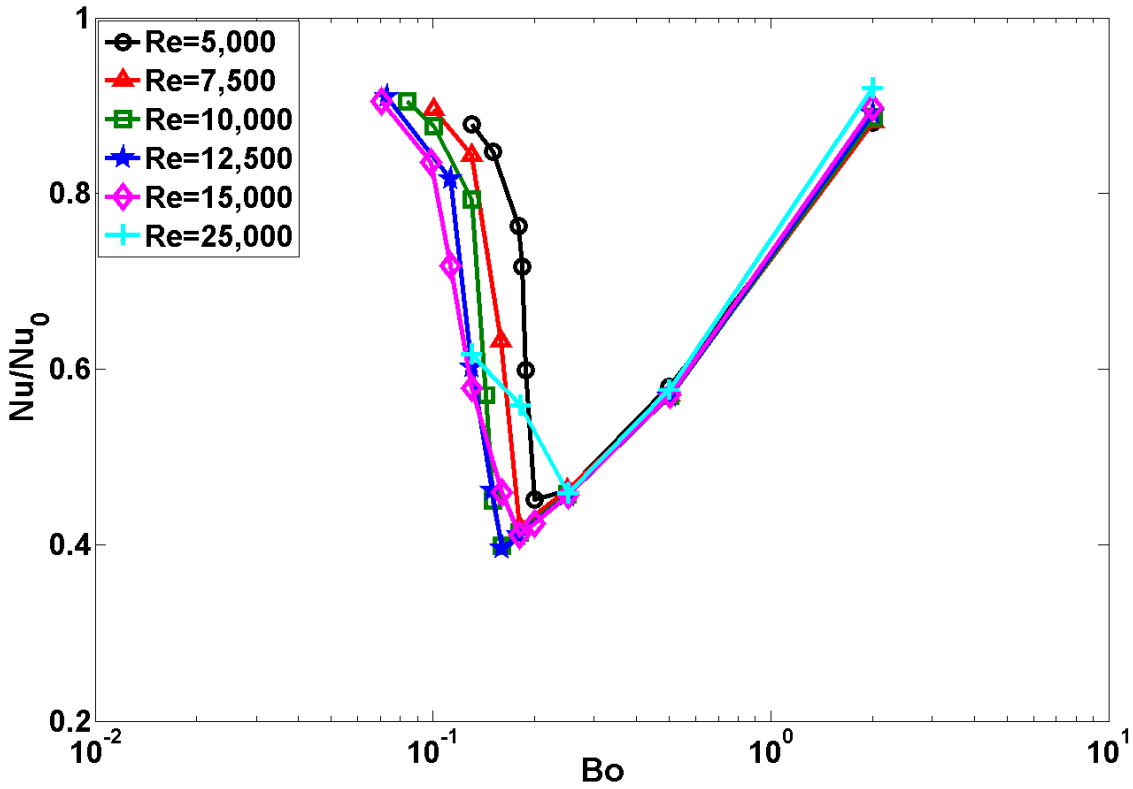

Figure 5.30 – Normalized Nusselt number impairment and enhancement against the buoyancy parameter for different Reynolds numbers.

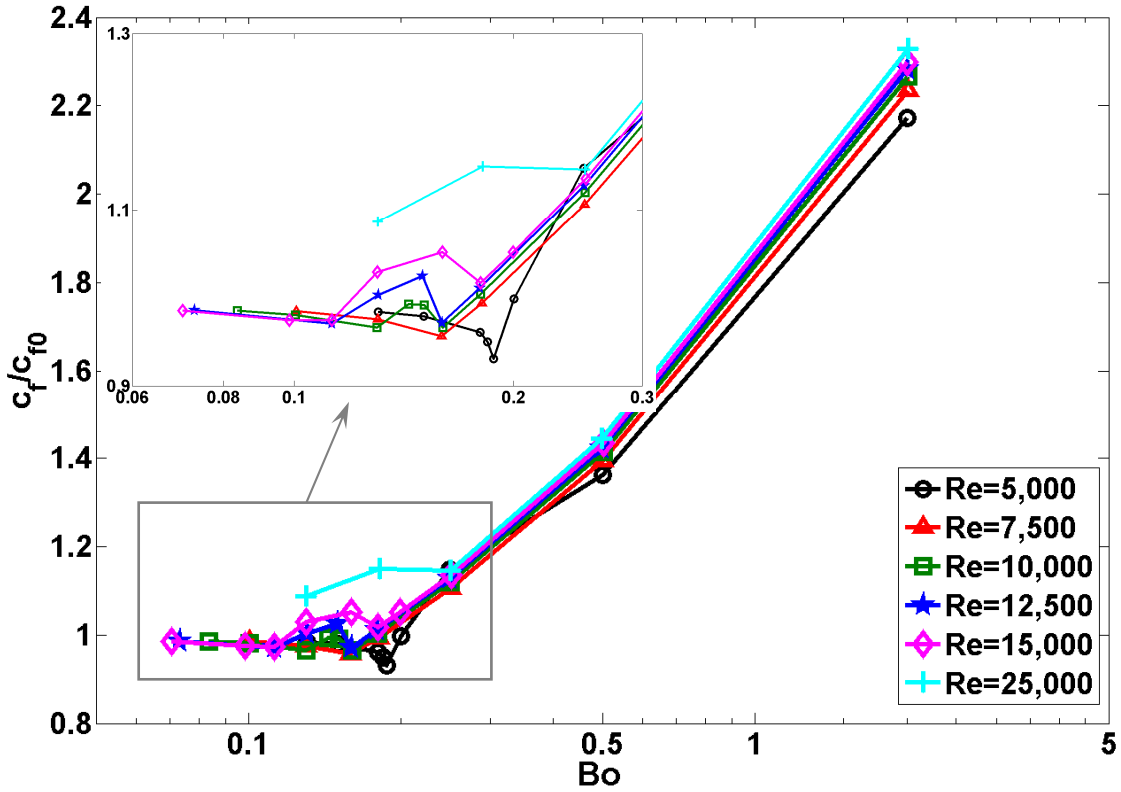

Figure 5.31 – Normalized Friction coefficient impairment and enhancement against the buoyancy parameter for different Reynolds numbers.

CHAPTER 6

2-DIMENSIONAL RIB-ROUGHENED SURFACES

6.1 PRELIMINARY REMARKS

As was mentioned in Chapter 1, rough surfaces have been used as a tool to enhance heat transfer by increasing the level of turbulence mixing in the flow. One of the objectives of the present work is to study the rib-roughened fuel pins of the UK fleet of Advanced Gas-cooled Reactors (AGRs). This chapter is mainly concerned with studying different factors which can influence the thermal-hydraulic performance of these fuel pins. Some current practical issues associated with fuel pins such as the effects of carbon deposition on the roughened surfaces are also addressed.

The commercial code 'STAR-CD' version 4.02 (CD-Adapco, 2006) was used to generate results for this part of the study. In the CFD simulations reported in the present chapter, the focus is on the data of Rau et al. (1998) who employed two geometrically

(and dynamically) similar square cross-section test lengths: a smaller one for heat transfer measurements and a larger version designed to give good resolution of the flow field. Air was the working fluid, and the Reynolds number based on the bulk velocity and equivalent diameter was fixed at Re = 30,000. In both cross-sections square ribs could be mounted on the lower surface only ('1s'; Figure 2.4), or on both the lower and upper surfaces ('2s'). In all cases, a large blockage ratio was imposed (k/H = 0.1) and the surfaces may be considered to have a high degree of roughness. Rau et al. reported 1s channel results for P/k = 6, 9, and 12, while P/k was set to 9 in the 2s section.

In this chapter, the effects of eight different 'design parameters' are tested on 2-dimensional rib-roughened surfaces. These design parameters are divided into two categories: 1) Discrete design parameters, and 2) Continuous design parameters.

The discrete design parameters include the selection of one of four different turbulence models, two different rib profiles, two different near-wall treatments, and two different mesh types (Table 6.1). The continuous design parameters studied here consist of three rib pitch-to-height ratios (P/k), four rib height-to-channel height ratios (k/H), three rib width-to-height ratios (b/k) and two Reynolds numbers (Re) (Table 6.2). Unlike the discrete design parameters, it is possible to define upper and lower limits for the continuous design parameters, as indicated in Table 6.2.

Design Parameters	**Tests**
Turbulence models	k-ε, k-ω-SST, v^2-f and Suga
Rib shape	Square and Multi-Start
Near-wall treatment	Low-Reynolds-number and Standard Wall Function
Mesh type	Cartesian structured mesh and Polyhedral unstructured mesh

Table 6.1 – Discrete design parameters along with their details.

Design Parameters	Lower limit	Upper limit	Number of tests
P/k	6	12	3 (for 1s) + 1 (for 2s)
k/H	0.05	0.1	4
b/k	0.5	1.5	3
Re	30,000	100,000	2

Table 6.2 – Continuous design parameters along with their details.

The numerical details of the simulations carried out using these design parameters are discussed below.

6.2 CASE DESCRIPTION

6.2.1 Two-Dimensional Channel Approximation

In CFD simulations, it is common to reduce the computational domain to 2-dimensions by making use of symmetry boundary conditions and thereby reducing both computational power requirements and time. These 2D domains are especially desirable for carrying out 'parametric studies' where a large number of runs might be required. A general assumption in 2D simulations of channel flow is that they represent conditions along the centre-plane of the true 3D configuration. Clearly, the accuracy of this assumption greatly depends on the degree of secondary flows present along the centre-plane of the configuration, i.e. the lower the level of these secondary flows, the higher the accuracy of the 2D assumption.

As was noted before, in the present study the main focus is on the experimental work of Rau et al. (1998) in which square cross-sections were used. The question arises as to whether or not a 2D approximation is valid for this case. To address this question, the results along the centre-line of a 3D case are compared with the results of a 2D simulation. The results are discussed in the context of mesh sensitivity (see Section 6.3.2.1).

6.2.2 Numerical Procedures

In the simulations presented in this chapter, all fluid properties are assumed to be constant. The momentum and turbulence transport equations are discretized using second-order central and first-order upwind schemes, respectively. The energy equation is discretized using the 'Monotone Advection and Reconstruction Scheme' (MARS) (CD-Adapco, 2006) (see Section 4.7.2.3). The SIMPLE algorithm is adopted for pressure-velocity correction. The maximum residual tolerance (convergence criterion) for all the simulations was set to 10^{-6}. The turbulent Prandtl number is set to a constant value, $\sigma_t = 0.9$ for all simulations.

6.2.3 Geometry and Grids

In total, twelve different meshes were used in this chapter to test the effects of all eight design parameters (Table 6.3 below). Despite their differences, all these grids have some common features; they all consist of 2-dimensional channels, the lower walls of which are roughened by square ribs of height *k*. The computational domain is of length 2*P*, i.e. it includes 2 ribs. Streamwise periodicity is assumed and cyclic (periodic) boundary conditions are applied at the inlet and outlet planes, which not only reduces the grid size, but also reduces the uncertainty in the results associated with approximate inlet boundary conditions (see Section 4.7.2.2 for more details on periodic boundary conditions as implemented in STAR-CD). In the 1s case the domain is of height *H* (Figure 6.2), whereas for the 2s channel symmetry permits the use of a domain of height *H*/2 (Figure 6.3). The thermal boundary conditions at both the lower and upper walls of the 1s case consist of the same uniform wall heat flux. As noted above, the upper boundary of the 2s domain is a symmetry plane.

The hydraulic diameter (D_e=4×[flow area]/[wetted perimeter]) of the present 2D channels is 0.1m. The rib height to channel hydraulic diameter ratio in the present simulations is k/D_e = 0.05, and the blockage ratio (k/H) is 10% (except for the case where the effects of changing k/H ratio is studied). As in Rau et al. (1998), the Reynolds number based on hydraulic diameter is fixed at Re = 30,000 (except for the case where the effects of Reynolds number is studied). Prandtl number is set to 0.71.

Mesh No.	Design parameters	No. of rough walls	P/k	k/H	b/k	Near-wall treatment	Rib shape	No. of cells
1	1) Turb. models 2) P/k ratio	1	6	0.1	1	LRN	square	133,000
2	1) Turb. models 2) P/k ratio 3) Rib shape 4) Reynolds number	1	9	0.1	1	LRN	square	161,000
3	1) Turb. models 2) P/k ratio 3) Near-wall treatment 4) k/H ratio 5)b/k ratio	2	9	0.1	1	LRN	square	111,000
4	1) Turb. models 2)P/k ratio	1	12	0.1	1	LRN	square	189,000
5	Rib shape	1	9	0.1	1	LRN	MSRP	112,000
6	Near-wall treatment	2	9	0.1	1	HRN	square	6,480
7	k/H ratio	2	9	0.090	1	LRN	square	111,000
8	k/H ratio	2	9	0.075	1	LRN	square	111,000
9	k/H ratio	2	9	0.050	1	LRN	square	103,400
10	b/k ratio	2	9	0.1	1.5	LRN	square	107,000
11	b/k ratio	2	9	0.1	0.5	LRN	square	113,000
12	Mesh type	1	9	0.1	1	Unstructured - LRN	square	147,144

Table 6.3 – The properties of the grids used to test different design parameters.

The results presented in this chapter were generated using structured Cartesian grids (except for the case where the effects of mesh type are tested). Since low-Reynolds-number turbulence models are employed, the grids were generated so as to be very fine near walls (the wall-adjacent cell typically extends only to $y^+ \leq 0.5$, except for the case

where standard wall functions are tested). Table 6.3 lists the features of all the grids used in this chapter, except those used for sensitivity tests which will be discussed separately in Section 6.3.2.2.

6.3 PRELIMINARY RESULTS

6.3.1 Preliminary Remarks

In this section, after presenting results for a 3-dimensional ribbed case (P/k = 9; 2s), grid-independence tests are carried out using 2-dimensional grids with different mesh refinements. The performance of the various turbulence models is then tested by applying them to a smooth channel. Later, the effects of each design parameter on 2D channels are presented.

In the results presented in this section, local Nusselt number is defined as

$$Nu = \frac{\dot{q}\, D_e}{\lambda (T_w - T_b)} \tag{6.1}$$

where $\dot{q}$ is the heat flux, D_e the channel hydraulic diameter, λ the fluid conductivity, and T_w and T_b represent the wall and bulk temperatures, respectively. In the present work, the average Nusselt number, Nu_{av} is defined as the Nusselt number averaged over the first near-wall cell within the gap between the ribs.

Following Rau et al. (1998), all Nusselt number distributions for the ribbed duct calculations are normalized by the value associated with a smooth passage (the Dittus-Boelter equation):

$$Nu_0 = 0.023\, Re^{0.8}\, Pr^{0.4} \tag{6.2}$$

For the continuous design parameters studied in the present work (Section 6.5), the average Nusselt number is compared against the correlations of Ravigururajan and Bergles (1996). These correlations are based on a number of experimental data obtained

for a wide range of roughness and flow parameters. Ravigururajan and Bergles take into account many factors including the ratios of *k/H*, *P/k* and *b/k*, as well as the Reynolds and Prandtl numbers. The Ravigururajan and Bergles correlation for the normalized average Nusselt number is given as

$$Nu / Nu_s = \left\{1 + \left[2.64 (Re)^{0.036} (k / H)^{0.212} (P / H)^{-0.21} (Pr)^{0.024}\right]^7\right\}^{1/7} \tag{6.3}$$

where Nu_s is the smooth-tube heat transfer correlation proposed by Petukhov and Popov (1963):

$$Nu_s = (f / 2) Re\ Pr / \left[1 + 12.7 (f / 2)^{0.5} \left(\mathrm{Pr}^{2/3} - 1\right)\right] \tag{6.4}$$

where f is the friction factor (= 4 c_f). For the sake of simplicity, in the present work this smooth-tube correlation has been replaced by the Dittus-Boelter correlation given in Eqn. (6.2). This is justified on the basis that both the Dittus-Boelter and Petukhov-Popov correlations return satisfactorily close values for the present flow condition (Iaccarino et al. 2002; Yu et al. 2002).

While in a smooth channel the friction coefficient can be directly linked to the shear stress at the wall, this is not true for a ribbed channel. In the present work, the friction coefficient, c_f is defined as

$$c_f = \frac{\Delta p\, D_e}{2 \rho U_b{}^2 L} \tag{6.5}$$

where Δp is the pressure drop over the whole domain, ρ is fluid density, U_b is the bulk velocity, and L is the axial length of the domain. The average friction coefficient, $c_{f\mathrm{av}}$ is obtained from the pressure drop across the whole domain. Thus, the average friction coefficient is the sum of two components: 1) Form drag and 2) Wall drag. In the present rib-roughened channel simulations, the rib form drag is the dominant contribution to the average friction coefficient, $c_{f\mathrm{av}}$.

All friction coefficients are normalized using the value for a smooth tube (the Blasius equation):

$$c_{f0} = 0.079\ Re^{-0.25} \tag{6.6}$$

It is also useful to define the efficiency index, η, in order to represent the overall thermal-hydraulic performance of ribbed channels:

$$\eta = \frac{Nu/Nu_0}{(c_f/c_{f0})^{1/3}} \tag{6.7}$$

Other researchers including Han et al. (1985), Taslim and Wadsworth (1997) and Kim and Kim (2004) have also used this efficiency index to evaluate the overall performance of their test cases. In the present work, the efficiency index is calculated for each continuous design parameter to indicate the optimum configuration for each case.

The pressure coefficient is defined here as

$$C_p = \frac{p - p_{ref}}{0.5\rho U_b^{\,2}} \tag{6.8}$$

where p is the static pressure on the wall and p_{ref} is a reference pressure. Note that C_p in all cases is offset to the experimental value at x/k = 0.5 (the trailing edge of the upstream rib, see Figure 6.1).

6.3.2 Sensitivity Tests

6.3.2.1 Simulation using a 3D mesh (P/k = 9; 2s)

In this section, the validity of the 2-dimensional channel assumption is first assessed and then a grid-independence test for such channels is carried out.

As was noted earlier, in order to evaluate the accuracy of the 2D channel assumption, one needs to carry out a 3-dimensional computation and compare flow

distributions along the centre-line. Based upon the experimental results of Rau et al. (1998), the case of $P/k = 9$; 2s is examined here.

For the 3D simulation, a grid with 1.3 million cells is used (Figure 6.4). Since in '2s' simulations, symmetry is imposed at the top of the domain ($y/H = 0.5$) and at the spanwise mid-duct ($z/H = 0$), only one quarter of the domain needs to be computed. Other boundary conditions used for this simulation are indicated in Figure 6.4. Simulations are carried out using the v^2-f model.

Figure 6.5 shows a contour plot of the streamwise velocity on a plane parallel to the floor of the passage located at $y/k = 0.1$ (or $y/H = 0.01$). In this figure, it is seen that near the side wall ($z/H > 0.45$), there is no clear region of reattachment. In this figure the reattachment line is indicated with a dashed line which, near the symmetry line ($z/H = 0$), is at $x/k \approx 5.2$. The data of Rau et al., however, suggests that the reattachment point in the symmetry plane occurs at $x/k \approx 4$.

A contour plot of the streamwise velocity on a plane parallel to the ribs and between the two ribs ($x/k = 4.5$) is shown in Figure 6.6. From this figure, it is clear how the upstream rib has affected the boundary layer on the bottom wall and its effects are felt up to $y/H \approx 0.18$. This is nearly 18 times greater than the thickness of the boundary layer on the smooth side wall. This figure also shows that the $x/k = 4.5$ plane lies within the separation region. The spanwise flow structure at the same plane is shown in Figure 6.7 (a) and is compared with the LDV data of Liou et al. (1993b) which was obtained for $P/k = 10$; 2s and $Re = 30{,}000$, but at the $x/k = 2$ plane (shown in Figure 6.7 b). The data of Liou et al. shows that one secondary flow cell exists in each quadrant of the channel cross-section and the centre of this secondary flow is towards the side wall ($y/H \approx 0.3$ and $z/H \approx 0.45$). However, the present simulation does not show such a structure, although some 'impinging' on the side wall can be seen close to the channel floor.

Contours of Nu/Nu_0 on the floor ($y/H = 0$) of the 3D channel are shown in Figure 6.8. The region with the highest levels of heat transfer corresponds to the reattachment zone. For higher P/k ratios ($P/k \geq 10$) Rau et al. identified a second region of high heat transfer upstream of the ribs. The maximum value of Nu/Nu_0 at the symmetry line in Figure 6.8 is 3.5, while Rau et al. found the maximum to be $Nu/Nu_0 \approx 3$.

A contour plot of Nu/Nu_0 on the side wall ($z/H = 0.5$) is shown in Figure 6.9 (b). The maximum heat transfer rate occurs upstream of and above the ribs. These high heat transfer zones are related to the deflection of the downward-directed secondary flow motion above the ribs towards the smooth side wall (Rau et al., 1998). It can be seen that there is fairly good agreement between the simulations and the data of Rau et al. (Figure 6.9 a).

The local Nusselt number enhancement factor on the side wall at a distance k upstream from a rib is shown in Figure 6.10. The v^2-f model returns satisfactory results, except for a local minimum between $0.13 < y/H < 0.20$ which corresponds to the region between two high heat transfer zones upstream of the rib (as seen in the detail).

6.3.2.2 Mesh Sensitivity

The results obtained from the 3D case considered above are now compared with four 2D grids (shown in Figure 6.11 to Figure 6.14) for the purposes discussed above. The number of cells and the average Nu/Nu_0 (averaged over the gap between the two ribs) computed for each mesh is listed in Table 6.4. The value of Nu/Nu_0 found by Rau et al. (1998) is also included in this table for comparison. It can be seen that finer meshes return values of Nu/Nu_0 which are closer to that of the 3D channel. However, the 3D channel itself over-predicts the value of Nu/Nu_0 by about 10% compared to the data of Rau et al. (1998).

The question raised earlier concerning the validity of the 2D approximation can now be addressed by comparing various distributions, particularly the heat transfer distribution shown in Figure 6.15. It can be seen that, despite some discrepancies, the average Nu/Nu_0 on the centre of the 3D channel is similar to those of the 2D cases. The largest discrepancy between the 2D and 3D simulations occurs in the region upstream of a rib ($5 < x/k < 8$), but even there the maximum discrepancy does not exceed 10%. Similar trends were reported by Bredberg (2002) who compared 3D and 2D simulations for a $P/k = 9;1s$ configuration.

Mesh type	No. of cells	Average Nu/Nu_0	Difference %
3D – P/k=9; 2s	1,324,000	2.73	–
2D – P/k=9; 2s – Fine	444,000	2.69	– 1.5
2D – P/k=9; 2s – Medium	111,000	2.69	– 1.5
2D – P/k=9; 2s – Coarse	29,500	2.63	– 3.7
2D – P/k=9; 2s – Very Coarse	9,080	2.60	– 4.8
Data of Rau et al. (1998)	–	2.48	– 9.2

Table 6.4 – Comparison of grids used in the sensitivity tests and the corresponding values of Nu/Nu_0.

Results obtained using four different 2D grids with different mesh refinements are also included as a grid-independency test. As can be seen, refining the mesh has only a marginal effect on the results. The medium mesh with 111,000 cells was consequently considered to be fine enough for the computations in the present work.

The discrepancy between the 2D and 3D cases is even smaller for the velocity distributions shown in Figure 6.16 and Figure 6.17. The maximum differences are found in the region $1 < x/k < 3$ for the streamwise velocity and over $2 < x/k < 4$ for the wall-normal velocity distribution. However, the discrepancy for the friction coefficient is somewhat larger, especially in the recirculating region which is again due to secondary flow effects present in the 3D case (Figure 6.18).

It is worth noting that there is perhaps another reason for obtaining somewhat different results for 2D and 3D case. This is due to an unavoidable discrepancy between the 3D square cross-sectioned experimental channel and the present 2D simulations, namely that the equivalent diameter of the square channel is equal to H, whereas $D_e = 2H$ in the 2D case. In order to overcome this difficulty, at least partially, the bulk velocity is set to one-half of the experimental value (and hence the Reynolds numbers based on equivalent diameter are equal). The rib height, k is maintained at the experimental value and therefore the blockage ratio, k/H, rather than k/D_e, is matched. There remains, however, a lack of geometric similarity, this being due to the differing ratios of ribbed-to-smooth surfaces in the experimental and computational cases (1:3 vs. 1:1 in the 1s case; 1:1 vs. 1:0 for the 2s channel).

In the light of above findings, it was concluded that the 2D representation of the 3D channel is adequate for carrying out parametric studies and therefore all the results presented in the remainder of this chapter were obtained using 2D grids.

6.3.2.3 Thermal Boundary Conditions on the Ribs

In this section, two alternative thermal boundary conditions on the ribs are compared. This test provides some assessment of the uncertainties present in the experimental conditions. These uncertainties are usually associated with the measurement techniques, the rib and channel wall material properties, and the presence of unsteady effects (Iaccarino et al., 2002).

In the first case, the thermal boundary condition on both the ribs and the bottom wall is one of the same uniform wall heat flux, Figure 6.19 (a). In the second case, the ribs are insulated (adiabatic walls), shown in Figure 6.19 (b).

The v^2-f model was used to carry out the simulations to compare the effects of these two thermal boundary conditions. It was found that the thermal field was slightly

affected especially, in regions near the ribs. Nu/Nu_0 distributions for both cases are shown in Figure 6.20. While both cases have similar heat transfer patterns, it is evident that the case with insulated ribs has higher levels of heat transfer. It can also be seen that for the case with heated ribs, the heat transfer levels immediately downstream and upstream of the ribs are much lower than those of the insulated rib. Similar results were reported by Iaccarino et al. (2002).

The reason that different heat transfer levels are obtained in the vicinity of the ribs can be better understood by comparing the temperature contours of both cases, see Figure 6.21. When the rib is heated (Figure 6.21 a), the maximum temperatures occur in the corners upstream and downstream of the ribs. However, when the ribs are insulated the high temperature zones near the ribs become much smaller giving larger temperature gradients which leads to higher heat transfer levels.

From the above findings, it can be concluded that the thermal boundary conditions on the ribs affect heat transfer levels only in the regions near the ribs, while naturally for a forced convection flow the dynamic field is not affected by the thermal boundary condition.

6.3.2.4 Smooth Channel

In this section, the *k-ε*, *k-ω-SST* and v^2*-f* models are applied to a smooth 2D channel with 30,000 cells at Re = 30,000. The friction coefficient obtained using each model is compared with that found from the Blasius equation:

$$c_f = 0.079 Re^{-0.25} \tag{6.9}$$

Table 6.5 shows that compared to the value found from the Blasius equation, the v^2*-f* model returns the most accurate prediction.

Model	c_f	Discrepancy %
Blasius Equation	6.00×10^{-3}	–
k-ε model	5.78×10^{-3}	– 3.8
k-ω-SST model	5.86×10^{-3}	– 2.4
v^2-f model	6.11×10^{-3}	+ 1.8

Table 6.5 – The value friction coefficient for a smooth channel using different turbulence models.

6.4 RESULTS FOR DISCRETE EFFECTS

6.4.1 Effects of Turbulence Models

Four turbulence models of the eddy viscosity class are examined in the present study. These are the low-Reynolds-number *k-ε* model of Lien, Chen and Leschziner (1996) ('*k-ε* model'), the non-linear *k-ε* model of Suga (1995; Craft, Launder and Suga, 1996b) ('Suga model'), the *k-ω-SST* model of Menter (1994) ('*k-ω-SST* model'), and a variant of Durbin's v^2-*f* model due to Iaccarino (2001) ('v^2-*f* model'). While all four closures eventually trace their roots to the 'standard', or 'parent', EVM of Launder and Spalding (1974), they embody quite distinct modifications to that scheme. The models do, however, share common features in that they are of the 'low-Reynolds-number' type (in common with the widely-adopted extension of the Launder-Spalding scheme proposed by Launder and Sharma, 1974). With the exception of the Suga model, all the models tested here use a linear stress-strain relationship. In low-Reynolds number formulations the systems of governing equations are integrated over the entire flow domain, there being no need to employ wall functions in wall-adjacent regions (the effects of using Standard Wall Functions however, will be discussed in Section 6.4.3). Full details of all these turbulence models can be found in Chapter 3 and in the STAR-CD manual (CD-Adapco, 2006). The models as coded into STAR-CD conform to the original published versions (di Mare, 2008).

In Chapter 5 two of the turbulence models in STAR-CD, namely the *k-ω-SST* and Suga models were validated against the models as implemented in in-house and industrial codes (CONVERT and Code_Saturne) – see also Keshmiri et al., 2008a; 2008b.

Figure 6.22 compares the heat transfer results of the *k-ε*, *k-ω-SST*, v^2*-f* and Suga models against the experimental data of Rau et al. (1998) for the 1s channel with P/k = 9 (mesh number 2). The *k-ε* model clearly returns levels of heat transfer that are far too high. Such a result might be anticipated from the findings of Bredberg et al. (2000) and Iacovides and Raisee (2001): the length scale correction which Iacovides and Raisee (2001) employed in combination with a low-Reynolds-number *k-ε* model acts to increase ε and thus reduce ν_t (however *Nu* was still over-predicted by the maximum of 50%, which is a smaller margin than that seen here). From Figure 6.23 it is clear that the *k-ε* model also predicts the shortest reattachment length (similar findings have also been found for a backward-facing step - see Momeni, 2008, for example). This could provide another reason for the model returning such high heat transfer levels. It is noted that Iaccarino et al. (2002) applied the Launder-Sharma *k-ε* model to a rib-roughened channel (with $10 \leq P/k \leq 30$ and $0.1 \leq k/H \leq 0.3$) and found approximately 15-20% over-prediction of heat transfer levels compared to the results of the v^2*-f* model.

In Figure 6.22 it is seen that the results of the *k-ω-SST* model is closer to the data compared to those of the *k-ε* and Suga models, but it is the v^2*-f* formulation that is in the closest, although still not excellent, accord with the measurements.

Using a v^2*-f* formulation that differs only slightly from the present form, Ooi et al. (2002) also made comparison with the data of Rau et al. (1998). The 3D computations of Ooi et al. for P/k = 9; 1s returned a Nusselt number distribution on the line of symmetry of the channel floor that was slightly *lower* than the data (although the average Nu/Nu_0 was around 20% lower than the data). The discrepancy between the

findings of Ooi et al. and Figure 6.22 perhaps gives some measure of the errors incurred by the present adoption of a 2D computational framework.

Furthermore, in Figure 6.22 unlike the other turbulence models, the Suga model shows two maxima at $x/k \approx 2.5$ and 6 and under-predicts the heat transfer levels. This can be explained by looking at streamlines shown in Figure 6.23. It is seen that streamline pattern predicted by the Suga model is somewhat deflected towards above the rib which in turn results in predicting a 'taller' recirculation bubble (extending up to $y/H \approx 0.15$) making it more difficult for the flow to be renewed within the inter-rib gap. Again somewhat similar streamlines were found by Raisee et al. (2004) using the Suga model, but there with the modified Yap term included in the ε-equation. The overall performance of the Suga model with two different versions of the Yap term (Raisee et al., 2004) was much better than the present results.

In the present work the Suga model has shown to have numerical stability problems both in the rib-roughened channels and mixed convection flows in vertical pipes. As was discussed in Chapter 5, Raisee (1999) showed that severe problems of numerical stability were encountered when applying the Suga model to a rib-roughened channel. Raisee traced these stability problems to the form of the dependence of C_μ on the strain rate, which, in flows over sharp corners, led to very abrupt changes in turbulent viscosity. Raisee overcame these stability problems by smoothing the variation of C_μ.

In general, the turbulence length scale plays a critical role in the computation of separated flows. It was remarked in Chapter 2 that the use of a high-Reynolds-number k-ε model coupled with wall functions (Acharya et al., 1993) gave rise to an *under*-prediction of heat transfer levels. The same result was found when a k-ε model was blended with a near-wall k-l form (l being a prescribed length scale; Iacovides, 1998 and Ooi et al., 2002). In fact, there are two related mechanisms at work – one alluded to already that concerns the diffusivity of the thermal field, and the other is an 'indirect'

effect related to the mean dynamic field and hence the advective terms of the Energy Equation:

$$U_j \frac{\partial T}{\partial x_j} = \frac{\partial}{\partial x_j}\left[\left(\frac{\nu}{Pr} + \frac{\nu_t}{\sigma_t}\right)\frac{\partial T}{\partial x_j}\right] \tag{6.10}$$

This point is expanded below in connection with Figure 6.25.

Streamlines obtained by all four turbulence models are shown in Figure 6.23. The *k-ε* and *k-ω-SST* models return the smallest and largest separation bubbles, respectively. The latter is due to a turbulent viscosity limiter (Eqn. (3.75)) that exists in the *k-ω-SST* model which limits the shear stress when the production of *k* exceeds its dissipation rate (by about an order of magnitude, for example). This limiter tends to eliminate the unrealistic build-up of eddy viscosity in the stagnation regions (Menter, 1994; Kral, 1998). Furthermore, in Figure 6.23 it is seen that the Suga model returns the largest counter-rotating separation bubble near the upstream face of the rib compared to the other models.

Figure 6.24 shows the normalized streamwise velocity distributions for *P/k* = 9; 1s at one-tenth of the rib height. The recirculation region and reattachment point are evident in the data and the v^2-*f*, Suga and *k-ε* model results, while the *k-ω-SST* model indicates that the flow remains reversed at this elevation. The *k-ω-SST* model therefore fails to predict flow renewal in the inter-rib cavity and consequently its relatively good agreement with the heat transfer data of Figure 6.22 must be viewed as being largely fortuitous. The reattachment point predicted by the Suga model is the closest to that found by Rau et al. (1998).

Results for the wall-normal velocity at rib height are presented in Figure 6.25. The v^2-*f* model is in reasonably good agreement with the data as, to a somewhat lesser degree, is the baseline *k-ε* formulation. The *k-ω-SST* model generally under-predicts the magnitude of the wall-directed velocity. The Suga model has the worst predictions in

this figure mainly due to the size of its predicted separation region which was shown in Figure 6.23. Comparing Figure 6.25 and Figure 6.22, it is seen that there is a direct correspondence between the magnitude of the downward-going velocity in the recirculation region and the level of heat transfer. This raises the question of the importance of advection in determining the thermal characteristics of recirculating flows, i.e. in a mathematical sense there is now a focus on the left hand side of Eqn. (6.10). First, it is remarked that identical mean flow equations are employed in conjunction with the four turbulence models considered here, and that the only input of a turbulence model to Momentum and Energy equations is the turbulent viscosity, v_t. The discussion above has identified the importance of the turbulence length scale as a determinant of model performance. It is clear though that the length scale exerts an influence on the thermal field via its role in the *dynamic* field (the right hand side of the Momentum equation). Thus, in relation to the Energy Equation, length scale effects are manifest indirectly via the advective terms and directly via turbulence diffusion.

Figure 6.26 shows the distribution of the normalized friction coefficient, c_f/c_{f0}. This essentially shows how wall shear stress varies along the gap between the ribs, since:

$$c_f = \frac{\tau_w}{0.5\rho U_b^{\,2}} \tag{6.11}$$

where the wall shear stress is calculated as

$$\tau_w = \mu\left(\frac{\partial U}{\partial y}\right)_{y=0} \tag{6.12}$$

where the velocity gradient is evaluated at the near-wall cell. Therefore, the distribution of the friction coefficient is naturally very similar to the streamwise velocity distribution shown in Figure 6.24.

Normalized streamwise velocity profiles at two wall-normal planes, namely over the rib-top (x/k = 0) and in the separation region (x/k = 4) are shown in Figure 6.27 and

Figure 6.28, respectively. The prediction of the k-ε model over the rib-top is the closest to the data, while the k-ω-*SST* and v^2-f models both over-predict the magnitude of the velocity. Once again, the Suga model returns an unstable distribution.

At $x/k = 4$, Figure 6.28 shows that both the k-ω-*SST* and v^2-f models yield longer separation bubble compared to the data (similar to the findings from Figure 6.23), while in contrast, the k-ε and Suga models predict shorter reattachment lengths than that found by Rau et al. (1998). Further away from the wall ($y/H > 0.2$), except for the k-ε model, the velocity magnitude returned by the turbulence models are in relatively good agreement with the data.

Attention is turned next to the inter-rib pressure distribution. Impingement on the upstream face of the rib leads to high static pressure, while there is a low pressure zone downstream of the rib. These effects can be seen in Figure 6.29, where the pressure coefficient distributions between the two ribs are plotted against x/k. This figure shows that the k-ε model overestimates C_p, whereas the k-ω-*SST* model returns values that are too low. Within the recirculation zone, at least, the v^2-f model is in good agreement with the data. The Suga model returns nearly a constant value for C_p downstream of the reattachment point which can be explained by comparing these results with the streamlines shown in Figure 6.23, where the Suga model predicted only a very small recirculation bubble upstream of the second rib. It is worth noting that in Figure 6.29 the data of Rau et al. does not extend all the way to the upstream face of the second rib, but if one assumes a linear extrapolation (since all simulations show a quasi-linear distributions) then the predicted pressure drop by the v^2-f model would appear very close to the data.

Contours of the streamwise velocity of all four turbulence models are shown in Figure 6.30. It can be seen that ribs affect the flow field only up to $y/H \approx 0.4$. Beyond that ($y/H \geq 0.4$), all the models return very similar results, except for the top wall, where

the Suga model predicts a boundary layer with the largest thickness. On the rough wall, each model returns a different recirculation region/length, as was also evident in Figure 6.23.

Pressure contours are shown in Figure 6.31. The pressure difference between forward and backward faces of the ribs gives a measure of the 'form drag' which is a large contribution to the total head loss (a key parameter in fuel pin designs). As can be seen from Figure 6.31 and Figure 6.29 the models exhibit very large differences, much larger than on velocity profiles (Figure 6.27 and Figure 6.28). This is due to the fact the in the present work, constant mass flow rate was imposed at inlet/outlet boundaries rather than a pressure drop.

Contours of the normalized turbulent kinetic energy are shown in Figure 6.32. The k-ε and Suga models respectively, return the highest and lowest levels of turbulent kinetic energy. Generally, all the models predict that the maximum level of turbulent kinetic energy occurs around upstream and above the rib. Again a dramatic difference can be seen between the performances of the various models. It is worth noting that overall turbulent kinetic energy levels are in the same order as pressure drop; energy coming from the mean flow is an average pressure drop times (constant) mass flow rate which feeds into the turbulent kinetic energy and in turn is transferred into heat via the dissipation of turbulent kinetic energy.

The results for k-ε, k-ω-*SST*, and v^2-f models for the 2s channel with P/k = 9 (i.e. P/k = 9; 2s) are discussed next.

Local Nusselt number distributions are shown in Figure 6.33. The findings are similar to those of Figure 6.22 where it can be seen that, again the v^2-f model is in quite close agreement with the data, and the k-ε and k-ω-*SST* models over-predict and under-predict the results, respectively.

Streamwise velocity distributions shown in Figure 6.34 indicate that now none of the models are in good agreement with the data. The v^2-f and k-ω-SST models significantly under-predict the magnitude of the positive velocity especially for $x/k > 4$, the reason being the over-prediction of the recirculation length by these two models (Figure 6.23).

Wall-normal velocity distributions shown in Figure 6.35 indicate that compared to the data, all three models generally under-predict the magnitude of the normal velocity over a wide length within the inter-rib cavity, therefore, none of the models can be said to be in very good agreement with the data.

It is worth noting that, in all the results presented in this chapter, the turbulent Prandtl number was set to a constant value, $\sigma_t = 0.9$. According to Bredberg et al. (2002), a decrease of the turbulent Prandtl number to $\sigma_t = 0.8$ results in a general increase in the Nusselt number by 5%. Bredberg et al. also tested a more advanced definition for σ_t by using an algebraic relation proposed by Kays and Crawford (1993) but the predicted heat transfer levels were only marginally different from the case of $\sigma_t = 0.9$. Thus, the value of σ_t was kept unchanged throughout this chapter.

6.4.2 Effects of Rib Profile

In the previous sections, all the computations were carried out for ribs with a square cross-section (profile). However, in an earlier design of Advanced Gas-cooled Reactors (AGRs), fuel pins had a different rib profile. The rib profile of the latter design is known as the 'Transverse Rib Profile' (TRP). Later, this initial design was replaced by a new and more efficient design, called the 'Multi-Start' rib design (Figure 6.36). The description of these two designs will be discussed further in conjunction with the 3D AGR fuel elements in Chapter 7. In Table 6.6 below, real dimensions of the Transverse

and Multi-Start designs are compared with the dimensions of the 'Square Rib Profile' design adopted by Rau et al. (1998).

Properties	Square Rib Profile	Transverse Rib Profile	Multi-Start Rib Profile
Reference	Rau et al. (1998)	Gotts (2008)	Gotts (2008)
Rib height (k)	5	0.3	0.457
Rib width (w)	5	0.3	0.22
Rib base (b)	5	0.706	0.44
Radius of the lower corner (R_1)	–	0.203	0.051
Radius of the upper corner (R_2)	–	0.025	0.025
Pitch (P)	30, 45 and 60	2.16	2.98
Pitch-to-rib height ratio (P/k)	6, 9 and 12	7.0	5.5 – 6.5*

* The exact value depending upon whether pitch is measured normal to the ribs or in the axial direction.

Table 6.6 – Real dimensions of Square, Transverse and Multi-start rib profile designs (all dimensions are in mm).

Properties	Square Rib Profile	Multi-Start Rib Profile
Reference	Rau et al. (1998)	Gotts (2008)
Rib height (k)	5	5
Rib width (w)	5	2.4
Rib base (b)	5	4.81
Radius of the lower corner (R_1)	–	0.558
Radius of the upper corner (R_2)	–	0.274
Pitch (P)	45	45
Pitch-to-rib height ratio (P/k)	9	9

Table 6.7 – Transformed dimensions of Square and Multi-start rib profile designs in the present work (all dimensions are in mm).

In this section, the effects of changing the rib profile are examined by comparing the 'Square Rib Profile' (SRP) to the 'Multi-Start Rib Profile' (MSRP). Clearly, these two rib profiles have different dimensions and since the data of Rau et al. is for the

square rib profiles, the dimensions of the MSRP is transformed so that rib heights are matched in both cases i.e. k = 5 mm (Table 6.7 above).

The grids used for the computations of the SRP and MSRP cases are shown in Figure 6.37 and Figure 6.38, respectively. The mesh used for the SRP case is the same as that used in the simulations of Section 6.4.1 (mesh number 2 in Table 6.3), while for the MSRP case, a structured grid with 112,000 cells is used (mesh number 5 in Table 6.3).

The v^2-f and k-ω-*SST* models were used to generate results in this section. In Figure 6.39 it can be seen that both models suggest that there is little effect on the Nusselt number distribution in-between the two ribs, and indeed it was noted in Chapter 2 that Han et al. (1978) found that changes to the rib cross-section had only a very limited effect on heat transfer levels. In fact Han et al. showed that the influence of the rib profile on heat transfer completely disappeared for the range Re = 10,000 – 30,000, where the flow was in a completely rough region. In addition, the experiments of Liou and Hwang (1993) on three different rib profiles, namely triangular, semi-circular and square revealed that these profiles have comparable thermal performances, while the square ribs had the highest average friction factor.

Figure 6.40 and Figure 6.41 compare normalized streamwise and wall-normal velocity distributions, and again it is seen that both models return similar results for the SRP and MSRP cases. In Figure 6.40 the maximum difference between the two cases occurs in the recirculation regions, where both models return slightly higher streamwise velocity magnitude for the MSRP design.

Figure 6.42 shows larger differences in the results of the friction coefficient distributions of both cases, with the MSRP having slightly higher friction levels. Although these results seem to be in contrast with the experimental data of Liou and Hwang (1993) (where the triangular ribs had less friction compared to the square ribs),

one has to note that in the experiment, the triangular rib had a wider width than the square one, while in the present work the MSRP case has a smaller width than the SRP; the width of the SRP design is 5mm whereas the MSRP design has an average width of 3.6 mm – see Table 6.7. This width difference could also be one of the reasons for obtaining slightly different heat transfer levels in Figure 6.39. This point will be expanded later in connection with the effects of rib width, in Section 6.5.3.

Velocity profiles at two wall-normal planes shown in Figure 6.43 and Figure 6.44, indicate that both models return nearly identical results for both SRP and MSRP cases. The results in Figure 6.43 are in good agreement with the data as, to a somewhat lesser degree, is the velocity profile in Figure 6.44, although the recirculation length is severely over-predicted by both models.

In Figure 6.45, while the v^2-f model returns very similar results for both SRP and MSRP cases, the k-ω-*SST* model returns slightly higher C_p for the MSRP case near the upstream face of the rib.

Figure 6.46 and Figure 6.47 show broadly similar streamlines for both rib profiles, although the recirculation length of the SRP case is slightly larger than that of the MSRP case. In addition, the counter-rotating separation bubbles at the corners are slightly larger for the SRP, clearly due to its sharper corners. Larger separation bubbles are predicted by the k-ω-*SST* model in comparison to the v^2-f model (consistent with the findings from Figure 6.23).

In Figure 6.48 to Figure 6.50 contours of the streamwise velocity, relative pressure, and turbulent kinetic energy for both SRP and MSRP cases, generally show similar results. The pressure levels in Figure 6.49, however, suggest higher pressure levels upstream of the ribs for the SRP case, again due to its sharper edges which consequently have resulted in higher stagnation pressures. Contours in Figure 6.50 indicate slightly higher levels of turbulent kinetic energy for the MSRP case between $0.05 < y/H < 0.2$; it

is not clear why this should be, however, it is consistent with the fact that MSRP yields higher Nu/Nu_0 levels (Figure 6.39), in spite of velocity profile shapes being hardly affected (Figure 6.40 and Figure 6.41).

6.4.3 Effects of Near-Wall Treatment

All the results presented so far (including the results of Chapter 5), were obtained using Low-Reynolds Number (LRN) turbulence models which resolve the equations all the way down to the wall. These turbulence models, therefore, require a fine near wall mesh in order to resolve the large gradients of the turbulent flow properties i.e. the first cell should usually satisfy $y^+ < 1$. Despite advances in computing power, this near-wall resolution requirement makes LRN models expensive in complex three-dimensional flow problems. Another disadvantage associated with the LRN models (with a notable exception of the v^2-f model) is that they make use of various damping functions. These damping functions are still empirical and thus, only mimic the turbulence reduction in the near-wall regions rather than taking the actual source into account (see Section 3.5.2.1 for more detail). Therefore, industrial CFD practitioners still tend to make use of classical wall function approaches, despite successful performance of LRN models. However, not so many researchers focused on development of wall functions over the last few decades after the establishment of the Standard Wall Function (SWF). As was discussed in Section 3.5.3.2 the SWF approach (Launder and Spalding, 1972) is based on the log-law and it is well-known that such a condition does not apply in flows with strong pressure gradients and separation such as the rib-roughened channel in the present work.

To further this point, velocity profiles at a number of monitoring planes on, and between, two ribs are shown in Figure 6.51. Here $P/k = 9$; 1s (mesh number 2 in Table 6.3) and the v^2-f model is employed. The recirculation region (Planes 2-5) may be

identified and the profiles in the recovery region (Planes 6-8) are characteristic of a laminar, rather than a turbulent boundary layer.

An alternative presentation of the velocity profiles is given in Figure 6.52 which shows $U^+ = U/U_\tau$ vs. $y^+ = yU_\tau/\nu$ plotted on semi-logarithmic axes. (The local friction velocity is defined as $U_\tau = \sqrt{|\tau_w|/\rho}$.) As would be expected, the flow is highly 'non-universal' within the separation bubble (for comparison, the inset to Figure 6.52 shows the conventional 'law of the wall'). It is now seen more clearly that the recovery region takes the form of a developing laminar boundary layer (here large U^+ is associated primarily with low values of U_τ).

From these figures, it is apparent that the rib-roughened surface is a challenging case for conventional wall functions. In the past, a few attempts have been made in applying high-Reynolds number turbulence models with wall functions to rib-roughened surfaces and it was found that wall functions are generally inadequate for thermal predictions of ribbed duct flows, this being due to predicting inaccurate near-wall turbulence field which is necessary for predicting heat transfer levels (Acharya et al., 1993; Liou et al., 1993a; Prakash and Zerkle, 1995).

Case	A	B	C	D [m]	y_0 [m]
1	8.5	0	1	0	0.005
2	8.5	0	1	0.0025	0.0025

Table 6.8 – The value of the constants used in the calculations of the SWF.

In this section, the performance of the HRN k-ε model with the SWF implemented in STAR-CD is tested against the results of the LRN k-ε model for the case of P/k = 9; 2s. The SWF in STAR-CD has a distinctive formulation for the semi- and fully-rough surfaces, the description of which is given in Section 4.7.2.4. Two sets of constants, as shown in Table 6.8 were used here (see Figure 4.5) and since no significant difference

was identified between the results, only the results of Case 1 are presented in this section.

Schematic of the mesh used for the HRN calculations (mesh number 6 in Table 6.3) is shown in Figure 6.53. The mesh used for the LRN calculation in this section is the Medium mesh used in the 'sensitivity test' section (Section 6.3.2.2 – see Figure 6.13).

Heat transfer levels are shown in Figure 6.54. This figure shows that although both near-wall treatment techniques return similar shapes for the Nu/Nu_0 distribution, the HRN model under-predicts the average Nu/Nu_0 by about 15% compared to the LRN k-ε model. Compared to the data of Rau et al. (1998), however, both models over-predict the heat transfer levels. Note that as was shown in Figure 6.22, the LRN k-ε model available in STAR-CD greatly over-predicts the heat transfer levels, mainly due to under-predicting the recirculation length and over-predicting the turbulence levels.

Streamlines for both near-wall treatments are shown in Figure 6.55. This figure clearly shows that the recirculation bubble within the inter-rib cavity is not predicted correctly by the HRN k-ε model. This model also fails to predict any recirculation bubble near the upstream face of the second rib. It should be noted, however, that since there are only two cells across the height of the rib in the HRN mesh, the streamline representation of the flow may not provide a very correct picture of the mean field. The streamwise velocity distributions in Figure 6.56 give a better image of the separation region. In the figure it is apparent that the HRN k-ε model predicts a very small recirculation bubble and reattachment length. Consequently, the magnitude of the positive velocity is over-predicted throughout the inter-rib region.

The magnitude of the wall-normal velocity at the y/k = 1 plane, shown in Figure 6.57 is also greatly over-predicted by the HRN k-ε model, while the predictions of the LRN k-ε model is in good agreement with the data.

As shown in Figure 6.58, for the pressure coefficient distributions, the HRN k-ε model returns levels that are too low compared to the results of the LRN model. As was mentioned earlier, the value of C_p in all cases is offset to the experimental value at x/k = 0.5 (the trailing edge of the upstream rib). However, as shown as an inset to Figure 6.58, if the pressure coefficient distribution of the HRN k-ε model is offset to the value obtained by the LRN k-ε model at x/k = 4.5 (middle of the inter-rib cavity), the differences between the results of the two models are much smaller; the largest discrepancies occur near the ribs.

Contours of the streamwise velocity, relative pressure, and turbulent kinetic energy are shown in Figure 6.59 to Figure 6.61. The recirculation bubble within the inter-rib cavity of both cases is evident in Figure 6.59, where it is seen that the HRN k-ε model fails to predict a realistic separation region. In Figure 6.60, the HRN k-ε model generally under-predicts the pressure levels compared to the LRN k-ε model. Similar under-predictions can also be seen for the turbulent kinetic energy in Figure 6.61.

From the results presented in this section, it is clear that the HRN k-ε model with the SWF fails to return satisfactory results. From economical point of view, however, the HRN k-ε model computations were faster by 1 to 2 orders of magnitude. This is clearly a very attractive feature especially for industrial applications and therefore, the development of more efficient and advanced wall functions is still very desirable.

6.4.4 Effects of Mesh Type

In general, there are two main classes of grids, which differ in the way in which the mesh points are connected to each other. If the internal points are connected to their neighbours in a way independent of their position, the mesh is called ‘structured’. When the pattern of the connections varies from point to point, the mesh is called ‘unstructured’. In the structured case, the connectivity of the grid is implicitly taken into

account by storing the point data into the elements of a matrix. On the contrary, the connectivity of unstructured grids must be explicitly described by an appropriate data structure, thus making the solution algorithms on unstructured grids more expensive than those on structured grids (Rebay, 1993).

All the results presented so far, have been generated using structured grids. However, complex geometries such as 3-dimensional AGR fuel elements (to be presented in Chapter 7) require greater geometrical flexibility which is only offered by unstructured grids. Therefore, the aim of this section is to compare the results of a structured and an unstructured grid for the same flow problem.

Mesh number 2 (which was shown in Figure 6.37) is chosen as a structured grid. As for the unstructured grid, mesh number 12 in Table 6.3 (shown in Figure 6.62) is used which is a hybrid mesh composed of 5 layers of prismatic elements near the wall and polyhedral elements for the rest of the domain. The wall-adjacent cell typically extends only to $y^+ \leq 0.5$. For both grids, the convergence criterion is set to 10^{-6}. Computations are undertaken using the v^2-f model and the same numerical inputs are used for both grids.

Heat transfer levels obtained from both grids are compared in Figure 6.63, where relatively large discrepancies are evident in the results. The maximum discrepancies of about 30% occur in the middle of the inter-rib cavity. This is in spite of both grids having similar values of y^+ for the wall-adjacent cell.

Normalized streamwise velocity distributions at $y/k = 0.1$ are shown in Figure 6.64. While the general trend is similar for both grids, magnitude of the positive velocity returned by the unstructured mesh is slightly lower than that obtained by the structured mesh for $x/k > 3.5$. However, wall-normal velocity distributions at $y/k = 1$, shown in Figure 6.65 are quite similar for both grids, with very small differences within the recirculation region.

From friction coefficient distributions in Figure 6.66, it is evident that the results of the unstructured mesh indicate that the flow remains reversed in the near-wall cell within the entire inter-rib cavity. The value of the friction coefficient in the recirculation region obtained by the unstructured mesh is also lower than that found by the structured mesh. These differences in the near-wall cell could be a source of discrepancies which were evident in the heat transfer levels in Figure 6.63.

Pressure coefficient distributions shown in Figure 6.67 indicate that the unstructured mesh returns lower pressure levels compared to the structured mesh. However, as shown as an inset to Figure 6.67, by offsetting the results of the unstructured mesh to the value obtained by the structured mesh at x/k = 4.5, the agreement between the results improves.

Contours of the streamwise velocity and relative pressure obtained by both grids are shown in Figure 6.68 and Figure 6.69, respectively. It is seen that the results produced by both grids are very similar. However, as shown in Figure 6.70, large discrepancies are evident in the contours of the turbulent kinetic energy, with the structured mesh returning much higher turbulence levels compared to the unstructured mesh, especially near the ribs.

As a final comparison, the mesh density and velocity vector representation of a small section near the downstream face of the first rib for the structured and unstructured meshes are shown in Figure 6.71 and Figure 6.72, respectively. It can be seen that the unstructured mesh is not as good as the structured mesh in capturing the very sharp velocity gradients in this region, despite having very similar values of y^+ in the near-wall cells.

In the light of above findings, it seems that further work would be required in order to investigate the reasons for obtaining different results with structured and unstructured grids in this part of the study.

6.5 RESULTS FOR CONTINUOUS EFFECTS

6.5.1 Effects of Pitch-to-Rib Height Ratio (P/k)

In this section the effects of varying the rib pitch-to-height ratio (*P/k*) is investigated. The results presented here are for 1s channels and three *P/k* ratios of 6, 9, and 12 (mesh numbers 1, 2 and 4 – see Table 6.3) and comparison is made against the experimental data of Rau et al. (1998). Computations are undertaken using the *k-ω-SST* and v^2-*f* models. (For comparison, the helical ribs of AGR fuel pins have a pitch-to-height ratio $P/k \approx 5.5 - 6.5$, the exact value depending upon whether pitch is measured normal to the ribs or in the axial direction; Fairbairn, 2009.)

***k-ω-SST* model**

Figure 6.73 compares heat transfer levels for various *P/k* ratios using the *k-ω-SST* model. The results in this figure indicate that the model broadly under-predicts the heat transfer levels, except for $P/k = 6$, where the model returns the most accurate results. In general, in Figure 6.73 the largest discrepancies between the predictions and the data are near ribs. This is due to the *k-ω-SST* model predicting relatively large counter-rotating vortices near rib corners (Figure 6.74), except for $P/k = 6$, where only one vortex is evident downstream of the first rib. The reattachment length returned by the *k-ω-SST* model is also not in agreement with the data; another reason for under-predicting the heat transfer levels.

Figure 6.75 shows the streamwise velocity distributions at $y/k = 0.1$. Large discrepancies are evident especially for $P/k = 9$ where the *k-ω-SST* model indicates that the flow remains reversed in the entire inter-rib cavity which is in contrast with the data of Rau et al. (1998). For $P/k = 12$, the recirculation length is over-predicted by about 50% compared to the data. This in turn results in an under-prediction of the velocity magnitude in the recovery region. As was discussed in Section 6.4.1, this over-

prediction of the separation bubble and reattachment length is due to a turbulent viscosity limiter that exists in the *k-ω-SST* model.

In Figure 6.76 it is evident that except for P/k = 12, the wall-normal velocity distributions at y/k =1 are in relatively good agreement with the data. In addition, Rau et al. (1998) noted that the maximum wall-normal velocity was slightly higher for P/k = 9 compared to 6 and 12, while the *k-ω-SST* model indicates that by increasing the P/k ratio, the maximum wall-normal velocity increases too, as shown in the inset to Figure 6.76.

The friction coefficient distributions shown in Figure 6.77 have similar trends to the streamwise velocity distributions in Figure 6.75. It can be seen that within the primary recirculation region, c_f/c_{f0} is negative and there are two negative peaks within the inter-rib cavity for P/k = 9 and 12. For P/k = 6 the peaks are more difficult to distinguish. According to the DNS data of Leonardi et al. (2003), one negative peak exists for $P/k \leq 4$ and two for $P/k \geq 7$. In addition, from Figure 6.77 it can be seen that by increasing P/k ratio, the intensity of the recirculation zone increases which increases the magnitude of c_f/c_{f0} in this region i.e. the size of the first negative peak increases.

v^2-f model

Figure 6.78 compares heat transfer levels for various P/k ratios using the v^2-f model. In general, it is seen that the model tends to overestimate levels of heat transfer. The v^2-f model returns the least accurate results for P/k = 6, where it over-predicts the maximum heat transfer level by approximately 50%. The most accurate results are for P/k = 9.

Streamlines for all three P/k ratios are shown in Figure 6.79. This figure indicates that there is no reattachment point for P/k = 6, a result that is in agreement with the data (Figure 6.80 below). The recirculation lengths for P/k = 9 and 12, are nearly the same; however, the model over-predicts the measurements of Rau et al. (1998).

Figure 6.80 shows normalized streamwise velocity distributions at $y/k = 0.1$. The v^2-f model clearly underestimates the velocity magnitude in the separation region before the downstream rib. Consistent with Figure 6.79, there is no reattachment of the flow for $P/k = 6$. From Figure 6.80, it is also clear that the magnitude of the streamwise velocity increases for higher P/k ratios as there is a longer recovery region where the flow can accelerate. This in turn results in higher impingement force on the front face of the downstream rib.

Results for the wall-normal velocity at rib-height are presented in Figure 6.81. The results of the v^2-f model are in close agreement with the data except for $P/k = 12$, where the model under-predicts the magnitude of the downward normal velocity in the recovery region. Ooi et al. (2002) also found similar results for $P/k = 12$ and argued that this under-prediction of the downward velocity leads to an under-prediction of the impingement strength which in turn results in under-predicting the heat transfer from the floor between the two ribs. This argument, however, is not true in the present results (see heat transfer levels in Figure 6.78). In addition, in contrast to the results of Rau et al. (but consistent with the predictions of the k-ω-SST model), the v^2-f model shows that the maximum wall-normal velocity increases with the P/k ratio (inset to Figure 6.81).

Friction coefficient distributions are shown in Figure 6.82. Similar to the results of the k-ω-SST model (Figure 6.77), it can be seen that within the cavity, c_f / c_{f0} is negative underneath the primary recirculation region with two negative peaks. This figure also indicates that for $P/k = 9$ and 12, the distance over which the mean viscous shear is positive, increases with the P/k ratio. Compared to the data of Rau et al., the recirculation length for $P/k = 9$ and 12 are over-predicted by the v^2-f model by about 20%.

Normalized average Nusselt number for all three P/k ratios using the k-ω-SST and v^2-f models are shown in Figure 6.83. The experimental data of Rau et al. (1998) and the

correlation of Ravigururajan and Bergles (1996) are also shown in this figure. The correlation suggests that heat transfer levels continuously decrease as the *P/k* ratio increases. The experimental data of Rau et al., however, indicates that *P/k* = 9 has the highest average Nusselt number, a result that is also consistent with the predictions of the *k-ω-SST* model. In contrast, the v^2*-f* model returns the lowest heat transfer levels for *P/k* = 9 (although this value is in a good agreement with both the experimental data and correlation). Consistent with the findings of Rau et al., three other earlier experimental works of similar flow problem have found that heat transfer levels were maximized for *P/k* = 8.5 – 10 (Taslim and Wadsworth, 1997; Okamoto et al. 1993; Liou et al. 1990).

In Figure 6.84 normalized average friction coefficient for various *P/k* ratios are shown. In agreement with the experimental data of Rau et al. (1998) and Okamoto et al. (1993), the v^2*-f* model shows that *P/k* = 9 has the highest c_f/c_{f0}. The *k-ω-SST* model, however, predicts *P/k* = 12 to have the highest friction coefficient.

Table 6.10 below lists the values of the normalized average heat transfer and friction coefficient as well as the efficiency index (see Eqn. (6.7)). The latter represents the overall thermal-hydraulic performance of each case. It can be seen that from the predictions of the *k-ω-SST* model, *P/k* = 9 is the optimum configuration, while the v^2*-f* model predicts *P/k* = 6 to be the optimum design.

P/k ratio	Method	Nu_{av}/Nu_0	$c_{f\,av}/c_{f0}$	$\eta=(Nu_{av}/Nu_0)/(c_{f\,av}/c_{f0})^{1/3}$
6	k-ω-SST model	1.634	2.931	1.141
9	k-ω-SST model	2.384	4.045	1.496
12	k-ω-SST model	1.905	4.168	1.184
6	v^2-f model	2.426	3.949	1.535
9	v^2-f model	2.248	4.329	1.379
12	v^2-f model	2.446	4.084	1.530

Table 6.9 – Average heat transfer levels, friction coefficients, and efficiency indices for various *P/k* ratios.

Contours of the streamwise velocity obtained using the v^2-f model, are shown in Figure 6.85. It is clear that for P/k = 6, there is no reattachment point and the inter-rib cavity is filled with a recirculating bubble. In addition, from this figure it can be seen the recirculation length for P/k = 9 and 12 are nearly the same.

P/k ratio	Method	Nu_{av}/Nu_0	$c_{f\,av}/c_{f0}$	$\eta=(Nu_{av}/Nu_0)/(c_{f\,av}/c_{f0})^{1/3}$
6	k-ω-SST model	1.634	2.931	1.141
9	k-ω-SST model	2.384	4.045	1.496
12	k-ω-SST model	1.905	4.168	1.184
6	v^2-f model	2.426	3.949	1.535
9	v^2-f model	2.248	4.329	1.379
12	v^2-f model	2.446	4.084	1.530

Table 6.10 – Average heat transfer levels, friction coefficients, and efficiency indices for various P/k ratios.

Pressure contours in Figure 6.86 indicate that the pressure at the upstream faces of the ribs becomes greater for higher P/k ratios due to higher rate of flow renewal in the inter-rib cavity. The magnitude of the negative pressure downstream of the ribs also increases by increasing the P/k ratio.

Contours of the turbulent kinetic energy are shown in Figure 6.87. The maximum value in all three cases occurs at upstream and above the ribs. It is clear that P/k = 9 has the highest levels of turbulent kinetic energy and the region with the maximum level of turbulence extends over the entire rib crest. The reason for P/k = 9 having higher levels of k could perhaps be associated with the magnitude of the streamwise and wall-normal velocity components near the top corner of the ribs.

6.5.2 Effects of Rib Height (k/H)

All the computations presented so far have been carried out for a constant rib height (for 1s channels: k/H = 0.1 or k/D_e = 0.05). In this section, the aim is to see the effects of

reducing the rib height on the mean flow and heat transfer. This analysis has relevance to one of the current problems that all AGRs are facing due to carbon particle deposition on the fuel pins. This deposition results in an overall reduction of the effective rib height. Based on the data provided by British Energy, this rib height reduction in AGRs due to carbon deposition is typically between 1.2-14.6% (Gotts, 2008).

In addition, the present author estimates on the basis of design data provided by Fairbairn (2009) that k/D_e ratio in a typical AGR fuel channel is an order of magnitude less than that in the experiments of Rau et al. (1998). Nevertheless, the ratio of k to D_e in AGRs is still sufficiently high to raise the possibility that there will be significant restructuring of the logarithmic layer. (Also, the distance between adjacent fuel pins is somewhat less than D_e; consequently normalization of k by inter-pin distance will indicate a greater degree of relative roughness.)

In this section, four k/H ratios are investigated: a) 0.100, b) 0.090, c) 0.075, and d) 0.050 (which respectively correspond to 0, 10, 25 and 50% rib height reduction). Computations are undertaken using the v^2-f model and four different grids with P/k = 9; 2s (mesh numbers 3, 7, 8 and 9 – see Table 6.3).

In Figure 6.88, it is evident that reducing the rib height results in a decrease in heat transfer levels. By reducing the rib height by 10%, the average Nu/Nu_0 decreases by 3.8%, while further reduction of the rib height by 25%, decreases the average Nu/Nu_0 by 11.5%. From Figure 6.88 it can also be seen that the shape of the Nusselt number distribution becomes rather skewed towards the upstream rib by reducing the rib height.

The streamwise velocity at the y/k = 0.1 plane is shown in Figure 6.89. It can be seen that the smaller the rib height, the shorter the recirculation length becomes. The maximum positive velocity is also higher for shorter ribs i.e. higher flow renewal within the cavity. It is also seen that the size of the primary recirculation bubble downstream of

the first rib is very different for various rib heights, although the size of the second separation vortex upstream of the second rib remains nearly unchanged.

Figure 6.90 shows the magnitude of the wall-normal velocity at rib height (i.e. y/k = 1). This figure shows that different rib heights have similar distributions, except for y/k = 0.05, which has the smallest downward velocity magnitude, especially in the recovery region ($3 < x/k < 6$).

The local friction coefficient distributions in Figure 6.91 again indicate that for smaller k/H ratios, the size of the separation bubble becomes smaller and consequently the distance over which the friction coefficient is positive becomes larger. It can also be seen that by reducing the rib height for example by 50%, the reattachment length too reduces by about 50%.

Figure 6.92 shows the pressure coefficient distributions. All the distributions are offset to the same value at x/k = 0.5. This figure shows the pressure coefficient near the second rib decreases by decreasing the rib height. The implication of this is that the pressure drop due to form drag decreases by decreasing the rib height.

In Figure 6.93 average Nu/Nu_0 for all k/H ratios using the v^2-f model is shown. The data of Rau et al. (1998) for k/H = 0.1 and the correlation of Ravigururajan and Bergles (1996) (Eqn. (6.3)) are also shown in this figure. Consistent with the correlation, the v^2-f model shows that normalized average heat transfer decreases by reducing the rib height. However, the gradient of the line connecting the results of the v^2-f model is about 2.5 times greater than that of the correlation. The present simulations predict that reducing the rib height by 50% results in 27% drop in heat transfer levels, while for the same rib height reduction, the correlation gives 15% heat transfer impairment. Moreover, consistent with the correlation, the DNS data of Nagano et al. (2004) for 1s channel and

P/k = 4 also found that the average heat transfer levels drop only by 15% when the rib height is reduced by 50%.

Normalized average c_f/c_{f0} for all four *k/H* ratios are shown in Figure 6.94. It is seen that the friction coefficient decreases by reducing the rib height. The v^2-*f* model predicts a reduction of 64% in the friction coefficient when the rib height is reduced by 50%, while for the same rib height reduction, the DNS data of Nagano et al. (2004) returned a drop of only 27%. (Note, however, that the inconsistencies between the present simulations and those of Nagano et al. (2004) could be associates with the differences in the Reynolds number, *P/k* ratio and number of roughened walls in the simulated channel.)

Table 6.11 lists the values of the average Nu/Nu_0, c_f/c_{f0}, and the efficiency index, η, for each rib height. The maximum value of η is obtained for *k/H* = 0.05 which indicates that this is the optimum rib height. Similarly, Nagano et al. (2004) concluded that ribs with smaller heights have better overall thermal-hydraulic performances.

k/H ratio	**Turbulence model**	$\mathbf{Nu_{av}/Nu_0}$	$\mathbf{c_{f\,av}/c_{f0}}$	$\boldsymbol{\eta=(Nu_{av}/Nu_0)/(c_{f\,av}/c_{f0})^{1/3}}$
0.100	v^2-f model	2.687	12.350	1.163
0.090	v^2-f model	2.585	10.523	1.179
0.075	v^2-f model	2.379	7.840	1.198
0.050	v^2-f model	1.968	4.396	1.201

Table 6.11 – Average heat transfer levels, friction coefficients, and efficiency indices for various *k/H* ratios.

Contours of the streamwise velocity are shown in Figure 6.95. Recirculation regions downstream of the ribs are clearly evident. The size of these separation regions is proportional to the rib height. It is also seen that in all four cases the flow reattaches within the inter-rib cavity.

Contours of the relative pressure are shown in Figure 6.96. In this figure it is seen that by reducing the rib height, the stagnation pressure upstream of the ribs also decreases, which results in lower form drag i.e. lower pressure loss.

Contours of the turbulent kinetic energy are shown in Figure 6.97, where the levels of turbulent kinetic energy can be seen to be affected throughout the domain by changing the rib height. As before, the region with the maximum level of turbulent kinetic energy occurs at upstream and above the ribs for all *k/H* ratios. The maximum level of turbulent kinetic energy decreases by reducing the rib height.

6.5.3 Effects of Rib Width (b/k)

In this section, the effects of rib width on the mean flow and heat transfer are examined. Three different rib width-to-height ratios, *b/k* are tested: 1) 0.5, 2) 1.0, and 3) 1.5. Three grids with *P/k* = 9; 2s (mesh numbers 3, 10 and 11 – see Table 6.3) are used and computations are undertaken using the v^2-*f* model.

Figure 6.98 compares heat transfer levels for various *b/k* ratios. It is seen that the highest rate of heat transfer is predicted for the case with the minimum width i.e. *b/k* = 0.5 mainly because in this case, the inter-rib cavity between the two ribs is wider, which in turn leads to higher rate of flow renewal in the cavity.

Streamwise velocity distributions are shown in Figure 6.99. The results indicate that while similar trends are found for all three *b/k* ratios, the case with the minimum rib width has the highest velocity magnitude in both the recirculation and recovery regions.

In Figure 6.100 it can be seen that by changing the rib width, wall-normal velocity distributions are affected only marginally in the regions near the ribs. In fact, these distributions are nearly identical over a wide range ($1.5 < x/k < 6.5$) within the cavity.

Friction coefficient distributions in Figure 6.101 indicate that decreasing the rib width results in an increase in the intensity of the recirculation region while the size of

the recirculation bubble upstream of the rib (represented by the second negative peak) is the same for all three cases. It can also be seen that unlike b/k = 0.5 and 1, for b/k = 1.5 the flow does not have any reattachment point i.e. the flow remains reversed in the near-wall cell throughout the cavity.

As was noted earlier, by decreasing the rib width, heat transfer enhances (Figure 6.98). This, however, is achieved with the penalty of having higher friction (form drag) as a result of higher pressure difference between upstream and downstream regions of the ribs, as shown in Figure 6.102. (As before, the distribution in the figure are offset to the same value at x/k = 0.5.)

Table 6.12 lists the values of average Nu/Nu_0, c_f/c_{f0}, and η for different b/k ratios. The values of average Nu/Nu_0 and c_f/c_{f0} are also plotted against b/k ratio in Figure 6.103 and Figure 6.104, respectively. From these figures, it is clear that increasing the rib width results in a decrease in both heat transfer and friction. Wilkie (1966) also found a similar decreasing trend for the normalized friction coefficient.

As before, an overall thermal-hydraulic performance of each configuration is better represented by the efficiency index, η. The results in Table 6.12 indicate that the case with the smallest rib width is an optimum design.

b/k ratio	Turbulence model	Nu_{av}/Nu_0	$c_{f\,av}/c_{f0}$	$\eta=(Nu_{av}/Nu_0)/(c_{f\,av}/c_{f0})^{1/3}$
0.5	v^2-f model	2.877	14.116	1.190
1.0	v^2-f model	2.687	12.350	1.163
1.5	v^2-f model	2.561	11.411	1.137

Table 6.12 – Average heat transfer levels, friction coefficients, and efficiency indices for various b/k ratios.

In Figure 6.105 very similar patterns can be seen in the contours of the streamwise velocity for all three b/k ratios. Pressure contours in Figure 6.106, however, show that the pressure drop due to the form drag increases by reducing the rib width. In Figure

6.107 it is seen that the levels of turbulent kinetic energy are higher for smaller rib widths since the streamwise (and wall-normal velocity to a lesser extent) are higher for wider inter-rib cavities (Figure 6.99 and Figure 6.100).

6.5.4 Effects of Reynolds Number

It was remarked in Section 6.2.3 that in the present 2D simulations, the bulk velocity was set so that the Reynolds number based on hydraulic diameter is the same as that in the experiments of Rau et al. (1998) i.e. Re = 30,000. In relation to AGR fuel channels, however, the Reynolds number based on hydraulic diameter is estimated to be $Re \approx 0.6\times10^6 - 1.2\times10^6$ (Gotts, 2009). Therefore, it is important to study the effects of the Reynolds number on the flow field and heat transfer. For this reason, the 1s channel configuration with P/k = 9 (mesh number 2 in Table 6.3) is used and earlier computations are now repeated for Re = 100,000 using both the *k-ω-SST* and v^2-*f* models. (Even though Re = 100,000 is still much smaller than the value of the Reynolds number in a typical AGR fuel passage, it can provide a measure of how much mean flow and heat transfer are affected by the Reynolds number in a rib-roughened channel.)

***k-ω-SST* model**

Figure 6.108 compares heat transfer levels obtained by the *k-ω-SST* model with the experimental data of Rau et al. (1998). As was discussed earlier (Figure 6.22), compared to the data the *k-ω-SST* model under-predicts the local Nusselt number distribution at Re = 30,000. Figure 6.108 shows that increasing the Reynolds number to Re = 100,000 results in a decrease in heat transfer levels with the maximum difference of about 12% near the centre of the cavity.

Figure 6.109 shows that the streamlines for both Reynolds numbers are similar. In both cases, a relatively large separation region is predicted within the inter-rib cavity. Two counter-rotating recirculation vortices are also predicted upstream and downstream

of the ribs. No reattachment point can be seen in either of these cases (this point will be further discussed in relation to Figure 6.113).

In Figure 6.110 at one-tenth of the rib height the streamwise velocity distributions of Re = 100,000 show slightly greater velocity gradient. In addition, at Re = 30,000 the k-ω-*SST* model predicts that the flow remains reversed at this elevation, while a positive velocity peak is seen between $x/k = 6 - 7.5$ for Re = 100,000.

However, wall-normal velocity and pressure coefficient distributions for both cases are nearly identical, as shown in Figure 6.111 and Figure 6.112, respectively.

Friction coefficient distributions are shown in Figure 6.113. Clearly, in both cases the k-ω-*SST* model fails to predict any reattachment point. It is also seen that the magnitude of the friction coefficient decreases with increasing the Reynolds number. This implies that the magnitude of the reversed streamwise velocity in the first near-wall cell is reduced by increasing the Reynolds number. This could be the reason for predicting lower levels of heat transfer at Re = 100,000 (Figure 6.108).

Normalized streamwise velocity profiles at two wall-normal planes, namely over the rib-top ($x/k = 0$) and in the separation region ($x/k = 4$) are shown in Figure 6.114 and Figure 6.115, respectively. In both figures, the velocity magnitude is slightly lower for Re = 100,000 for the range $0.2 < y/H < 0.8$, while closer to the top smooth wall ($y/H > 0.8$), the velocity magnitude at Re = 100,000 becomes somewhat higher, indicating smaller boundary layer thickness for higher Reynolds numbers. In addition, in Figure 6.115 it is seen that compared to the data of Rau et al. (1998), the k-ω-*SST* model under-predicts the velocity magnitude especially for $y/H < 0.2$. This is mainly due to an over-prediction of the reattachment length in the cavity (Figure 6.109).

v^2-f model

Figure 6.116 shows that heat transfer levels obtained by the v^2-f model are similar for both Reynolds numbers. Near the downstream rib, however, the v^2-f model predicts slightly higher levels of heat transfer for Re = 100,000.

While the streamlines in Figure 6.117 are similar for both Reynolds numbers, it is seen that the v^2-f model predicts a somewhat shorter reattachment length for Re = 100,000. This results in a slightly longer recovery region (i.e. distance between the reattachment point and the next rib) for Re = 100,000 which in turn leads to a slightly higher maximum velocity magnitude for this case compared to Re = 30,000. This is indicated in Figure 6.118 where the streamwise velocity distributions at the y/k = 0.1 plane are shown.

Similar to the results of the k-ω-*SST* model, in Figure 6.119 and Figure 6.120 the wall-normal velocity and pressure coefficient distributions for both Reynolds numbers are principally the same.

Consistent with the findings of Figure 6.117, the friction coefficient distributions shown in Figure 6.121 indicate that the v^2-f model predicts a slightly smaller recirculation bubble and reattachment length for Re = 100,000 i.e. the negative area underneath the primary recirculation bubble is smaller. It is worth noting that the experimental results of Liou et al. (1990) for Re = 12,000 - 120,000 suggest that the reattachment length is a 'weak function' of the Reynolds number.

Figure 6.122 and Figure 6.123 show that the streamwise velocity profiles at two wall-normal planes, one over the rib-top and the other one in the recirculation bubble, are nearly identical for both Reynolds numbers. In Figure 6.122 there is good agreement with the data for flow over the rib-top. However, within the inter-rib cavity (Figure 6.123), the size of the recirculation bubble is over-predicted by the v^2-f model.

Figure 6.124 shows the normalized average Nusselt number obtained using the k-ω-*SST* and v^2-f models. As before, the present results are compared against the

experimental data of Rau et al. (1998) and the correlation of Ravigururajan and Bergles (1996). The experimental results of Park et al. (1992) on a channel with a square cross-section with P/k = 10; 2s are also included in this figure (and also in Figure 6.125). It can be seen that the v^2-f model returns values that are in fairly good agreement with the data and correlation; they all suggest a slight increase in heat transfer levels by increasing the Reynolds number (this is also in agreement with the RANS simulations of Iaccarino et al., 2002). In contrast, the k-ω-*SST* model predicts a lower heat transfer level for Re = 100,000.

The average friction coefficients returned by the k-ω-*SST* and v^2-f models are shown in Figure 6.125. Although both models predict the same trend, the results of the v^2-f model is in somewhat better agreement with the data of Park et al. (1992).

Table 6.13 shows the values of average Nu/Nu_0, c_f/c_{f0}, and η using the k-ω-*SST* and v^2-f models for both Reynolds numbers. It is seen that the efficiency index decreases with increasing the Reynolds number. This is consistent with the findings of Taslim and Wadsworth (1997).

Re	Turbulence model	Nu_{av}/Nu_0	$c_{f\,av}/c_{f0}$	$\eta=(Nu_{av}/Nu_0)/(c_{f\,av}/c_{f0})^{1/3}$
30,000	k-ω-SST model	1.719	4.045	1.079
100,000	k-ω-SST model	1.526	5.559	0.862
30,000	v^2-f model	2.248	4.329	1.379
100,000	v^2-f model	2.281	5.810	1.269

Table 6.13 – Average heat transfer levels, friction coefficients, and efficiency indices for two different Reynolds numbers.

6.6 SUMMARY

In this chapter, numerical simulations of the flow and heat transfer in 2-dimensional rib-roughened ducts were performed using a commercial CFD package, 'STAR-CD' version 4.02. Several careful sensitivity tests were carried out to confirm the accuracy of

the computational procedures adopted. These sensitivity tests included comparing the results of four 2-dimensional grids with different cell counts against the results obtained at a centre-line of a 3-dimensional channel. Furthermore, the effects of four discrete and four continuous design parameters on the dynamic and thermal fields were investigated and comparison was made against the experimental data of Rau et al. (1998). The discrete design parameters studied in this chapter included four turbulence models, two rib profiles, two near-wall treatments and two mesh types. The continuous design parameters examined included three pitch-to-rib height ratios, four rib height-to-channel height ratios, three rib width-to-height ratios, and two Reynolds numbers. For each continuous design parameter, the optimum ratio represented by the value of the efficiency index was also determined.

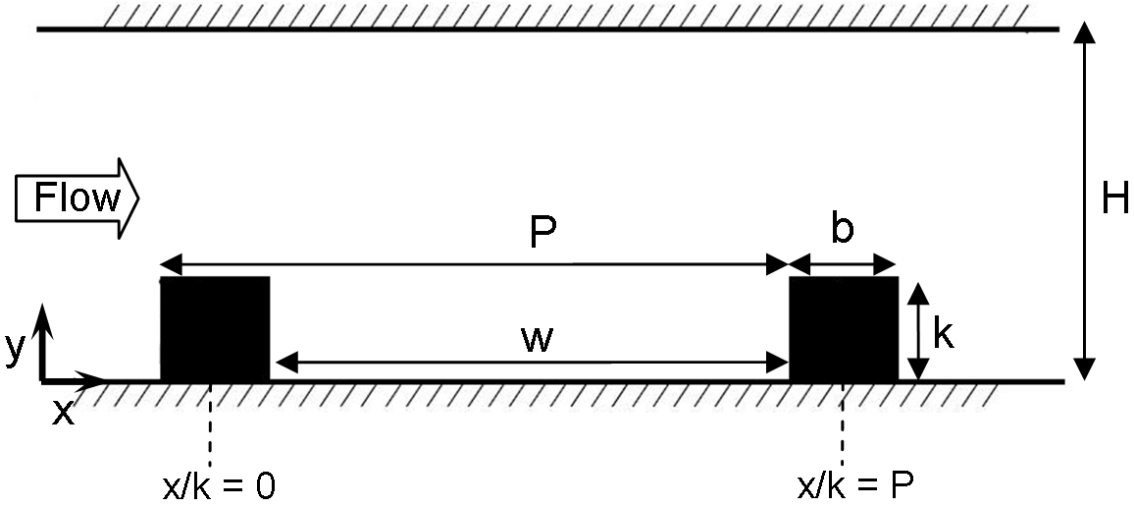

Figure 6.1 – Schematic diagram of a rib-roughened surface.

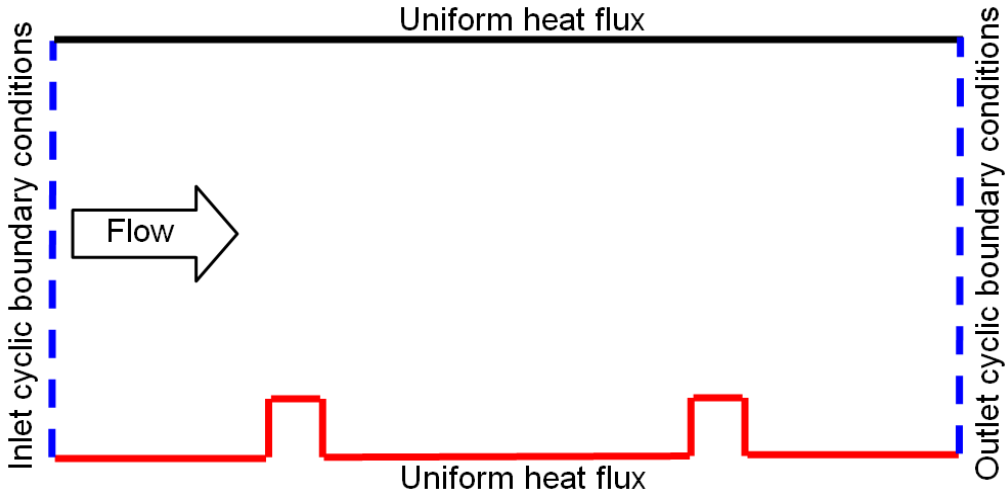

Figure 6.2 – The computational domains used in the present work for 1s configuration.

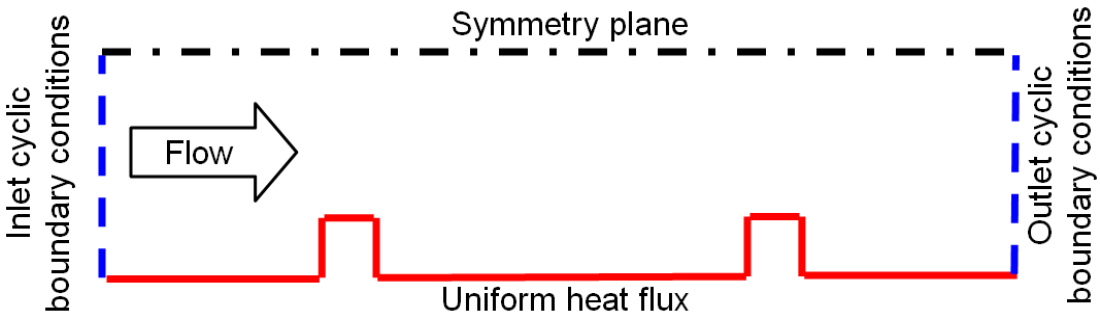

Figure 6.3 – The computational domains used in the present work for 2s configuration.

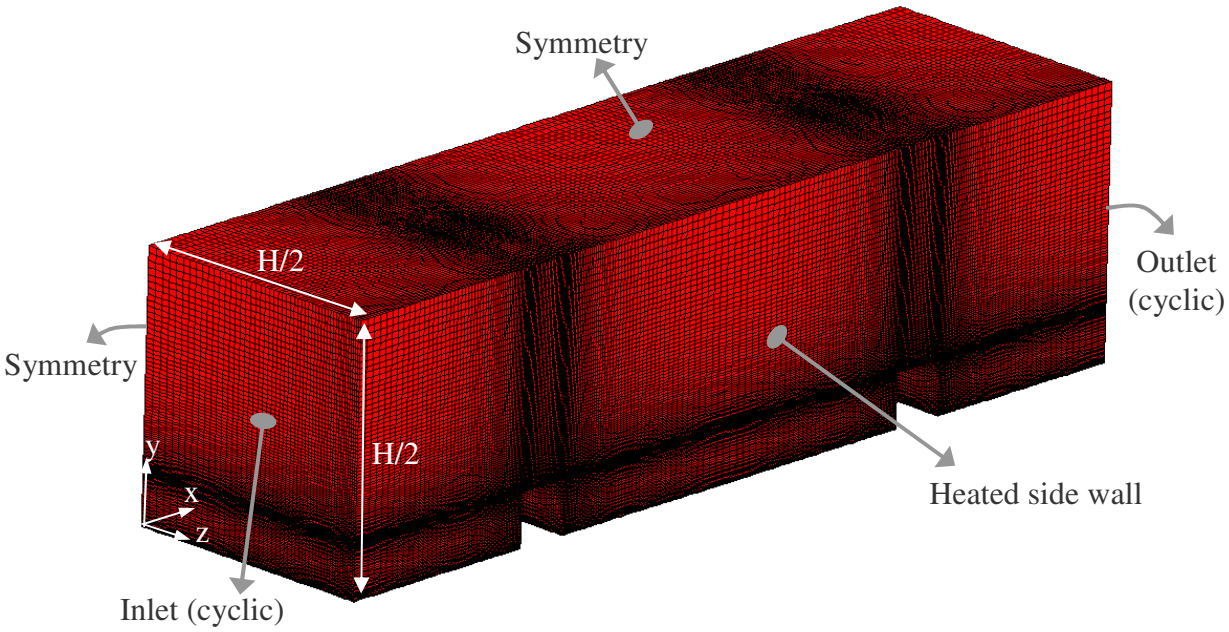

Figure 6.4 – Schematic of the 3D mesh (P/k = 9; 2s).

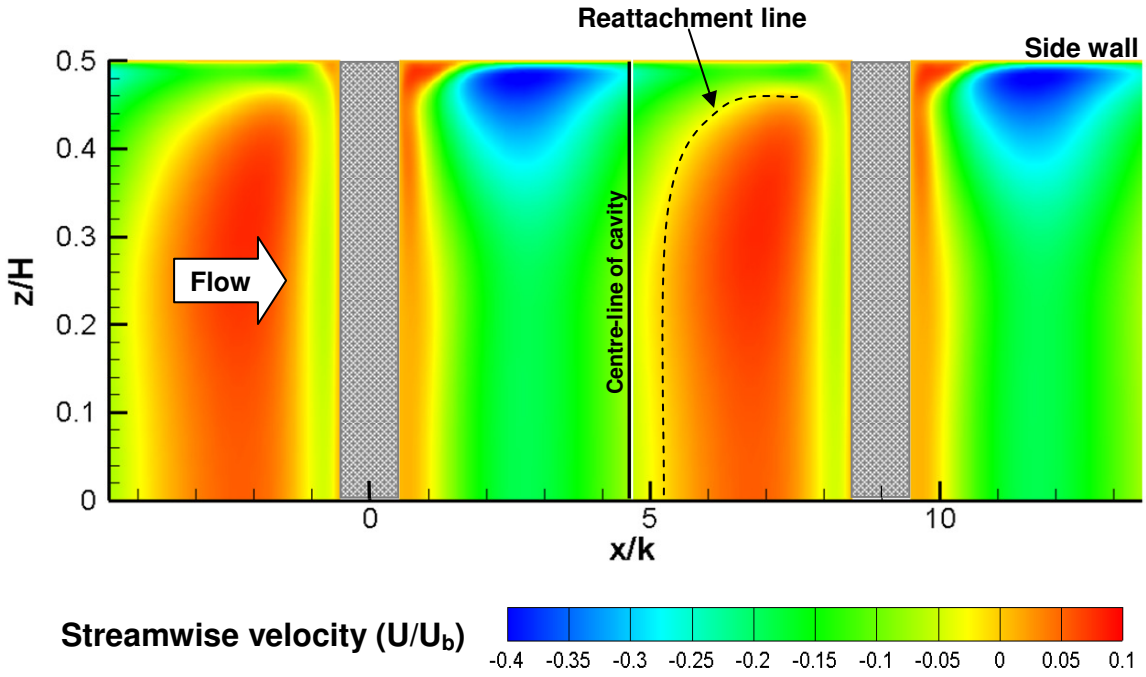

Figure 6.5 – Plan view contours of the streamwise velocity for the 3D case (P/k = 9; 2s) at the y/k = 0.1 plane using the v^2-f model.

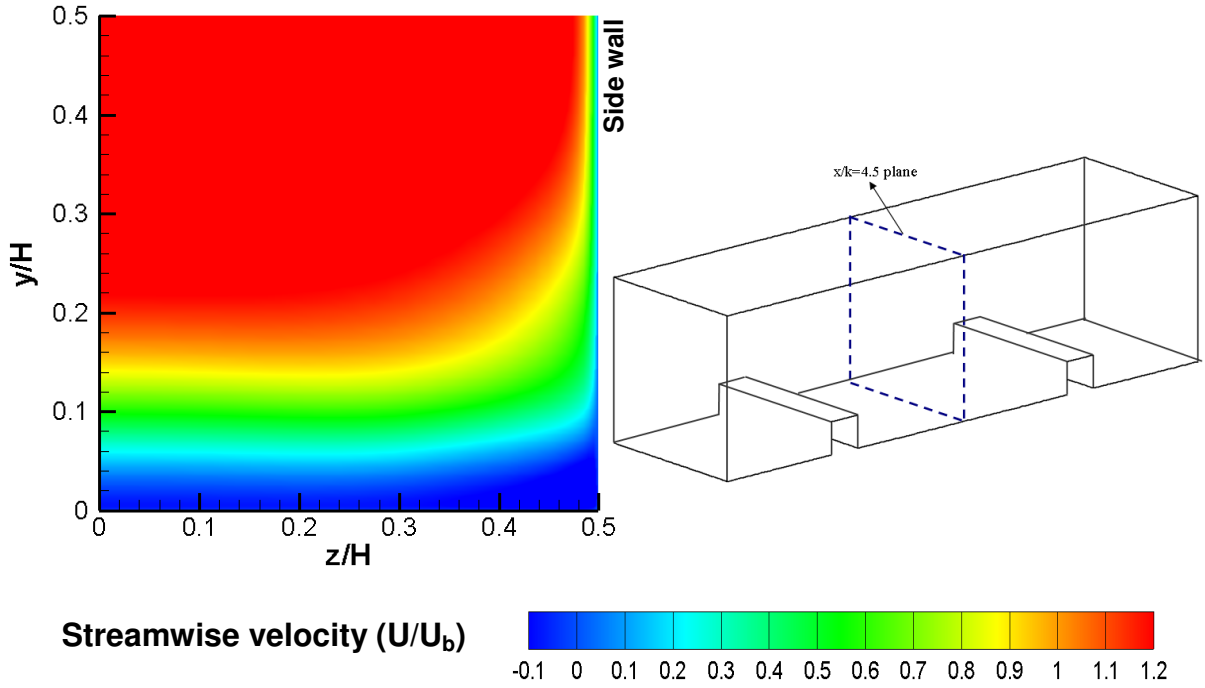

Figure 6.6 – Spanwise plane contour plot of the streamwise velocity for the 3D case (P/k = 9; 2s) at the mid-section between the two ribs (x/k = 4.5) using the v^2-f model.

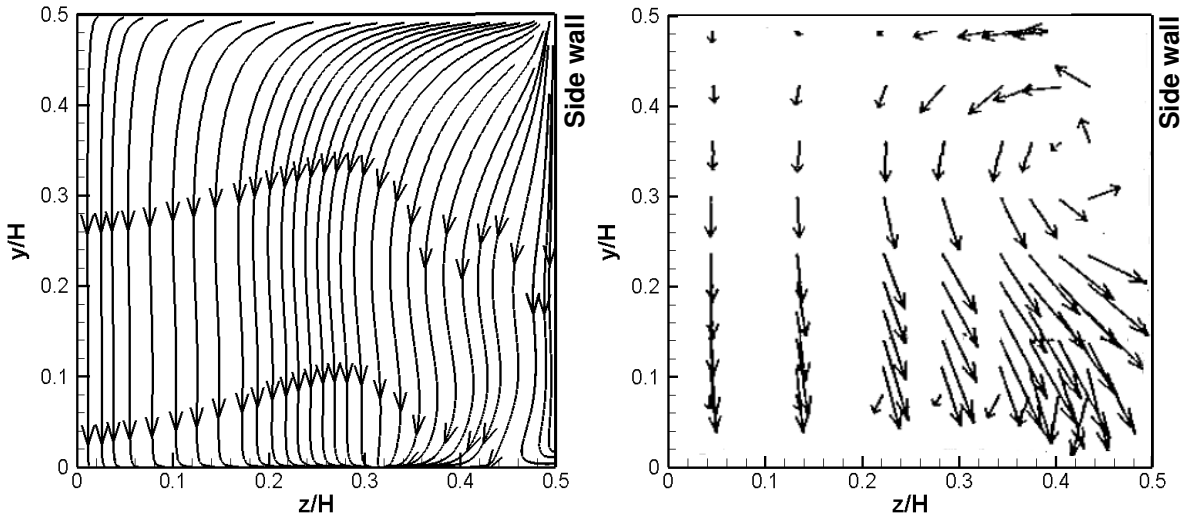

Figure 6.7 – Spanwise flow structure. (a) Present v^2-f model for the 3D case (P/k = 9; 2s) at x/k = 4.5 (b) LDV measurements of Liou et al. (1993b) for P/k = 9:2s at x/k = 2 plane.

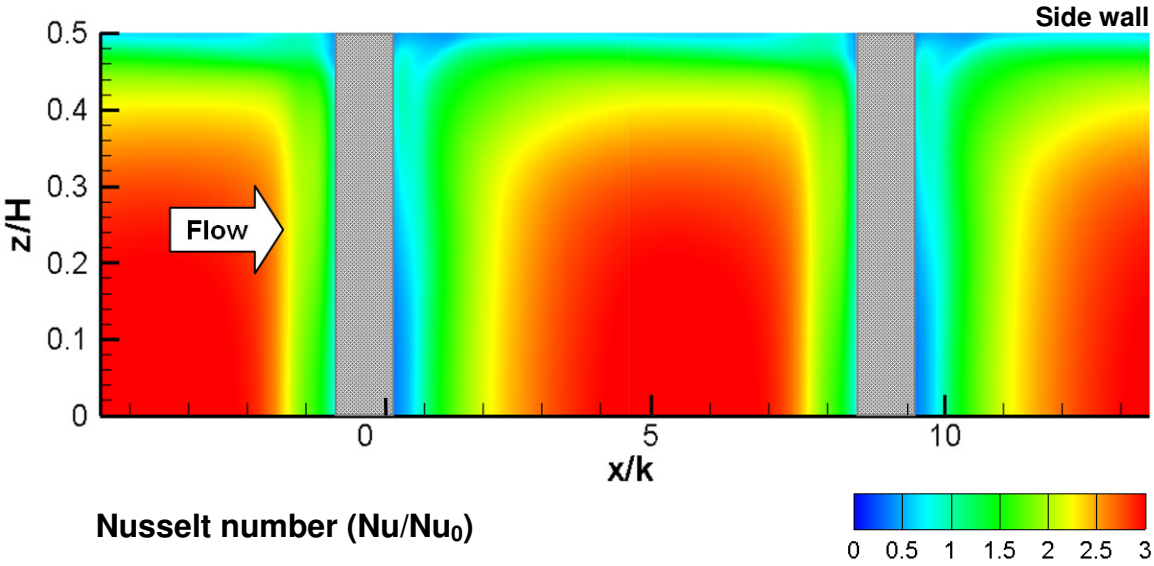

Figure 6.8 – Plan view contour of Nu/Nu_0 on the floor of the channel for the 3D case (P/k = 9; 2s) using the v^2-f model.

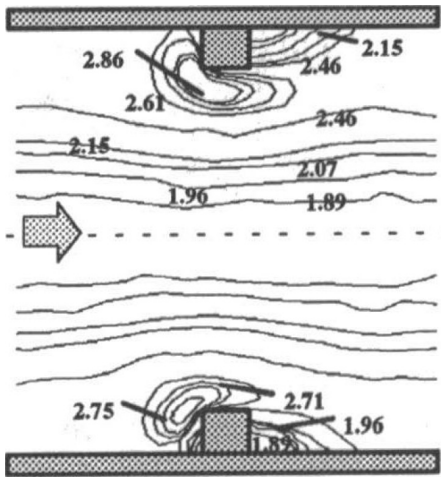

(a)

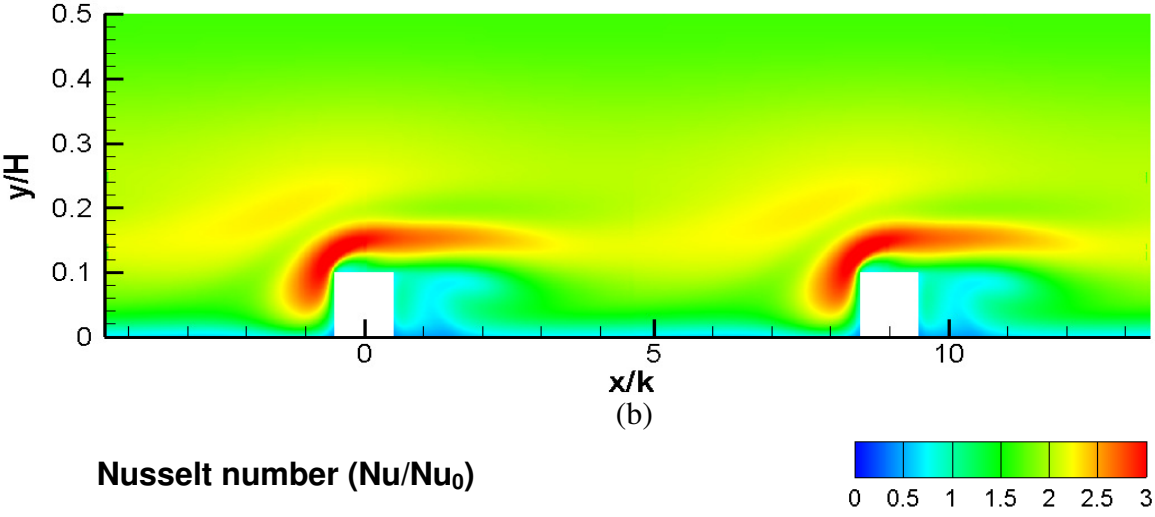

(b)

Figure 6.9 – Contour plot of Nu/Nu_0 on the side wall for the 3D case (P/k = 9; 2s) (a) experimental data of Rau et al. (1998) (b) the present v^2-f model.

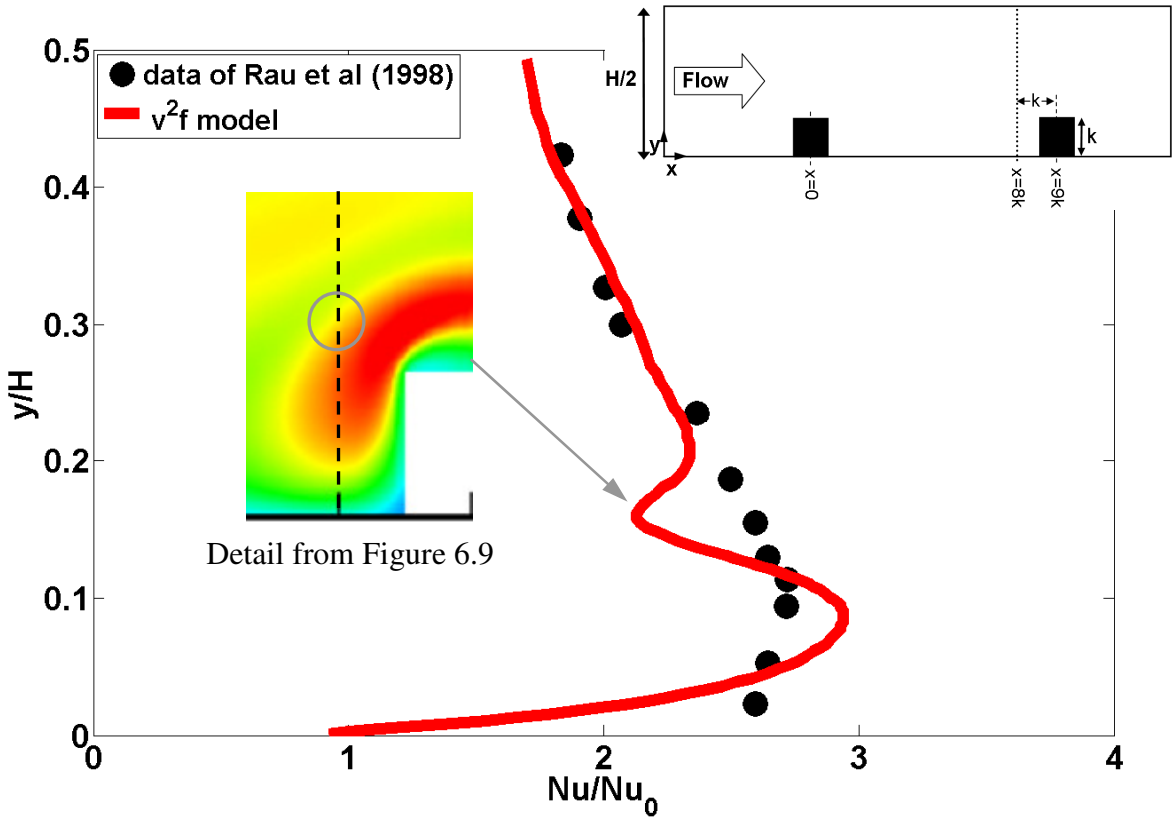

Figure 6.10 – Nusselt number distribution on the side wall of the 3D case (P/k = 9; 2s) at a distance k upstream from a rib using the v^2-f model.

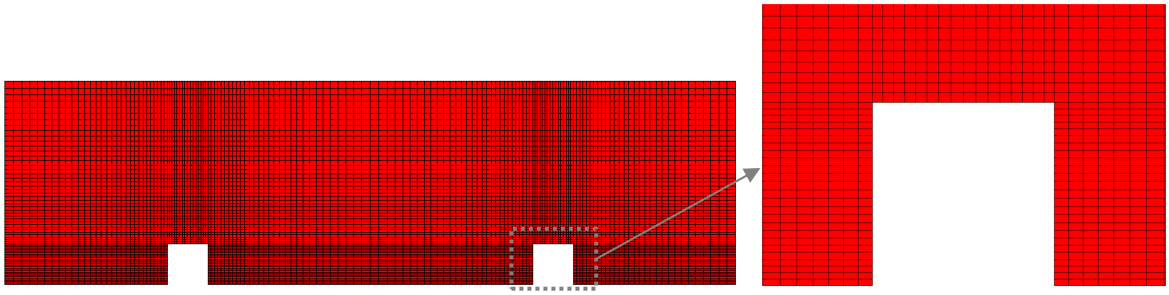

Figure 6.11 – 2D very coarse mesh (*P/k*=9; 2s).

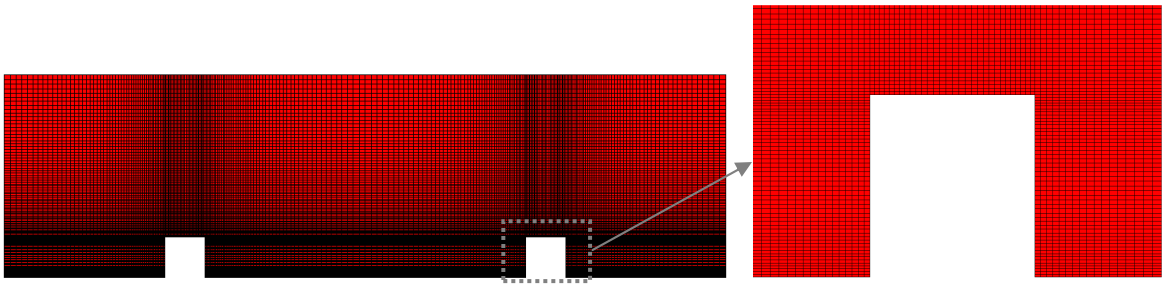

Figure 6.12 – 2D coarse mesh (*P/k* = 9; 2s).

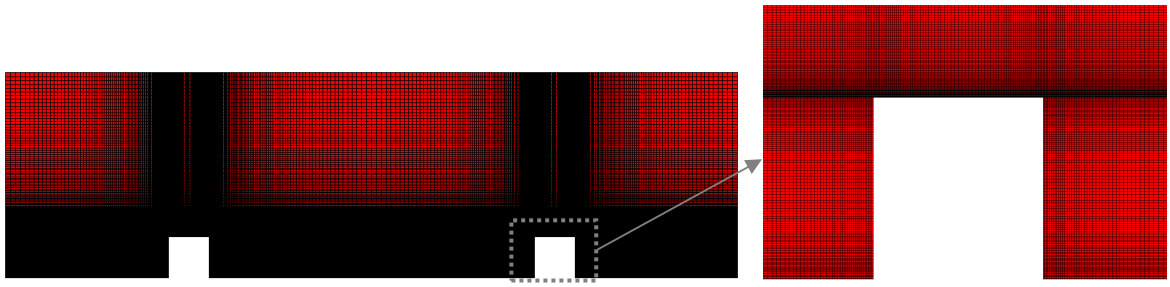

Figure 6.13 – 2D medium mesh (*P/k* = 9; 2s).

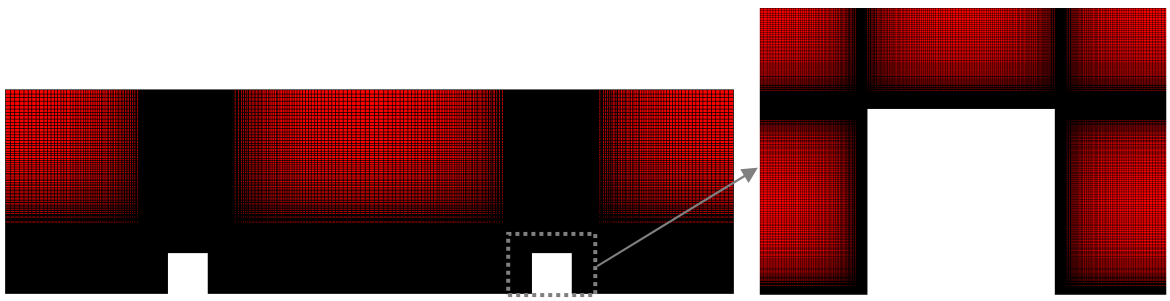

Figure 6.14 – 2D fine mesh (*P/k* = 9; 2s).

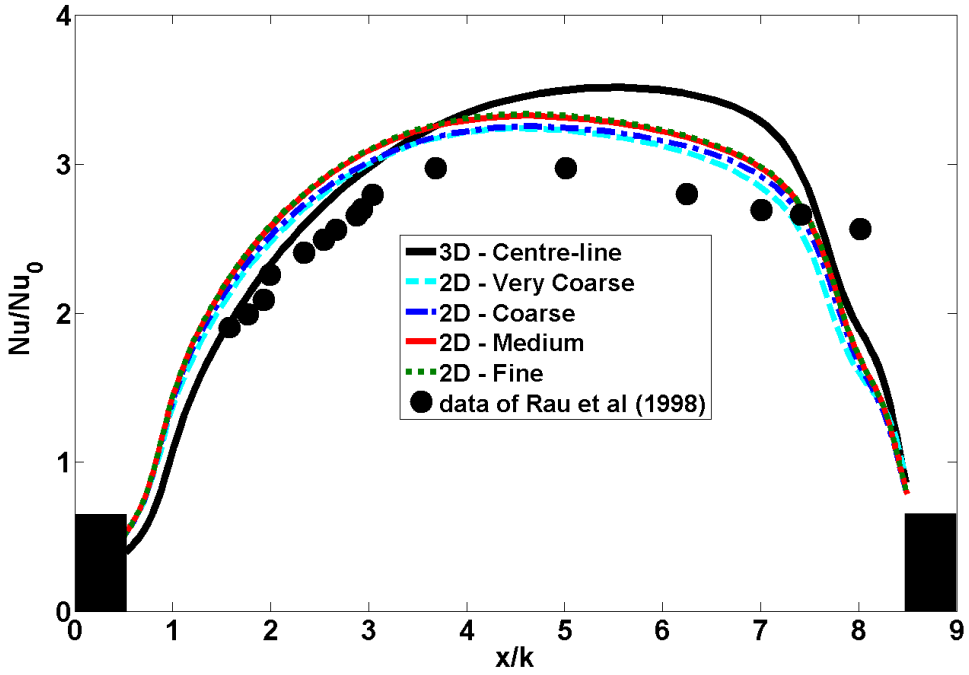

Figure 6.15 – Mesh sensitivity test and comparison of 2D vs 3D case (P/k = 9; 2s) for the Nusselt distribution using the v^2-f model.

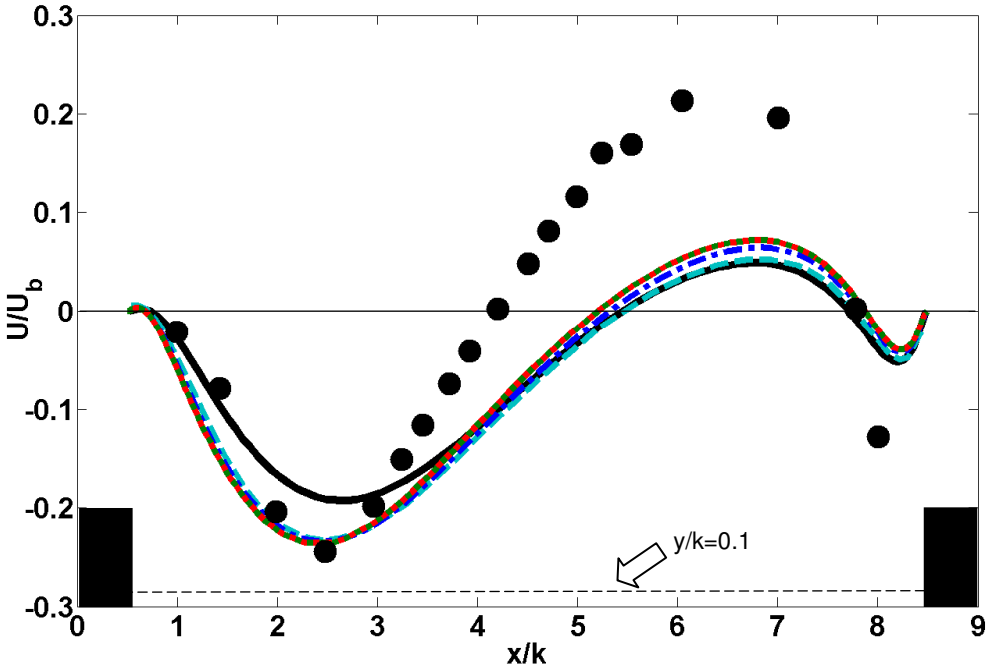

Figure 6.16 – Mesh sensitivity test and comparison of 2D vs 3D case (P/k = 9; 2s) for the streamwise velocity distribution at y/k = 0.1 using the v^2-f model.

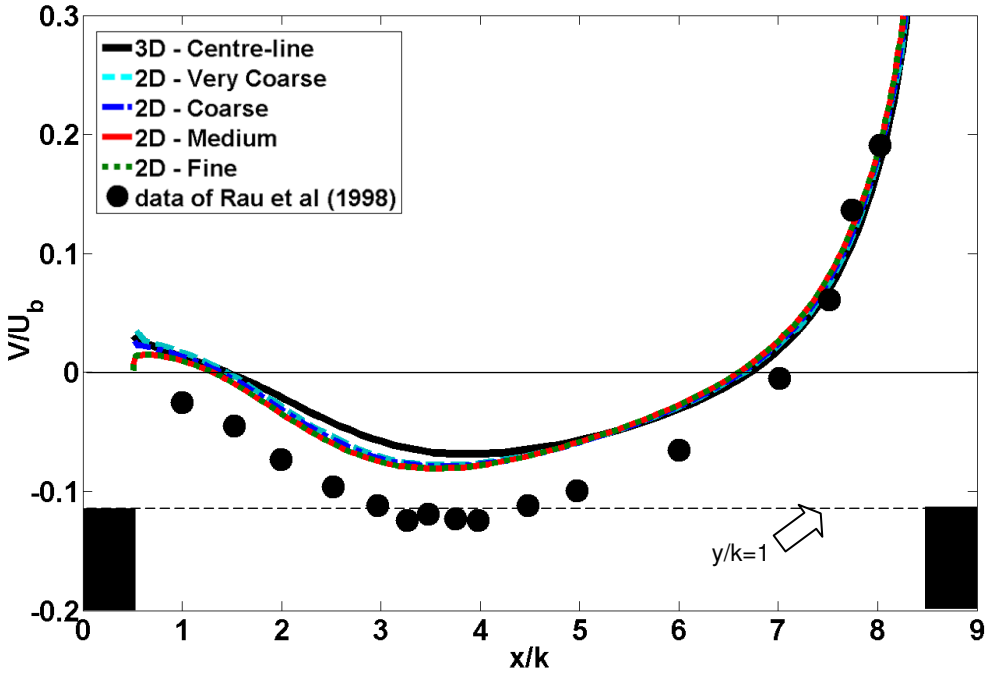

Figure 6.17 – Mesh sensitivity test and comparison of 2D vs 3D case (P/k = 9; 2s) for the wall-normal velocity distribution at y/k = 1 using the v^2-f model.

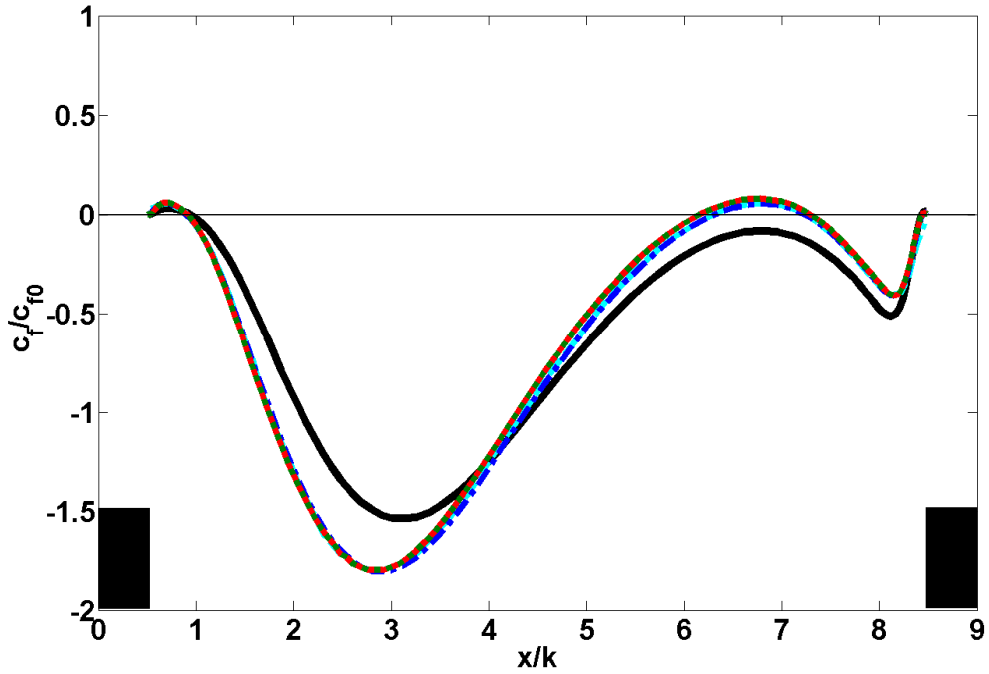

Figure 6.18 – Mesh sensitivity test and comparison of 2D vs 3D case (P/k = 9; 2s) for the friction coefficient distribution using the v^2-f model.

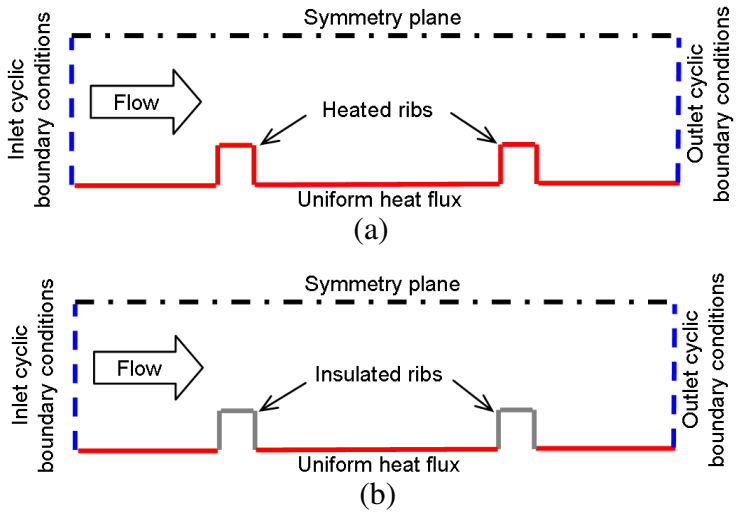

Figure 6.19 – The computational domains used for 2s configuration with different rib thermal boundary conditions (a) Heated ribs (b) Insulated ribs

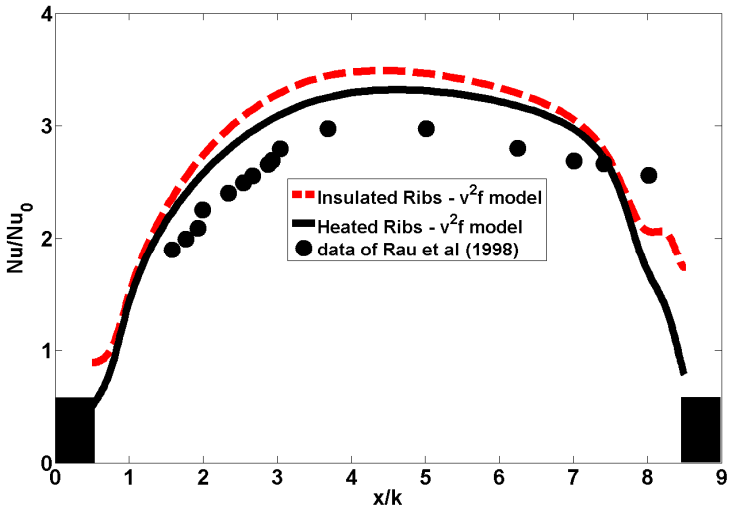

Figure 6.20 – Nusselt distribution for P/k = 9; 2s and two different rib thermal boundary conditions.

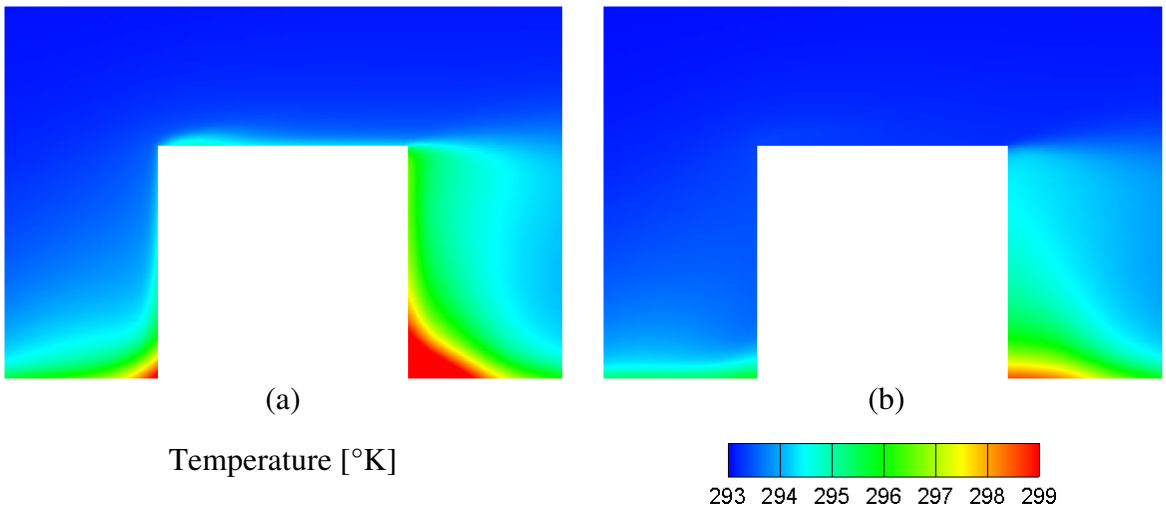

Figure 6.21 – Contour plots of temperature in the vicinity of the rib with different rib thermal boundary condition (a) Uniform heat flux at the ribs (b) Insulated ribs

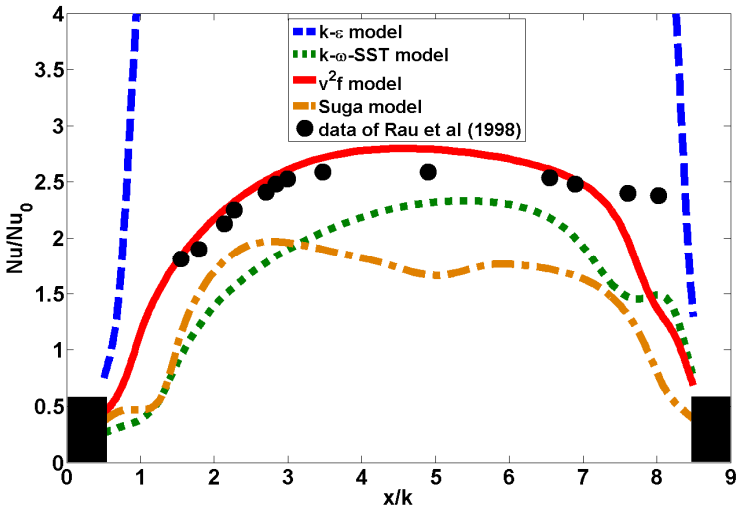

Figure 6.22 – Nusselt distribution for *P/k* = 9; 1s and various turbulence models.

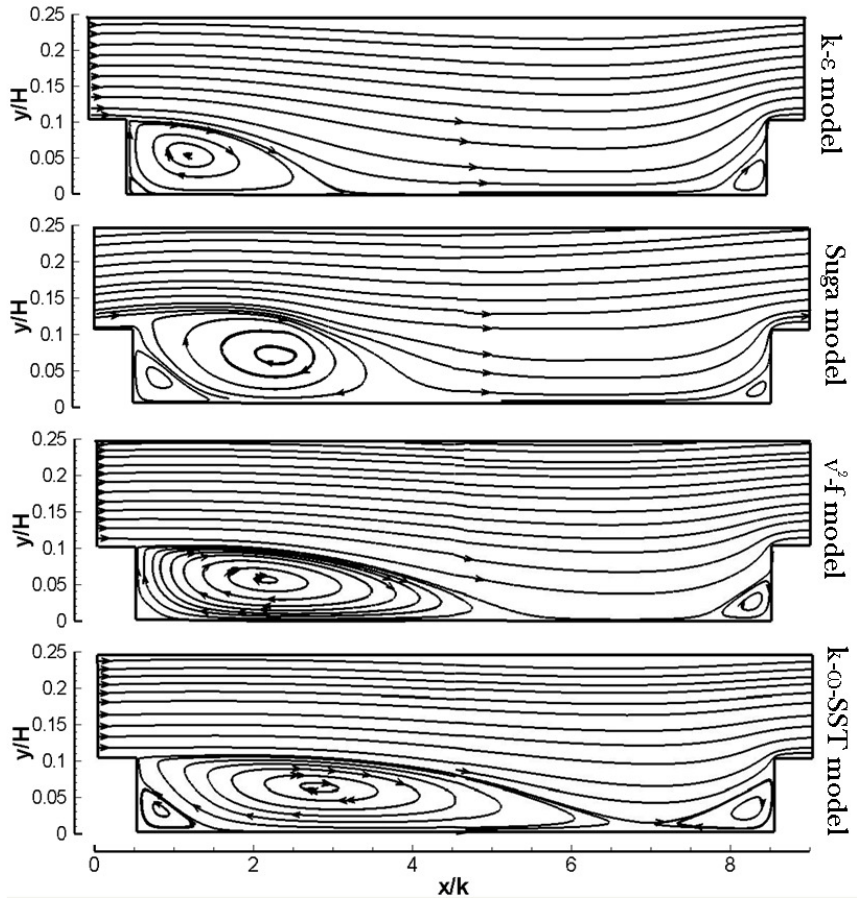

Figure 6.23 – Streamlines for *P/k* = 9; 1s and various turbulence models.

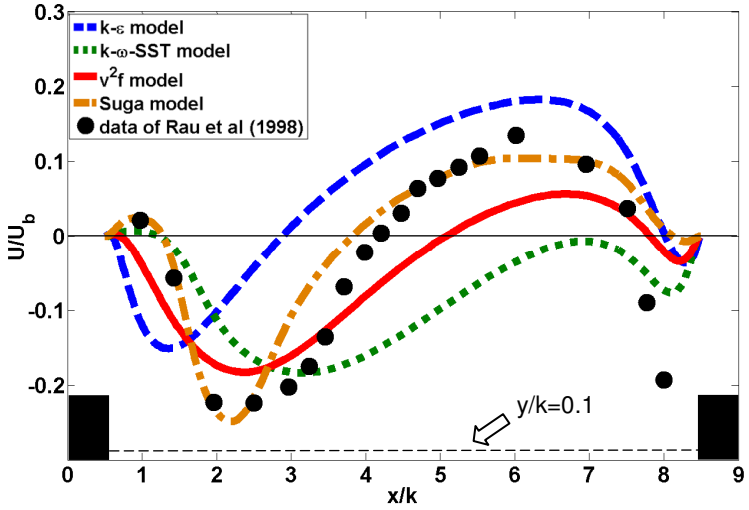

Figure 6.24 – Streamwise velocity distributions for $P/k = 9$; 1s at $y/k = 0.1$ for various turbulence models.

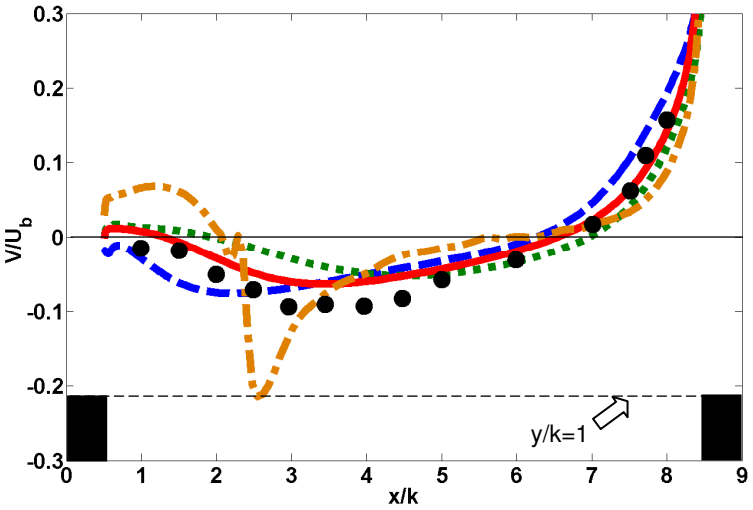

Figure 6.25 – Wall-normal velocity distributions for $P/k = 9$; 1s at $y/k = 1$ for various turbulence models.

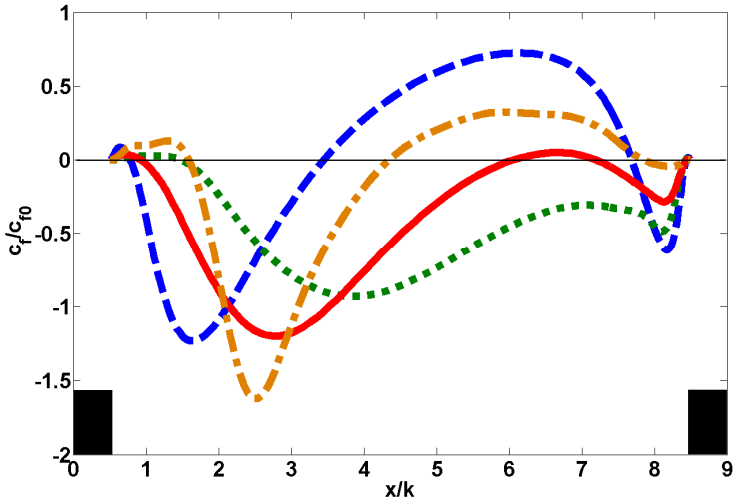

Figure 6.26 – Friction coefficient distributions for various turbulence models.

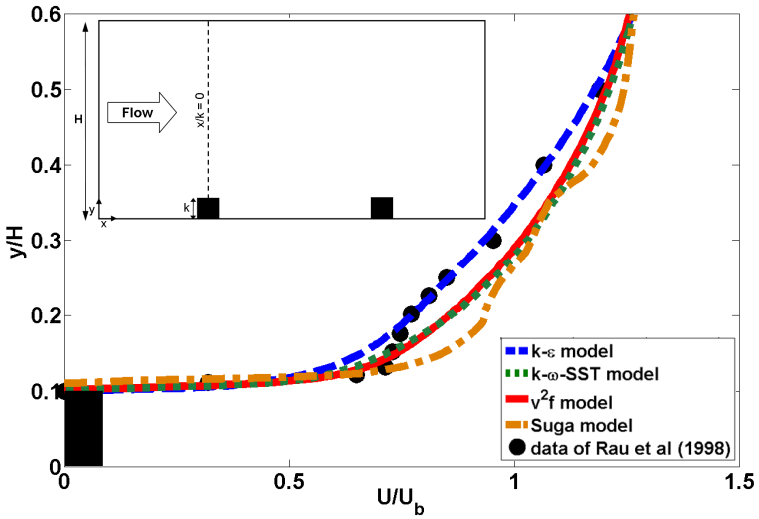

Figure 6.27 – Streamwise velocity profiles for $P/k = 9$; 1s on the rib-top ($x/k = 0$) for various turbulence models.

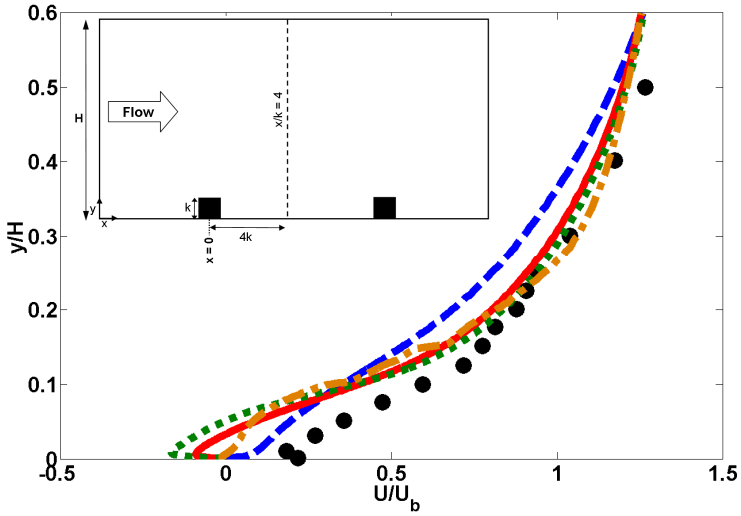

Figure 6.28 – Streamwise velocity profiles for $P/k = 9$; 1s at $x/k = 4$ for various turbulence models.

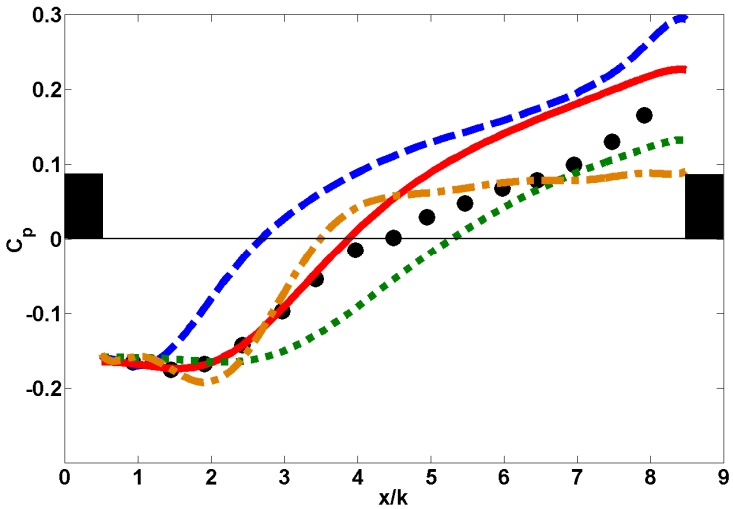

Figure 6.29 – Pressure coefficient distributions for $P/k = 9$; 1s for various turbulence models.

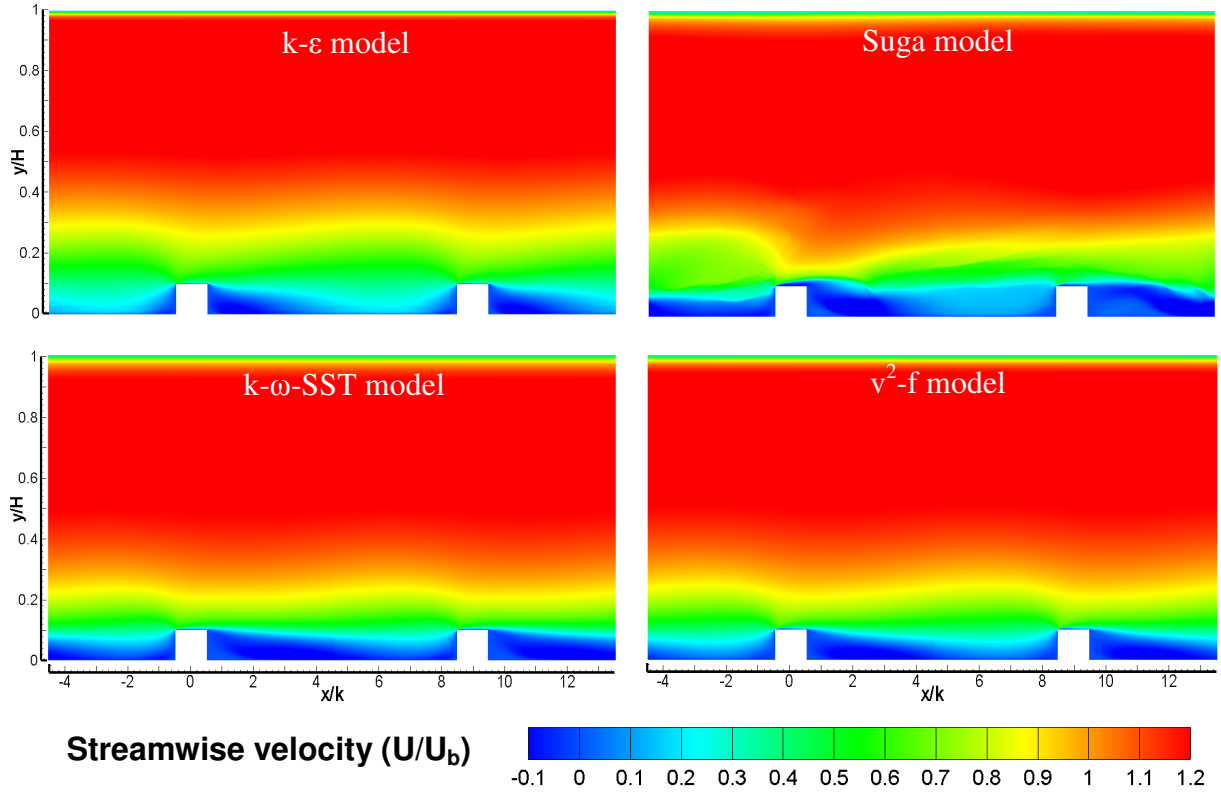

Figure 6.30 – Contour plots of the streamwise velocity for *P/k* = 9; 1s for various turbulence models.

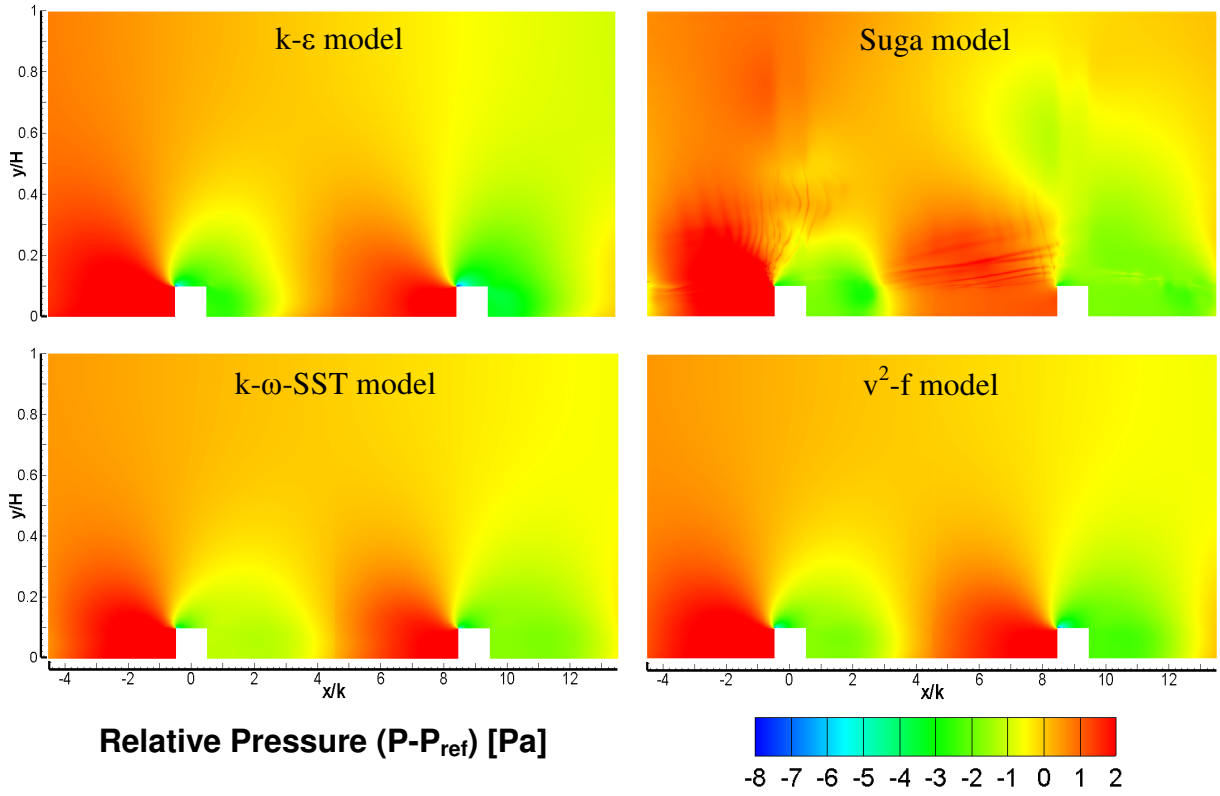

Figure 6.31 – Contour plots of the relative pressure for *P/k* = 9; 1s for various turbulence models.

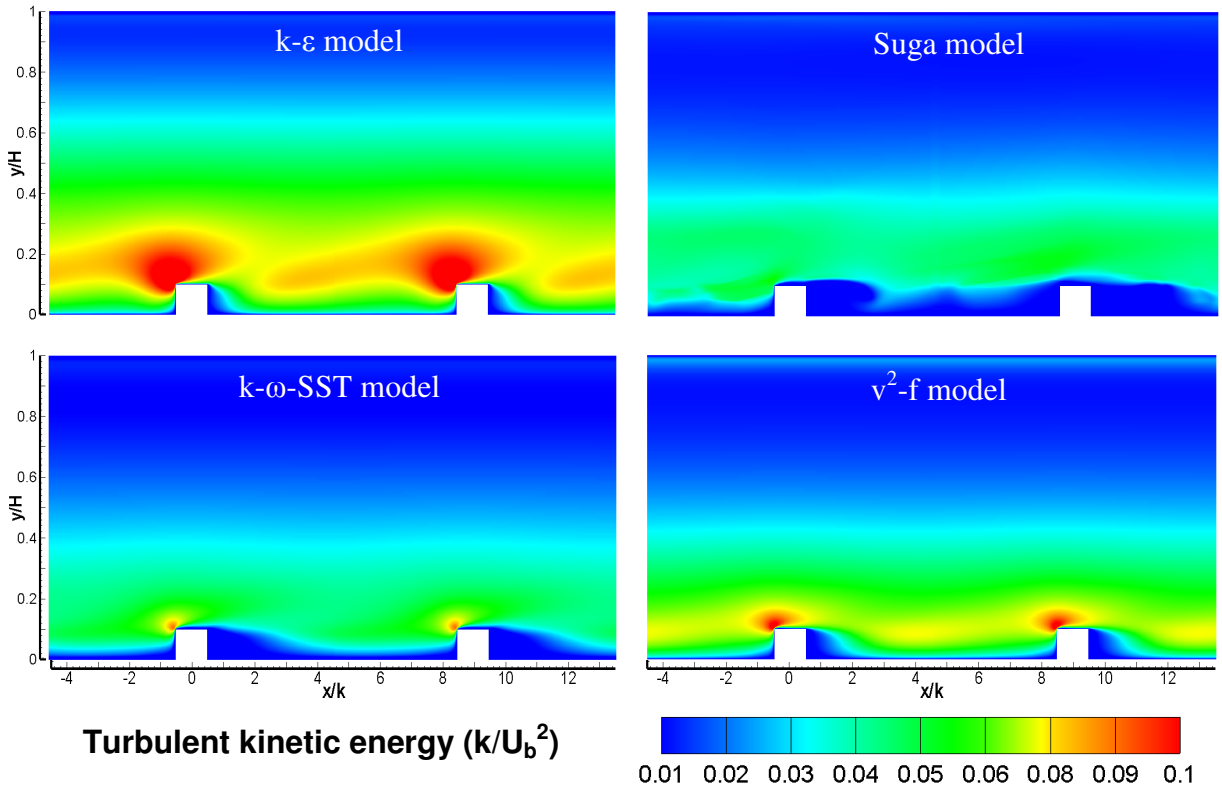

Figure 6.32 – Contour plots of the turbulent kinetic energy for *P/k* = 9; 1s for various turbulence models.

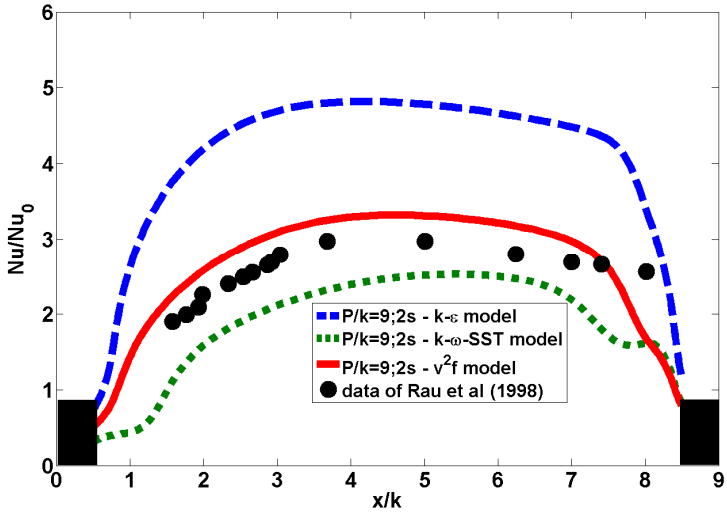

Figure 6.33 – Nusselt distributions for *P/k* = 9; 2s and various turbulence models.

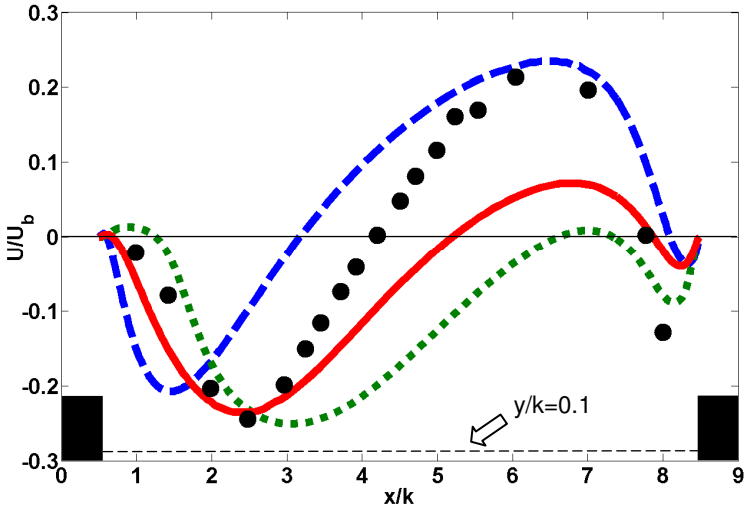

Figure 6.34 – Streamwise velocity distributions for *P/k* = 9; 2s at *y/k* = 0.1 for various turbulence models.

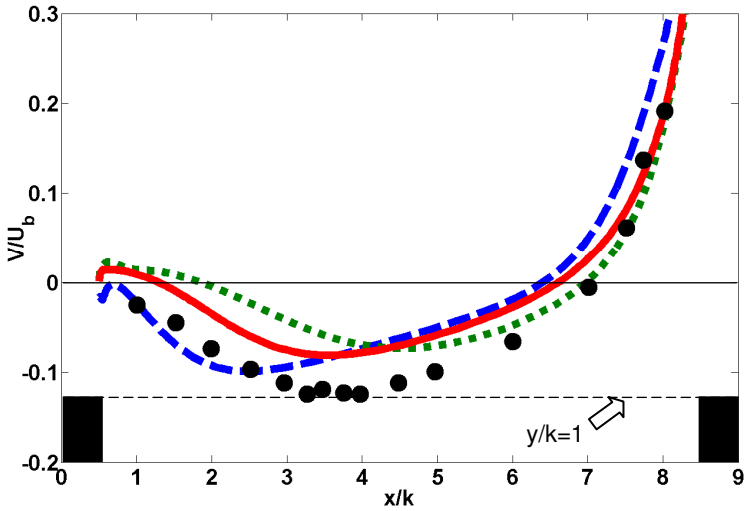

Figure 6.35 – Wall-normal velocity distributions for *P/k* = 9; 2s at *y/k* = 1 for various turbulence models.

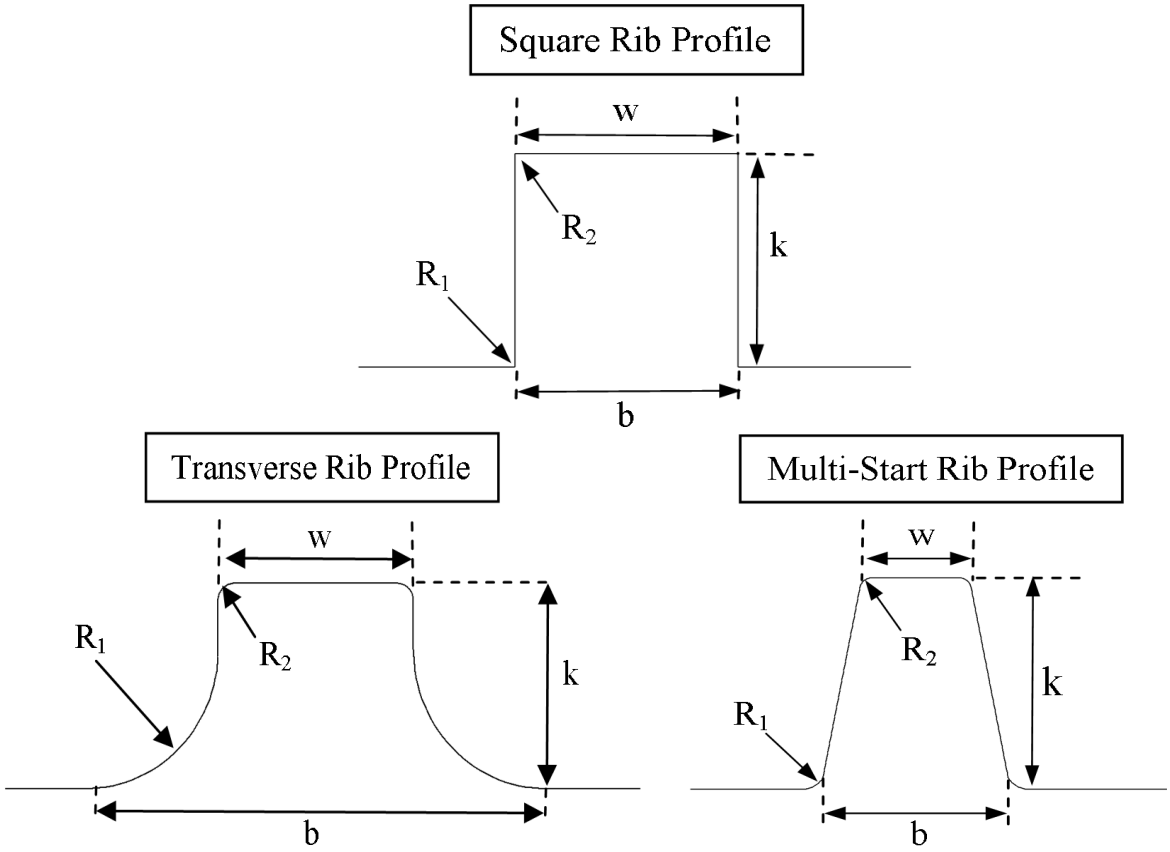

Figure 6.36 – Schematic of the Square, Transverse and Multi-Start Rib Profile designs.

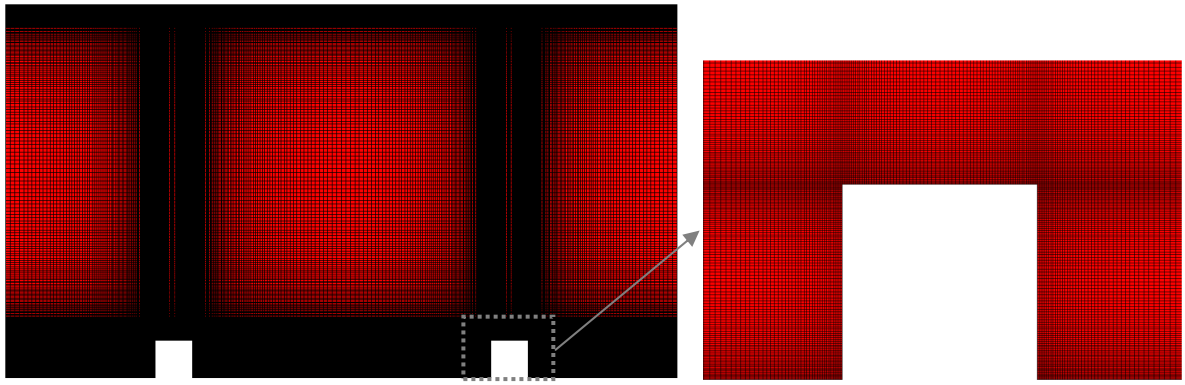

Figure 6.37 – Schematic of *P/k* = 9; 1s mesh with square rib profile (Mesh number 2).

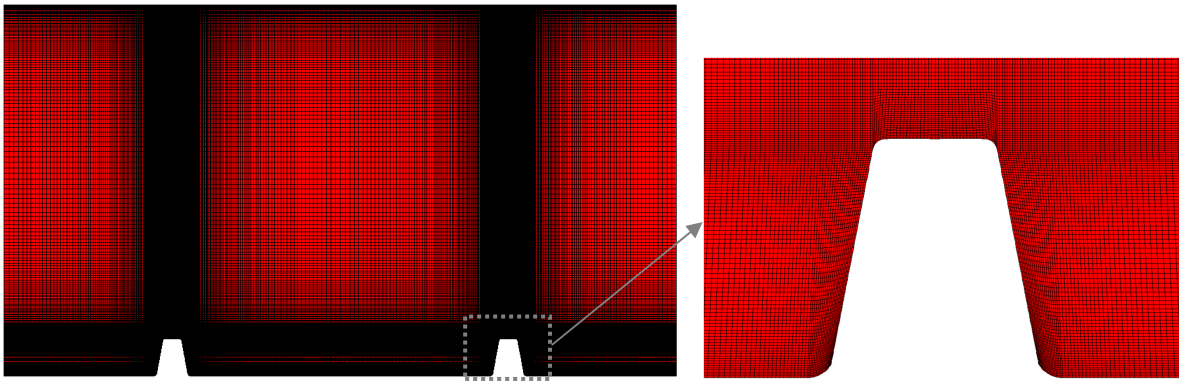

Figure 6.38 – Schematic of *P/k* = 9; 1s mesh with multi-start rib profile (Mesh number 5).

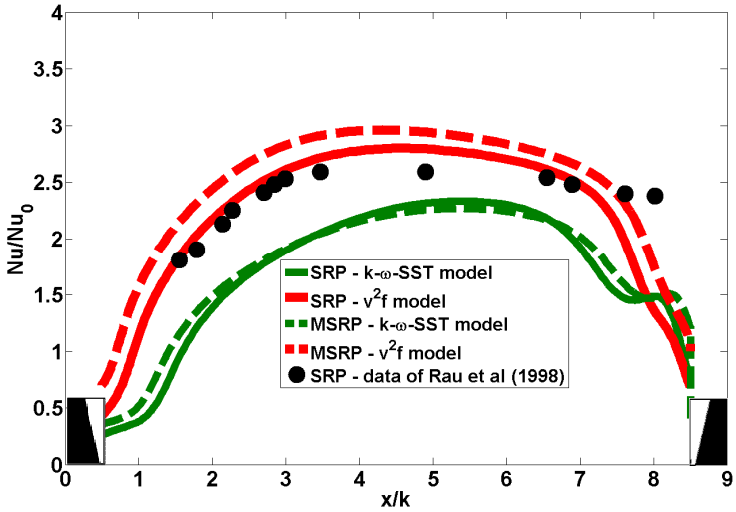

Figure 6.39 – Nusselt number distributions for P/k = 9; 1s and different rib profiles using the v^2-f and k-ω-SST models.

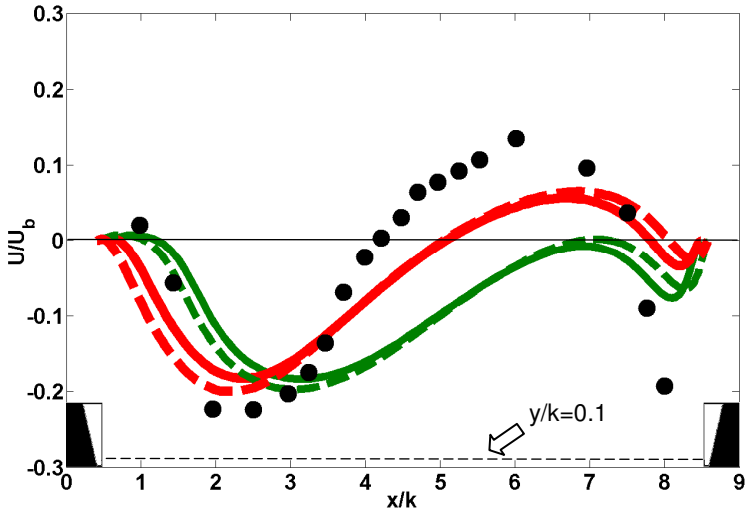

Figure 6.40 – Streamwise velocity distributions for P/k = 9; 1s at y/k = 0.1 and different rib profiles using the v^2-f and k-ω-SST models.

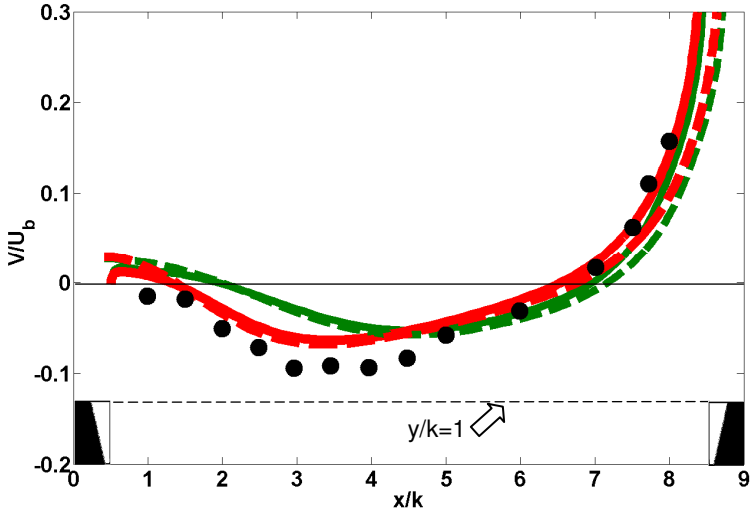

Figure 6.41 – Wall-normal velocity distributions for P/k = 9; 1s at y/k = 1 and different rib profiles using the v^2-f and k-ω-SST models.

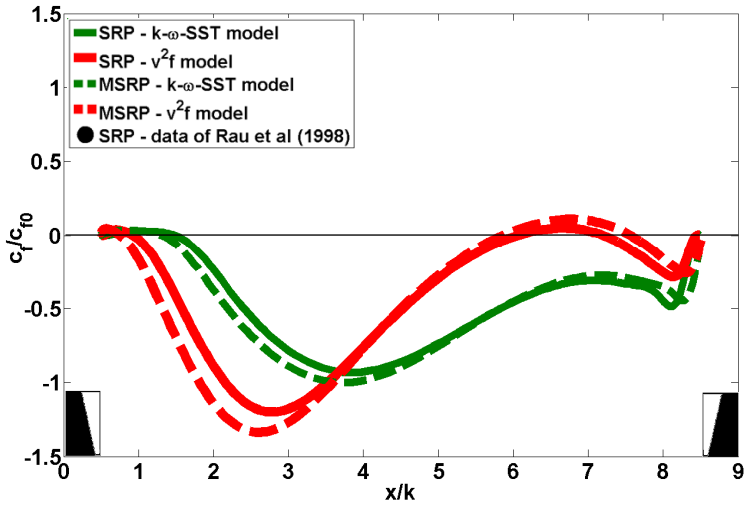

Figure 6.42 – Friction coefficient distributions for $P/k = 9$; 1s and different rib profiles using the v^2-f and k-ω-SST models.

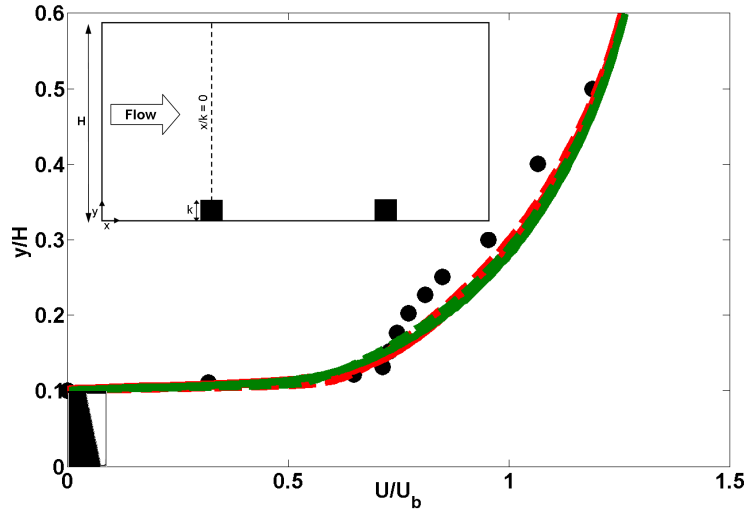

Figure 6.43 – Streamwise velocity distributions for $P/k = 9$; 1s on the rib-top ($x/k = 0$) for different rib profiles using the v^2-f and k-ω-SST models.

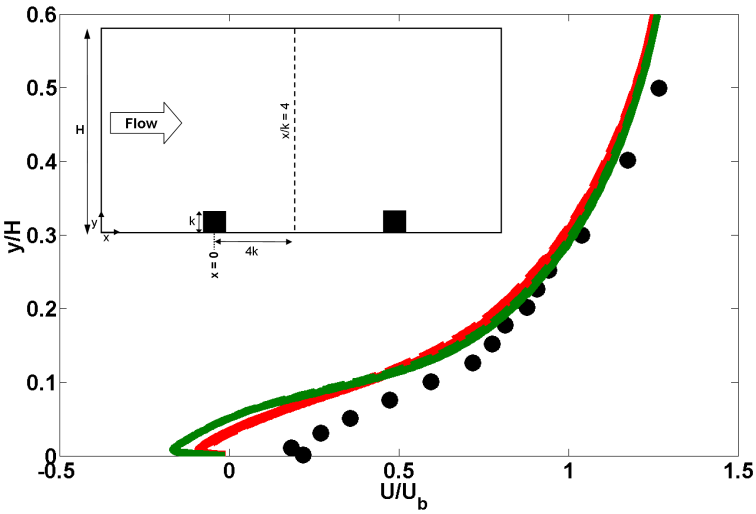

Figure 6.44 – Streamwise velocity distributions for $P/k = 9$; 1s at $x/k = 4$ and different rib profiles using the v^2-f and k-ω-SST models.

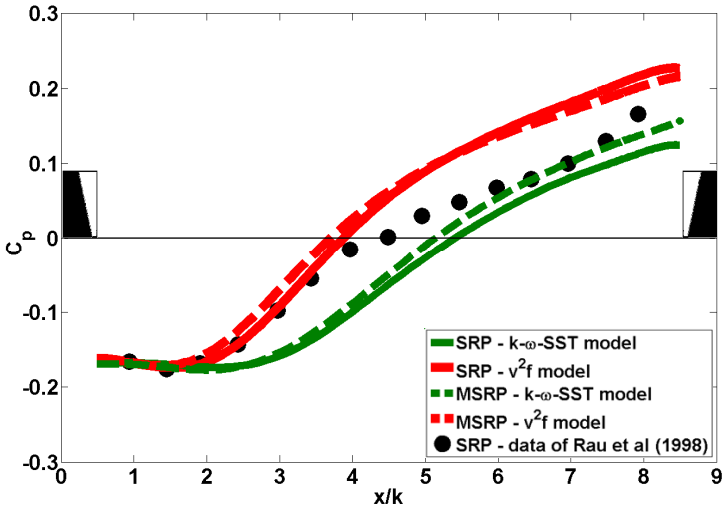

Figure 6.45 – Pressure coefficient distributions for P/k = 9; 1s and different rib profiles using the v^2-f and k-ω-SST models.

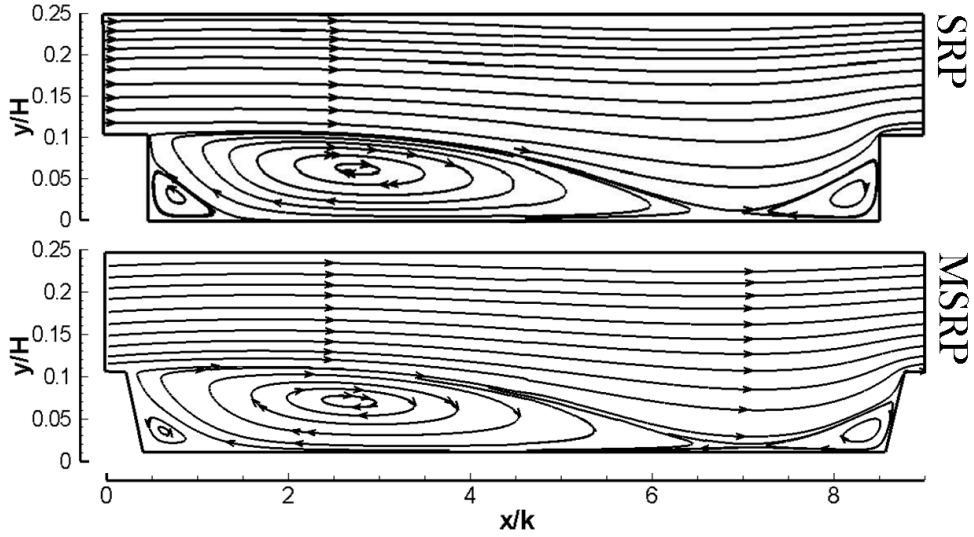

Figure 6.46 – Streamlines for P/k = 9; 1s and different rib profiles using the k-ω-SST model.

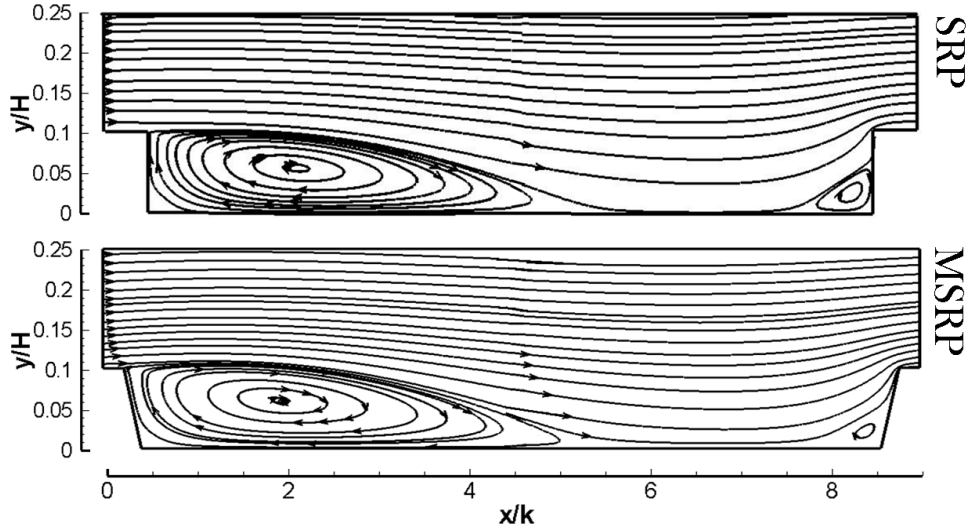

Figure 6.47 – Streamlines for P/k = 9; 1s and different rib profiles using the v^2-f model.

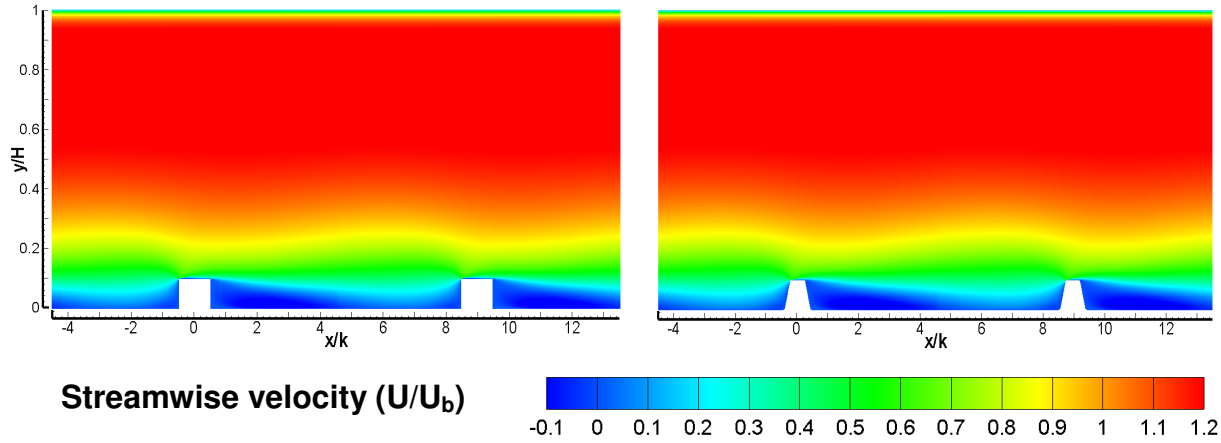

Figure 6.48 – Contour plots of the streamwise velocity for P/k = 9; 1s and different rib profiles using the v^2-f model.

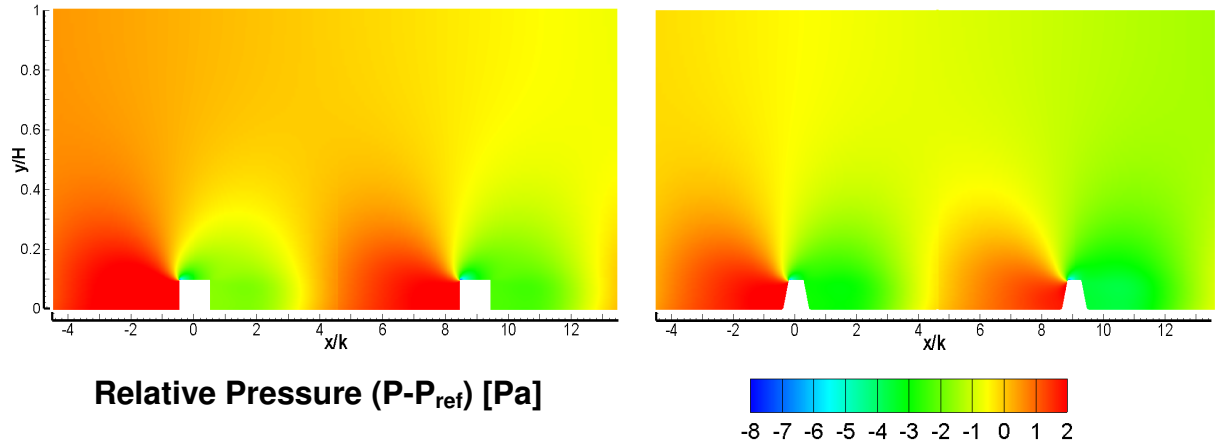

Figure 6.49 – Contour plots of the relative pressure for P/k = 9; 1s and different rib profiles using the v^2-f model.

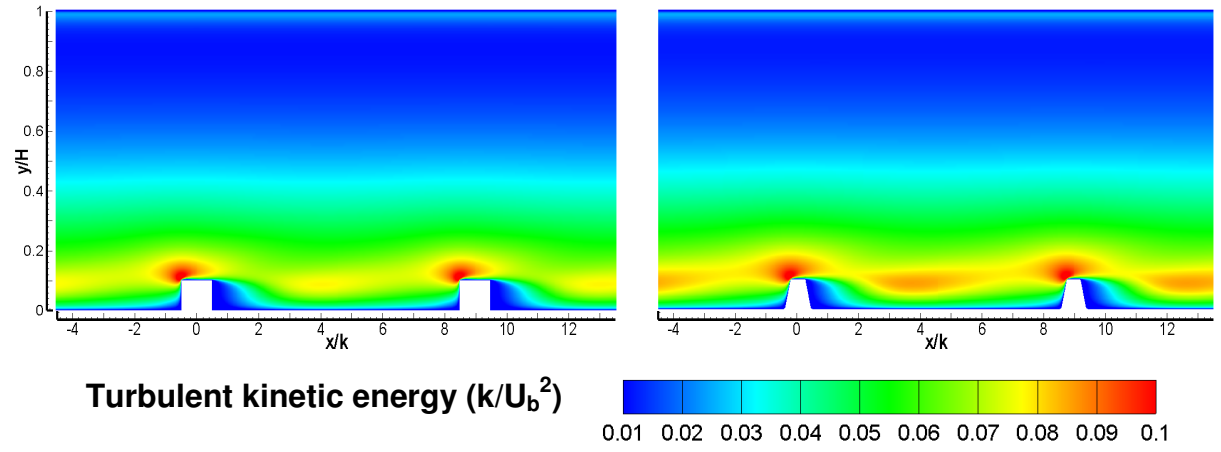

Figure 6.50 – Contour plots of the turbulent kinetic energy for P/k = 9; 1s and different rib profiles using the v^2-f model.

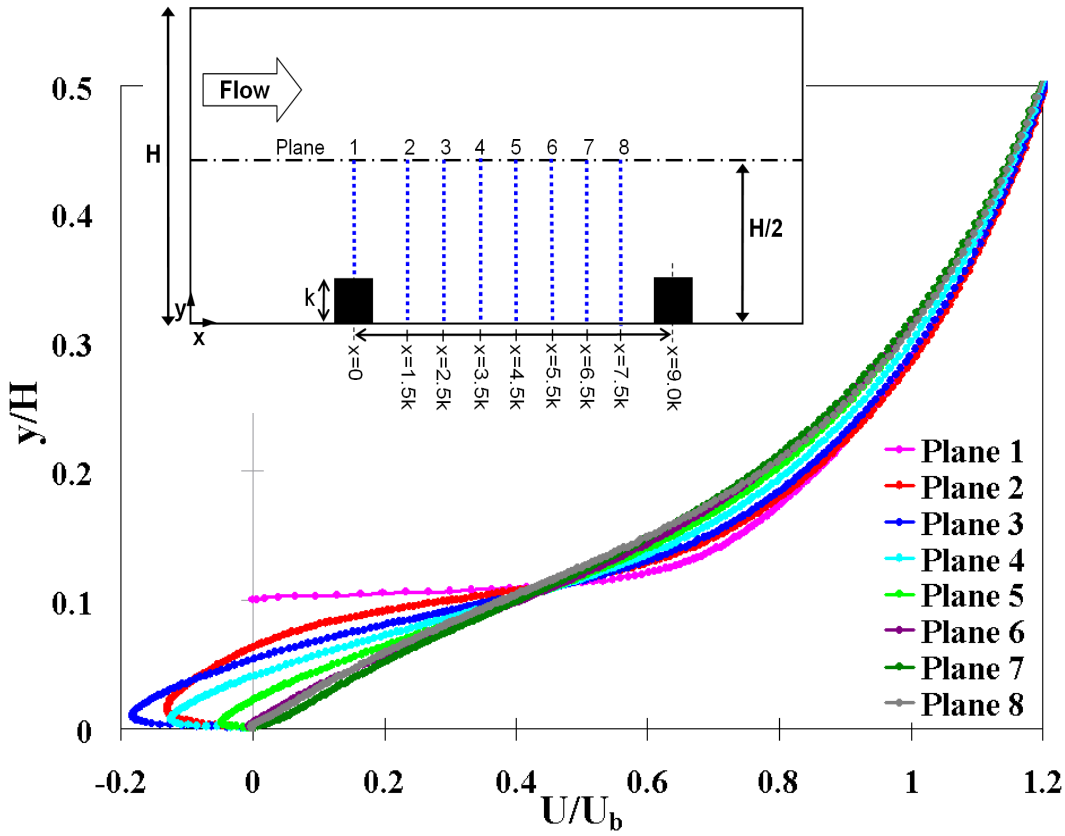

Figure 6.51 – Velocity profiles plotted on linear axes for $P/k = 9$; 1s using the v^2-f model.

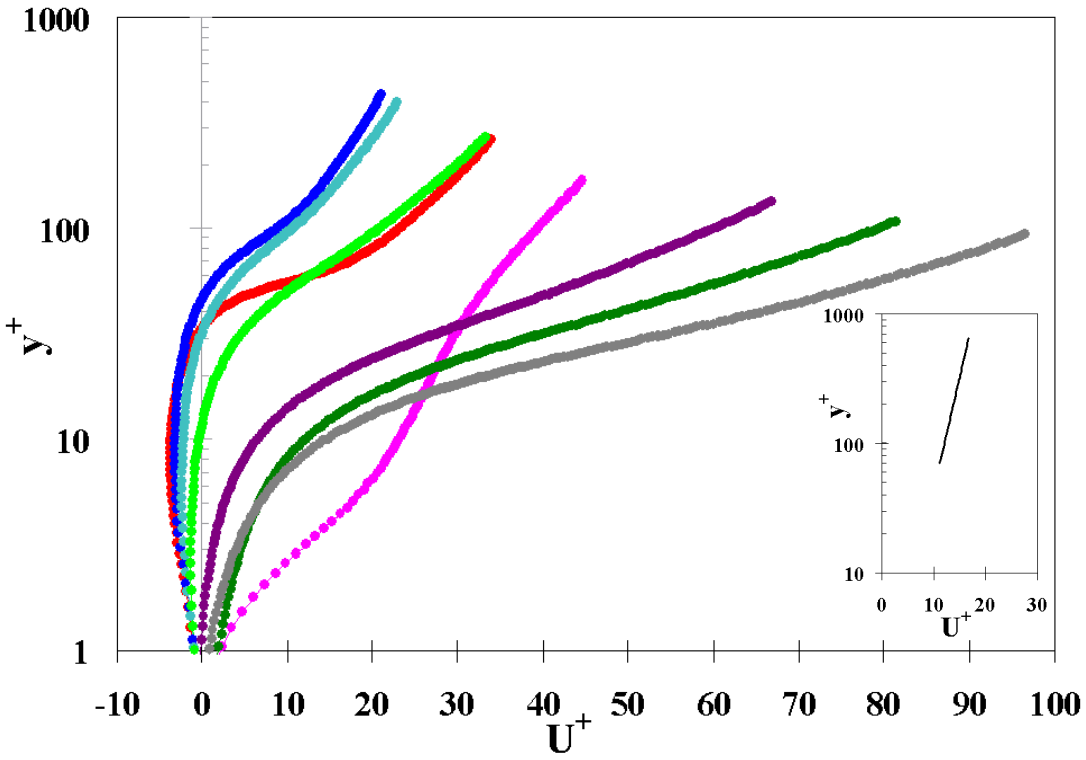

Figure 6.52 – Velocity profiles plotted on semi-logarithmic axes for $P/k = 9$; 1s using the v^2-f model.

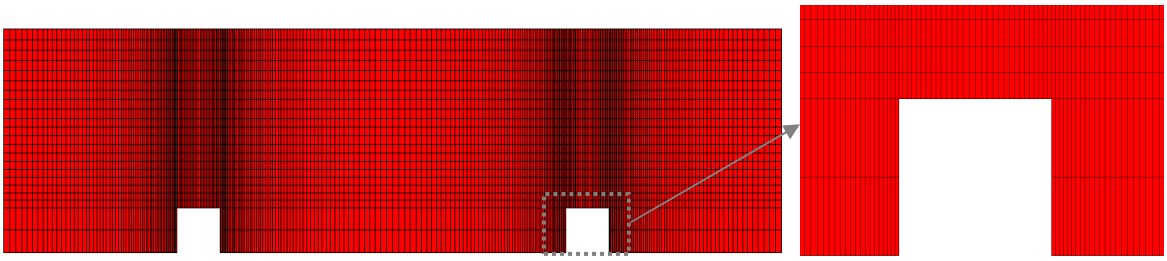

Figure 6.53 – Schematic of *P/k* = 9; 2s mesh for simulations with wall function (Mesh number 6).

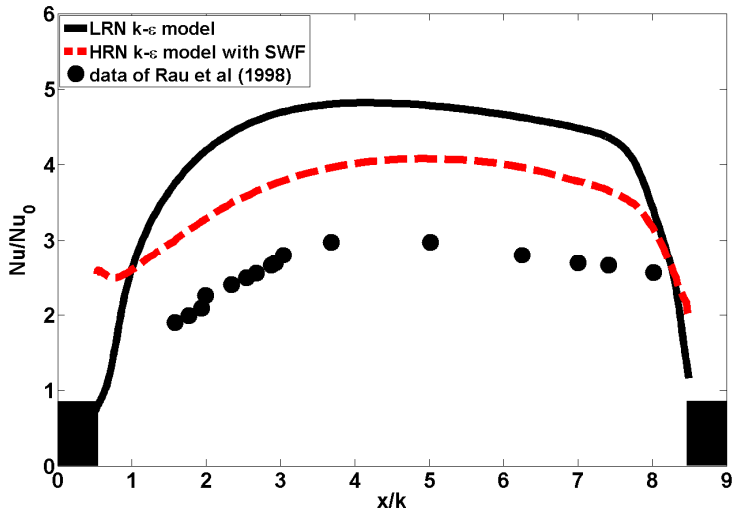

Figure 6.54 – Nusselt number distributions for *P/k* = 9; 2s and different near-wall treatments.

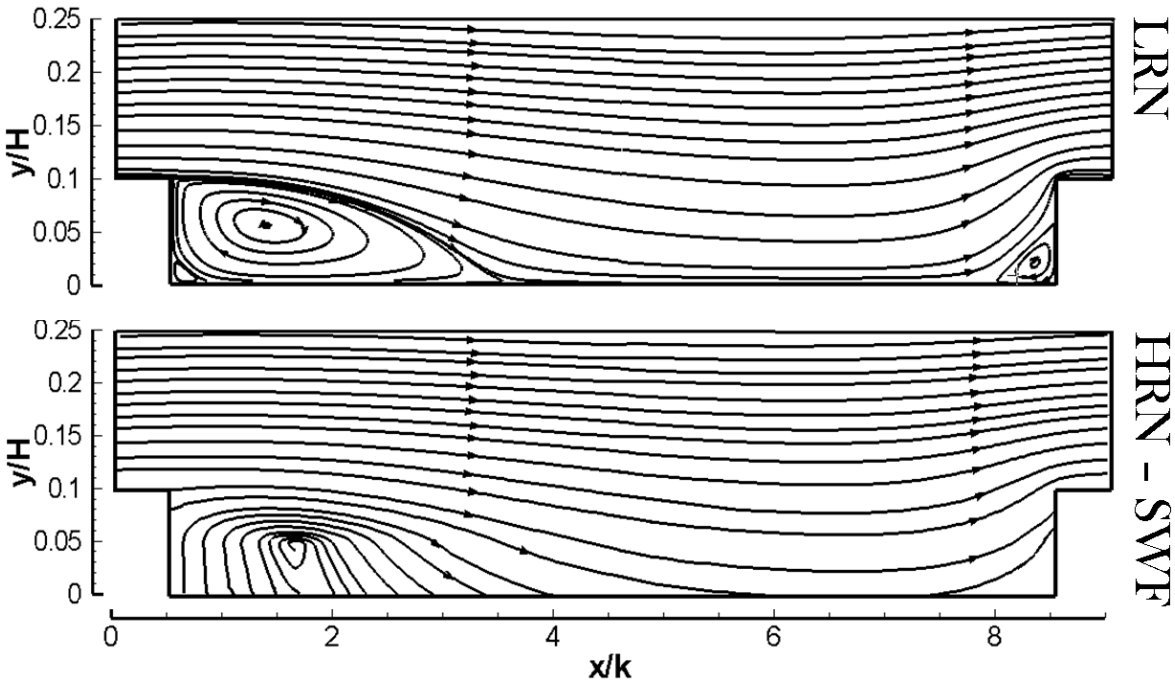

Figure 6.55 – Streamlines for *P/k* = 9; 2s and different near-wall treatments using the LRN and HRN *k-ε* model.

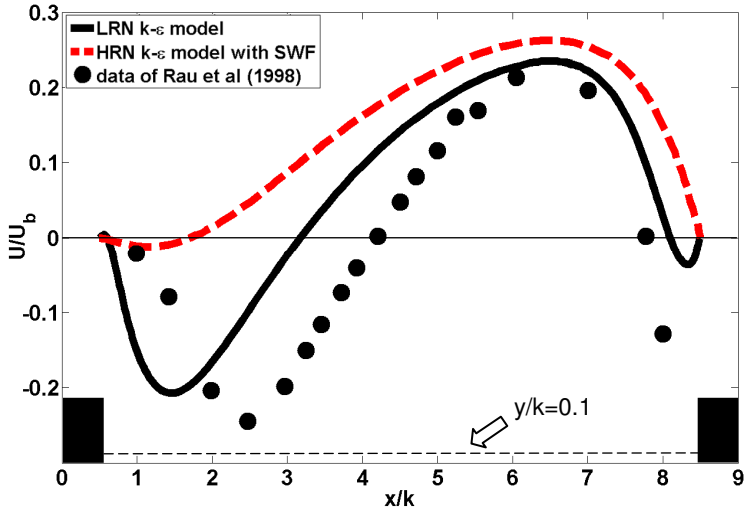

Figure 6.56 – Streamwise velocity distributions for P/k = 9; 2s at y/k = 0.1 for different near-wall treatments.

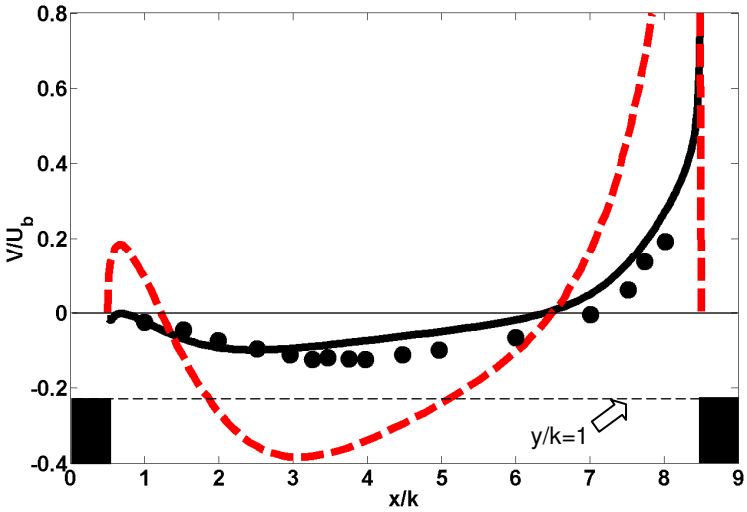

Figure 6.57 – Wall-normal velocity distributions for P/k = 9; 2s at y/k = 1 for different near-wall treatments.

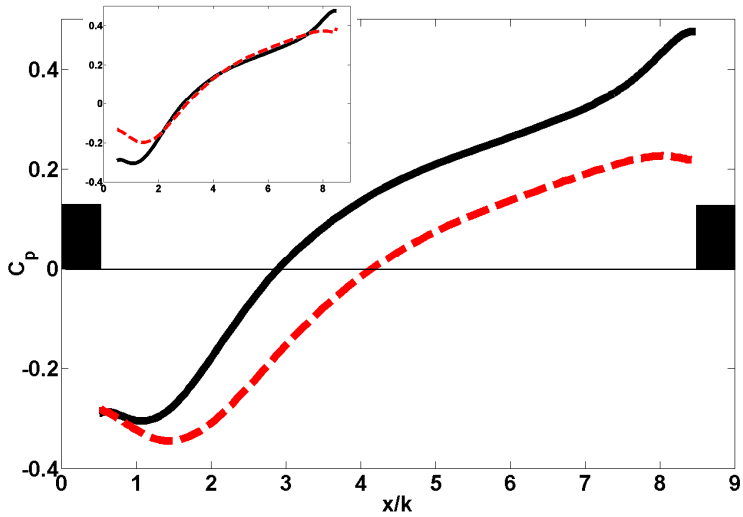

Figure 6.58 – Pressure coefficient distributions for P/k = 9; 2s and different near-wall treatments.

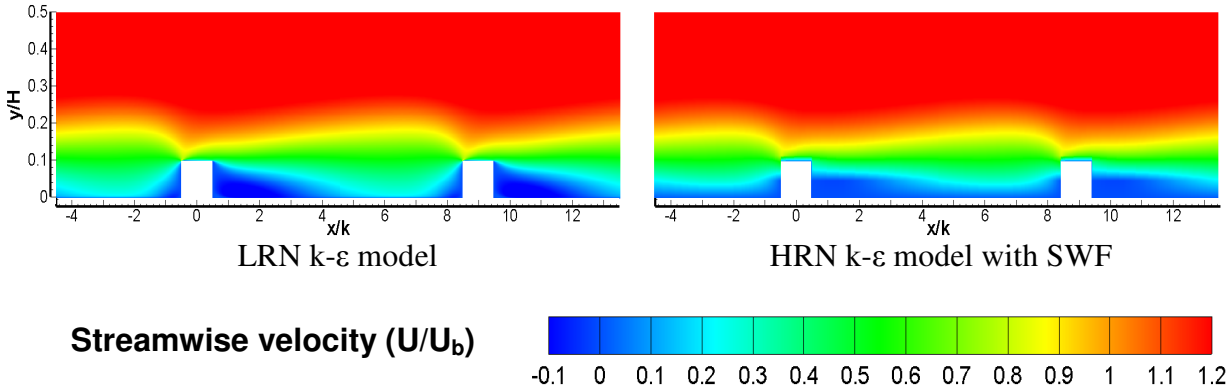

Figure 6.59 – Contour plots of the streamwise velocity for *P/k* = 9; 2s and different near-wall treatments.

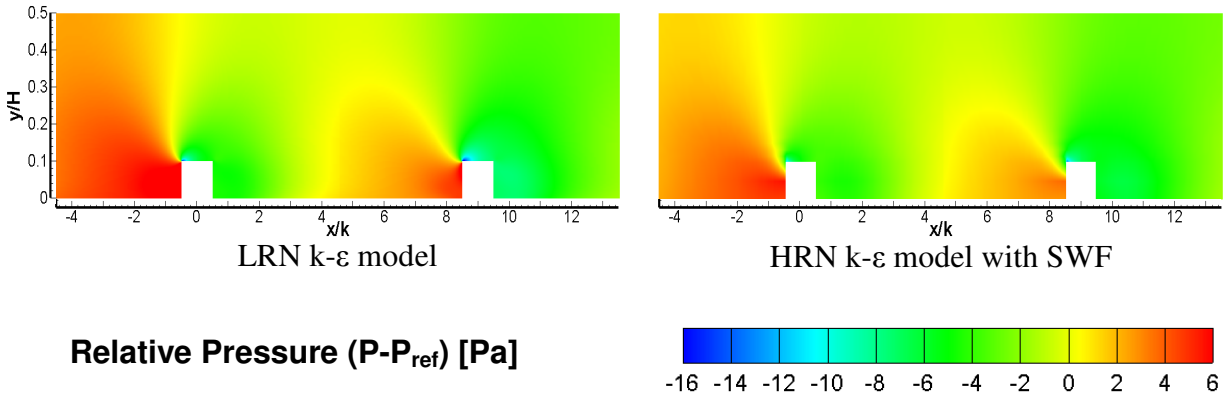

Figure 6.60 – Contour plots of the relative pressure for *P/k* = 9; 2s and different near-wall treatments.

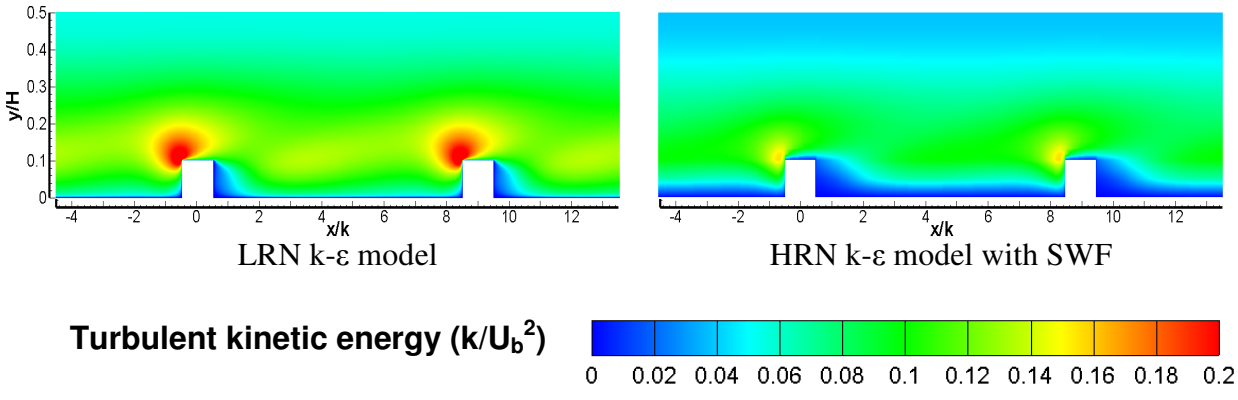

Figure 6.61 – Contour plots of the turbulent kinetic energy for *P/k* = 9; 2s and different near-wall treatments.

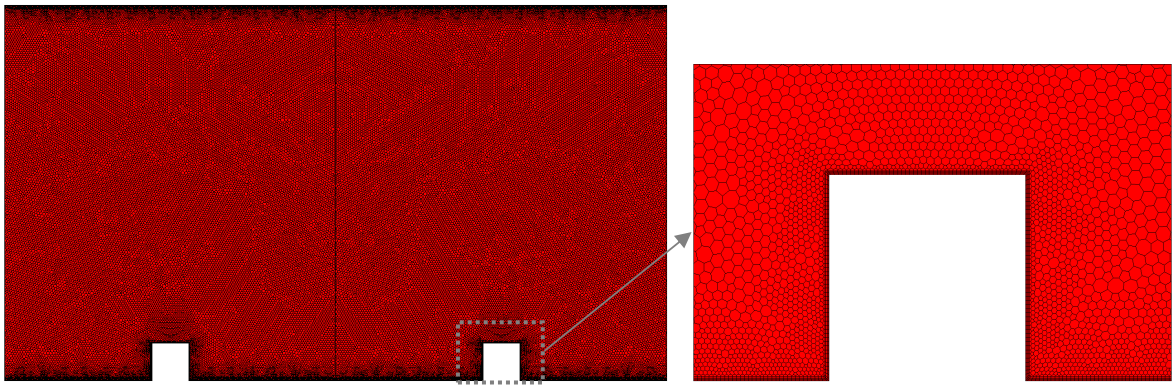

Figure 6.62 – Schematic of *P/k* = 9; 1s mesh with polyhedral unstructured cells (Mesh number 12).

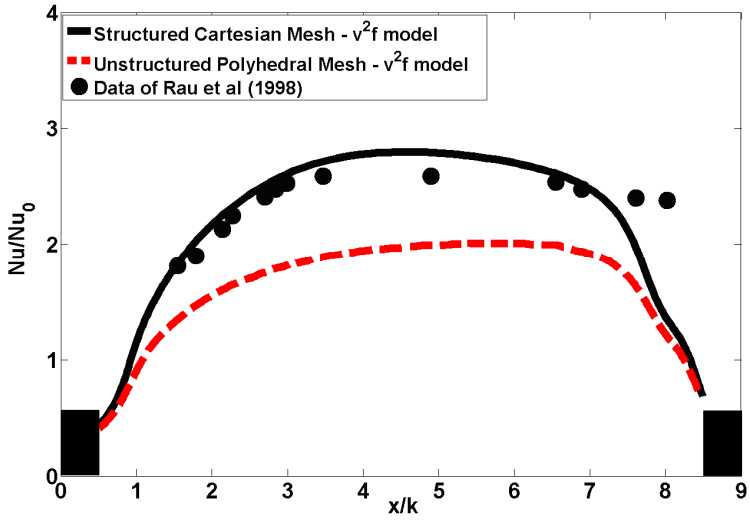

Figure 6.63 – Nusselt number distributions for *P/k* = 9; 1s with structured and unstructured meshes using the v^2-*f* model.

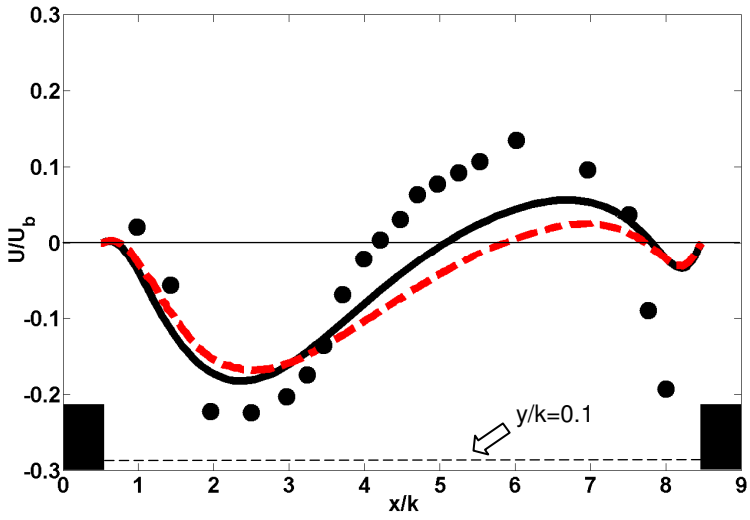

Figure 6.64 – Streamwise velocity distributions for *P/k* = 9; 1s with structured and unstructured meshes using the v^2-*f* model.

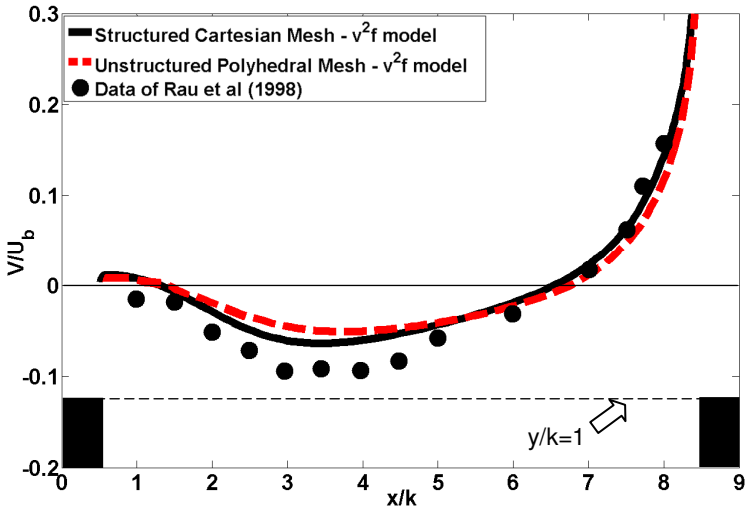

Figure 6.65 – Wall-normal velocity distributions for P/k = 9; 1s with structured and unstructured meshes using the v^2-f model.

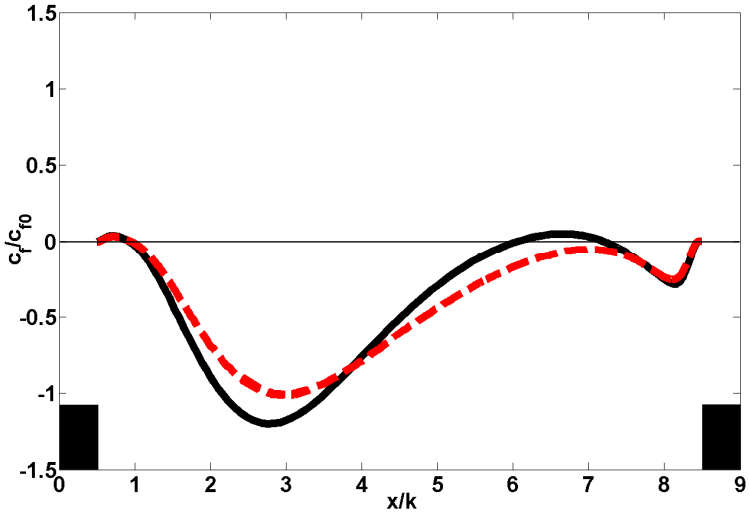

Figure 6.66 – Friction coefficient distributions for P/k = 9; 1s with structured and unstructured meshes using the v^2-f model.

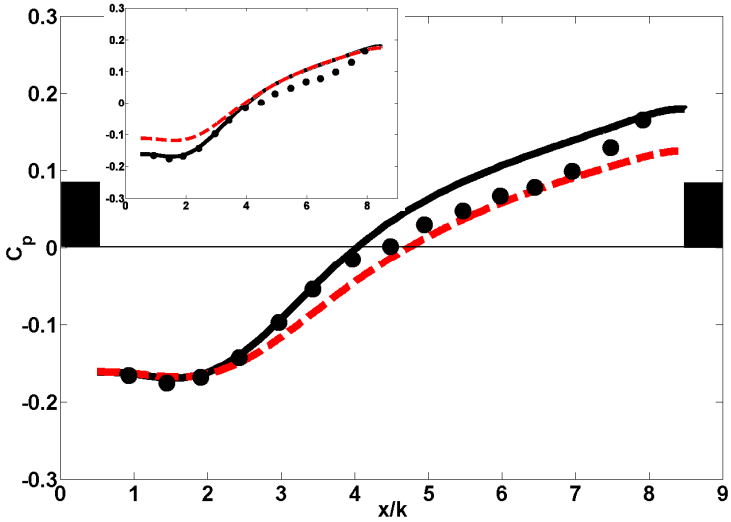

Figure 6.67 – Pressure coefficient distributions for P/k = 9; 1s with structured and unstructured meshes using the v^2-f model.

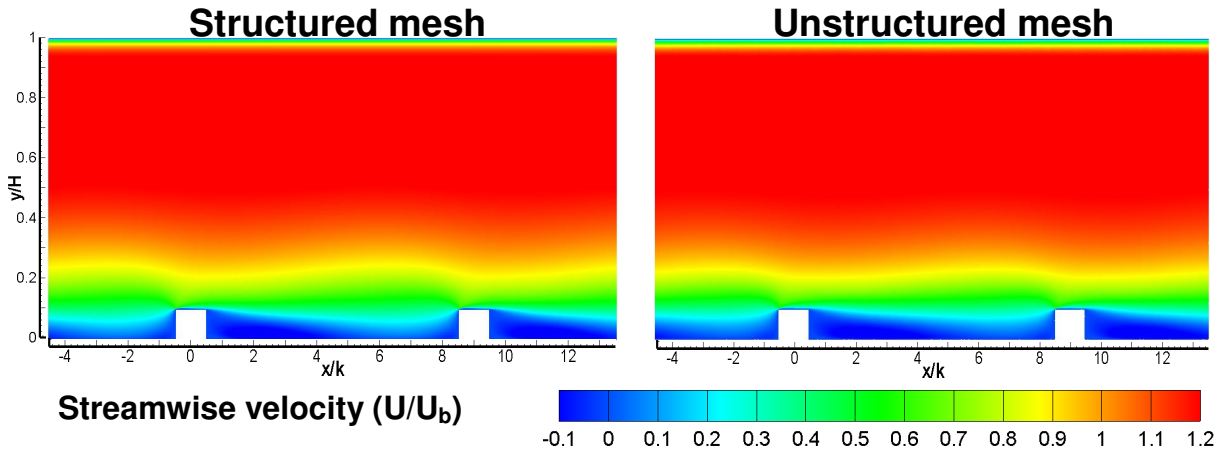

Figure 6.68 – Contour plots of the streamwise velocity for P/k = 9; 1s and different mesh types using the v^2-f model.

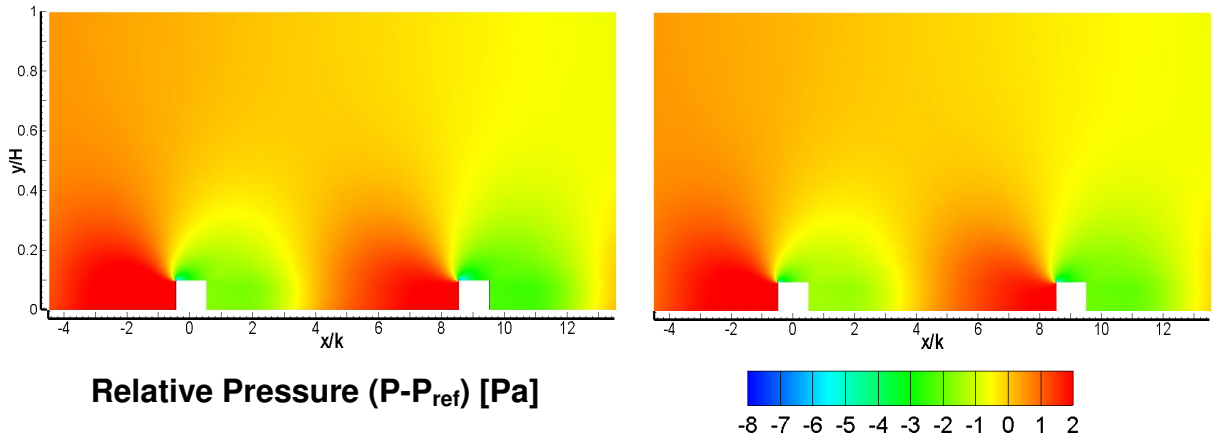

Figure 6.69 – Contour plots of the relative pressure for P/k = 9; 1s and different mesh types using the v^2-f model.

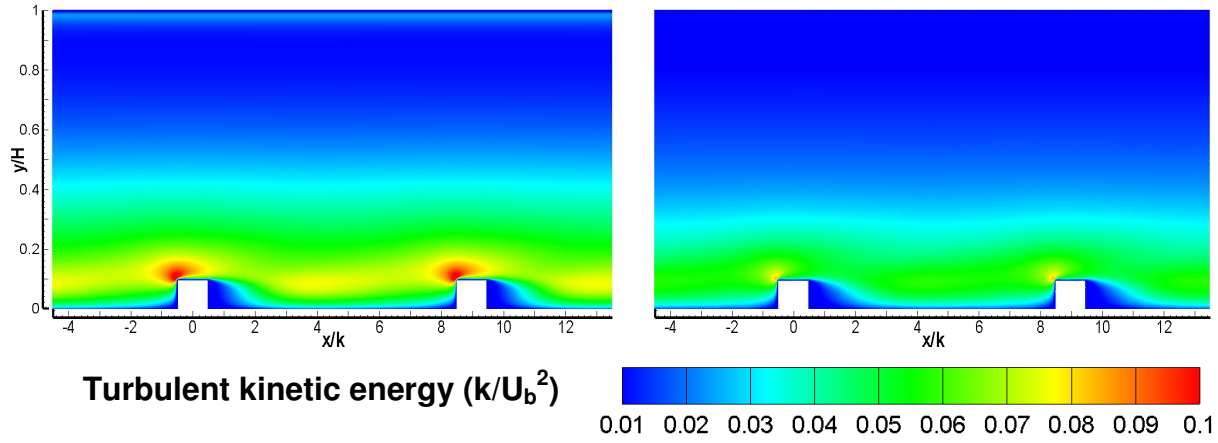

Figure 6.70 – Contour plots of the turbulent kinetic energy for P/k = 9; 1s and different mesh types using the v^2-f model.

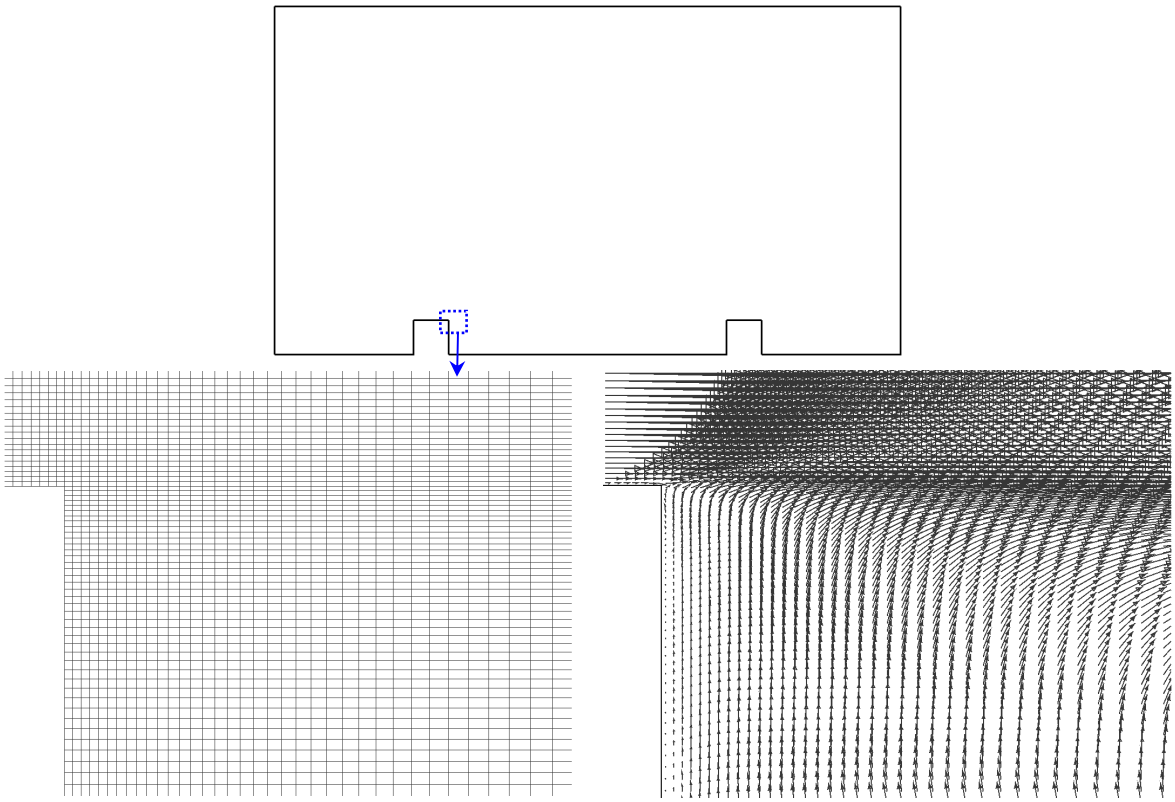

Figure 6.71 – Schematic of the mesh and a velocity vector representation of a small section near a rib for the structured mesh.

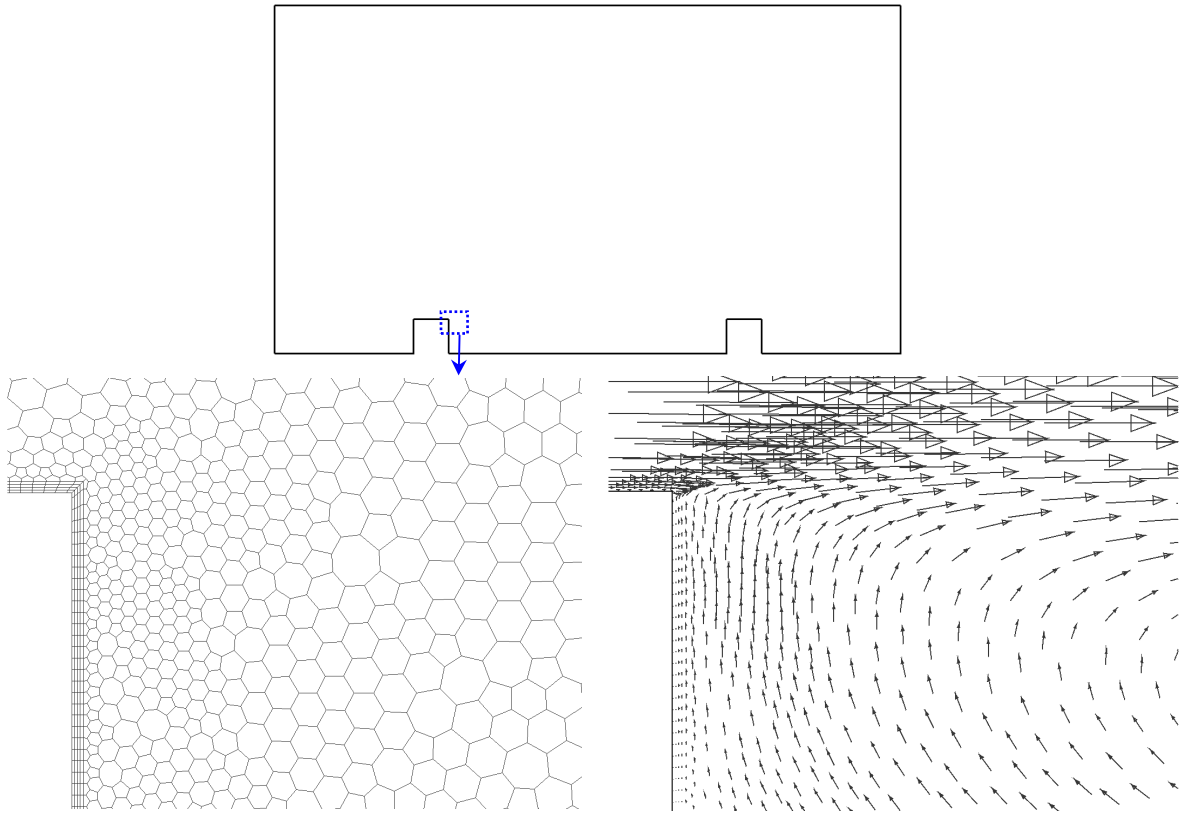

Figure 6.72 – Schematic of the mesh and a velocity vector representation of a small section near a rib for the unstructured mesh.

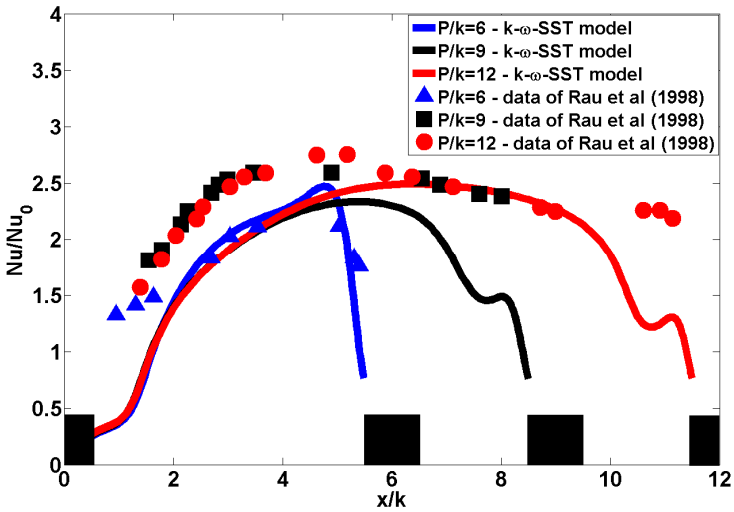

Figure 6.73 – Nusselt number distributions for *P/k* = 6, 9 and 12 using the *k-ω-SST* model.

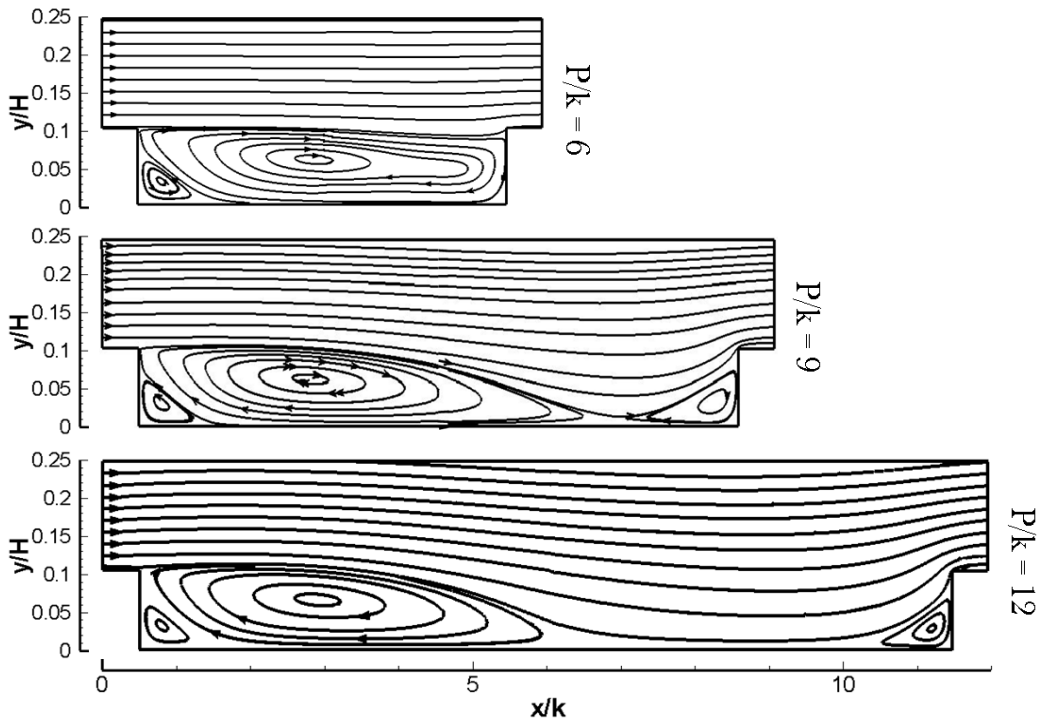

Figure 6.74 – Streamlines for *P/k* = 6, 9 and 12 using the *k-ω-SST* model.

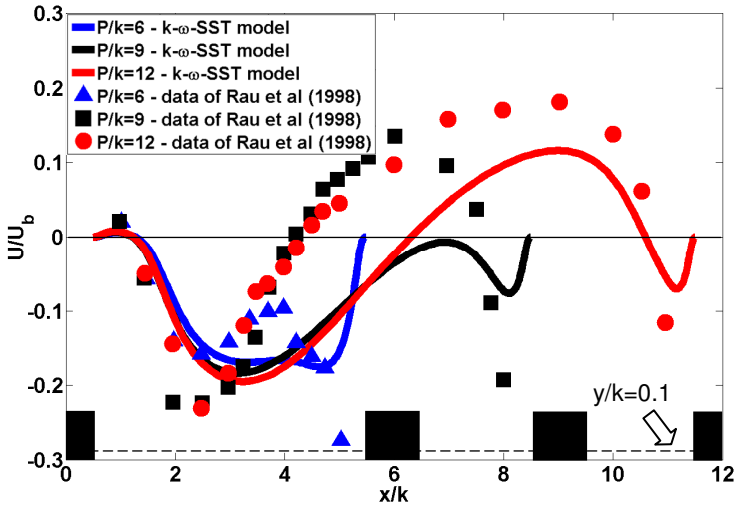

Figure 6.75 – Streamwise velocity distributions for P/k = 6, 9 and 12 at y/k = 0.1 using the *k-ω-SST* model.

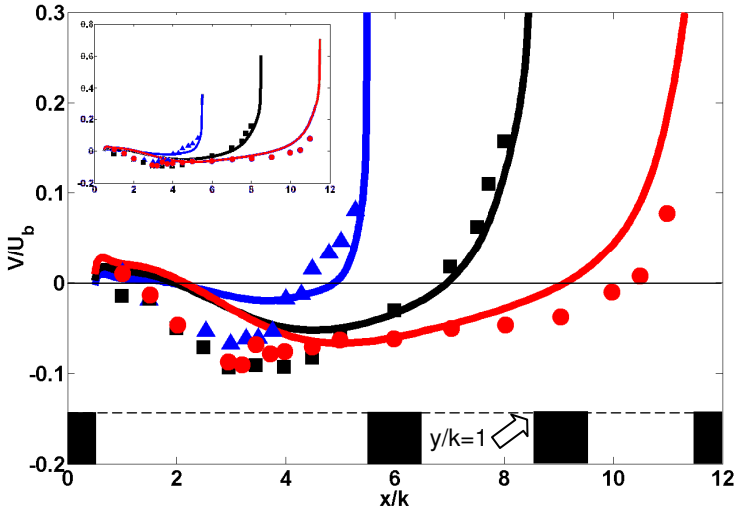

Figure 6.76 – Wall-normal velocity distributions for P/k = 6, 9 and 12 at y/k = 1 using the *k-ω-SST* model.

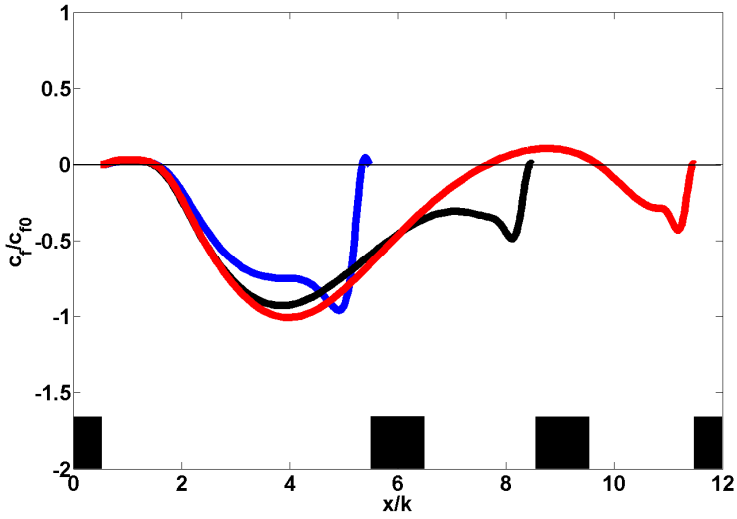

Figure 6.77 – Friction coefficient distributions for P/k = 6, 9 and 12 using the *k-ω-SST* model.

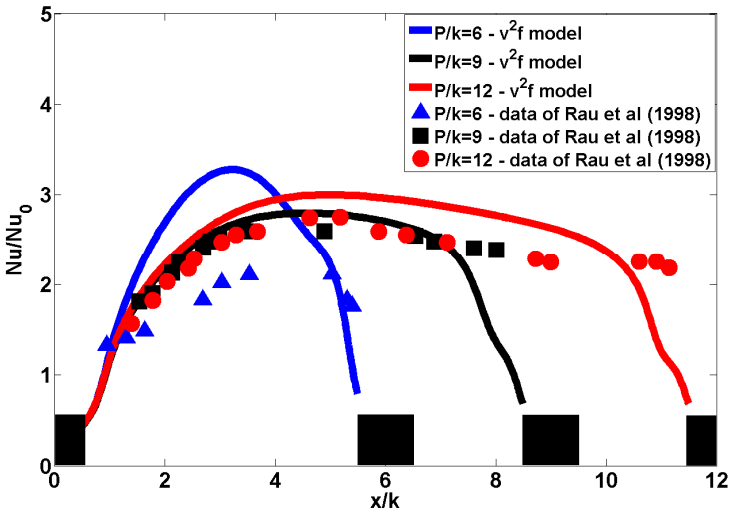

Figure 6.78 – Nusselt number distributions for *P/k* = 6, 9 and 12 using the v^2-*f* model.

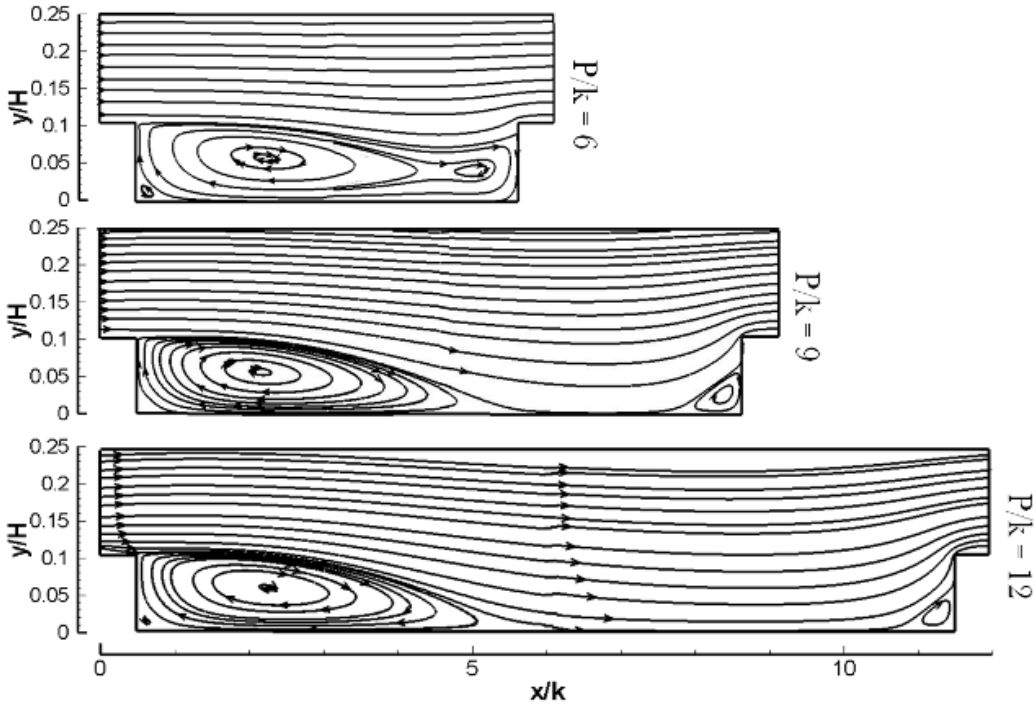

Figure 6.79 – Streamlines for *P/k* = 6, 9 and 12 using the v^2-*f* model.

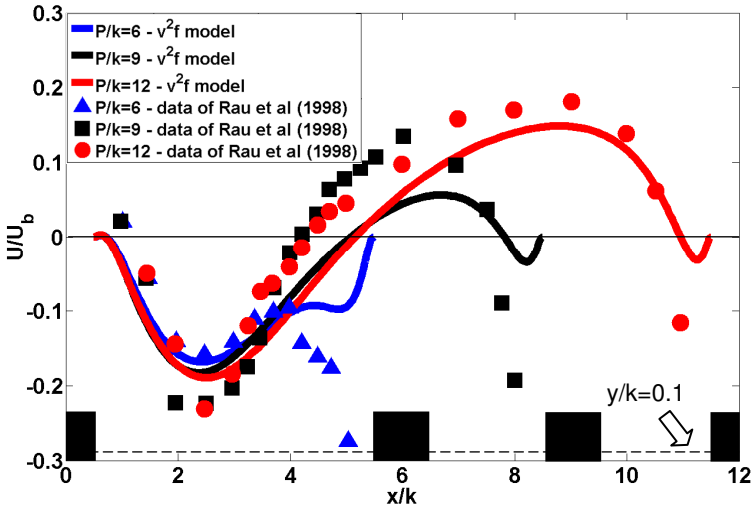

Figure 6.80 – Streamwise velocity distributions for P/k = 6, 9 and 12 at y/k = 0.1 using the v^2-f model.

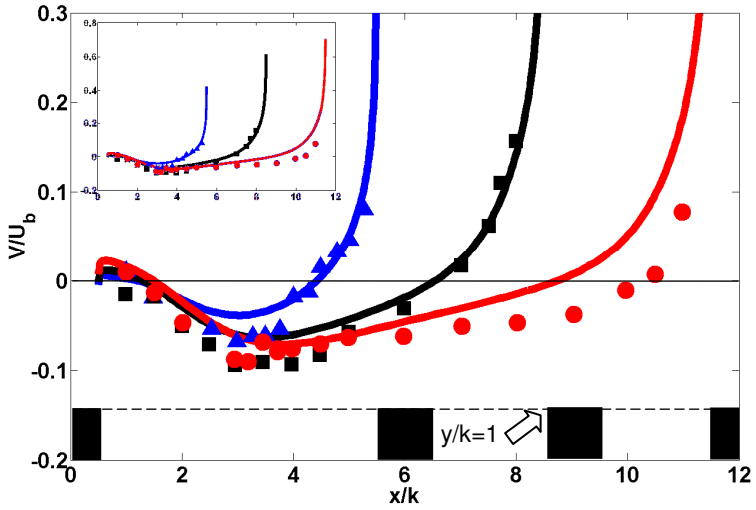

Figure 6.81 – Wall-normal velocity distributions for P/k = 6, 9 and 12 at y/k = 1 using the v^2-f model.

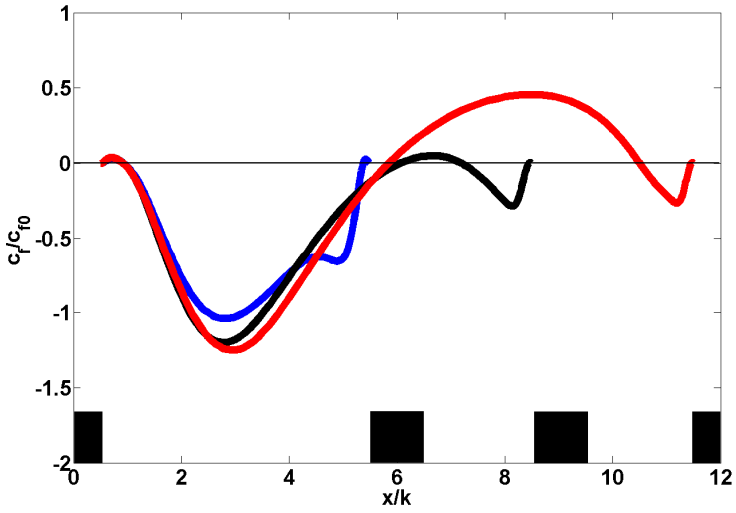

Figure 6.82 – Friction coefficient distributions for P/k = 6, 9 and 12 using the v^2-f model.

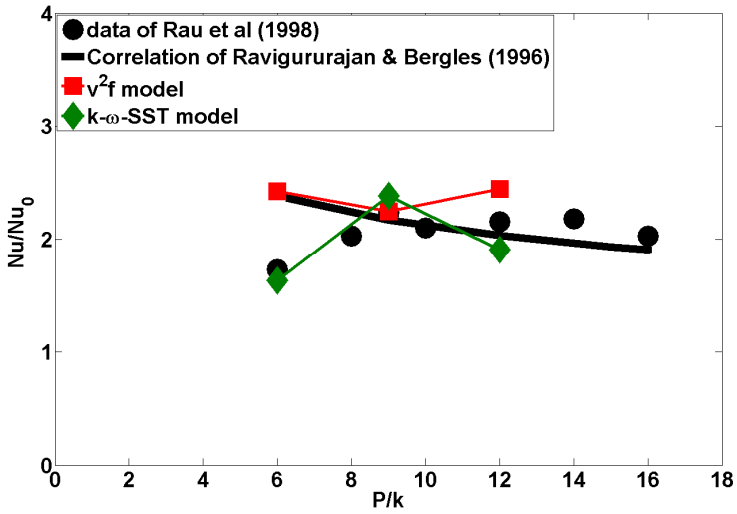

Figure 6.83 – Normalized average Nusselt number for various *P/k* ratios using the v^2-*f* and *k*-ω-*SST* models.

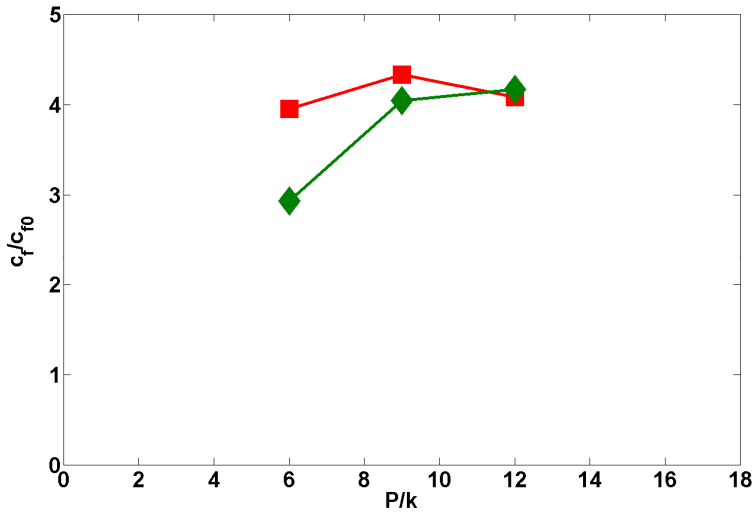

Figure 6.84 – Normalized average friction coefficient for various *P/k* ratios using the v^2-*f* and *k*-ω-*SST* models.

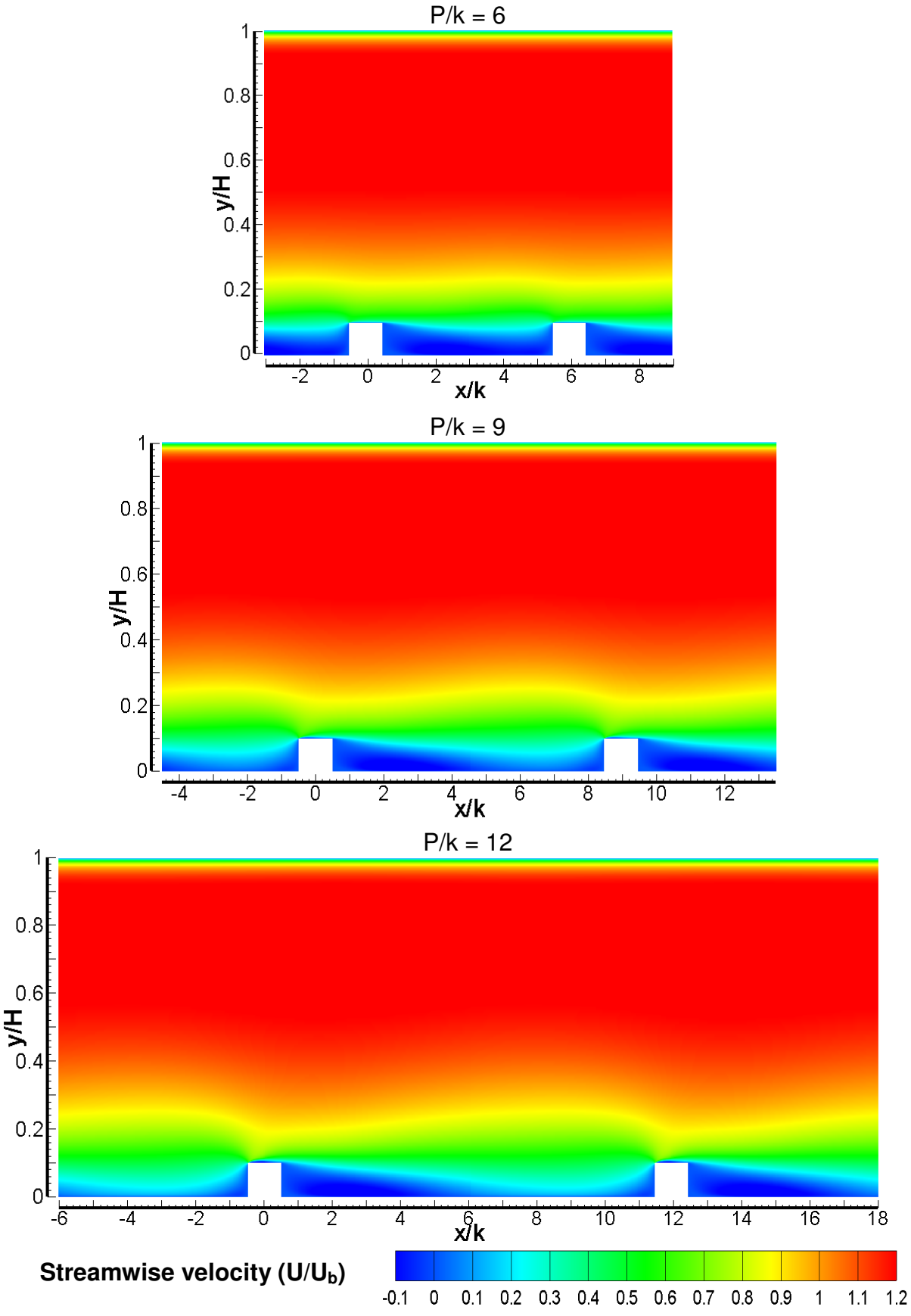

Figure 6.85 – Contour plot of the streamwise velocity for P/k = 6, 9 and 12 using the v^2-f model.

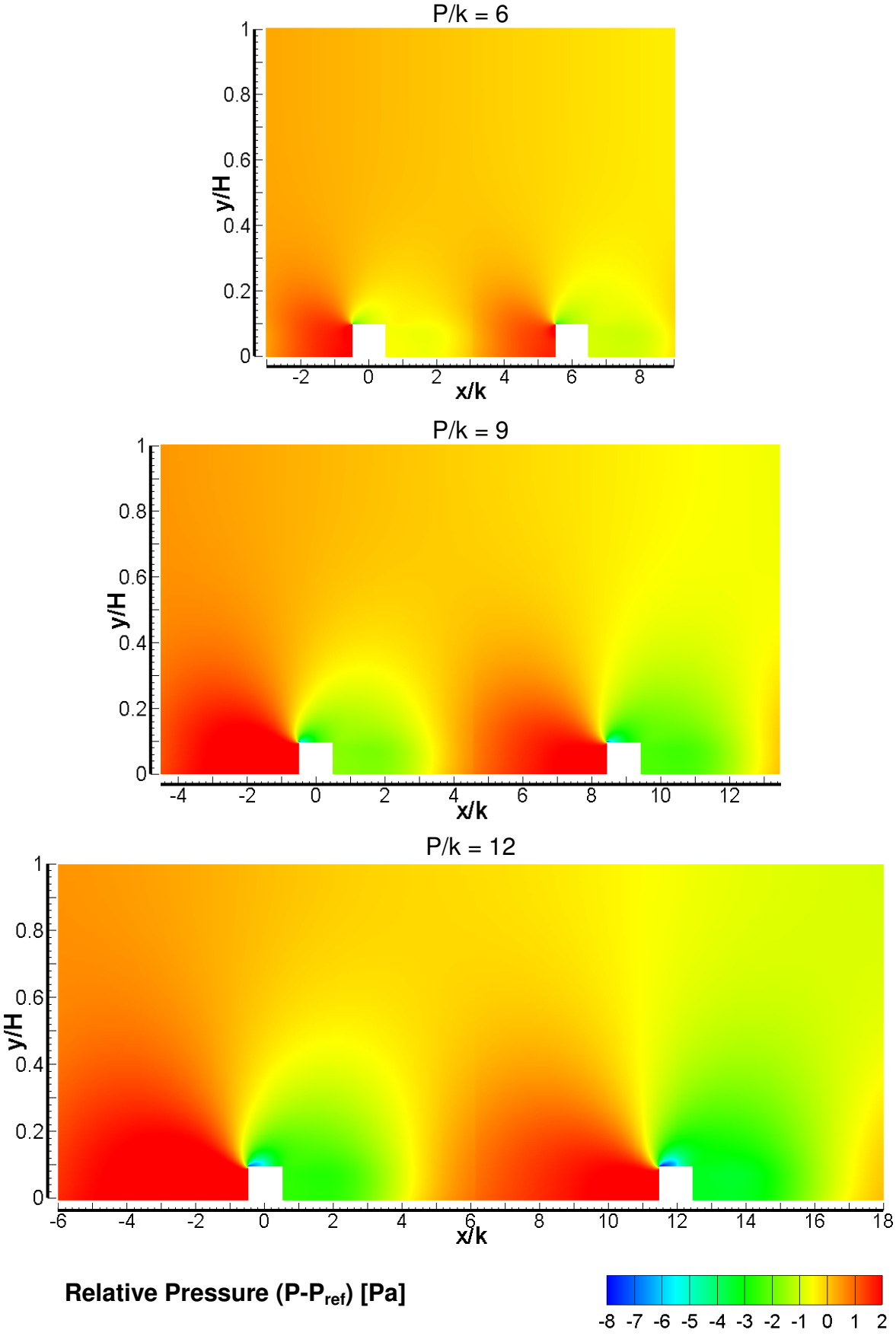

Figure 6.86 – Contour plot of the relative pressure for P/k = 6, 9 and 12 using the v^2-f model.

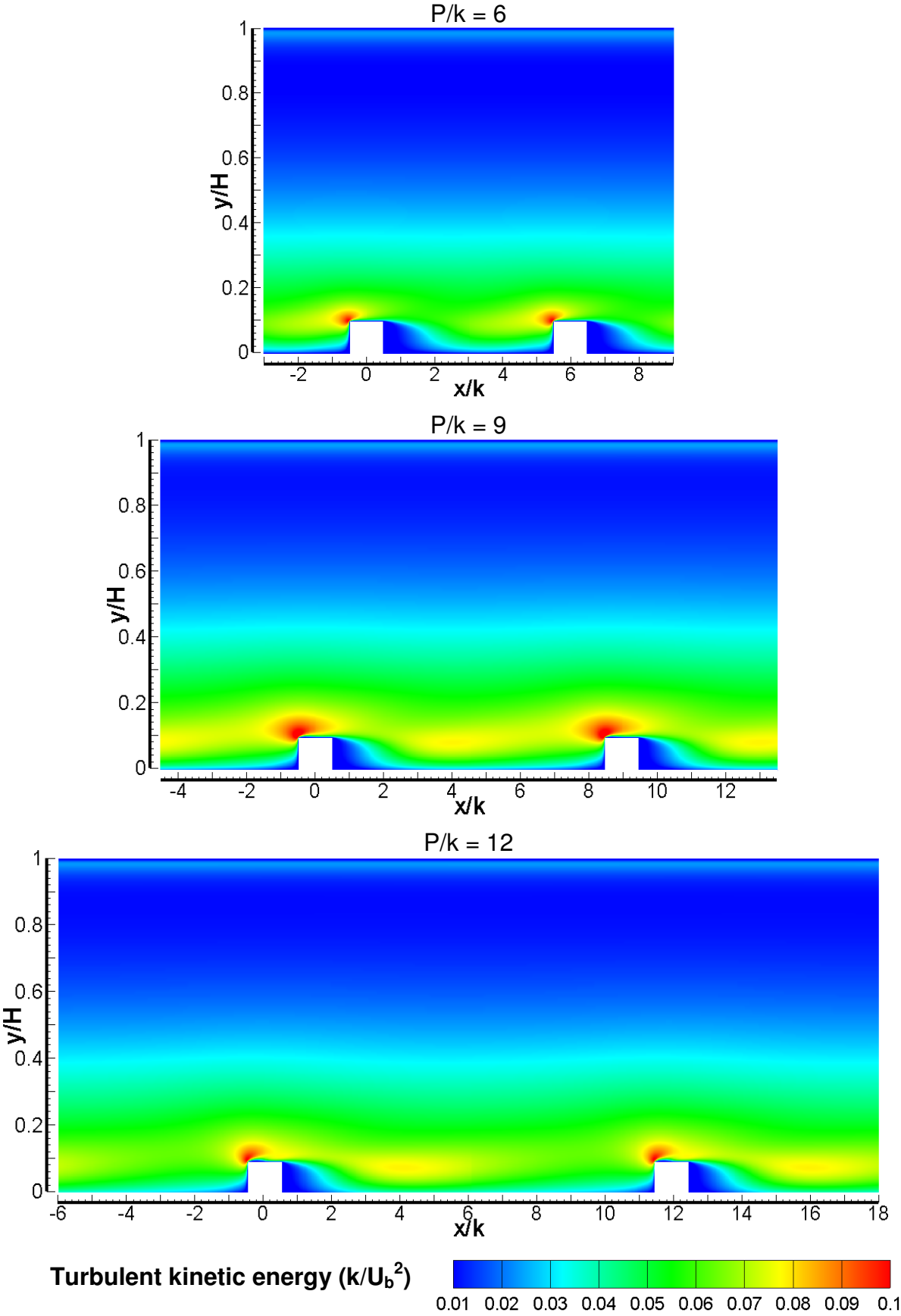

Figure 6.87 – Contour plot of the turbulent kinetic energy for P/k = 6, 9 and 12 using the v^2-f model.

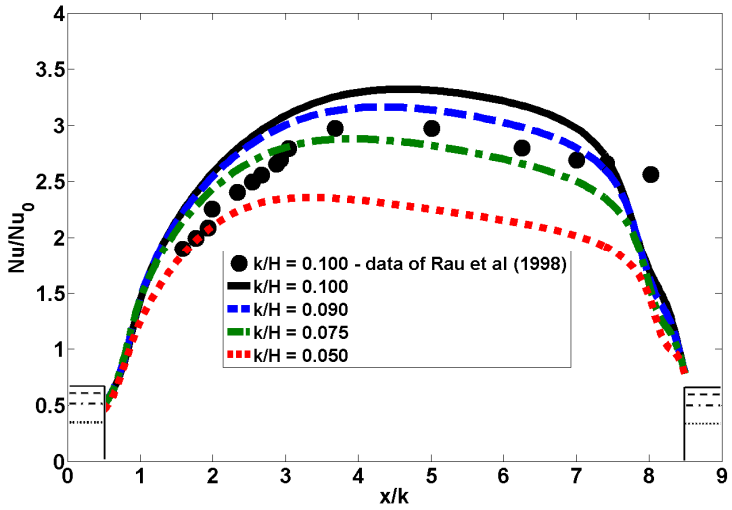

Figure 6.88 – Nusselt number distributions for P/k = 9; 2s and different rib heights using the v^2-f model.

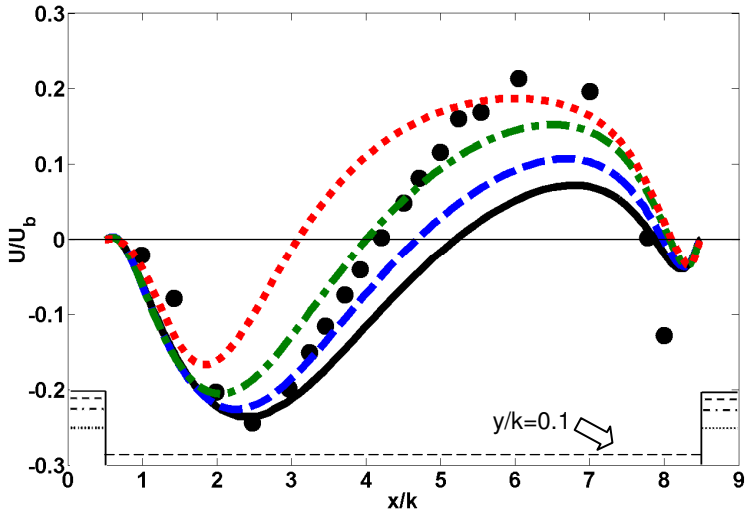

Figure 6.89 – Streamwise velocity distributions at y/k = 0.1 for P/k = 9; 2s and different rib heights using the v^2-f model.

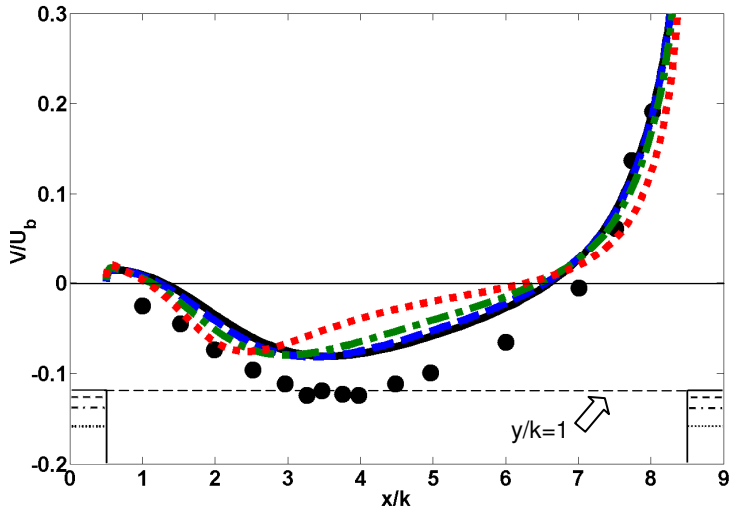

Figure 6.90 – Wall-normal velocity distributions at y/k = 1 for P/k = 9; 2s and different rib heights using the v^2-f model.

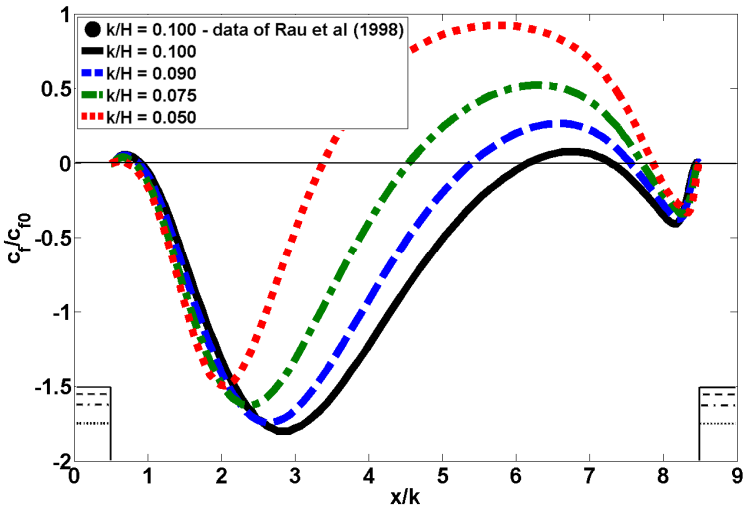

Figure 6.91 – Friction coefficient distributions for $P/k = 9$; 2s and different rib heights using the v^2-f model.

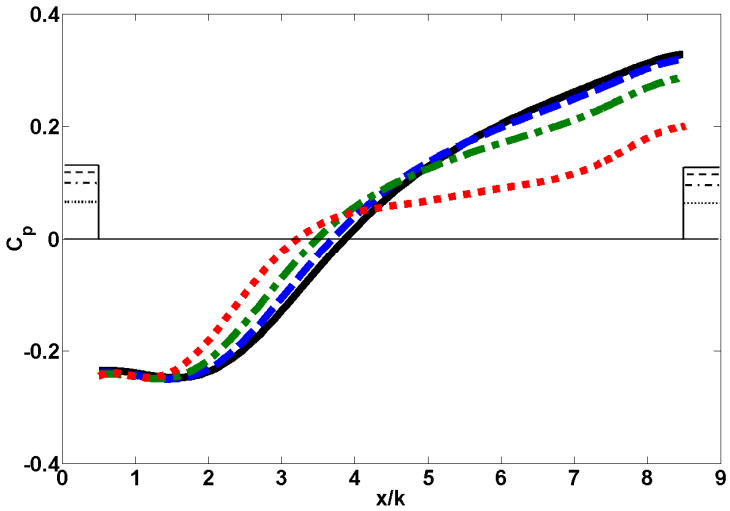

Figure 6.92 – Pressure coefficient distributions for $P/k = 9$; 2s and different rib heights using the v^2-f model.

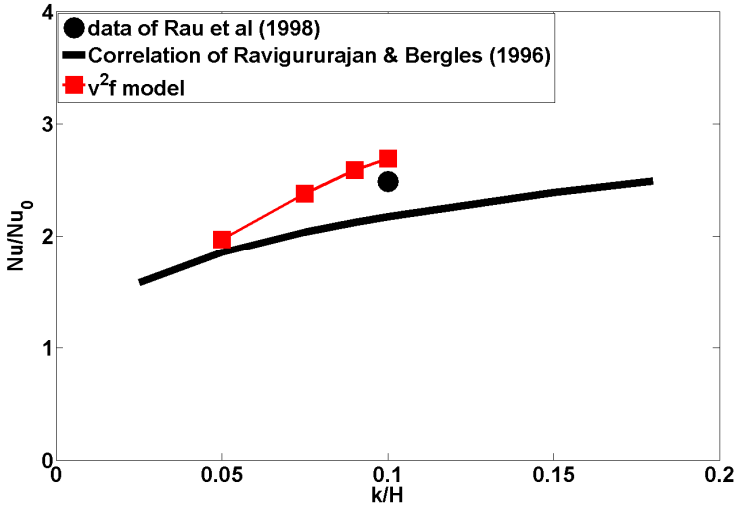

Figure 6.93 – Normalized average Nusselt number for $P/k = 9$; 2s and different rib heights using the v^2-f model.

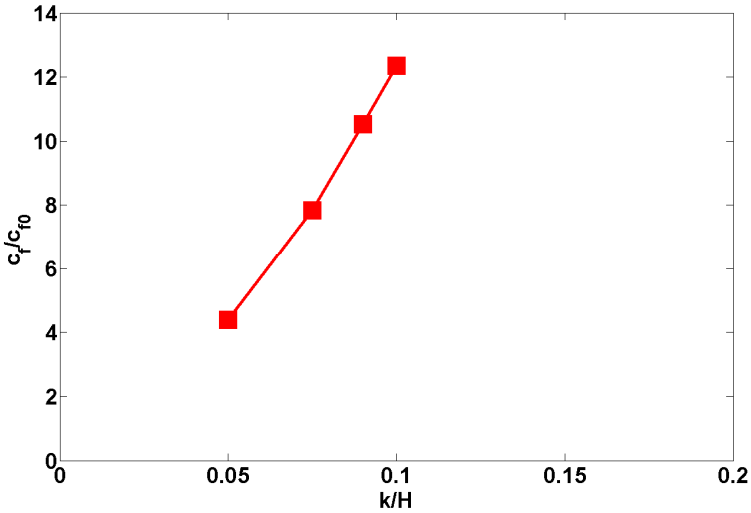

Figure 6.94 – Normalized average friction coefficient for $P/k = 9$; 2s and different rib heights using the v^2-f model.

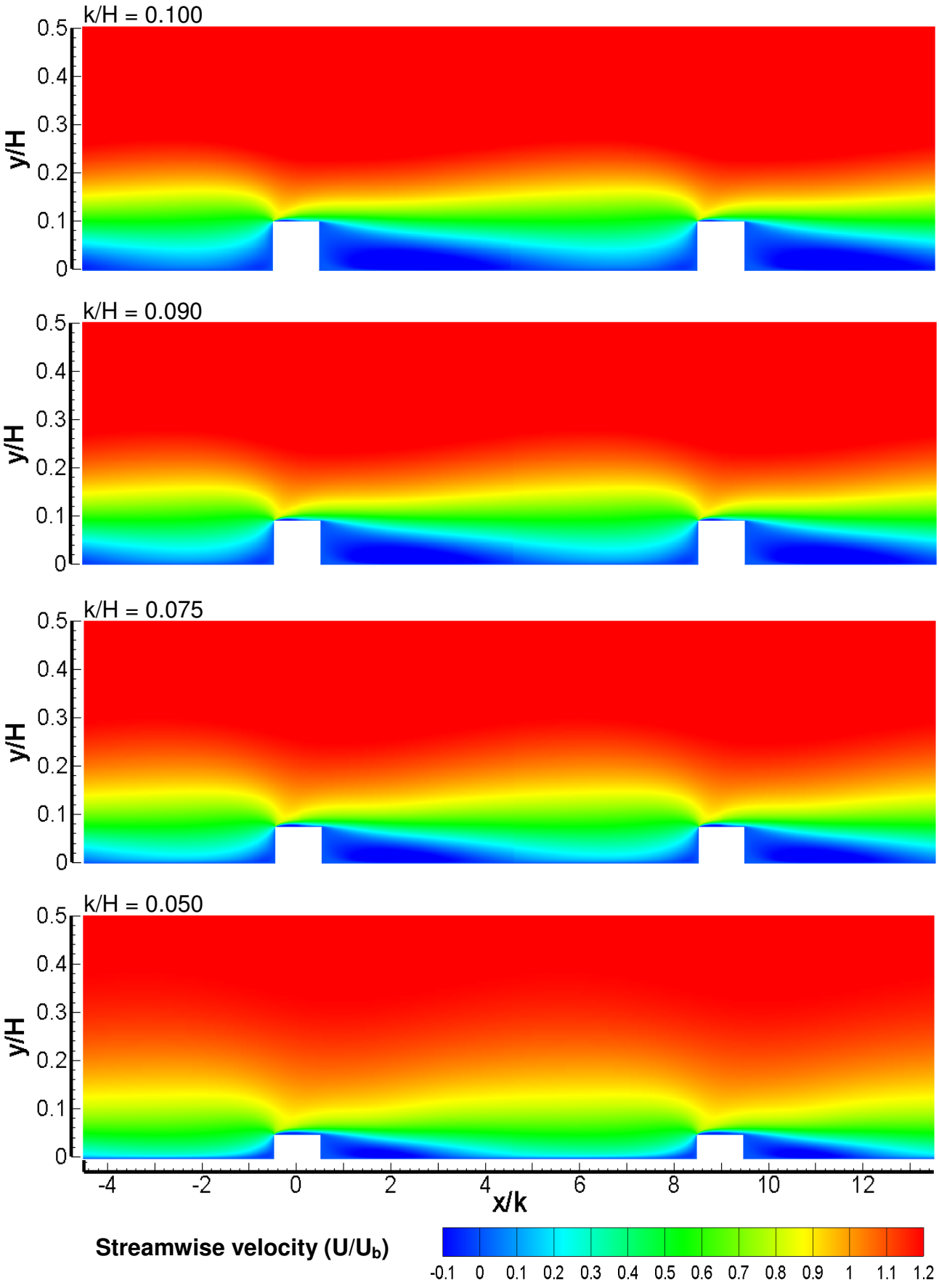

Figure 6.95 – Contour plots of the streamwise velocity for P/k = 9; 2s and different rib heights using the v^2-f model.

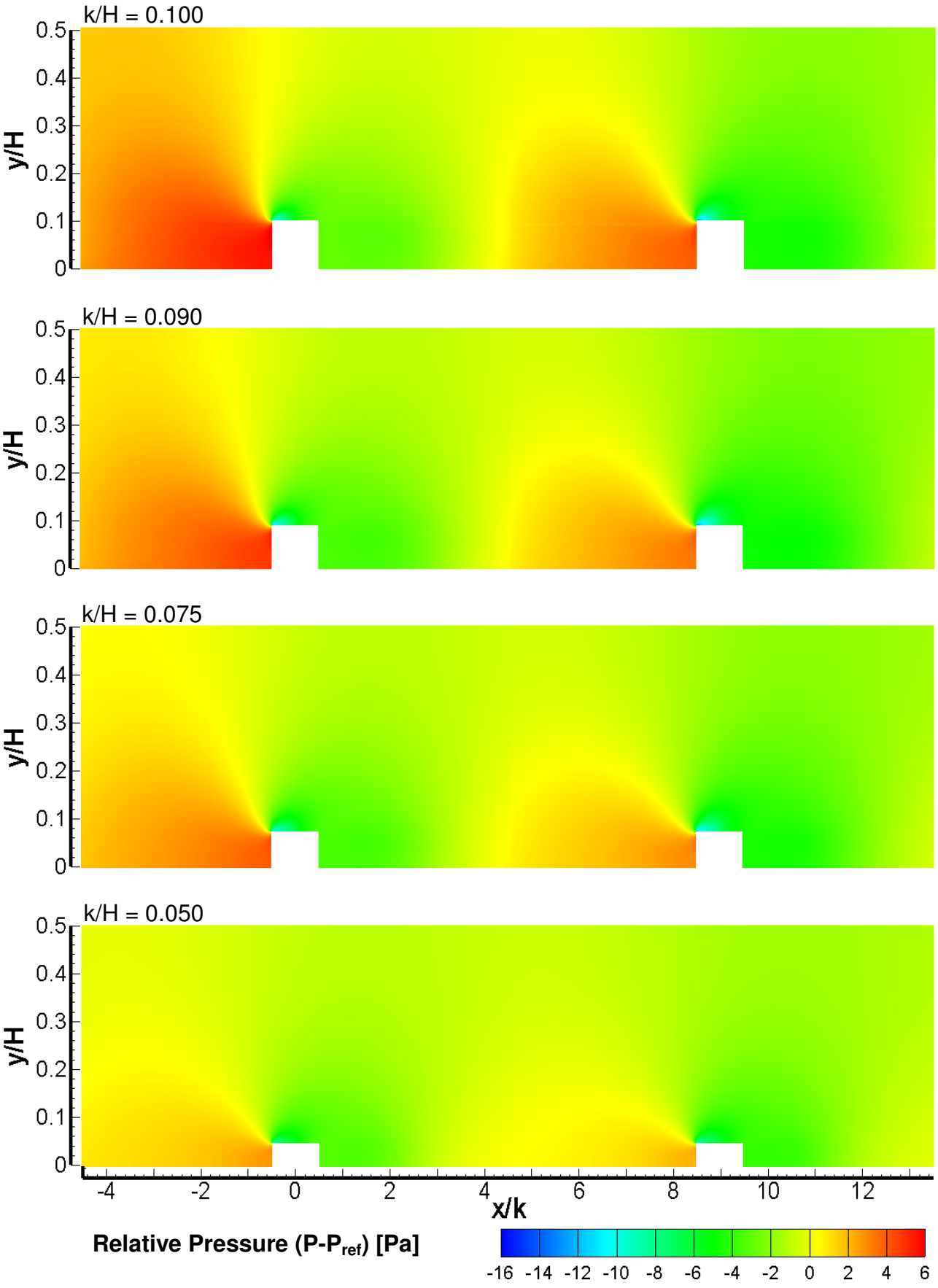

Figure 6.96 – Contour plots of the relative pressure for $P/k = 9$; 2s and different rib heights using the v^2-f model.

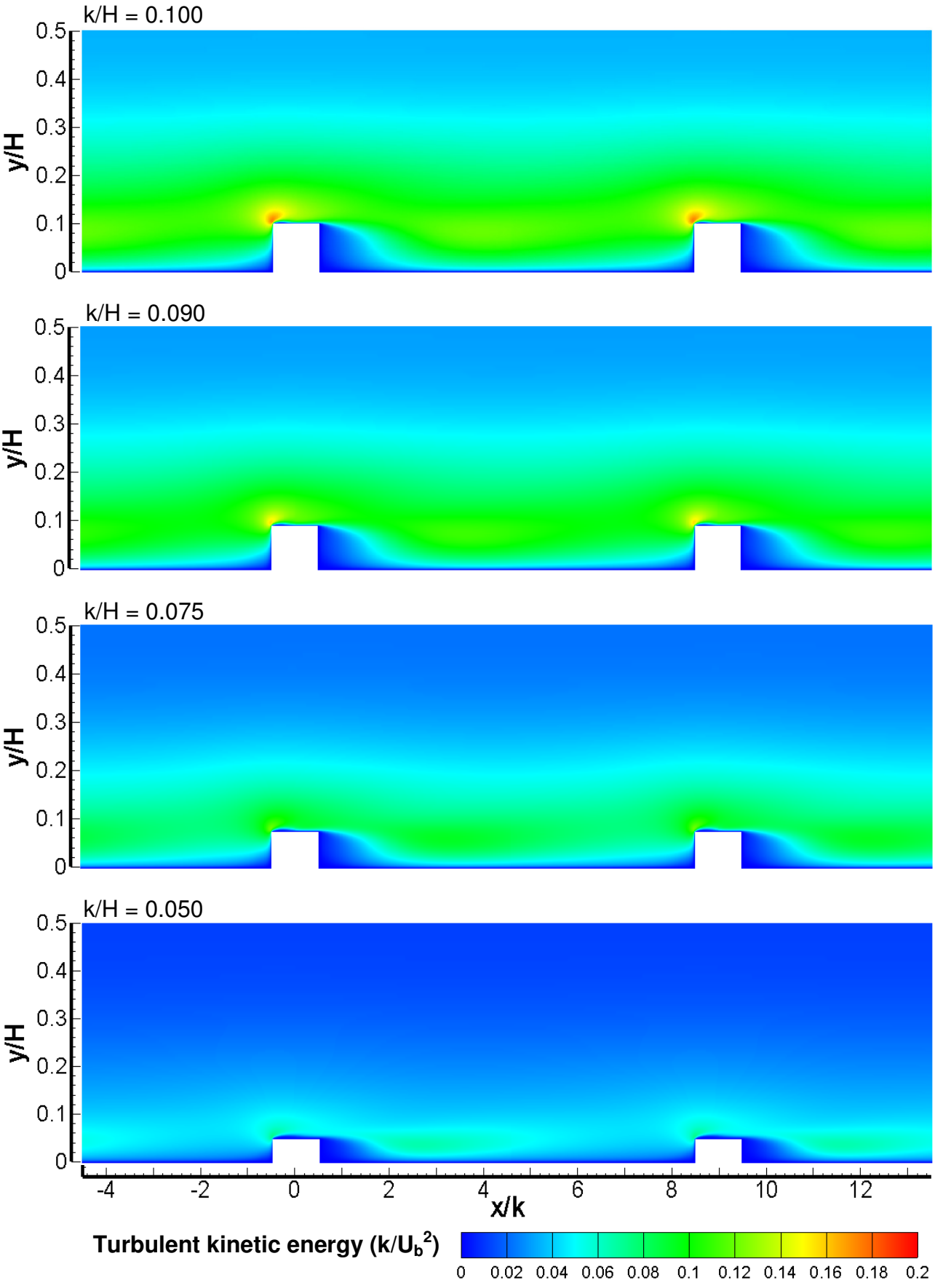

Figure 6.97 – Contour plots of the turbulent kinetic energy for P/k = 9; 2s and different rib heights using the v^2-f model.

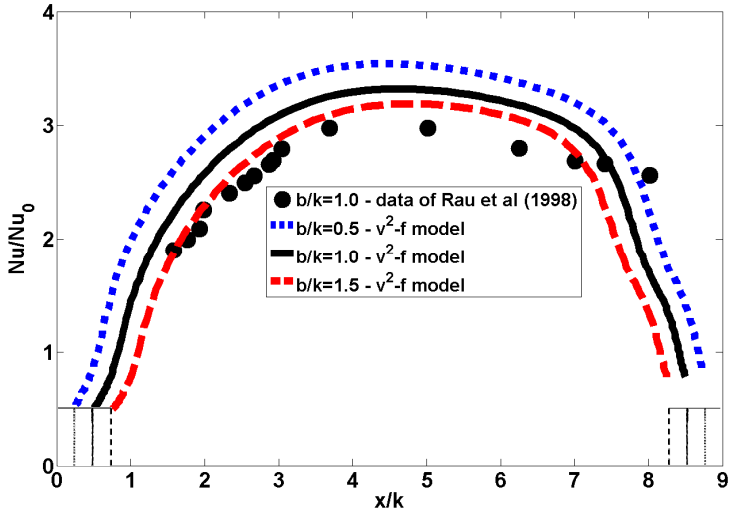

Figure 6.98 – Nusselt number distributions for $P/k = 9$; 2s and different rib widths using the v^2-f model.

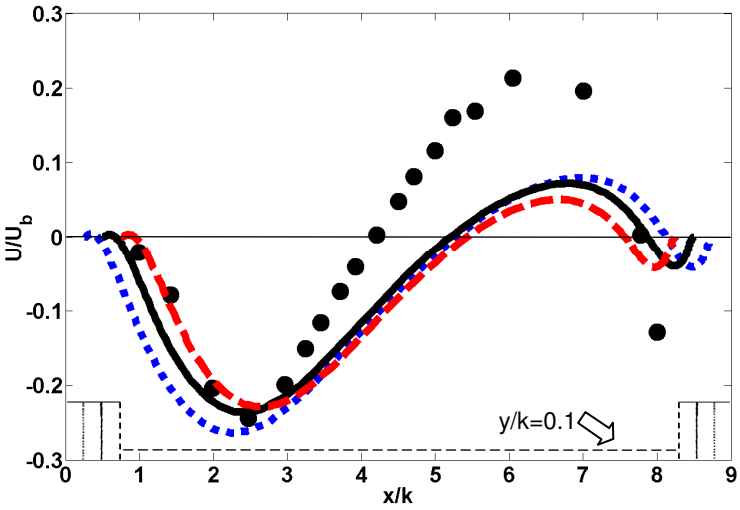

Figure 6.99 – Streamwise velocity distributions at $y/k = 0.1$ for $P/k = 9$; 2s and different rib widths using the v^2-f model.

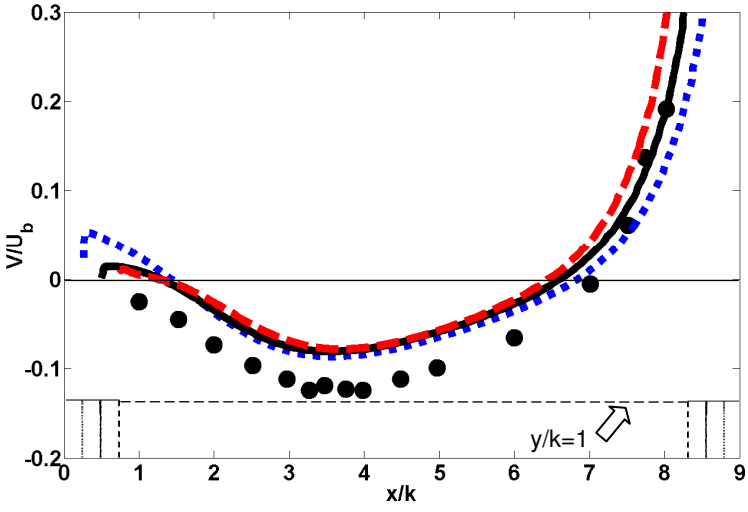

Figure 6.100 – Wall-normal velocity distributions at $y/k = 1$ for $P/k = 9$; 2s and different rib widths using the v^2-f model.

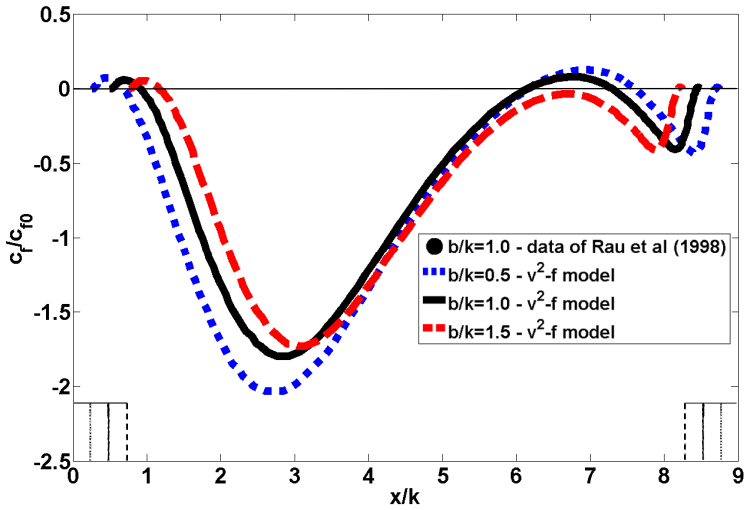

Figure 6.101 – Friction coefficient distributions for $P/k = 9$; 2s and different rib widths using the v^2-f model.

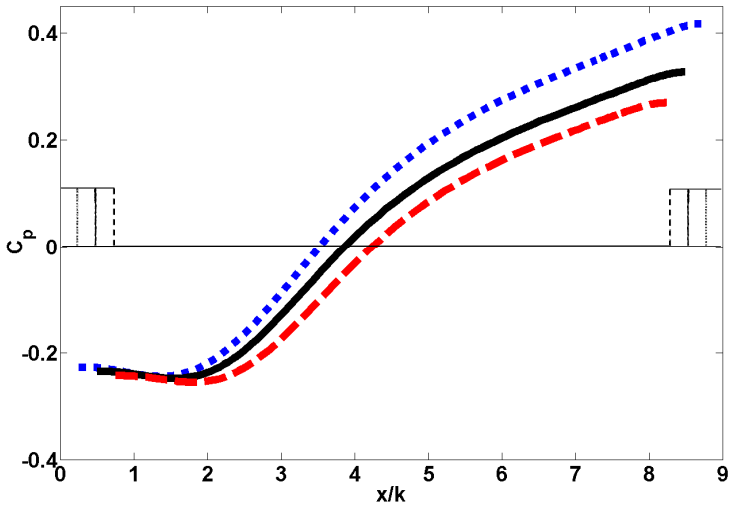

Figure 6.102 – Pressure coefficient distributions for $P/k = 9$; 2s and different rib widths using the v^2-f model.

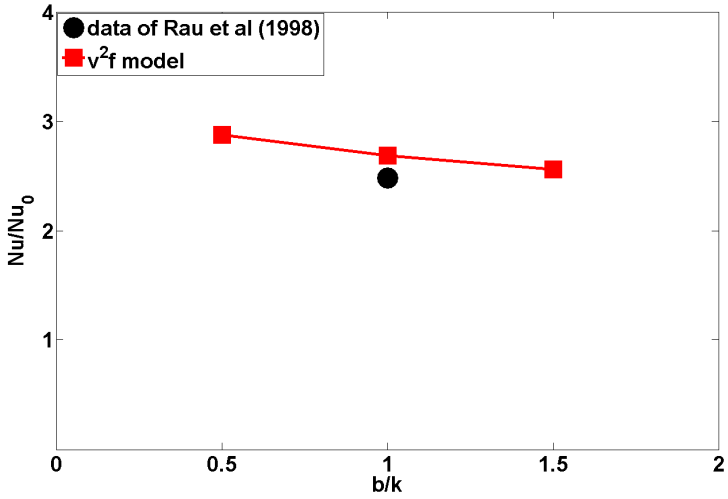

Figure 6.103 – Normalized average Nusselt number for P/k = 9; 2s and different rib widths using the v^2-f model.

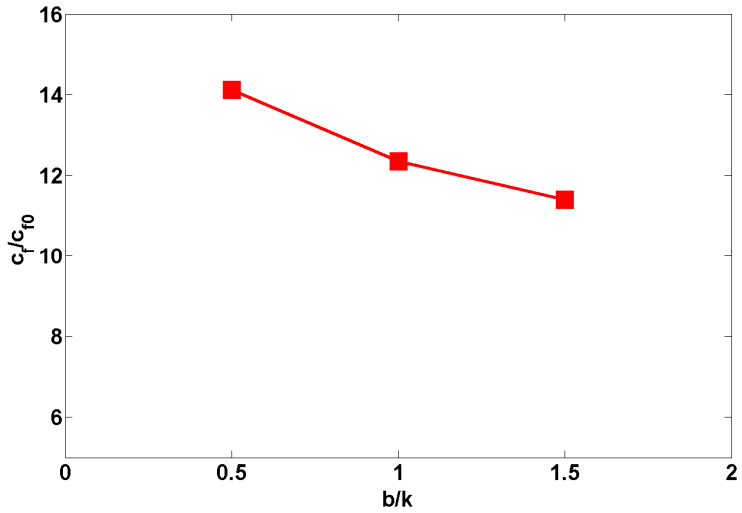

Figure 6.104 – Normalized average friction coefficient for P/k = 9; 2s and different rib widths using the v^2-f model.

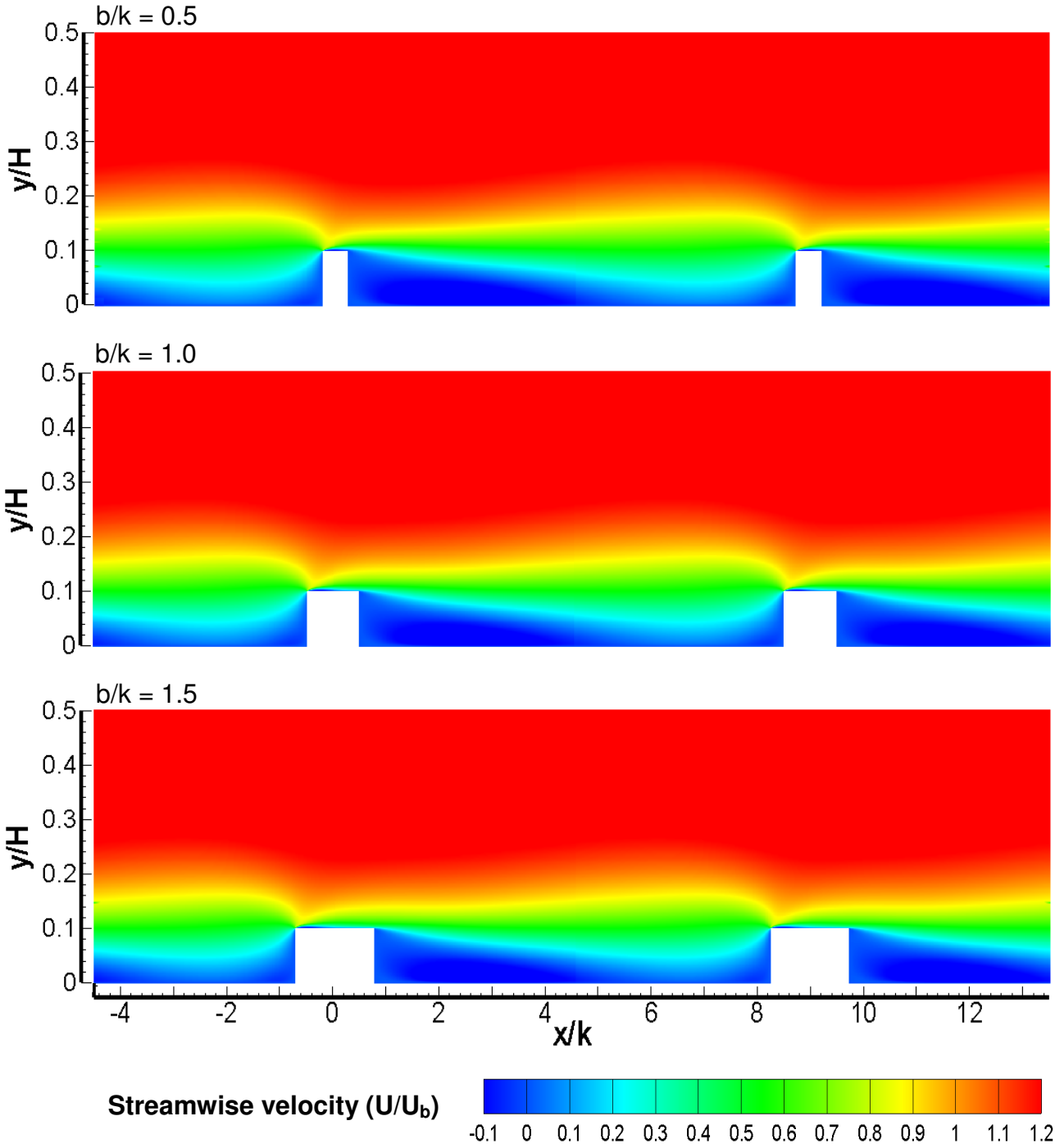

Figure 6.105 – Contour plot of the streamwise velocity for $P/k = 9$; 2s and different rib widths using the v^2-f model.

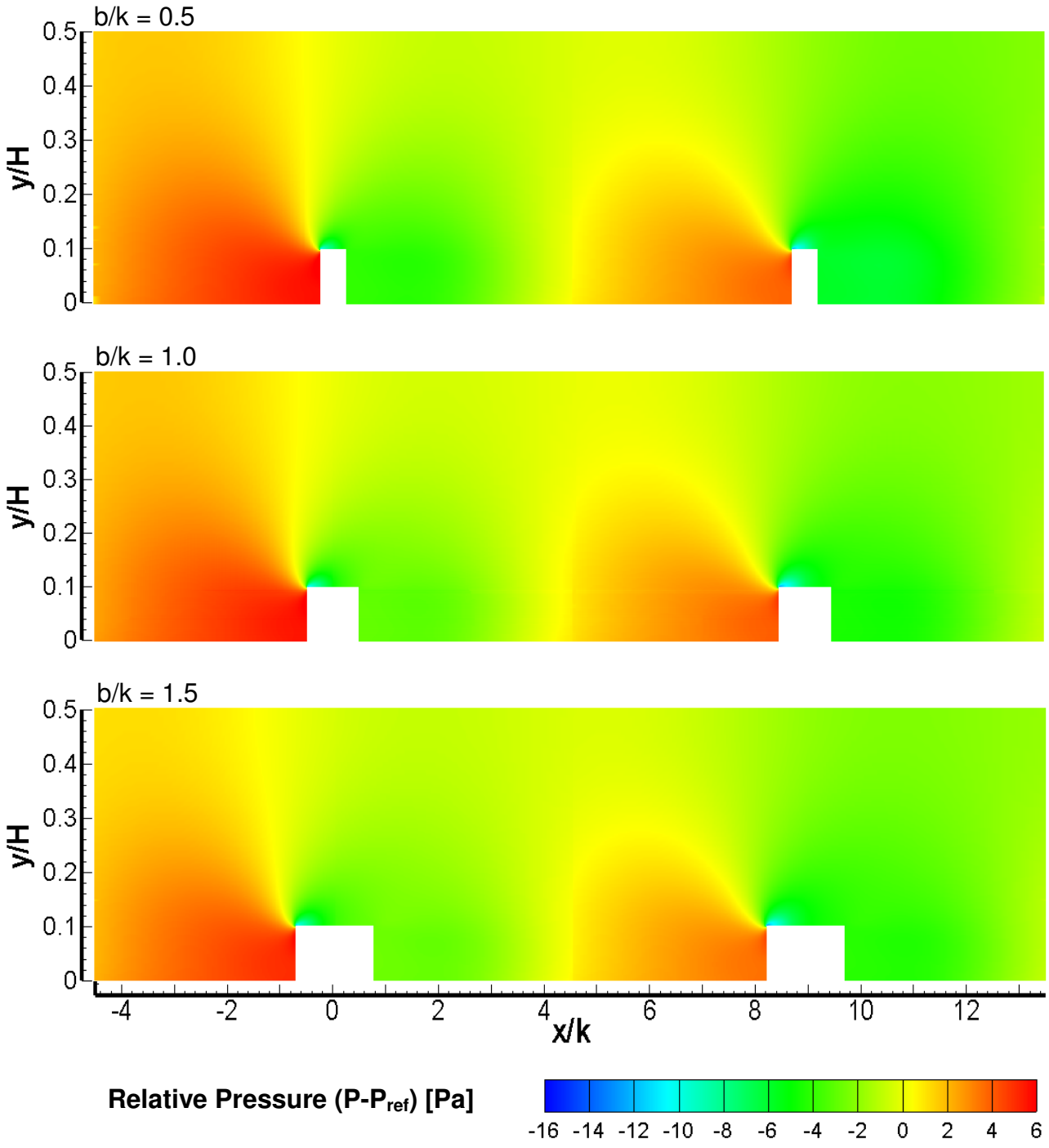

Figure 6.106 – Contour plot of the relative pressure for P/k = 9; 2s and different rib widths using the v^2-f model.

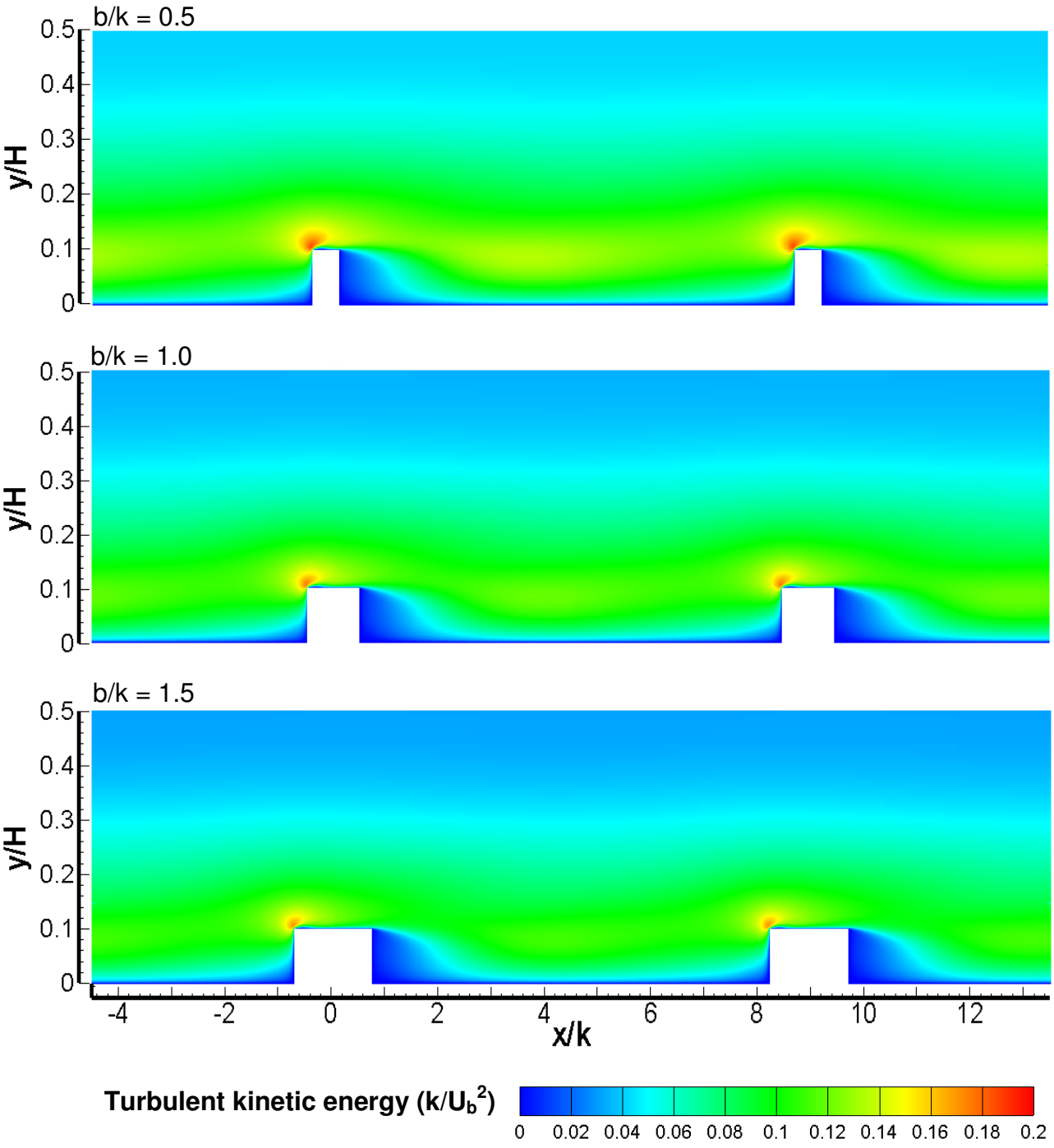

Figure 6.107 – Contour plot of the turbulent kinetic energy for P/k = 9; 2s and different rib widths using the v^2-f model.

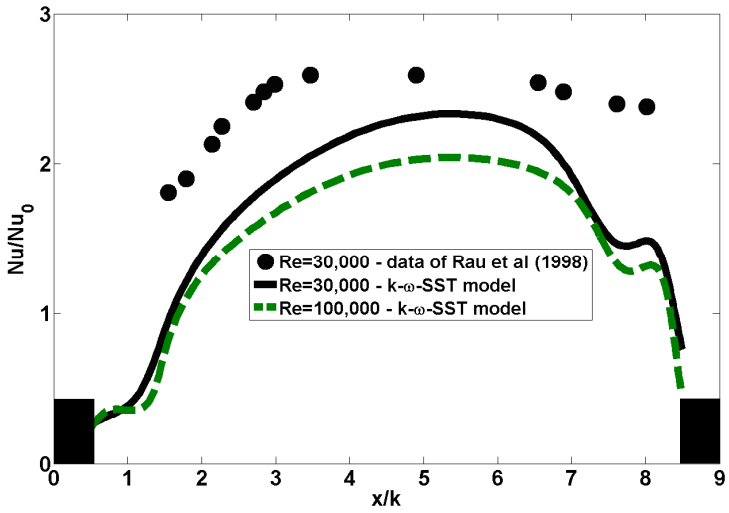

Figure 6.108 – Nusselt number distributions for *P/k* = 9; 1s for different Reynolds numbers using the *k-ω-SST* model.

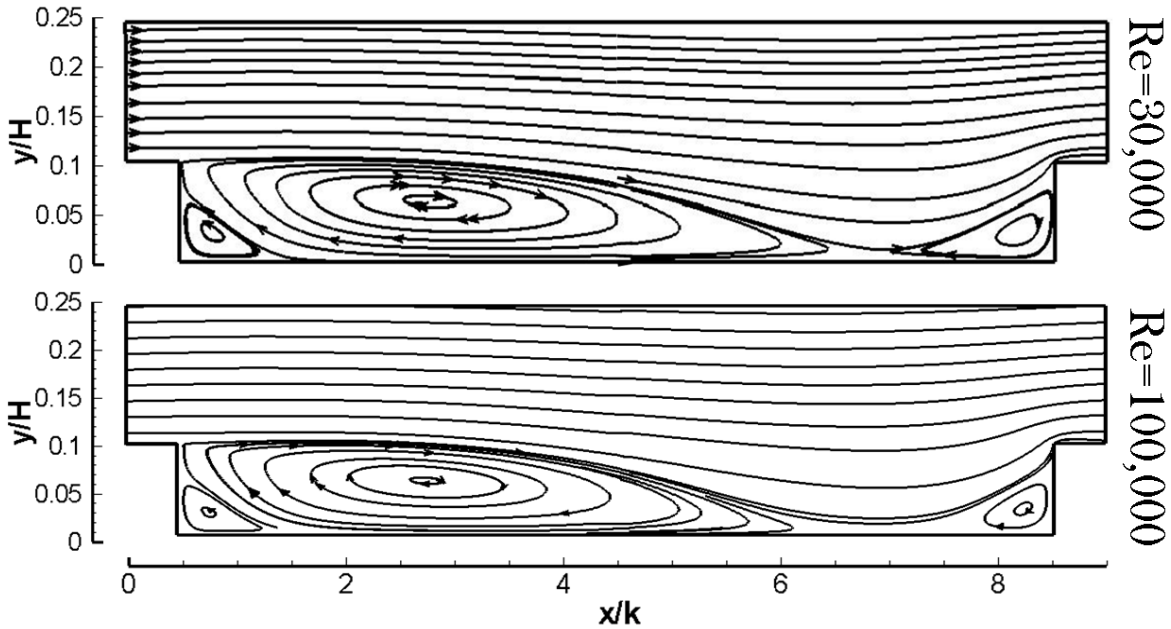

Figure 6.109 – Streamlines for *P/k* = 9; 1s for different Reynolds numbers using the *k-ω-SST* model.

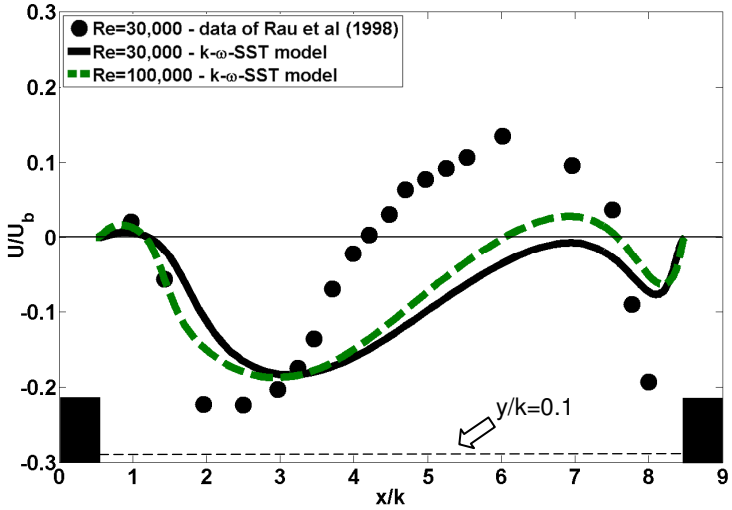

Figure 6.110 – Streamwise velocity distributions for *P/k* = 9; 1s for different Reynolds numbers using the *k-ω-SST* model.

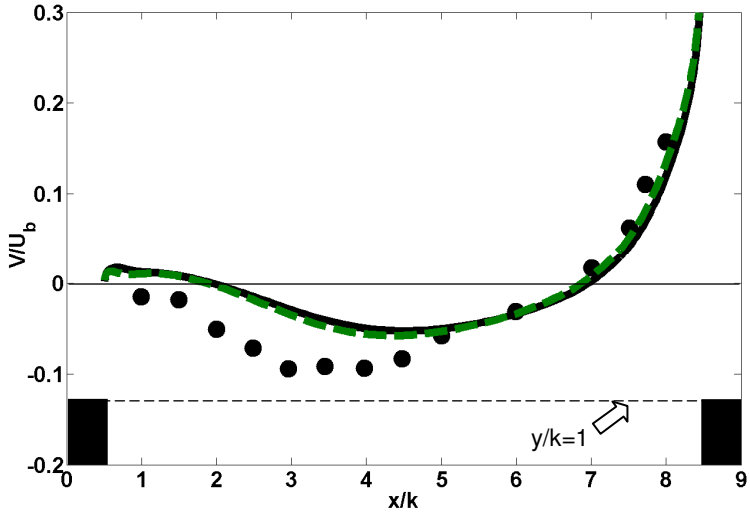

Figure 6.111 – Wall-normal velocity distributions for *P/k* = 9; 1s for different Reynolds numbers using the *k-ω-SST* model.

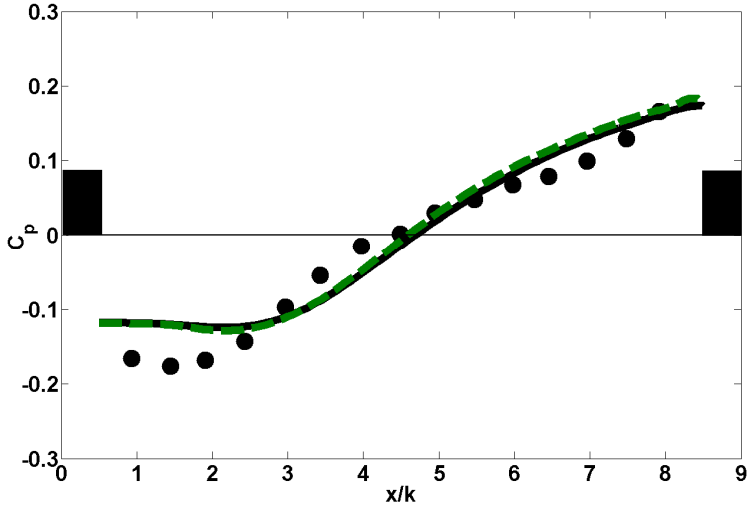

Figure 6.112 – Pressure coefficient distributions for *P/k* = 9; 1s for different Reynolds numbers using the *k-ω-SST* model.

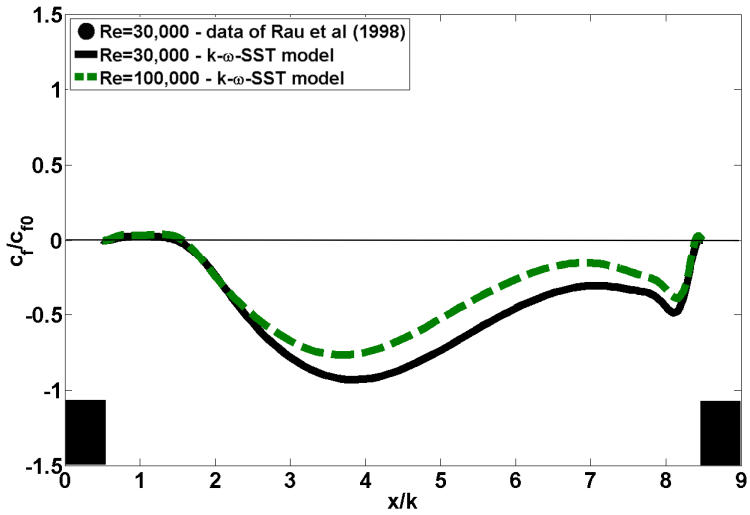

Figure 6.113 – Friction coefficient distributions for *P/k* = 9; 1s for different Reynolds numbers using the *k-ω-SST* model.

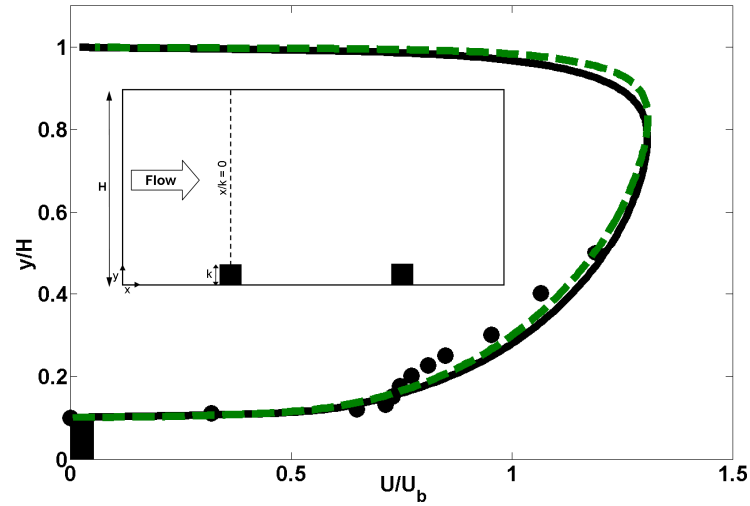

Figure 6.114 – Streamwise velocity profiles for *P/k* = 9; 1s on the rib-top for different Reynolds numbers using the *k-ω-SST* model.

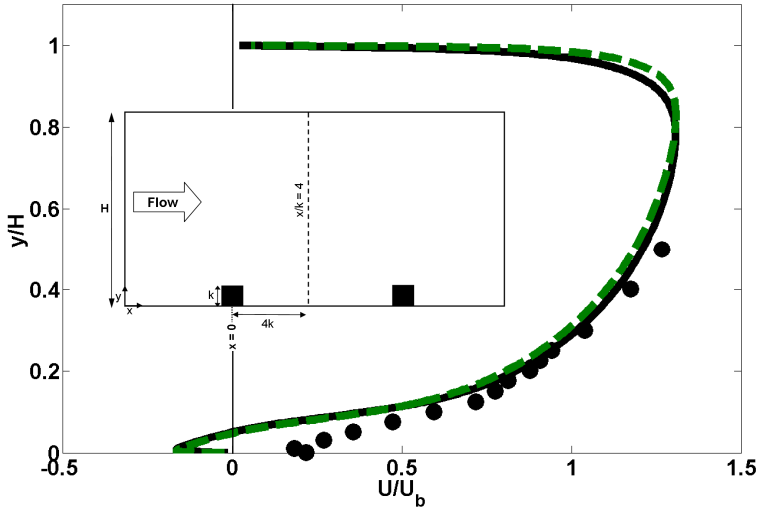

Figure 6.115 – Streamwise velocity profiles for *P/k* = 9; 1s at *x/k* = 4 for different Reynolds numbers using the *k-ω-SST* model.

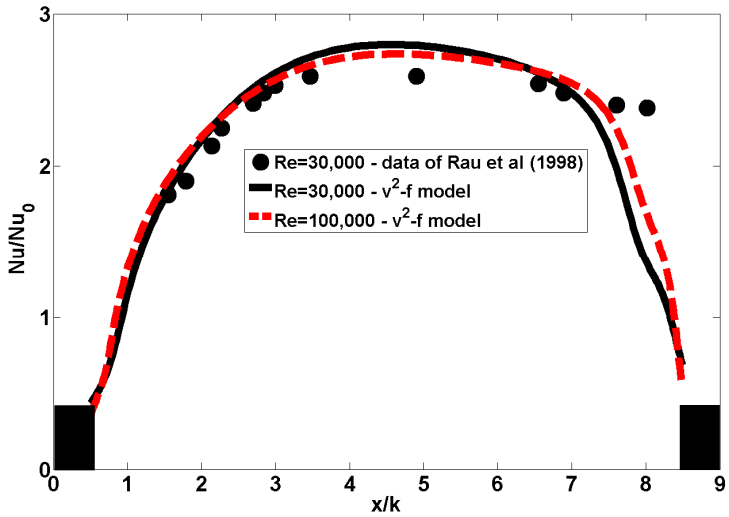

Figure 6.116 – Nusselt number distributions for $P/k = 9$; 1s for different Reynolds numbers using the v^2-f model.

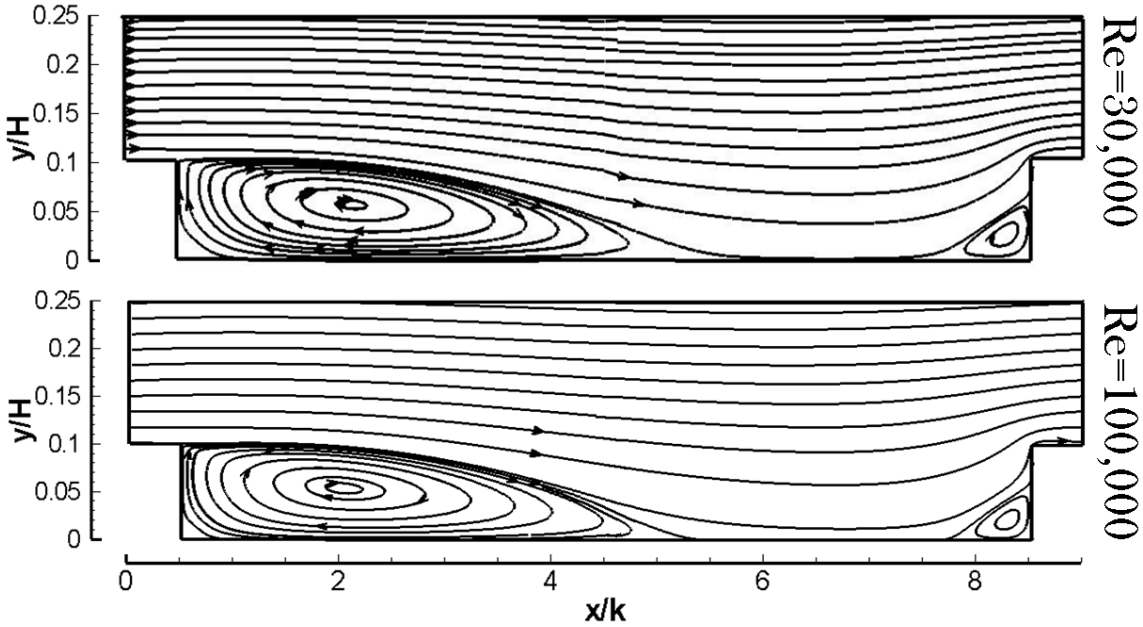

Figure 6.117 – Streamlines for $P/k = 9$; 1s for different Reynolds numbers using the v^2-f model.

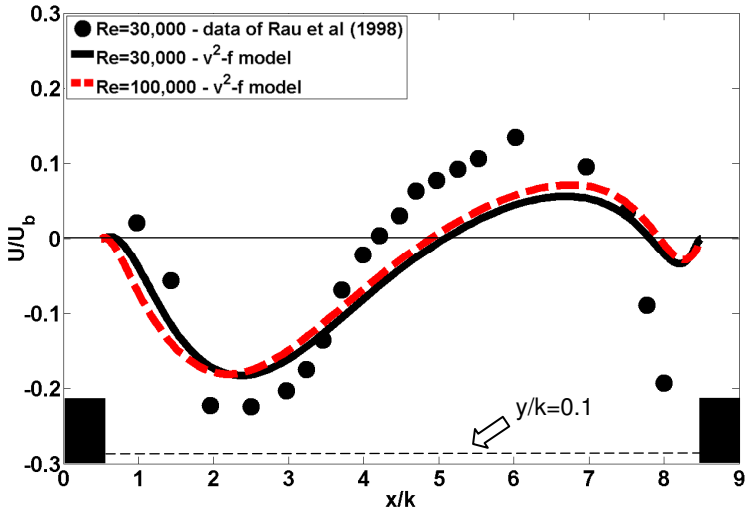

Figure 6.118 – Streamwise velocity distributions for $P/k = 9$; 1s for different Reynolds numbers using the v^2-f model.

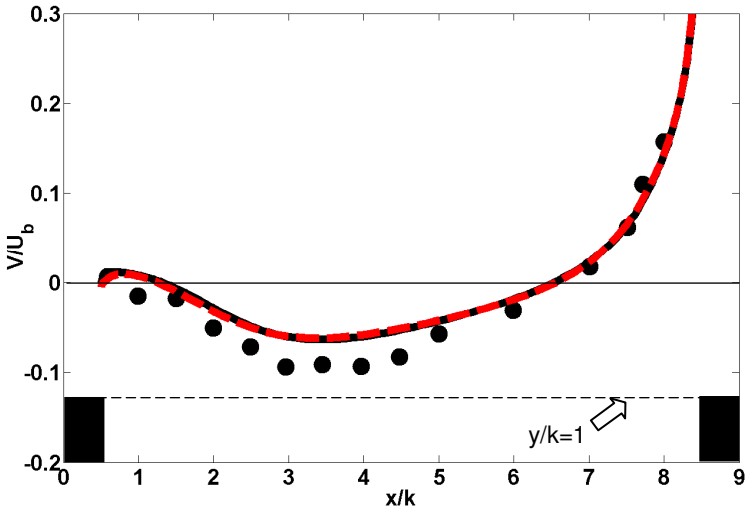

Figure 6.119 – Wall-normal velocity distributions for $P/k = 9$; 1s for different Reynolds numbers using the v^2-f model.

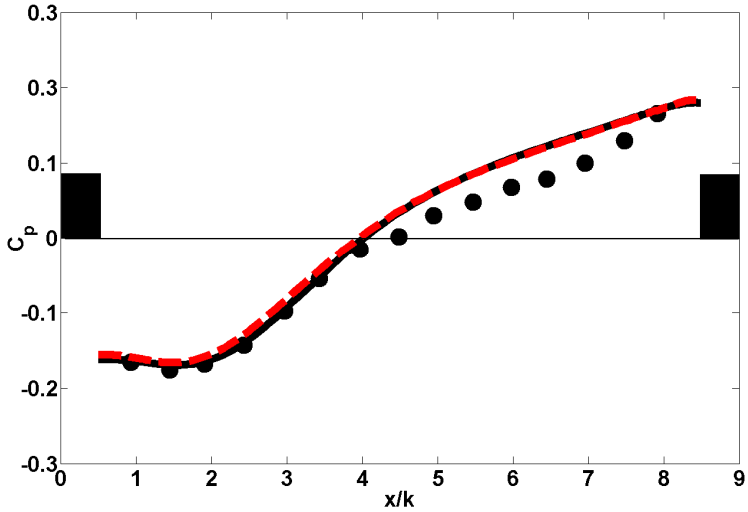

Figure 6.120 – Pressure coefficient distributions for $P/k = 9$; 1s for different Reynolds numbers using the v^2-f model.

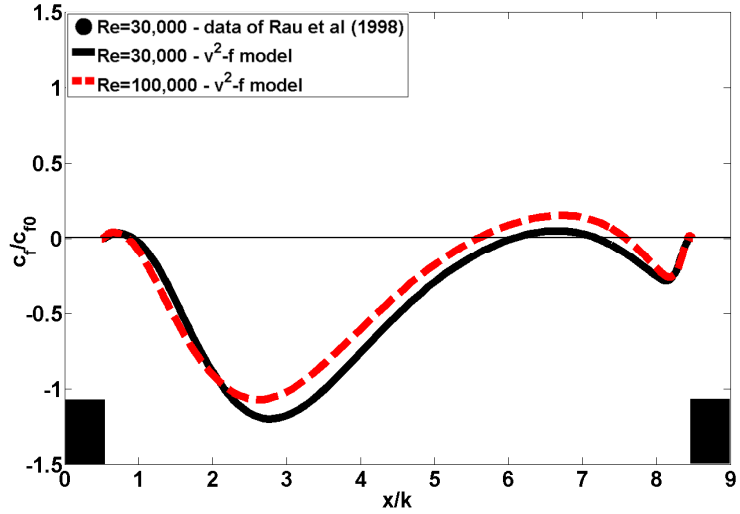

Figure 6.121 – Friction coefficient distributions for $P/k = 9$; 1s for different Reynolds numbers using the v^2-f model.

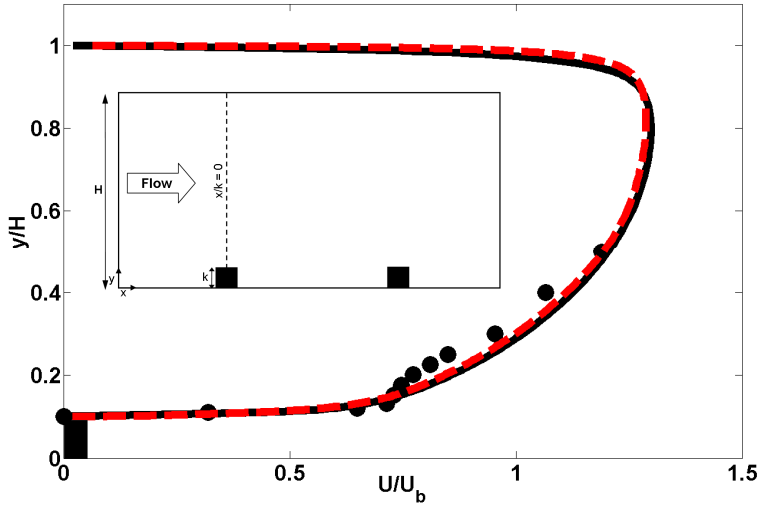

Figure 6.122 – Streamwise velocity profiles for $P/k = 9$; 1s on the rib-top for different Reynolds numbers using the v^2-f model.

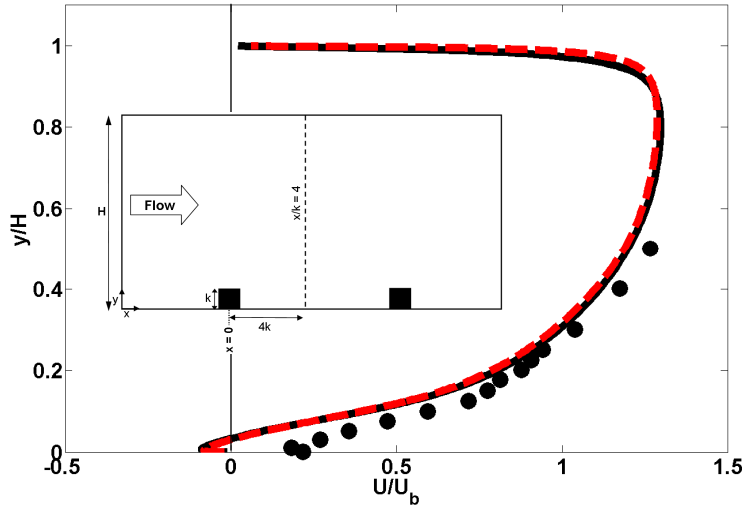

Figure 6.123 – Streamwise velocity profiles for $P/k = 9$; 1s at $x/k = 4$ for different Reynolds numbers using the v^2-f model.

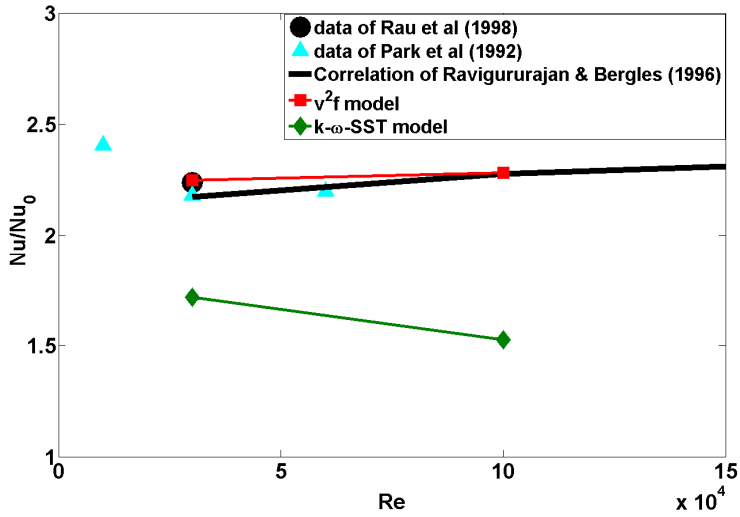

Figure 6.124 – Normalized average Nusselt number for different Reynolds numbers using the v^2-f and k-ω-SST models.

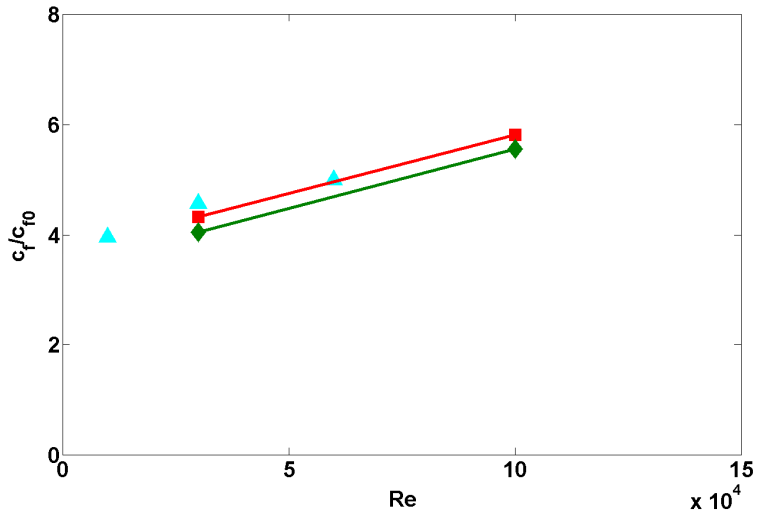

Figure 6.125 – Normalized average friction coefficient for various P/k ratios using the v^2-f and k-ω-SST models.

CHAPTER 7

3-DIMENSIONAL AGR FUEL ELEMENTS

7.1 PRELIMINARY REMARKS

In Chapter 6, 2-dimensional rib-roughened channels were examined and the effects of various 'design parameters' on heat transfer and mean flow were investigated. The conclusions which have emerged from the 'parametric study' in Chapter 6 have provided very important information for simulation of flow over accurately represented Advanced Gas-cooled Reactor (AGR) fuel elements.

Generally, in a 36-fuel pin passage (representing a complete AGR fuel element), three different sub-channels (defined as the area surrounded by fuel pins) exist including triangular, square, and wall sub-channels. This makes the simulations conducted using simple 2D channels or even triangular or square sub-channels dubious. Therefore, 3-dimensional simulations of a fuel element are required to capture possible interactions

among different fuel pins and sub-channels, in addition to computing the pressure, temperature and velocity distributions across the whole fuel element's cross-section.

For these reasons, in this chapter a simplified design of an AGR fuel element is simulated using a 3-dimensional approach and comparison is made against the results of a 2-dimensional rib-roughened channel, similar to those used in Chapter 6.

As was briefly discussed in Chapter 1, the rib-roughened fuel pins of the UK fleet of AGRs can be divided into the following two categories:

1. 'Multi-Start' Configuration – as shown in Figure 7.1, in this design 12 helices configured at an angle of approximately 50^{o} to the horizontal cover the outer surface of the fuel pin. As indicated in Figure 7.1 (c), the fuel elements of this design consist of a combination of 36 right- and left-hand fuel pins. The minimum section to be simulated for this configuration would be a 120^{o} sector, as indicated in the figure.
2. 'Transverse' Configuration – as shown in Figure 7.2, in this design a single-start continuous helix at a small angle of pitch to the horizontal covers the outer surface of the fuel pin. As indicated in Figure 7.2 (c), the fuel elements of this design consist of 36 identical fuel pins. Therefore, the minimum section to be simulated for this configuration would be a 60^{o} sector.

The Transverse configuration was the first design used in AGRs. However, this configuration was later replaced by the Multi-Start design following the findings of a number of researchers in this field including Wilkie (1983b, b) and Pirie (1987), who revealed the advantages of using the Multi-Start configuration in place of its predecessor.

7.2 CASE DESCRIPTION

In the present work, a simplified fuel element consisting of fuel pins with parallel and uniformly spaced ribs is simulated (Figure 7.3). In the present configuration, a simple square rib profile is chosen since it was shown in Chapter 6 that a rib profile has an insignificant effect on the mean flow and heat transfer.

Parameter	Notation	Multi-Start (360° sector)	Transverse (360° sector)	Present (30° sector)
Rib width at base [m]	b	0.00044	0.00071	0.00030
Rib width at tip [m]	w	0.00022	0.00030	0.00030
Rib height [m]	k	0.00042	0.00030	0.00030
Radius at base [mm]	R_1	0.051	0.203	–
Radius at tip [mm]	R_2	0.025	0.025	–
Pitch-to-height ratio	P/k	5.5	7.0	7.0
Graphite sleeve inner diameter [m]	D_s	0.19231	0.19231	0.1920
Fuel pin diameter [m]	D_p	0.01532	0.01532	0.01505
Guide tube diameter [m]	D_g	0.01627	0.01627	0.01627
Free flow area [m^2]	A	0.0222	0.0222	0.00186
Rough perimeter [m]	P_R	1.7326	1.7326	0.1418
Smooth perimeter [m]	P_S	0.6553	0.6553	0.0545
Total perimeter [m]	P_T	1.8637	1.8637	0.1527
Hydraulic diameter [m] – using P_T in Eqn. (7.3)	D_e	0.0372	0.0372	0.0378
Hydraulic diameter [m] – using P_T in Eqn. (7.4)	D_e	0.0477	0.0477	0.0488
Length of fuel element/computational domain [m]	L	0.9789	0.9789	0.0042

Table 7.1 – Geometrical data for the Multi-Start, Transverse, and the present configurations.

Table 7.1 compares the dimensions of the present domain to the real dimensions of the Transverse and Multi-Start configurations provided by the British Energy (Gotts,

2008). In Table 7.1 it is seen that the pitch-to-rib height ratio of the present geometry matches that of the Transverse configuration. It is noted, however, that generally both the Transverse and Multi-start configurations have the same dimensions, except for those corresponding to their rib profiles, pitch and height.

Taking advantage of azimuthal symmetry of a complete fuel element in order to reduce the computational requirements, the present simulation employed a symmetry boundary condition on the two azimuthal faces and computed the flow in only a 30° sector of the circular cross section (Figure 7.4). (Note that for the present configuration if a periodic boundary condition was to be used at the azimuthal faces, a 60° sector would have been required, although the results of both cases should be the same.)

Streamwise periodic boundary condition maintaining a constant mass flow rate and constant bulk temperature was applied at the top and bottom faces of the domain. The computational domain was chosen to be of length $2P$ (i.e. 0.0042m) in the streamwise direction to include 2 complete ribs. The latter length combined with a streamwise periodic boundary condition was found to be sufficiently long for the attainment of fully developed flow. Similar to the simulations in Chapter 6, temperature in the present computations is solved as a passive scalar. The thermal boundary conditions at all ribbed walls (i.e. Fuel pin numbers 1-5 in Figure 7.5) consist of the same uniform wall heat flux, while both the guide-tube and outer graphite sleeve faces were set as adiabatic walls. Dimensions of the present configuration are given in Figure 7.6.

The results presented in this chapter were generated using the v^2-f model (which was found to be generally the most accurate turbulence model in the precursor 2D simulations in Chapter 6) and since this is a low-Reynolds-number turbulence model, the grid was generated so as to be very fine near the wall. As shown in Figure 7.7, an unstructured hybrid mesh with approximately 821,000 cells composed of prismatic elements for the near-wall (the wall-adjacent cell typically extends only to $y^+ \leq 0.5$) and

polyhedral elements for the core regions was used. The present mesh was generated using STAR-CCM+ Version 4.04.011 (CD-Adapco, 2008).

All computations were carried out using the commercial code, STAR-CD Version 4.02 (CD-Adapco, 2006). The Reynolds number based on hydraulic diameter (defined below) was fixed at Re = 30,000 and Prandtl number was set to Pr = 0.71. All fluid properties were assumed to be constant. The momentum and turbulence transport equations were discretized using first-order upwind differencing scheme. The energy equation was discretized using the 'Monotone Advection and Reconstruction Scheme' (MARS) (see Section 4.7.2.3). The SIMPLE algorithm was adopted for pressure-velocity correction. The convergence criterion was set to 10^{-6}.

The hydraulic diameter of the present geometry is defined as

$$D_e = \frac{4A}{P_T} \tag{7.1}$$

where A is the free flow area and P_T the total wetted perimeter (Table 7.1). The free flow area for a 30° sector is calculated as

$$A = \alpha \frac{\pi}{4}\left[\left(D_s{}^2\right) - \left(36 \times D_p{}^2\right) - \left(D_g{}^2\right)\right] \tag{7.2}$$

and the total wetted perimeter is given by:

$$P_T = \alpha\left[\underbrace{36\pi D_p}_{\text{Rough Perimeter}} + \underbrace{\pi\left(D_s + D_g\right)}_{\text{Smooth Perimeter}}\right] \tag{7.3}$$

where α=1/12 for the present 30° sector. The rough perimeter is that of the fuel pins, while the smooth perimeter corresponds to the guide tube and graphite sleeve.

Morrison (2003) has suggested an improved definition of the wetted perimeter in which the perimeters are weighted according to their friction factors, thus giving more weight to the pin roughened surfaces:

$$P_T = \alpha\left[\underbrace{36\pi D_p}_{\text{Rough Perimeter}} + 0.2\underbrace{\pi\left(D_s + D_g\right)}_{\text{Smooth Perimeter}}\right] \tag{7.4}$$

In the present work, however, the wetted perimeter was calculated according to Eqn. (7.3) in order to be consistent with earlier analyses in Chapter 6.

7.3 RESULTS

In this section, results are presented in the form of contours of the normalized streamwise velocity, temperature, and pressure obtained at streamwise mid-plane (Figure 7.8) and four other planes along one of the azimuthal faces (hereafter referred to as 'azimuthal planes'; Figure 7.9).

Figure 7.10 shows the magnitude of the normalized streamwise velocity at the mid-plane. As one would expect, local maxima ($U/U_b \approx 1.2$) form in the centres of all sub-channels, while the flow is slowed down near fuel pins, guide tube and graphite sleeve. As was mentioned earlier, three different sub-channels including triangular, square and wall sub-channels can be indentified in Figure 7.10. The highest local velocity maxima is observed to occur in the square sub-channel between fuel pins in the second and third rings, followed by that in the triangular sub-channel between the two fuel pins in the third ring. The local maxima surrounding the central guide tube, however, has an average velocity magnitude of approximately 0.8 which is about 30% lower than that found in other sub-channels. It can also be seen that excluding boundary layers, the variation of the streamwise velocity is relatively mild in the sub-channels. In addition, iso-contours bulge towards the gaps, indicating that the local velocity is increased within the gap between the fuel pins. The inset to Figure 7.10 provides an overview of the streamwise velocity distribution over the whole computational domain.

Contours of the normalized streamwise velocity at the azimuthal planes are shown in Figure 7.11. The first picture to emerge from comparing the contours in Figure 7.11

is that the maximum velocity magnitude in Plane2 is the largest compared to the other 3 planes since it has the largest height and consequently the lowest *k/H* ratio (this will be further discussed in connection with Figure 7.19 and Figure 7.20, below). It should be noted that the magnitude of the average streamwise velocity in each plane is not only a function of plane height, but is also significantly affected by the value of local maxima in the near sub-channel. This is why the velocity contours in Figures 7.11 (b) and (c) are different despite of having the same type of thermal boundary condition and similar plane height (see Table 7.2 below for the dimensions of the azimuthal planes).

Within the inter-rib cavity, however, all 4 planes show similar trends, indicating a recirculation bubble downstream of the first rib. Similar trends were also found in Chapter 6 for a 2D channel with P/k = 6; 1s (where '1s' indicates one-side ribbed channel).

Attention is turned next to the thermal-field results. A contour of the relative temperature (T-T_{ref}) at the mid-plane is shown in Figure 7.12. Iso-thermal lines are also plotted in this figure. It is seen that the maximum temperature generally occurs around the fuel pins, especially near fuel pin numbers 2-4, where the gap between the fuel pins is relatively small. Clearly, the lowest temperatures can be found around the guide tube and graphite sleeve, at which adiabatic wall boundary condition was imposed. The inset to Figure 7.12 shows a temperature contour of the whole computational domain and it is evident how different the temperature levels are at the fuel pins in the inner and outer rings. Since in the inner rings the gaps between different fuel pins are smaller, much higher temperatures and lower streamwise velocities occur in these regions, resulting in fuel pin numbers 3, 2 and 4 having the highest temperature levels.

Temperature contours at the azimuthal planes are shown in Figure 7.13. Each plane shows a considerably different range of temperatures which depends on three main factors: 1) The type of thermal boundary condition imposed on the plane, 2) The

position of the surrounding fuel pin within the fuel element (e.g. in the 1st, 2nd or 3rd ring), and 3) The magnitude of the average streamwise velocity in the plane. As was mentioned above, the third factor itself depends on the local velocity maxima in the near sub-channel and the *k/H* ratio. In Figure 7.13 it is clear that Plane1 has the lowest temperature levels due to an adiabatic wall boundary condition being imposed at the graphite sleeve, in addition to a relatively large distance between the two fuel pins in the third ring. The importance of the latter can be understood better by comparing Figures 7.13 (a) and (d), where it is seen that much higher temperature levels are obtained in Plane4 despite both planes having a similar thermal boundary condition and streamwise velocity magnitudes.

Results of the relative pressure are next considered. Figure 7.14 shows a contour of the relative pressure at the mid-plane. Clearly, the pressure magnitude further away from the ribbed walls in the sub-channels is negligible. The inset to Figure 7.14 shows the pressure contour from a different angle, in which high- and low-pressure regions near the ribs are more visible.

A better representation of the pressure variations near the ribs is given in Figure 7.15 where the relative pressure at the azimuthal planes is shown. It can be seen that all four planes show very similar patterns which include high-pressure zones upstream and low-pressure zones downstream of the ribs. Broadly similar patterns (and similar values) were found in the simulations of 2D channels in Chapter 6.

Comparison against a 2D simulation

In the previous section, the results of the present test case were reported qualitatively by showing contours of normalized streamwise velocity, temperature, and pressure. In this section, the aim is to compare the results obtained using the present 3D configuration with a 2-dimensional channel simulation. This comparison would be an assessment on

the validity and relevance of the precursor 2D channel approximation employed in Chapter 6 to the present 3D configuration.

The first step for carrying out a 2D simulation is to choose one of the azimuthal planes of the present 3D configuration. As shown in Figure 7.16 the azimuthal face between fuel pin numbers 1 and 2 (which contains 'Plane2') is selected. In order to generate a 2D configuration, the selected face is extruded in the spanwise direction (z-direction) to have 1 cell thickness. Symmetry boundary condition is then imposed on the spanwise faces. Other boundary conditions used are also indicated in Figure 7.16. The present 2D grid would now have the same geometrical properties (i.e. the same mesh resolution and *P/k* and *k/H* ratios) as 'Plane2' defined earlier in Figure 7.9. This grid consists of 1,800 cells and the wall-adjacent cell extends only to $y^+ \leq 0.3$. The computations are then carried out on this grid using STAR-CD Version 2.04 with the same numerical inputs (including the same turbulence model i.e. the v^2-f model) as in the 3D case. It should be noted that the present 2D configuration is much coarser compared to the 2D grids used in Chapter 6 i.e. direct comparison between them would be dubious. However, this is an unavoidable inconsistency since it is not possible to have the same level of refinement in the present 3D configuration due to time and computational limitations.

Case	Number of rough walls	H [m]	k/H	Effective k/H	P/k	Re
Plane 1	1	0.0106	0.028	0.028	7	30,000
Plane 2	2	0.0121	0.025	0.050	7	30,000
Plane 3	2	0.0111	0.027	0.054	7	30,000
Plane 4	1	0.0089	0.034	0.034	7	30,000
2D simulation	2	0.0121	0.025	0.025	7	16,000

Table 7.2 – Comparison of the 4 planes on the symmetry line of the 3D simulation with the 2D case.

Some of the features of the cases compared in this section are listed in Table 7.2. The 'Effective *k/H* ratio' indicated in the table is as defined as [*k/H*]×[Number of rough walls]. Also note that, as can be seen in Table 7.2, the Reynolds number based on hydraulic diameter is different for the 2D simulation, that is due to the fact that the hydraulic diameter of the 2D channel is smaller ($D_e = 2H = 0.0242$) compared to that of the present 3D case ($D_e = 0.0378$), while the value of the bulk velocity, U_b for both configurations are the same.

Figure 7.17 shows a contour of the streamwise velocity obtained using the present 2D channel. Comparing the results of Figure 7.17 and Figure 7.11, it can be seen that while similar patterns are present between 2D and 3D results, the maximum velocity magnitude predicted by the 2D mesh is generally higher than that found at the azimuthal planes of the 3D case (this will be discussed further below in connection with Figure 7.19 and Figure 7.20).

Figure 7.18 shows the normalized streamwise velocity at one-tenth of the rib height ($y/k = 0.1$). Two recirculation regions, represented by two negative velocity peaks are evident in all cases. All four azimuthal planes have similar recirculation bubbles, while the magnitude of the primary recirculation bubble obtained by the 2D case is nearly twice of that found by Plane2. In addition, the velocity distributions found by azimuthal planes 1-3 indicate that the flow remains reversed at this elevation. The velocity distributions for the 2D channel and Plane4, however, suggest that the flow may reattach within the cavity; this is indicated by a small region between $x/k \approx 4.5 - 5.5$ where $U/U_b \geq 0$.

Results for the streamwise velocity profiles over the rib-top ($x = 0$) and at the middle of the inter-rib cavity ($x/k = 3.5$) are shown in Figure 7.19 and Figure 7.20, respectively. It can be seen that the velocity magnitude of the 2D channel is generally higher than that of the azimuthal planes (the maximum of 20% difference compared to

the distributions of Plane2). As was discussed earlier, the velocity magnitude of the azimuthal planes depends on both the magnitude of the velocity maxima in the near sub-channel and the *k/H* ratio. This has resulted in Plane2 and Plane4 having respectively, the highest and lowest velocity magnitudes compared to the other azimuthal planes.

Furthermore, the inset to Figure 7.20 shows more clearly the recirculation regions (represented by $U/U_b < 0$). It can be seen that except for Plane1, the size of the recirculation region at the middle of the inter-rib cavity is relatively similar for all cases. The recirculation bubble of Plane1, however, is the largest followed by that of Plane4. It is noted that the single-side ribbed planes (i.e. '1s') show larger recirculation regions compared to the double-side ribbed planes. The size of the recirculation bubble is also affected by the *k/H* ratio. In addition, the results shown in the inset of Figure 7.20 are also consistent with the results of the streamwise velocity magnitudes at $x/k = 3.5$ shown in Figure 7.18.

Figure 7.21 shows the wall-normal velocity distributions at rib height. It can be seen that while the magnitude of the wall-normal velocity is similar for all four azimuthal planes, the 2D channel generally returns higher velocity magnitude especially within the primary recirculation region ($x/k = 0.5 – 4.0$). The discrepancies between the results of the 2D channel and azimuthal planes in Figure 7.21 are in part related to the differences in the streamwise velocity magnitude within the inter-rib cavity (seen in Figure 7.18 to Figure 7.20).

The discrepancies found above (Figure 7.18 to Figure 7.21) between the mean flow results of the 2D channel and Plane2 of the 3D case are mainly related to the 3D effects and spanwise velocity component which is non-zero in the azimuthal planes. In the case of a 2D channel, however, there is no velocity component in the spanwise direction due to a symmetry boundary condition being imposed on both spanwise faces.

Attention is turned next to the results of the relative temperature. Figure 7.22 shows a contour of the relative temperature obtained using the 2D grid. Comparing this figure with the contours obtained for the azimuthal planes (Figure 7.13) reveals a considerably different heat transfer levels between 2D and 3D results (note that the scales are different in Figure 7.13 and Figure 7.22). It is seen that the 2D configuration has approximately 60% lower temperature levels compared to Plane2, due to higher streamwise velocity magnitudes in the 2D configuration (see Figure 7.19 and Figure 7.20) which results in higher turbulence mixing and consequently higher heat transfer levels.

Figure 7.23 compares the distributions of the local Nusselt number, Nu ($=\dot{q}.D_e/[\lambda(T_w - T_b)]$) between the ribs for both 2D and 3D configurations. It is seen that Plane1 has the highest levels of heat transfer which is again mainly due to the effects of imposing adiabatic wall boundary condition at the graphite sleeve. As could be anticipated from the contours presented in Figure 7.13, Plane3 has the lowest levels of heat transfer due to the plane being heated from both sides (from fuel pin numbers 2 and 3) and to a lesser degree due to slightly lower streamwise velocity magnitude in this plane. An interesting picture to emerge from Figure 7.23 is the excellent agreement between the results of the 2D channel and Plane2. It should be noted, however, that such good agreement is obtained in spite of having different temperature levels (compare Figure 7.22 to Figure 7.13 b). This is due to the fact in the 2D simulation, the smaller temperature difference ($T_w - T_b$) in the denominator of the Nusselt number definition is compensated by the smaller hydraulic diameter in its numerator. This implies such good agreement between the results of the 2D channel and Plane2 should be viewed as being largely fortuitous.

Results of the relative pressure are next discussed. Figure 7.24 shows a contour of the relative pressure obtained using the 2D channel. It can be seen that while the

patterns of the pressure distributions are broadly similar in Figure 7.24 and Figure 7.15 (i.e. high-pressure zones upstream and low-pressure zones downstream of the ribs), the pressure levels especially downstream of the ribs are much lower in the 2D channel compared to the azimuthal planes. This can be better quantified in the next figure.

Inter-rib pressure distributions represented by the pressure coefficient, C_p ($=(p-p_{ref})/(0.5\rho U_b^2)$) are shown in Figure 7.25 (note that C_p in all cases is offset to zero at the middle of the cavity). It can be seen that all four azimuthal planes of the 3D configuration have similar distributions. However, the pressure at the downstream face of the first rib is much lower in the 2D channel compared to the azimuthal planes, resulting in much higher form drag in the 2D case. This is due to the 2D channel having a higher streamwise velocity magnitude (Figure 7.20) within the cavity in comparison with the azimuthal planes. In the inset to Figure 7.25 the pressure coefficient distributions of the azimuthal planes are re-plotted but now C_p has been offset to the same value at $x/k = 0.5$ for all four cases. It is seen that the pressure difference within the cavity (or the pressure drop over a rib) has the same order as the streamwise velocity magnitude (Figure 7.20) i.e. higher the velocity, higher the pressure at the upstream face of the rib. Therefore, Plane2 and Plane4 have respectively, the maximum and minimum pressure differences within the inter-rib cavity.

In the light of above findings, it appears that although a 2D approach is extremely useful and economical for parametric studies, it does not provide an accurate representation of the 3D fuel element configuration, especially for the velocity and pressure coefficient distributions, where large discrepancies were found between the results of the 2D channel and azimuthal planes of the 3D case.

7.4 SUMMARY

In the present chapter, a 3-dimensional simulation of a simplified design of a fuel element employed in the UK fleet of Advanced Gas-cooled Reactors was presented using a 30° sector representation. The computations were undertaken using the commercial CFD package, STAR-CD Version 4.02. The v^2-f formulation, which was shown to be one of the most accurate turbulence models in the earlier simulations of 2D rib-roughened channel, was employed. For the 3D configuration, results were presented using contours of the streamwise velocity, temperature, and pressure at the mid-plane and four other planes on one of the azimuthal faces. In order to assess the validity and relevance of the earlier 2D approach, comparison was made against a 2D channel which was geometrically similar to one of the azimuthal planes of the 3D case. The streamwise velocity magnitude was found to be generally higher for the 2D channel. In addition, the pressure difference within the inter-rib cavity in the 2D channel was also shown to be approximately 55% higher than that in Plane2 of the 3D configuration. Nevertheless, heat transfer results of the 2D channel was found to be in good agreement with the azimuthal planes which was shown to be rather fortuitous. The discrepancies between the 2D and 3D results are mainly associated with the 3D effects which cannot be captured using a 2D approach.

The present results have important implications that deserve consideration in the analyses of nuclear reactor operation and safety. It appears that conventional CFD methods including RANS are attractive alternatives to experimentation, at least in the stages of proof-of-concept and optimization of new fuel element designs. Although the configuration studied in this chapter was somewhat idealized, the present approach could be followed and applied in simulating more realistic and complex designs such as the Multi-Start configuration. As computational power continuously increases, it is

expected that CFD techniques would become suitable for simulations at higher Reynolds numbers using even more refined and accurately-represented grids.

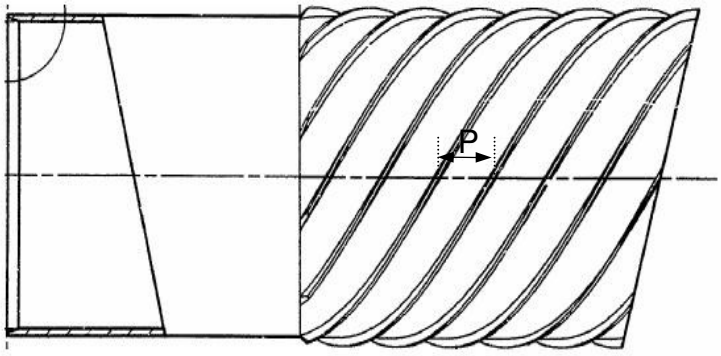

(a)

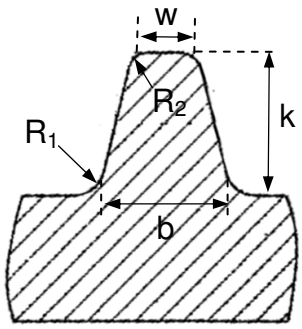

(b)

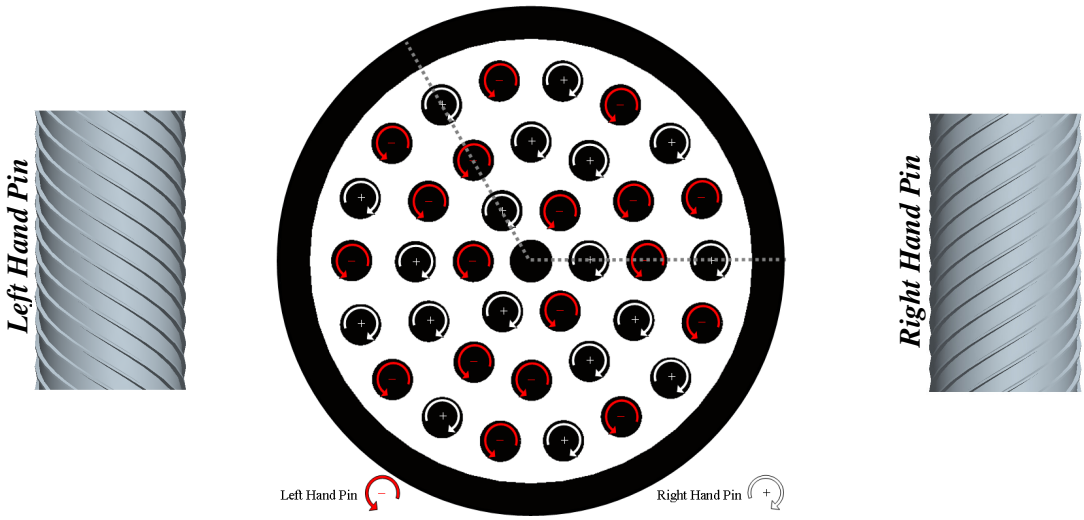

(c)

Figure 7.1 –The 'Multi-Start' configuration (a) Schematic of a fuel pin (b) Rib profile (c) Schematic of a fuel element and the minimum sector to be simulated. (Figures 7.1 (a) and (b) have been provided by J. Gotts from British Energy.)

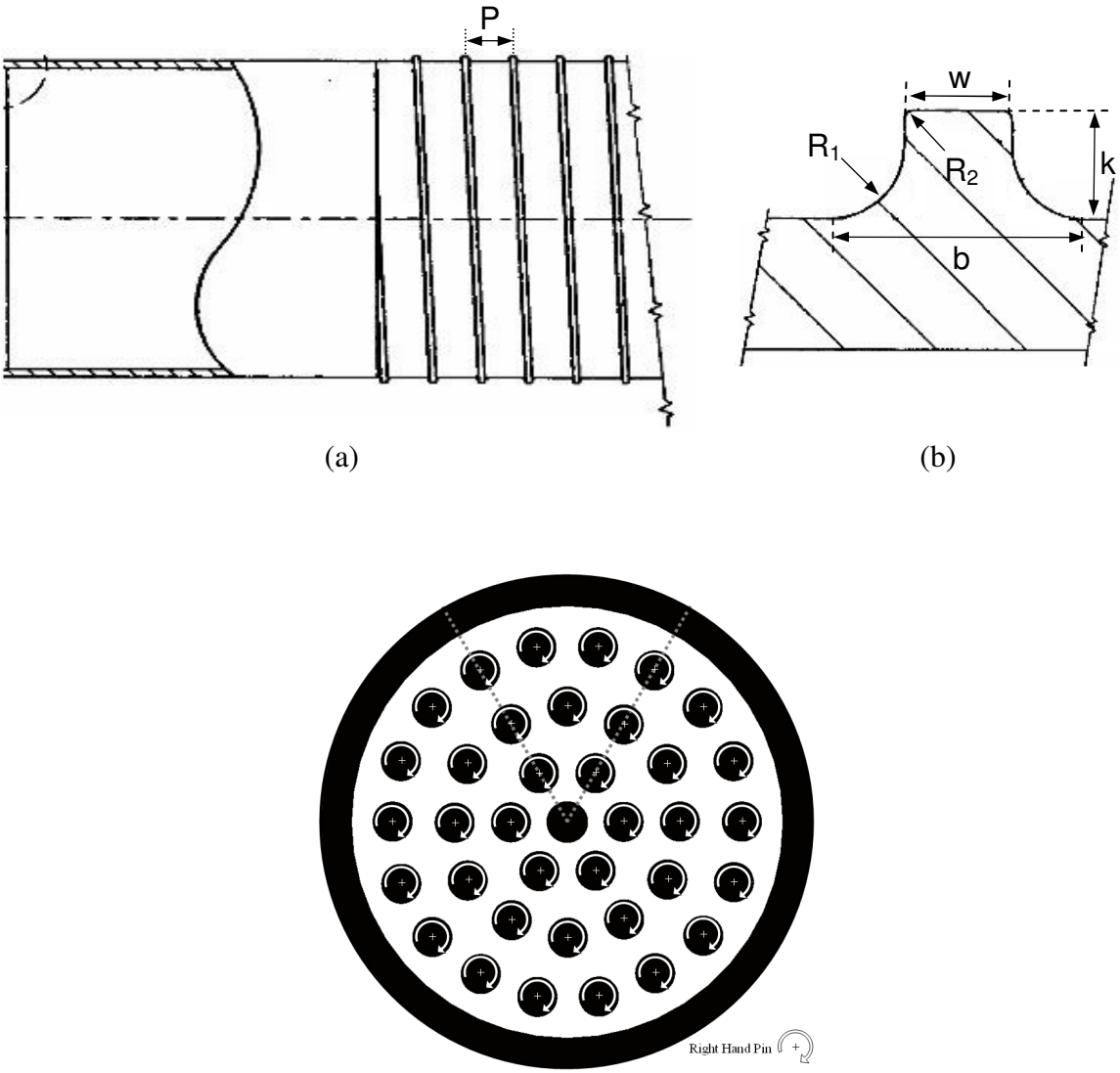

(a) (b)

(c)

Figure 7.2 – The 'Transverse' configuration (a) Schematic of a fuel pin (b) Rib profile (c) Schematic of a fuel element and the minimum sector to be simulated. (Figures 7.2 (a) and (b) have been provided by J. Gotts from British Energy.)

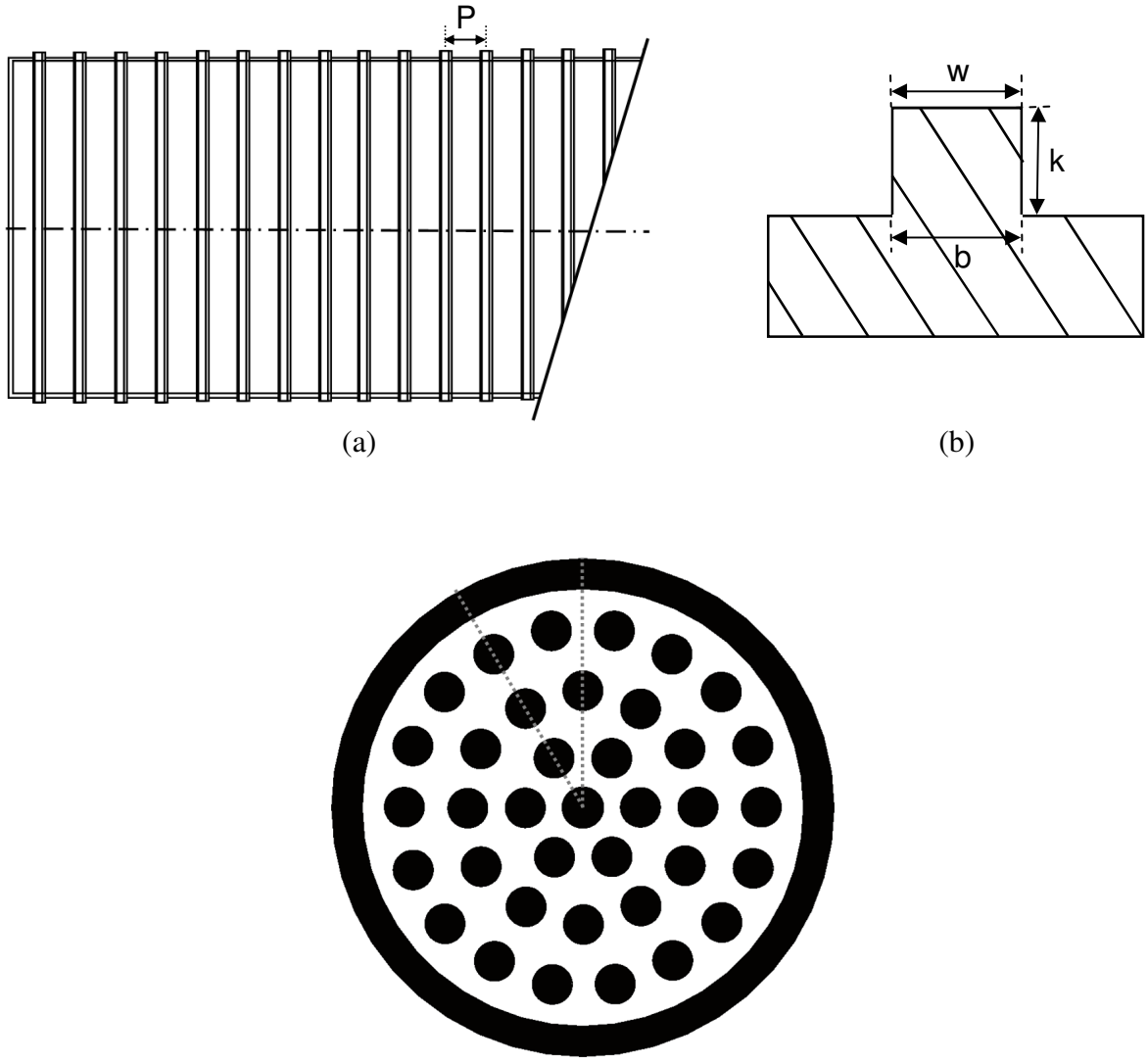

(a) (b)

(c)

Figure 7.3 – The present configuration (a) Schematic of a fuel pin (b) Rib profile (c) Schematic of a fuel element and the minimum sector to be simulated.

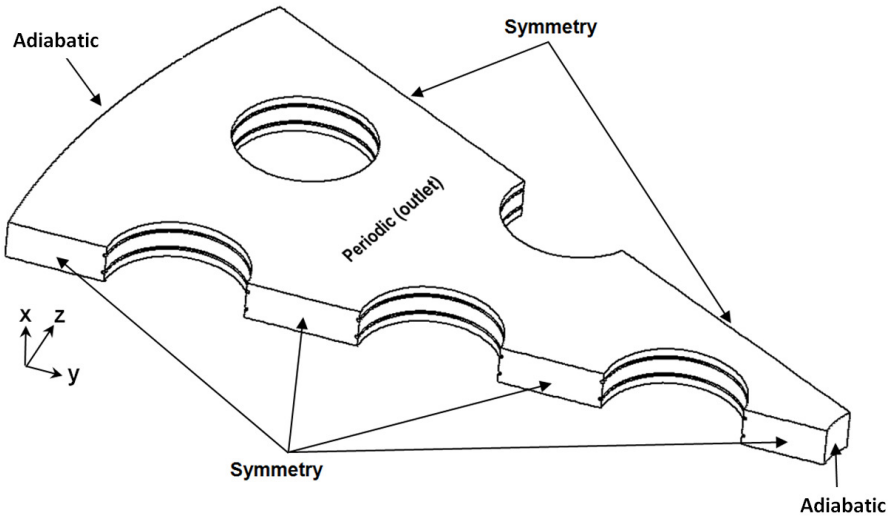

Figure 7.4 – Boundary conditions used in the domain.

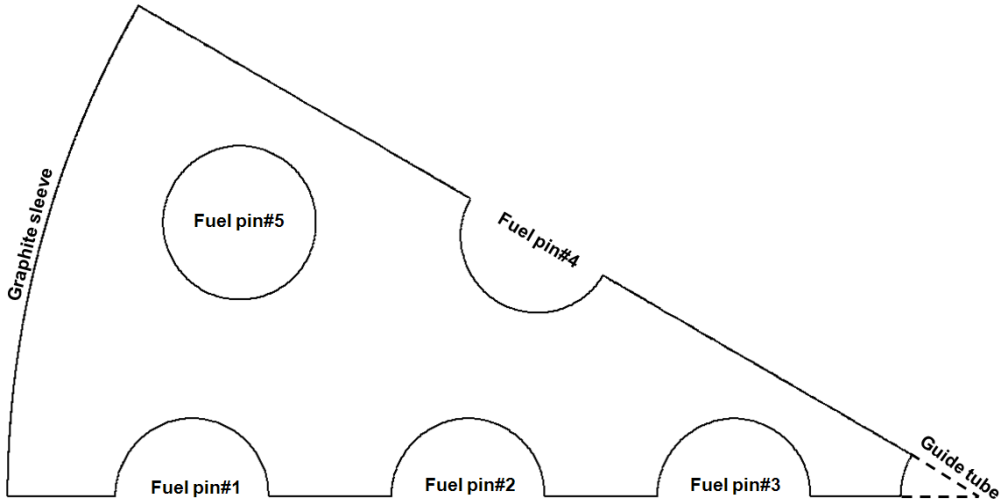

Figure 7.5 – Notations of different elements in the present computational domain.

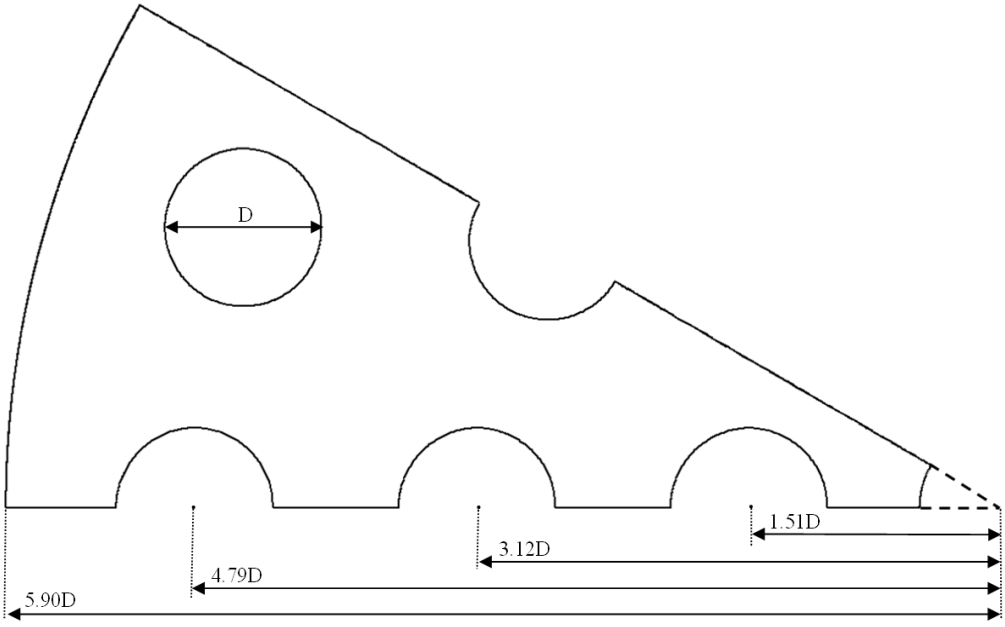

Figure 7.6 – Dimensions of the present configuration.

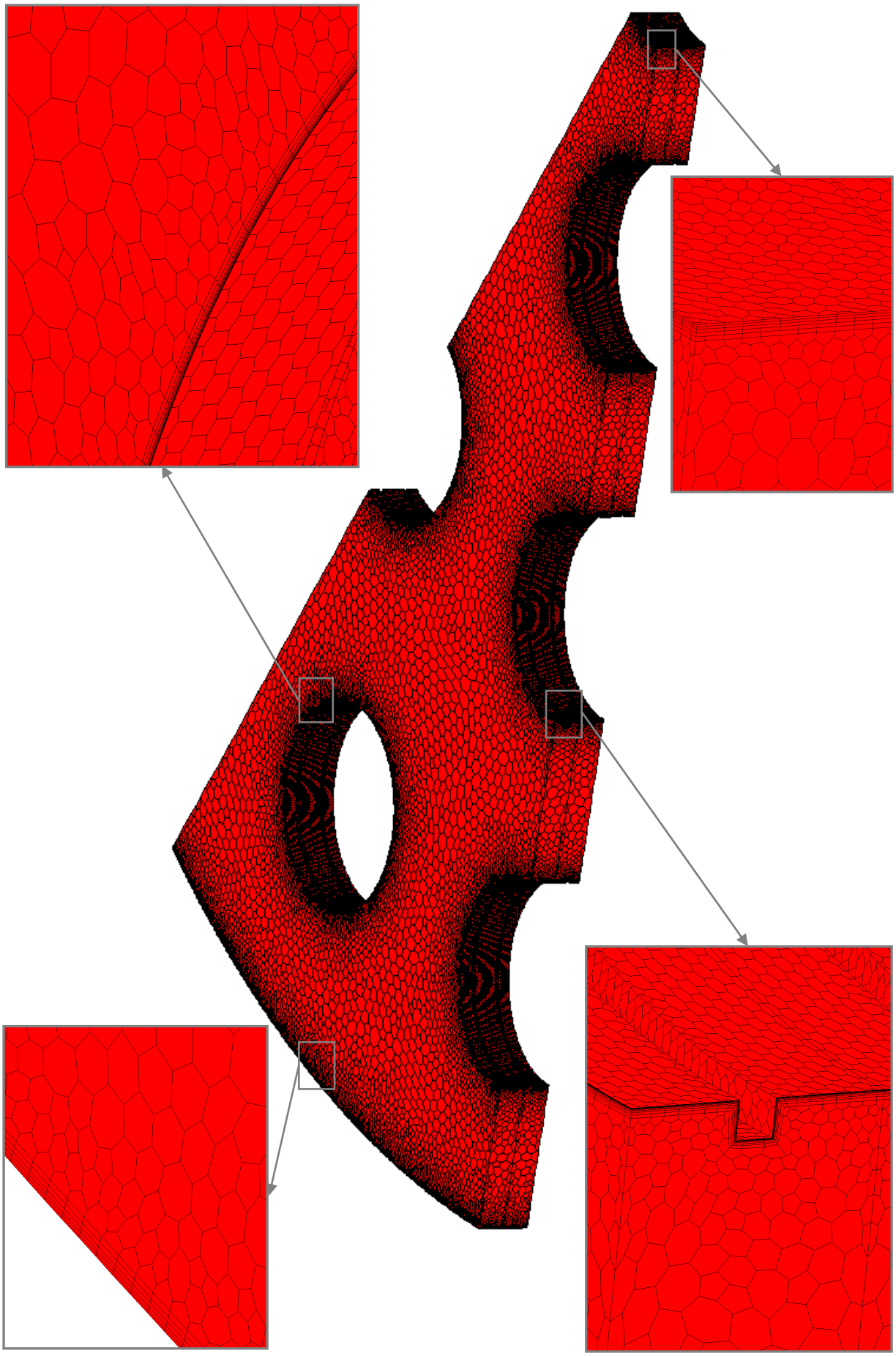

Figure 7.7 – Schematic of the mesh used for the present 3D configuration.

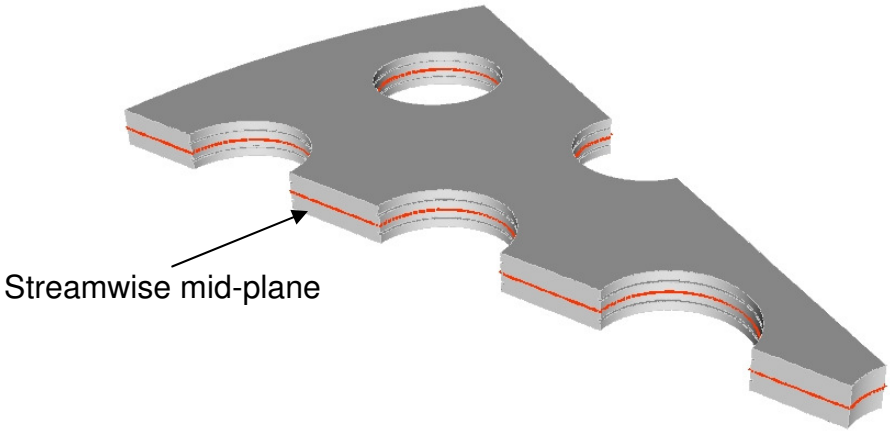

Figure 7.8 – Definition of domain's streamwise 'mid-plane'.

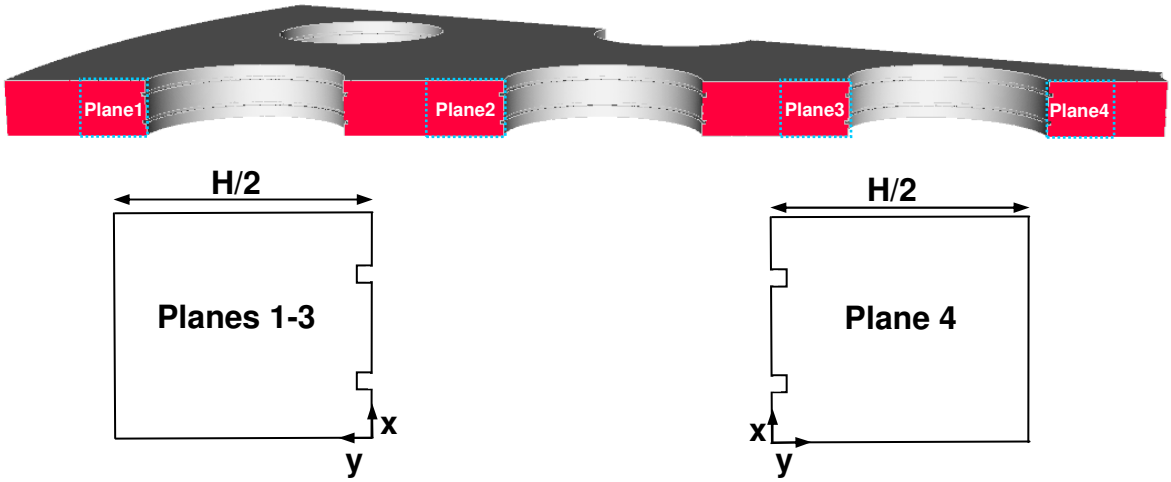

Figure 7.9 – Definition of 'azimuthal planes' (Planes 1-4).

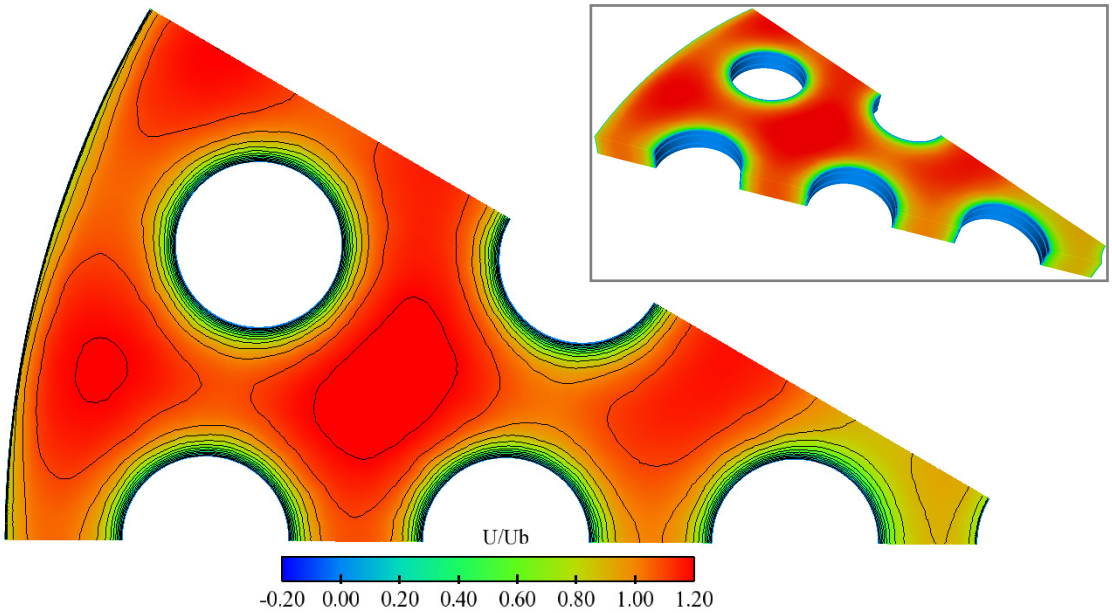

Figure 7.10 – Contour of the normalized streamwise velocity at the mid-plane (iso-contours vary from -0.2 to 1.2 with an increment of 0.1).

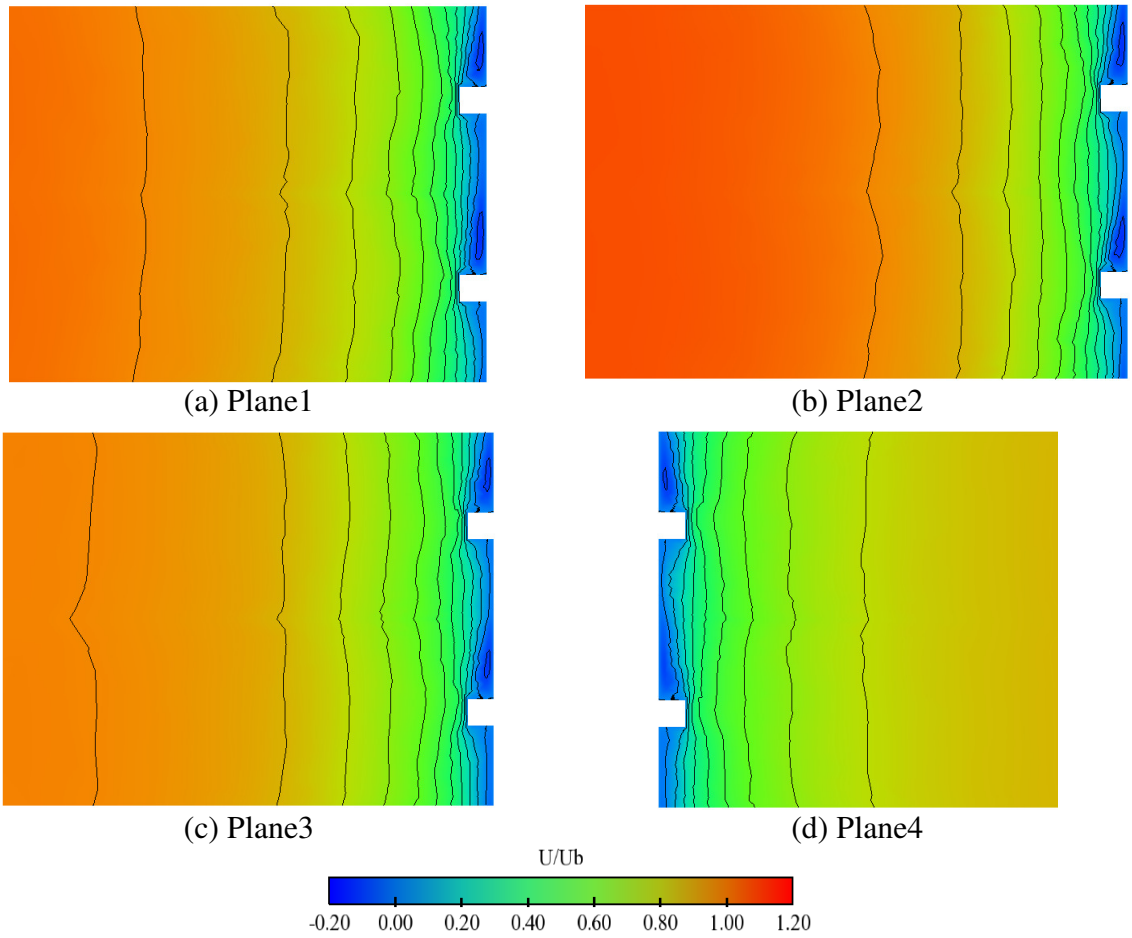

(a) Plane1 (b) Plane2

(c) Plane3 (d) Plane4

Figure 7.11 – Contours of the normalized streamwise velocity at the azimuthal planes (iso-contours vary with an increment of 0.1).

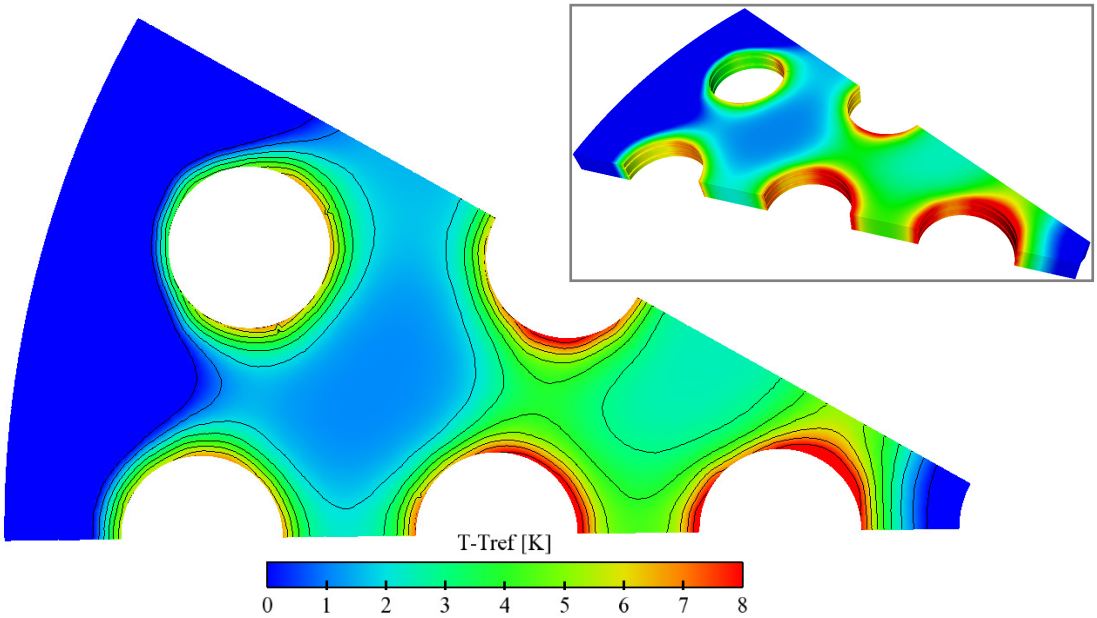

Figure 7.12 – Contour of the relative temperature at the mid-plane (iso-contours vary from 0 to 8, with an increment of 1).

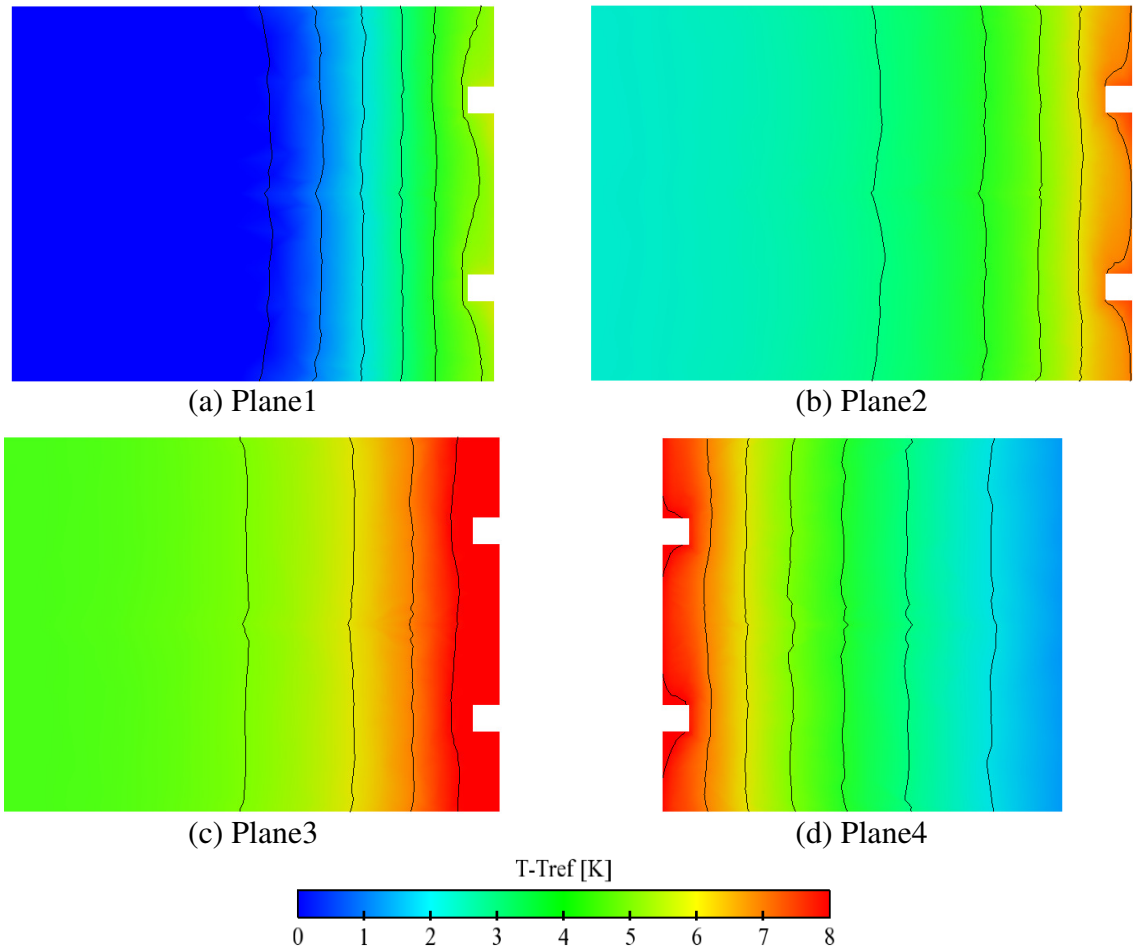

Figure 7.13 – Contours of the relative temperature at the azimuthal planes (iso-contours vary with an increment of 1).

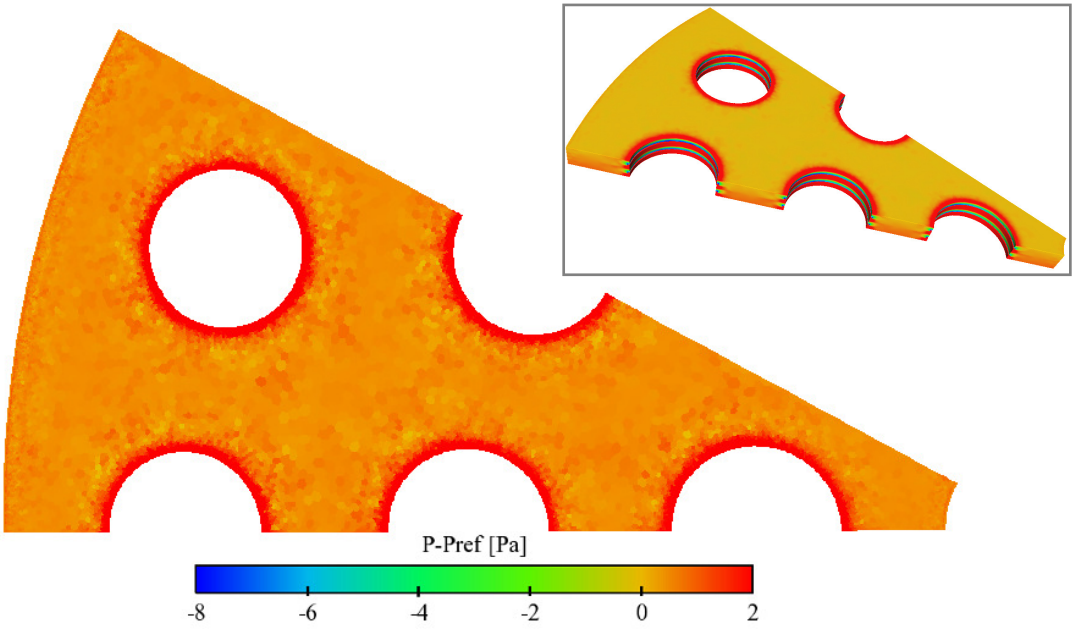

Figure 7.14 – Contour of the relative pressure at the mid-plane.

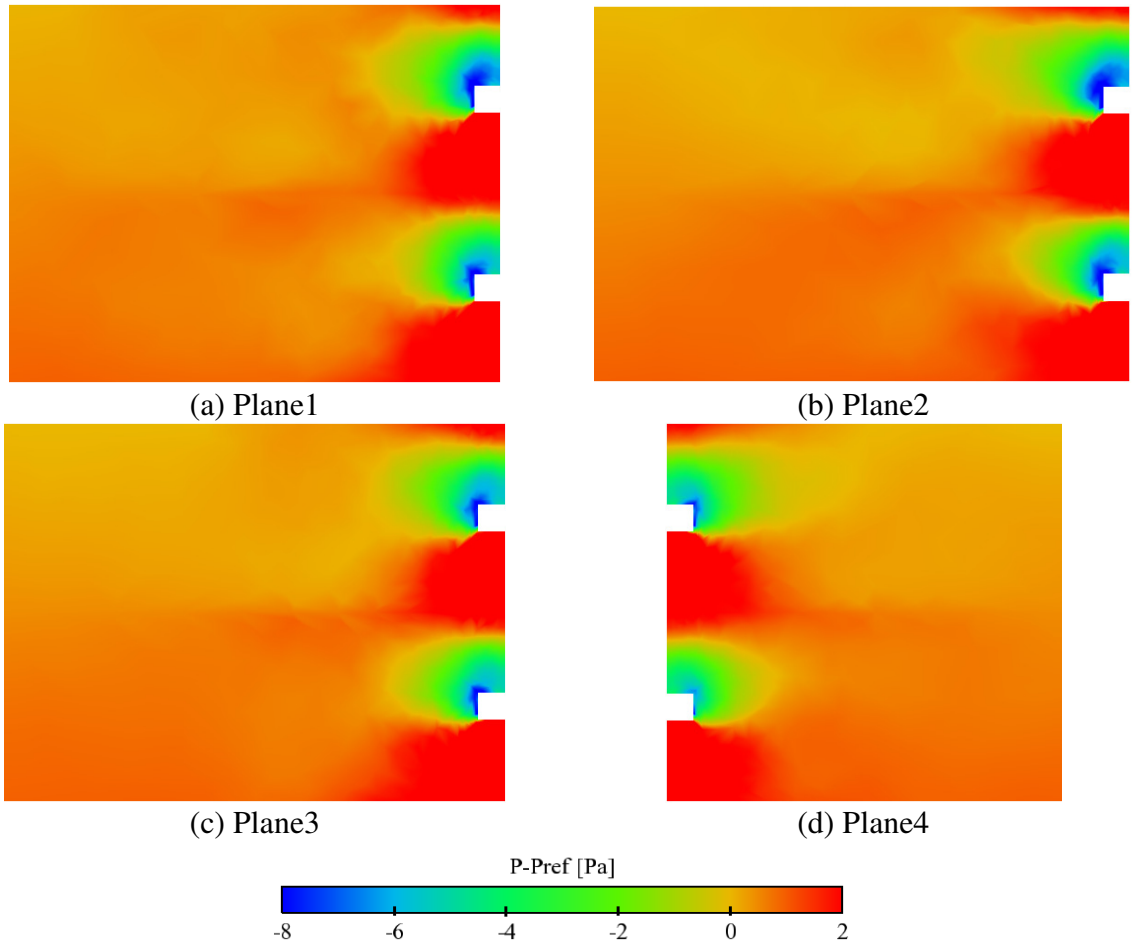

(a) Plane1 (b) Plane2

(c) Plane3 (d) Plane4

Figure 7.15 – Contours of the relative pressure at the azimuthal planes.

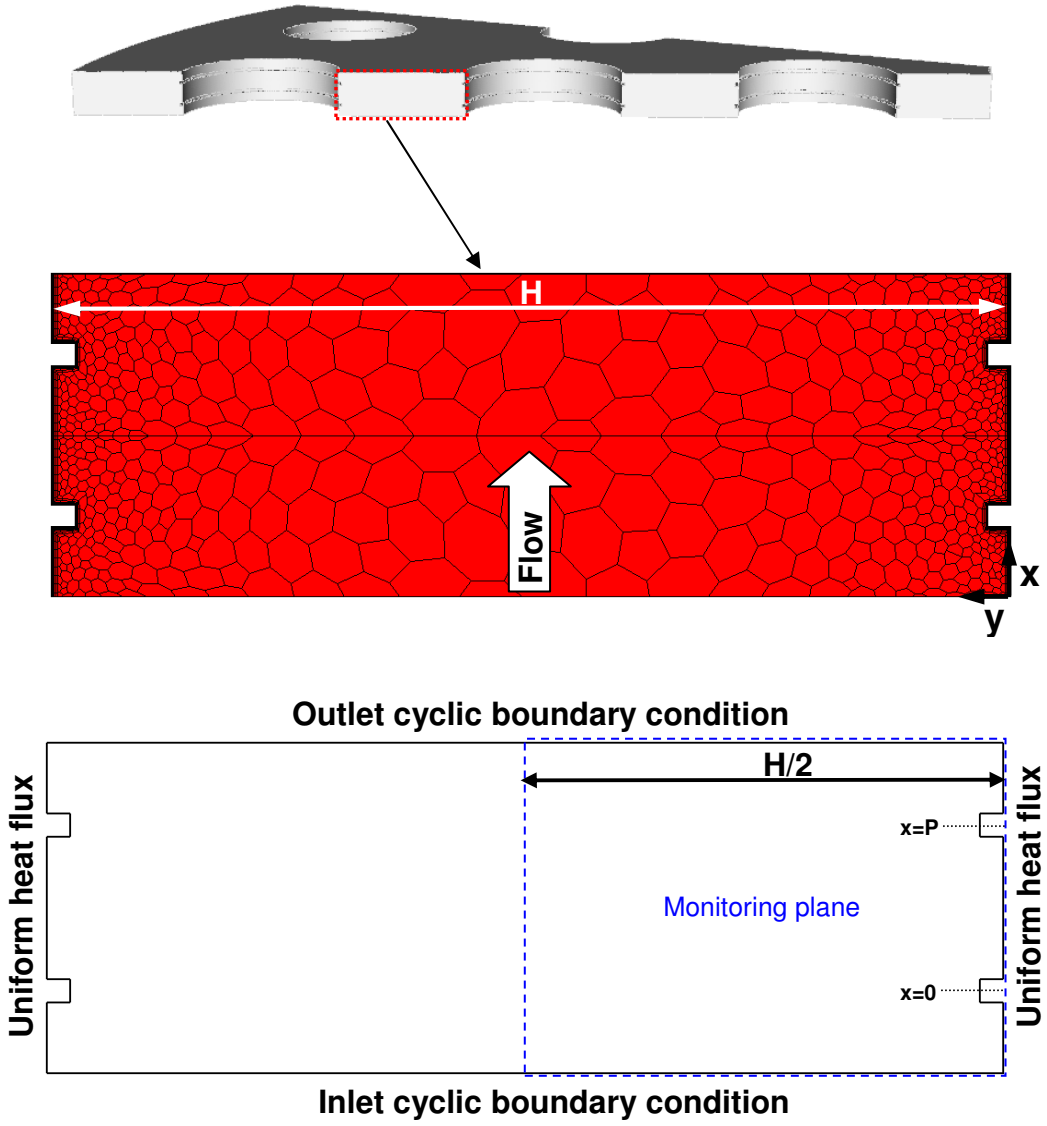

Figure 7.16 – Schematic of the mesh used for the 2D simulation and the monitoring plane.

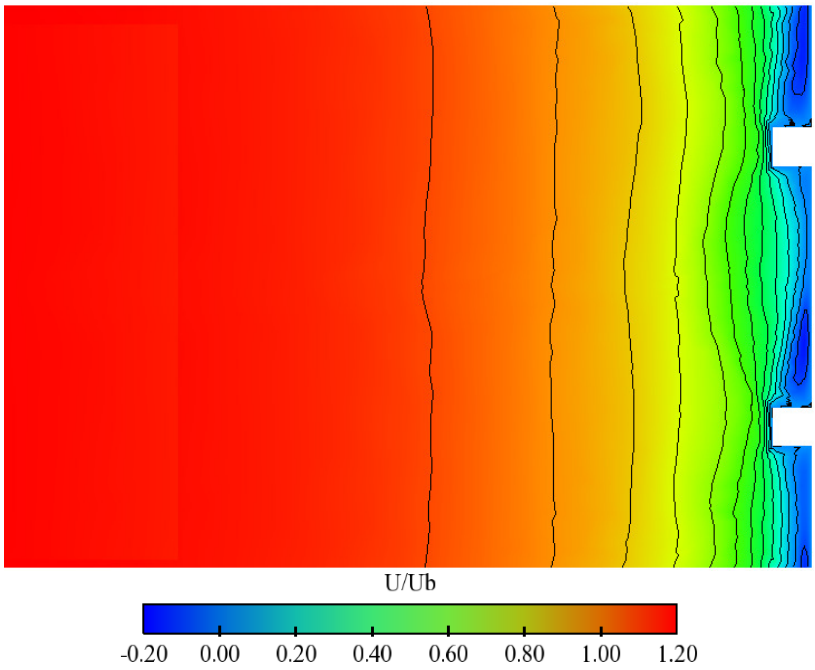

Figure 7.17 – Contour of the normalized streamwise velocity obtained using the 2D simulation (iso-contours vary from -0.2 to 1.2 with an increment of 0.1).

.

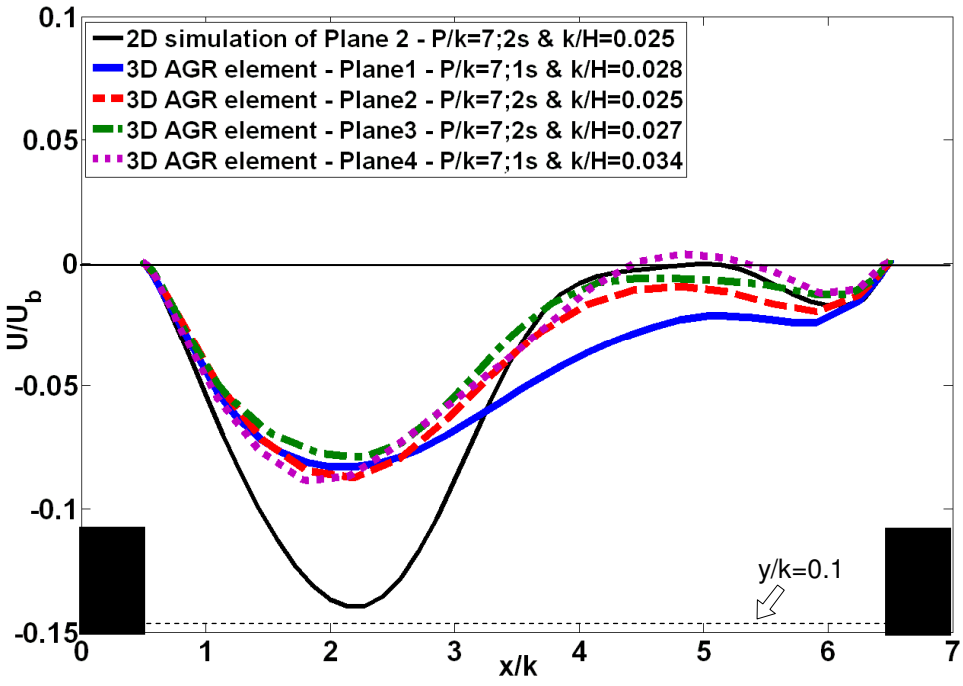

Figure 7.18 – Streamwise velocity distributions at *y/k* = 0.1 for the azimuthal planes compared against the 2D simulation.

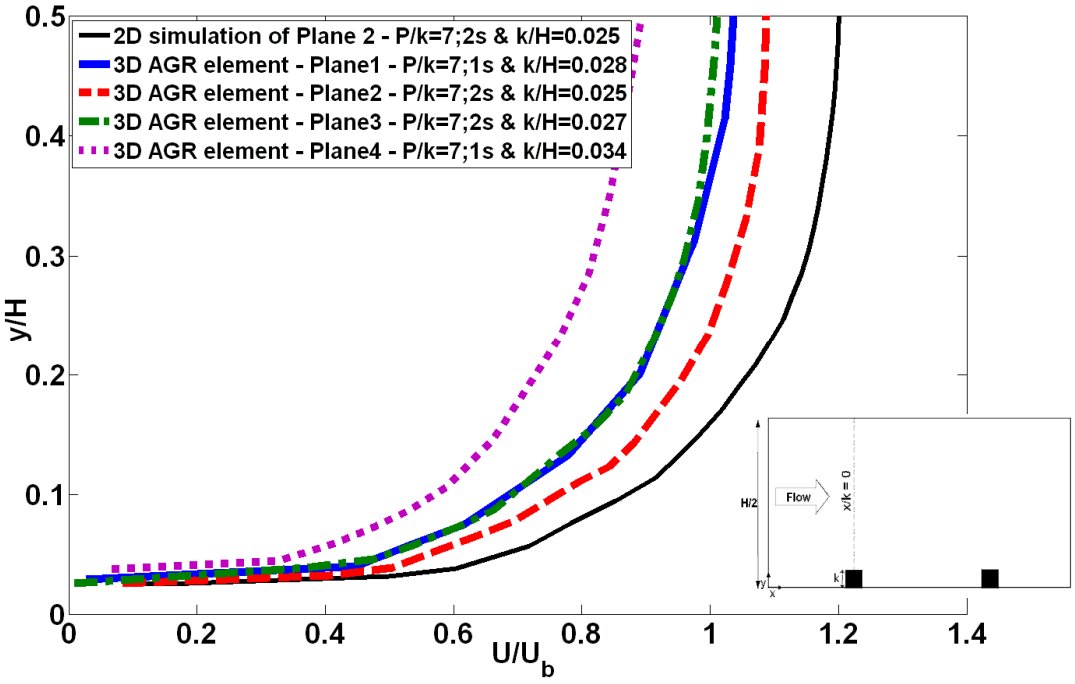

Figure 7.19 – Streamwise velocity profiles on the rib-top for the azimuthal planes compared against the 2D simulation.

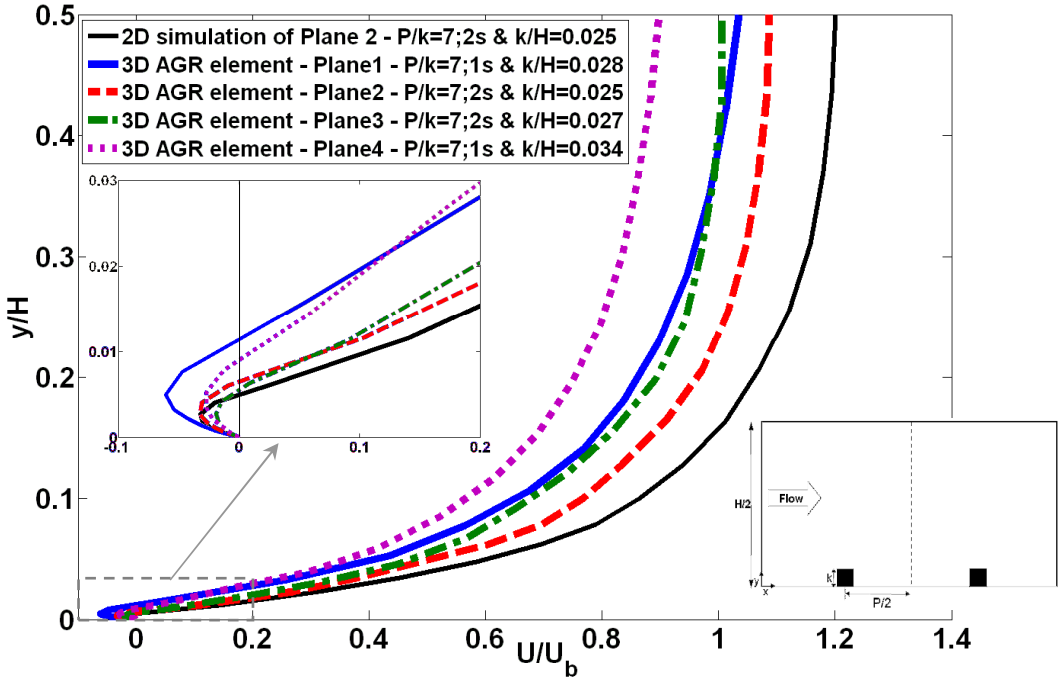

Figure 7.20 – Streamwise velocity profiles at the middle of the cavity for the azimuthal planes compared against the 2D simulation.

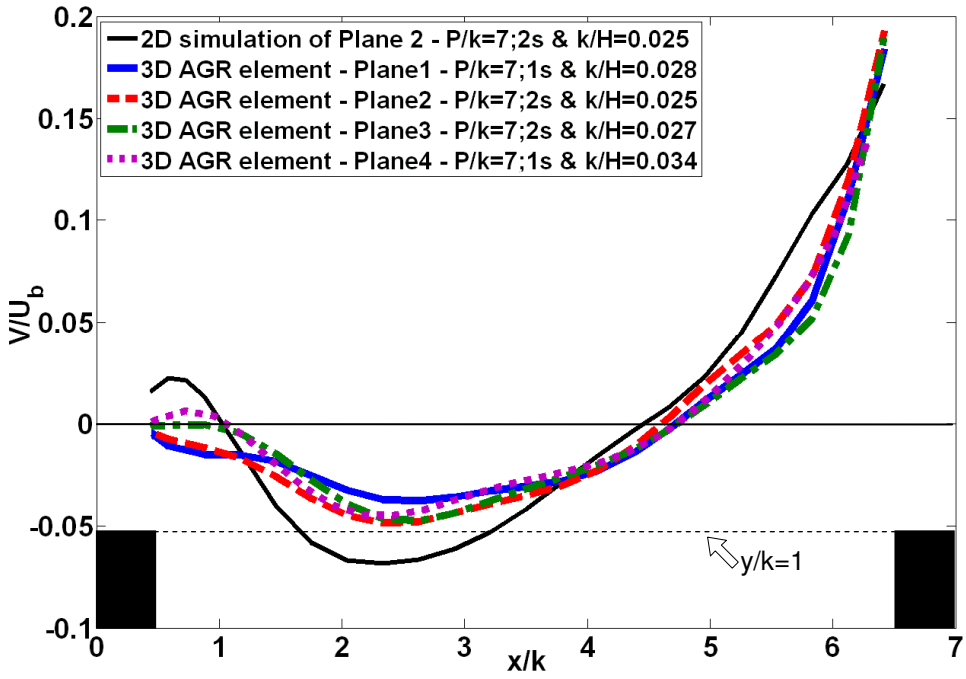

Figure 7.21 – Wall-normal velocity distributions at $y/k = 1$ for the azimuthal planes compared against the 2D simulation.

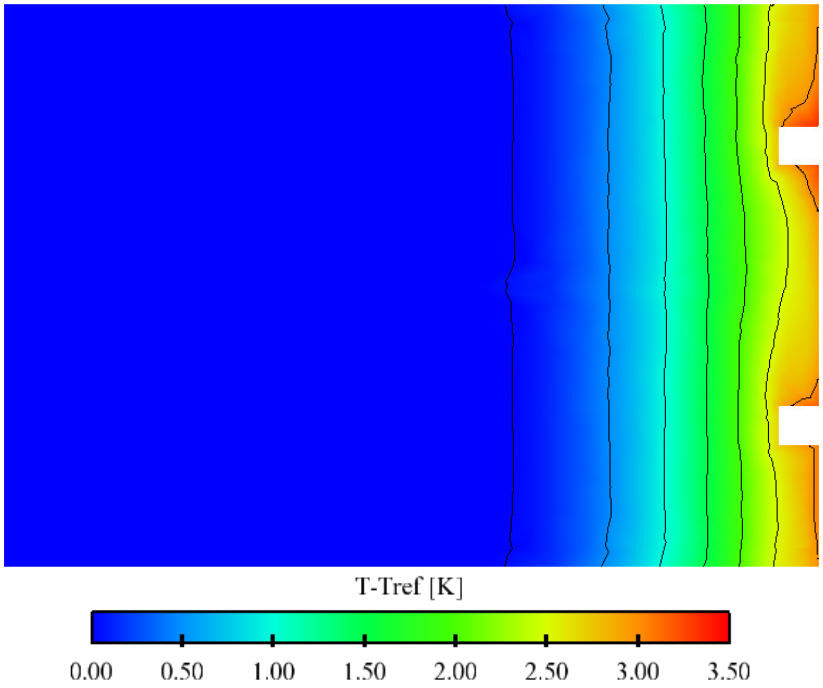

Figure 7.22 – Contour of the relative temperature obtained using the 2D simulation (iso-contours vary from 0 to 3.5 with an increment of 0.5).

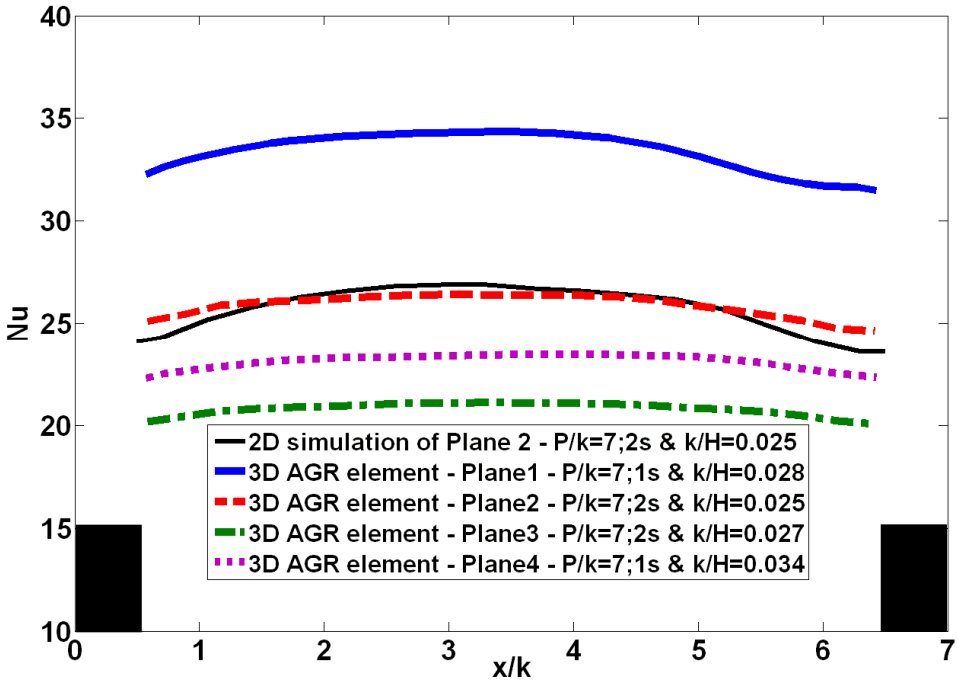

Figure 7.23 – Nusselt number distributions for the azimuthal planes compared against the 2D simulation.

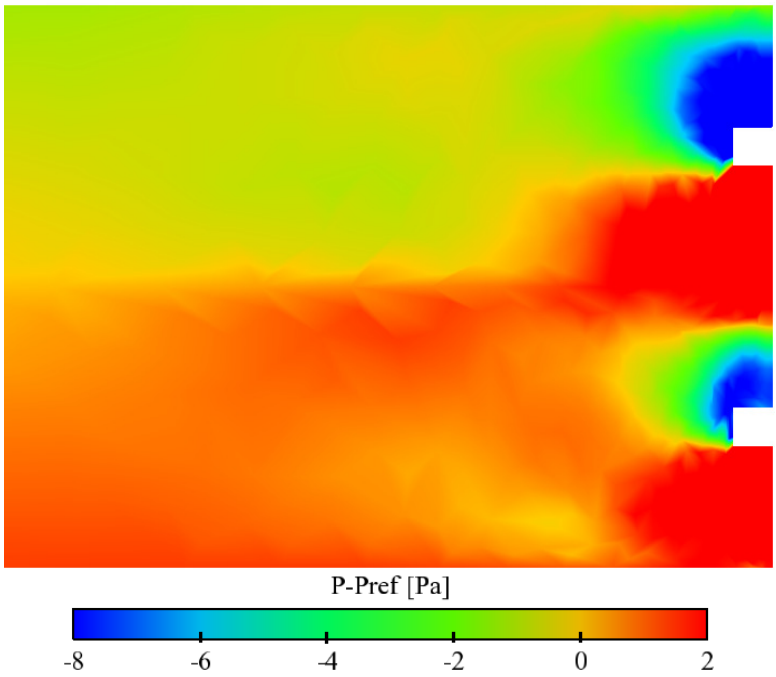

Figure 7.24 – Contour of the relative pressure obtained using the 2D simulation.

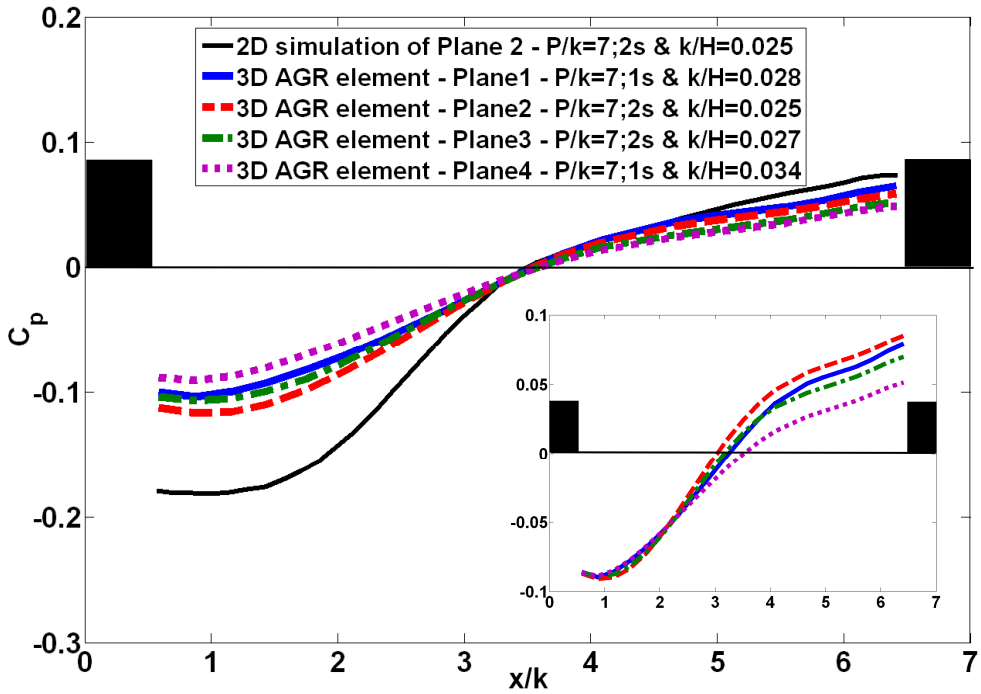

Figure 7.25 – Pressure coefficient distributions for the azimuthal planes compared against the 2D simulation.

CHAPTER 8

CONCLUSIONS AND FUTURE WORK

8.1 PRELIMINARY REMARKS

In this thesis a numerical study has been undertaken to investigate turbulent flow and heat transfer in a number of flow problems, representing the gas-cooled reactor core flows. The first part of the research consisted of a meticulous assessment of various advanced RANS models of fluid turbulence against experimental and numerical data for buoyancy-modified mixed convection flows, such flows being representative of low-flow-rate flows in the cores of nuclear reactors (both presently-operating Advanced Gas-cooled Reactors and proposed 'Generation IV' designs). For this part of the project, an in-house code ('CONVERT'), a commercial CFD package ('STAR-CD') and an industrial code ('Code_Saturne') were used to generate results. Wide variations in turbulence model performance were identified.

The research described above concerned flow in smooth passages; a second distinct contribution made in this thesis concerned the thermal-hydraulic performance of rib-roughened surfaces, these being representative of the fuel elements employed in the UK fleet of Advanced Gas-cooled Reactors (AGRs). This part of the research took various design factors into consideration including the effects of rib profile, rib height-to-channel height ratio, rib width-to-height ratio, rib pitch-to-height ratio and Reynolds number. Through comparison with experimental data, the performance of different RANS turbulence models was also assessed. In addition, the effects of applying standard wall function and using unstructured grids were also investigated.

The final stage of the study involved a simulation of a simplified 3-dimensional representation of an AGR fuel element using a 30° sector configuration. The v^2-f model was employed and comparison was made against the results of a 2D rib-roughened channel in order to assess the validity and relevance of the precursor 2D simulations of rib-roughened channels.

8.2 CONCLUSIONS

Results have already been discussed on a case-by-case basis in each Chapter, but salient points for each case are repeated here in order to emphasize the principal conclusions.

8.2.1 Mixed Convection Heat Transfer

The following conclusions could be drawn from the work on mixed convection heat transfer in a vertical heated pipe:

- Initial comparison of the studied turbulence model results with forced convection data generated by You et al. (2003) produced a somewhat inconsistent picture, whereby a given model might return a reasonably accurate value for Nusselt number, but not local friction coefficient (or vice-versa). However, the CI model

results were closest to the DNS figure for local friction coefficient, whereas the Suga model was in best agreement with the DNS value of Nusselt number.

- Comparison with the DNS data of You et al. (2003) showed that the LS model best captures the phenomenon of heat transfer impairment (characterized as Nu/Nu_0) that occurs in the ascending flow case; both v^2-f formulations (STAR-CD and Manchester v^2-f models) also performed well. Except at lower values of Bo, the performance of the LCL k-ε model is very similar to that of the LS model. The CI model indicated that impairment occurs at higher values of Bo, while the Suga model under-predicted the extent of impairment. Large Eddy Simulations showed an earlier onset of heat transfer impairment. The k-ω-*SST* model was found to be in the poorest agreement with the data.

- For friction coefficient, of the turbulence models considered, both v^2-f schemes were in closest agreement with the three DNS points of You et al. (2003) and the data of Carr et al. (1973). The LS, CI, Suga and k-ω-*SST* models indicated little or no reduction in mixed convection c_f below the c_{f0} level (in the case of the LS model this was in part related to its under-prediction of c_{f0}). The Large Eddy Simulations showed an early onset of c_f-reduction; in fact, the LES computations returned the lowest values of c_f / c_{f0} found in the present study. There was considerable scatter in the experimental measurements, especially for higher Bo.

- All formulations were able to resolve the DNS flow and turbulence profiles at forced convection (case A) and early-onset of mixed convection (case B).

- At the maximum impairment condition (case C), where the flow is largely laminarized, the DNS flow and turbulence profiles were resolved most accurately by the LS and v^2-f models. It should be noted, however, that no single scheme could be said to be in excellent agreement with the DNS data.

- Satisfactory agreement between CONVERT and STAR-CD was obtained when using the Suga model, although some discrepancies were found in the turbulent kinetic energy profiles. Stability problems were encountered in both codes for cases with higher buoyancy influence; these problems were found to be associated with the functional form of C_μ. The pipe length in CONVERT had to be reduced to only 50D and no solution could be obtained for $Bo > 0.18$ in STAR-CD. Consequently, the discrepancies between the results could be related to the difference in the pipe length in both codes.

- Reasonable agreement between Code_Saturne and STAR-CD was obtained when using the *k-ω-SST* model, although some discrepancies mainly in the turbulence profiles were occurred especially for the recovery regime.

- In an ascending flow problem, including the Yap correction term and/or buoyancy production term showed to have negligible effects on the heat transfer and friction coefficient results.

- Mean flow and turbulence profiles at four different streamwise locations (x/D = 200, 300, 350, 500) were compared for the laminarized case (case C) using the LS model in CONVERT. Wide variations were found between the profiles and it was shown that for the laminarized case, the pipe length should be at least 500D in order to reach a fully-developed solution.

- The LS, CI and Suga models were evaluated in comparison with the data of Polyakov and Shindin (1988) for developing forced and mixed convection flows. The CI scheme was in the best agreement with the forced convection case; however, the LS model was found to be superior in the computation of mixed convection flows.

- Computations were carried out for six different Reynolds numbers (Re = 5,000 – 25,000) using the LS model. At each Reynolds number, the three thermal-hydraulic regimes of 'early-onset of mixed convection', 'laminarization', and 'recovery' were present. It was shown that the original definition of Bo (Eqn. (5.1)) results in collapsing curves of Nu/Nu_0 obtained at different Re in recovery region i.e. $Bo > 0.25$. It is, however, unable to produce a satisfactory collapse of the family of curves at lower levels of buoyancy influence.

8.2.2 2D Rib-Roughened Channels

The following conclusions could be derived from the simulations carried out using 2D rib-roughened channels:

- Simulations were initially carried out for a 3D square cross-sectioned rib-roughened channel with P/k = 9; 2s using the v^2-f model and results were compared against the experimental data of Rau et al. (1998), where relatively good agreement was found between the results.

- Sensitivity tests using four 2D grids with different levels of refinement were carried out and it was revealed that flow over the centre-line of the 3D channel studied by Rau et al. (1998) can be represented by a 2D configuration with relatively good accuracy, resulting in significant savings in computation power and time required i.e. suitable for carrying out parametric studies.

- Two different variations of thermal boundary conditions on the ribs were tested and it was found that they affect the heat transfer levels only in the regions near the ribs, while naturally for a forced convection flow the dynamic field is not affected by the thermal boundary condition.

- The performance of four low-Reynolds number eddy viscosity models including the *k-ε*, *k-ω-SST*, v^2*-f*, and Suga models were investigated. Of the four models, the v^2*-f* was found to be in the best agreement with the dynamic and thermal field data of Rau et al. (1998) as, to a somewhat lesser degree were the results of the *k-ω-SST* model. The *k-ε* and Suga models performed poorly in comparison to the experimental data. The wide variation in turbulence model performance was attributed primarily to model determination of the turbulence length scale, and the role of the length scale in affecting both the advective and diffusive terms of the Energy Equation.

- Computations using the v^2*-f* and *k-ω-SST* models indicated that there is little difference between the dynamic and thermal performance of channels with square ribs and those with AGR rib profiles i.e. 'Multi-Start' rib profile.

- Results of the low-Reynolds number *k-ε* model were compared against the results obtained by the high-Reynolds number *k-ε* formulation coupled with the Standard Wall Function (SWF). Large discrepancies were found between the results and it was seen that the SWF as implemented in STAR-CD is not suitable for recirculating flows mainly due to the flow being highly 'non-universal' within the separation bubble. However, it has to be noted that using a mesh different from the one used in this part of the study could affect the overall performance of the SWF in STAR-CD.

- The effects of mesh type were examined by comparing the results obtained using structured and unstructured grids. The largest discrepancies occurred in the levels of heat transfer and turbulent kinetic energy. However, relatively good agreement was found for the mean flow profiles; streamwise velocity and pressure contours obtained by both grids were very similar. Comparing a velocity vector plot

obtained for a small section near a rib, revealed that the unstructured mesh was not as good as the structured one in capturing the very sharp velocity gradients near the ribs, despite having very similar values of y^+ in the near-wall cells.

- Configurations with rib pitch-to-height ratios (*P/k*) of 6, 9, and 12 were studied using the v^2-*f* and *k*-ω-*SST* closures. The results of the v^2-*f* model showed that *P/k* = 6 was the optimum ratio (i.e. having the highest value of efficiency index), while the *k*-ω-*SST* model indicated *P/k* = 9 to be the optimum ratio.

- The effects of rib height were examined using the v^2-*f* model. The rib height-to-channel height ratios (*k/H*) of 0.1, 0.09, 0.075, and 0.05 were tested. The results showed that the average Nusselt number and friction coefficient decrease with reducing the rib height. The configuration with the shortest rib height (*k/H* = 0.05) was found to be the optimum design.

- The effects of rib width were examined by testing the rib width-to-height ratios (*b/k*) of 0.5, 1, and 1.5. The computations using the v^2-*f* model showed that the average Nusselt number and friction coefficient decrease by increasing the rib width. It was found that the configuration with *b/k* = 0.5 gives the highest value of efficiency index.

- Computations using the v^2-*f* and *k*-ω-*SST* models were carried out at two Reynolds numbers of *Re* = 30,000 and 100,000. The results of both models indicated little difference between the dynamic performances of channels at both Reynolds numbers. By increasing the Reynolds number, the v^2-*f* model showed small increase in the value of average Nusselt number; in contrast, the *k*-ω-*SST* model returned lower value of Nu/Nu_0 for *Re* = 100,000. Both models predicted higher average friction coefficient for *Re* = 100,000. Accordingly, both models found that a higher efficiency index is obtained at *Re* = 30,000.

8.2.3 3D AGR Fuel Element

The conclusions which could be drawn from the work on the 3D simulation of an AGR fuel element are as follows:

- A computational domain consisting of a 30° sector along with an assumption of streamwise periodicity at inlet and outlet was shown to be suitable for representing the 3D flow over a simplified design of an AGR fuel passage with parallel ribs.
- The computational domain broadly consisted of three different sub-channels including triangular, square, and wall sub-channels. This makes the simulations conducted using simple 2D channels or even triangular or square sub-channels dubious.
- The results of the streamwise velocity showed that local maxima form in the centres of all sub-channels, while the flow is slowed down near fuel pins, guide tube and graphite sleeve.
- The results of the temperature showed that the maximum temperature generally occurs around fuel pins, especially near fuel pins in the 2 inner rings, where the gap between the fuel pins is relatively small. The lowest temperatures were found to be near the guide tube and graphite sleeve, at which adiabatic wall boundary condition was imposed.
- The results along one of the azimuthal faces of the 3D case were compared against the results of a 2D configuration with similar geometrical and numerical properties to one of the azimuthal planes (i.e. 'Plane2'). Magnitudes of the streamwise and wall-normal velocities were generally higher in the 2D simulation. Pressure difference within the inter-rib cavity was also significantly

higher in the 2D channel compared to the azimuthal planes of the 3D configuration. On the other hand, heat transfer levels of the 2D channel (represented by the local Nusselt number) were found to be in quite close agreement with the results of Plane2, although this agreement was shown to be largely fortuitous.

- It was shown that although a 2D approach can be extremely useful and economical for 'parametric studies', it does not provide an accurate representation of a 3D fuel element configuration, especially for the velocity and pressure coefficient distributions, where large discrepancies were found between the results of the 2D channel and azimuthal planes of the 3D case.
- The main source of discrepancy between the results of the 2D channel and Plane2 of the 3D case was found to be related to the 3D effects which can only be captured by a 3D configuration.

8.3 FUTURE WORK

Although the present work has made some significant progress towards the original objectives outlined in Introduction, the present contribution could be developed in the following areas:

8.3.1 Mixed Convection Heat Transfer

- **Application of RSM:** In the present work, although a broad range of low-Reynolds-number turbulence models were tested on the flow in a vertical heated pipe, future work could focus on applying more complex RANS models such as Reynolds Stress Models.
- **Effects of Prandtl number:** The value of Prandtl number was set to 0.71 throughout the present work. The effects of increasing the Prandtl number on heat

transfer and friction coefficient could be tested in the context of mixed convection heat transfer (see Seng, 2009, for example).

- **New Buoyancy parameter:** In the present work, heat transfer impairment/enhancement against Buoyancy parameter (originally developed by Hall and Jackson, 1969) was tested for a range of Reynolds numbers. At each Reynolds number, the three thermal-hydraulic regimes of 'early-onset of mixed convection', 'laminarization', and 'recovery' were present. Further work can be done on advancing a low-Reynolds-number extension of the buoyancy parameter (which was initiated by Cotton and Keshmiri, 2008) to further improve the collapse of computed heat transfer results. If successful, this could result in deriving a new correlation for heat transfer performance of mixed convection flows.

8.3.2 2D Rib-Roughened Channels

- **Other design factors:** The effects of several continuous and discrete design factors on heat transfer and friction coefficient were examined in the present work. It might be worthwhile to explore the effects of other geometrical factors such as defining a groove in between the ribs and varying the distance between opposite ribs on 2-side ribbed channels.
- **Optimization techniques:** The results obtained for various design factors can be used as an input to optimization techniques such as Response Surface Method and Multi-Objective Optimization.
- **LES/DNS of 3D channels:** It would be of great interest to simulate the 3D rib-roughened channels of Rau et al. (1998) using Large Eddy Simulation or even Direct Numerical Simulation, if computational resources permit.

- **Structured vs. Unstructured grids:** During the course of this work, some discrepancies were found between the results of structured and unstructured grids. It would be beneficial to explore the reasons for these discrepancies. Making use of methods such as 'adaptive mesh refinement' is also desirable in order to create an optimum mesh.
- **Equivalent Sand-Grain Roughness:** A further aspect of the investigation could examine the extent to which classical (Schlichting, 1979), and extended (Jiménez, 2004) concepts of 'Equivalent Sand-Grain Roughness' can be applied to the discrete forms of roughness used in AGR fuel pin designs.

8.3.3 3D AGR Fuel Element

- **Simulation of Multi-Start configuration:** Simulations could be carried out for flow over an accurately-represented 120° sector of an AGR fuel passage of Multi-Start configuration. Preliminary studies in this field including mesh generation have already been carried out as part of the present work (Appendix C), but further research is required in order to bring this work to its proper fruition. To date, there is no other 3D simulation of this type and therefore, this could represent the first attempt to simulate an accurate representation of an AGR fuel element using CFD.
- **Comparison with experimental results:** A few experiments (Pirie, 1987, for example) have been carried out by British Energy to measure the pressure drop and flow resistance of a fuel stringer at different mass flow rates ($\dot{m}/\mu = 4\times10^4 - 4.5\times10^5$ corresponding to reactor flows in the range of approximately 7 - 80% where full channel flow is taken as 17 kg/s; Morrison, 2003). These experiments provide a valuable source for validation of CFD results and therefore, could be used as an extension of the present work.

- **LES of a 3D fuel element:** Given the computational resources available including parallel mesh generation packages and High Performance Computing (HPC) facilities, it is possible and certainly of interest to use Large Eddy Simulation techniques to simulate the flow over 3D AGR fuel passages.

BIBLIOGRAPHY

[1] Abdelmeguid, A.M. and Spalding, D.B., 1979. Turbulent flow and heat transfer in pipes with buoyancy effects. *J. Fluid Mech.*, 94, 383-400.

[2] Abe, K., Kondoh, T. and Nagano, Y., 1994. A new turbulence model for predicting fluid flow and heat transfer in separating and reattaching flows - I. Flow field calculations. *Int. J. Heat and Mass Transfer*, 37 (1), 139-151.

[3] Abid, R., Rumsey, C. and Gatski, T.B., 1995. Prediction of nonequilibrium turbulent flows with explicit algebraic stress models. *AIAA J.*, 33, 2026-2031.

[4] Acharya, S., Dutta, S., Myrum, T.A. and Baker, R.S., 1993. Periodically developed flow and heat transfer in a ribbed duct. *Int. J. Heat Mass Transfer*, 36, 2069-2082.

[5] Addad, Y. and Laurence, D., 2008. Computational investigation of vertically heated pipes using the large-eddy simulations approach. In: *Proc. 7th Int. ERCOFTAC Symp. on Engineering Turbulence Modelling and Measurements 'ETMM7'*, Limassol, Cyprus, pp. 400-405.

[6] Archambeau, F., Mechitoua, N. and Sakiz, M., 2004. A finite volume method for the computation of turbulent incompressible flows – Industrial applications. *Int. J. Finite Volumes (electronic journal)*, 1(1).

[7] Ashrafian, A., 2004. Numerical investigation of turbulent flow in a channel with rough walls, *thesis,* Ph.D. thesis, Dept. of Energy and Process Eng., Norwegian University of Science and Technology, Trondheim, Norway.

[8] Ashrafian, A., Andersson, H.I. and Manhart, M., 2004. DNS of turbulent flow in a rod-roughened channel. *Int. J. Heat Fluid Flow*, 25, 373-383.

[9] Axcell, B.P. and Hall, W.B., 1978. Mixed convection to air in a vertical Pipe. In: *Proc. 6th Int. Heat Transfer Conference*, Toronto, Canada, Paper MC-7.

[10] Behnia, M., Parneix, S. and Durbin, P.A., 1998. Prediction of heat transfer in an axisymmetric turbulent jet impinging on a flat plate. *Int. J. Heat Mass Transfer*, 12, 1845-1855.

[11] Billard, F., 2010. Near-wall turbulence RANS modelling and its applications to industrial cases, *Ph.D. thesis,* School of Mechanical, Aerospace and Civil Engineering, University of Manchester, UK.

[12] Billard, F., Uribe, J.C. and Laurence, D., 2008. A new formulation of the v^2-f model using elliptic blending and its application to heat transfer prediction. In: *Proc. 7th Int. ERCOFTAC Symp. on Engineering Turbulence Modelling and Measurements 'ETMM7'*, Limassol, Cyprus, pp. 89-94.

[13] Bredberg, J., 2002. Turbulence modelling for internal cooling of gas-turbine blades, *Ph.D. thesis,* Department of Thermo and Fluid Dynamics, Chalmers University of Technology, Göteborg, Sweden.

[14] Bredberg, J. and Davidson, L., 1999. Prediction of flow and heat transfer in a stationary 2-D rib roughened passage using low-Re turbulent models. In: *3rd European Conference on Turbomachinery*, IMechE, pp. 963-972.

[15] Bredberg, J., Davidson, L. and Iacovides, H., 2000. Comparison of near-wall behavior and its effect on heat transfer for k-ω and k-ε turbulence models in rib-roughened 2D channels. In: *3rd International Symposium on Turbulence Heat and Mass Transfer*, Aichi Shuppan, Nagano Y., Hanjalic, K., Tsuji, T. (eds.).

[16] Bredberg, J., Peng, S.H. and Davidson, L., 2002. An improved k-ω turbulence model applied to recirculating flows. *Int. J. Heat Fluid Flow*, 23, 731-743.

[17] Buhr, H.O., Horsten, E.A. and Carr, A.D., 1974. The distortion of turbulent velocity and temperature profiles on heating of mercury in a vertical pipe. *Trans. ASME C, J. Heat Transfer*, 96, 152-158.

[18] Burridge, D.P. and Naylor, J.E., 1991. Development of graphite for fuel element sleeves in advanced gas cooled reactors. In: *Proc. of a specialists meeting on the status of graphite development for gas cooled reactors (IAEA-TECDOC-690)*, 9-12 September 1991, Tokai-mura, Japan pp. 134-139.

[19] Buyucalaca, O., 1993. Studies of convective heat transfer to water in steady and unsteady pipe flow, *Ph.D. thesis,* Dept. of Engineering, University of Manchester, UK.

[20] Byrne, J.E. and Ejiogu, E., 1971. Combined free and forced convection heat transfer in a vertical pipe. *IMechE Symp. on Heat and Mass Transfer by Combined Forced and Natural Convection*, Manchester, UK, Paper C118/71, pp. 40-46, 1971.

[21] Carr, A.D., Connor, M.A. and Buhr, H.O., 1973. Velocity, temperature and turbulence measurements in air for pipe flow with combined free and forced convection. *J. Heat Transfer*, 95 (Trans. ASME C), 445-452.

[22] CD-Adapco, 2006. STAR-CD Methodology, Version 4.02.

[23] CD-Adapco, 2008. STAR-CCM+ User Guide, Version 3.04.009.

[24] Chen, H.C. and Patel, V.C., 1988. Near-wall turbulence models for complex flows including separation. *AIAA J.*, 26 (6), 641-648.

[25] Chien, K.Y., 1982. Prediction of channel and boundary-layer flows with a low-Reynolds-number turbulence model. *AIAA J.*, 20, 33-38.

[26] Ciofalo, M. and Collins, M.W., 1992. Large-eddy simulation of turbulent flow and heat transfer in plane and rib-roughened channels. *Int. J. Numer. Methods Fluids*, 15, 453-489.

[27] Cokljat, D., Kim, S.E., Iaccarino, G. and Durbin, P.A., 2003. A comparative assessment of the v^2f model for recirculating flows. *AIAA J.*, 0765.

[28] CORE, 1999. Nuclear transports in Britain: Feeding Sellafield's pollution (available from 'http://www.kare-uk.org/coreguide/trainguide.htm').

[29] Cotton, M.A., 1987. Theoretical studies of mixed convection in vertical tubes, *Ph.D. thesis,* Dept. of Engineering, University of Manchester, UK.

[30] Cotton, M.A. and Ismael, J.O., 1998. A strain parameter turbulence model and its application to homogeneous and thin shear flows. *Int. J. Heat Fluid Flow*, 19, 326-337.

[31] Cotton, M.A., Ismael, J.O. and Kirwin, P.J., 2001. Computations of post-trip reactor core thermal hydraulics using a strain parameter turbulence model. *Nuclear Eng. and Design*, 208, 51-66.

[32] Cotton, M.A. and Jackson, J.D., 1990. Vertical tube air flows in the turbulent mixed convection regime calculated using a low-Reynolds-number k-ε model. *Int. J. Heat Mass Transfer*, 33, 275-286.

[33] Cotton, M.A., Jackson, J.D. and Yu, L.S.L., 1989. Application of a low-Reynolds-number two-equation turbulence model to mercury and sodium flows in the turbulent mixed convective regime. In: *Proc. 7th Symp. on Turbulent Shear Flows*, Stanford University.

[34] Cotton, M.A. and Keshmiri, A., 2008. Turbulent mixed convection flows computed using low-Reynolds-number and strain parameter eddy viscosity schemes. In: *Proc. 7th Int. ERCOFTAC Symp. on Engineering Turbulence Modelling and Measurements 'ETMM7'*, Limassol, Cyprus, pp. 274-279.

[35] Cotton, M.A. and Kirwin, P.J., 1995. A variant of the low-Reynolds-number two-equation turbulence model applied to variable property mixed convection flows. *Int. J. Heat Fluid Flow*, 16, 486-492.

[36] Craft, T.J., Gerasimov, A.V., Iacovides, H. and Launder, B.E., 2002. Progress in the generalization of wall-function treatments. *Int. J. Heat Fluid Flow*, 23 (2), 148-160.

[37] Craft, T.J., Iacovides, H. and Yoon, J.H., 1999. Progress in the use of non-linear two-equation models in the computation of convective heat transfer in impinging and separated flows. *Flow, Turbulence and Combustion*, 63, 59-80.

[38] Craft, T.J., Ince, N.Z. and Launder, B.E., 1996a. Recent developments in second-moment closure for buoyancy-affected flows. *Dynamics of Atmospheres and Oceans*, 23, 99-114.

[39] Craft, T.J., Launder, B.E. and Suga, K., 1996b. Development and application of a cubic eddy-viscosity model of turbulence. *Int. J. Heat Fluid Flow*, 17, 108-115.

[40] Cui, J., Patel, V.C. and Lin, C.L., 2003. Large-eddy simulation of turbulent flow in a channel with rib roughness. *Int. J. Heat Fluid Flow* 24, 372-388.

[41] Daly, B.J. and Harlow, F.H., 1970. Transport equations in turbulence. *Phvsics Fluids*, 13, 2634-2649.

[42] di Mare, F., 2008. Personal communication.

[43] Drain, L.E. and Martin, S., 1985. Two-component velocity measurements of turbulent flow in a ribbed-wall flow channel. *Int. Conf. on Laser Anenometry - Advances and Applications*, Manchester, UK, pp. 99-112, 1985.

[44] Durbin, P., 1993. A Reynolds-stress model for near-wall turbulence. *J. Fluid Mech.*, 249, 465-498.

[45] Durbin, P.A., 1991. Near-wall turbulence closure modeling without damping functions. *Theoret. Comput. Fluid Dynamics*, 3, 1-13.

[46] Durbin, P.A., 1995. Separated flow computations with the k-ε-v^2 model. *AIAA J.*, 33, 659-664.

[47] Easby, J.P., 1978. The effect of buoyancy on flow and heat transfer for a gas passing down a vertical pipe at low Reynolds numbers. *Int. J. Heat Mass Transfer*, 21, 791-801.

[48] ERCOFTAC, 2000. Best Practice Guidelines. *Special Interest Group on Quality and Trust in industrial CFD*.

[49] Fairbairn, S.A., 2009. Personal communication.

[50] Gant, S.E., 2003. Development and application of a new wall function for complex turbulent flows, *Ph.D. thesis,* Dept. of Mechanical, Aerospace and Manufacturing Engineering, UMIST (now University of Manchester), UK.

[51] Gerasimov, A.V., 2003. Development and validation of an analytical wall-function strategy for modelling forced, mixed and natural convection flows, *Ph.D. thesis,* Dept. of Mechanical, Aerospace and Manufacturing Engineering, UMIST (now University of Manchester), UK.

[52] Gotts, J., 2008. Personal communication.

[53] Gotts, J., 2009. Personal communication.

[54] Gotts, J. and Xu, B., 2006. An investigation of heat transfer impairment modelling arising from fuel pin carbon deposition. *British Energy Generation Limited, Engineering Division, Report E/REP/BBDB/0057/AGR/05, RAWG/P(05)08*.

[55] Gray, D.D. and Giorgini, A., 1976. The Validity of the Boussinesq Approximation for Liquids and Gases. *Int. J. Heat Mass Transfer*, 19, 545-551.

[56] Grotjans, H. and Menter, F.R., 1998. Wall functions for general application CFD codes. In: *Proc. ECCOMAS 98, Papaolou et al., editors*, pp. 1112-1117.

[57] Hall, W.B., 1962. Heat transfer in channels having rough and smooth surfaces. *J. Mech. Eng. Science*, 4 (3), 287-291.

[58] Hall, W.B. and Jackson, J.D., 1969. Laminarization of a turbulent pipe flow by buoyancy forces. *ASME Paper*, 69-HT-55.

[59] Han, J.C., 1988. Heat transfer and friction characteristics in rectangular channels with rib turbulators. *ASME J. Heat Transfer*, 110, 321–328.

[60] Han, J.C., Glicksman, L.R. and Rohsenow, W.M., 1978. An investigation of heat transfer and friction for rib-roughened surfaces. *Int. J. Heat Mass Transfer*, 21, 1143-1156.

[61] Han, J.C., Park, J.S. and Lei, C.K., 1985. Heat transfer enhancement in channels with turbulence promoters. *ASME J. Eng. for Gas Turbines and Power*, 107, 628-635.

[62] Hanjalić, K., Popovac, M. and Hadziabdic, M., 2004. A robust near-wall elliptic-relaxation eddy-viscosity turbulence model for CFD. *Int. J. Heat Fluid Flow*, 24, 1047-1051.

[63] Hirsch, C., 1990. Numerical Computation of Internal and External Flows. Volume 2: Computational Methods for Inviscid and Viscous Flows. John Wiley & Sons.

[64] Hunt, J.C.R. and Carruthers, D.J., 1990. Rapid distortion theory and the 'problems' of turbulence. *J. Fluid Mech.*, 212, 497-532.

[65] Iaccarino, G., 2001. Predictions of a turbulent separated flow using commercial CFD codes. *J. Fluids Eng.*, 123, 819-828.

[66] Iaccarino, G., Ooi, A., Durbin, P.A. and Behnia, M., 2002. Conjugate heat transfer predictions in two-dimensional ribbed passages. *Int. J. Heat Fluid Flow*, 23, 340-345.

[67] Iacovides, H., 1998. Computation of flow and heat transfer through rotating ribbed passages. *Int. J. Heat Fluid Flow*, 19, 393-400.

[68] Iacovides, H., 2006. Convective heat and mass transfer. *Lecture notes of Advanced Heat Transfer,* The University of Manchester.

[69] Iacovides, H. and Raisee, M., 1999. Recent progress in the computation of flow and heat transfer in internal cooling passages of turbine blade. *Int. J. Heat Fluid Flow*, 20, 320-328.

[70] Iacovides, H. and Raisee, M., 2001. Computation of flow and heat transfer in two-dimensional rib-roughened passages, using low-Reynolds-number turbulence models. *Int. J. Numerical Methods for Heat and Fluid Flow*, 11, 138-155.

[71] Ikeda, T. and Durbin, P.A., 2007. Direct numerical simulation of a rough-wall channel flow. *J. Fluid Mech.*, 571, 235-263.

[72] Ince, N.Z. and Launder, B.E., 1989. On the computation of buoyancy-driven turbulent flows in rectangular enclosures. *Int. J. Heat Fluid Flow*, 10 (2), 110-117.

[73] Jackson, J.D., 2006. Studies of buoyancy-influenced turbulent flow and heat transfer in vertical passages. *Keynote lecture, 13th Int. Heat Transfer Conference, 'IHTC13'*, Sydney, Australia, 2006.

[74] Jackson, J.D., Cotton, M.A. and Axcell, B.P., 1989. Studies of mixed convection in vertical tubes. *Int. J. Heat Fluid Flow*, 10, 2-15.

[75] Jacoby, J.K., 1972. Free convection distortion and eddy diffusivity effects in turbulent mercury heat transfer, *M.Sc. thesis,* Purdue University.

[76] Jiménez, J., 2004. Turbulent flows over rough walls. *Annual Review of Fluid Mechanics*, 36, 173-196.

[77] Jones, W.P. and Launder, B.E., 1972. The prediction of laminarization with a two-equation model of turbulence. *Int. J. Heat Mass Transfer*, 15, 301-314.

[78] Kamali, R. and Binesh, A.R., 2008. The importance of rib shape effects on the local heat transfer and flow friction characteristics of square ducts with ribbed internal surfaces. *Int. Commun. in Heat Mass Transfer*, 35, 1032-1040.

[79] Kamali, R. and Binesh, A.R., 2009. Heat transfer and friction characteristics optimization with compound turbulators in roughened ducts. *J. of Mechanics*, 25 (3), 271-278.

[80] Kasagi, N. and Nishimura, M., 1997. Direct numerical simulation of combined forced and natural turbulent convection in a vertical plane channel. *Int. J. Heat Fluid Flow*, 18, 88-99.

[81] Kays, W. and Crawford, M., 1993. Convective Heat and Mass Transfer. McGraw-Hill Inc., New York.

[82] Kays, W.M. and Leung, E.Y., 1963. Heat transfer in annular passages - Hydrodynamically developed turbulent flow with arbitrarily prescribed heat flux. *Int. J. Heat Mass Transfer*, 6, 537-557.

[83] Kays, W.M. and Perkins, H.C., 1973. Forced Convection, Internal Flow in Ducts, Section 7 of Handbook of Heat Transfer, Eds. Rohsenow, W.M. and Hartnett, J.P., McGraw-Hill, New York.

[84] Kenning, D.B.R., Shock, R.A.W. and Poon, J.Y.M., 1974. Local reduction in heat transfer due to buoyancy effects in upward turbulent flow. In: *Proc. 5th Int. Heat Transfer Conference*, Tokyo, Japan, Paper NC 4.3.

[85] Keshmiri, A., Addad, Y., Cotton, M.A., Laurence, D.R. and Billard, F., 2008a. Refined eddy viscosity schemes and large eddy simulations for ascending mixed convection flows. In: *Proc. 4th Int. Symp. on Advances in Computational Heat Transfer, 'CHT08', Paper CHT-08-407*, Marrakech, Morocco.

[86] Keshmiri, A., Cotton, M.A., Addad, Y. and Laurence, D.R., 2009. Thermal-hydraulic analysis of rib-roughened fuel pin performance in gas-cooled nuclear reactors. In: *Proc. 6th International Symposium on Turbulence, Heat and Mass Transfer*, Rome, Italy, pp. 1011-1014.

[87] Keshmiri, A., Cotton, M.A., Addad, Y., Rolfo, S. and Billard, F., 2008b. RANS and LES investigations of vertical flows in the fuel passages of gas-cooled nuclear reactors. In: *Proc. 16th ASME Int. Conf. on Nuclear Engineering, 'ICONE16', Paper ICONE16-48372*, Orlando, Florida, USA.

[88] Kim, H.M. and Kim, K.Y., 2004. Design optimization of rib-roughened channel to enhance turbulent heat transfer. *Int. J. Heat Mass Transfer*, 47, 5159-5168.

[89] Kim, J., Moin, P. and Moser, R., 1987. Turbulence statistics in fully developed channel flow at low Reynolds number. *J. Fluid Mechanics Digital Archive*, 177, 133-166.

[90] Kim, W.S., Jackson, J.D. and He, S., 2008. Assessment by comparison with DNS data of turbulence models used in simulations of mixed convection. *Int. J. Heat and Mass Transfer*, 51, 1293-1312.

[91] Kirwin, P.J., 1995. Investigation and development of two-equation turbulence closures with reference to mixed convection in vertical pipes, *Ph.D. thesis,* Dept. of Engineering, University of Manchester, UK.

[92] Kral, L.D., 1998. Recent experience with different turbulence models applied to the calculation of flow over aircraft components. *Progress in Aerospace Sciences*, 34 (7-8), 481-541.

[93] Krogstad, P.A., Andersson, H.I., Bakken, O.M. and Ashrafian, A., 2005. An experimental and numerical study of channel flow with rough walls. *J. Fluid Mech.*, 530, 327-352.

[94] Launder, B.E., 1984. Numerical computation of convective heat transfer in complex turbulent flows: Time to abandon wall functions. *Int. J. Heat and Mass Transfer*, 27, 1485-1490.

[95] Launder, B.E., 1986. Low-Reynolds-number turbulence near walls. Dept. of Mechanical Engineering, UMIST (now School of MACE, The University of Manchester) Report TFD/86/4. Manchester, UK.

[96] Launder, B.E., 1988. On the computation of convective heat transfer in complex turbulent flows. *J. heat transfer*, 110, 1112-1128.

[97] Launder, B.E., 1989. Review; Second-moment closure:present and future? *Int. J. Heat Fluid Flow*, 10 (4), 282-300.

[98] Launder, B.E., Reece, G.J. and Rodi, W., 1975. Progress in the development of a Reynolds stress turbulence closure. *J. Fluid Mech.*, 68, 537-566.

[99] Launder, B.E. and Sharma, B.I., 1974. Application of the energy dissipation model of turbulence to the calculation of flow near a spinning disc. *Lett. Heat Mass Transfer*, 1, 131-138.

[100] Launder, B.E. and Spalding, D.B., 1972. Lectures in mathematical models of turbulence. Academic Press, London.

[101] Launder, B.E. and Spalding, D.B., 1974. The numerical computation of turbulent flows. *Comp. Meth. in Appl. Mech. Eng.*, 3, 269-289.

[102] Laurence, D.R., Uribe, J.C. and Utyuzhnikov, S.V., 2004. A robust formulation of the v^{2-}f model. *Flow, Turbulence and Combustion*, 73, 169-185.

[103] Lee, S., Kim, J.H. and Sung, H.J., 2008. PIV measurements of turbulent boundary layer over a rod-roughened wall. *Int. J. Heat Fluid Flow*, 29, 1679-1687.

[104] Leonardi, S., Orlandi, P., Smalley, R.J., Djenidi, L. and Antonia, R.A., 2003. Direct numerical simulations of turbulent channel flow with transverse square bars on one wall. *J. Fluid Mech.*, 491, 229-238.

[105] Leschziner, M.A., 1980. Practical evaluation of three finite difference schemes for the computation of steady-state recirculating flows. *Computer Methods in Applied Mech. and Eng.*, 23 (3), 293-312.

[106] Leschziner, M.A., 1982. An introduction and guide to the computer code PASSABLE. *Report,* Dept. of Mech. Engineering, UMIST (now University of Manchester), UK.

[107] Li, J.K., 1994. The interaction between forced and free convection in a heated vertical tube with both fan-driven and thermally induced flow, *Ph.D. thesis,* Dept. of Engineering, University of Manchester, UK.

[108] Lien, F. and Kalitzin, G., 2001. Computations of transonic flow with the v^2-f turbulence model. *Int. J. Heat Fluid Flow*, 22, 53-61.

[109] Lien, F.S., Chen, W.L. and Leschziner, M.A., 1996. Low-Reynolds-number eddy-viscosity modelling based on non-linear stress-strain/vorticity relations. In: *Proc. 3rd Int. Symp. on Engineering Turbulence Modelling and Experiments*, Crete, Greece, Rodi W., Bergeles, G. (eds.), pp. 91–100.

[110] Lien, F.S. and Durbin, P.A., 1996. Non-linear k-ε-v^2 modelling with application to high lift. In: *Proceedings of the Summer School Program*, NASA Ames/Stanford University Centre for Turbulence Research, pp. 5-25.

[111] Liou, T.M., Chang, Y. and Hwang, D.W., 1990. Experimental and computational study of turbulent flows in a channel with two pairs of turbulent promoters in tandem. *J. Fluids Eng.*, 112, 302-310.

[112] Liou, T.M. and Hwang, J.J., 1993. Effect of ridge shapes on turbulent heat transfer and friction in a rectangular channel. *Int. J. Heat Mass Transfer*, 36, 931-940.

[113] Liou, T.M., Hwang, J.J. and Chen, S.H., 1993a. Simulation and measurement of enhanced turbulent heat transfer in a channel with periodic ribs on one principal wall. *Int. J. Heat Mass Transfer*, 36, 507-517.

[114] Liou, T.M., Wu, Y.Y. and Chang, Y., 1993b. LDV measurements of periodic fully developed main and secondary flows in a channel with rib-disturbed walls. *J. Fluids Eng.*, 115, 109-114.

[115] Liu, y., Tucker, P.G. and Iacono, G.L., 2006. Comparison of zonal RANS and LES for a non-isothermal ribbed channel flow. *Int. J. Heat Fluid Flow*, 27, 391-401.

[116] Manceau, R., 2005. An improved version of the elliptic blending model. Application to non-rotating and rotating channel flows. In: *Proc. 4th Symp. Turb. Shear Flow Phenomena*, Williamsburg, Virginia, USA, pp. 259-264.

[117] Manceau, R., Parneix, S. and Laurence, D., 2000. Turbulent heat transfer predictions using the model on unstructured meshes. *Int. J. Heat Fluid Flow*, 21, 320-328.

[118] Manceau, R., Wang, M. and Laurence, D., 2001. Inhomogeneity and anisotropy effects on the redistribution term in Reynolds-averaged Navier-Stokes modelling. *J. Fluid Mech.*, 438, 307-338.

[119] Mantle, P.L., 1985. A review of the method for determining the effect of carbonaceous deposition on the heat transfer from CAGR fuel pins. *British Energy Generation Limited, Engineering Division, Report TPRD/B/PS/409/M85, HTSG/P(85)29.*

[120] Maxey, M.R., 1982. Distortion of turbulence in flows with parallel streamlines. *J. Fluid Mech.*, 124, 261-282.

[121] McAdams, W.H., 1954. Heat Transmission. 3rd Edn., McGraw-Hill, New York.

[122] Menter, F.R., 1994. Two-equation eddy-viscosity turbulence models for engineering applications. *AIAA J.*, 32, 1598–1605.

[123] Menter, F.R., 2002. CFD Best Practice Guidelines for CFD Code Validation for Reactor Safety Applications. *EVOL-ECORA D01.*

[124] Menter, F.R., Kuntz, M. and Langtry, R., 2003. Ten years of industrial experience with the SST turbulence model. *Turbulence, Heat and Mass Transfer*, 4, 1-8.

[125] Michelassi, V., Rodi, W. and Scheuerer, G., 1991. Testing a low-Reynolds-number k-ε turbulence model based on direct simulation data. In: *Proc. 8th Symposium on Turbulent Shear Flows*, Munich, Germany.

[126] Mikielewicz, D.P., 1994. Comparative studies of turbulence models under conditions of mixed convection with variable properties in heated vertical tubes, *Ph.D. thesis,* Dept. of Engineering, University of Manchester, UK.

[127] Miyake, Y., Tsujimoto, K. and Nakaji, M., 2001. Direct numerical simulation of rough-wall heat transfer in a turbulent channel flow. *Int. J. Heat Fluid Flow*, 22, 237-244.

[128] Moin, P. and Kim, J., 1982. Numerical investigation of turbulent channel flow. *J. Fluid Mech.*, 118, 341-377.

[129] Momeni, P., 2008. Modelling the effect of pulsation on flow and heat transfer in turbulent separated and reattaching flows, *Ph.D. thesis,* School of Mechanical, Aerospace and Civil Engineering, University of Manchester, UK.

[130] Morrison, A.M., 2003. Task team F phase 3: Fuel resistance for increased sleeve bore and machined brace. *British Energy Generation Limited, Engineering Division, Report E/REP/BBDB/0002/AGR/03, RAWG/P(03)02*.

[131] Nagano, Y., Hattori, H. and Houra, T., 2004. DNS of velocity and thermal fields in turbulent channel flow with transverse-rib roughness. *Int. J. Heat Fluid Flow*, 25, 393-403.

[132] Nicklin, G.J.E., 1998. Augmented heat transfer in a square channel with asymmetrical turbulence promotion. *Final year project report,* Dept. of Mech. Eng., UMIST, Manchester, UK.

[133] Okamoto, S., Seo, S., Nakaso, K. and Kawai, I., 1993. Turbulent shear flow and heat transfer over the repeated two-dimensional square ribs on ground plane. *Trans. ASME J. Fluids Eng.*, 115, 631-637.

[134] Ooi, A., Iaccarino, G., Durbin, P.A. and Behnia, M., 2002. Reynolds averaged simulation of flow and heat transfer in ribbed ducts. *Int. J. Heat Fluid Flow*, 23, 750-757.

[135] Park, J.S., Han, J.C., Huang, Y., Ou, S. and Boyle, R.J., 1992. Heat transfer performance comparisons of five different rectangular channels with parallel angled ribs. *Int. J. Heat and Mass Transfer*, 35 (11), 2891-2903.

[136] Parlatan, Y., Todreas, N.E. and Driscoll, M.J., 1996. Buoyancy and property variation effects in turbulent mixed convection of water in vertical tubes. *J. Heat Transfer*, 118, 381-387.

[137] Patel, V.C., Rodi, W. and Scheuerer, G., 1985. Turbulence models for near-wall and low Reynolds number flows: A Review. *AIAA J.*, 23, 1308-1319.

[138] Peng, S.H., Davidson, L. and Holmberg, S., 1997. A modified low-Reynolds-number k-ω model for recirculating flows. *J. Fluid Engineering*, 119, 867-875.

[139] Perry, A.E., Schofield, W.H. and Joubert, P.N., 1969. Rough wall turbulent boundary layers. *J. Fluid Mechanics*, 37, 383-413.

[140] Petukhov, B.S. and Polyakov, A.F., 1988. Heat Transfer in Turbulent Mixed Convection. Launder B.E.(ed.), Hemisphere, Bristol, PA, USA.

[141] Petukhov, B.S. and Popov, V.N., 1963. Theoretical calculation of heat exchange and frictional resistance in turbulent flow in tubes of an incompressible fluid with variable physical properties. *High Temp. Heat Phys.* , 1, 69-83.

[142] Pirie, M.A.M., 1987. Pressure drop measurements on nominal 7.5 inch diameter stage 2 CAGR fuel elements containing CE05 multi-start fuel cans. *Report TPRD/B/PS/589/M88, HTSG/P(87)27, FADC/P1516*.

[143] Polyakov, A.F. and Shindin, S.A., 1988. Development of turbulent heat transfer over the length of vertical tubes in the presence of mixed air convection. *Int. J. Heat Mass Transfer*, 31, 987-992.

[144] Pope, S., 1975. A more general effective viscosity hypothesis. *J. of Fluid Mechanics*, 72, 331-340.

[145] Pope, S.B., 2000. Turbulent Flows. Cambridge University Press.

[146] Prakash, C. and Zerkle, R., 1995. Prediction of turbulent flow and heat transfer in a ribbed rectangular duct with and without rotation. *J. Turbomachinery*, 117 (2), 255-264.

[147] Raisee, M., 1999. Computation of flow and heat transfer through two- and three-dimensional rib-roughened passages, *Ph.D. thesis,* Dept. of Mechanical Engineering, UMIST (now University of Manchester), UK.

[148] Raisee, M., Noursadeghi, A. and Iacovides, H., 2004. Application of a non-linear k-ε model in prediction of convective heat transfer through ribbed passages. *Int. J. Heat Fluid Flow*, 14, 285-304.

[149] Raithby, G.D. and Schneider, G.E., 1979. Numerical solution of problems in incompressible fluid flow: Treatment of the velocity–pressure coupling. *Numer. Heat Transfer*, 2, 417–440.

[150] Rau, G., Çakan, M., Moeller, D. and Arts, T., 1998. The effect of periodic ribs on the local aerodynamic and heat transfer performance of a straight cooling channel. *ASME J. Turbomach.*, 120, 368-375.

[151] Raupach, M.R., Antonia, R.A. and Rajagopalan, S., 1991. Rough-wall turbulent boundary layers. *Appl. Mech. Rev.*, 44, 1-25.

[152] Ravigururajan, T.S. and Bergles, A.E., 1996. Development and verification of general correlations for pressure drop and heat transfer in single-phase turbulent flow in enhanced tubes. *Experimental Thermal and Fluid Science*, 13 (1), 55-70.

[153] Rebay, S., 1993. Efficient unstructured mesh generation by means of delaunay triangulation and Bowyer-Watson algorithm. *J. Computational Physics*, 106 (1), 125-138.

[154] Richards, A.H., Spall, R.E. and McEligot, D.M., 2004. An assessment of turbulence models for strongly-heated internal gas flows. In: *Proc. 15th IASTED Int. Conf. on Modeling and Simulation*, Marina Del Rey, California, USA.

[155] Rodi, W. and Leschziner, M.A., 1981. Calculation of annular and twin parallel jets using various discretization schemes and turbulence-model variations. *Trans. ASME J. Fluids Eng.*, 103, 352-360.

[156] Rosten, H.I. and Worrell, J.K., 1988. Generalized wall functions for turbulent flow. *PHOENICS Journal*, 1, 81-109.

[157] Rouai, N.M., 1987. Influences of buoyancy and imposed flow transients on turbulent convective heat transfer in a tube, *Ph.D. thesis,* Dept. of Engineering, University of Manchester, UK.

[158] Ryu, D.N., Choi, D.H. and Patel, V.C., 2007a. Analysis of turbulent flow in channels roughened by two-dimensional ribs and three-dimensional blocks. Part II: Heat Transfer. *Int. J. Heat Fluid Flow*, 28, 1112-1124.

[159] Ryu, D.N., Choi, D.H. and Patel, V.C., 2007b. Analysis of turbulent flow in channels roughened by two-dimensional ribs and three-dimensional blocks. Part I: Resistance. *Int. J. Heat Fluid Flow*, 28, 1098-1111.

[160] Satake, S., Kunugi, T., Shehata, A.M. and McEligot, D.M., 2000. Direct numerical simulation for laminarization of turbulent forced gas flows in circular tubes with strong heating. *Int. J. Heat Fluid Flow*, 21, 526-534.

[161] Schlichting, H., 1968. Boundary Layer Theory. 6th ed. McGraw Hill, New York.

[162] Schlichting, H., 1979. Boundary Layer Theory. 7th ed. McGraw Hill, New York.

[163] Seng, Q., 2009. Mixed convection heat transfer in vertical tube, *M.Sc. thesis,* School of Mechanical, Aerospace and Civil Engineering, University of Manchester, UK.

[164] Shehata, A.M. and McEligot, D.M., 1995. Turbulence structure in the viscous layer of strongly heated gas flows. *Tech. report INEL-95/0223,* Idaho National Engineering Laboratory.

[165] Shehata, A.M. and McEligot, D.M., 1998. Mean turbulence structure in the viscous layer of strongly-heated internal gas flows. Measurements. *Int. J. Heat Mass Transfer*, 41, 4297-4313.

[166] Spalart, P.R., 2000. Strategies for turbulence modelling and simulations. *Int. J. Heat Fluid Flow*, 21 (3), 252-263.

[167] Spalart, P.R. and Allmaras, S.R., 1992. A one equation turbulence model for aerodynamic flows. *AIAA Paper 92-0439*.

[168] Speziale, C.G., 1987. On nonlinear k-l and k-ε models of turbulence. *J. Fluid Mech.*, 178, 459-475.

[169] Steiner, A., 1971. On the reverse transition of a turbulent flow under the action of buoyancy forces. *J. Fluid Mech.*, 47, 503-512.

[170] Suga, K., 1995. Development and application of a non-linear eddy viscosity model sensitized to stress and strain invariants, *Ph.D. thesis,* Dept. of Mechanical Engineering, UMIST (now University of Manchester), UK.

[171] Tanaka, H., Maruyama, S. and Hatano, S., 1987. Combined forced and natural convection heat transfer for upward flow in a uniformly heated vertical pipe. *Int. J. Heat Mass Transfer*, 30, 165-174.

[172] Taslim, M.E. and Wadsworth, C.M., 1997. An experimental investigation of the rib surface-averaged heat transfer coefficient in a rib-roughened square passage. *J. Turbomachinery*, 119 (2), 381-389.

[173] Townsend, A.A., 1970. Entrainment and the structure of turbulent flow. *J. Fluid Mech.*, 41, 13-46.

[174] Uribe, J.C., 2006. An industrial approach to near-wall turbulence modelling for unstructured finite volume methods, *Ph.D. thesis,* School of Mechanical, Aerospace and Civil Engineering, University of Manchester, UK.

[175] Versteeg, H.K. and Malalasekera, W., 1995. An Introduction to Computational Fluid Dynamics: The Finite Volume Method. PEARSON Education Limited.

[176] Vilemas, J.V., Poškas, P.S. and Kaupas, V.E., 1992. Local heat transfer in a vertical gas-cooled tube with turbulent mixed convection and different heat fluxes. *Int. J. Heat Mass Transfer*, 35, 2421-2428.

[177] Walklate, P.J., 1976. A comparative study of theoretical models of turbulence for the numerical prediction of boundary layer flows, *Ph.D. thesis,* Dept. of Mech. Engineering, UMIST (now University of Manchester), UK.

[178] Webb, R.L., Eckert, E.R.G. and Goldstein, R.J., 1971. Heat transfer and friction in tubes with repeated-rib roughness. *Int. J. Heat Mass Transfer*, 14, 601-617.

[179] Weinberg, R.S., 1972. Experimental and theoretical study of buoyancy effects in forced convection to supercritical pressure carbon dioxide, *Ph.D. thesis,* Dept. of Engineering, University of Manchester, UK.

[180] White, L. and Wilkie, D., 1967. The heat transfer and pressure loss characteristics of some multi-start ribbed surfaces. *United Kingdom Atomic Energy Authority, TRG Report 1504 (W).*

[181] Wilcox, D.C., 1988. Reassessment of the scale-determining equation for advanced turbulence models. *AIAA J.*, 26 (11), 1299-1308.

[182] Wilcox, D.C., 1993a. Comparison of two-equation turbulence models for boundary layers with pressure gradient. *AIAA J.*, 31, 1414-1421.

[183] Wilcox, D.C., 1993b. Turbulence Modeling for CFD. DCW Industries Inc., La Cañada, California.

[184] Wilcox, D.C., 1998. Turbulence Modeling for CFD. 2nd ed., DCW Industries Inc., La Cañada.

[185] Wilkie, D., 1966. Forced convection heat transfer from surfaces roughened by transverse ribs. *Third International Heat Transfer Conference, 1-19 August 1966*, Chicago, USA, American Institute of Chemical Engineers, Paper 1, 1966.

[186] Wilkie, D., 1983a. Heat transfer development of AGR fuel. In: *Proc. Gas-cooled reactors today, BNES*, 20-24 September 1982, Bristol, UK, Vol. 4, pp. 227-234.

[187] Wilkie, D., 1983b. Alternative heat transfer surfaces for AGR fuel pins. In: *Proc. Gas-cooled reactors today, BNES*, 20-24 September 1982, Bristol, UK, Vol. 4, pp. 235-240.

[188] Xu, X., Lee, J.S., Pletcher, R.H., Shehata, A.M. and McEligot, D.M., 2004. Large eddy simulation of turbulent forced gas flows in vertical pipes with high heat transfer rates. *Int. J. Heat and Mass Transfer*, 47, 4113-4123.

[189] Yap, C.R., 1987. Turbulent heat and momentum transfer in recirculating and impinging flows, *Ph.D. thesis,* Dept. of Mech. Engineering, Faculty of Technology, UMIST (now the University of Manchester), UK.

[190] You, J., Yoo, J.Y. and Choi, H., 2003. Direct numerical simulation of heated vertical air flows in fully developed turbulent mixed convection. *Int. J. Heat Mass Transfer*, 46, 1613-1627.

[191] Yu, L.S.L., 1991. A computational study of turbulent mixed convection in vertical tubes, *Ph.D. thesis,* Dept. of Engineering, University of Manchester, UK.

[192] Yu, W., France, D.M., Wambsganss, M.W. and Hull, J.R., 2002. Two-phase pressure drop, boiling heat transfer, and critical heat flux to water in a small-diameter horizontal tube. *International Journal of Multiphase Flow*, 28 (6), 927-941.

APPENDIX A

LIST OF PUBLICATIONS

Peer-reviewed publications:

1. **Keshmiri, A.**, Cotton, M.A., Addad, Y. & Laurence, D.R, '*Turbulence Modelling and LES for Ascending Mixed Convection Flows',* Submitted to Journal of Heat and Fluid Flow, 2010.

2. **Keshmiri, A.**, Cotton, M.A., Addad, Y. & Laurence, D.R., *'Thermal-Hydraulic Analysis of Rib-Roughened Fuel Pin Performance in Gas-Cooled Nuclear Reactors'*, Proc. 6th International Symposium on Turbulence, Heat and Mass Transfer, Rome, Italy, 14-18 September 2009.

3. **Keshmiri, A.**, Cotton, M.A. & Addad, Y., 2009, *'Numerical Simulations of Flow and Heat Transfer over Rib-Roughened Surfaces'*, 17th Annual conference of CFD society of Canada, Ottawa, Canada, 3-5 May 2009.

4. Cotton, M.A. & **Keshmiri, A.**, '*Turbulent Mixed Convection Flows Computed Using Low-Reynolds-Number and Strain Parameter Eddy Viscosity Schemes',* Proc. 7th Int. ERCOFTAC Symp. on Engineering Turbulence Modelling and Measurements 'ETMM7', Vol. 1, pp. 274-279, Limassol, Cyprus, 4-6 June 2008.

5. **Keshmiri, A.**, Cotton, M.A., Addad, Y., Laurence, D.R. & Billard, F., '*Refined Eddy Viscosity Schemes and LES for Ascending Mixed Convection Flows',* 4th Int. Symp. on Advances in Computational Heat Transfer, 'CHT-08', Marrakech, Morocco, 11-16 May 2008.

6. **Keshmiri, A.**, Cotton, M.A., Addad, Y., Rolfo, S. & Billard, F., '*RANS and LES Investigations of Vertical Flows in the Fuel Passages of Gas-Cooled Nuclear Reactors',* 16th ASME Int. Conf. on Nuclear Engineering, 'ICONE16', Orlando, Florida, USA, 11-15 May 2008.

Conference presentations:

1. **Keshmiri, A.**, Rolfo, S. & Cotton, M.A., '*CFD Analysis of Operating Reactor Systems and a Proposed Generation IV Design*', Universities' Nuclear Technology Forum, University of Cambridge, 18-20 March 2009.

2. **Keshmiri, A.**, Cotton, M.A. & Laurence, D.R., *'RANS-LES Investigations of Buoyancy-modified Vertical Flows'*, Postgraduate Research Conference, University of Manchester, 27 June 2008.

3. **Keshmiri, A.** & Rolfo, S., *'Numerical Investigation of Vertical Flows in Advanced Gas-cooled Reactors'*, Postgraduate Research Conference, University of Manchester, 12 June 2007.

Publications under preparation:

1. **Keshmiri, A.** & Cotton, M.A, '*Heat Transfer Developments in Ascending Mixed Convection Flows*', To be submitted to Journal of Heat and Fluid Flow, 2010.

2. **Keshmiri, A.**, Cotton, M.A. & Laurence, D.R, '*Thermal-Hydraulic Analysis of Four Geometrical Design Parameters on Fuel Pins in AGR Core Flows',* To be submitted to Journal of Computers and Fluids, 2010.

3. Karim, O., **Keshmiri, A.**, & Benhamadouche, S., '*RANS and LES Investigation of Rib-Roughened Channels with Heat Transfer',* To be submitted to Journal of Heat and Mass Transfer, 2010.

4. **Keshmiri, A.**, Addad, Y. & Pepin, V., '*Simulation of a 3-Dimensional AGR Fuel Element Using Adaptive Mesh Generation Method',* To be submitted to Journal of Nuclear Engineering and Design, 2010.

Other contributions:

1. Goddard, A.J.H., Pain, C.C., Laurence, D.R., Cotton, M.A., Grimes, R., Marsden, B., Fitzpatrick, M. E., Edwards, L. & Allen, R.W.K., 2007. '*Safety and Performance for Innovative Reactors',* Nuclear Future (Journal of the I. Nuc. E. and BNES – Issue 5; a KNOO special edition), Vol. 3, pp. 257-268.

2. Walker, S.P., Ammirabile, L., Cotton, M.A., Hewitt, G. and Laurence, D.R., 2007. '*Multi-pin PWR Re-Flood Studies and Large Eddy CFD Simulation',* Nuclear Future (Journal of the I. Nuc. E. and BNES – Issue 5; a KNOO special edition), Vol. 3, pp. 223-229.

APPENDIX B

B1. Verification and Validation Tests for the Suga Model (CONVERT)

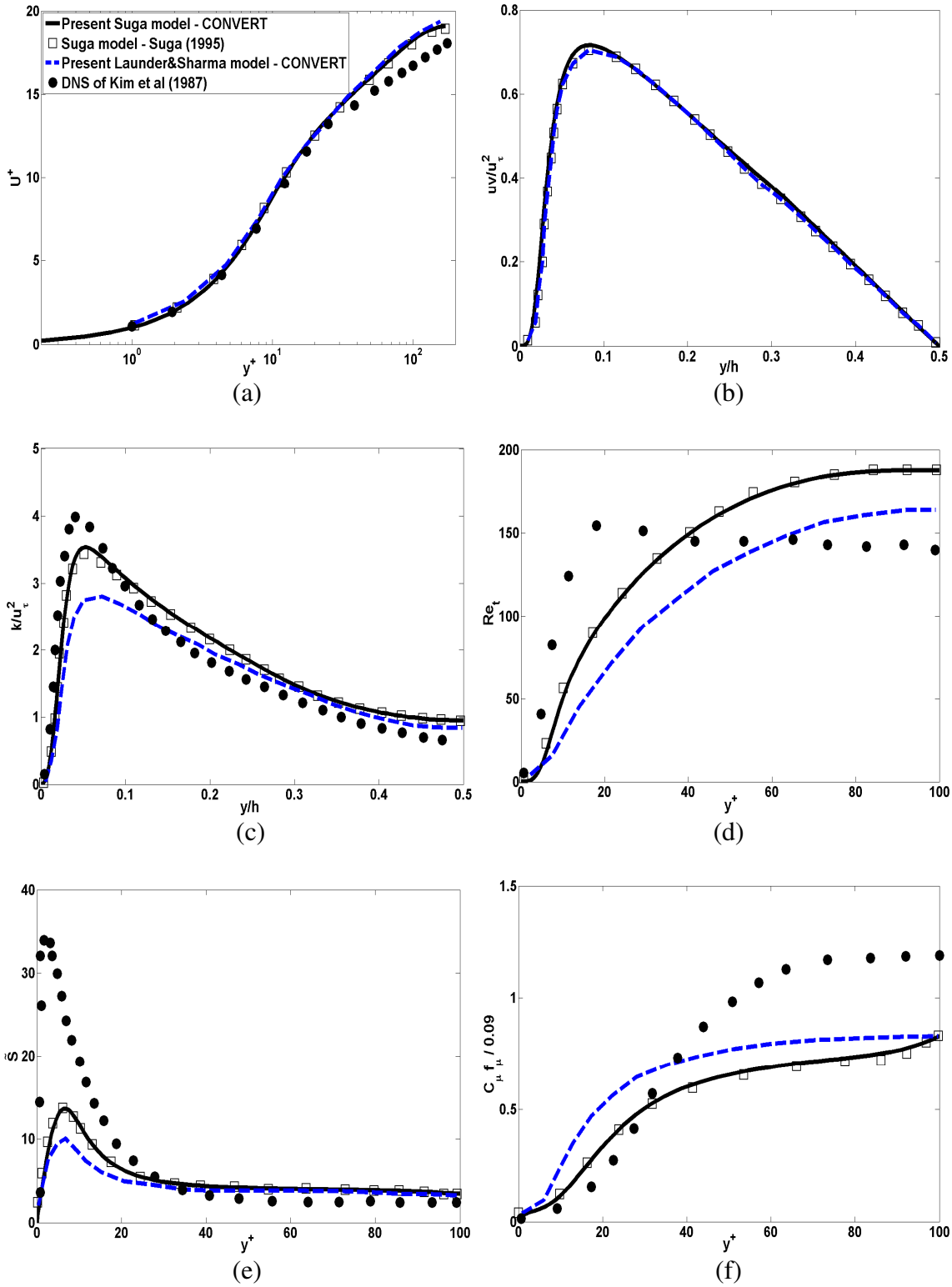

Figure B.1 – Verification and validation tests for the Suga model implemented in CONVERT for *Re* = 5,600 compared against the results of Craft et al. (1996b).

B2. Results of the Manchester v^2-f Model (Code_Saturne)

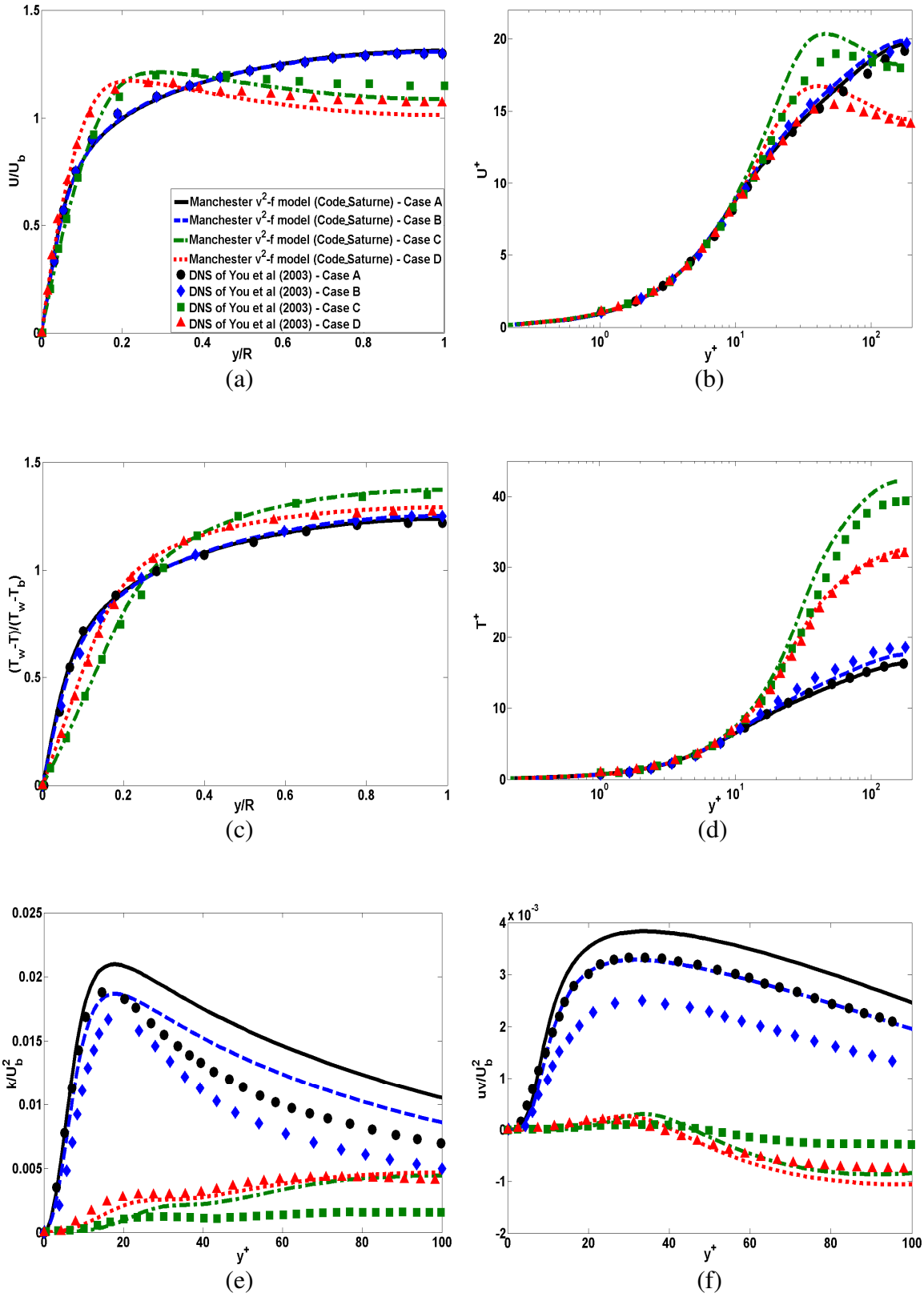

Figure B.2 – Mean flow and turbulence profiles for an ascending flow problem in a vertical heated pipe at Re = 5,300 using the Manchester v^2-f model implemented in Code_Saturne (Billard et al., 2008).

B3. Results of Large Eddy Simulation (STAR-CD)

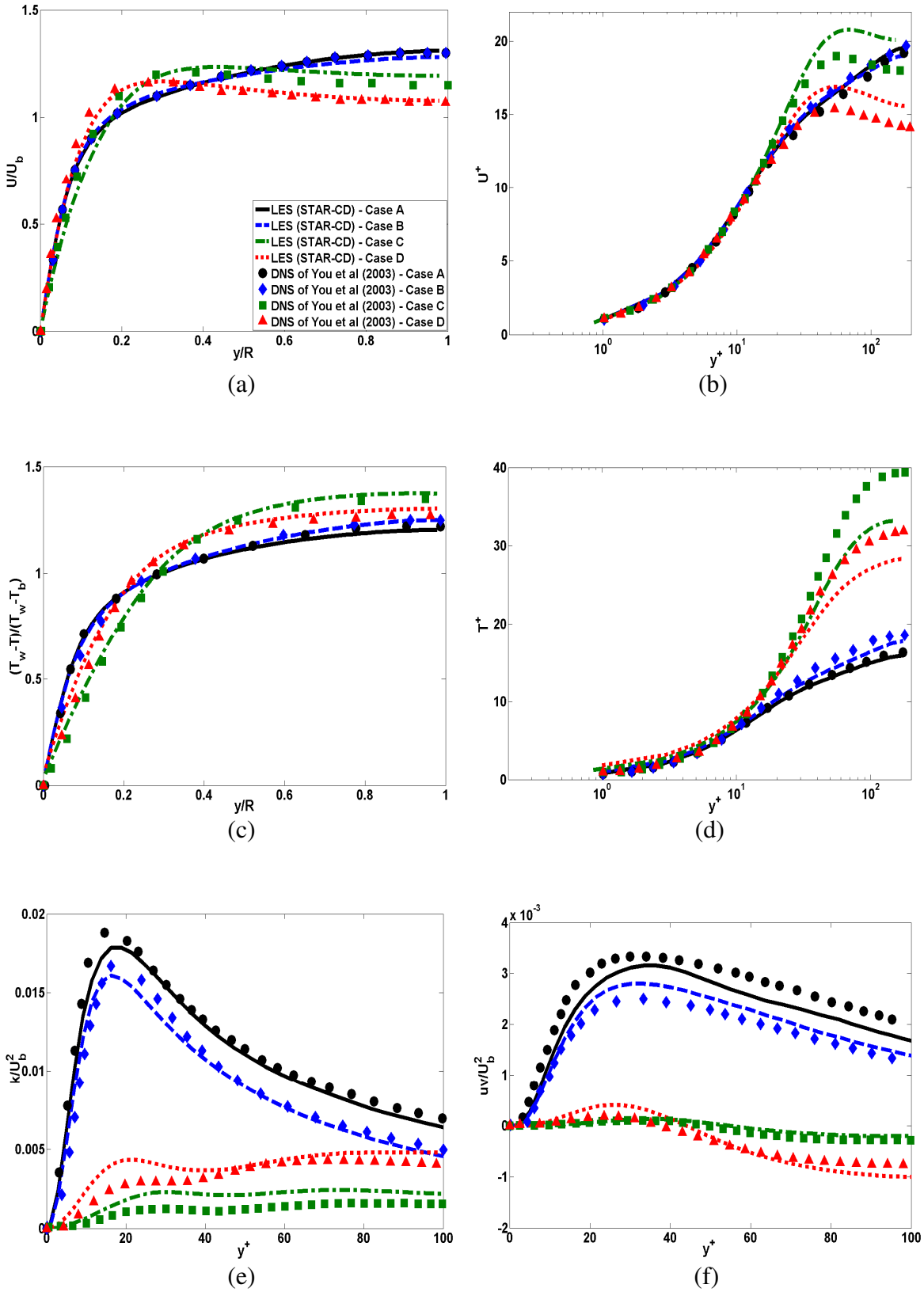

Figure B.3 – Mean flow and turbulence profiles for an ascending flow problem in a vertical heated pipe at *Re* = 5,300 using Large Eddy Simulation in STAR-CD (Addad and Laurence, 2008).

APPENDIX C

MULTI-START CONFIGURATION

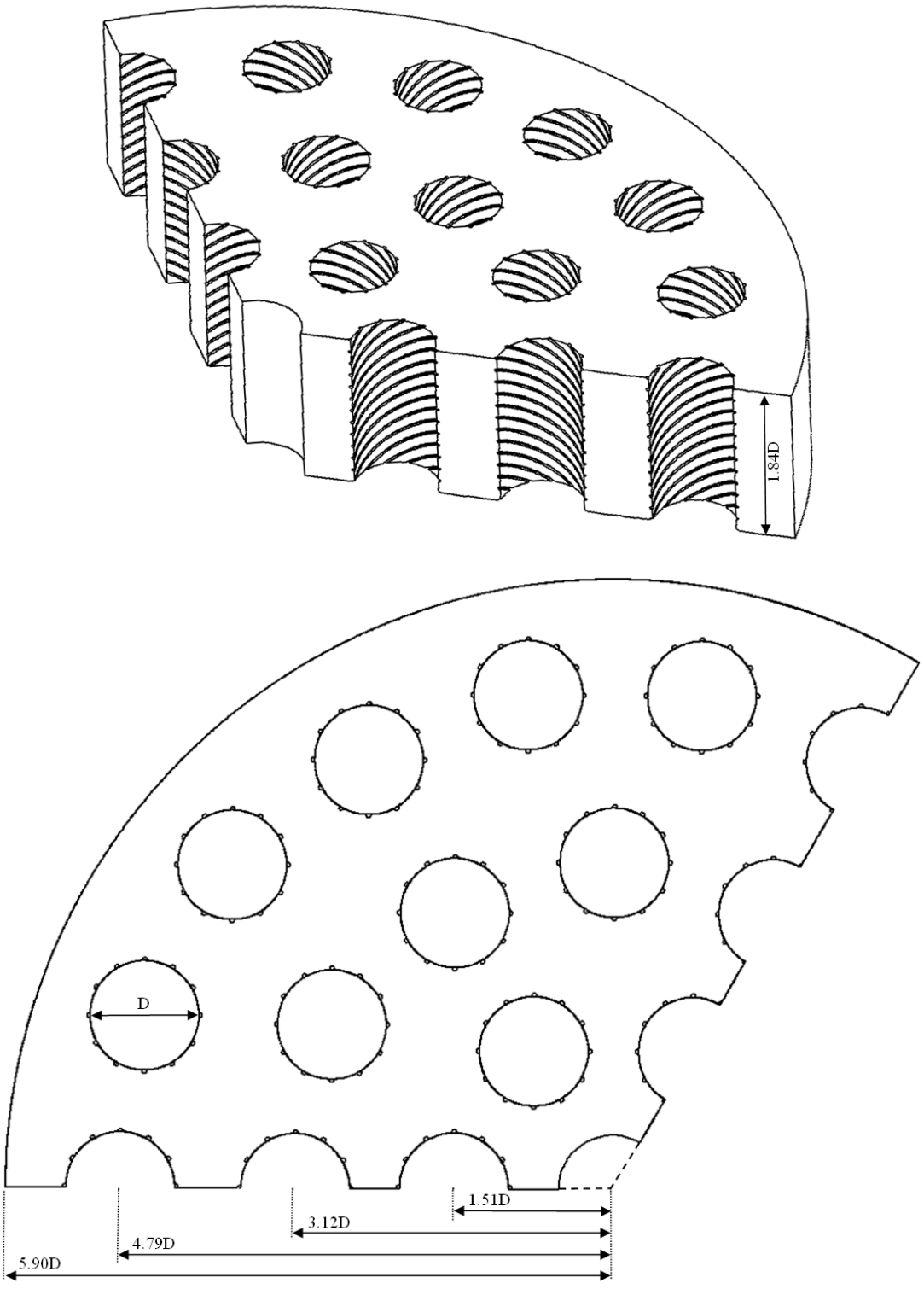

Figure C.1 – Dimensions of the present Multi-Start configuration.

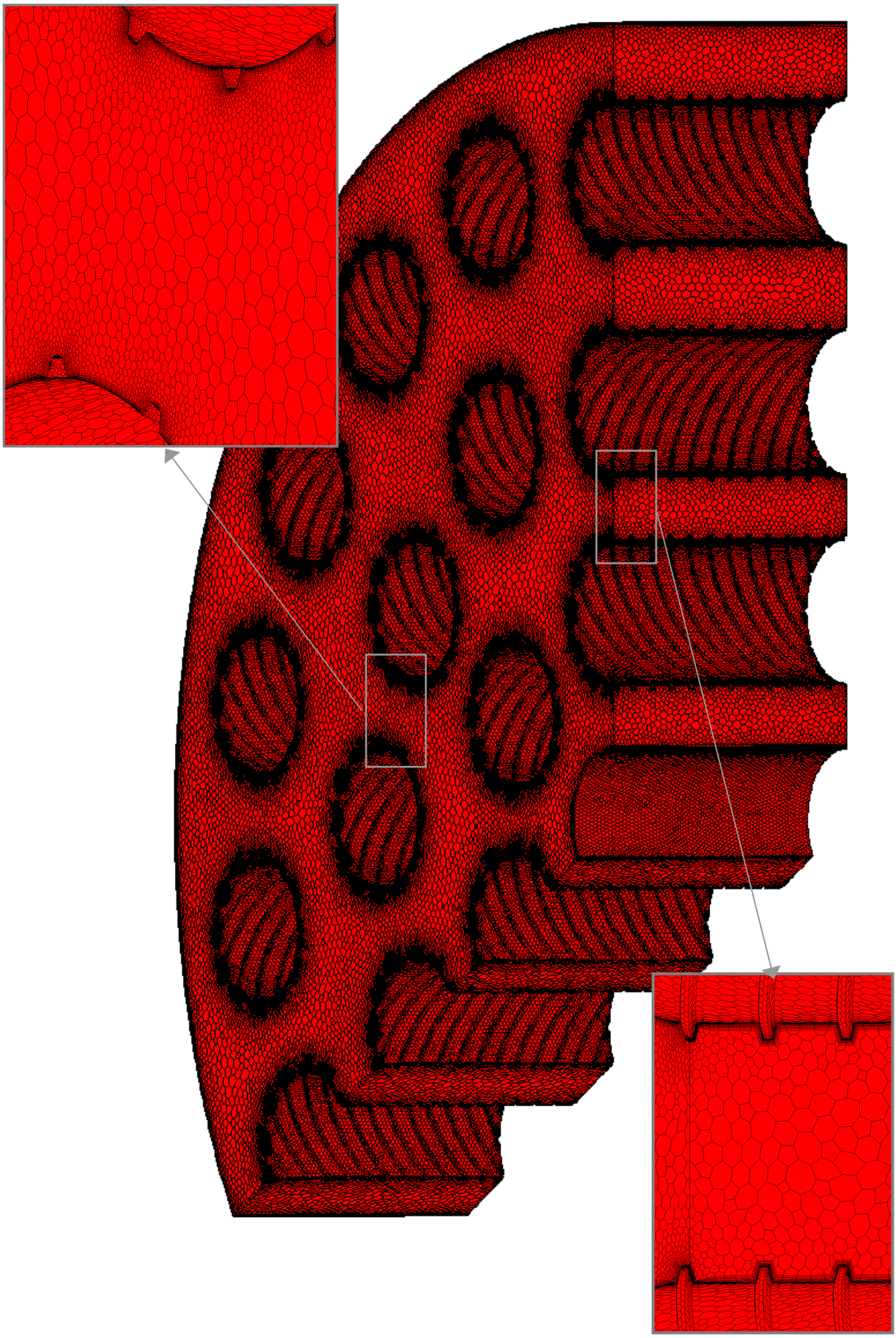

Figure C.2 – Schematic of the mesh representing a 120° sector of the Multi-Start design.